J. Astrophys. Astr. (1981) **2,** 1–27

General Relativistic Analysis of Structure and Stability of Charged Fluid Disks Around Compact Objects

A. R. Prasanna and D. K. Chakraborty* *Physical Research Laboratory, Navrangpura, Ahmedabad 380009*

Received 1980 April 1; accepted 1981 January 5

Abstract. In this paper we give a detailed general relativistic formulation of the study of structure and stability of charged fluid disks around com pact objects like black holes neglecting the self-gravitation of the disk itself. Having presented the general equations for equilibrium as well as for perturbations we solve explicitly the cases of rigidly and differentially rotating thin disks, with constant charge density and zero pressure, confined to the equatorial plane of the black hole. By using normal mode analysis we have analysed the stability of such disks under purely radial perturbations and find that the disks are generally stable.

Key words: general relativity— black holes— accretion disks— stability

1. Introduction

One of the most important topics of discussion in present day astrophysics is accretion disks around compact objects. Accretion disk models have been proposed in many cases of galactic as well as extragalactic high energy sources like X-ray sources, quasars, Seyfert galaxies and the like. Well known among such models are those of Rees (1978), Eardley *et al.* (1978), Shapiro, Lightman and Eardley (1976) and Bisnovatyi-Kogan and Blinnikov (1977). It is generally believed that electromagnetic emission from such sources is due to plasma processes in these disks. As it is very important to understand the structure and stability of such disks there have been a number of attempts to consider the dynamics of such accretion disks. The most recent of such investigations is due to Okuda (1980) who considers accretion disks around compact objects like neutron stars and black holes. Earlier attempts in this direction are due to Pringle and Rees (1972), Shakura and Sunyaev (1973), Novikov and Thorne (1973), Lightman (1974 a, b), Fishbone and Moncrief (1976), Abramowicz,

*On leave of absence from Government College, Jagadalpur 494005

Jaroszynski and Sikora (1977), Hoshi and Shibazaki (1977) and Shibazaki (1978). These disks have been considered in Newtonian and relativistic formulations by different authors. Almost all discussions restrict the disks to be such that the inner edge is beyond 6 m in the case of a Schwarzschild black hole, giving the reason that the last stable circular orbit for a particle in Schwarzschild spacetime is at 6 m.

Recently Prasanna and Varma (1977) have shown that even a very weak magnetic field associated with the Schwarzschild geometry results in a stable orbit for the charged particle very close to the event horizon $r \simeq 2.1\ m$. This made us consider the structure and stability of disks in a more detailed way in general relativistic formulation; for if the inner edge could get so close to the horizon then the general relativistic effects would be dominant. Further, another problem that we consider is to solve the entire system of fluid equations and Maxwell's equations self consistently on a curved background such that the disk is under the influence of the gravitational field of the black hole and the electromagnetic field produced by its own motion. The effect of the geometry in the electromagnetic field is taken through solving Maxwell's equations on the curved background so that the coupling between the fields is well taken care of. As far as we know such a formulation has not been made earlier and thus a detailed discussion even for simple cases would possibly provide guidelines for the treatment of more complicated problems.

The scenario we consider is as follows: We take a light thin disk whose mass is negligible in comparison to that of the Central compact object so that the Schwarzschild geometry produced by the compact object is unaffected. The disk made up of charged as well as neutral fluid is taken to be rotating and hence the motion of the charged particles produces an electromagnetic field. This electromagnetic field is also taken to be a test field. Thus it would not affect the geometry while it is modified by the background geometry. The dynamical equations that govern the system are the set of fluid equations and the Maxwell's equations which are to be solved together self consistently on the assumed background geometry. We do take such a system, solve for two simple cases of pressureless thin disk confined to the equatorial plane and then consider their stability under purely radial perturbation using normal mode analysis.

In Section 2 we first develop the complete set of dynamical equations for a general curved background as seen by the local Lorentz observer and later restrict them to the Schwarzschild background. In Section 3, we give the general linearised equations governing the perturbations. Section 4 presents steady state solutions for two particular cases of differential and rigid rotation with pressure zero. In Section 5 we take up the perturbation equations for the restricted case of radial perturbations and consider the stability analysis. In Section 6 we discuss the results and draw some conclusions.

2. Equations governing the disk

The general system that we consider in these studies consists of a thin disk, with either charged fluid or plasma, in the gravitational field surrounding a central mass such that the mass of the disk is negligible in comparison with the central mass. With this assumption the spacetime is governed only by the curvature produced by the central mass whereas the self gravitation, of the disk is negligible. The

disk is then supported entirely by the gravitational field of the central mass and the centrifugal and the electromagnetic field produced by the disk itself. The electromagnetic field produced by the motion of charged particles of the disk gets modified due to the background geometry. The equations of structure are given by the fluid equations and are expressed through the conservation laws

$$T^{j}_{i;j} = 0 \tag{2.1}$$

with

$$T^{j}_{i} = (\rho + p/c^2)\, u_i\, u^j - (p/c^2)\, \delta^{j}_{i} - \frac{1}{4\pi c^2}(F_{ik}\, F^{jk} - \tfrac{1}{4}\, \delta^{j}_{i}\, F_{kl}\, F^{kl}) \tag{2.2}$$

and the Maxwell's equations

$$F^{ij}{}_{;j} = -\frac{4\pi}{c}\, J^i, \tag{2.3}$$

$$F_{ij,k} + F_{ki,j} + F_{jk,i} = 0; \tag{2.4}$$

wherein

$$J^i = c\, \epsilon\, u^i + \sigma\, F^{ij}\, u_j. \tag{2.5}$$

In these equations ρ, p, u^i , ε and σ denote the matter density, the matter pressure, the fluid 4-velocity, the charge density and the conductivity respectively. As u^i satisfies the normalisation condition $u^i u_i = 1$ and as F_{ij} is antisymmetric the equation (2.1) may be resolved into the equation of continuity

$$\rho_{,j}\, u^j + (\rho + p/c^2)\, u^{j}_{;j} = \frac{\sigma}{c^3} F_{ij}\, F^{j}{}_{k}\, u^i\, u^k \tag{2.6}$$

and the momentum equation

$$(\rho + p/c^2)\, u^{i}_{;j}\, u^j = \frac{1}{c^2}(g^{ij} - u^i\, u^j)\, p_{,j} + \frac{\epsilon}{c^2} F^{i}{}_{j}\, u^j$$

$$+ \frac{\sigma}{c^3}(F^{i}{}_{j}\, F^{j}{}_{k}\, u^k - u^i\, F_{jl}\, F^{i}{}_{k}\, u^j\, u^k). \tag{2.7}$$

In order to compare with the corresponding Newtonian equations we introduce the 3-velocity V^α such that $u^\alpha = V^\alpha u^0/c$, wherein $u^0 = dx^0/ds$, x^0 being the time coordinate expressed in length units ($x^0 = ct$). Further we write the equations in terms of proper Lorentz frame components defined by the orthonormal tetrad $\lambda^{(i)}_{j}$ appropriate to the metric corresponding to the background geometry. The momentum equations (2.7) reduce to

$$(\rho + p/c^2)(u^0)^2 \left[\frac{\partial V^\alpha}{\partial t} + V^\beta \frac{\partial V^\alpha}{\partial x^\beta} + c^2 \left(\Gamma^\alpha_{00} - \frac{V^\alpha}{c}\Gamma^0_{00}\right) + 2c\, V^\beta \left(\Gamma^\alpha_{0\beta} - \frac{V^\alpha}{c}\Gamma^0_{0\beta}\right)\right.$$

$$\left. + V^\beta V^\gamma \left(\Gamma^\alpha_{\beta\gamma} - \frac{V^\alpha}{c}\Gamma^0_{\beta\gamma}\right)\right] = \left(g^{\alpha 0} - g^{00}\frac{V^\alpha}{c}\right)\frac{\partial p}{c\partial t} + \left(g^{\alpha\beta} - g^{0\beta}\frac{V^\alpha}{c}\right)\frac{\partial p}{\partial x_\beta}$$

$$+ \epsilon u^0 \left[F^\alpha_{\ 0} + \frac{1}{c}F^\alpha_{\ \beta} V^\beta - \frac{1}{c^2}F^0_{\ \beta} V^\alpha V^\beta\right] + \frac{u^0 \sigma}{c}\left[\left(F^\alpha_{\ i} - \frac{V^\alpha}{c}F^0_{\ i}\right)F^i_{\ 0}\right.$$

$$\left. + \frac{1}{c}\left(F^\alpha_{\ i} - \frac{V^\alpha}{c}F^0_{\ i}\right) F^i_{\ \beta} V^\beta\right], \tag{2.8}$$

while the continuity equation (2.6) reduces to

$$\left(\rho + \frac{p}{c^2}\right)\left[V^\alpha_{,\alpha} - \Gamma^0_{0\alpha} V^\alpha + c\,\Gamma^\alpha_{\ \alpha} + \Gamma^\beta_{\alpha\beta} V^\alpha - \Gamma^0_{\alpha\beta}\frac{V^\alpha V^\beta}{c}\right]$$

$$+ \left(\frac{\partial \rho}{\partial t} + V^\alpha \frac{\partial \rho}{\partial x^\alpha}\right) - \frac{1}{c^2}\left(\frac{\partial p}{\partial t} + V^\alpha \frac{\partial p}{\partial x^\alpha}\right) + \frac{1}{c}\frac{1}{(u^0)^2}\left(g^{00}\frac{\partial p}{c\partial t} + g^{0\alpha}\frac{\partial p}{\partial x^\alpha}\right)$$

$$+ \frac{1}{u^0 c^2}\left[\epsilon F^0_{\ \alpha} V^\alpha + \sigma\left\{F^0_{\ \alpha} F^\alpha_{\ 0} + \frac{1}{c}F^0_{\ \alpha} F^\alpha_{\ \beta} V^\beta\right\}\right] = 0 \tag{2.9}$$

with

$$\frac{V^\alpha}{c} = (\lambda^\alpha_{(\beta)} V^{(\beta)} + c\,\lambda^\alpha_{(0)}) / (\lambda^0_{(\beta)} V^{(\beta)} + c\,\lambda^0_{(0)}),$$

$$(u^0)^2 = (g_{00} + 2g_{0\alpha} V^\alpha/c + g_{\alpha\beta} V^\alpha V^\beta/c^2)^{-1},$$

$$F^i_{\ j} = \lambda^i_{\ (l)} \lambda^{(m)}_j F^{(l)}_{\ (m)}.$$

Here, and in what follows, we adopt the notation that the Latin indices take values from 0 to 3 whereas Greek indices range from 1 to 3. In the following, we consider the background geometry to be that given by the Schwarzschild spacetime representing the gravitational field of a non-rotating mass M. Hence,

$$ds^2 = \left(1 - \frac{2m}{r}\right)c^2 dt^2 - \left(1 - \frac{2m}{r}\right)^{-1} dr^2 - r^2 (d\theta^2 + \sin^2\theta\, d\phi^2), \tag{2.10}$$

wherein $m = MG/c^2$. The corresponding local (proper) Lorentz frame is defined by the tetrad,

$$\lambda_t^{(t)} = \left(1 - \frac{2m}{r}\right)^{1/2}, \ \lambda_r^{(r)} = \left(1 - \frac{2m}{r}\right)^{-1/2},$$

$$\lambda_\theta^{(\theta)} = r, \quad \lambda_\phi^{(\phi)} = r \sin\theta. \tag{2.11}$$

The components of velocity as well as of electromagnetic field are therefore given by

$$V^{(r)} = \left(1 - \frac{2m}{r}\right)^{-1} V^r, \quad V^{(\theta)} = r\left(1 - \frac{2m}{r}\right)^{-1/2} V^\theta, \quad V^{(\phi)} = r \sin\theta \left(1 - \frac{2m}{r}\right)^{-1/2} V^\phi,$$

$$F_{(r)(\theta)} = \frac{1}{r}\left(1 - \frac{2m}{r}\right)^{1/2} F_{r\theta}, \qquad F_{(r)(t)} = F_{rt},$$

$$F_{(r)(\phi)} = \frac{1}{r \sin\theta}\left(1 - \frac{2m}{r}\right)^{1/2} F_{r\phi}, \qquad F_{(\theta)(t)} = \frac{1}{r}\left(1 - \frac{2m}{r}\right)^{-1/2} F_{\theta t},$$

$$F_{(\theta)(\phi)} = \frac{1}{r^2 \sin\theta} F_{\theta\phi}, \qquad F_{(\phi)(t)} = \frac{1}{r \sin\theta}\left(1 - \frac{2m}{r}\right)^{-1/2} F_{\phi t}. \tag{2.12}$$

Presently we restrict ourselves to the case of non-conducting charged fluid ($\sigma = 0$, $\varepsilon \neq 0$). In addition to the momentum equations (2.8) and Maxwell's equations (2.4) and (2.5), we now have the conservation equation for both mass and charge expressed through

$$(\rho + p/c^2)\left(\frac{\partial}{\partial t} + V^\alpha \frac{\partial}{\partial x^\alpha}\right)(\epsilon) = \epsilon\left(\frac{\partial}{\partial t} + V^\alpha \frac{\partial}{\partial x^\alpha}\right)(\rho), \tag{2.13}$$

wherein we have explicitly used the charge continuity equation

$$\epsilon_{,i}\, u^i + \epsilon\, u^i_{;i} = 0. \tag{2.14}$$

Thus the complete system of equations that govern the dynamics of such a disk is given by:

(a) the momentum equations

$$\begin{aligned}(\rho + p/c^2)\left\{\frac{DV^{(r)}}{Dt} + \frac{mc^2}{r^2}\left(1 - \frac{V^{(r)2}}{c^2}\right) - \left(1 - \frac{2m}{r}\right)\left[\frac{V^{(\theta)^2} + V^{(\phi)^2}}{r}\right]\right\}&\\ = -(1 - V^2/c^2)\left[\left(1 - \frac{2m}{r}\right)\frac{\partial p}{\partial r} + \frac{V^{(r)}}{c^2}\frac{\partial p}{\partial t}\right] + \epsilon\left(1 - \frac{2m}{r}\right)^{1/2}(1 - V^2/c^2)^{1/2}&\\ \times\left[F^{(r)}{}_{(t)} + \frac{1}{c}\{F^{(r)}{}_{(\theta)} V^{(\theta)} + F^{(r)}{}_{(\phi)} V^{(\phi)}\}\right.&\\ \left. - \frac{V^{(r)}}{c^2}\{F^{(t)}{}_{(r)} V^{(r)} + F^{(t)}{}_{(\theta)} V^{(\theta)} + F^{(t)}{}_{(\phi)} V^{(\phi)}\}\right],\end{aligned} \tag{2.15}$$

$$(\rho + p/c^2)\left\{\frac{DV^{(\theta)}}{Dt} + \left(1 - \frac{3m}{r}\right)\frac{V^{(r)}\,V^{(\theta)}}{r} - \left(1 - \frac{2m}{r}\right)^{1/2}\frac{\cot\theta}{r}\,V^{(\phi)^2}\right\}$$

$$= -\left(1 - \frac{V^2}{c^2}\right)\left[\left(1 - \frac{2m}{r}\right)^{1/2}\frac{1}{r}\,\frac{\partial p}{\partial\theta} + \frac{V^{(\theta)}}{c^2}\,\frac{\partial p}{\partial t}\right] + \epsilon\left(1 - \frac{2m}{r}\right)^{1/2}(1 - V^2/c^2)^{1/2}$$

$$\times\left[F^{(\theta)}{}_{(t)} + \frac{1}{c}\{F^{(\theta)}{}_{(r)}\,V^{(r)} + F^{(\theta)}{}_{(\phi)}\,V^{(\phi)}\}\right.$$

$$\left. - \frac{V^{(\theta)}}{c^2}\{F^{(t)}{}_{(r)}\,V^{(r)} + F^{(t)}{}_{(\theta)}\,V^{(\theta)} + F^{(t)}{}_{(\phi)}\,V^{(\phi)}\}\right], \tag{2.16}$$

$$(\rho + p/c^2)\left\{\frac{DV^{(\phi)}}{Dt} + \left(1 - \frac{3m}{r}\right)\frac{V^{(r)}\,V^{(\phi)}}{r} + \left(1 - \frac{2m}{r}\right)^{1/2}\frac{\cot\theta}{r}\,V^{(\theta)}\,V^{(\phi)}\right\}$$

$$= -(1 - V^2/c^2)\left[\left(1 - \frac{2m}{r}\right)^{1/2}\frac{1}{r\sin\theta}\,\frac{\partial p}{\partial\phi} + \frac{V^{(\phi)}}{c^2}\,\frac{\partial p}{\partial t}\right]$$

$$+ \epsilon\left(1 - \frac{2m}{r}\right)^{1/2}(1 - V^2/c^2)^{1/2}\left[F^{(\phi)}{}_{(t)} + \frac{1}{c}\{F^{(\phi)}{}_{(r)}\,V^{(r)} + F^{(\phi)}{}_{(\theta)}\,V^{(\theta)}\}\right.$$

$$\left. - \frac{V^{(\phi)}}{c^2}\{F^{(t)}{}_{(r)}\,V^{(r)} + F^{(t)}{}_{(\theta)}\,V^{(\theta)} + F^{(t)}{}_{(\phi)}\,V^{(\phi)}\}\right]; \tag{2.17}$$

(b) the continuity equation

$$(\rho + p/c^2)\,\frac{D\epsilon}{Dt} = \epsilon\,\frac{D\rho}{Dt}\;; \tag{2.18}$$

(c) Maxwell's equations

$$\frac{1}{c}\frac{\partial}{\partial t}\left[r\left(1 - \frac{2m}{r}\right)^{-1/2}F_{(r)(\theta)}\right] + \frac{\partial}{\partial r}\left[r\left(1 - \frac{2m}{r}\right)^{1/2}F_{(\theta)(t)}\right] + \frac{\partial}{\partial\theta}\left[F_{(t)\,(r)}\right] = 0, \tag{2.19}$$

$$\frac{1}{c}\frac{\partial}{\partial t}\left[r\sin\theta\left(1 - \frac{2m}{r}\right)^{-1/2}F_{(r)(\phi)}\right] + \frac{\partial}{\partial r}\left[r\sin\theta\left(1 - \frac{2m}{r}\right)^{1/2}F_{(\phi)(t)}\right]$$

$$+ \frac{\partial}{\partial\phi}\left[F_{(t)\,(r)}\right] = 0, \tag{2.20}$$

$$\frac{1}{c}\frac{\partial}{\partial t}\left[r^2\sin\theta\,F_{(\theta)(\phi)}\right] + \frac{\partial}{\partial\theta}\left[r\sin\theta\left(1 - \frac{2m}{r}\right)^{1/2}F_{(\phi)(t)}\right]$$

$$+ \frac{\partial}{\partial\phi}\left[r\left(1 - \frac{2m}{r}\right)^{1/2}F_{(t)(\theta)}\right] = 0, \tag{2.21}$$

$$\frac{\partial}{\partial r}[r^2 \sin\theta\, F_{(\theta)(\phi)}] + \frac{\partial}{\partial\theta}\left[r\sin\theta\left(1-\frac{2m}{r}\right)^{-1/2} F_{(\phi)(r)}\right]$$

$$+\frac{\partial}{\partial\phi}\left[r\left(1-\frac{2m}{r}\right)^{1/2} F_{(r)(\theta)}\right] = 0, \tag{2.22}$$

$$\frac{1}{c}\frac{\partial}{\partial t}[F_{(r)(t)}] - \frac{1}{\sin\theta}\frac{\partial}{\partial\theta}\left[\frac{\sin\theta}{r}\left(1-\frac{2m}{r}\right)^{1/2} F_{(r)(\theta)}\right]$$

$$-\frac{\partial}{\partial\phi}\left[\frac{1}{r\sin\theta}\left(1-\frac{2m}{r}\right)^{1/2} F_{(r)(\phi)}\right] = \frac{4\pi\epsilon}{c}\left(1-\frac{2m}{r}\right)^{1/2}\left(1-\frac{V^2}{c^2}\right)^{-1/2} V^{(r)}, \tag{2.23}$$

$$\frac{1}{c}\frac{\partial}{\partial t}F_{(\theta)(t)} - \frac{1}{r}\left(1-\frac{2m}{r}\right)^{1/2}\frac{\partial}{\partial r}\left[r\left(1-\frac{2m}{r}\right)^{1/2} F_{(\theta)(r)}\right]$$

$$-\frac{\partial}{\partial\phi}\left[\frac{1}{r\sin\theta}\left(1-\frac{2m}{r}\right)^{1/2} F_{(\theta)(\phi)}\right] = \frac{4\pi\epsilon}{c}\left(1-\frac{2m}{r}\right)^{1/2}\left(1-\frac{V^2}{c^2}\right)^{-1/2} V^{(\theta)}, \tag{2.24}$$

$$\frac{1}{c}\frac{\partial}{\partial t}F_{(\phi)(t)} - \frac{1}{r}\left(1-\frac{2m}{r}\right)^{1/2}\frac{\partial}{\partial r}\left[r\left(1-\frac{2m}{r}\right)^{1/2} F_{(\phi)(r)}\right]$$

$$-\frac{\partial}{\partial\theta}\left[\frac{1}{r}\left(1-\frac{2m}{r}\right)^{1/2} F_{(\phi)(\theta)}\right] = \frac{4\pi\epsilon}{c}\left(1-\frac{2m}{r}\right)^{1/2}\left(1-\frac{V^2}{c^2}\right)^{-1/2} V^{(\phi)}, \tag{2.25}$$

$$\frac{1}{r}\frac{\partial}{\partial r}[r^2 F_{(t)(r)}] + \frac{1}{\sin\theta}\frac{\partial}{\partial\theta}\left[\sin\theta\left(1-\frac{2m}{r}\right)^{-1/2} F_{(t)(\theta)}\right]$$

$$+\frac{\partial}{\partial\phi}\left[\frac{1}{\sin\theta}\left(1-\frac{2m}{r}\right)^{-1/2} F_{(t)(\phi)}\right] = 4\pi\epsilon r\left(1-\frac{2m}{r}\right)^{-1/2}\left(1-\frac{V^2}{c^2}\right)^{-1/2}, \tag{2.26}$$

Wherein

$$\frac{D}{Dt} = \frac{\partial}{\partial t} + \left(1-\frac{2m}{r}\right)^{1/2}\left\{\left(1-\frac{2m}{r}\right)^{1/2} V^{(r)}\frac{\partial}{\partial r} + \frac{V^{(\theta)}}{r}\frac{\partial}{\partial\theta} + \frac{V^{(\phi)}}{r\sin\theta}\frac{\partial}{\partial\phi}\right\} \tag{2.27}$$

and

$$V^2 = V^{(r)2} + V^{(\theta)2} + V^{(\phi)2}. \tag{2.28}$$

3. Equations governing the perturbation

In general one can consider perturbations in the respective physical quantities as given by

$$p = p_0 + \delta p, \qquad \rho = \rho_0 + \delta\rho, \qquad \epsilon = \epsilon_0 + \delta\epsilon,$$

$$V^{(a)} = V_0^{(a)} + \delta V^{(a)}, \quad F_{(i)(j)} = F_{0(i)(j)} + \delta F_{(i)(j)},$$

wherein subscript ' 0 ' refers to the steady state parameters. Introducing these expressions in the general equations (2.15) to (2·26) and keeping only the linear terms in perturbations we get the linearised set of equations governing the perturbations:

$$\left(\rho_0+\frac{p_0}{c^2}\right)\left[\frac{\partial}{\partial t}\,\delta V^{(r)}+\left(1-\frac{2m}{r}\right)^{1/2}\left\{\left(1-\frac{2m}{r}\right)^{1/2}\left(V_0^{(r)}\,\frac{\partial}{\partial r}\,\delta V^{(r)}+\delta V^{(r)}\,\frac{\partial V_0^{(r)}}{\partial r}\right)\right.\right.$$
$$+\frac{1}{r}\left(V_0^{(\theta)}\,\frac{\partial}{\partial\theta}\,\delta V^{(r)}+\delta V^{(\theta)}\,\frac{\partial V_0^{(r)}}{\partial\theta}\right)+\frac{1}{r\sin\theta}\left(V_0^{(\phi)}\,\frac{\partial}{\partial\phi}\,\delta V^{(r)}+\delta V^{(\phi)}\,\frac{\partial V_0^{(r)}}{\partial\phi}\right)\Bigg\}$$
$$\left.-\frac{2}{r}\left(1-\frac{2m}{r}\right)\left(V_0^{(\theta)}\,\delta V^{(\theta)}+V_0^{(\phi)}\,\delta V^{(\phi)}\right)-\frac{2m}{r^2}\,V_0^{(r)}\,\delta V^{(r)}\right]$$
$$+\,(\delta\rho+\delta p/c^2)\left[\left(1-\frac{2m}{r}\right)^{1/2}\left\{\left(1-\frac{2m}{r}\right)^{1/2}V_0^{(r)}\,\frac{\partial}{\partial r}\,V_0^{(r)}+\frac{V_0^{(\theta)}}{r}\,\frac{\partial}{\partial\theta}\,V_0^{(r)}\right.\right.$$
$$\left.\left.+\frac{1}{r\sin\theta}\,V_0^{(\phi)}\,\frac{\partial}{\partial\phi}\,V_0^{(r)}\right\}-\frac{1}{r}\left(1-\frac{2m}{r}\right)\left(V_0^{(\theta)^2}+V_0^{(\phi)^2}\right)+\frac{mc^2}{r^2}\left(1-\frac{V_0^{(r)^2}}{c^2}\right)\right]$$
$$=-\left(1-\frac{2m}{r}\right)\left[\left(1-\frac{V_0^2}{c^2}\right)\left\{\frac{\partial}{\partial r}\,\delta p+\left(1-\frac{2m}{r}\right)^{-1}\frac{V_0^{(r)}}{c^2}\,\frac{\partial}{\partial t}\,\delta p\right\}-\frac{2\,V_0\,\delta V}{c^2}\,\frac{\partial p_0}{\partial r}\right]$$
$$-\left(1-\frac{2m}{r}\right)^{1/2}\left[F_{0(r)(t)}+\frac{1}{c}\left(F_{0(r)(\theta)}\,V_0^{(\theta)}+F_{0(r)(\phi)}\,V_0^{(\phi)}\right)\right.$$
$$\left.+\frac{V_0^{(r)}}{c^2}\left(F_{0(t)(r)}\,V_0^{(r)}+F_{0(t)(\theta)}\,V_0^{(\theta)}+F_{0(t)(\phi)}\,V_0^{(\phi)}\right)\right]$$
$$\times\left[\left\{\left(1-\frac{V_0^2+2V_0\,\delta V}{c^2}\right)^{1/2}-\left(1-\frac{V_0^2}{c^2}\right)^{1/2}\right\}\epsilon_0+\delta\epsilon\left(1-\frac{V_0^2}{c^2}\right)^{1/2}\right]$$
$$-\epsilon_0\left(1-\frac{2m}{r}\right)^{1/2}\left(1-\frac{V_0^2}{c^2}\right)^{1/2}\left[\delta F_{(r)(t)}+\frac{1}{c}\left\{\delta F_{(t)(\theta)}\,V_0^{(\theta)}+F_{0(t)(\theta)}\,\delta V^{(\theta)}\right.\right.$$
$$+\delta F_{(r)(\phi)}\,V_0^{(\phi)}+F_{0(r)(\phi)}\,\delta V^{(\phi)}\Big\}+\frac{V_0^{(r)}}{c^2}\left\{\delta F_{(t)(r)}\,V_0^{(r)}+F_{0(t)(r)}\,\delta V^{(r)}\right.$$
$$\left.\left.+\delta F_{(t)(\theta)}\,V_0^{(\theta)}+F_{0(t)(\theta)}\,\delta V^{(\theta)}+\delta F_{(t)(\phi)}\,V_0^{(\phi)}+F_{0(t)(\phi)}\,\delta V^{(\phi)}\right\}$$
$$\left.+\frac{\delta V^{(r)}}{c^2}\left\{F_{0(t)(r)}\,V_0^{(r)}+F_{0(t)(\theta)}\,V_0^{(\theta)}+F_{0(t)(\phi)}\,V_0^{(\phi)}\right\}\right], \tag{3.1}$$

$$\left(\rho_0+\frac{p_0}{c^2}\right)\left[\frac{\partial}{\partial t}\,\delta V^{(\theta)}+\left(1-\frac{2m}{r}\right)^{1/2}\left\{\left(1-\frac{2m}{r}\right)^{1/2}\left(V_0^{(r)}\,\frac{\partial}{\partial r}\,\delta V^{(\theta)}+\delta V^{(r)}\,\frac{\partial}{\partial r}\,V_0^{(\theta)}\right)\right.\right.$$
$$+\frac{1}{r}\left(V_0^{(\theta)}\,\frac{\partial}{\partial\theta}\,\delta V^{(\theta)}+\delta V^{(\theta)}\,\frac{\partial}{\partial\theta}\,V_0^{(\theta)}\right)+\frac{1}{r\sin\theta}\left(V_0^{(\phi)}\,\frac{\partial}{\partial\phi}\,\delta V^{(\theta)}+\delta V^{(\theta)}\,\frac{\partial}{\partial\phi}\,V_0^{(\phi)}\right)\Bigg\}$$

$$
\begin{aligned}
&-\frac{2}{r}\left(1-\frac{2m}{r}\right)^{1/2}\cot\theta\, V_0^{(\phi)}\,\delta V^{(\phi)}+\left(1-\frac{3m}{r}\right)\frac{1}{r}\left(V_0^{(r)}\,\delta V^{(\theta)}+\delta V^{(r)}\,V_0^{(\theta)}\right)\Big]\\
&+\left(\delta\rho+\frac{\delta p}{c^2}\right)\Big[\left(1-\frac{2m}{r}\right)^{1/2}\left\{\left(1-\frac{2m}{r}\right)^{1/2}V_0^{(r)}\frac{\partial}{\partial r}V_0^{(\theta)}+\frac{V_0^{(\theta)}}{r}\frac{\partial}{\partial\theta}V_0^{(\theta)}\right.\\
&\left.+\frac{1}{r\sin\theta}V_0^{(\phi)}\frac{\partial}{\partial\phi}V_0^{(\theta)}\right\}-\frac{V_0^{(\phi)^2}}{r}\left(1-\frac{2m}{r}\right)^{1/2}\cot\theta+\left(1-\frac{3m}{r}\right)\frac{V_0^{(r)}\,V_0^{(\theta)}}{r}\Big]\\
&=-\left(1-\frac{V_0^2}{c^2}\right)\left\{\left(1-\frac{2m}{r}\right)^{1/2}\frac{1}{r}\frac{\partial}{\partial\theta}\delta p+\frac{V_0^{(\theta)}}{c^2}\frac{\partial}{\partial t}\delta p\right\}+\frac{2\,V_0\,\delta V}{r\,c^2}\left(\frac{\partial}{\partial\theta}p_0\right)\left(1-\frac{2m}{r}\right)^{1/2}\\
&\quad-\left(1-\frac{2m}{r}\right)^{1/2}\Big[F_{0(\theta)(t)}+\frac{1}{c}\left\{F_{0(\theta)(r)}\,V_0^{(r)}+F_{0(\theta)(\phi)}\,V_0^{(\phi)}\right\}\\
&\quad+\frac{V_0^{(\theta)}}{c^2}\left\{F_{0(t)(r)}\,V_0^{(r)}+F_{0(t)(\theta)}\,V_0^{(\theta)}+F_{0(t)(\phi)}\,V_0^{(\phi)}\right\}\Big]\\
&\quad\times\Big[\left\{\left(1-\frac{V_0^2+2\,V_0\,\delta V}{c^2}\right)^{1/2}-\left(1-\frac{V_0^2}{c^2}\right)^{1/2}\right\}\epsilon_0+\delta\epsilon\left(1-\frac{V_0^2}{c^2}\right)^{1/2}\Big]\\
&\quad-\epsilon_0\left(1-\frac{2m}{r}\right)^{1/2}\left(1-\frac{V_0^2}{c^2}\right)^{1/2}\Big[\delta F_{(\theta)(t)}+\frac{1}{c}\left\{\delta F_{(\theta)(r)}\,V_0^{(r)}+F_{0(\theta)(r)}\,\delta V^{(r)}\right.\\
&\quad\left.+\delta F_{(\theta)(\phi)}\,V_0^{(\phi)}+F_{0(\theta)(\phi)}\,\delta V^{(\phi)}\right\}+\frac{V_0^{(\theta)}}{c^2}\left\{\delta F_{(t)(r)}\,V_0^{(r)}+F_{0(t)(r)}\,\delta V^{(r)}\right.\\
&\quad\left.+\delta F_{(t)(\theta)}\,V_0^{(\theta)}+F_{0(t)(\theta)}\,\delta V^{(\theta)}+\delta F_{(t)(\phi)}\,V_0^{(\phi)}+F_{0(t)(\phi)}\,\delta V^{(\phi)}\right\}\\
&\quad+\frac{\delta V^{(\theta)}}{c^2}\left\{F_{0(t)(r)}\,V_0^{(r)}+F_{0(t)(\theta)}\,V_0^{(\theta)}+F_{0(t)(\phi)}\,V_0^{(\phi)}\right\}\Big],
\end{aligned}
\tag{3.2}
$$

$$
\begin{aligned}
&\left(\rho_0+\frac{p_0}{c^2}\right)\Big[\frac{\partial}{\partial t}\delta V^{(\phi)}+\left(1-\frac{2m}{r}\right)^{1/2}\left\{\left(1-\frac{2m}{r}\right)^{1/2}\left(V_0^{(r)}\frac{\partial}{\partial r}\delta V^{(\phi)}+\delta V^{(r)}\frac{\partial}{\partial r}V_0^{(\phi)}\right)\right.\\
&+\frac{1}{r}\left(V_0^{(\theta)}\frac{\partial}{\partial\theta}\delta V^{(\phi)}+\delta V^{(\theta)}\frac{\partial}{\partial\theta}V_0^{(\phi)}\right)+\frac{1}{r\sin\theta}\left(V_0^{(\phi)}\frac{\partial}{\partial\phi}\delta V^{(\phi)}+\delta V^{(\phi)}\frac{\partial}{\partial\phi}V_0^{(\phi)}\right)\\
&+\frac{1}{r}\left(1-\frac{2m}{r}\right)^{1/2}\cot\theta\,(V_0^{(\theta)}\delta V^{(\phi)}+\delta V^{(\theta)}\,V_0^{(\phi)})+\left(1-\frac{3m}{r}\right)\frac{1}{r}\left(V_0^{(r)}\delta V^{(\phi)}\right.\\
&\left.\left.+\delta V^{(r)}V_0^{(\phi)}\right)\right\}\Big]+\left(\delta\rho+\frac{\delta p}{c^2}\right)\Big[\left(1-\frac{2m}{r}\right)^{1/2}\left\{\left(1-\frac{2m}{r}\right)^{1/2}V_0^{(r)}\frac{\partial}{\partial r}V_0^{(\phi)}+\frac{V_0^{(\theta)}}{r}\frac{\partial}{\partial\theta}V_0^{(\phi)}\right.
\end{aligned}
$$

$$+\frac{V_0^{(\phi)}}{r\sin\theta}\frac{\partial}{\partial\phi}V_0^{(\phi)}\Big\}+\frac{V_0^{(\theta)}V_0^{(\phi)}}{r}\left(1-\frac{2m}{r}\right)^{1/2}\cot\theta+\left(1-\frac{3m}{r}\right)\frac{V_0^{(r)}V_0^{(\phi)}}{r}\Big]$$

$$=-\left(1-\frac{V_0^2}{c^2}\right)\Big\{\frac{1}{r\sin\theta}\left(1-\frac{2m}{r}\right)^{1/2}\frac{\partial}{\partial\phi}\delta p+\frac{V_0^{(\phi)}}{c^2}\frac{\partial}{\partial t}\delta p\Big\}+\frac{2V_0\delta V}{c^2}\frac{1}{r\sin\theta}\left(1-\frac{2m}{r}\right)^{1/2}\frac{\partial p_0}{\partial\phi}$$

$$-\left(1-\frac{2m}{r}\right)^{1/2}\Big[F_{0(\phi)(t)}+\frac{1}{c}\Big\{F_{0(\phi)(r)}V_0^{(r)}+F_{0(\phi)(\theta)}V_0^{(\theta)}\Big\}$$

$$+\frac{V_0^{(\phi)}}{c^2}\Big\{F_{0(t)(r)}V_0^{(r)}+F_{0(t)(\theta)}V_0^{(\theta)}+F_{0(t)(\phi)}V_0^{(\phi)}\Big\}\Big]$$

$$\times\Big[\Big\{\left(1-\frac{V_0^2+2V_0\delta V}{c^2}\right)^{1/2}-\left(1-\frac{V_0^2}{c^2}\right)^{1/2}\Big\}\epsilon_0+\delta\epsilon\left(1-\frac{V_0^2}{c^2}\right)^{1/2}\Big]$$

$$-\epsilon_0\left(1-\frac{2m}{r}\right)^{1/2}\left(1-\frac{V_0^2}{c^2}\right)^{1/2}\Big[\delta F_{(\phi)\,(t)}+\frac{1}{c}\Big\{\delta F_{(\phi)\,(r)}V_0^{(r)}+F_{0\,(\phi)\,(r)}\delta V^{(r)}$$

$$+\delta F_{(\phi)\,(\theta)}V_0^{(\theta)}+F_{0(\phi)(\theta)}\delta V^{(\theta)}\Big\}+\frac{V_0^{(\phi)}}{c^2}\Big\{\delta F_{(t)\,(r)}V_0^{(r)}+F_{0(t)(r)}\delta V^{(r)}$$

$$+\delta F_{(t)\,(\theta)}V_0^{(\theta)}+F_{0(t)(\theta)}\delta V^{(\theta)}+\delta F_{(t)\,(\phi)}V_0^{(\phi)}+F_{0(t)(\phi)}\delta V^{(\phi)}\Big\}$$

$$+\frac{\delta V^{(\phi)}}{c^2}\Big\{F_{0(t)(r)}V_0^{(r)}+F_{0(t)(\theta)}V_0^{(\theta)}+F_{0(t)(\phi)}V_0^{(\phi)}\Big\}\Big], \tag{3.3}$$

$$\left(\rho_0+\frac{p_0}{c^2}\right)\Big[\frac{\partial}{\partial t}\delta\epsilon+\left(1-\frac{2m}{r}\right)^{1/2}\Big\{\Big(1-\frac{2m}{r}\Big)^{1/2}\Big(V_0^{(r)}\frac{\partial}{\partial r}\delta\epsilon+\delta V^{(r)}\frac{\partial}{\partial r}\epsilon_0\Big)$$

$$+\frac{1}{r}\Big(V_0^{(\theta)}\frac{\partial}{\partial\theta}\delta\epsilon+\delta V^{(\theta)}\frac{\partial}{\partial\theta}\epsilon_0\Big)+\frac{1}{r\sin\theta}\Big(V_0^{(\phi)}\frac{\partial}{\partial\phi}\delta\epsilon+\delta V^{(\phi)}\frac{\partial\epsilon_0}{\partial\phi}\Big)\Big\}\Big]$$

$$+\left(\delta\rho+\frac{\delta p}{c^2}\right)\Big[\Big(1-\frac{2m}{r}\Big)^{1/2}\Big\{\Big(1-\frac{2m}{r}\Big)^{1/2}V_0^{(r)}\frac{\partial\epsilon_0}{\partial r}+\frac{V_0^{(\theta)}}{r}\frac{\partial\epsilon_0}{\partial\theta}+\frac{V_0^{(\phi)}}{r\sin\theta}\frac{\partial\epsilon_0}{\partial\phi}\Big\}\Big]$$

$$=\epsilon_0\Big[\frac{\partial}{\partial t}\delta\rho+\Big(1-\frac{2m}{r}\Big)^{1/2}\Big\{\Big(1-\frac{2m}{r}\Big)^{1/2}\Big(V_0^{(r)}\frac{\partial}{\partial r}\delta\epsilon+\delta V^{(r)}\frac{\partial}{\partial r}\rho_0\Big)$$

$$+\frac{1}{r}\Big(V_0^{(\theta)}\frac{\partial}{\partial\theta}\delta\rho+\delta V^{(\theta)}\frac{\partial}{\partial\theta}\rho_0\Big)+\frac{1}{r\sin\theta}\Big(V_0^{(\phi)}\frac{\partial}{\partial\phi}\delta\rho+\delta V^{(\phi)}\frac{\partial}{\partial\phi}\rho_0\Big)\Big\}\Big]$$

$$+\delta\epsilon\Big[\Big(1-\frac{2m}{r}\Big)^{1/2}\Big\{\Big(1-\frac{2m}{r}\Big)^{1/2}V_0^{(r)}\frac{\partial}{\partial r}\rho_0+\frac{V_0^{(\theta)}}{r}\frac{\partial\rho_0}{\partial\theta}+\frac{V_0^{(\phi)}}{r\sin\theta}\frac{\partial\rho_0}{\partial\phi}\Big\}\Big], \tag{3.4}$$

$$\frac{1}{c}\frac{\partial}{\partial t}\left[\, r\,\left(1-\frac{2m}{r}\right)^{-1/2}\delta F_{(r)(\theta)}\,\right]+\frac{\partial}{\partial r}\left[\, r\,\left(1-\frac{2m}{r}\right)^{1/2}\delta F_{(\theta)(t)}\,\right]$$

$$+\frac{\partial}{\partial\theta}\,[\delta F_{(t)(r)}]=0, \tag{3.5}$$

$$\frac{1}{c}\frac{\partial}{\partial t}\left[\, r\sin\theta\left(\,1-\,\frac{2m}{r}\right)^{-1/2}\delta F_{(r)(\phi)}\,\right]+\frac{\partial}{\partial r}\left[\, r\sin\,\theta\,\left(1-\frac{2m}{r}\right)^{1/2}\delta F_{(\phi)(t)}\,\right]$$

$$+\frac{\partial}{\partial\phi}\,[\delta F_{(t)(r)}]=0. \tag{3.6}$$

$$\frac{1}{c\partial t}\,[r^2\sin\theta\,\delta F_{(\theta)(\phi)}]+\frac{\partial}{\partial\theta}\left[\, r\sin\,\theta\,\left(1-\frac{2m}{r}\right)^{1/2}\delta F_{(\phi)\,(t)}\,\right]$$

$$+\frac{\partial}{\partial\phi}\left[\, r\left(\,1-\frac{2m}{r}\right)^{1/2}\delta F_{(t)(\theta)}\,\right]=0, \tag{3.7}$$

$$\frac{\partial}{\partial r}[r^2\sin\,\theta\,\delta F_{(\theta)(\phi)}]+\frac{\partial}{\partial\theta}\left[r\sin\,\theta\left(\,1-\frac{2m}{r}\right)^{-1/2}\delta F_{(\phi)(r)}\right]$$

$$+\frac{\partial}{\partial\phi}\left[\, r\,\left(1-\frac{2m}{r}\right)^{-1/2}\delta F_{(r)(\theta)}\,\right]=0, \tag{3.8}$$

$$\frac{1}{c}\frac{\partial}{\partial t}\delta F_{(r)\,(t)}-\frac{1}{\sin\theta}\frac{\partial}{\partial\theta}\left[\frac{\sin\,\theta}{r}\left(1-\frac{2m}{r}\right)^{1/2}\delta F_{(r)(\theta)}\,\right]$$

$$-\frac{\partial}{\partial\phi}\left[\frac{1}{r\sin\,\theta}\left(1-\frac{2m}{r}\right)^{1/2}\delta F_{(r)(\phi)}\,\right]$$

$$=\frac{4\pi}{c}\left(1-\frac{2m}{r}\right)^{1/2}\left\{\epsilon_0\,V_0^{(r)}\left[\left(1-\frac{V_0^2+2V_0\,\delta V}{c^2}\right)^{-1/2}-\left(1-\frac{V_0^2}{c^2}\right)^{-1/2}\right]\right.$$

$$\left.+\left(1-\frac{V_0^2}{c^2}\right)^{-1/2}\left(\epsilon_0\,\delta V^{(r)}+\delta\epsilon\;V_0^{(r)}\right)\right\}, \tag{3.9}$$

$$\frac{1}{c}\frac{\partial}{\partial t}\,\delta F_{(\theta)\,(t)}-\frac{1}{r}\left(1-\frac{2m}{r}\right)^{1/2}\frac{\partial}{\partial r}\left[r\left(1-\frac{2m}{r}\right)^{1/2}\delta F_{(\theta)\,(r)}\,\right]$$

$$-\frac{\partial}{\partial\phi}\left[\frac{1}{r\sin\,\theta}\left(1-\frac{2m}{r}\right)^{1/2}\,\delta F_{(\theta)\,(\phi)}\right]=\frac{4\pi}{c}\left(1-\frac{2m}{r}\right)^{1/2}$$

$$\times\left\{\epsilon_0\,V_0^{(\theta)}\left[\left(1-\frac{V_0^2+2V_0\,\delta V}{c^2}\right)^{-1/2}-\left(1-\frac{V_0^2}{c^2}\right)^{-1/2}\right]\right.$$

$$\left.+\left(1-\frac{V_0^2}{c^2}\right)^{-1/2}\left(\epsilon_0\,\delta V^{(\theta)}+\delta\epsilon\;V_0^{(\theta)}\right)\right\}, \tag{3.10}$$

$$\frac{1}{c}\frac{\partial}{\partial t}\delta F_{(\phi)\,(t)} - \frac{1}{r}\left(1-\frac{2m}{r}\right)^{1/2}\frac{\partial}{\partial r}\left[r\left(1-\frac{2m}{r}\right)^{1/2}\delta F_{(\phi)\,(r)}\right]$$

$$-\frac{\partial}{\partial\theta}\left[\frac{1}{r}\left(1-\frac{2m}{r}\right)^{1/2}\delta F_{(\phi)(\theta)}\right]$$

$$=\frac{4\pi}{c}\left(1-\frac{2m}{r}\right)^{1/2}\left\{\epsilon_0\, V_0^{(\phi)}\left[\left(1-\frac{V_0^2+2V_0\delta V}{c^2}\right)^{-1/2}-\left(1-\frac{V_0^2}{c^2}\right)^{-1/2}\right]\right.$$

$$\left.+\left(1-\frac{V_0^2}{c^2}\right)^{-1/2}\left(\epsilon_0\,\delta V^{(\phi)}+\delta\epsilon\; V_0^{(\phi)}\right)\right\}, \tag{3.11}$$

$$\frac{1}{r}\frac{\partial}{\partial r}\left[r^2\,\delta F_{(t)\,(r)}\right]+\frac{1}{\sin\theta}\frac{\partial}{\partial\theta}\left[\sin\,\theta\left(1-\frac{2m}{r}\right)^{-1/2}\delta F_{(t)\,(\theta)}\right]$$

$$+\frac{\partial}{\partial\phi}\left[\frac{1}{\sin\theta}\left(1-\frac{2m}{r}\right)^{-1/2}\delta F_{(t)\,(\phi)}\right]$$

$$=4\pi r\left(1-\frac{2m}{r}\right)^{-1/2}\left\{\epsilon_0\left[\left(1-\frac{V_0^2+2V_0\,\delta V}{c^2}\right)^{-1/2}-\left(1-\frac{V_0^2}{c^2}\right)^{-1/2}\right]\right.$$

$$\left.+\delta\epsilon\,(1-V_0^2/c^2)^{-1/2}\right\} \tag{3.12}$$

With

$$V_0\,\delta V = V_0^{(r)}\,\delta V^{(r)} + V_0^{(\theta)}\,\delta V^{(\theta)} + V_0^{(\phi)}\,\delta V^{(\phi)}. \tag{3.13}$$

4. Steady state solutions

The general set of equations governing the system in equilibrium under the gravitational, centrifugal and electromagnetic forces are equations (2.15) to (2.26). We now restrict ourselves to the case of an axisymmetric disk implying thereby that all physical parameters are independent of azimuthal coordinate ϕ and further that $V_0^{(r)} = 0$, $V_0^{(\theta)} = 0$. The equations governing the steady state motion then reduce to

$$\left(\rho_0+\frac{p_0}{c^2}\right)\left\{\frac{mc^2}{r^2}-\left(1-\frac{2m}{r}\right)\frac{V_0^{(\phi)^2}}{r}\right\}=-\left(1-\frac{V_0^{(\phi)^2}}{c^2}\right)\left(1-\frac{2m}{r}\right)\frac{\partial p_0}{\partial r}$$

$$-\epsilon_0\left(1-\frac{2m}{r}\right)^{1/2}\left(1-\frac{V_0^{(\phi)^2}}{c^2}\right)^{1/2}\left[F_{0(r)(t)}+\frac{V_0^{(\phi)}}{c}F_{0(r)\,(\phi)}\right], \tag{4.1}$$

$$\left(\rho_0 + \frac{p_0}{c^2}\right) \frac{\cot\theta}{r} V_0^{(\phi)^2} = \left(1 - \frac{V_0^{(\phi)^2}}{c^2}\right) \frac{1}{r} \frac{\partial p_0}{\partial \theta}$$

$$+ \epsilon_0 \left(1 - \frac{V_0^{(\phi)^2}}{c^2}\right)^{1/2} \left[F_{0\,(\theta)\,(t)} + \frac{V_0^{(\phi)}}{c} F_{0\,(\theta)\,(\phi)}\right]. \tag{4.2}$$

$$F_{0\,(\phi)\,(t)} \left(1 - \frac{V_0^{(\phi)^2}}{c^2}\right) = 0, \tag{4.3}$$

$$\frac{\partial}{\partial r}\left[r\left(1 - \frac{2m}{r}\right)^{1/2} F_{0\,(\theta)\,(t)}\right] + \frac{\partial}{\partial \theta} F_{0\,(t)\,(r)} = 0, \tag{4.4}$$

$$\frac{\partial}{\partial r}\left[r\left(1 - \frac{2m}{r}\right)^{1/2} F_{0\,(\phi)\,(t)}\right] = 0, \tag{4.5}$$

$$\frac{\partial}{\partial r}\left[\sin\theta\, F_{0\,(\phi)\,(t)}\right] = 0, \tag{4.6}$$

$$\frac{\partial}{\partial r}\left[r^2 \sin\theta\, F_{0\,(\theta)\,(\phi)}\right] + \frac{\partial}{\partial \theta}\left[r \sin\theta \left(1 - \frac{2m}{r}\right)^{-1/2} F_{0\,(\phi)\,(r)}\right] = 0, \tag{4.7}$$

$$\frac{\partial}{\partial \theta}\left[\sin\theta\, F_{0(r)\,(\theta)}\right] = 0, \tag{4.8}$$

$$\frac{\partial}{\partial r}\left[r\left(1 - \frac{2m}{r}\right)^{1/2} F_{0(\theta)\,(r)}\right] = 0, \tag{4.9}$$

$$\frac{1}{r}\left(1 - \frac{2m}{r}\right)^{1/2} \frac{\partial}{\partial r}\left[r\left(1 - \frac{2m}{r}\right)^{1/2} F_{0(\phi)\,(r)}\right]$$

$$+ \frac{\partial}{\partial \theta}\left[\frac{1}{r}\left(1 - \frac{2m}{r}\right)^{1/2} F_{0\,(\phi)\,(\theta)}\right] = -\frac{4\pi\epsilon_0}{c}\left(1 - \frac{2m}{r}\right)^{1/2}\left(1 - \frac{V_0^{(\phi)^2}}{c^2}\right)^{-1/2} V_0^{(\phi)}, \tag{4.10}$$

$$\frac{1}{r}\frac{\partial}{\partial r}\left[r^2 F_{0\,(t)\,(r)}\right] + \frac{1}{\sin\theta}\frac{\partial}{\partial \theta}\left[\sin\theta \left(1 - \frac{2m}{r}\right)^{-1/2} F_{0(t)\,(\theta)}\right]$$

$$= 4\pi\epsilon_0 r\left(1 - \frac{2m}{r}\right)^{-1/2}\left(1 - \frac{V_0^{(\phi)^2}}{c^2}\right)^{-1/2}. \tag{4.11}$$

The continuity equation is identically satisfied. Our aim is to solve this set of equations self consistently and then consider the corresponding perturbation equations. Equation (4.3) directly implies that the toroidal electric field $F_0(t)(\phi)$ is identically zero, which is consistent with two of the Maxwell's equations (4.5) and (4.6).

Similarly we find that the toroidal magnetic field is not coupled with any of the physical parameters of the system and hence without loss of generality it is taken to be zero consistent with equations (4.8) and (4.9). This reduces our system of equations to six equations connecting six variables which are thus completely determined.

Presently we shall consider two special cases:

Case 1. Differential rotation: u^{ϕ} and ε_0 are constant, where ε_0 is the charge density as seen by the comoving observer.

Case 2. Rigid rotation: u^{ϕ}/u^{0} and b are constant, where $b = \epsilon_0 \left(1 - \frac{2m}{r}\right)^{-1/2} (1 - V_0^{(\phi)^2}/c^2)^{-1/2}$ is the charge density as seen by the observer at infinity.

4.1 *Case 1. Differential Rotation*

Since ε_0 = constant, $u^{\phi} = \Omega/c$ with Ω = constant, the azimuthal component of 3-velocity in local Lorentz frame would be $V_0^{(\phi)} = r\,\Omega \sin\theta\,(1 + r^2\,\Omega^2 \sin^2\theta/c^2)^{-1/2}$. The equations (4.7) and (4.10) involving magnetic field components become similar to the ones considered by Ginzburg and Ozernoi (1965) except for the source term in (4.10). Adopting the same procedure as used by these authors we assume the magnetic field components to have the form

$$F_{0(\phi)(\theta)} = B_r = (2\mu \cos\theta/r^3)\, f(r)$$

and

$$F_{0(r)(\phi)} = B_\theta = (\mu \sin\theta/r^3)\, g(r) \tag{4.12}$$

with μ the dipole moment, and 'f ' and ' g ' giving the contributions to the field components from the curvature of the background geometry. Substituting these in equations (4.7) and (4.10) we get the equations for f and g to be

$$\frac{d}{dr}\left(\frac{f}{r}\right) + \frac{g}{r^2}\left(1 - \frac{2m}{r}\right)^{-1/2} = 0 \tag{4.13}$$

and

$$\frac{d}{dr}\left[\frac{g}{r^2}\left(1 - \frac{2m}{r}\right)^{1/2}\right] + \frac{2f}{r^3} = \frac{4\pi\,\Omega\,\epsilon_0}{\mu c} r^2. \tag{4.14}$$

Hence

$$f = C_1 f_1 + C_2 f_2 - \frac{2\pi}{5}\frac{\Omega\,\epsilon_0 r^5}{\mu c} h_1,$$

where

$$f_1 = \frac{r^3}{m^3}\left[\ln\left(1-\frac{2m}{r}\right)+\frac{2m}{r}\left(1+\frac{m}{r}\right)\right],$$

$$f_2 = r^3/2m^3,$$

and

$$h_1 = 1+\frac{4m}{r}+\frac{8m^2}{r^2}\ln(r/2m-1); \tag{4.15}$$

$$g = -C_1 g_1 - C_2 g_2 + \frac{8\pi}{5}\frac{\Omega\epsilon_0 r^5}{\mu c}h_2,$$

where

$$g_1 = \frac{2r^2}{m^2}\left[\frac{r}{m}\ln\left(1-\frac{2m}{r}\right)+\left(1-\frac{2m}{r}\right)^{-1}+1\right]\left(1-\frac{2m}{r}\right)^{1/2}$$

$$g_2 = (r^3/m^3)\,(1-2m/r)^{1/2},$$

and

$$h_2 = \left[1+\frac{3m}{r}+\frac{4m^2}{r^2}\ln\left(\frac{r}{2m}-1\right)+\frac{m}{r}\left(\frac{r}{2m}-1\right)^{-1}\right](1-2m/r)^{1/2}. \tag{4.16}$$

C_1 and C_2 are the constants of integration. In order to determine these constants of integration we expect the fields to be continuous at inner and outer boundaries r_a and r_b. At the outer boundary we take the fields similar to the Ginzburg-Ozernoi fields whereas at the inner boundary, the fields are as obtained in Appendix.

In order to solve for electrical fields we now consider the fact that Maxwell's equations should be solved consistently with the fluid equations. In view of this we solve for the components of electric field from momentum equations (4.1) and 4.2) getting

$$F_{0(t)(r)} = E_r = \left(\rho_0+\frac{p_0}{c^2}\right)\frac{c^2}{\epsilon_0 r}\left\{\frac{m}{r}-\left(1-\frac{3m}{r}\right)\frac{r^2\Omega^2}{c^2}\sin^2\theta\right\}\left(1-\frac{2m}{r}\right)^{-1/2}$$

$$\times\left(1+\frac{r^2\Omega^2}{c^2}\sin^2\theta\right)^{-1/2}+\frac{1}{\epsilon_0}\left(1+\frac{r^2\Omega^2\sin^2\theta}{c^2}\right)^{-1/2}\left(1-\frac{2m}{r}\right)^{1/2}\frac{\partial p_0}{\partial r}$$

$$+\frac{r\Omega}{c}\sin\theta\left(1+\frac{r^2\Omega^2\sin^2\theta}{c^2}\right)^{-1/2}\frac{\mu\sin\theta}{r^3}g, \tag{4.17}$$

$$F_{0(t)(\theta)} = E_\theta = -\left(\rho_0 + \frac{p_0}{c^2}\right)\frac{c^2}{\epsilon_0 r}\left(1+\frac{r^2\,\Omega^2\sin^2\theta}{c^2}\right)^{-1/2}\frac{r^2\,\Omega^2}{c^2}\sin\theta\cos\theta$$

$$+\left(1+\frac{r^2\,\Omega^2}{c^2}\sin^2\theta\right)^{-1/2}\frac{1}{r\epsilon_0}\frac{\partial p_0}{\partial\theta}$$

$$-\frac{r\Omega}{c}\sin\theta\left(1+\frac{r^2\,\Omega^2\sin^2\theta}{c^2}\right)^{-1/2}\frac{2\mu\cos\theta}{r^3}\,f. \tag{4.18}$$

Using these expressions for the electric field in (4.4) and (4.11) we get the constraint equations for p_0 and p_0 as follows:

$$R\frac{\partial}{\partial R}\Big[\left(\rho_0+\frac{p_0}{c^2}\right)\sin\theta\cos\theta\,R^2\,\omega^2\,(1+R^2\,\omega^2\sin^2\theta)^{-1/2}\left(1-\frac{2}{R}\right)^{1/2}$$

$$+\omega\sin\theta\cos\theta\,(1+R^2\,\omega^2\sin^2\theta)^{-1/2}\left(1-\frac{2}{R}\right)^{1/2}\left\{\frac{2\alpha}{R}\,(C_1 f_1+C_2 f_2)\right.$$

$$\left.-\frac{4\pi}{5}\,\omega\,R^4\,h_1\,\beta\right\}-(1+R^2\,\omega^2\sin^2\theta)^{-1/2}\,\frac{1}{c^2}\frac{\partial p_0}{\partial\theta}\left(1-\frac{2}{R}\right)^{1/2}\Big]$$

$$+\frac{\partial}{\partial\theta}\Big[\left(\rho_0+\frac{p_0}{c^2}\right)\left\{\frac{1}{R}-\left(1-\frac{3}{R}\right)R^2\,\omega^2\sin^2\theta\right\}(1+R^2\,\omega^2\sin^2\theta)^{-1/2}\left(1-\frac{2}{R}\right)^{-1/2}$$

$$+\omega\sin^2\theta\,(1+R^2\,\omega^2\sin^2\theta)^{-1/2}\left\{\frac{\alpha}{R}(-C_1\,g_1-C_2\,g_2)+\frac{8\pi}{5}\,\omega\,R^4\,h_2\,\beta\right\}$$

$$+(1+R^2\,\omega^2\sin^2\theta)^{-1/2}\,(1-2/R)^{1/2}\,\frac{R}{c^2}\,\frac{\partial p_0}{\partial R}\Big]=0, \tag{4.19}$$

$$\frac{\partial}{\partial R}\Big[\left(\rho_0+\frac{p_0}{c^2}\right)R\left\{\frac{1}{R}-\left(1-\frac{3}{R}\right)R^2\,\omega^2\sin^2\theta\right\}\left(1-\frac{2}{R}\right)^{-1/2}(1+R^2\,\omega^2\sin^2\theta)^{-1/2}$$

$$+\omega\sin^2\theta\,(1+R^2\,\omega^2\sin^2\theta)^{-1/2}\left\{\alpha\,(-C_1\,g_1-C_2\,g_2)+\frac{8\pi}{5}\,\omega\,R^5\,h_2\,\beta\right\}$$

$$+R^2\,(1+R^2\,\omega^2\sin^2\theta)^{-1/2}\left(1-\frac{2}{R}\right)^{1/2}\frac{1}{c^2}\,\frac{\partial p_0}{\partial R}\Big]$$

$$-\frac{1}{\sin\theta}\left(1-\frac{2}{R}\right)^{-1/2}\frac{\partial}{\partial\theta}\Big[\left(\rho_0+\frac{p_0}{c^2}\right)\cos\theta\sin^2\theta\,R^2\,\omega^2\,(1+R^2\,\omega^2\sin^2\theta)^{-1/2}$$

$$+\omega\sin^2\theta\cos\theta\,(1+R^2\,\omega^2\sin^2\theta)^{-1/2}\left\{\frac{2\alpha}{R}\,(C_1 f_1+C_2 f_2)-\frac{4\pi}{5}\,\omega\,R^4\,h_1\,\beta\right\}$$

$$- (1 + R^2\omega^2 \sin^2\theta)^{-1/2} \frac{1}{c^2} \sin\theta \frac{\partial p_0}{\partial \theta}\Bigg]$$

$$= 4\pi\beta R^2 \left(1 - \frac{2}{R}\right)^{-1/2} (1 + R^2\omega^2 \sin^2\theta)^{1/2}, \tag{4.20}$$

wherein

$$R = \frac{r}{m}, \quad \omega = \frac{m\Omega}{c}, \quad \alpha = \frac{\mu\epsilon_0}{m^2c^2}, \quad \beta = \frac{m^2\epsilon_0^2}{c^2}. \tag{4.21}$$

Thus in principle we have the entire system solved self-consistently. But in practice it is formidable to solve these two equations completely for ρ_0 and p_0. We resort in this paper to the case of incoherent fluid disk which has $p_0 = 0$ and further treat the disk to be infinitesimally thin and confined to the equatorial plane. In order to bring in the last requirement we introduce a 'height coordinate' $h = r(\pi/2 - \theta) = Rm(\pi/2 - \theta)$ and further express the 3densities ρ_0, α, β in terms of corresponding 2-densities, $\bar{\rho}_0$, $\bar{\alpha}$, $\bar{\beta}$ as

$$\rho_0 = \bar{\rho}_0 (R)\, \delta(h), \qquad \alpha = \bar{\alpha}\, \delta(h), \qquad \beta = \bar{\beta}\, \delta(h) \tag{4.22}$$

ensuring $\bar{\alpha}$ and $\bar{\beta}$ to be independent of R. Putting these in (4.20) and integrating the resulting equation with respect to h we get

$$\frac{d}{dR}\Bigg[\bar{\rho}_0 R\left\{\frac{1}{R} - \left(1 - \frac{3}{R}\right) R^2\omega^2\right\}\left(1 - \frac{2}{R}\right)^{-1/2} (1 + R^2\omega^2)^{1/2}$$

$$+ \omega (1 + R^2\omega^2)^{-1/2} \left\{\bar{\alpha}(- C_1 g_1 - C_2 g_2) + \frac{8\pi}{5} \omega R^5 h_2 \bar{\beta}\right\}\Bigg]$$

$$= 4\pi\bar{\beta}\, R^2 (1 - 2/R)^{-1/2} (1 + R^2\omega^2)^{1/2}, \tag{4.23}$$

while the equation (4.20) becomes identically zero. To solve this equation we expand the factor $(1 - 2/R)^{1/2}$ binomially, keeping the terms upto $(2/R)^6$ and obtain the solution:

$$\bar{\rho}_0 = \left[4\pi\bar{\beta} D - \omega(1 + R^2\omega^2)^{-1/2}\left\{\bar{\alpha}(- C_1 g_1 - C_2 g_2) + \frac{8\pi}{5}\omega R^5 h_2 \bar{\beta}\right\} + C_3\right]$$

$$\times \frac{1}{R}\left(1 - \frac{2}{R}\right)^{1/2} (1 + R^2\omega^2)^{-1/2}\left\{\frac{1}{R} - \left(1 - \frac{3}{R}\right) R^2\omega^2\right\}^{-1}, \tag{4.24}$$

wherein

$$D = (1 + R^2\omega^2)^{3/2}\left(\frac{R}{4\omega^2} - \frac{231}{48 R^3} + \frac{1}{3\omega^2}\right)$$

A.—2

$$+ (1+R^2\,\omega^2)\,(5/2 - 31/8R - 63/10\,R^2 - R/8\omega^2)$$

$$+ \ln\,[R\,\omega + (1+R^2\,\omega^2)^{1/2}]\,(41 - 1/\omega^2)\,1/8\omega$$

$$+ \frac{1}{4}\ln\left[\frac{(1+R^2\,\omega^2)^{1/2}-1}{(1+R^2\,\omega^2)^{1/2}+1}\right]\left(5+\frac{63}{8}\omega^2\right) \tag{4.25}$$

and C_3 is the constant of integration which can be evaluated by assuming the average density $\bar{\rho}_{0c}$ at the mid point of the disk.

From the expression (4.24) we find that $\bar{\rho}_0$ has singularities at the values of R given by the roots of the equation

$$(R-2)^{1/2}\,(R^3\,\omega^2 - 3\,R^2\,\omega^2 - 1) = 0. \tag{4.26}$$

The second factor of (4.26) has a pair of complex conjugate roots and one real root as given by

$$R_{\text{sing}} = 1 + \frac{1}{(2\omega)^{1/3}}\left[\{1+2\omega^2+(1+4\omega^2)^{1/2}\}^{1/3} + \{1+2\omega^2-(1+4\omega^2)^{1/2}\}^{1/3}\right] \tag{4.27}$$

Thus for any given value of ω we can evaluate R_{sing} where we have a singularity in addition to the one at $R = 2$. For lower values of ω, R_{sing} lies far out and as ω increases R_{sing} approaches the value 3 asymptotically. Hence we can consider two kinds of disks, (1) $R_b < R_{\text{sing}}$, in which case the disk is necessarily slowly rotating and (2) $R_a > R_{\text{sing}}$, which would allow slow as well as fast rotation for the disk.

To get the equations for electromagnetic field for the infinitesimally thin disk considered above we also introduce surface charge density $\bar{\epsilon}_0$ by

$$\epsilon_0 = \bar{\epsilon}_0\,\delta\,(h) \tag{4.28}$$

and obtain

$$(B_r)_{\theta=\pi/2} = 0,$$

$$X = \frac{m\,\bar{\epsilon}_0}{c^2}(B_\theta)_{\theta=\pi/2} = \frac{\bar{a}}{R^3}(-C_1\,g_1 - C_2\,g_2) + \frac{8\pi}{5}\,\omega\,R^2\,h_2\,\bar{\beta},$$

$$(E_\theta)_{\theta=\pi/2} = 0,$$

$$Y = \frac{m\,\bar{\epsilon}_0}{c^2}(E_r)_{\theta=\pi/2} = \frac{\bar{\rho}_0}{R}\left\{\frac{1}{R} - \left(1-\frac{3}{R}\right)R^2\,\omega^2\right\}\left(1-\frac{2}{R}\right)^{-1/2}(1+R^2\omega^2)^{-1/2}$$

$$+ R\omega\,(1 + R^2\omega^2)^{-1/2}\,X. \tag{4.29}$$

Taking various values of R_a, R_b, $\bar{\alpha}$, $\bar{\beta}$ and $\bar{\rho}_{0c}$ we have computed $\bar{\rho}_0$, B_θ and E_r profiles, some of which are presented in Tables 1 to 6. Because of the approximation

Table 1. Differential rotation $R_b < R_{\text{sing}}$

$R_a = 4{\cdot}5, \quad R_b = 6, \quad \omega = 0{\cdot}093$

$\bar{\alpha} = 1{\cdot}08, \ \bar{\beta} = 1{\cdot}0 \times 10^{-6}, \ \bar{\rho}_{0_c} = 1{\cdot}80 \times 10^{3}$

R	$\bar{\rho}_0 \times 10^3$	$E_r \times 10^{10}$	$B_\theta \times 10^3$
4·5	1·10	3·48	−3·27
4·7	1·18	3·26	−1·93
4·8	1·28	3·06	−0·78
5·0	1·41	2·88	0·21
5·1	1·57	2·71	1·07
5·3	1·80	2·56	1·82
5·4	2·12	2·42	2·48
5·6	2·62	2·29	3·06
5·7	3·49	2·17	3·58
5·9	5·42	2·06	4·03

Table 2. Differential rotation $R_b < R_{\text{sing}}$

$R_a = 3{\cdot}5, \quad R_b = 100, \quad \omega = 0{\cdot}0010$

$\bar{\alpha} = 1{\cdot}32 \times 10^{3}, \quad \bar{\beta} = 0{\cdot}1 \times 10^{-6}, \quad \bar{\rho}_{0_c} = 2{\cdot}83$

R	$\bar{\rho}_0$	$E_r \times 10^6$	$B_\theta \times 10^6$
3·5	1·37	102·22	−2·01
4·0	1·47	78·96	−0·95
4·5	1·55	62·82	−0·38
4·9	1·61	51·17	−0·06
5·4	1·66	42·49	0·15
5·9	1·70	35·84	0·28
7·1	1·77	24·73	0·48
8·1	1·81	19.19	0·56
13·1	1·93	7·28	0·70
22·9	2·05	2·47	0·75
37·3	2·30	1·00	0·77
51·8	2·83	0·60	0·78
71·1	4·78	0·43	0·79
85·5	10·16	0·39	0·80
100·0	1625·44	0·36	0·81

Table 3. Differential rotation $R_a > R_{\text{sing}}$

$R_a = 4{\cdot}5, \quad R_b = 25, \quad \omega = 0.19$

$\bar{\alpha} = 9{\cdot}81 \times 10^{2}, \quad \bar{\beta} = 1.0 \times 10^{-6}, \quad \bar{\rho}_{0_c} = 46{\cdot}79$

R	$\bar{\rho}_0 \times 10$	$E_r \times 10^{11}$	$B_\theta \times 10^7$
4·5	6585·53	−4·17	−3·22
5·5	418·77	−2·77	−2·48
6·6	158·26	−1·97	0·30
7·6	78·86	−1·47	1·67
9·6	27·59	−0·91	2·90
12·7	8·66	−0·52	3·56
14·8	4·68	−0·39	3·76
18·9	1·72	−0·24	3·96
21·9	0·93	−0·18	4·04
25·0	0·55	−0·14	4·09

Table 4. Differential rotation $R_a > R_{\text{sing}}$

$R_a = 3{\cdot}5$, $R_b = 100$, $\omega = 0.46$

$\bar{\alpha} = 6{\cdot}09 \times 10^5$, $\bar{\beta} = 1.0 \times 10^{-6}$, $\bar{\rho}_{0c} = 2{\cdot}83$

R	$\bar{\rho}_0 \times 10^4$	$E_r \times 10^{12}$	$B_\theta \times 10^8$
3·5	207·26	−96·16	−9·23
4·0	27·77	−74·27	−4·34
4·5	11·91	−59·09	−1·77
4·9	6·49	−48·12	0·26
5·4	3·96	−39·95	0·69
5·9	2·60	−33·70	1·32
7·1	1·09	−23·24	2·21
8·1	0·62	−18·02	2·58
13·2	0·08	−6·81	3·22
22·8	$0{\cdot}79 \times 10^{-3}$	−2·27	3·45
37·3	$0{\cdot}11 \times 10^{-2}$	−0·85	3·54
51·8	$0{\cdot}22 \times 10^{-3}$	−0·44	3·59
71·1	$0{\cdot}79 \times 10^{-4}$	−0·23	3·64
85·2	$0{\cdot}37 \times 10^{-4}$	−0·16	3·68
100·0	$0{\cdot}20 \times 10^{-4}$	−0·12	3·72

Table 5. Differential rotation $R_a > R_{\text{sing}}$

$R_a = 4{\cdot}5$, $R_b = 25$, $\omega = 19{\cdot}2$

$\bar{\alpha} = 9{\cdot}31 \times 10^4$, $\bar{\beta} = 1{\cdot}0 \times 10^{-4}$, $\bar{\rho}_{0c} = 46{\cdot}79$

R	$\bar{\rho}_0 \times 10^2$	$E_r \times 10^{17}$	$B_\theta \times 10^9$
4·5	103·47	−3·98	−9·22
5·5	35·59	−2·64	−4·14
6·6	15·85	−1·86	−2·03
7·6	8·19	−1·40	−0·95
10·7	1·85	−0·71	0·46
12·7	0·88	−0·50	0·99
14·8	0·47	−0·37	1·45
17·8	0·21	−0·25	2·15
21·9	0·09	−0·17	3·20
25·0	0·05	−0·13	4·09

Table 6. Differential rotation $R_a > R_{\text{sing}}$

$R_a = 3{\cdot}5$, $R_b = 80$, $\omega = 46{\cdot}5$

$\bar{\alpha} = 2{\cdot}49 \times 10^7$, $\bar{\beta} = 1{\cdot}0 \times 10^{-4}$, $\bar{\rho}_{0c} = 4{\cdot}42$

R	$\bar{\rho}_0 \times 10$	$E_r \times 10^{18}$	$B_\theta \times 10^{10}$
3·5	$3{\cdot}9 \times 10^4$	−63·06	−7·32
7·3	642·09	−14·40	−5·49
11·2	102·65	−6·21	−5·55
22·6	53·77	−1·51	−5·23
30·3	16·35	−0·84	−4·71
41·8	4·43	−0·44	−3·57
49·4	2·24	−0·32	−2·60
60·9	0·10	−0·21	−0·81
72·4	0·05	−0·15	1·35
80·0	0·03	−0·12	3·00

made in expanding the factor $(1 - 2/R)^{-1/2}$ in evaluating ρ_0 we restrain ourselves from going too near to the event horizon. We find that R_a as small as 3·5 is a reasonably good choice for the inner edge of the disk.

4.2 *Case 2. Rigid Rotation*

We solve this case exactly on the same lines as for case 1 with b = constant, $u^\phi / \mu^0 = \Omega/c$, Ω, = constant. We now have $V_0{}^{(\phi)} = r\,\Omega \sin\theta\,(1-2m/r)^{-1/2}$. The expression for magnetic fields (4.15) and (4.16) remain unchanged except for the fact that ε_0 gets replaced by b. The components of the electric field as calculated from momentum equations become

$$F_{0(t)(r)} = E_r = (\rho_0 + p_0/c^2)\ \frac{c^2}{br}\left(1 - \frac{2m}{r} - \frac{r^2\,\Omega^2}{c^2}\sin^2\theta\right)^{-1}$$

$$\times\left(\frac{m}{r} - \frac{r^2\,\Omega^2}{c^2}\sin^2\theta\right) + \frac{1}{b}\frac{\partial p_0}{\partial r} + \frac{r\Omega}{c}\left(1 - \frac{2m}{r}\right)^{-1/2}\frac{\mu g}{r^3}\sin^2\theta\,, \tag{4.30}$$

$$F_{0(t)(\theta)} = E_\theta = -(\rho_0 + p_0/c^2)\ \frac{c^2}{br}\left(1 - \frac{2m}{r}\right)^{-1/2}\left(1 - \frac{2m}{r} - \frac{r^2\,\Omega^2}{c^2}\sin^2\theta\right)^{-1}$$

$$\times\frac{r^2\Omega^2}{c^2}\sin\theta\cos\theta + \left(1 - \frac{2m}{r}\right)^{-1/2}\frac{1}{br}\frac{\partial p_0}{\partial\theta}$$

$$-\frac{r\Omega}{c}\left(1 - \frac{2m}{r}\right)^{-1/2}\frac{2\mu f}{r^3}\sin\theta\cos\theta. \tag{4.31}$$

Substituting these in Maxwell's equations, using

$$a = \mu\, b/m^2c^2,\ \ \beta = m^2b^2/c^2,\ p_0 = 0 \tag{4.32}$$

and integrating with respect to h after putting δ function as in the previous case, we get the following expression for $\bar{\rho}_0$ and the electromagnetic field components

$$\bar{\rho}_0 = \left[\frac{4\pi}{3}\bar{\beta}\,R^2 - \frac{\omega}{R}\left(1 - \frac{2}{R}\right)^{-1/2}\left\{\bar{a}\,(-C_1\,g_1 - C_2\,g_2)\right.\right.$$

$$\left.\left. + \frac{8\pi}{5}\,\omega\,R^5\,h_2\,\bar{\beta}\right\} + C_3\right]\left(1 - \frac{2}{R} - R^2\,\omega^2\right)\left(\frac{1}{R} - R^2\,\omega^2\right)^{-1}, \tag{4.33}$$

$$X = \frac{m\bar{b}}{c^2}(B_\theta)_{\theta=\pi/2} = \frac{\bar{a}}{R^3}(-C_1\,g_1 - C_2\,g_2) + \frac{8\pi}{5}\,\omega R^2\,h_2\,\bar{\beta}, \tag{4.34}$$

$$Y = \frac{m\bar{b}}{c^2}(E_r)_{\theta=\pi/2} = \frac{\bar{\rho}_0}{R}\left(1 - \frac{2}{R} - R^2\,\omega^2\right)^{-1}\left(\frac{1}{R} - R^2\,\omega^2\right) + R\omega\left(1 - \frac{2}{R}\right)^{-1/2}X. \tag{4.35}$$

The constants C_1, C_2, C_3 are evaluated exactly as in the previous case. The expression for ρ_0 in this case is exact and we can put the inner edge of the disk very near to the event horizon. The singularity point in this case is given by

$$R_{\text{sing}} = \omega^{-2/3} \tag{4.36}$$

Because of the nature of the velocity function $V_0^{(\phi)}$, in this case we have to confine only to the slowly rotating disks with $R_b < R_{\text{sing}}$ The limitation comes from the consideration that the maximum linear velocity $V_0^{(\phi)}$ ' at R_b, should be less than c, the velocity of light. Tables 7 and 8 present two cases of $\bar{\rho}_0$, B_θ and E_r profiles for chosen values of the parameters.

Table 7. rigid rotation

$R_a = 2{\cdot}1$, $R_b = 10$, $\omega = 0{\cdot}03$

$\bar{\alpha} = 4{\cdot}07$, $\bar{\beta} = 1{\cdot}0\times10^{-8}$, $\bar{\rho}_{0_c} = 2{\cdot}96\times10^{2}$

R	$\bar{\rho}_0 \times 10^2$	$E_r \times 10^{10}$	$B_\theta \times 10^6$
2·1	0·16	4·99	−1·69
2·9	1·13	2·63	1·65
3·7	1·71	1·62	2·22
4·5	2·14	1·10	2·49
5·3	2·53	0·80	2·66
6·1	2·96	0·60	2·77
6·8	3·52	0·47	2·85
7·6	4·39	0·38	2·92
8·4	6·04	0·31	2·97
9·2	10·62	0·26	3·00
10·0	87·59	0·22	3·04

Table 8. Rigid rotation

$R_a = 4{\cdot}5$, $R_b = 1000$, $\omega = 3{\cdot}16\times10^{-3}$

$\bar{\alpha} = 4{\cdot}1\times10^{-11}$, $\bar{\beta} = 1{\cdot}0\times10^{-11}$, $\bar{\rho}_{0_c} = 28{\cdot}3$

R	$\bar{\rho}_0 \times 10^2$	$E_r \times 10^{14}$	$B\theta \times 10^7$
4·5	0·14	735·51	$-7{\cdot}4\times10^{-10}$
7·0	0·18	304·79	−6·51
9·5	0·20	165·73	−7·95
12·0	0·21	103·96	−8·46
21·9	0·22	30·97	−9·07
31·9	0·23	14·65	−9·24
41·8	0·24	8·51	−9·31
51·8	0·24	5·55	−9·35
104.1	0·24	1·38	−9·37
203·6	0·25	0·36	−9·12
303·2	0·25	0·16	−8·65
402·7	0·26	0·09	−7·99
502·2	0·28	0·06	−7.13
751·1	0·42	0·03	−4.16
1000·0	826.10	0·01	$2{\cdot}5\times10^{-10}$

5. Stability analysis

We shall now take up the analysis of stability of such disks as mentioned in Section 4 under purely radial perturbations. We use the normal mode analysis to set up the characteristic value equation and analyse the stability by trial function method as has been done by Chandrasekhar (1964) for relativistic fluid spheres. Among the perturbed quantities we take $\delta V^{(\theta)} = 0$, $\delta V^{(\phi)} = 0$ and $\delta p = 0$, and get the governing system of equations from Section 3. Making use of the proper δ functions we get after simplification the pulsation equation in the following form

$$(\bar{\rho}_0 Z - X)\frac{m^2}{c^2}\frac{\partial^2}{\partial t^2}\delta V^{(r)} - \frac{1}{R}\left(1-\frac{2}{R}\right)^{1/2}\frac{d}{dR}\left[\left(1-\frac{2}{R}\right)\frac{d}{dR}\left\{R\left(1-\frac{2}{R}\right)^{1/2}\right.\right.$$

$$\left.\left. -(\bar{\rho}_0 Z + X)\,\delta V^{(r)}\right\}\right] = -\frac{4\pi}{R}\left(1-\frac{2}{R}\right)^{1/2}\omega\,\bar{\beta}\,\frac{d}{dR}\,[R^2\,(1-2/R)\,\delta V^{(r)}], \tag{5.1}$$

wherein $\bar{\rho}_0$ and X corresponding to the two different cases are given by (4.24), (4.29) and (4.33), (4.34) and the corresponding Z values are given by

$$Z = 2\omega\,(1-2/R)^{1/2} \tag{5.2}$$

for differential rotation and by

$$Z = \omega\,(1-2/R)^{1/2}\,(1-2/R-R^2\,\omega^2)^{-2}\,(2-5/R-R^2\,\omega^2) \tag{5.3}$$

for rigid rotation

With $\delta V^{(r)} = a(r)\exp(i\sigma t)$ we get the characteristic value equation

$$\frac{d}{dR}\left[\left(1-\frac{2}{R}\right)\frac{d}{dR}\{(-\bar{\rho}_0 Z+X)\,y\}\right] - 4\pi\,\omega\,\bar{\beta}\,\frac{d}{dR}\,[R\,(1-2/R)^{1/2}\,y]$$

$$+(1-2/R)^{-1}\,(-\bar{\rho}_0 Z+X)\,(m^2\sigma^2/c^2)\,y = 0 \tag{5.4}$$

wherein $y=R\,(1-1/R)^{1/2}\,a$. To bring (5.4) into the self-adjoint form we impose the boundary condition $y=0$ at the two edges R_a and R_b and integrate it by parts after multiplying by $(-\bar{\rho}_0 Z+X)y$. The resultant equation is

$$\frac{m^2\sigma^2}{c^2}\int_{R_a}^{R_b}(1-2/R)^{-1}\,(-\bar{\rho}_0 Z+X)^2\,y^2\,dR = \int_{R_a}^{R_b}(1-2/R)\left[\frac{d}{dR}\{(-\bar{\rho}_0 Z+X)\,y\}\right]^2 dR$$

$$+2\omega\,\pi\,\beta\int_{R_a}^{R_b} y^2\,\{(-\bar{\rho}_0 Z+X)\,(1-2/R)^{-1/2}\,(1-1/R)$$

$$-R\,(1-2/R)^{1/2}\,\frac{d}{dR}(-\bar{\rho}_0 Z+X)\}\,dR. \tag{5.5}$$

Equation (5.5) is the variational base corresponding to the characteristic value equation

$$\frac{d}{dR}\left[(1-2/R)\frac{d}{dR}\{(-\bar{\rho}_0 Z+X)\, y\}\right]-2\pi\,\omega\,\bar{\beta}\left[(1-2/R)^{-1/2}\,(1-1/R)\right.$$

$$\left.-R(1-2/R)^{1/2}\,(-\bar{\rho}_0 Z+X)^{-1}\,\frac{d}{dR}\,(-\bar{\rho}_0 Z+X)\right] y$$

$$+\frac{m^2\sigma^2}{c^2}\,(1-2/R)\,(-\bar{\rho}_0 Z+X)\, y=0, \tag{5.6}$$

which is clearly a characteristic value equation of a self-adjoint operator. We now take trial functions for y which satisfy the prescribed boundary condition but otherwise are completely arbitrary, express the integrands appearing on right hand side of (5.5) as coefficients of $\bar{\alpha}$, $\bar{\beta}$ and ρ_{oc} and perform the integration numerically. We compute critical value of one of these parameters $\bar{\beta}$ for given values of $\bar{\alpha}$ and $\bar{\rho}_{0c}$ which will make the right hand side of (5.5) zero. This critical choice of the parameters gives a sufficient condition for the disk to be unstable. We have considered a number of cases for different choices of the parameters R_a, R_b and ω and looked for the onset of instability in the manner indicated above with the trial function

$$y = (R - R_a)\,(R_b - R). \tag{5.7}$$

For every choice that we have made, we find that the equation $\sigma^2=0$ cannot be satisfied for real positive $\bar{\beta}$. Thus it indicates that for real values of the physical parameters, there is no region of instability among the cases we have considered. In fact we notice from the expression (5.5) for σ^2 that the only term which can become negative is

$$I = 2\pi\,\omega\,\bar{\beta}\int_{R_a}^{R_b} y^2\left(1-\frac{2}{R}\right)^{-1/2}\left\{(-\bar{\rho}_0 Z+X)\,(1-1/R)\right.$$

$$\left.-(R-2)\,\frac{d}{dR}\,(-\bar{\rho}_0 Z+X)\right\} dR \tag{5.8}$$

and hence for σ^2 to be either zero or negative this term has to be negative and also equal to or greater than the other terms. On the contrary, we find that for certain choice of $\bar{\alpha}$, $\bar{\beta}$, and $\bar{\rho}_{oc}$ this term is positive and thus σ^2 is positive indicating that the disk is stable under perturbation. Table 9 gives a choice of parameters for which I, and therefore σ^2, is positive.

Table 9. A choice of parameters for which the disk is stable

R_a	R_b	ω	$\bar{\alpha}$	$\bar{\beta}$	$\bar{\rho}_{0c}$
Rigid rotation					
3·5	12·0	0·024	$6{\cdot}4\times10^{-4}$	1·0	$2{\cdot}15\times10^{3}$
3·5	12·0	0·024	$6{\cdot}4\times10^{-4}$	0·1	$2{\cdot}15\times10^{2}$
3·5	6·0	0·066	0·99	$1{\cdot}0\times10^{-2}$	$1{\cdot}19\times10^{3}$
3·5	6·0	0·066	0·99	$1{\cdot}0\times10^{-4}$	1·19
4·5	6·0	0·066	0·99	$1{\cdot}0\times10^{-6}$	$1{\cdot}80\times10^{3}$
Differential rotation					
3·5	6·0	0·09	1·40	$1{\cdot}0\times10^{-4}$	$1{\cdot}2\times10^{3}$
3·5	6·0	0·09	13·96	$1{\cdot}0\times10^{-4}$	$1{\cdot}2\times10^{3}$
4·5	6·0	0·09	1·07	$1{\cdot}0\times10^{-6}$	$1{\cdot}8\times10^{3}$
4·5	6·0	0·09	10·70	$1{\cdot}0\times10^{-6}$	$1{\cdot}8\times10^{2}$

6. Discussion

We have considered in this paper pressureless thin disks of charged fluid with differential as well as rigid rotation and have found that in all cases the disk is stable under radial pulsations. While obtaining the solution for the density distribution in steady state, the only approximation that we have introduced is in the case of differential rotation. Here for the purpose of integration while solving for $\bar{\rho}_0$ we consider a binomial expansion of the factor $(1—2/R)^{-½}$ choosing terms upto $(1/R^6)$. The disk which is in equilibrium under gravitational, centrifugal and electromagnetic forces seems to adjust its material and field structure such that it can always retain the stability under perturbation. As we have mentioned in Section 4, the disk should either have its inner edge R_a beyond the singularity R_{sing} or have R_{sing} beyond its outer edge R_b, in order to avoid the singularity in $\bar{\rho}_0$. In the case of rigid rotation R_{sing} is always beyond R_b and this naturally restricts us to the case of slowly rotating disks (see equation 4.37). On the other hand such restrictions are not present in the case of differential rotation. Hence fast rotation is possible with $R_a > R_{\text{sing}}$. From the results presented in Tables 1 and 2 it is evident that the density $\bar{\rho}_0$ increases from the inner edge to the outer edge for slowly rotating disks whereas the electrical field (E_r) decreases from R_a to R_b in the outgoing direction. The magnetic field (B_θ) shows a change in sign indicating its role in confining the fluid. The disk is stable in this case since the centrifugal force is quite small. On the other hand in the case of fast rotating disks (Tables 3-6) the density distribution as well as the electric field change their profiles such that the density decreases towards the outer edge whereas E_r increases and is directed inwards. This is again completely compatible with the increased centrifugal force. The magnetic field still remains a confining field. In essence, depending upon the centrifugal force the matter in the pressureless disks adjusts itself with the help of electric fields to such a distribution that the forces balance each other completely and allow the magnetic field to keep the fluid in a stable configurtion under radial perturbations. It is in fact important to notice that we have several examples of disks which have their inner edge well within 6 m limit and are stable under perturbations. This supports our view expressed in the beginning concerning the significance of general relativistic effects in the study of disk structure.

In this analysis, though $B_r = 0$ along the equatorial plane $\theta = \pi/2$ to which the disk is confined, it should be recognized that the B_r field outside the disk (above and below $\theta = \pi/2$ plane) will give rise to vertical forces which in general compress the disk from above and below. Naturally these do not affect the perturbations in the radial direction but could give rise to plasma instabilities like ' pinch' and ' tearing mode ' for more general perturbations. Hence a more rigorous treatment including the role of such forces will be worth consideration. With the general system of equations developed here systems with finite conductivity, radial motion, non-zero pressure etc. can be treated. Our present set of equations also allows us to consider disks with finite meridional extension. In conclusion we may mention that further detailed analysis of disks should take into account viscous and shear forces and more general perturbations. It is also important to consider the possible modes of exciting the perturbations through passage of electromagnetic waves in such disks.

Acknowledgements

It is a pleasure to thank Dr. K. S. Rao for useful discussions regarding numerical computations and the referees for valuable suggestions. One of us (D.K.C.) would like to thank University Grants Commission for the award of teacher fellowship.

Appendix

In order to determine C_1 and C_2 appearing in the expression for magnetic field components we take the Ginzburg-Ozernoi field for $R > R_b$ which gives

$$(X)_{R > R_b} = (3/8)\, \bar{\alpha}\, g_1/R^3. \tag{A-1}$$

To obtain another boundary condition we take the familiar results of magnetic field in the interior of a circular current loop in the $\theta = \pi/2$ plane restricting only to the lower order terms. In the present case of the disk these fields appear as

$$F_{(r)(\phi)} = B_\theta = -\mu\, D' \sin\theta\, g'(r),$$

$$F_{(\phi)(\theta)} = B_r = \mu\, D' \cos\theta\, f'(r), \tag{A-2}$$

wherein $D' = 4\,(R_b - R_a)/[m^3\,(R_b^4 - R_a^4)]$ and f' and g' represent the correction due to curvature of spacetime. Substituting these in Maxwell's equations governing magnetic field we get

$$\frac{d}{dr}[r^2 f'] - 2rg'\left(1 - \frac{2m}{r}\right)^{-1/2} = 0 \tag{A-3}$$

and

$$\frac{d}{dr}\left[r\left(1 - \frac{2m}{r}\right)^{1/2} g'\right] - f' = 0. \tag{A-4}$$

This set of simultaneous differential equations can be solved by a process similar to the one adopted by Ginzburg and Ozernoi yielding

$$f' = C_1' \left[\ln (1-2m/r) + (2m/r)\,(1+m/r)\right] + C_2' \tag{A-5}$$

and

$$g' = \left\{C_1' \left[\ln (1-2m/r) + (m/r) + (m/r)\,(1-2m/r)^{-1}\right] + C_2'\right\} \left(1 - \frac{2m}{r}\right)^{1/2}. \tag{A-6}$$

We choose $C_1' = 0$ in order to avoid the singularity at $r = 2m$ and take $C'_2 = 1$ to obtain the flat spacetime limit ($m \to 0$). With these we get for $R < R_a$

$$(X)_{R < R_a} = -\bar{a}\, D'\, (1-2/R)^{1/2} m^3. \tag{A-7}$$

References

Abramowicz, M., Jaroszynski, M., Sikora, M. 1977, *Astr. Astrophys,,* **63**, 221.
Bisnovatyi-Kogan, G. S., Blinnikov, S. I. 1977, *Astr. Astrophys.*, **59,** 111.
Chandrasekhar, S. 1964, *Astrophys. J.*, **140,** 417.
Eardley, D. M., Lightman, A. P., Payne, D. G., Shapiro, S. L. 1978, *Astrophys. J.*, **224,** 53.
Fishbone, L. G., Moncrief, V. 1976, *Astrophys. J.*, **207**, 962.
Ginzburg, V. L., Ozernoi, L. M. 1964, *Soviet Phys. JETP*, **20,** 689
Hoshi, R. 1977, *Progress theor. Phys*., **58,** 1191.
Hoshi, R., Shibazaki, N. 1977, *Progress theor. Phys*., **58,** 1759.
Lightman, A. P. 1974a, *Astrophys. J.*, **194,** 419.
Lightman, A. P. 1974b, *Astrophys. J.*, **194,** 429.
Novikov, I. D., Thorne, K. S. 1973, *in Les Houches: Black Holes*, Eds C. DeWitt and B. S. DeWitt, Gordon and Breach, New York, p. 343.
Okuda, T. 1980, *Publ. astr. Soc. Japan*, **32**, 127.
Prasanna, A. R., Varma, R. K. 1977, *Pramana*, **8**, 229.
Pringle, J. E., Rees, M. J. 1972, *Astr. Astrophys.,* **21,** 1.
Rees, M. J. 1978, *Observatory,* **98**, 210.
Shakura, N. I. Sunyaev, R. A. 1973, *Astr. Astrophys.,* **24**, 337.
Shapiro, S. L., Lightman, A. P., Eardley, D. M. 1976, Astrophys. *J.*, **204**, 187.
Shibazaki, N.1978, *Progress theor. Phys.*, **60,** 985.

J. Astrophys. Astr. (1981) **2,** 29–41

An Analysis of the Orbital Periods of Some Eclipsing Binaries Suspected to be in the Pre-Main Sequence Contraction Phase of Evolution

T. Panchatsaram and K. D. Abhyankar *Centre of Advanced study in Astronomy, Osmania University, Hyderabad 500007*

Received 1980 September 4; accepted 1981 January 5

Abstract. An analysis of the available photoelectric times of minima of KO Aql, TV Cas and Z Her, which are suspected to be in pre-main sequence phase of evolution, reveals that KO Aql shows a secular increase in its orbital period at the rate of 4.34×10^{-8} day per cycle while the period of TV Cas has been decreasing at the rate of $4{\cdot}08 \times 10^{-9}$ day per cycle. Z Her does not show any period change at all. The orbital period of any binary system which is in the pre-main sequence phase will be systematically affected because of ' shrinking' dimensions of the components. A simple formula for the characteristic period change, defined by (P/P), is derived from a consideration of the conservation of total energy and total angular momentum for a binary system whose components are still in the process of contraction or expansion. The derived formula is applied to the above systems to see whether theoretical characteristic period changes agree with the observed values. The systems are assumed to evolve independently in the pre-main sequence phase in accordance with the model calculations of Iben (1965). It is found that there is no agreement between theoretical and observed characteristic period changes. This suggests that KO Aql and TV Cas may not be in the pre-main sequence phase. We do not have sufficient data for Z Her to judge its evolutionary status by the present procedure; this is also true of TT Hya. We suspect that the period changes observed in KO Aql and TV Cas may be due to light-time effect.

Key words: eclipsing binaries—period changes—pre-main sequence evolution

1. Introduction

Kopal (1959) identified a group of close binary systems in which the subgiant secondary components appear to be smaller than their Roche lobes. Hall (1974) analysed a sample of 25 such binaries to see whether the secondaries are really undersize. Of these, he suspected only KO Aql, S Cnc and SX Cas, to be potential candidates for this class of binaries. Of course, for these 3 suspected systems he maintained that he did not have accurate data. When accurate elements for KO Aql became available (Blanco and Criztaldi 1974) it was learnt that this system also did not have an undersize subgiant (Hall 1975). Hall (1974) did not believe in the existence of such a class of systems, since it is an established notion that Algols are remnants of post-main sequence mass transfer, and hence the existence of such undersize components cannot be explained. Even for systems suspected by him to have undersize components he did not have reliable data. Recent accurate observations of some of these systems show the existence of undersize subgiants. For example, the discussion of KO Aql by Hayasaka (1979) reveals an undersize subgiant. Similarly, Kulkani's (1979) analysis of the photoelectric data of TT Hya shows the secondary to be undersized. One can, therefore, find the revival of the old idea of undersize subgiants in close binary systems.

If such systems are really in existence, then great importance should be attached to their evolutionary status. The only possible explanation for the existence of undersize subgiants, if at all they exist, is based on the assumption that the subgiant component is in the pre-main sequence contraction phase of evolution, while the primary has almost reached the main sequence. Roxburgh (1966 a, b), using Iben's (1965) evolutionary calculations and his fission theory, found that KO Aql is currently in the pre-main sequence phase of evolution. Field (1969) using a modified version of Roxburgh's method examined the undersize subgiant systems listed by Kopal (1959) to see whether they are in the pre-main sequence phase. Among the 18 systems listed by Kopal, he found only four systems, KO Aql, TV Cas, WW Cyg and Z Her in the pre-main sequence contraction phase. We present here a different approach, in order to confirm whether these undersize systems are in the pre-main sequence stage. We have taken for our analysis only those suspected systems for which photoelectric observations of minima exist for a few decades. These systems are KO Aql, TV Cas and Z Her. If these three systems are in the pre-main sequence phase of evolution, it may be inferred that their orbital period would be affected systematically. Therefore an accurate analysis of the behaviour of the orbital periods of these systems will definitely provide us with valuable information regarding their evolutionary status. The necessary details are presented in Sections 3, 4 and 5.

2. (*O*—*C*) Diagrams

The photoelectric times of minima available in the literature for the three systems KO Aql, TV Cas and Z Her are presented in Tables 1, 2 and 3 respectively. The light-elements for KO Aql used in the computations of time residuals have been taken from ' *Supplemento ad Annuario Cracoviense*, *No. 49* (*1978*)'. For TV Cas and Z Her the light-elements used are those given by Koch, Sobieski and Wood (1963). A plot of the observed minus computed (*O*—*C*) time residuals versus the

number of cycles elapsed E, is shown for each of the systems in Figs 1, 2 and 3. It can be seen from these that the orbital periods of KO Aql and TV Cas change secularly while that of Z Her remains practically constant. The orbital period of KO Aql secularly increases and TV Cas shows a secular decrease of period. The points in the (O—C) diagrams of KO Aql and TV Cas were fitted with parabolas while that of Z Her with a straight line using the least squares method and assigning equal weights to all the points. The resulting ephemerides for the primary times of minima along with the standard errors are:

$$\text{KO Aql}: \mathrm{JD}_\odot\ 2441887{\cdot}4731 + 2^{\mathrm{d}}{\cdot}8640440\ E + 0{\cdot}217\times10^{-7}\ E^2$$
$$\pm 13 \qquad \pm 18 \qquad \pm 32$$

$$\text{TV Cas}: \mathrm{JD}_\odot\ 2436483{\cdot}8094 + 1^{\mathrm{d}}{\cdot}8126107\ E - 0{\cdot}204\times10^{-8}\ E^2$$
$$\pm 5 \qquad \pm 3 \qquad \pm 9$$

$$\text{Z Her}: \mathrm{JD}_\odot\ 2413086{\cdot}352 + 3^{\mathrm{d}}{\cdot}9928006\ E$$
$$\pm 13 \qquad \pm 19$$

It can be seen from the above quadratic ephemeris that the rate of increase of the orbital period is $4{\cdot}34 \times 10^{-8}$ day per cycle for KO Aql and the rate of decrease of the period is $4{\cdot}08 \times 10^{-9}$ day per cycle for TV Cas. Let us now define the characteristic period change by ($\dot{P}/P$) where P is the period used in the computation of the time

Table 1. Photoelectric times of primary minima of KO Aql.

	JD⊙	E	$(O-C)$ d	Reference
243	8937.5280	−1030	+0.00750	Pohl and Kizilirmak (1966)
	8980.4940	−1015	+0.01305	Blanco and Cristaldi (1974)
	9361.4030	− 882	+0.00606	Blanco and Cristaldi (1974)
	9696.4920	− 765	+0.00355	Blanco and Cristaldi (1974)
	9762.3640	− 742	+0.00286	Blanco and Cristaldi (1974)
244	0355.2140	− 535	−0.00135	Blanco and Cristaldi (1974)
	0435.4076	− 507	−0.00059	Pohl and Kizilirmak (1970)
	1148.5600	− 258	+0.00834	Pohl and Kizilirmak (1972)
	1827.3238	− 21	−0.00297	Hayasaka (1979)
	1887.4710	0	−0.00040	Kizilirmak and Pohl (1974)
	2245.4798	+ 125	+0.00465	Pohl and Kizilirmak (1975)
	2637.8558	+ 262	+0.00854	Margrave *et al.* (1978)
	2652.1712	+ 267	+0.00379	Hayasaka (1979)
	2947.1727	+ 370	+0.01020	Hayasaka (1979)
	3010.1771	+ 392	+0.00594	Hayasaka (1979)
	3305.1815	+ 495	+0.01525	Hayasaka (1979)
	3348.1400	+ 510	+0.01330	Hayasaka (1979)
	3351.0080	+ 511	+0.01727	Hayasaka (1979)
	3766.3019	+ 656	+0.02682	Cristescu, Oprescu and Suran (1979)
	4135.7568	+ 785	+0.02185	Margrave (1979b)

Table 2. Photoelectric times of primary minima of TV Cas

	JD⊙	E	$(O-C)$ d	Reference
243	2827.7665	−2017	−0·00218	Huffer and Kopal (1951)
	3181.2282	−1822	−0·00002	Tchudovichev (1958)
	3184·8515	−1820	−0·00194	Huffer and Kopal (1951)
	3213·8516	−1804	−0·00365	Huffer and Kopal (1951)
	6483·8091	0	0·0	Chou (1959)
	8472·2386	+1097	−0·00696	Lavrov (1966)
	8733·2560	+1241	−0·00583	Kristenson (1966)
	8791·2585	+1273	−0·00694	Lavrov (1966)
	8829.3230	+1294	−0·00732	Lavrov (1966)
	8840·1985	+1300	−0·00750	Lavrov (1966)
	9389.4182	+1603	−0.00953	Popovici (1968)
244	0056.4558	+1971	−0·01352	Pohl and Kizilirmak (1970)
	0105.3960	+1998	−0·01387	Pohl and Kizilirmak (1970)
	0105.3977	+1998	−0·01217	Pohl and Kizilirmak (1970)
	0154.3360	+2025	−0·01442	Bakos and Tremko (1973)
	0183.3372	+2041	−0·01503	Bakos and Tremko (1973)
	0194.2127	+2047	−0·01521	Bakos and Tremko (1973)
	0201.4632	+2051	−0.01516	Bakos and Tremko (1973)
	0203.2765	+2052	−0.01447	Popovici (1968)
	0203.2770	+2052	−0.01397	Pohl and Kizilirmak (1970)
	0442.5406	+2184	−0.01528	Walter (1979)
	0493.2930	+2212	−0.01605	Pohl and Kizilirmak (1970)
	0502·3569	+2217	−0·01522	Popovici (1970)
	0859.4399	+2414	−0·01698	Walter (1979)
	0899·3175	+2436	−0·01686	Pohl and Kizilirmak (1972)
	0948·2560	+2463	−0·01891	Grauer *et al.* (1977)
	0986·3210	+2484	−0·01879	Grauer *et al.* (1977)
	1207·4605	+2606	−0·01807	Walter (1979)
	1575·4190	+2809	−0·02001	Papousek (1974)
	1593·5455	+2819	−0·01964	Walter (1979)
	1595·3584	+2820	−0·01936	Papousek (1974)
	1604·4213	+2825	−0·01952	Papousek (1974)
	1671·3000*	+2862	−0·20750	Kizilirmak and Pohl (1974)
	1749·4291	+2905	−0·02076	Grauer *et al.* (1977)
	1919·8125	+2999	−0·02298	Scarfe and Barlow (1978)
	1981·4405	+3033	−0·02382	Walter (1979)
	1990·5030	+3038	−0·02439	Tremko and Bakos (1977)
	1992·3150	+3039	−0·02500	Tremko and Bakos (1977)
	2016·4240*	+3052	+0·52003	Pohl and Kizilirmak (1977)
	2019·5040	+3054	−0·02520	Tremko and Bakos (1977)
	2289·5820	+3203	−0·02653	Pohl and Kizilirmak (1975)
	2320.3969	+3220	−0·02606	Walter (1979)
	2590.4729	+3369	−0·02939	Pohl and Kizilirmak (1976)
	2659·3513	+3407	−0·03029	Pohl and Kizilirmak (1976)
	2775.3610	+3471	−0·02782	Tremko and Bakos (1977)
	3063.5585	+3630	−0.03579	Grauer *et al.* (1977)
	3090.7471	+3645	−0.03638	Grauer *et al.* (1977)
	3130.6234	+3667	−0.03757	Grauer *et al.* (1977)
	3442.3897	+3839	−0.04070	Ebersberger, Pohl and Kizilirmak (1978)
	3786.7774*	+4029	−0.04947	Margrave (1979a)
	3795.8442	+4034	−0.04574	Margrave (1979a)
	4094.9219	+4199	−0·04918	Margrave (1979b)
	4114.8601	+4210	−0.04973	Margrave (1979b)

*not included in the analysis

Table 3. Photoelectric times of primary minima of Z Her.

	JD⊙	E	$(O-C)$ d	Reference
243	3801·0030	+5188	+0·01754	Baglow (1952)
	3852·9058	+5201	+0·01401	Popper (1956)
244	0740·4884	+6926	+0·02523	Kizilirmak (1971)
	0752·5671	+6929	+0·02555	Kizilirmak (1971)
	0772·4314	+6934	+0·02587	Kizilirmak (1971)
	0816.3533	+6945	+0·02703	Kizilirmak (1971)
	0832.3241	+6949	+0.02665	Kizilirmak (1971)
	1111.8211	+7019	+0·02800	Scarfe *et al.* (1973)
	2217.8226	+7296	+0.02528	Scarfe and Barlow (1978)

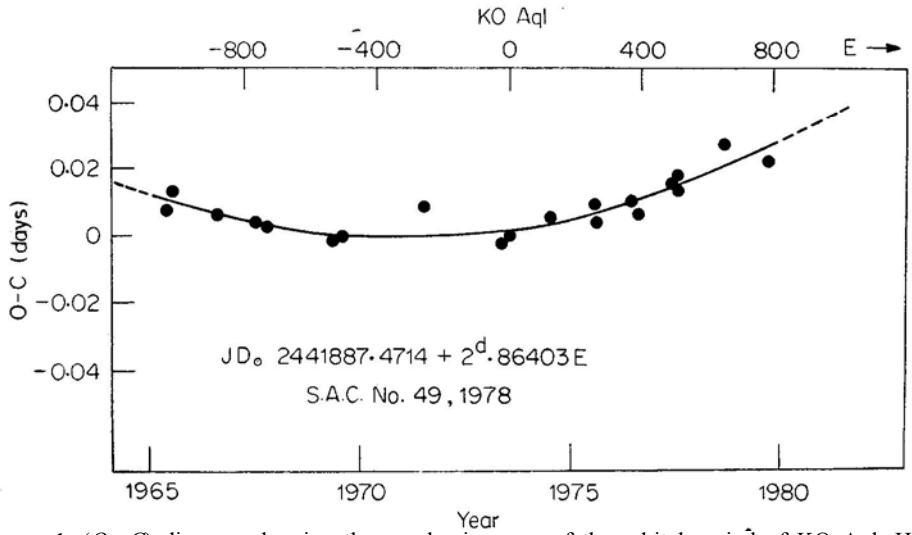

Figure 1. (O—C) diagram showing the secular increase of the orbital period of KO Aql. Here S.A.C. stands for *Supplemento ad Annuario Cracoviense*

residuals and P its time derivative. With this definition the observed values of the characteristic period change become

$$(\dot{P}/P) = +61{\cdot}24 \times 10^{-15}\ \mathrm{s}^{-1} \text{ for KO Aql,}$$

$$(\dot{P}/P) = -14{\cdot}37 \times 10^{-15}\ \mathrm{s}^{-1} \text{ for TV Cas,}$$

$$(\dot{P}/P) = 0 \qquad \text{For Z Her}$$

It is to be noted that the periods assumed by us are slightly different from those given in the fifth edition of the *Finding List for Observers of Interacting Binary Stars* (Wood *et al*. 1980). However, this does not alter the analysis because the least squares fit gives the best values of the initial epoch, period and $\dot{P}/P$ that satisfy all the data used.

3. An equation for $\dot{P}/P$

Almost all investigators in the field of eclipsing binaries have completely neglected the crucial role of rotational angular momentum and rotational energy in their

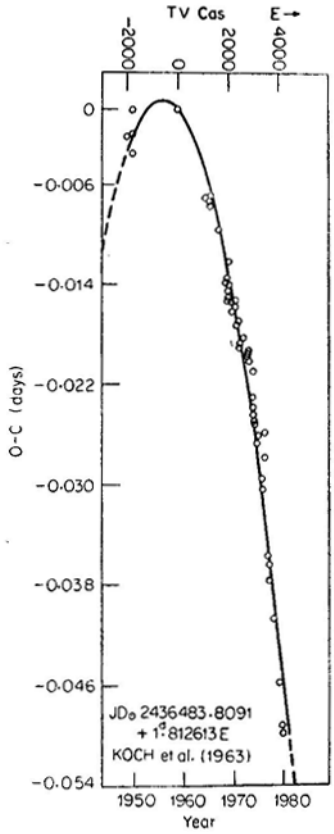

Figure 2. (*0— C*) diagram showing the secular decrease of the orbital period of TV Cas.

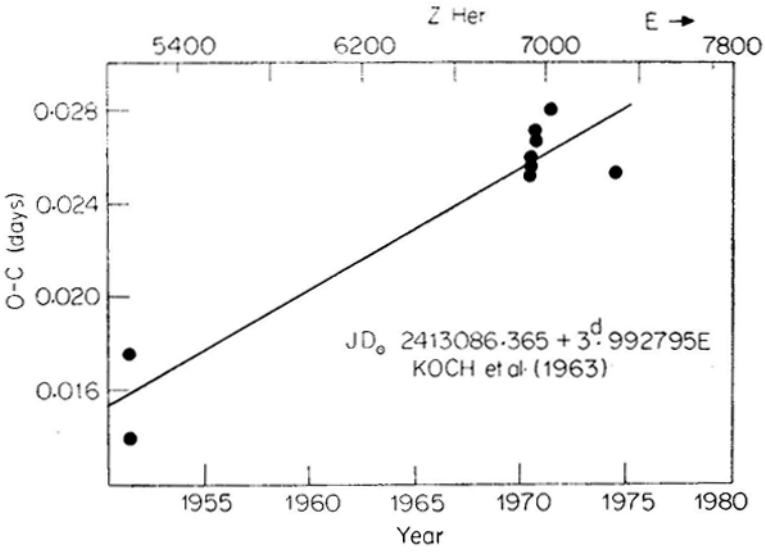

Figure 3. (*O*—*C*) diagram showing the constancy of the orbital period of Z Her.

studies. This practice becomes highly objectionable when the dimensions of the components are nearly comparable with the distance separating them. Therefore, any analysis of the behaviour of the orbital period of binaries should invariably include the contribution of angular momentum as well as energy arising out of the rotation of the components of the system.

We wish to consider here the effect of contraction (or expansion) of the components of a close binary system on the orbital period. It is easy to derive a simple formula for the characteristic period change of a binary system whose components undergo changes in their physical dimensions during their course of evolution. Let us make the following reasonable assumptions:

(1) Total mass of each component of the binary system remains constant;
(2) Orbit is circular.
(3) Orbital motion and rotation are synchronized.
(4) Total angular momentum, *i.e*. the sum of rotational and orbital angular momenta is conserved.
(5) Total energy of the system is conserved.
(6) Stars are spherical, *i.e*. distortions due to proximity effects and rotation are neglected.

Now the total angular momentum J of the system is given by

$$J=I_1W+I_2W+m_1r^2_1W+m_2r^2_2W, \tag{1}$$

where I_1, I_2 = the moments of inertia of the primary and secondary,
m_1, m_2 = the masses of the primary and secondary,
W = Keplerian angular velocity,
r_1, r_2 = the distances of the centres of the primary and secondary from the common centre of mass of the system.

The first two terms in equation (1) represent the rotational part of the total angular momentum. Using $m_1r_1=m_2r_2$ equation (1) becomes

$$J=I_1W+I_2W+\mu a^2\ W, \tag{2}$$

where $a=r_1+r_2$ and $\mu=m_1m_2/(m_1+m_2)$.

Differentiating equation (2) with respect to time and equating J to zero, we get

$$\dot{a} = -\frac{(I_1+I_2+\mu a^2)\ (\dot{W}/W)+(\dot{I}_1+\dot{I}_2)}{2\mu a}. \tag{3}$$

Let E represent the total energy of the system, then

$$E=\tfrac{1}{2}I_1W^2+\tfrac{1}{2}I_2W^2+\tfrac{1}{2}\mu a^2W^2-(Gm_1m_2/a), \tag{4}$$

where G is the gravitational constant. But $Gm_1m_2/a = \mu a^2 W^2$ according to virial theorem for a stable and steady dynamical system. Hence

$$E = \tfrac{1}{2} I_1 W^2 + \tfrac{1}{2} I_2 W^2 - \tfrac{1}{2} \mu a^2 W^2. \tag{5}$$

Differentiating equation (5) with respect to time and equating $\dot{E}$ to zero, we have

$$\dot{a} = + \frac{2(I_1 + I_2 - \mu a^2)\,(\dot{W}/W) + (\dot{I}_1 + \dot{I}_2)}{2\mu a}. \tag{6}$$

Equating right hand sides of equation (3) and (6), we get

$$\frac{\dot{W}}{W} = - \frac{2(\dot{I}_1 + \dot{I}_2)}{3I_1 + 3I_2 - \mu a^2}$$

or

$$\frac{\dot{P}}{P} = \frac{2(\dot{I}_1 + \dot{I}_2)}{3I_1 + 3I_2 - \mu a^2}. \tag{7}$$

Let $I = kmR^2$, then

$$\dot{I} = 2kmR\dot{R} + mR^2\dot{k} = 2I(\dot{R}/R) + I(\dot{k}/k). \tag{8}$$

However for homologous contraction or expansion, which will be valid for a small period of time, k can be taken as constant. Hence equation(7)becomes

$$\frac{\dot{P}}{P} = \frac{4(I_1\dot{R}_1/R_1 + I_2\dot{R}_2/R_2)}{3I_1 + 3I_2 - \mu a^2}, \tag{9}$$

where R_1 and R_2 are radii of primary and secondary components respectively. We would like to point out here that the dominant term (μa^2) in the denominator on the right hand side of equation (9) is negative which makes the sign of the period change opposite to that of the change in radius.

Equation (9) involves the moments of inertia of the components and their contractional rates. If we have a fair estimate of these quantities then the characteristic period change ($\dot{P}/P$) can be theoretically calculated. We can then apply equation (9) to systems whose components have been suspected to be in the pre-main sequence contraction phase of evolution, and see how far theoretical ($\dot{P}/P$) agrees with observed ($\dot{P}/P$).

4. Contractional rates of the components of the systems

Iben (1965) has discussed in detail the pre-main sequence evolution of single stars of various masses. Let us assume that each component of the system evolves similar

to single stars in this phase of evolution. Therefore, we can confine our attention to those model calculations for stars whose masses correspond to the masses of the individual components of our systems. For example, Iben's (1965) calculations for $3M_{\odot}$ and $1{\cdot}5M_{\odot}$ model stars can be used for the components of TV Cas because these represent fairly well the masses of its components. From the graphs (Iben 1965) relating age with radius of model stars, both the age and contractional rate of the component in question can be estimated from the known value of its radius. For example, in the $3M_{\odot}$ track, the radius $3{\cdot}08R_{\odot}$ of the primary component of TV Cas gives its age to be about $1{\cdot}06\times10^{6}$ years. The slope at this point ($3{\cdot}08R_{\odot}$, $1{\cdot}06\times10^{6}$ years) gives the contractional rate of this component at the present time to be $-0{\cdot}087$ mm s^{-1} or $-2{\cdot}75$ km yr^{-1}. Thus using the appropriate evolutionary tracks the relative contractional rates have been estimated for different components of the systems. These values are given in Table 4. We also list the absolute dimensions used in our discussion taken from the literature. We have included in the table the system of TT Hya, the secondary of which is suspected to be in the pre-main sequence phase by Kulkarni (1979).

5. Moments of inertia of components

The moments of inertia of stars can be calculated easily assuming uniform distribution of density. But seldom does it represent the actual state of affairs in the stars. Based on the available information one can assume some specific polytropic distribution inside the stars, and hence calculate the moments of inertia. From Iben's (1965) graph relating age with the central density ρ_c for a particular mass of star, the ratio of central to mean density ρ_c/ρ_m can be obtained, finding ρ_c through the known age of the star. ρ_c / ρ_m values for the components of the four binaries have been given in Table 5.

Table 4. Dimensions and contraction rates.

Star	Component	Mass $M_{\odot}$	Radius $R_{\odot}$	Age 10^6 yr	Relative contractional rate $\dot{R}/R$ 10^{-15} s^{-1}	Distance between the components $R_{\odot}$	Reference
KO Aql	Primary	2.91	2.7	1.17	−44.79	13.06	Hayasaka (1979)
	Secondary	0.58	2.6	0.83	−16.99		
TV Cas	Primary	3.10	3.08	1.06	−40.67	10.50	Tremko and Bakos (1977)
	Secondary	1.39	3.36	0.70	−18.37		
Z Her	Primary	1.22	1.6	3.66	− 1.98	14·08	Popper (1956)
	Secondary	1.10	2.6	0.87	−10.78		
TT Hya	Primary	2.61	2.01	1.50	− 8.25	22.80	Kulkarni (1979)
	Secondary	0.70	5.53	0.10	− 9.84		

By comparing ρ_c/ρ_m values of the components with Eddington's (1926) table giving ρ_c/ρ_m values for different polytropic indices, we can fix the polytropic index η for each component of the systems. These are given in column (4) of Table 5. Eddington (1926) has reproduced Emden's tables, giving the masses interior to different points on the radii of stars of various polytropic indices. For a star of particular polytropic index these tabulated values were modified to its mass and radius. The moments of inertia were computed using the formula

$$I = \frac{2}{5}\sum_{i=1}^{N} m_i \frac{R_i^5 - R_{i-1}^5}{R_i^3 - R_{i-1}^3},$$

where R_i and R_{i-1} represent the outer and inner radii of the ith shell of mass m_i. N indicates the total number of shells. It should be mentioned here that for n1·5 and 3·0 we took N=12 and 17, respectively. The moments of inertia thus calculated are shown in last column of Table 5.

6. Discussion

Taking relevant data from Tables 4 and 5, the theoretical value of $(\dot{P}/P)$ can be calculated using equation (9). The observed and theoretical characteristic period changes have been given in Table 6. It is quite obvious from this table that there is

Table 5. Moments of inertia

Star	Component	Central condensation	Polytropic index n	Moment of inertia 10^{46} kg m^2
KO Aql	Primary	127·73	3	162·16
	Secondary	6·31	1·5	79·75
TV Cas	Primary	108·54	3	224·76
	Secondary	6·92	1·5	319·21
Z Her	Primary	7·36	1·5	63·53
	Secondary	6·31	1·5	151·26
TT Hya	Primary	64·69	3	80·61
	Secondary	—	1·5	435·00

Table 6. Comparison of theoretical and observed period changes.

System	$(\dot{P}/P)_{th}$ 10^{-15} s^{-1}	$(\dot{P}/P)_{obs}$ 10^{-15} s^{-1}
KO Aql	+4·77	+61·24
TV Cas	+7·00	−14·37
Z Her	+0·67	0
TT Hya	+0·76	—

no agreement at all between the theoretical and the observed values of $(\dot{P}/P)$. For KO Aql the observed value is about an order of magnitude higher than the theoretical value. This points to the fact that the period change occurring in these systems is not dimensional changes. However, it may be noted that the period variations occurring due to dimensional changes are not small enough to be neglected in the case of KO Aql and TV Cas. They are sufficiently large to be detectable photometrically over a time interval of a few decades. Any suspicion that these systems belong to the pre-main sequence can therefore be ruled out.

In the case of Z Her, $(\dot{P}/P)_{th}$ is very small. Therefore, the variation in its orbital period owing to changing dimensions cannot be detected at present due to insufficient data. In addition, Kulkarni's (1979) speculation that TT Hya is in the pre-main sequence phase can neither be confirmed nor rejected by analysing minima over a brief period of time, since $(\dot{P}/P)_{th}$ is very small for this system. We have not analysed the variation of period of this system for lack of accurately determined minima. The other two systems, KO Aql and TV Cas are probably not in the pre-main sequence phase of evolution, since there is no agreement between $(\dot{P}/P)_{obs}$ and $(\dot{P}/P)_{th}$ Therefore, the idea of subgiant secondaries being undersized is also doubtful. This supports Hall's (1974) conclusion that no system exists with undersize secondaries. Also, Field's (1969) belief that KO Aql and TV Cas are in pre-main sequence appears to be invalid. In this connection, we may note that in the recent discussion of TV Cas, Cester *et al*. (1979) have shown that the secondary is almost filling its Roche lobe.

We would like to point out that equation (9) for characteristic period change is derived on the assumption of continuous synchronisation between the orbital and angular motions. Our justification for this is based on the following reasons. (1) We have to make this simplifying assumption, in order to be able to evaluate the effect of the changing sizes of stars; (2) The assumption is not totally invalid in close binary systems where tidal forces are strong; and (3) All theoretical calculations of binary evolution invoke Roche model which presupposes circular orbit and complete synchronization of orbital and angular motions. But even if there were no instantaneous synchronization, contrary to our assumption, then the effect of changing size on period change will be less and we would get a lower estimate for $(\dot{P}/P)$ due to shrinking dimensions of the components of the binary. Thus the $(\dot{P}/P)$ values obtained by us represent the upper limit of the expected values and even this is inadequate to explain the observed period changes. It seems probable, therefore, that the observed period changes in KO Aql and TV Cas may be due to some other cause as discussed below.

It has been suspected that the period change found in TV Cas may be due to a third body (Frieboes Conde and Herczeg 1973, Grauer *et al*. 1977). Some authors (Tremko and Bakos 1977; Chaubey 1979; Wood *et al*. 1980) believe that the period change in TV Cas is due to mass transfer. But we support the former view although at present it is an indecisive conclusion. If there is mass transfer from the secondary component to the primary component then there should be a secular increase in the period contrary to what we observe. So mass transfer and mass loss do not seem to be appropriate to explain the observed period change in TV Cas.

Further, we suspect that the period change observed in KO Aql may also be attributed to light-time effect. However one can assume that there is mass transfer from

Secondary to primary, if the secondary is not undersize. Then the conservative mass transfer equation gives a mass flow rate of about 0.47×10^{-6} M yr $^{-1}$It may be noted that both KO Aql and TV Cas appear more or less similar in some respects. There fore the mechanism responsible for the period change in both cases should also be the same. If this is the case then mass transfer and mass loss cannot be the mechanism causing the period changes. But the third body hypothesis seems fairly reason able for these systems. The solution of third body orbit will lead to highly uncertain elements at present. To attain best representative values for the third body orbital elements, precise astrometric studies of these binaries are very essential. The import ance of such studies for all eclipsing binaries should be realised.

References

Baglow, R. L. 1952, *Pub. David Dunlap Obs.*, **2,**'No. 1.
Bakos, G. A., Tremko, J. 1973, *Bull. astr. Inst. Csl*., **24,** 304.
Blanco, C., Criztaldi, S. 1974, *Publ. astr. Soc. Pacific*, **86**, 187.
Cester, B., Fedel, B., Giuricin, G., Mardirossian, F., Mezzetti, M., Predolin, F. 1979, *Mem. Soc. astr. Ital*.,**50**, 551.
Chaubey, U. S. 1979, *Astrophys. Sp. Sci*., **63**, 247.
Chou, K. C. 1959, *Astr. J.,* **64**, 468.
Cristescu, C., Oprescu, G., Suran, M. D. 1979, *Inf. Bull. Var. Stars,* No. 1589.
Ebersberger, J., Pohl, E., Kizilirmak, A. 1978, *Inf. Bull. Var. Stars,* No. 1449.
Eddington, A. S. 1926, *The Internal Constitution of the Stars,* Cambridge Univ. Press, London, p. 82.
Field, F. V. 1969, *Mon. Not. R. astr. Soc.,* **144**, 419.
Frieboes-Conde, H., Herczeg, T. 1973, *Astr. Astrophys. Suppl. Ser*., **12**,1.
Grauer, A. D., McCall, J., Reaves, L. C., Trible, T. L. 1977, *Astr. J*., **82**, 740.
Hall, D.S.1968, *Publ. astr. Soc. Pacific,* **80**, 477.
Hall, D. S. 1974, *Acta Astr.,* **24**, 215.
Hall, D. S. 1975, *Acta Astr*., **25**, 95.
Hayasaka, T.1979, *Publ.astr.Soc.Japan,* **31**, 271.
Huffer, C. M., Kopal, Z. 1951, *Astrophys. J*., **114,** 297.
Iben, I. 1965, *Astrophys. J*., **141,** 1002.
Kizilirmak, A. 1971, *Inf. Bull. Var. Stars*, No. 530.
Kizilirmak, A., Pohl, E. 1974, *Inf. Bull. Var. Stars,* No. 937.
Koch, R. H., Sobieski, S., Wood, F. B. 1963, *Publ. Univ. Pα. astr. Ser*., **9**.
Kopal, Z. 1959, *Close Binary System,* Chapman and Hall, London, p. 467.
Kristenson, H. 1966, *Bull. astr. Inst. Csl*., **17**,123.
Kulkarni, A. G. 1979, *PhD thesis,* Osmania University, Hyderabad.
Lavrov, M. I. 1966, *Contr. astr. Inst. Kazan*, No.31,91.
Margrave, T. E. 1979a, *Inf. Bull. Var. Stars,* No. 1631.
Margrave, T. E. 1979b, *Inf. Bull. Var. Stars,* No. 1694.
Margrave, T. E., Doolittle, J. H., Cutlillo, D., Scherrer, J. S. 1978, *Inf. Bull. Var. Stars,* No. 1478.
Papousek, J. 1974, *Bull. astr. Inst. Csl*., **25**, 152.
Pohl, E., Kizilirmak, A. 1966, *Astr. Nachr.,* **289**,191.
Pohl, E., Kizilirmak, A. 1970, *Inf. Bull. Var. Stars,* No. 436.
Pohl, E., Kizilirmak, A. 1972, *Inf. Bull. Var. Stars,* No. 647.
Pohl, E., Kizilirmak, A. 1975, *Inf. Bull. Var. Stars,* No. 1053.
Pohl, E., Kizilirmak, A. 1976, *Inf. Bull. Var. Stars,* No. 1163.
Pohl, E., Kizilirmak, A. 1977, *Inf. Bull. Var. Stars,* No. 1358.
Popovici, C. 1968, *Inf. Bull. Var. Stars,* No. 322
Popovici, C. 1970, *Inf. Bull. Var. Stars,* No. 419.
Popper, D. M. 1956, *Astrophys. J*., **124,** 196.
Roxburgh, I. W. 1966a, *Astrophys, J*., **143**, 111,

Roxburgh, I. W. 1966b, *Astr. J.* **71**, 133.
Scarfe, C. D., Barlow, D. J. 1978, *Inf. Bull. Var. Stars,* No. 1379.
Scarfe, C. D., Niehaus, R. J., Barlow, D. J. Baldwin, B. W. 1973, *Inf. Bull. Var. Stars,* No. 844.
Tchudovichev, N. I. 1958, *Astr. Cirk.*, **188**. 25.
Tremko, J., Bakos, G. A. 1977, *Bull. astr. Inst. Csl.*, **27**, 41.
Walter, K. 1979, *Astr. Astrophys., Suppl. Ser.*, **35,** 281.
Wood, F. B., Oliver, J. P., Florkowski, D. R., Koch, R. H., 1980, *Publ. Dept. Astr. Univ. Florida,* **1**,17.

J. Astrophys. Astr. (1981) **2,** 43–58

Extragalactic Sources with One-sided Radio Structure

Vijay K. Kapahi *Tata Institute of Fundamental Research, Radio Astronomy Group, Indian Institute of Science Campus, Bangalore 560012*

Received 1980 October 31; accepted 1981 February 9

Abstract. A list has been compiled of 49 extragalactic sources, most of them identified with quasars, that appear to have a one-sided (D_2 type) radio structure characterized by a single outer component displaced from a compact central (nuclear) component coincident with the optical object. The observed properties of a subsample of 28 D_2 quasars that have an overall angular size larger than 5 arcsec are briefly discussed and compared with those of normal (D_1 type) double quasars. It is found that the central components in most D_2 sources account for more than half the total flux density at high frequencies in contrast to the D_1 quasars which generally have less than 20 per cent of their total flux density in a central component. This makes it very unlikely that D_2 sources are just those D_1s in which there is a large intrinsic difference in the flux densities or separations of the two outer components. The observed properties of D_2 sources are easier to understand in the relativistic beaming interpretation in which their axes are inclined at smaller angles with the line of sight compared to D_1 sources.

Key words: quasars and radio galaxies—double radio sources—asymmetric structure—relativistic beaming

1. Introduction

A vast majority of powerful extragalactic radio sources either have a double structure with the two radio lobes more or less symmetrically placed on either side of the optical object or have only a compact structure ($\lesssim$ 1 arcsec) coincident with the optical object. Observations of double sources with high sensitivity often show up an additional weak and compact central component at the position of the optical identification. In recent years a number of radio sources have, however, been found to consist of a single radio lobe displaced from a compact central component. Such sources are now often referred to as D_2 type doubles (after Miley 1971) in contrast to the classical doubles (with or without central components) being referred to as of

D1 type. Most D2 sources are identified with quasars; 3C 273, the first to have shown a one-sided radio structure (Hazard, Mackey and Shimmins 1963), is the standard example of this type. It is not clear if such sources result from one-sided ejections from galactic nuclei or whether they are double sources in which for some reason (intrinsic or extrinsic to the source) one of the outer components remains invisible to us. Three kinds of explanations in the latter category have been suggested.

(a) *Projection effects*. If the axis defined by the outer components does not pass through the nuclear component, then, for some directions of view the superposition of components can make a source appear to consist of only 2 components, one of them coincident with the optical object.

(b) *Intrinsic asymmetries.* Due to intrinsic asymmetry in the brightness or linear displacement of the two outer components, a source can appear to be of the D2 type if one component is either too weak to be detected by the observing instrument or too close to the nuclear component to be resolved by the instrument.

(c) *Relativistic beaming.* If the outer components are moving out at relativistic speeds, a large apparent asymmetry can arise in the observed flux densities provided the source axis makes a small angle with the line of sight.

The phenomena of apparent faster-than-light expansion (*e.g*. Cohen *et al.* 1977) and of the considerable bending of radio structure close to the nucleus (Readhead *et al*. 1978), observed by VLBI techniques in the cores of a few compact and D2 type sources have also been explained by the relativistic beaming of radio waves from narrow jets aimed close to our line of sight (Readhead *et al*. 1978; Scheuer and Readhead 1979; Cohen *et al*. 1979; Blandford and Königl 1979). Observations of a larger sample of D2 sources are clearly needed to test the beaming model and to understand the asymmetry in such sources. The purpose of this paper is to compile a list of radio sources that appear to belong to the D2 category. The list of 49 such sources found, most of them identified with quasars, is presented in Section 2. The fairly common occurrence of D2 structures implies that their explanation in terms of chance superposition of components in non-collinear double sources can be discarded because it predicts that most double sources should depart strongly from collinearity, contrary to observations.

Thirty three of the 49 sources have an overall angular size >5 arcsec and are probably free from serious selection effects. The observed properties of the 28 quasars in this sample are briefly discussed in Section 3 and compared with those of D1 quasars. The comparison leads us to rule out intrinsic asymmetries as a general explanation for the D2 phenomenon and to provide some support to the beaming hypothesis.

For brevity we shall henceforth refer to the central components as CCs and to the outer components as OCs.

2. List of D2 sources

Brightness distributions across hundreds of radio sources, determined with a variety of telescopes at several different observing frequencies have been reported in the literature. We have considered a radio source to be of the D2 type if it consists of one component coincident with an optical object and one or more secondary components located on one side of the optical identification. Since the observations span a

wide range in sensitivity and angular resolution, any list of D2 sources compiled from the literature is unlikely to be homogeneous and free from various observational selection effects. In order to restrict the number of doubtful entries in the list and to be fairly objective in our selection we have adopted the following procedure.

(1) We have generally used only the observations made with aperture synthesis telescopes (mainly the Cambridge 5-km telescope, the Westerbork synthesis array, the NRAO 3-lement interferometer and the Very Large Array) or by the lunar occultation technique (mainly using the Ooty Radio Telescope). Most of the synthesis observations have been made at cm wavelengths (frequencies near 1·4, 2·7, 5 and 8 GHz) with angular resolutions ranging between about 1 and 20 arcsec. The lunar occultation observations at 327 MHz have similar angular resolutions.

(2) We have only considered the sources that are optically identified and for which the accurate optical positions (~l arcsec accuracy or better) are known. Apart from excluding ' empty field ' sources, the necessary requirement of an optical identification can discriminate against D2 sources that have very weak or no detected CCs. Such sources would show a genuine displacement between the true optical identification and the observed radio position and could therefore be wrongly considered as unidentified. This possibility has been discussed in Section 3.2 where we have argued that D2 sources in which the CCs contribute only a small fraction of the total flux density at high frequencies are likely to be quite rare.

(3) Although the spectral indices of most CCs in Dl sources and of the few well known D2 sources are known to be relatively flat ($\alpha<0{\cdot}5$, with the definition $S \propto \nu^{-\alpha}$), it is important not to introduce a bias in the sample with regard to spectral information. We have therefore considered a restricted sample of D2 sources that have an LAS (largest angular size; in the present case the separation between the CC and the OC)>5 arcsec. The criterion of agreement in the radio and optical positions (both generally known to an accuracy of ~1 arcsec or better) of the CCs alone has been used in this sample to make the D2 classification, regardless of any available spectral information. For sources with LAS<5 arcsec, positional coincidence alone may not be sufficient in most cases and we have therefore imposed a restriction that the suspected CC be known to have a flat spectral index ($\alpha<0{\cdot}5$). Only the restricted sample with LAS>5 arcsec has been used for the purpose of a statistical investigation of the properties of D_2 sources.

(4) We do not include the well known head-tail sources which are generally found in clusters of galaxies and have a one-sided radio structure.

The list of 33 sources with LAS>5 arcsec that satisfy the above criteria and the 16 sources with LAS<5 arcsec is presented in Table 1 which is arranged as follows:

Columns 1 *and* 2. The source name in coordinate designation and one alternate name or the catalogue in which the source appears.

Column 3. Optical identification;Q = QSO; G=galaxy; BSO=blue stellar object and RO = red object.

Columns 4 *and* 5. The redshift and a coded reference for it, or the approximate magnitude and reference to the optical identification if redshift is not known. The references are given at the foot of the Table.

Columns 6 *and* 7. The observed LAS and the corresponding linear size (calculated for q_0 =0·5, H_o =50 km s $^{-1}$ Mpc $^{-1}$).

Table 1. Radio sources with one-sided (D2 type) structure.

(1)	(2)	(3)	(4)	(5)	(6)	(7)	(8)	(9)	(10)	(11)	(12)
Source	Other name	Optical Identification			LAS (arcsec)	Lin size (kpc)	Ref to radio structure	Spect indices		f_c	Notes
		Type	z	Ref				α_c	α_e		
0003−003	3C 2	Q	1·037	1	6	51	PW, J80	0·7	0·9	0·63	*
0051+291	4C 29·01	Q	1·828	1	2·7	23	PW, RP	0·1	0·7	0·63	
0115+027	4C 02·04	Q	0·672	1	9	71	MH			0·58	
0241+622	4U	Q	0·044	1	3·8	5	TSMB	−0·2	0·7	0·92	*
0309+411	S4	G	m = 18	2	87		K79	−0·2			
0409+229	4C 22·08	Q	12·13	1	3·4	29	PW, SN				*
0615+578	4C 57·12	BSO	m = 18	3	6·6		OPN	1·1		(0·8)	*
0740+380	3C 186	Q	1·063	1	100	857	S80, RP, HC	1·0	0·8	0.9	*
0742+376	4C 37·19	BSO	m = 20	4	56		KLP			(0·34)	
0814+201	OTL	RO	m = 20	5	12		SG				*
0821+394	4C 39·23	Q	1·216	1	24	207	K80, PW, SN	0·1		0·85	
0836+195	4C 19·31	Q	1·691	1	18	152	JPR, MH			0·31	
0836+710	4C 71·07	Q	m = 16·5	6	1·5		PFJ	0·4	1·7		
0919+218	4C 21·25	Q	1·421	1	6	52	PW	0·6	1·0	0·41	
0932+022	4C 02·27	Q	0·659	1	38	298	MH, BHSS	0·5	0·9	0·51	
0945+408	4C 40·24	Q	1·252	1	4.1	35	PFJ	0·2	0·7	0·9	
1012+232	4C 23·24	Q	0·565	1	11·2	84	PW	−0·3	1·0	0·92	
1040+123	3C 245	Q	1·029	1	4·6	39	JPR, L72	0·6	0·9	0·72	*
1047+096	4C 09·37	Q	0·786	1	71	582	MH	0·9	1·1	0.81	
1055+201	4C 20·24	Q	1·110	1	23	198	MH	<0		0·42	*
1055+018	4C 01·28	Q	0·890	1	1·5	13	SGV	0·1			*
1132+303	4C 30·22	Q	0·614	1	7·8	60	PW	0·8	1·2	0·50	
1136−135	PKS	Q	0·554	1	9	67	MH			0·69	
1203+109	4C 10·34	Q	1·088	1	10	86	MH			0·94	
1222+216	4C 21·35	Q	0·435	1	10·1	68	PW	0·5	0·9	0·78	
1226+023	3C 273	Q	0·158	1	21	75	MH, PFJ	−0·3	0·8	0·93	
1320+29	B2	BSO	m = 20·5	7	52		F77, F79	0·3	0·9	(0·53)	*
1347+539	4C 53·28	BSO	m = 17	3	31·3		OPN	0·0		(>0·9)	

1350+316	3C 293	G	0·045	8	85	103	ARP	0·7	0·7	0·83	*
1354+195	4C 19·44	Q	0·720	1	15	120	MH			0·84	*
1415+463	4C 46·29	Q	1·552	1	12·7	108	OPN, K80	0·0		0·82	*
1419+31	B2	BSO	m = 20	7	128		F77, F79	−0·1	1·6	(0·77)	
1433+177	4C 17·59	Q	1·203	1	4·6	40	W79	0·2	0·9	0·47	
1509+158	4C 15·45	Q	0·828	1	8·2	68	W79	0·8	1·1	0·56	
1547+309	4C 30·29	G	0·111	9	11	30	CBV, KLP	1·0	1·1	0·68	
1636+473	4C 47·44	BSO	m = 18·5	6	18		K80	<0		(0·76)	*
1637+574	OS 562	Q	0·745	1	8·8	71	OPN	0·0		0·92	
1641+399	3C 345	Q	0·595	1	2·8	21	PJ, DSC	0·0	1·0	0·97	
1642+690	4C 69·21	Q	m = 19	3	4		PFJ	−0·7	1·3		
1729+501	4C 50·43	Q	1·111	1	20·8	179	OPN		0·9	0·09	
1741+279	4C 27·38	Q	0·372	1	4	25	PW	0·4	0·7	0·57	
1800+440	OU 401	Q	0·660	1	2·6	20	OPN, K80	−0·4			
1807+698	3C 371	G	0·050	8	3·3	4	PJ	−0·2	1·1	0·96	
1828+487	3C 380	Q	0·692	1	1·2	10	S77				*
1842+681	JB	BSO	m = 18	3	2·8		OPN	−0·4			
2037+511	3C 418	Q	1·686	1	1·6	14	PJ	0·2	1·2	0·94	
2041−149	OTL	RO	m = 20·5	10	28		SGV				*
2251+158	3C 454·3	Q	0.859	1	5·4	45	DSC	0.0	1.0	0·9	*
2251+134	4C 13·85	Q	0·673	1	6·6	52	W79	0·3	0·6	0·75	

References to redshift or optical identification:

1. Hewitt and Burbidge (1980)
2. Kapahi (1979)
3. Cohen *et al.* (1977)
4. Katgert-Merkelijn *et al.* (1980)
5. Subrahmanya and Gopal-Krishna (1979)
6. Kühr (Personal communication)
7. Fanti *et al.* (1975)
8. Sandage (1966)
9. Sargent (1973)
10. Singal *et al.* (1979)

Additional notes to Table 1.

0003—003 (*3C 2*): The one-sided structure of this source was first pointed out by Lyne (1972) from a lunar occultation at 408 MHz. A recent occultation observation at 327 MHz, (Joshi 1980) with the Ooty Radio Telescope has enabled the strip brightness distributions along and perpendicular to the source axis to be determined with a resolution of 0·6 arcsec. These show the outer component which accounts for ~ 30 per cent of the total flux density to have a narrow jet-like structure extending to ~ 6 arcsec from the CC in PA 196°. The CC itself consists of two compact components (< 1 arcsec) with a separation of~ l·2 arcsec along the source axis. The stronger of the two accounts for ~ 60 per cent of the total source flux density and lies at the extreme and opposite the jet. The location of the two with respect to the optical nucleus is, however, unclear. All the observed components appear to have normal spectral indices.

0241+622: This low redshift quasar is identified with the X-ray source 4U 0241 + 61 (Apparao *et al,* 1978).

0409+229: A model fit at 2·7 GHz (Potash and Wardle 1979) shows a single component of size 3·4 ± 0·7 arcsec. From the observed flux densities at 2·7 and 8·1 GHz and a position difference of ~ 1 arcsec at the two frequencies, Potash and Wardle conclude that the source is almost certainly a D2 double whose components have different spectral indices.

0615+578: The stronger component lies 1·7 arcsec from the optical position and has a steep spectral index ($\alpha = 1{\cdot}1$) between 2·7 and 8·1 GHz (Owen, Porcas and Neff 1978). There is therefore some doubt about its being the CC.

0740+380 (*3C 186*): Recent VLA observations at λ=6 cm (Schilizzi, Personal communication) show that the CC could itself be double with a separation of ~ 1·5 arcsec along the source axis. The OC which is ~ 100 arcsec away is therefore likely to be physically associated with the source. The total spectrum of the source is straight ($\alpha \sim 1$) except for a kink around 20 MHz (Veron, Veron and Witzel 1974), which could arise from synchrotron self absorption in one of the two components near the quasar.

0814+201: Structure based on lunar occulation at 327 MHz (Subrahmanya and Gopal-Krishna 1979). The two components have roughly equal flux density. Spectra of individual components are not known; the total spectral index is ~ 0·4 between 327 MHz and 2·7 GHz.

1040+123 (*3C 245*): Lunar occulations at 408 and 240 MHz (Lyne 1972) indicate that the CC may consist of two components with a separation of ~ 1·5 arcsec. The outer of the two then has $\alpha = 1{\cdot}2$ and the inner $\alpha = 0{\cdot}4$ between 240 MHz and 2·7 GHz. The spectral indices given in columns 9 and 10 are from Lyne (1972) for the total flux density from the CC.

1055+201: The total spectrum is flat at high frequencies (Kuhr *et al*. 1979) implying that the CC must have $\alpha < 0$ near 5 GHz.

1055+018: Structure based on lunar occultations at 327 MHz. The two components have a flux density ratio of about 2:1. The source is a radio variable even at metre wavelengths (McAdam 1976) and is known to have a flat spectrum from metre to cm wavelengths (Veron, Veron and Witzel 1974). The stronger component at 327 MHz is almost certainly the CC.

1320+29: There are two OCs on the same side of the CC.

1350+316 (*3C 293*): The central component has been resolved into a close double (separation ~1·5arcsec) at15GHz, in a PA quite different from that of the OC (Argue, Riley and Pooley 1978). All components have normal spectra.

1354+195: Structure based on limited angular resolution comparable to the LAS.

415+463: The model fit at 2·7 GHz (Owen, Porcas and Neff 1978) indicates that there could be two compact components separated by ~ 1·7 arcsec, close to the optical position.

1636+473: The total spectrum (Kühr *et al*. 1979) implies that the CC must have $\alpha < 0$ near 5 GHz.

1828+487 (*3C 380*): A 15.GHz map in Scott (1977) shows two components separated by 1·2 arcsec in PA — 37°. As the total spectrum is known to be flat at such high frequencies the stronger component is likely to be the CC. There could be an additional extended component or halo at lower frequencies.

2041—149: Structure based on lunar occultations at 327 MHz. The two components have roughly equal flux density. While the CC is not resolved (< 2·5 arcsec) the OC could have a narrow jet like structure.

2251+158 (3C 454·3): The spectral indices given in the table are estimated from the figure in Davis Stannard and Conway (1977).

Column 8. Reference to best available measurements of the radio structure.

ARP	Argue, Riley and Pooley (1978)	MH	Miley and Hartsuijker (1978)
BHSS	Bentley *et al.* (1976)	OPN	Owen, Porcas and Neff (1978)
CBV	Conway, Burn and Vallee (1977)	PFJ	Perley, Foimalont and Johnston (1980)
DSC	Davis, Stannard and Conway (1977)	PJ	Perley and Johnston (1979)
F77	Fanti *et al.* (1977)	PW	Potash and Wardle (1979)
F79	Fanti *et al.* (1979)	RP	Riley and Pooley (1975)
HC	Hiigbom and Carlsson (1974)	S80	Schilizzi, R. T. (Personal Communication)
JPR	Jenkins, Pooley and Riley (1977)	S77	Scott (1977)
J80	Joshi (1980)	SGV	Singal, Gopal-Krishna and Venugopal (1979)
K79	Kapahi (1979)	SN	Stannard and Neal (1977)
K80	Kapahi (1980)	SG	Subrahmanya and Gopal-Krishna (1979)
KLP	Katgert-Merkelijn, Lari and Padrielli (1980)	TSMB	Tzanetakis *et al.* (1978)
L72	Lyne (1972)	W79	Wills (1979)

Columns 9 and 10. The approximate spectral indices, α_c and α_e of the central and outer components respectively, if available. For most of the sources these refer to the frequency range of either 2·7 to 8·1 GHz or 1·4 to 5 GHz.

Column 11. The fraction of the total source flux density contained in the CC referred to a constant frequency of 8 GHz in the frame of reference of the source. For sources with unknown redshift the value is given in parenthesis and refers to the observed frequency of 5 GHz and therefore corresponds to 8 GHz at the source for a redshift of 0·6.

Column 12. Indication of additional notes on some sources at the foot of the table.

While scanning the literature we came across several cases where better observations indicated that a particular source previously considered to be of the D2 type was actually not so. In most of them an additional component on the other side of the optical object had been missed in the earlier observations either because of its low flux density or low surface brightness. It is quite possible that such weaker components exist also for the sources listed in Table 1. The upper limits on the flux densities of such undetected components depend not only on the characteristics of the telescopes used in the observations but also on the size of such components. For unresolved components we estimate that only in 4 or 5 sources with LAS>5 arcsec could the ratio of the flux density of the observed OC to that of the missing OC be < 3. In several cases this ratio is likely to exceed 10.

3. Observed properties and comparison with DI quasars

Of the 49 sources listed in Table 1 as many as 43 are identified with QSOs (33 confirmed QSOs and 10 BSOs of unknown redshift) and only 4 are identified with galaxies. The remaining two are faint red objects of unknown redshift. It thus appears that QSOs are much more likely to have one-sided radio structure than galaxies. It was pointed out by Riley and Jenkins (1977) that such a difference exists in the 3CR sample even when the comparison is restricted to QSOs and galaxies of comparable total luminosity. Although many more deep galaxy identifications and redshifts have recently become available (*e.g.* Smith and Spinrad 1980) no 3CR galaxy

with redshift >0·1 appears to have a D2 structure. Since the D2 quasars generally have dominant CCs (see Section 3·3) the paucity of such structures among galaxies could be related to the fact that their CCs are usually found to be much weaker than those of quasars (Riley and Jenkins 1977; Miley 1980).

In view of the predominance of QSOs in the D2 sample we shall compare the observed properties of the 22 QSOs and 6 BSOs with LAS> 5 arcsec and listed in Table 1, with a sample of DI type quasars (Kapahi and Saikia 1981). Although the DI sample contains all QSOs with known redshift that have been reported in the literature (from aperture synthesis observations at high frequencies) we consider only the 93 sources with LAS> 10 arcsec, because the average minimum separation of an individual from the central object would then be the same in the two samples. Since most of the DI and D2 sources have been found from the structural determinations of the same samples of QSOs, largely selected from low frequency surveys, there is no significant bias in the two samples with regard to flux density or the distribution of redshifts. It should also be noted that every double quasar in our sample has been classified either as DI or as D2. As the number of ambiguous cases, mainly in the D2 sample (e.g. 0003—003 and 0615+578), is quite small, this is unlikely to affect the comparisons seriously.

3.1 *Spectral Indices*

The distributions of spectral indices, α_c and α_e, whenever available, for the central and outer components are shown in Fig. 1. While the OCs have a fairly narrow distribution peaked around α_e =0·9 as is well known for DI sources, the CCs appear to have a much wider distribution extending from —0·4 to about +1. Spectral information regarding the total flux density, extending from about 178 MHz to 10 GHz is available in the literature for about half the sources in the sample. In all such cases for which α_c is flatter than 0·5 the total spectrum is flat or inverted at high frequencies ($\gtrsim$2·7 GHz) and shows a steep component at low frequencies. D2 sources have generally been associated exclusively with this spectral class (*e.g.* Stannard and Neal 1977: Davis, Stannard and Conway 1977).

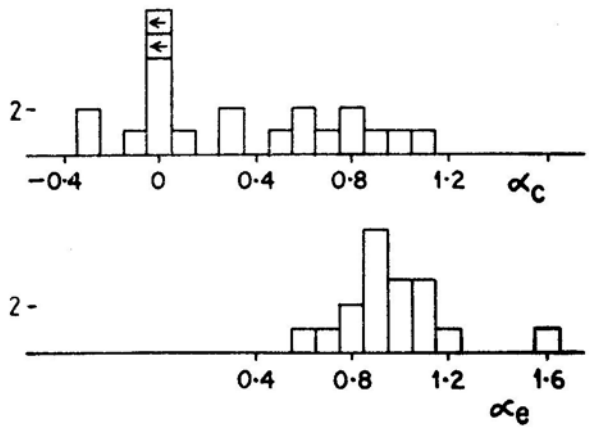

Figure 1. Distributions of spectral indices of the central (α_c) and outer (α_e) components of D2 quasars with LAS > 5 arcsec.

It is not clear how the D2 sources with $\alpha_c > 0{\cdot}5$ differ from the well known flat spectrum variety. Although the width of the α_c distribution is quite broad also for the CCs of D1 quasars (Kapahi and Saikia 1981), the fraction of D2 quasars with $\alpha_c > 0{\cdot}5$ (~38 per cent) is somewhat larger than the corresponding fraction for D1 quasars (~25 per cent). Values of $\alpha_c > 0{\cdot}5$ are unlikely to have been caused by flux variations because in the few cases where spectral information on total emission is available over a wide range of frequencies there is no evidence of any flattening of the spectra at high frequencies as is known to be the case for strongly variable sources. It is possible that the CCs of such sources have compact double structure or are synchrotron self absorbed at low frequencies. The core components of several double radio galaxies are known to have steep spectra and double structure on a scale of a few kpc (Bridle and Fomalont 1978). The CCs of two D2 quasars in our sample (*viz*. 3C 2 and 3C 186) do appear to have a double structure (on a scale of ~10 kpc; $\lesssim 1{\cdot}5$ arcsec) but the exact location of the components with respect to the optical nucleus is uncertain. Another possibility is that such CCs consist of both flat and steep spectrum components, *e.g*. core and jet, or core and other OC close together, since in most cases it is found that $\alpha_c < \alpha_e$. As the D2 classification in the latter case would be incorrect we shall keep this possibility in mind in the subsequent discussion.

3.2 *Luminosities of Central and Outer Components*

The distributions of the calculated luminosities at 5 GHz of the CCs and OCs in D1 and D2 sources are shown in Figs 2 and 3 respectively. It is seen that the CCs in D2 quasars tend to be more powerful than those in D1 quasars while the luminosities of

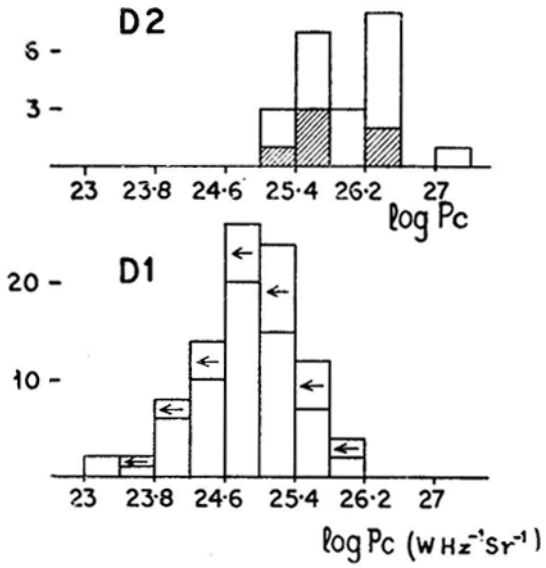

Figure 2. Histograms of the 5 GHz luminosity of the central components of D1 and D2 quasars Upper limits to the luminosities in D1 quasars without detected CCs are indicated by arrows. In this and subsequent figures the shaded portion refers to D2 quasars in which the CCs have a spectral index $\alpha_c > 0{\cdot}5$.

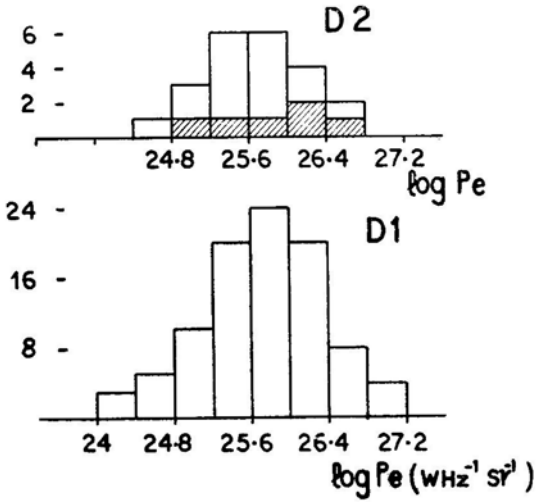

Figure 3. Histograms of the 5 GHz luminosities of the outer components of D1 and D2 quasars.

the OCs do not appear to be significantly different. The difference in the CC luminosities is unlikely to be a result of observational selection effects as quasars of both types have been selected basically from the same flux density limited samples, mostly at low frequencies where the CCs in most sources are unlikely to make a significant contribution to the total flux density.

3.3 *Fractional Flux Density in Central Components*

Because most of the D2 quasars appears to have very prominent CCs, we have calculated the fractional flux density in CCs, f_c ,at a standard frequency of 8 GHz in the rest frame of each source. This choice of frequency should minimize errors due to unknown spectral indices in many cases as the best measurements of flux density are generally available at 2·7 and 5 GHz. We have used the values of α_c and α_e if known. Where these are unknown we have assumed α_c=0·2 and α_e =0·9 which are the median observed values. The resulting distribution of f_c is shown in Fig. 4 together with the corresponding distribution for D1 quasars.

It is clear from Fig. 4 that the f_c distributions for the two types are markedly different. While most of the Dls have f_c <20 per cent, most of the D2s have f_c>50 per cent. It is important to know to what extent the difference can arise from observational selection effects. Two such effects may be important. First, a D2 quasar with very weak or no detectable CC could remain optically unidentified and therefore not be recognized as belonging to this class. Second, due to the larger positional errors for weak CCs a D2 quasar may be misclassified as Dl. In order to investigate the former effect we have considered two complete samples of sources from the 4C and 3CR catalogues that appear to be the most suitable for this purpose.

For a sample with S(178 MHz) > 2·5 Jy selected from the 4C catalogue, optical identifications with 69 suspected QSOs were proposed by Olsen (1970), on the basis of positional coincidences. As the radio position errors in this study were of the

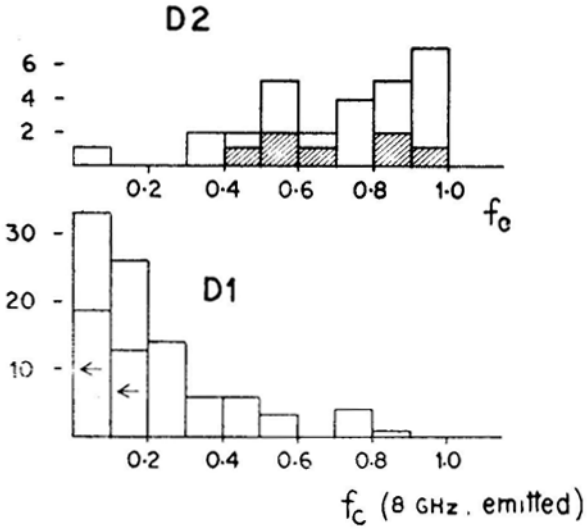

Figure 4. Distributions of the parameter f_c (fractional flux density in the central component) in D1 and D2 quasars. D1 quasars without detected CCs are indicated by upper limits and have been equally distributed in the first two bins.

order of 20 arcsec and the search area was at least ±30 arcsec around the radio position most of the possible D2 quasars would have been considered identified. Spectroscopic observations of the candidates (Schmidt 1974) have confirmed 48 QSO identifications. Of the remaining 21, 17 are stars, 2 have a continuous spectrum and 2 have inconclusive spectra. Brightness distributions (determined with the NRAO 3-element interferometer by Potash and Wardle, 1979) for 46 of the confirmed QSOs for which redshifts are available indicate that 25 are of the D1 type, 6 of the D2 type (included in Table 1) and 15 are classified as single, most of them being unresolved. Nine of the single sources have a spectral index steeper than 0·5 (between 2·7 and 8·1 GHz) but in no case is there any significant difference between the radio and the optical positions (most of which have rms errors of the order of 0·5 arcsec) implying that they cannot be D2 quasars without CCs.

The 3CR complete sample of 166 radio sources (Jenkins, Pooley and Riley 1977) has the best available information both on radio structures as well as on optical identifications. If an unknown D2 quasar without a CC exists in this sample it has to be one of the as yet unidentified sources. After the recent work on optical identifications reaching faint optical magnitudes (Riley, Longair and Gunn 1980, and references therein) there are only 18 sources in the sample that either still remain unidentified or for which the proposed identifications need further confirmation. Sixteen of these sources, however, appear to be classical doubles (LAS>7 arcsec) with nearly equal flux densities in the two components. The remaining 2 sources (3C 241 and 3C 454· 1) are smaller than 2 arcsec and no possible QSO is known to lie within ~ 1 arcmin of the radio positions.

The selection effect associated with larger positional errors of weak CCs is also unlikely to be important because a D2 source with $f_c \leqslant 0{\cdot}2$ would then appear as a D1 with a flux density ratio $\geqslant 4$. In the sample of D1 quasars there are only 6 such sources and in none of them is the Dl classification in doubt because of position errors.

We conclude from the above arguments that selection effects in the data are very unlikely to be responsible for the different distributions of f_c among Dl and D2 quasars.

3.4 *Projected Linear Sizes*

The distribution of projected linear sizes for the twenty two D2 quasars of LAS>5 arcsec with known redshift is shown in Fig. 5 together with the distribution for Dl quasars of LAS> 10 arcsec. Note that in order to compare the distributions directly we have reduced the sizes of Dl quasars by a factor of 2 so that they represent the average projected separation of an individual OC from the optical object. The median sizes for the Dl and D2 samples are about 125 kpc and 75 kpc respectively (if the 6 quasars with $\alpha_c > 0{\cdot}5$ are excluded the median size for the D2 sample rises to about 85 kpc), but the formal statistical significance of the difference is only marginal. There is a suggestion in Fig. 5, however, that the shapes of the two distributions could be different. Since many quasars with sizes < 50 kpc would have angular sizes <5 arcsec, which is the limiting value for the two samples it is seen from Fig. 5 that the peak of the distribution for the D2 sample could be lower than 50 kpc unlike that for the Dl sample. Such a possibility is indicated also by the distributions of the observed angular sizes shown in Fig. 6 and is further supported by extending the histograms to sizes upto 2·5 arcsec (note that only D2 quasars with known redshift and $\alpha_c < 0{\cdot}5$ are included in the LAS range of 2·5 to 5 arcsec). Although Fig. 6 suggests that the typical projected sizes of D2 quasars could be more than 2 times smaller than the corresponding sizes of Dl quasars, the non-homogeneous nature of the samples and the uncertainty in the D2 classification of some sources, particularly those with $\alpha_c > 0{\cdot}5$, makes it difficult to assess the significance of the two distributions.

If the comparison of linear sizes is confined to the largest available complete and homogeneous sample of 52 QSOs from the 4C catalogue whose structure has been determined by Potash and Wardle (1979), there are eight D2 quasars of LAS > 2·5 arcsec with a median size of about 55 kpc and 25 Dl quasars of LAS > 5 arcsec with a median size (corresponding to half the LAS) of about 115 kpc.

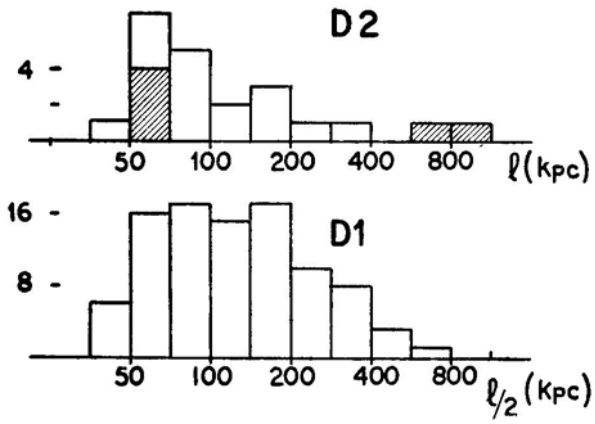

Figure 5. Distributions of projected linear sizes for Dl and D2 quasars.

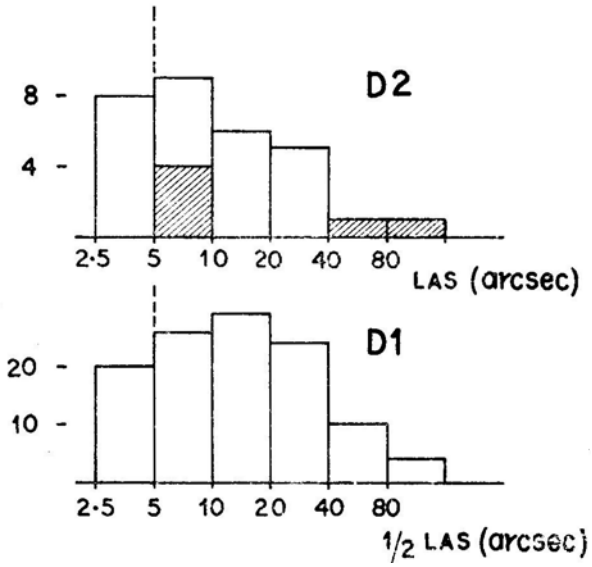

Figure 6. Distributions of the observed angular sizes for D1 and D2 quasars.

4. Discussion

If the D2 sources are essentially those Dl sources in which the two OCs have large intrinsic ratios of flux density, R_s, or of angular separations from the CC, R_θ, and if the relative strengths of the central and outer components are assumed to be independent of the orientation of the source axis, it is hard to understand the difference in the distributions of f_c shown in Fig. 4, unless there is a strong intrinsic correlation between the luminosity of the CC and the asymmetry in the OCs. No such correlation is however observed in the sample of Dl quasars (Kapahi and Saikia 1981). As most of the CCs in our sample of D2 quasars have luminosities P_{cc}(5 GHz) > 2 X 10^{25} W $Hz^{-1}sr^{-1}$ it is seen from Fig. 2 that less than 20 per cent of the Dl quasars have CCs as bright as this. Furthermore, as only about 15 per cent of the Dl quasars are observed to have a flux ratio R_s > 3, at the most only 3 out of a sample of 100 Dl quasars could be expected to be classified in the D2 category.

A similar argument applies also to the displacement ratio R_θ, since less than 10 per cent of the Dl quasars have R_θ > 2, whereas most of the D2 quasars in our sample (LAS>5 arcsec) must be of this type if the OCs are of comparable flux den sity. It therefore seems very unlikely that the D2 sources represent just the extreme end of a continuous distribution of intrinsic flux density or displacement ratios.

In the relativistic beaming model the apparent strengths of the central and the outer components depend on source orientation due to the strong Doppler enhancement of the flux density of the approaching components for smaller angles of orientation of the source ejection axis. The larger observed values of f_c and of luminosities of the CCs of D2 quasars as compared to those for Dl quasars can both be understood in this model if the bulk velocities of the radiating material near the nuclei are considerably higher than those of the outer components. While velocities $\gtrsim$ 0·9c have been proposed in the jets close to the nuclear source (*e.g.* Scheuer and

Readhead 1979, Blandford and Königl 1979) those in the OCs of double sources have generally inferred, from the observed distributions of the separation ratio R_θ to be $\lesssim$ 0·25c for most sources (Longair and Riley 1979; Katgert-Merkelijn, Lari and Padrielli 1980; Banhatti 1980; and Swarup and Banhatti 1980).

In beam models, if the oppositely directed jets are identical, the apparent flux density ratio is given by

$$R_s = \left\{\frac{1+(v/c)\cos\phi}{1-(v/c)\cos\phi}\right\}^{2+\alpha}$$

where v is the velocity of recession of the OCs, ϕ the orientation angle and α the spectral index. We shall ignore the fact that the two components are seen at slightly different ages due to the difference in light travel times. For velocities of 0·25c, and assuming α=0·9, values of R_s of only about 4 can be obtained for $\phi < 30°$. Since many D2 sources are likely to have larger flux density ratios, somewhat larger values of u appear to be required. For v =0·4 for example, R_s can attain values of about 5 to 12 for $\phi < 45°$. Furthermore, because of the strong apparent enhancement of the total flux density of a source with decreasing ϕ due to the Doppler boosting in the approaching as compared to the case for ϕ =90°, an increasing number of D2 sources with small values of ϕ can appear in a flux limited sample from the larger population of intrinsically less luminous or more distant sources. The OCs of only a small fraction of all double sources may therefore be required to have v >0·25c in order to explain the D2 phenomenon. The flux density enhancement could also explain the observed distribution of projected linear sizes of D2 quasars which appears to be more concentrated towards smaller sizes as compared to the case for Dl quasars.

5. Conclusion

A search through the literature has resulted in a list of 49 sources that appear, from the existing observations, to have one-sided (D2 type) radio structure. Most of the sources are associated with quasars. The central components, coincident with the optical objects, in several cases appear to have steep spectral indices, α_c>0·5. Better angular resolutions are needed to decide if these could be normal doubles with a large spatial asymmetry.

A comparison of the observed properties of Dl and D2 quasars indicates that unlike the Dl class, the D2 quasars are characterized by strong central components that account for most of their total flux density at high frequencies. This difference in the properties of the 2 types is very unlikely to have been caused by observational selection effects or by the uncertainty in the D2 classification of some sources and appears to rule out the possibility that most D2 sources are a subset of Dl sources with large intrinsic flux density ratios or separation ratios of the two outer components.

The higher relative strengths of the central components observed for the D2 quasars appear, at least qualitatively, to be consistent with the relativistic beaming interpretation in which the axes of such sources are supposed to make small angles with our lines of sight. Although the projected linear sizes of D2 quasars do appear to

be generally smaller than those of D1 quasars, suggestive of smaller orientation angles, the evidence cannot at present be considered conclusive because of the heterogeneous nature of the quasar samples and the uncertainty in the D2 classification of several sources, particularly those that have central components of steep spectral indices or for which insufficient spectral information is available.

Observations with higher angular resolution and sensitivity would be quite valuable in understanding the nature of the asymmetry in D2 sources.

Acknowledgement

I wish to thank D. J. Saikia for help with literature search and an anonymous referee for his valuable comments.

References

Apparao, K. M. V., Bignami, G. F., Maraschi, L., Helmken, H., Margon, B., Hjellming, R., Bradt, H. V., Dower, R. G. 1978, *Nature,* **273**,450.
Argue, A. N., Riley, J. M., Pooley, G. G. 1978, *Observatory*, **98,**132.
Banhatti, D. G. 1980, Astr. *Asrtophys.,* **84**,112.
Bentley, M., Haves, P., Spencer, R. E., Stannard, D. 1976, Mon. Not. *R. astr. Soc.,* **176**, 275.
Blandford, R. D., Königl, A. 1979, *Astrophys. J*., **232**, 34.
Bridle, A. H., Fomalont, E. B. 1978, *Astr. J*., **83,** 704.
Cohen, A. M., Porcas, R, W., Browne, I. W. A., Daintree, E. J., Walsh, D. 1977, *Mem. R. astr. Soc*., **84**, 1.
Cohen, M. H., Kellermann, K. I., Shaffer, D. B., Linfield, R. P., Moffet, A. T., Romney, J. D., Seielstad, G. A., PaulinyToth, I.I. K., Preuss, E., Witzel, A., Schilizzi, R. T., Geldzahler, B. J. 1977, Nature, **268**, 405.
Cohen, M. H., Pearson, T. J., Readhead, A. C. S., Seielstad, G. A., Simon, R. S., Walker, R. C. 1979,*Astrophys. J*., **231**,293.
Conway, R. G., Burn, B. J., Vallee, J. P. 1977, *Astr. Astrophys. Suppl. Ser*., **27**, 155.
Davis, R. J., Stannard, D., Conway, R. G. 1977, *Nature,* **267,** 596.
Fanti, C., Fanti, R., Ficarra, A., Formiggini, L., Giovannini, G., Lari, C., Padrielli, L. 1975, *Astr. Astrophys. Suppl. Ser.*, **19**,143.
Fanti, C., Fanti, R., Formiggini, L., Lari, C., Padrielli, L. 1977, *Astr. Astrophys. Suppl. Ser*., **28,** 351.
Fanti, R., Feretti, L., Giovannini, G., Padrielli, L. 1979, *Astr. Astrophys. Suppl. Ser*., **35**, 169.
Hazard, C., Mackey, M. B., Shimmins, A. J. 1963, *Nature*, **197,**1037.
Hewitt, A., Burbidge, G. 1980, *Astrophys. J. Suppl. Ser*., **43**, 57.
Högbom, J. A., Carlsson, I. 1974, *Astr.Astrophys.,* **34**, 341.
Jenkins, C. J., Pooley, G. G., Riley, J. M. 1977, *Mem. R. astr. Soc.*, **87**, 61.
Joshi, M. N. 1980, *Mon. Not. R. astr. Soc.*, (in press).
Kapahi, V. K. 1979, *Astr. Astrophys*., **74**, L11.
Kapahi, V. K. 1980, *Astr. Astrophys. Suppl. Ser*., (in press).
Kapahi, V. K., Saikia, D. J. 1981, In preparation.
Katgert-Merkelijn, J., Lari, C, Padrielli, L. 1980, *Astr. Astrophys. Suppl. Ser.*, **40,** 91
Kühr, H., Nauber, U., PaulinyToth, I.I.K., Witzel, A. 1974, *Preprint*
Longair, M. S., Riley, J. M. 1979, *Mon. Not. R. astr. Soc.*, **188**, 625.
Lyne, A. G. 1972, *Mon. Not. R. astr. Soc.*, **158**, 431.
McAdam, W. B. 1976, *Proc. astr. Soc. Austr*., **3**, 86.
Miley, G. K., 1971, *Mon. Not. R. astr. Soc.,* **152**, 477.
Miley, G.K.,1980, *A. Rev. Astr. Astrophys*., **18**, 165.
Miley, G. K., Hartsuijker, A. P. 1978, *Astr. Astrophys. Suppl. Ser.*, **34**, 129.

Olsen, E. T. 1970, *Astr.J*., **75**, 764.
Owen, F. N., Porcas, R. W., Neff, S. G. 1978, *Astr. J.*. **83**,1009.
Perley, R. A., Johnston, K. J. 1979, *Astr. J.* **84**,1247.
Perley, R. A., Fomalont, E. B., Johnston, K. J. 1980, *Astr. J*., **85**, 649.
Potash, R. I., Wardle, J. F. C. 1979, *Astr. J.,* **84**, 707.
Readhead, A. C. S., Cohen, M. H., Pearson, T. J., Wilkinson, P. N. 1978, *Nature,* **276**, 768.
Riley, J. M., Jenkins, C. J. 1977, in *IAU Symp.* **74**: *Radio Astronomy and Cosmology*, Ed. D. L. Jauncey, D. Reidel, Dordrecht, p. 237.
Riley, J. M., Longair, M. S., Gunn, J. E. 1980, *Mon. Not. R. astr. Soc.,* **192,** 233.
Riley, J. M., Pooley, G. G. 1975, *Mem. R. astr. Soc.,* **80**, 105.
Sandage, A. 1966, *Astrophys. J*., **145**, 1.
Sargent, W. L. W. 1973, *Astrophys. J*., **182**, L13.
Scheuer, P. A. G., Readhead, A. C. S. 1979, *Nature,* **277**, 182.
Schmidt, M. 1974, *Astrophys*. *J.*, **193**, 505.
Scott, M. A. 1977, *Mon. Not. R. astr. Soc.,* **179,** 377.
Singal, A. K., GopalKrishna, Venugopal, V. R. 1979, *Mem. astr. Soc. India,* **1,**14.
Smith, H. E., Spinrad, H. 1980, *Preprint*.
Stannard, D., Neal, D. S. 1977, *Mon. Not. R. astr, Soc.,* **179,** 719.
Subrahmanya, C. R., Gopal-Krishna, 1979, *Mem. astr. Soc. India*, **1**, 2.
Swarup, G., Banhatti, D. G. 1980, *Mon. Not. R. astr. Soc*. (in press).
Tzanetakis, A., Spencer, R. E., Masson, C. R., Baldwin, J. E. 1978, *Mon. Not. R. astr. Soc.,* **185**, 63.
Veron, M. P.,Veron, P., Witzel, A. 1974, *Astr. Astrophys. Suppl. Ser*., **13**, 1.
Wills, D. 1979, *Astrophys. J. Suppl Ser*., **39**, 291.

Note added in proof

Recent observations at 6 cm and 2 cm λ of the sources in Table 1 with LAS > 15 arcsec, made with Very Large Array (G. Swarup, personal communication) indicate that three of them (*viz*. 0932+022, 1047+096 and 1354+195) have a triple structure with an additional weak OC on the opposite side of the CC.

J. Astrophys. Astr. (1981) **2,** 59–65

Pulsating Radio Emission at Decametre Wavelengths from the Sun

Ch. V. Sastry, V. Krishan and K. R. Subramanian *Indian Institute of Astrophysics, Bangalore 560034 and Raman Research Institute, Bangalore 560080*

Received 1980 November 24; accepted 1981 February 5

Abstract. Observations on the pulsation pattern in the time profile of short duration solar radio bursts at decametre wavelengths are presented. The pulsations are found to be present predominantly in the saturation phase of the burst. A tentative physical model based on the non-linear development of the waves interacting in a turbulent medium is invoked to explain the origin of the pulsations.

Key words: explosive instability—pulsating burst

1. Introduction

The periodical temporal variations in the intensity of solar radio emission have been reported by several workers, *e.g.* Rosenberg (1970), Mclean *et al.* (1971), Abrami. (1972) and Tapping (1978). Most of these observations were made at wavelengths of approximately 2 m and less. These pulsations occurred during some phases of type IV events. These are broad band and are seen at all phases *i.e.* growth, plateau and decay of that burst. Santin (1971) reported his observations on quasi-oscillatory decay in type III radio bursts. In the decametre wavelength range, we have already reported some observations on quasi-periodic variations of enhanced background emission during intense noise storms (Sastry 1969). Achong (1974) observed similar pulsation of the enhanced continuum in the frequency range of 24-26 MHz. In this paper, we report our observations on a different type of pulsation pattern in the intensity time profile of short duration radio bursts at decametre wavelengths. A tentative physical model to explain the observed characteristics is proposed.

2. Equipment

These observations were made with the N-S arm of the Gauribidanur decametre wave radio telescope. This radio telescope is a Mill's ' T ' type array operating in the

frequency range 25 to 35 MHz. The N-S array of the radio telescope has a collecting area of approximately 15,000 m^2 and beam-widths of 15°and 0·5° in the E-W and N-S directions respectively. The receiving system consists of eight channels with centre frequencies around 34·5 MHz. The separation between channels is 50 kHz and the bandwidth of each channel is 15 kHz. The time constant used is 20 milliseconds.

3. Observations

We observed the Sun each day for about an hour centred at local noon during storm periods. Since the sensitivity of the system is very high a large number of new and peculiar bursts hither to unclassified were detected. On several occasions we recorded a burst in which there is a smooth growth of intensity to a maximum in a short time and during the maximum phase the intensity exhibits quasiperiodic pulsations and then decays with the same smoothness. The basic distinct feature of these profiles is the presence of oscillations or pulsations during the saturation phase of the radio emission. Typical examples are shown in Figs la, b and c. In Fig. la one can see a rise in the intensity starting around $06^h\ 51^m\ 58^s$ UT and then going into oscillations with an approximate period of 2 seconds. After three oscillations the intensity decays to the preburst level. The total duration of the burst is about 6 seconds. A similar burst is shown in Fig. lb starting around $06^h\ 29^m\ 41^s$ UT. Here the total duration and the period of oscillation are larger *i.e.* 10 and 3 s respectively. Another burst with twice the number of oscillations is shown in Fig. lc. The total number of events recorded during the period April-July 1980 is 22. As pointed out here, all these bursts occurred during periods of intense noise storms where the base level of emission is already very high.

We have derived several characteristics of these bursts from the observed time and frequency profiles. The various measured parameters of the burst are illustrated in Fig. 2. Fig. 3a shows a histogram of the number of bursts versus the pulse repetition rate. It can be seen that the most common value of the pulse repetition period lies between 2 and 5 seconds. A histogram of the number of bursts versus total durations is given in Fig. 3b and it is clear that the total duration, τ, ranges from 5 to 15 seconds. A modulation index m defined as

$$m = \frac{\Delta I}{2I - \Delta I},$$

is calculated for each burst. From the histogram of Fig. 3c it can be seen that the value of m lies between 0·2 and 0·4 in a majority of cases. We have also looked for correlations between the various parameters of the bursts. Fig. 4 is a scatter plot of the average peak intensity $\langle I \rangle$ and the average pulse amplitude, $\langle \Delta I \rangle$. It is obvious that these two parameters are positively correlated and the linear correlation coefficient is found to be +0·7. A plot of $\langle I \rangle$ versus the pulse repetition period, $\langle \Delta\tau \rangle$ showed no significant correlation. A similar result is obtained for correlation between the pulse amplitude, $\langle \Delta\tau \rangle$ and the pulse repetition period, $\langle \Delta\tau \rangle$ No correlation is also found between the modulation index, m, and the pulse repetition period, $\langle \Delta\tau \rangle$ The average individual pulse profile is found to be.

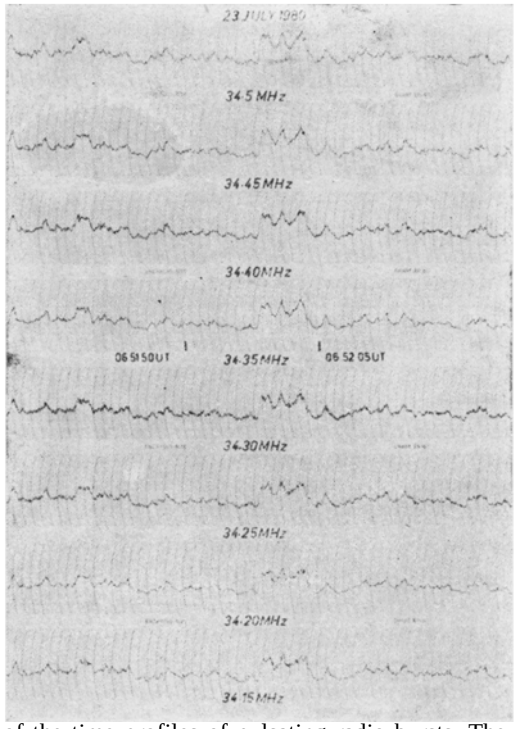

Figure 1a. Examples of the time profiles of pulsating radio bursts. The ordinate is the receiver output voltage (1980 July 23).

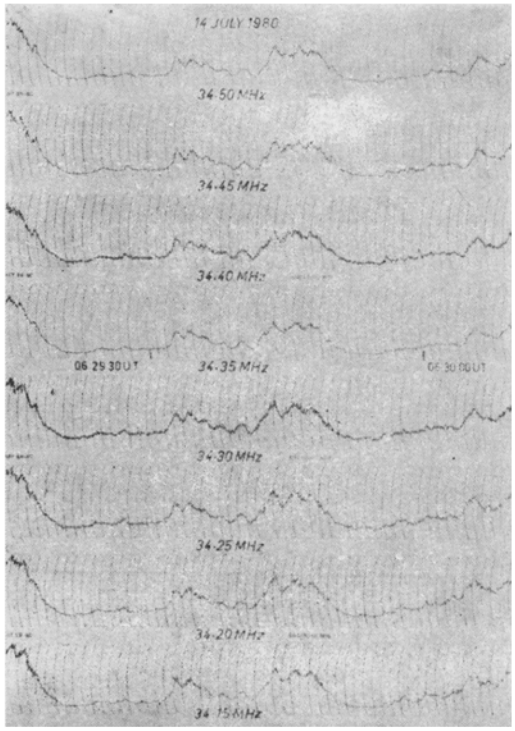

Figure 1b. Examples of the time profiles of pulsating radio bursts. The ordinate is the receiver output voltage (1980 July 14).

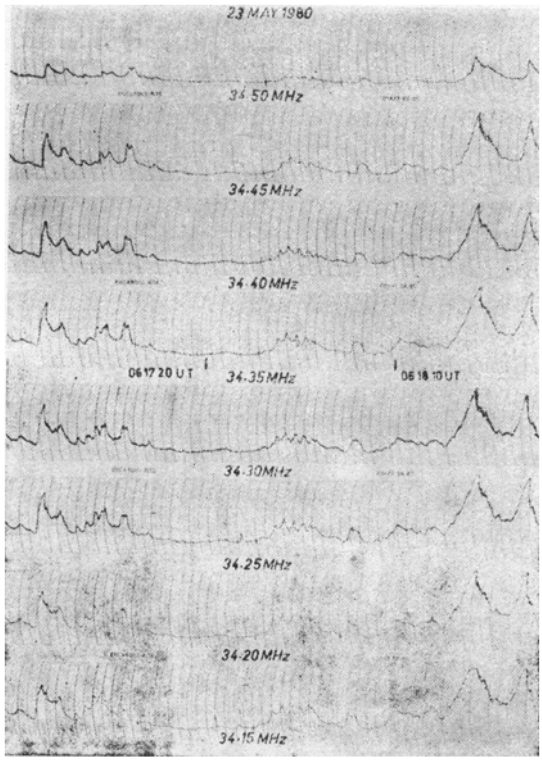

Figure 1c. Examples of the time profiles of pulsating radio bursts. The ordinate is the receiver output voltage (1980 May 23).

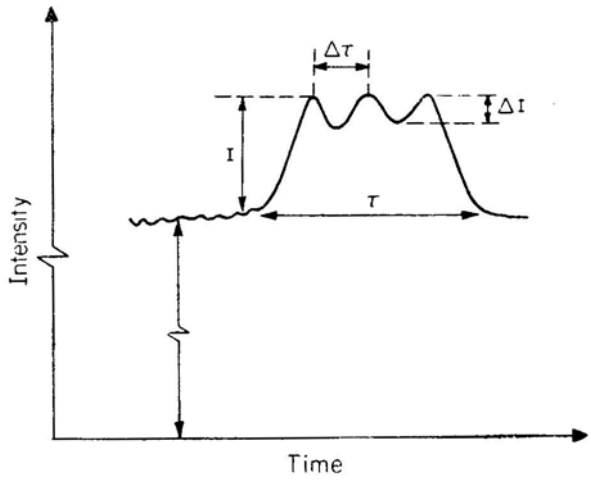

Figure 2. Explanation of the burst parameters.

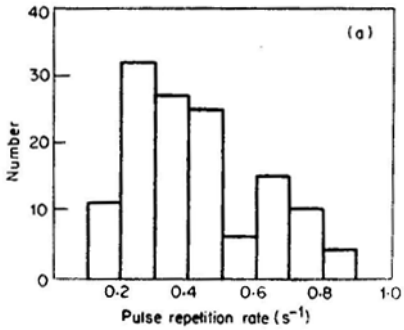

Figure 3a. Histogram of the number of bursts versus the pulse repetition rate

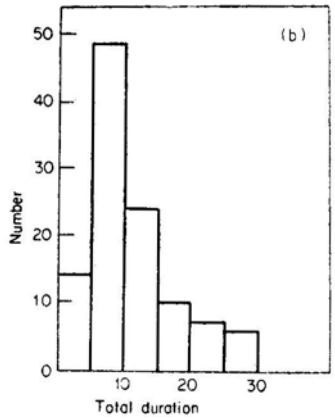

Figure 3b. Histogram of the number bursts of versus the total duration

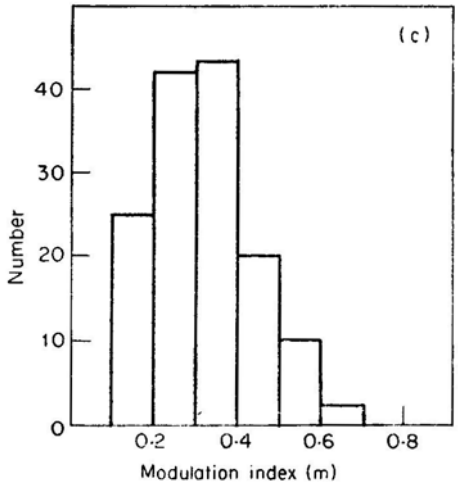

Figure 3c. Histogram of the number of bursts versus the modulation index.

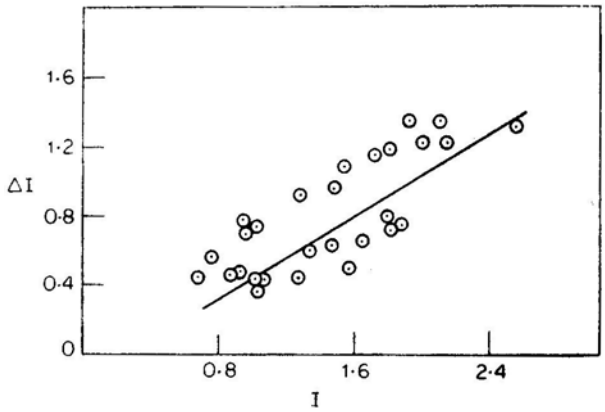

Figure 4. A plot between the average peak intensity $\langle I \rangle$ and the average pulse amplitude $\langle \Delta I \rangle$ shows a strong correlation between $\langle I \rangle$ and $\langle \Delta I \rangle$·

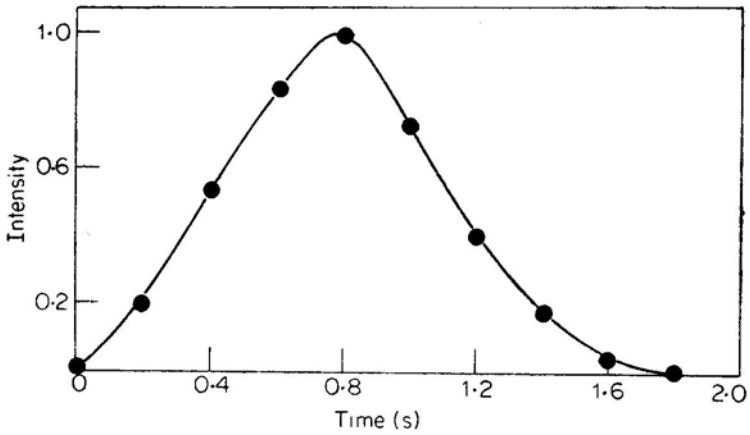

Figure 5. The average time profile of a pulse.

symmetric (Fig. 5). These results do not agree with those obtained by Tapping (1978) and McLean and Sheridan (1973).

In conclusion, one can identify these bursts by the following distinct characteristics.

1 The pulsations are seen only in the saturation phase of the burst.
2 The pulse repetition period lies within 2–5 seconds.
3 The amplitude of the individual pulse remains approximately constant during the pulsating phase.

4. Discussion

Rosenberg (1970) and McLean *et al.* (1971) proposed that the modulated radio emission was due to synchrotron emission in a magnetic flux tube and the pulsations are introduced due to the radial oscillations of the flux tube. Abrami (1972) noticed that the above model fails to account for the arrest of emission increase accompanying the start of pulsations.

We have sought a physical model where the oscillations can set in only during the saturation phase of the burst since this is a distinct feature of the bursts we observed. The basic system responsible for these modulated bursts is an electron beam-plasma system. This system has been shown to support positive as well as negative energy waves. The coupling of the positive and negative energy waves gives rise to an explosive instability where the amplitude can become infinite in a finite interval of time, although due to various nonlinear effects mentioned below, the growth of the amplitude will be arrested. The initial growing phase of the observed burst can be attributed to this explosive instability. The excitation of the explosive instability is a threshold effect. Since the background level of emission over which the burst is superimposed is very high, the conditions for the explosive interaction of the waves are satisfied. The time of explosion is a function of the initial amplitudes of the interacting waves. The saturation of the explosive instability is due to the non-linear complex amplitude-dependent frequency shift caused by three wave coupling.

Further the non-linear frequency shifts combined with the linear dissipation effects set the saturation stage into an oscillatory mode. It can be shown that the time period of pulsations is a function of the level of the initial enhanced background and not the peak intensity I. This would explain the absence of correlation between the pulse repetition rate $(\Delta\tau)^{-1}$ and $\langle I \rangle$, $\langle \Delta\tau \rangle$ and pulse amplitude $\langle \Delta I \rangle$ and therefore $\langle \Delta\tau \rangle$and the modulation index m. The significant correlation observed between the average pulse amplitude $\langle \Delta I \rangle$ and the average peak intensity $\langle I \rangle$ is a natural consequence of this mechanism since the pulsations come into play only when I attains a certain value at which the nonlinear effects become predominant. The solution of the non-linear wave equations including three wave coupling is given with and without linear dissipation by Oraevskii *et al.* (1973), Weiland and Wilhelmsson (1973) and Weiland Wilhelmsson (1977). The time period of the pulsations has been determined in Fukai, Krishan and Harris (1971). The theoretical results of the above investigations predict the pulsations to continue throughout the decay phase unlike our observations, where the decay phase is almost pulsation free. This last stage of the burst could be a consequence of the passage of the electron beam out of the interaction region. The decay of the remaining field could then be due to collisional or collisionless processes.

Acknowledgement

The Low Frequency Radio Astronomy Project at Gauribidanur owes its existence to the keen interest and continuous support of M. K. V. Bappu and V. Radhakrishnan. We would also like to thank Rajasekhara and Nanje Gowda for their help in collecting data.

References

Abrami, A. 1972, *Nature,* **238**, 25.
Achong, A. 1974, *Solar Phys.,* **37,** 477.
Fukai, J., Krishan, S, Harris, E. G. 1969, *Phys. Rev. Lett.,* **23**, 910.
McLean, D. J., Sheridan, K. V. 1973, *Solar Phys.,* **32**, 485.
McLean, D. J., Sheridan, K. V., Stewart, R. T., Wild, J. P. 1971, *Nature,* **234**, 140.
Oraevskii, V. N., Wilhelmsson, H., Kogan, E. Ya., Pavlenko, V. P. 1973, *Phys. Scripta,* **7,** 217.
Rosenberg, H. 1970, *Astr. Astrophys.,* **9**, 159.
Santin, P. 1971, *SolarPhys.,* **18**, 87.
Sastry, Ch. V. 1969, *SolarPhys.,* **10**, 429.
Tapping, K. P. 1978, *SolarPhys.,* **59**, 145.
Weiland, J., Wilhelmsson, H. 1973, *Phys. Scripta,* **7,** 222.
Weiland, J., Wilhelmsson, H. 1977, *Coherent Non-Linear Interaction of Waves in Plasmas,* Pergamon Press, Oxford.

J. Astrophys. Astr. (1981) **2,** 67–79

Luminosity-H I Velocity Width Relation for Spirals

N. Visvanathan *Mount Stromlo and Siding Spring Observatories, Research School of Physical Sciences, The Australian National University, Australia*

Received 1980 December 12; accepted 1981 February 18

Abstract. Multicolour and multiaperture photometry of 22 late-type Virgo cluster galaxies in a new *V* (5500 Å), *r* (6738 Å), *IV* (10500 Å) system confirm the previously known correlations between the luminosity and H I velocity width, and show them to be strongly wavelength dependent with the slope of the relation reaching a maximum value of ~ – 10 at 10500 Å and remaining constant at longer wavelengths. The scatter in the luminosity-H I width relation is nearly the same, whether we use $(V)^{c}_{-0\,5,}$ $(r)^{c}_{-0\,5,}$ $(IV)^{c}_{-0\,5,}$ or $(H)^{c}_{-0\,5}$ magnitudes. The error in the determination of the corrected magnitudes is much less than the scatter in the luminosity-H I width relations as evidenced by the fact that the residuals of individual galaxies in *V, r, IV,* and *H* are correlated with one another. An attempt to use a ' kinematic magnitude' instead of an isophotal magnitude shows the slope of the luminosity-H I width relations to be reduced substantially.

Observations in the *V, r,* and *IV* system for fifteen field galaxies and three galaxies in the Cancer and Zw 74-23 clusters have been obtained and combined with the H I velocity width to derive their differences in distance modulus, between the galaxy and the Virgo cluster, through the luminosity-H_I width relations of the Virgo cluster galaxies. The three independent differences in the distance modulus of each galaxy agree with one another indicating that the relations using *V, r* and *IV* magnitudes have the same zero point in absolute magnitude, independent of the wavelength of observations. The distance modulus difference from the Virgo cluster to the three galaxies U 4334, U 8942 and U 8944, which are outside the Local Supercluster, are +1·50, +3·45 and +2·81 mag respectively and are in agreement with those of +1·75,+3·23 and +2·46 mag derived for the same galaxies by Aaronson *et al.* (1980) through *H* magnitudes.

The scatter in the velocity distance relation of the field galaxies compares well with the mean error derived in the luminosity-H_I width relations and hence is intrinsic.

Key words: spiral galaxies—photometry—luminosity-H_I velocity width relation

I. Introduction

The luminosity-H I velocity width, relation for late-type galaxies was studied by Tully and Fisher (1977) and Sandage and Tammann (1976) using blue magnitudes and by Aaronson, Huchra and Mould (1979) using the infrared *H* magnitudes. The slope of the relation changes from ~ –7 at blue wavelength to ~ – 10 at the infrared-*H* wavelength, mainly due to the difference in the population content of stars at these wavelengths. Mould, Aaronson, and Huchra, 1980 (hereafter MAH) and Aaronson *et al.* (1980), used this relation to obtain, independent distances to the Virgo cluster and other clusters with $4000 < v_0 < 6000$ km s^{-1} on the assumption that the relation is similar from cluster to cluster. They found that the value of the Hubble constant for more distant clusters is ~ 40 per cent larger than that for the Virgo cluster. Their results are in disagreement with the measured departures of the velocity field (from a uniform expansion) derived through the cluster and field E, SO galaxies with v_0 <6500 km s^{-1} (Visvanathan and Sandage 1977 and Visvanathan 1979) and through other methods (Sandage and Tammann 1975; Rubin *et al.* 1976; Tammann, Sandage and Yahil 1980). Hence we have started an observing programme to study the luminosity-H I width relation for late-type spirals and irregulars, using magnitudes at the visual (5500 Å), red (6738 Å)'and the near infrared wavelengths (10500 Å), in order to check independently both the slope and the zero point of the relation from cluster to cluster. This paper describes our first results obtained for the Virgo cluster as well as some field galaxies.

2. Magnitudes at *V, r* and *IV* wavelengths

2.1 *Instrument and Observational Procedure*

We have obtained multiaperture photoelectric data for 40 late-type spirals, through three filters, *V, r* and *IV,* centred at 5500 Å, 6738 Å and 10500 Å respectively at the Cassegrain focus of the 1-m telescope of the Siding Spring Observatory. The *V* filter is a standard broadband filter (GG14+BG38; $\Delta\lambda$~800 Å) and the *r* and *IV* filters are broad band interference filters with bandwidths of 300 Å and 800 Å respectively.

The automatic scanner (Visvanathan 1972; Visvanathan and Sandage 1977) was used in the single channel mode for all the observations. A Varian photo-multiplier tube with InGaiAsP cathode was used with an SSR preamplifier. The tube was operated with 2000 volts at the dry ice temperature. The data system was modified to operate with the standard computer-controlled photometer system.

The filters *V, r* and *IV* were mounted in the filter wheel that was rotated by a stepping motor and programmed to dwell for predetermined times in each filter position. The exposures were 68, 168 and 368 units of 15·0 ms respectively. The total time for a single scan was 10·5 s. To maintain a control of the sky variation, the number of scans for any one observation was kept to eight, and the galaxy observation was always preceded and succeeded by a sky observation.

The net galaxy count was converted into magnitudes and reduced to outside the atmosphere using the average extinction coefficients. (The zero point of the *V* magnitude was set equal to that of the *UBV* system.) The zero point of our *r* and *IV*

magnitude system was set equal to zero for an A0 V star: The standard stars were taken from Glass (1974) and Frogel *et al.* (1978).

2.2 *Data for the Virgo Cluster and Field Spiral Galaxies*

The *V, r* and *IV* data were obtained for 22 Virgo cluster galaxies, 15 field galaxies and one galaxy each in Cancer cluster (Humason, Mayall, and Sandgae 1956, hereafter HMS) and *Zw 74-23, through 22·6, 45·4, 64·9 and 90·6 arcsec apertures. Before these data are used for the study of the luminosity -H I velocity width relation, four corrections must be made to the measured magnitudes: 1. Correction to a Standard fixed fraction of each galaxy's size by the method in HMS (Appendix A) (We chose the Standard size as log $A/D(0)=$ 0·5 where A is the measuring aperture and $D(0)$ is the corrected face-on diameter of the galaxy); 2. Correction for internal absorption; 3. Correction for galactic extinction; 4. Correction for redshift. The diameter D_{25} for each galaxy was taken from the *Second Reference Catalogue of Bright Galaxies* (de Vaucouleurs, de Vaucouleurs and Corwin, 1976; hereafter RC2) and reduced to face-on value $D(0)$ after correcting for inclination and galactic extinction, as described by Aaronson, Mould and Huchra (1980). All our observations of galaxies were used to construct Standard growth curves in *V, r* and *IV,* after normalising the data to log A/D (0)= — 0·5. The growth curves were found to be nearly linear in the observed range of $A/D(0)=$ — 0·2to — 0·8. These growth curves were used to reduce the observed magnitudes to log $A/D(0)=$ — 0·5 as described in Sandage and Visvanathan (1978). The reduced magnitudes with the same filter, of the same galaxy, from several apertures were averaged.

The internal absorption correction was the same as adopted by Sandage and Tammann (1976). The values of α at *V, r* and *IV* were obtained by reducing those at *B* by factors 0·71, 0·53 and 0·22 respectively according to van de Hülst reddening curve No. 15 (Johnson 1966). Corrections due to local absoprtion in our Galaxy were adopted to be a function of galactic latitude alone (Sandage and Visvanathan 1978). The adopted gradients at *V, r* and *IV* are 0·10, 0·074 and 0·031 respectively. Adopted corrections for redshifts are proportional to the redshift z of the galaxy and are 1·8z, 0·8z and 0·3z at *V, r* and *IV* respectively.

The H I velocity widths at 20 per cent level were either taken or computed, from Whiteoak and Gardner (1977), Shostak (1978), MAH and Aaronson *et al* (1980). The velocity-widths were corrected for inclination to an edge-on value as suggested by Aaronson, Mould and Huchra (1980). Only disk galaxies that are inclined more than 45° were selected for the observations.

Table 1 lists the data for the Virgo cluster spirals: the first column is the NGC number or UGC number from the *Uppsala General Catalogue of Galaxies* (Nilson 1973; hereafter UGC); the second column is the morphological types taken from RC2 or UGC; the third column is the inclination angle taken from MAH; fourth, fifth and sixth columns are the average aperture-reduced magnitudes corrected for internal absorption, local galactic reddening and K-effect for $(V)^c_{-0\,5}$ $(r)^c_{-0\,5}$ $(IV)^c_{-0\,5}$ respectively. The last column lists the H I-velocity widths, log W $(0)^{,}$ corrected for inclination taken from MAH.

*In the catalogue of Zwicky *et al.* (1961-68), this cluster is called Zwicky 1400·4+0949. Here for the sake of brevity, we refer to this cluster as Zw 7423 as was described in Aaronson *et al.* (1980).

Table 1. Virgo cluster galaxies.

	Name	Type	i	$(V)^c_{-0.5}$	$(r)^c_{-0.5}$	$(IV)^c_{-0.5}$	log $W(0)$
			deg	mag	mag	mag	km s^{-1}
N	4178	SB (rs) dm	77	12·28	11·71	10·89	2·47
	4192	SX (s) ab	78	10·04	9·31	8·52	2·67
	4206	SA (s) bc:	78	12·46	11·89	11·18	2·48
	4216	SX (s) b:	81	9·25	8·83	7·93	2·73
	4294	SB (s) cd	70	12·65	12·67	11·95	2·41
	4380	SA (rs) b?	58	12·24	11·56	10·82	2·52
	4388	SA (s) b	81	10·85	10·43	9·85	2·60
	4438	SA (s) 0/a pec:	71	9·77	9·06	8·14	2·58
	4450	SA (s) ab	53	10·49	9·89	8·94	2·59
	4498	SX (s) cd	59	13·03	12·42	11·80	2·33
	4501	SA (rs) b	64	9·86	9·10	8·04	2·77
	4519	SB (rs) d	48	12·89	12·10	11·50	2·48
	4522	SB (s) cd:	79	12·76	12·06	11·71	2·37
	4532	IBm	70	12·61	11·96	11·53	2·44
	4535	SX (s) c	42	11·36	10·82	9·80	2·65
	4550	SBO+?	79	12·20	11·38	10·49	2·47
	4569	SX (rs) ab	64	9·71	9·13	8·10	2·59
U	7513	SB (s) cd	90	12·91	12·39	11·84	2·45
	4651	SA (rs) c	59	11·24	10·55	9·62	2·66
	4654	SX (rs) cd	55	11·47	10·76	9·84	2·58
	4698	SA (s) ab	68	10·92	10·20	9·39	2·66
	4758	SBb?	82	12·93	12·48	12·17	2·32

Table 2. Field and other cluster galaxies.

	Name	Type	i	v_0	$(V)^c_{-0.5}$	$(r)^c_{-0.5}$	$(IV)^c_{-0.5}$	log $W(0)$	Remarks
			deg	km s^{-1}	mag	mag	mag	km s^{-1}	
N	2835	SB (rs) c	47	617	11·40	10·74	10·20	2·48	
	3621	SA (s) cd	54	455	9·82	9·15	8·34	2·54	
	4273	SB (s) c	49	2224	12·37	11·60	11·00	2·60	G46 group
	4487	SAB (rs) cd	46	1029	12·29	11·62	11·13	2·54	G35 group
	4504	SA (s) cd	50	1029	12·46	11·86	11·12	2·52	G35 group
	4939	SA (s) bc	61	2957	11·58	10·83	10·07	2·73	
	5054	SA (s) bc	56	1587	11·52	10·76	9·76	2·60	
	5248	SAB (rs) bc	45	1106	10·71	9·95	8·98	2·61	
	5426	SA (s) c (pec)	61	2416	12·77	12·08	11·39	2·68	
	6070	SA (s) cd	61	2057	12·31	11·55	10·69	2·67	
	6118	SA (s) cd	66	1619	12·25	11·56	10·51	2·59	
	6221	SB (s) c	46	1213	10·88	10·17	9·30	2·63	G14 group
	6744	SAB (r) bc	53	592	9·08	8·36	7·43	2·62	
	6810	SA (s) ab	80	1821	10·73	10·10	9·30	2·69	
	6925	SA (s) bc	73	2605	11·32	10·63	9·81	2·75	
U	4334	Sb	67	3487	12·05	11·32	10·74	2·66	Cancer cluster?
U	8942	Pec	48	5893	14·19	13·45	13·18	2·63	Zw 74-23
U	8944	Sc	60	5893	13·98	13·20	12·57	2·60	Cluster

Table 2 lists the data for the field and other cluster galaxies: columns 1-2 are the NGC or UGC number and morphological type of the galaxy, from the RC2 or UGC; column 3 is the inclination angle taken from Danver (1942), RC2 or Aaronson *et al.* (1980); column 4 is the redshift of the galaxy corrected for solar motion relative to the assumed inertial frame of 300 sin l cos b km s^{-1}; columns 5, 6 and 7, give the average aperture-reduced magnitudes corrected for internal absorption, local galactic reddening and K-effect for $(V)^c_{-0.5}$ $(r)^c_{-0.5}$ $(IV)^c_{-0.5}$ respectively; the eighth column is the H I velocity widths at 20 per cent level log $W(0)$, corrected for inclination, taken or reduced from Whiteoak and Gardner (1977), Shostak (1978) and Aaronson *et al.* (1980); and the last column lists the group to which the galaxy belongs (de Vaucouleurs 1975).

3. Luminosity-H I velocity width relation for the Virgo spirals

The magnitudes $(V)^c_{-0.5}$ $(r)^c_{-0.5}$ $(IV)^c_{-0.5}$ given in Table 1 for the Virgo galaxies are plotted against log $W(0)$ in Fig. 1. All the galaxies are either within 6° of the cluster centre taken to be at $\alpha_{1950} = 12^h\ 25^m$, $\delta_{1950} = +\ 13°06'$, (Sandage and Tammann 1976a), or within a 6° circle centred on NGC 4486. They are all assumed to be at the same distance as the Virgo cluster.

In Fig. 1, the change in log $W(0)$ with magnitude at V, r and IV is pronounced, and well defined, even though the observed 'magnitude range is only 4.4. Formal least squares solutions were obtained by taking alternately magnitudes and log $W(0)$ as the independent variable. The averages of the regressions are given below:

$$(V)^c_{-0.5} = -8{\cdot}89 \log W(0) + 34{\cdot}236 \pm 0{\cdot}89; \text{ mean error} = \pm 0{\cdot}47 \text{ mag}; r = -0{\cdot}92, \quad (1)$$

$$(r)^c_{-0.5} = -9{\cdot}10 \log W(0) + 34{\cdot}158 \pm 0{\cdot}90; \text{ mean error} = \pm 0{\cdot}47 \text{ mag}; r = -0{\cdot}92, \quad (2)$$

$$(IV)^c_{-0.5} = -10{\cdot}29 \log W(0) + 36{\cdot}445 \pm 0{\cdot}86; \text{ mean error} = \pm 0{\cdot}46 \text{ mag}; r = -0{\cdot}94. \quad (3)$$

In Fig. 1, we have also plotted for all our Virgo galaxies $(H)^c_{-0.5}$ against log $W(0)$ taken from MAH in order to compare our results with those at the infrared H wavelength. The least squares fit to these data, gives the following solution:

$$(H)^c_{-0.5} = -9{\cdot}843 \log W(0) + 34{\cdot}387 \pm 0{\cdot}84; \text{ mean error} = 0{\cdot}45 \text{ mag}; r = -0{\cdot}94. \quad (4)$$

The galaxies N 4438 and N 4569 are given zero weight in the solutions (1)—(4) as they deviate by more than three mean errors.

Equations (1) to (4) as well as Fig. 1, indicate that the slope of the luminosity-H I velocity width relation, varies from ~ —8·9 at visible and red wavelengths to ~ —10 at near-infrared and infrared wavelengths. It is important to note that the slope of —10·3 at IV agrees well with that of —9·84 observed at the H wavelength (equation 4 and MAH). Further, the slopes of the relation at visual and red wavelengths agree with one another but are shallower than that at blue wavelengths (~ —7) (Tully and Fisher 1977, Sandage and Tammann 1976).

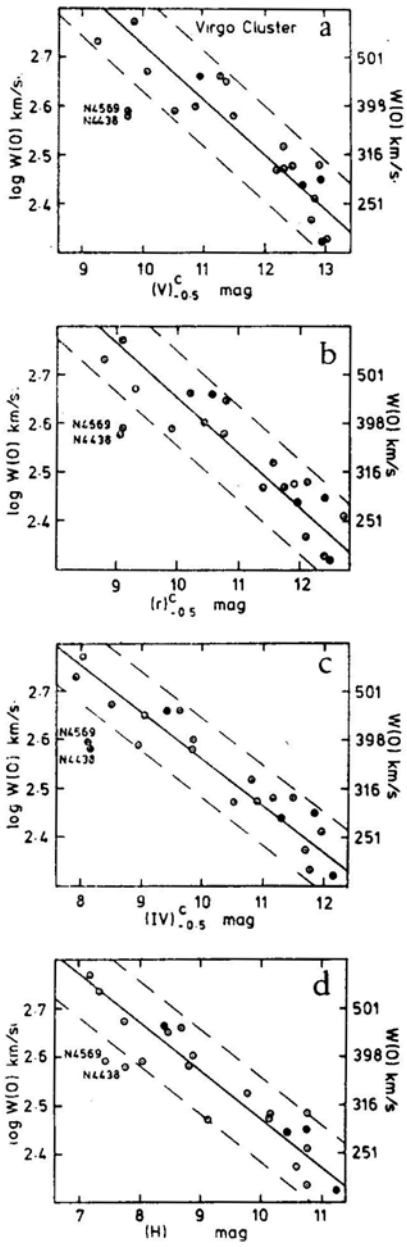

Figure 1. Corrected magnitudes at *V, r, IV* and *H* wavelengths plotted against the corrected velocity widths for Virgo cluster galaxies: open circles are galaxies within 6° of the cluster centre taken to be at $\alpha_{1950} = 12^h25^m$,$\delta_{1950} = +13°06'$; solid circles are galaxies within 6° circle centred on .N 4486 but not within 6° of the cluster centre. The solid lines represent (equations 1 to 4) in the text. The dotted lines are $\pm 2\sigma$ lines.

It is significant that the mean error of the relation, ± 0·46 mag, is nearly the same at *V, r* and *IV* and agrees well with that derived in *H* (equation 4 and MAH). This proves clearly that the uncertainties in the correction for internal absorption (large in *V* and small in *IV* and *H*) do not contribute significantly to the scatter.

It is now of interest to intercompare the scatter of the individual galaxies, in *V, r, IV* and *H* from the mean regression lines (equations 1 to 4) to understand its origin With this in mind, magnitude residuals $\delta (V)^{c}_{-0\,5}$,$\delta(r)^{c}_{-0\,5}$ and $\delta(IV)^{c}_{-0\,5}$ are computed and plotted against the magnitude residual $\delta(H)^{c}_{-0\,5}$ in Fig. 2 for our Virgo cluster galaxies, including N 4438 and N 4569.

The main result (Fig. 2) is that the residuals in the luminosity-H I velocity width relations at *V, r, IV* and *H* are correlated with one another. It follows that the errors in the magnitudes $(V)^{c}_{-0\,5}$ $(r)^{c}_{-0\,5}$ $(IV)^{c}_{-0\,5}$ and $(H)^{c}_{-0\,5}$ are only ± 0·15 mag (derived from Fig. 2) and are much smaller than the scatter observed in the luminosity-H I velocity width relation, ±0·46 mag (Fig. 1). This confirms our previous result that the additive random errors, introduced in the determination of magnitudes due to the adoption of the same growth curve for all types in any one wavelength, together with uncertainties in the amount of internal absorption at different wavelengths, and observational errors, are well within ±0·15 mag.

We conclude, that there is an excess scatter $(0{\cdot}47^2 - 0{\cdot}15^2)^{1/2}$ =0·45 mag in the relations and that is nearly the same in all the observed wavelengths, *V, r, IV* and *H.* Hence, it also follows that the distances to other clusters and groups could be obtained with nearly the same accuracy whether we use *r* or *IV* or *H* magnitudes in the luminosity-H I velocity width relation. It should be pointed out that bursts of star formation might be more important in field galaxies leading to, possibly, an increase in the scatter in *V* and *r* magnitudes.

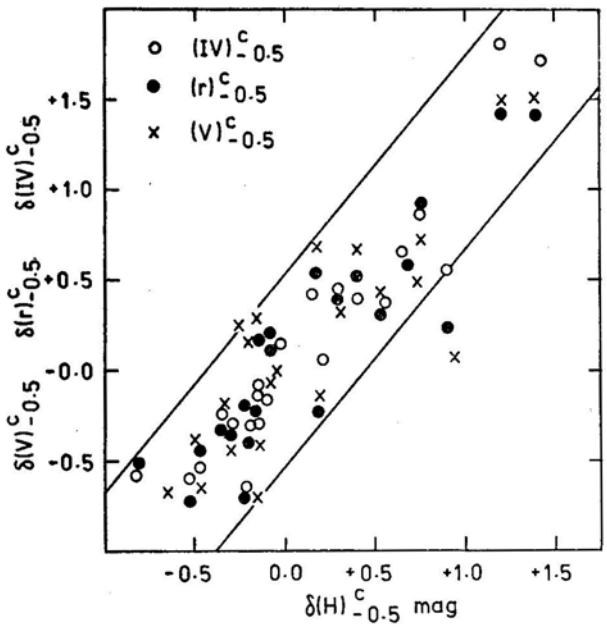

Figure 2. Residual in *H* magnitude from Fig. 1d, plotted against residuals in *V, r* and *IV* magnitudes derived from Fig. la, b and c respectively

The excess scatter of 0·45 mag cannot be explained fully by the error in log $W(0)$ estimated as 3 per cent corresponding to ~ ± 0·1 mag. A likely possibility to reduce the scatter in (equations 1 to 4) is the adoption of a ' kinematic magnitude' instead of the isophotal magnitudes $(V)^{c}_{-0\,5,}$ (r) $^{c}_{-0\,5,}$ (IV) $^{c}_{-0\,5,}$ (H) $^{c}_{-0\,5,}$ Kinematic magnitude represents the magnitude of the galaxy corresponding to $[r_{max}/D\ (0)]$ * which varies from galaxy to galaxy and hence is different from the adopted isophotal magnitude corresponding to a fixed $A/D(0)$ of the galaxy. The variation of $r_{max}/D(0)$ changes systematically from 0·1 for S0/*a*-*Sa* to ~ 0·5 for Sd-Sm galaxies (Brosche 1973; Huchtmeier 1975; Kormendy and Norman 1979). The kinematic magnitude for each Virgo galaxy has been derived by applying correction to isophotal magnitudes in Table 1 as follows:

$$\text{kinematic magnitude} = \text{isophotal magnitude} - K \log \frac{r_{max}}{D(0)} - 0{\cdot}5.$$

The value of K is the slope of the growth curve derived in *V, r, IV* or *H* wavelength in Section 2; r_{max}/D (0), for each Hubble type, is taken from Fig. 2 of Aaronson, Mould and Huchra (1980).

Fig. 3 represents the kinematic magnitude H I velocity width relations for our Virgo cluster galaxies. Kinematic magnitudes at *V, r, IV* and *H* are represented as $(V)^{c}_{-0\,5,K,}$ $(r)^{c}_{-0\,5,K,}(IV)^{c}_{-0\,5,K}$, $(H)^{c}_{-0\,5,K,}$ respectively. Formal least squares analysis gives the following solutions:

$$(V)^{c}_{-0.5,K} = -7{\cdot}14 \log W(0) + 29{\cdot}650; \text{ mean error} = \pm 0{\cdot}40 \text{ mag}, \quad (5)$$

$$(r)^{c}_{-0.5,K} = -7{\cdot}76 \log W(0) + 30{\cdot}75; \text{ mean error} = \pm 0{\cdot}41 \text{ mag}, \quad (6)$$

$$(IV)^{c}_{-0.5,K} = -8{\cdot}870 \log W(0) + 32{\cdot}825; \text{ mean error} = \pm 0{\cdot}42 \text{ mag}, \quad (7)$$

$$(H)^{c}_{-0.5,K} = -8{\cdot}389 \log W(0) + 30{\cdot}622; \text{ mean error} = \pm 0{\cdot}39 \text{ mag}. \quad (8)$$

It is evident from the above equations, that using kinematic magnitudes instead of isophotal magnitudes, makes the slope of the luminosity-H I velocity width relation less steep in all the observed wavelengths and the scatter is reduced only marginally from ± 0·47 to ± 0·40 mag. This indicates that the main source of scatter may not be the variation of r_{max} with type. However, it is to be noted that the scatter in r_{max} within each type is substantial. Due to the lack of rotation curve data for the galaxies in Table 1 we are not able to correct the isophotal magnitudes for this variation.

Our attempts to correlate the scatter in the luminosity-H I width relation at *V, r* and *IV* with morphological types, diameters and surface brightness of galaxies, and similar attempts by MAH at infrared *H,* did not give any positive results. It is possible that *M*/*L* variations within galaxies of the same absolute magnitude are responsible for the scatter in the relation.

4. Distances to field and other cluster galaxies relative to the Virgo cluster

In this section, we derive distances to the field spirals in Table 2 on the assumption that the Virgo cluster relations at *V, r,* and *IV* (equations 1 to 3) are universal.

*Here r_{max} = the radius at which the rotation curve has a maximum curvature and is $\simeq r_{max}$ rigid defined by Kormendy and Norman (1979),

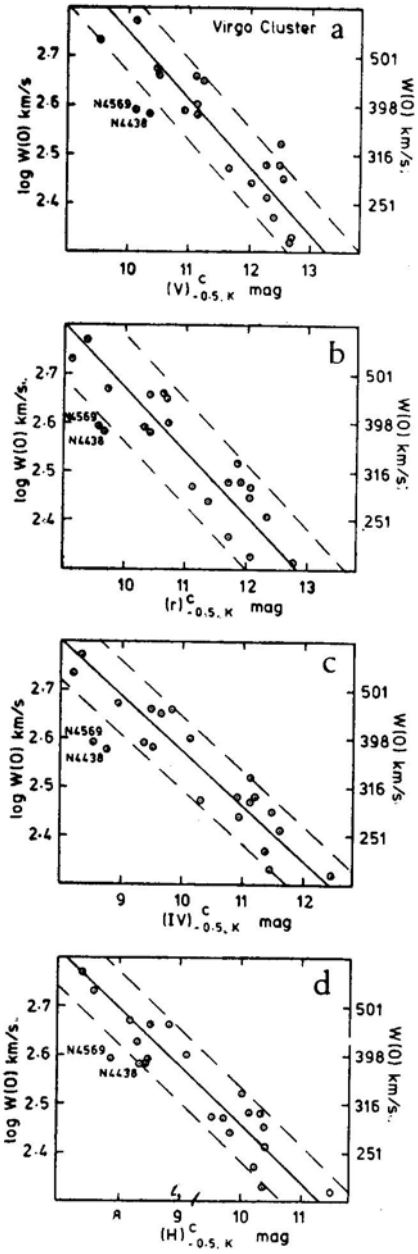

Figure 3. Same as **Fig. 1** except that the isophotal magnitudes are replaced by kinematic magnitudes, derived by correcting the isophotal magnitudes for the systematic variation of r_{max} with type. The solid lines represent (equations 5 to 8) in the text. Dotted lines are $\pm 2\sigma$ lines.

A Virgo-magnitude for each field spiral was obtained from the known log $W(0)$ of that galaxy through the Virgo relations. This Virgo-magnitude, M_{virgo}, when combined with the isophotal magnitude of the field galaxy, enables us to obtain the difference in distance modulus between the galaxy and the Virgo cluster. For each galaxy in Table 2, we list in Table 3 the three independent differences in distance moduli $\Delta\ (m–M)_{V,}$ $\Delta\ (m–M)_{r}$, $\Delta\ (m–M)_{IV}$ along with the average value $\Delta\ (m–M)_{\text{virgo}}$

It is seen from Table 3, that the three independent differences in distance moduli of each galaxy agree well with one another, and the mean error in $\Delta\ (m–M)_{\text{virgo}}$ from the intercomparisons, is ± 0·15 mag which is much less than the scatter (± 0·47 mag) in the luminosity-H I velocity width relations (equations 1 to 3). This low error for the field galaxies supports our earlier results from the Virgo cluster galaxies (Section 3) that our derivation of isophotal magnitudes is within ± 0·15 mag. Further, it also demonstrates that the zero points in the absolute magnitude in the luminosity-H I velocity width relations, are the same whether we use $(V)^{c}_{-0\,5,}$ $(r)^{c}_{-0\,5,}$ $(IV)^{c}_{-0\,5}$ for luminosity.

5. The velocity-distance relation

In Fig. 4, the average of the three distance moduli differences from the Virgo cluster, $\Delta\ (m–M)_{\text{virgo}}$, is plotted against the velocity, $v_{0,}$ for each of the field galaxies of Table 3. The galaxies in the Cancer cluster as well as in Zw 74-23 cluster are marked in the same figure by different symbols. The velocity-distance relation for the field galaxies is shown as a solid line in the figure, where a line of slope 5 for uniform expansion is assumed, and the fit is made for zero mean deviation of the points.

Table 3. Distance moduli of field and cluster galaxies with respect to the Virgo cluster.

Name	log v_0	$\Delta(m-M)_V$	$\Delta(m-M)_r$	$\Delta(m-M)_{IV}$	$\Delta(m-M)_{\text{Virgo}}$
N 2835	2·790	−0·79	−0·88	−0·73	−0·80
3621	2·658	−1·84	−1·91	−1·97	−1·91
4273	3·347	+1·25	+1·10	+1·30	+1·22
4487	3·012	+0·63	+0·56	+0·82	+0·67
4504	3·012	+0·62	+0·62	+0·60	+0·61
4939	3·471	+1·61	+1·53	+1·71	+1·62
5054	3·201	+0·40	+0·26	+0·06	+0·24
5248	3·044	−0·33	−0·46	−0·61	−0·47
5426	3·383	+2·36	+2·32	+2·52	+2·40
6070	3·313	+1·81	+1·69	+1·71	+1·74
6118	3·209	+1·04	+0·96	+0·71	+0·90
6221	3·084	+0·02	−0·06	−0·09	−0·04
6744	2·772	−1·87	−1·96	−2·06	−1·96
6810	3·260	+0·41	+0·43	+0·53	+0·46
6925	3·416	+1·53	+1·52	+1·66	+1·57
U 4334	3·543	+1·46	+1·37	+1·66	+1·50
U 8942	3·770	+3·33	+3·22	+3·79	+3·45
U 8944	3·770	+2·86	+2·70	+2·87	+2·81

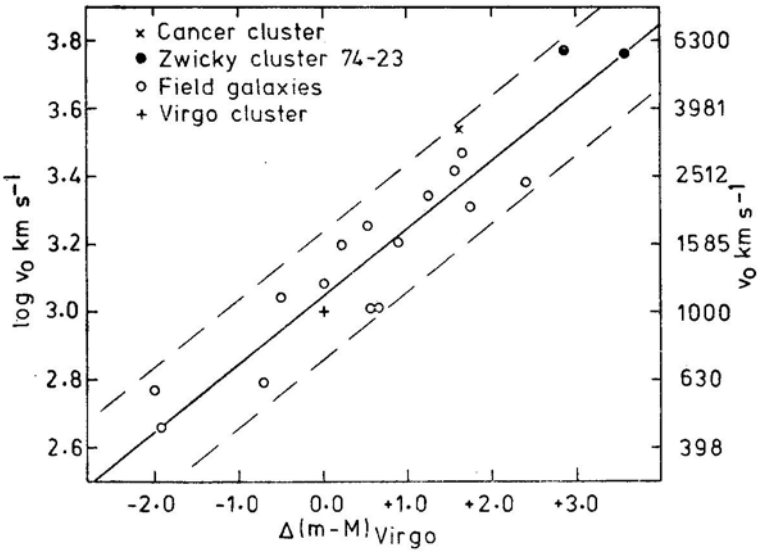

Figure 4. Redshift-distance relation for the field and cluster galaxies. The position of Virgo cluster is indicated and the distances are relative to the Virgo cluster The solid line is represented by $\Delta\,(m–M)_{\text{virgo}} = 5 \log v_0 – 15.28$ The dotted lines are $\pm 2\sigma$ lines.

This relation is represented by the following equation:

$$\Delta(m—M)_{\text{Virgo}} = 5 \log v_0 — 15{\cdot}28 \pm 0{\cdot}13. \tag{9}$$

The dispersion in $\Delta(m–M)_{\text{Virgo}}$ about the mean line in Fig. 4 is ± 0·51 mag, which compares well with the mean error of ± 0·47 mag, derived in the luminosity-log W (0) relations (equations 1 to 3). The Virgo cluster position is plotted in the figure, corresponding to a systemic velocity 1029 + 53 km s^{-1} (MAH) and $\Delta(m–M)_{\text{Virgo}}$ equal to zero.

The results in Fig. 4 could be interpreted as follows: 1. If we assume that the luminosity-H I velocity width relation has the same zero point in absolute magnitude from cluster to cluster, then the velocity-distance relation is closely linear for field galaxies. Of course, the difference in velocity between the mean ridge line of the field galaxies and the Virgo cluster position gives a measure of the perturbation of the local velocity field due to the Virgo cluster. This comes out to 109 ± 68 km S^{-1} which is well within our errors. 2. The three galaxies in the Zw 74-23 and the Cancer clusters, which are well outside the Local Supercluster, fall within 2σ of the mean ridge line. It is important to note that the above two interpretations are preliminary and hence are to be given low weight until we have proved the universality of the luminosity-H I velocity width relation in *V, r* and *IV* wavelengths, and until the mean ridge line in Fig. 4 is defined by an unbiased sample of field and group galaxies.

The distance modulus differences from the Virgo cluster to the Cancer galaxy U 4334, and Zw 74-23 galaxies U 8942, U 8944 (Table 3) are +1·50, +3·45 and +2·81 mag respectively. These are in agreement with the values of +1·75, +3·23, +2·46 derived for the same galaxies through *H* magnitudes by Aaronson *et al.* (1980). However, these three galaxies are not enough to derive a meaningful value of the Hubble constant for these clusters.

6. Conclusion

An investigation of the luminosity-H I width relation was made, using magnitudes at *V* (5500 Å), *r* (6738 Å) and *IV* (10500 Å) of the Virgo cluster spirals. The slopes of the relations vary from ~ — 9 at the visible and red wavelengths and to ~ — 10 at the near infrared and the infrared wavelengths. Intercomparison of residuals $\delta(V)^{c}_{-0.5,}\delta(IV)^{c}_{-0\,5,}\delta(H)^{c}_{-0\,5,}$ indicate that the scatter of ~ 0·46 mag in the luminosity-H I width relation is much higher than the errors in the final corrected magni tudes, ~ 0 15 rnag, in all the observed wavelengths. When we use 'kinematic' instead of isophotal magnitudes the scatter is reduced only marginally to ± 040 mag. We find that most of the scatter in the relation is intrinsic.

The corrected magnitudes $(V)^{c}_{-0\,5,}$ $(r)^{c}_{-0\,5,}$ $(IV)^{c}_{-0\,5}$ have been obtained for 15 field galaxies and three galaxies in Cancer and Zw 74-23 clusters. These were combined with the available-H I velocity widths and used to derive the distance moduli of these galaxies using the Virgo cluster relations. The three independent differences of distance modulus from the Virgo clusters derived for each galaxy in *V, r* and *IV* agree with one another, indicating that the zero point in absolute magnitude is the same in all the observed wavelenghts.

Acknowledgements

The author wishes to thank A. Kalnajs and A. W. Rodgers for many valuable discussions, and. Su Hong-Jun and N. Killeen for helping during the observations.

References

Aaronson, M., Huchra, J., Mould, J. 1979, *Astrophys. J.*, **229,**1.
Aaronson, M., Mould, J., Huchra, J. 1980, *Astrophys. J.,* **237,** 655.
Aaronson, M., Mould, J., Huchra, J., Sullivan III, W. T ., Schommer, R. A., Bothun, G. D. 1980, *Astrophys. J.,* **239**,12.
Brosche, P. 1973, *Astr. Astrophys.* **23**, 259.
Danver, C-G. 1942, *Ann, Obs. Lund.,* No. 10.
de Vaucouleurs, G. 1975, in *Galaxies and the Universe* Eds A. Sandage,M. Sandage and J. Kristian, University of Chicago Press, p. 557.
de Vaucouleurs, G., de Vaucouleurs, A., Corwin, H. G. 1976, *Second Reference Catalogue of Bright Galaxies,* University of Texas Press, Austin.
Frogel, J. A., Persson, S. E., Aaronson, M., Matthews, K. 1978, *Astrophys. J.* **220,** 75.
Glass, I. S. 1974, *Mon.* Notes *astr. Soc. Sth. Afr.,* **33**, 53.
Huchtmeier, W. K. 1975, *Astr. Astrophys.,* **45**, 259.
Humason, M. L., Mayall, N. U., Sandage, A. R. 1956, *Astr. J.,* **61**,97,
Johnson, H. L. 1966, in *Nebulae and Interstellar Matter,* Eds B. M. Middlehurst and L. H. Aller, University of Chicago Press, p. 167.
Kormendy, J., Norman, C. A. 1979, *Astrophys. J.*, **233,** 539.
Mould, J., Aaronson, M. Huchra, J. 1980, *Astrophys. J.,* **238**, 458.
Nilson, P. 1973, *Uppsala General Catalogue of Galaxies,* RoyalSociety of Sciences,Uppsala.
Rubin, V. C., Ford, W. K., Thonnard, N., Roberts, M. S., Graham, J. A. 1976, *Astr. J.*, **81**, 687.
Sandage, A., Tammann, G. A. 1975, *Astrophys. J.*, **197**, 265.
Sandage, A., Tammann, G. A. 1976, *Astrophys. J.*, **210**, 7.
Sandage , A., Tammann, G. A. 1976a, *Astrophys. J.*, **207**, LI.

Sandage, A., Visvanathan, N. 1978, *Astrophys. J.,* **223**, 707.
Shostak, G. S. 1978, *Astr. Astrophys.,* **68**, 321.
Tammann, G. A., Sandage, A., Yahil, A. 1980, *Phys. Scripta,* **21**, 630.
Tully, R. B., Fisher, J. R. 1977, *Astr. Astrophys.,* **54**, 661.
Visvanathan, N.,1972, *Publ. astr. Soc. Pacific,* **84**, 248.
Visvanathan, N., 1979, *Astrophys. J.,* **228,** 81.
Visvanathan, N., Sandage, A. 1977, *Astrophys. J.,* **216,** 214.
Whiteoak, J. B., Gardner, F. F. 1977, *Austr. J. Phys.,* **30**,187.
Zwicky, F., Wild, P., Herzog, E., Karpowicz, M., Koval, C. 196168, *Catalogue of Galaxies and Clusters of Galaxies,* 1-6, California Inst. Tech., Pasadena.

J. Astrophys. Astr. (1981) **2,** 81-86

Photon Escape Probabilities in Expanding Atmospheres

A. Peraiah, K. E. Rangarajan and D. Mohan Rao *Indian Institute of Astrophysics, Bangalore 560034*

Received 1980 December 30; accepted 1981 February 4

Abstract. A comparison of mean number of scatterings and escape probabilities has been made in isotropic scattering and dipole scattering by using the angle-averaged partial frequency redistribution function R_I. We have solved the equations of radiative transfer and statistical equilibrium simultaneously in a spherically symmetric expanding atmosphere. Two cases of atmospheric extension (*i.e.*) B/A=3 and 10 (where B and A are the outer and inner radii of the atmosphere) have been treated.

We find that the partial frequency redistribution gives a larger mean number of scatterings compared to that given by complete redistribution. Velocities tend to reduce the mean number of scatterings and in crease the mean escape probabilities.

Key words: mean number of scatterings—mean escape probability—partial redistribution function—isotropic scattering—dipole scattering

1. Introduction

It is well known that the radiative transfer effects in an optically thick resonance line are considerable and should be investigated by highly accurate methods. If the medium is optically thin, one can easily calculate, for example, the probability P_x that a photon, created at a given point in space and time, leaves the medium without being scattered or absorbed. If the optical depth at a normalized frequency x is given by τ_x then $P_x = \exp(-\tau_x)$. This relation is true in the case of certain subordinate lines. For resonance lines, τ_x is much larger and a rigorous treatment of radiative transfer is required. Several people have studied the problem of mean number of scatterings and photon escape probability in a resonance line (Osterbrock 1962; Hummer 1964; Panagia and Ranieri 1973; Kunasz and Hummer 1974a, b) with various assumptions regarding geometry and nature of the media. However, in all these studies the main assumption was complete redistribution of photons in the line. A few have solved the radiative transfer equation correctly for

the resonance line in a moving media relative to the rest frame. In these calculations the optical depths were assumed at line centre and mean number of scatterings and the mean escape probabilities were computed. In a general case one must reduce the number of free parameters such as optical depths, velocities etc. and obtain a consistent solution of line transfer in the resonance lines. There exist now fast and accurate techniques for obtaining simultaneous solutions of radiative transfer equation in a comoving frame and statistical equilibrium equation, for a resonance line (Peraiah 1980). The aim of this paper is to use such calculations to compute the mean number of scatterings and escape probabilities in a resonance line forming in a spherically symmetric expanding atmosphere. The mean number of scatterings and escape probabilities have been estimated with the partial redistribution function R_I . Isotropic and dipole scattering functions have been employed for the sake of comparison.

2. Brief description of procedure and discussion of the results

The procedure of obtaining a simultaneous solution of radiative transfer equation in a comoving frame and the statistical equilibrium equation for a non-LTE two-level atom with complete redistribution is described in Peraiah (1980 henceforth called Paper I). This procedure has been extended to include partial frequency redistribution (Peraiah 1981). We have made use of the redistribution functions to calculate the profile functions:

$$\phi(x) = \int_{-\infty}^{\infty} R(x, x')\, dx', \tag{1}$$

where

$$R_{I\text{-}AI}(x, x') = \frac{1}{\sqrt{\pi}} \int_{|\bar{x}|}^{\infty} \exp(-t^2)\, dt \tag{2}$$

for isotropic scattering (Unno 1952) and

$$R_{I\text{-}AD}(x, x') = \frac{3}{8}\left\{\frac{1}{\sqrt{\pi}} \int_{|\bar{x}|}^{\infty} \exp(-t^2)\, dt\, [3+2(x^2+x'^2)+4x^2x'^2] - (1/\sqrt{\pi}) \exp(-|\bar{x}|^2)\, |\bar{x}|\, (2|\bar{x}|^2+1)\right\}, \tag{3}$$

for dipole scattering in the angle-averaged redistribution function. The statistical equilibrium equation for a two-level atom that we have used is given by

$$N_1 \{B_{12} \int J_x \phi_x\, dx + C_{12}\} = N_2 \{B_{21} \int J_x \phi_x\, dx + C_{21} + A_{21}\}, \tag{4}$$

where N_1 and N_2 are the number densities in levels 1 and 2, B_{12}, B_{21} and A_{21} are Einstein coefficients, J_x is the mean intensity at the normalized frequency x and C_{12} and C_{21} are the collisional excitation and de-excitations rates (see Paper I). The quantity $\phi(x)$ is the absorption profile defined in equation (1). The probability that a photon is lost by collisional de-excitation is calculated by

$$\epsilon = \frac{C_{21}}{C_{21} + A_{21}\,[1 - \exp(-h\nu/kT)]^{-1}}. \tag{5}$$

The quantities C_{12} and C_{21} are given in Paper I. The quantity ϵ is given in Fig. 1. The iterative procedures are similar to those described in Paper I.

The mean number of scatterings N is calculated as the ratio of the number of emitted photons to those generated in unit time (see Kunasz and Hummer 1974b) and this is given by

$$\langle N \rangle = \frac{\int_A^B K_L(r)\, S_L(r)\, r^2\, dr}{\int_A^B K_L(r)\, \epsilon(r)\, B(r)\, r^2\, dr}. \tag{6}$$

Here $K_L(r)$ is the line centre absorption coefficient per unit frequency band width given by

$$K_L(r) = \frac{h\nu}{4\pi\Delta\nu_D}\,[N_1(r)\, B_{12} - N_2(r)\, B_{21}] \tag{7}$$

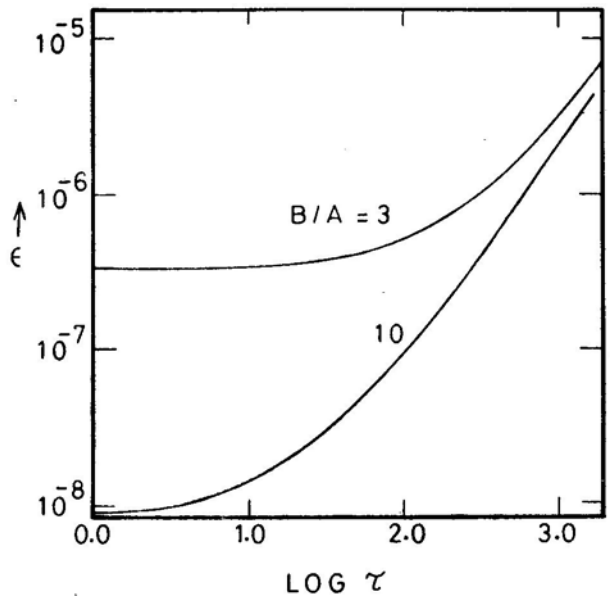

Figure 1. ϵ is given against τ.

$\Delta\nu_D$ being some standard frequency band width. We have taken $\Delta\ \nu_D$ here to be the Doppler width

$$\frac{\nu_0}{c}\left(\frac{2kT_0}{m}\right)^{1/2},$$

where T_0 is temperature and $S_L\ (r)$ is the line source function given in our case as

$$S_L\ (r) = \frac{N_2\ (r)\ A_{21}}{N_1\ (r)\ B_{12} - N_2(r)\ B_{21}} \tag{8}$$

Another important quantity we intend to study is the mean escape probability $\langle P\rangle$ This is given as the ratio of number of photons leaving the medium to those created (see Kunasz and Hummer 1974b) in the medium and is written as

$$\langle P\rangle = \frac{8\pi^2\ B^2 \int_{-\infty}^{\infty} dx \int_{-1}^{+1} I\ (x, \mu, r)\ \mu\ d\mu}{\int_A^B 4\pi\ r^2\ K_L\ (r)\ \epsilon\ (r)\ B\ (r)\ dr}, \tag{9}$$

where $I(x,\ \mu.\ r)$ is the specific intensity making an angle $\cos^{-1}\ \mu$ with the radius vector at the radial point r.

Initially we have assumed a certain variation of number density of the ions and the velocity with which the gas is expanding in accordance with the equation of continuity. When there is motion, we have given a constant velocity gradient $dV/d\tau$ with the velocity increasing outwards starting with 0 mean thermal units (mtu) at $r=A$ and taking the values $V_B = V_{\max}$ at $r=B$. The maximum velocity V_B is set equal to 5, 10, 30 mtu in addition to the static case. We have calculated the mean number of scatterings and the mean escape probability for isotropic and dipole scattering cases for the sizes of the atmospheres $B/A=3$ and 10. In Table 1a the mean number of scatterings per unit velocity gradient is given for the hydrogen Lyman α line.

Table la shows that, in general, dipole scattering gives greater mean number of scatterings than isotropic scattering. As the velocity increases the mean number of scatterings decreases. We also notice that media with higher optical depths have greater mean number of scatterings. We can make a fair comparison between our results (for $V=0$) and those of Panagia and Ranieri (1973, Table 1) which we have reproduced in Table lb. They have calculated the mean number of scatterings using a Voigt profile, assuming $V=0$ and complete redistribution. By comparing the results of Tables la and lb we find that the assumption of partial frequency redistribution gives a larger mean number of scatterings than that given by complete redistribution. This seems to be true in moving media also. For example, if we compare our results with those of Kunasz and Hummer (1974b, Table 1) we find that the mean number of scatterings in our case is greater (even at much higher velocities) than what they have obtained with complete redistribution at smaller velocities ($V=1$ or 2). These differences can be explained on the basis of the fact that we have considered an almost

purely scattering medium ($\epsilon \sim 10^{-5} - 10^{-8}$) whereas Kunasz and Hummer have investigated a medium with $\epsilon = 10^{-2}$.Inanycase, it is important to note that partial frequency redistribution gives higher mean number of scatterings than complete redistribution and this is further accentuated in the case of dipole scattering. The effects of high velocities are to reduce the mean number of scatterings both in the case of isotropic and dipole scattering. However, when the geometrical depth is increased from $B/A=3$ to $B/A=10$ the mean number of scatterings do not show an increase as shown in Panagia and Ranieri (1973, Fig. 1). This difference arises because our optical depth $T(B/A=10)<T(B/A=3)$ and this brings out the fact that the optical depth at the centre of the line plays a more important role than the greater geometrical thickness of the atmosphere.

In Table 2, the mean escape probabilities $\langle P \rangle$ is given for the same parametric values of V, B/A and T the total optical depth as given in Table 1.

There are three ways that a photon can escape the medium: (1) by diffusion of the photon through space, (2) by a line centre photon reaching into the wings after several scatterings and (3) by the translational motion of the gases towards the outward surface of the atmosphere. The solution of the radiative transfer in our calculations

Table 1a. Mean number of scatterings of a Lyman α photon for the total optical depth T.

	V	$R_{I\text{-iso}}$	$R_{I\text{-dip}}$
	0	$6{\cdot}68\ 10^4$	$1{\cdot}12\ 10^5$
B/A = 3	5	$1{\cdot}4\ 10^4$	$2{\cdot}2\ 10^4$
	10	$6{\cdot}97\ 10^3$	$1{\cdot}2\ 10^4$
T = 1986	30	$2{\cdot}13\ 10^3$	$3{\cdot}37\ 10^3$
	0	$5{\cdot}66\ 10^4$	$1{\cdot}43\ 10^5$
B/A = 10	5	$1{\cdot}327\ 10^4$	$2{\cdot}86\ 10^4$
	10	$5{\cdot}65\ 10^3$	$1{\cdot}6\ 10^4$
T = 1763	30	$1{\cdot}87\ 10^3$	$4{\cdot}73\ 10^3$

Table.1b. Mean number of scatterings: Results of Panagia and Ranieri (1973, Table 1)

B/A	3	12
T		
10^3	$2{\cdot}055\ 10^3$	$1{\cdot}732\ 10^3$
10^4	$9{\cdot}555\ 10^3$	$8{\cdot}789\ 10^3$

Table 2. Mean escape probabilities $\langle P \rangle$

	V	$R_{I\text{-iso}}$	$R_{I\text{-dip}}$
	0	0·028	0·013
B/A = 3	5	0·136	0·06
	10	0·278	0·1303
T = 1986	30	0·86	0·401
	0	0·0198	0·008
B/A = 10	5	0·10	0·042
	10	0·198	0·083
T = 1763	30	0·59	0·25

takes into account all these effects, together with the partial frequency redistribution of photons in the line. Here, our main concern is to study the difference that arises by using the partial redistribution with isotropic and dipole scattering functions.

Let us consider how photons diffuse through space. We have studied two cases of B/A=3 and 10, for the same set of velocities. We notice that when the photon has to diffuse through large distances, its probability of escape is reduced. This is true in both the cases of scattering functions. Therefore, the mean escape probabilities for all V's, for B/A=3 are consistently larger than those for B/A=10 for all V's. We have seen in Table 1 that the mean number of scatterings is smaller for T=1763 compared to those for T=1986. This means that a photon has lesser chance of reaching the wings and hence a small escape probability. However, these two effects are highly compensated by the radially moving matter. When the gases which emit and scatter radiation move rapidly towards the outer surface of the atmosphere, the photons are enabled to escape the medium more easily. At V= 30, the escape probability is nearly 0·9 in the case of B/A=3 and isotropic scattering. However, this is reduced to 0·6, when the geometry is extended by three times. A similar analysis holds good for the escape probability with dipole scattering. It is interesting to note that only twice as many photons escape by isotropic scattering compared to dipole scattering. More photons are back-scattered in the case of dipole scattering than in the case of isotropic scattering.

References

Hummer, D. G. 1964, *Astrophys. J.,* **140**, 276.
Kunasz, P. B., Hummer, D. G. 1974a, *Mon. Not. R. astr. Soc.,* **166**,19.
Kunasz, P. B., Hummer, D..G. 1974b, *Mon. Not. R. astr. Soc.,* **166,** 57.
Osterbrock, D. E. 1962, *Astrophys. J.*, **135,**195.
Panagia, N., Ranieri, M. 1973, *Astr. Astrophys.,* **24**, 219.
Peraiah, A. 1980, *J. Astrophys. Astr.,* **1**, 101.
Peraiah, A. 1981, In preparation.
Unno, W. 1952, *Pub. astr. Soc. Japan,* **3**, 158.

J. Astrophys. Astr. (1981) **2,** 87–93

On the Relationship Between Pulsars and Supernova Remnants

R. K. Kochhar *Indian Institute of Astrophysics, Bangalore 560034*

Received 1981 January 9; accepted 1981 February 4

Abstract. We propose that single stars in the mass range 4–6·5$M_{\odot}$, that explode as Supernovae of Type I, are totally disrupted by the explosion and form shell-type remnants. More massive single stars which explode as Supernovae of Type II also give rise to shell-type remnants, but in this case a neutron star or a black hole is left behind. The first supernova explosion in a close binary also gives rise to a shell-type supernova remnant. The Crab-like filled-centre supernova remnants are formed by the second supernova explosion in a close binary. The hybrid supernova remnants, consisting of a filled centre surrounded by a shell, are formed if there is an active neutron star inside the shell.

Key words: pulsars—Supernovae—supernova remnants

1. Introduction

On the basis of their radio observations, supernova remnants (SNRs) have been divided into two classes (Casewell 1979). Most of the SNRs are shell-type, in which radio emission comes from a shell. The filled-centre, Crab-like plerions are characterized by radio emission which has a peak at the centre and falls steadily to the periphery with no enhanced shells. Plerions have flat spectra ($\alpha \simeq 0.0$–$0{\cdot}3$, $S_\nu \sim \nu^{-\alpha}$) while the shell-type have steep spectra ($\alpha \simeq 0{\cdot}5$).

In both the types, radio emission is synchrotron in nature, but while in the shell sources the magnetic field and the relativistic electrons are most probably swept up from the interstellar medium, the relativistic electrons in Crab-like SNRs come from a central pulsar, as is suggested by the observed spatial distribution of the radio emission. X-ray spectrum of shell sources is thermal as evidenced by profuse line emission while the Crab Nebula X-ray spectrum is a featureless power law with $\alpha \simeq 1{\cdot}15$ and a continuation of synchrotron radio emission. Absence of thermal emission from the Crab Nebula implies that the SN 1054 produced at most a very weak shock wave (Schattenberg *et al.* 1980) unlike the shell SNRs which require strong shock waves for their formation.

Examples of shell-type SNRs are Cas A, Tycho, Kepler and SNR 1006. Crab and 3C 58 are two well known examples of plerions. Then there are hybrid SNRs which exhibit the characteristics of both the types. The SNR G 326·3 — 1·8 has a weak but well defined shell ($\alpha \simeq 0{\cdot}4$) surrounding the central feature ($\alpha \simeq 0{\cdot}0$) (Weiler and Panagia 1980). A similar object is CTB 80 (G 68·9+2·8) which has a Crab Nebula-type central radio source inside a weak extended broken shell (Angerhofer, Wilson and Mould 1980). This object is probably the remnant of SN 1408. Weiler and Panagia (1980) have argued that while the SNR Vela XYZ is shell type, the part Vela X which contains the pulsar is Crab-like. The SNR W 50 around SS 433 also perhaps belongs to this category (Weiler and Panagia 1980). It has the sharp outer edge and the integrated spectral index (α =0·45) typical of shell-type remnants but its central regions are plerionic.

From among the 120 or so SNRs known, only two, the Crab and the Vela SNRs are known to contain pulsars. Significantly, the Einstein Observatory has failed to find any evidence for pulsed or unpulsed X-ray emission from a neutron star at the centre of any of the historic SNRs, Cas A, Tycho, Kepler or 1006. Either, only some SN leave behind neutron stars, or else a cooling mechanism more efficient than neutrino cooling—pion cooling for example—may make the neutron star so cold that they are not detectable at X-ray wavelengths (Helfand, Chanan and Novick 1980). Since the cold neutron star at the centre of SNR 1006, if present, would be as old as the Crab pulsar, which is a source of thermal X-rays, it would then seem that pulsar radiation mechanisms heat up the neutron stars so that if a neutron star is not a radio pulsar, it would also not be a source of thermal X-rays.

Attempts have been made to relate the type of the SN, the morphology of the SNR and the presence or otherwise of pulsars in it. Weiler and Panagia (1978) suggested that plerions come from SN II and shell-type SNRs from SN I. According to Radhakrishnan and Srinivasan (1980), although shell-type SNRs do have neutron stars in them, their magnetic fields are such that pulsar activity does not take place (Shukre and Radhakrishnan 1980). Similarly Shklovsky (1980) feels that shell-type SNRs do have neutron stars which do not manifest themselves as pulsars and ' somehow X-ray astronomy fails to detect them'.

These hypotheses have many unsatisfactory features. Cas A is a shell-type SNR and a result of a SN II (Woltjer 1972). It is an obvious counter example to the above hypothesis that SN II form plerions. It is not clear where sources like G 326·3 —1·8, which have a weak shell surrounding a Crab-like feature, fit in this scheme. On the basis of the detection by the Einstein Observatory of an X-ray nebulosity, 80 arcsec in diameter, around the Vela pulsar (Harnden *et al*. 1979), Radhakrishnan and Srinivasan (1980) and Shklovsky (1980) have concluded that the Vela SNR is a plerion, In our view such a conclusion is erroneous. The radio sources Vela X, Y and Z are all parts of an incomplete and rather asymmetrical shell, about 5° in diameter (Milne 1968); the circular outline of the nebula is clearly visible in the ultraviolet light (Miller 1973). The soft X-ray emission also comes from the shell and is interpreted as thermal emission from a (mostly interstellar) plasma heated to about 4×10^6 K by shock waves (Moore and Garmire 1976). Thus the Vela SNR is characterized by radio emission from a shell and X-rays from shock heated plasma—features which are independent of the embedded pulsar. This is in contrast to the Crab Nebula, which owes its structure to the central pulsar. The non-thermal X-rays from a small region around the Vela pulsar and the thermal X-rays from the pulsar itself

are the signatures of a 10^4 yr old pulsar and *not* the defining characteristics of a SNR. We, therefore, conclude that Vela is a shell-type SNR and the Crab-like activity around the pulsar (Harnden *et al.* 1979, Weiler and Panagia 1980) is due to the pulsar. We thus have two morphologically distinct SNRs each containing a pulsar. We now discuss a hypothesis which attempts to relate the type of the SN with the morphology of the SNR and with the presence or otherwise of a compact star.

2. Shell-type supernova remnants

It has been suggested that SN come from short lived stars—SN I from stars in the mass range 46·5 $M_\odot$ and SN II from the more massive stars (Oemler and Tinsley 1979, Kochhar and Prabhu 1981a). Thus a typical elliptical galaxy, in which stars are atleast 10^{10} yr old, will not produce SN; only those will that went through a burst of star formation a few times 10^7 yr ago so that the stars formed then are exploding now. The stars formed would be of masses < 6·5 $M_\odot$; to form more massive stars the presence of density waves is essential (Kochhar and Prabhu 1981b).

It is well known that SN II are confined to the spiral arms whereas SN I belong to the interarm region (Maza and van den Bergh 1976). Since massive close binaries are confined to the spiral arms, it follows that SN occurring in massive close binaries should be of Type II. Moreover, since it is not possible to reproduce the light curve and the spectra of a SN II without a hydrogen envelope around the exploding star (Falk and Arnett 1977), it follows that the pre-SN star in a close binary should have a hydrogen envelope around it. Such an envelope could have survived the mass transfer phase. Or else, it could be transferred back and forth between the two stars if their masses are approximately the same. Alternatively, the matter lost from the system could form a shell around the binary to give a SN II light curve.

We now propose that stars in the mass range 4–6·5 $M_\odot$ exploding as SN I, are totally disrupted by carbon detonation (Arnett 1973) and form a shell-type SNR; More massive stars which explode as SN II also give rise to a shell-type SNR; but in this case a compact core—a neutron star or a black hole—is formed. The first SN explosion in a close binary in most cases is of Type II. Once again a shell SNR forms and a compact star is left behind. If the exploding star in a close binary is totally disrupted, the companion would become a runaway star (Kochhar 1978). Thus the SN explosion of a single star and the first SN explosion in a close binary would give rise to a shell-type SNR. If in the process a neutron star is formed, it would result in a Crab-like activity inside the shell. On the other hand, if no core is left behind by the SN explosion, or else a blackhole forms, the SNR will be a ' pure' shell-type.

W 50 is an example of a shell-type SNR formed as a result of the first supernova explosion in a close binary. The central filled-centre activity is attributed to the neutron star in the binary SS 433 which is exactly at the centre of W 50. We have here an example of Crab-like activity due to a neutron star which is not a pulsar.

We now propose that the shell SNR Cas A has a black hole inside it. A similar conclusion has been reached by Shklovsky (1979) by different arguments. In this context it should be noted that the X-ray emitting gas in Cas A, which must have been ejected from the pre-supernova star, has a mass exceeding 15 $M_\odot$ (Fabian *et al.* 1980) implying a very large mass for the progenitor star.

As for Tycho, Kepler and SNR 1006, which are all SN I (Woltjer 1972) we propose that they are the result of a total disruption of their progenitors caused by explosive carbon burning in degenerate cores (Arnett 1973). The major objection to the carbon detonation model for SN is that it produces too much of iron peak nuclei (Arnett 1973). The chemical composition of the gas in the star before the explosion is determined by the conditions after the helium burning phase in the stellar core. The gas consists of equal parts of ^{12}C and ^{16}O and two per cent of ^{22}Ne which arises in the following manner: all initial CNO nuclei (which have solar abundances) are converted into ^{14}N during hydrogen burning which in turn is converted into ^{18}O during helium burning. It is then assumed that all of the ^{18}O is burnt to ^{22}Ne before helium gets exhausted in the core (Arnett 1973).

Recently the ^{18}O (α, γ) ^{22}Ne reaction has been studied experimentally and the reaction rate compared with that of the competing ^{18}O (α, n) ^{2l}Ne (Trautvetter *et al.* 1978). The results indicate that at temperatures $\leqslant 6 \times 10^8$ K helium burning of ^{18}O proceeds predominantly through the ^{18}O (α, γ) ^{22}Ne reaction, synthesizing mainly the isotope ^{22}Ne. On the other hand at temperatures $> 1{\cdot}6 \times 10^9$ K the ^{18}O (α, n) ^{21}Ne reaction dominates by three orders of magnitude over the ^{18}O (α, γ) ^{22}Ne reaction and hence the isotopes ^{21}Ne and ^{22}Ne are produced in a ratio of 10^3:l (Trautvetter *et al.* 1972).

It would thus seem that the assumption that the pre-explosion gas contains two per cent of ^{22}Ne may not be valid and ^{18}O may be the main product of secondary nucleosynthesis in helium burning. Simulation of explosive-carbon-burning nucleosynthesis with an initial neutron rich mass fraction of two per cent of ^{18}O is found to yield much better agreement with solar system abundances than simulation with an initial two per cent of ^{22}Ne as hitherto used (Harris 1979). Thus after all the carbon detonation Supernovae may not be producing too much of iron peak nuclei.

The elemental abundances in SNR can be deduced from their X-ray spectra. Cas A, Tycho and Kepler all show strong line emission from helium-like species of Si, S and Ar (Becker *et al.* 1979, 1980a, b). If it is assumed that the emitting plasma is in collisional ionization equilibrium (CIE) the above observations imply that Si, S and Ar are greatly overabundant. However, there are enough indications that the emitting plasma is not in CIE (Pravdo and Smith 1979, Pravdo *et al.* 1980). In such a plasma, the line emission corresponds to a temperature much lower than the electron temperature, giving the impression of a two-temperature plasma in which both the high temperature lines and the low temperature continuum are missing. Consequently, the state of ionization is much lower than that predicted by CIE with the result that the intensities of some of the lines may differ from the predicted values by more than an order of magnitude (Itoh 1977). Thus the HEAO 1 and 2 X-ray spectra can be understood in terms of non-equilibrium line emission from a plasma with normal abundances and one need not invoke abnormal abundances (Pravdo and Smith 1979, Pravdo *et al.* 1980). Similarly the X-ray data on SNR 1006 (Becker *et al.* 1980c) can be interpreted in terms of thermal bremsstrahlung from a non-equilibrium plasma rather than as synchrotron emission from a pulsar which is not there (Helfand, Chanan and Novick 1980).

3. Crab-like supernova remnants

The Crab Nebula is characterized by an overabundance of helium without a corresponding excess of heavy elements (Woltjer 1972). Furthermore, as already mentioned, the absence of X-ray line emission implies that the SN 1054 did not produce any shock waves (Schattenberg *et al.* 1980). Kochhar (1979) has suggested that the Crab Nebula is the debris of a helium star in a close binary containing a neutron star. The helium star was totally disrupted by the spiraling-in of the neutron star which in the process was spun up and is identified with the Crab pulsar. The spiraling-in would occur in cases where the separation between the neutron star and the helium star is sufficiently small (if the separation is large, the helium star would evolve as a single star and explode leaving behind a compact star).

We now suggest that all filled-centre SNRs without outer shells are disrupted helium stars. Thus all plerions should have a chemical composition appropriate to a helium star. Since the progenitors of such systems have already undergone a SN explosion, their mean $|z|$ would be about 200 pc (Kochhar 1978).

Weiler and Panagia (1980) list six SNRs as well established plerions. Out of these, Vela X and the centre of G 326·3-1·8, are surrounded by shells. We have classified them, and W 50, as shell-type SNR with active neutron stars inside. The four 'genuine' plerions G 21·5-0·9, CTB 97, 3C 58 and the Crab have a mean $|z|$ of 240 pc. Of course, all plerions should have neutron stars embedded in them and attempts should be made to identify them.

4. Pulsar birthrates

We have argued that while all stars with $m > M_{\odot}$ end their lives as SN, only stars with $m > 6{\cdot}5\ M_{\odot}$ form pulsars. We now show that this is consistent with the recent estimates of pulsar birthrates and of star formation rates.

The computed pulsar birthrate depends on the electron density, n_e, of the interstellar medium which sets the pulsar distance scale and on the beaming factor, f, which specifies what fraction of the total pulsar population is observable. Taking $n_e = 0{\cdot}03$ cm^{-3} and f=0·2, Taylor and Manchester (1977) obtain a pulsar birthrate b_p=0·1 in units of pc^{-2} Gyr^{-1} which in terms of the stellar birthrate of Ostriker, Richstone and Thuan (1974) means that all stars more massive than $2{\cdot}5\ M_{\odot}$ must die as pulsars (If n_e is smaller than 0·03 cm^{-3}, b_p would be lower).

Hanson (1979) has pointed out that the proper motion data are very incomplete and strongly biased towards high velocity pulsars which are easily detected. Correcting for this bias reduces the pulsar birthrate by half. Thus for n_e=0·03 cm^{-3} Hanson (1979) obtains b_p=0·05. Recent studies show that the stellar birthrate of Ostriker, Richstone and Thuan (1974) is significantly too low (Miller and Scalo 1979, Shipman and Green 1980). Larson and Tinsley (1978) have noted that this birthrate does not reproduce the position of most galaxies in the *UBV* two-colour diagram.

The most recent pulsar birthrate is due to Shipman and Green (1980). They obtain the deathrate of all stars with $M_L < M < M_U$

$$b = (b_0/x)\,(M_L^{-x} - M_L^{-x}),$$

where b_0 = 2·08 and x=1·63. The birthrate of Ostriker, Richstone and Thuan (1974) corresponds to b_0 = 4·34 and x=2·57. Miller and Scalo obtain x=1·5 ($M < 10\ M_\odot$) and x=2·3 ($M > 10\ M_\odot$).

We now calculate the birthrates of pulsars and of SN as follows. We assume that all single stars with $M > 4\ M_\odot$ explode as SN. For a SN to occur in a close binary system, the mass of the star should be $M \geqslant 10$–$12\ M_\odot$ (van den Heuvel 1977; Massevitch, Tutukov and Yungelson 1976). Further we assume that 50 per cent of stars with $M < 4M_\odot$ are in binaries. Then following Shipman and Green (1980) we obtain a SN rate b_{SN}=0·08. If all single stars with M>6·5 $M_\odot$ and all double stars with $M > 10M_\odot$ become pulsars then the pulsar birthrate is b_p =0·045. We thus see that about 45 per cent of SN do not form any compact cores. Our derived pulsar birthrate of 0·045 should be compared with Hanson's (1979) estimates of b_p = 0·05 for n_e = 0·03 cm^{-3} and b_p = 0·03 for n_e= 0·025 cm $^{-3}$.

5. Conclusions

We have argued that shell-type SNRs form as a result of SN explosion of single stars and the first explosion in a close binary. The Crab-like SNRs are formed by the second SN explosion in a close binary. While a Crab-like SNR owes its existence to the embedded pulsar, the structure of a shell-type SNR is independent of the central pulsar. If at the centre of a shell-type SNR, there is an active neutron star, it will give rise to a Crab-like activity within the shell. On the other hand, if the shell SNR does not contain any neutron star or contains a black hole, we shall get a ' pure ' shell-type SNR.

We have further argued that single stars with $4<M/M_\odot < 6{\cdot}5$ explode as SN I and are totally disrupted while those with mass $>6{\cdot}5M_\odot$ exploding as SN II leave behind a neutron star or a black hole. In both cases a shell-type SNR forms.

Acknowledgements

The author thanks the Deutsche Forschungsgemeinschaft for partial financial support and Prof. Klaus Fricke for useful conversations.

References

Angerhofer, P. E., Wilson, A. S., Mould, J. R. 1980, *Astrophys. J.*, **236**, 143.
Arnett, W. D. 1969, *Astrophys. J.,* **157**,1369.
Arnett, W. D. 1973, *A. Rev. Astr. Astrophys.,* **11**, 73.
Becker, R. H., Holt, S. S., Smith, B. W., White, N. E., Boldt, E. A., Mushotzky, R. F., Serlemitsos, P. J. 1979, *Astrophys. J.,* **234**, L73.
Becker, R.H.,Holt, S.S.,Smith, B,W.,White,N. E., Boldt,E. A.,Mushotzky,R. F.,Serlemitsos, P. J. 1980a, *Astrophys. J.*, **235**, L5.
Becker, R. H., Boldt, E. A., Holt, S. S., Serlemitsos, P. J., White, N. E. 1980b, *Astrophys. J.*, **237**, L77.
Becker, R. H., Szymkowiak, A. E., Boldt, E. A., Holt, S. S., Serlemitsos, P. J. 1980c, *Astrophys. J.*, **240**, L33.
Caswell, J. L. 1979, *Man. Not. R. astr. Soc.,* **187**, 431.

Fabian, A. C., Willingale, R., Pye, J. P., Murray, S. S., Fabbiano, G. 1980, *Mon. Not. R. astr. Soc.,* **193**, 175.
Falk, S.W., Arnett, W. D. 1977, *Astrophys. J. Suppl. Ser.,* **33**, 515.
Hanson, R. B. 1979, *Mon. Not. R. astr. Soc.,* **186**, 357.
Harnden, F. R., Hertz, P., Gorenstein, P., Grindlay, J., Schreier, E., Seward, F. 1979, *Bull. Am. astr. Soc.,* **11**, 424.
Harris, M. J. 1979, *Observatory,* **99**,190.
Helfand, D. J., Chanan, G. A., Novick, R. 1980, *Nature,* **283**, 337.
Itoh, H. 1977, *Publ. astr. Soc. Japan,* **29***,* 813.
Kochhar, R. K. 1978, *Nature,* **271**, 528.
Kochhar, R. K. 1979, *Nature,* **277**,116.
Kochhar, R. K., Prabhu, T. P. 1981a, *Bull. astr. Soc. India,* (in press).
Kochhar, R. K., Prabhu, T. P. 1981b, In Preparation.
Larson, R. B., Tinsley, B. M. 1978, *Astrophys. J.,* **219**, 46.
Massevitch, A. G., Tutukov, A. V., Yungelson, L. R. 1976, *Astrophys. Sp. Sci.,* **40**, 115.
Maza, J., van den Bergh, S. 1976, *Astrophys. J.,* **204**, 519.
Miller, E. W. 1973, *Publ. astr. Soc. Pacific,* **85**, 764.
Miller, G. E., Scalo, J. M. 1979, *Astrophys. J. Suppl. Ser.,* **41**, 513.
Milne, D. K. 1968, *Austr. J. Phys.,* **21**, 201.
Moore, W. E., Garnure, G. P. 1976, *Astrophys. J.,* **206**, 247.
Oemler, A., Tinsley, B. M. 1979, *Astr. J.,* **84**, 985.
Ostriker, J. P., Richstone, D. O., Thuan, T. X. 1974, *Astrophys. J.,* **188**, L87.
Pravdo, S. H., Smith, B. W. 1979, *Astrophys. J.,* **234**, L195.
Pravdo, S. H., Smith, B. W., Charles, P. A., Tuohy, I. R. 1980, *Astrophys. J.,* **235**, L9.
Radhakrishnan, V.,Srinivasan, G.1980, *J. Astrophys. Astr.,* **1**, 25.
Schattenburg, M. L., Canizares, C. R., Berg, C. J., Clark, G. W., Markert, T. H., Winkler, P. F 1980, *Astrophys. J.,***241**,L151.
Shipman, H. L., Green, R. F. 1980, *Astrophys. J.,* **239**, L111.
Shklovsky, I. S. 1979, *Nature,* **279**, 703.
Shklovsky, I.S.1980, *Publ. astr. Soc. Pacific,* **92**,125.
Shukre, C. S., Radhakrishnan, V. 1980, in *IAU Symp. 95,* (in press).
Taylor, J. H., Manchester, R. N. 1977, *Astrophys. J.,* **215**, 885.
Trautvetter, H. P., Wiescher, M., Kettner, K-U., Rolfs, C. 1978, *Nucl. Phys.,* **A297**, 489.
van den Heuvel, E. P. J. 1977, *Ann. N. Y. Acad. Sci.,* **302**,14.
Weiler, K. W., Panagia, N. 1978, *Astr. Astrophys.,* **70**,419.
Weiler, K. W., Panagia, N. 1980, *Astr. Astrophys.,* **90**, 269.
Woltjer, L. 1972, *A. Rev. Astr. Astrophys.,* **10**,129.

J. Astrophys. Astr. (1981) **2,** 95–113

Intrinsic Properties of Carbon Stars. I. Effective Temperature Scale of N-type Carbon Stars

Takashi Tsuji *Tokyo Astronomical Observatory, University of Tokyo, Mitaka, Tokyo, 181 Japan*

Received 1981 January 27; accepted 1981 March 7

Abstract. It is shown that the infrared flux method for determining stellar effective temperatures (Blackwell and Shallis 1977; Blackwell, Petford and Shallis 1980) can be applied to cool carbon stars. Although the spectra of cool carbon stars are highly line blanketed, the spectral region between 3 and 4 μm (L-band in the infrared photometry system) is found to be relatively free from strong line absorption. The ratio R_L of bolometric flux to L flux can then be used as a measure of effective temperature. On the basis of the predicted line-blanketed flux based on model atmospheres, with an empirical correction for the effect of 3 μm absorption due to polyatomic species (HCN, C_2H_2), it is shown that R_L is roughly proportional to $T^3_{\rm eff}$. The high sensitivity of R_L to $T_{\rm eff}$ makes it a very good measure of effective temperature, and the usual difficulty due to differential line blanketing effect in the analyses of photometric indices of cool carbon stars can be minimized.

It is found that the majority of N-type carbon stars with small variability (SRb and Lb variables) are confined to the effective temperature range between 2400 and 3200 K, in contrast to M-giant stars (M0 III-M6 III, including SRb and Lb variables) that are confined to the effective temperature range between 3200 and 3900 K. The effective temperatures based on the infrared flux method show good agreement with those derived directly from angular diameter measurements of 5 carbon stars. On the basis of the new effective temperature scale for carbon stars, it is shown that the well known C-classification does not represent a temperature sequence. On the other hand, colour temperatures based on various photometric indices all show good correlations with our derived effective temperatures.

Key words: carbon stars—effective temperatures—line blanketing—spectral classification—stellar atmospheres

1. Introduction

Carbon stars play an important role in our understanding of both stars and galaxies. For example, the recent theory of stellar evolution made it possible to predict the details of stellar evolution at the advanced stages (*e.g.* Sugimoto and Nomoto 1974; Iben 1975). A carbon star could thus be a touchstone for the theory of stellar evolution at such late stages. Although carbon stars represent rather a minor constituent as compared with K–M giant stars in our Galaxy, it is found recently that carbon stars may form a more important population in other stellar systems such as the Magellanic Clouds (Blanco, Blanco and McCarthy 1978). This fact implies that carbon stars cannot necessarily be regarded as peculiar stars but rather they could represent a characteristic stage of normal stellar evolution. This fact also implies that carbon stars can be used as an important tracer of galactic evolution. Also, recent infrared and radio observations have revealed that many carbon stars are embedded in dust and molecular clouds (*e.g.* Merrill and Ridgway 1979; Zuckerman 1980), which implies that carbon stars are losing mass at a large rate and this has important bearings not only on stellar evolution but also on interstellar chemistry.

One important prerequisite to pursue these problems relating to carbon stars is to have an accurate knowledge of the intrinsic properties of carbon stars. This should in principle be determined from observations of nearby carbon stars. Unfortunately, this problem is still not adequately resolved possibly because of the great complexity of the spectra of cool carbon stars. For example, the effective temperature scale of carbon stars is not available. It is also uncertain whether any of the spectral classification schemes can be considered as a temperature sequence. Recently, spectral classification of carbon stars has been extended to a large sample by Yamashita (1967, 1972, 1975a), and major spectroscopic characteristics of these stars have been well worked out. On the other hand, Richer (1971) pointed out that C-classification is not compatible with colour temperatures based on infrared photometry, and he has proposed a new spectral classification scheme of carbon stars that may be more consistent with colour temperatures. Such an ambiguous situation can exist if either the C-classification does not represent the temperature sequence of carbon stars (*e.g.* Bergeat *et al.* 1976a; Scalo 1976), or if the interpretation of infrared photometry is incorrect because of the large differential line-blanketing effect in carbon stars (Yamashita 1975b). More recently, angular diameter measurements have also been made of some cool carbon stars (Ridgway, Wells and Joyce 1977; Ridgway, Jacoby, Joyce and Wells 1980, personal communication; Walker, Wild and Byrne 1979). The temperature scale of carbon stars can, in principle, be determined by this method. At present, however, the number of stars analyzed by this procedure is still too small to provide a definite conclusion. We show in this study a new possibility to settle the issue.

The infrared flux method for determining stellar effective temperature, first proposed by Blackwell and Shallis (1977) and further developed by Blackwell, Petford and Shallis (1980), can be applied to cool carbon stars. This success is due to locating an infrared spectral region that is free from strong line absorption in cool carbon stars. In fact, the L band ($\lambda_{\rm eff}$ =3·4 μm) measured by the current infrared photometric system can be regarded as a good quasi-continuum in cool carbon stars, and reasonably accurate prediction of the emergent stellar flux can be done on the basis of model

atmospheres presently available for these stars. This fact makes it possible to apply the infrared flux method to these. Hence an effective temperature scale for the cool carbon stars can be determined reliably for the first time, by the same and consistent method as for K–M giant stars (Tsuji 1979, 1980).

2. Method of analysis

There have been two major methods for the determination of stellar effective temperatures. The first one utilizes the observed angular diameter θ_{LD} and the bolometric flux at the Earth $f_{\rm bol}$ The effective temperature is obtained from

$$T_{\rm eff} = (4f_{\rm bol}/\sigma\ \theta_{LD})^{1/4}, \tag{1}$$

where σ is the Stefan-Boltzman constant. This method has recently been applied successfully to cool stars on the basis of angular diameters of 5 carbon stars that have been measured by the lunar occultation method.

The second one is the model atmosphere method in which the temperature dependence of the observed spectral energy distribution curve is analyzed by means of model atmospheres. Although this method has been applied recently to cool stars, the spectral energy distribution of cool carbon stars is much more complicated as compared with that of M-giant stars. This spectral energy distribution is shown in Fig. 1 where the predicted line blanketed flux, based on the model of a carbon star with $T_{\rm eff}$ =3400K, log g=0·0 and $V_{\rm tur}$ =5 km s^{-1} (solid line, Querci and Tsuji 1974), is also shown together with the predicted line blocking-free continuum evaluated for the same model (dashed line). As compared with the emergent flux of an M-giant star of the same effective temperature (Tsuji 1978) shown at the bottom of Fig. 1 the emergent flux of a carbon star is much more disturbed by strong molecular absorption. In the case of M-giant stars, some quasi-continua such as those around 1 and 3·5 μm, are still found. It is then possible to determine effective temperatures for these stars by the second method since such quasi-continuous fluxes can be predicted accurately on the basis of model atmospheres. However, for carbon stars, such an analysis will be more difficult because it is not easy to find such quasi-continua in these stars. It is in principle possible to compute emergent fluxes for strongly line blanketed regions, but the accuracy of these computations may not be very high because of the high sensitivity of the results to the uncertainties in the model atmospheres as well as in the molecular data. In such a case, the determination of effective temperature will further be difficult because line absorption depends on other parameters such as chemical composition, gravity, turbulent velocity etc.

A new method of determining stellar effective temperature has been proposed recently by Blackwell and Shallis (1977). This third method, which is referred to as the infrared flux method, is based on the estimate of stellar angular diameter by

$$\theta_{LD} = [4\, f_\lambda/\pi\, F_\lambda\, (T_{\rm eff}, g, \ldots)]^{1/2}, \tag{2}$$

where F_λ is the observed infrared flux received at the Earth and F_λ ($T_{\rm eff,}$ g, ...) is the emergent stellar flux. Then, with the bolometric flux, the effective temperature

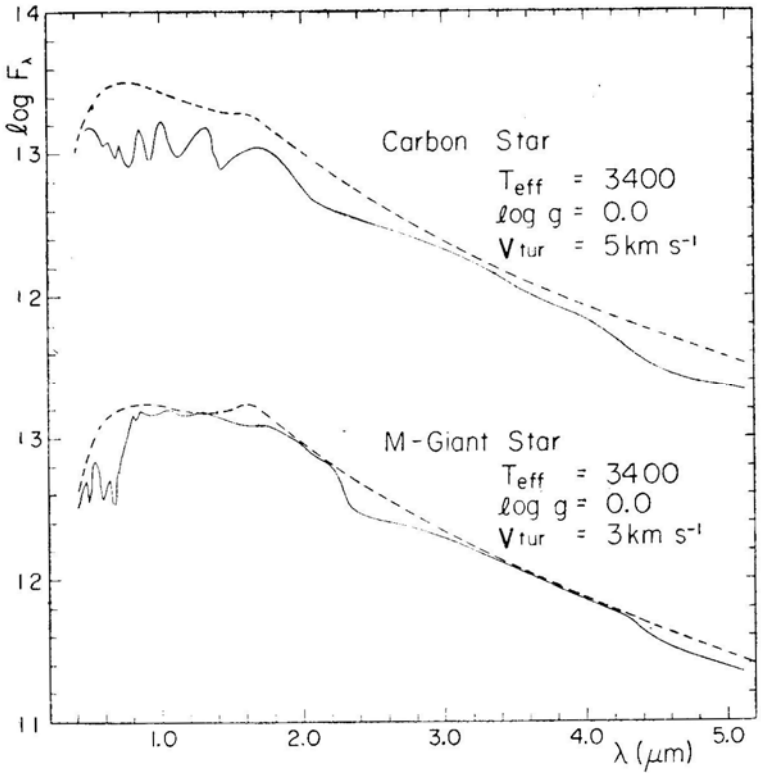

Figure 1. Spectral energy distribution of carbon stars (top) is shown in comparison with that of M-giant stars (bottom) of the same effective temperature. Predicted line blanketed flux is shown by solid line while line blocking free continuum based for the same model atmosphere is shown by dashed line in each model. It is to be noted that the spectral region between 3 and 4 μm is little disturbed by strong line blanketing even in a carbon star.

can be determined by equation (1). The final solution in this method should be determined by iterations since the emergent stellar flux in equation (2) already depends on the effective temperature and other stellar parameters. Recently, however, Blackwell, Petford and Shallis (1980) showed that the iterations can be avoided eliminating θ_{LD} from equations (1) and (2). Thus we derive

$$f_{\rm bol}/f_\lambda = T_{\rm eff}^4/\pi F_\lambda (T_{\rm eff}, g, \ldots) = R_\lambda (T_{\rm eff}, g, \ldots). \quad (3)$$

Then, the observed value of $f_{\rm bol}/f_\lambda$ can be interpreted in terms of R_λ ($T_{\rm eff}$, g, ...) that can be evaluated on the basis of model atmospheres, and the effective temperature can be estimated if the values of other parameters are known (or are not important). Also, infrared flux f_λ depends linearly on $T_{\rm eff}$ in the Rayleigh-Jeans region, and hence R_λ varies as $T_{\rm eff}$. Because of this high sensitivity of R_λ to $T_{\rm eff}$, R_λ can be used as a good stellar thermometer.

It is also desirable to apply the infrared flux method to the spectral region least disturbed by line absorption. In this method, however, it is necessary to find only one spectral region that is free from strong line absorption in the infrared. This is an important advantage of the method especially for carbon stars, because it is possible

to find a spectral region little disturbed by strong absorption even in cool carbon stars. In fact, the difference between the line blanketed and the line free fluxes is small in the spectral interval between 3 and 4 μm as seen in Fig. 1. This fact suggests that the *L* flux of carbon star is also a good quasi-continuum. Also, detailed spectrophotometric observations of this interval (*e.g.* Merrill and Stein 1976; Noguchi *et al.* 1977; Goebel *et al.* 1980) show that there is no strong absorption in the *L* band region except for the characteristic absorption centred at 3·07 μm. The spectral energy curve beyond this absorption is pretty smooth up to 4 μm especially in the non-Mira carbon stars. This fact implies that the emergent flux for *L* band can be predicted with reasonable accuracy even for cool carbon stars and thereby opens a new possibility of applying the infrared flux method to cool carbon stars.

3. Emergent fluxes and *R* values for carbon stars

Our problem is to evaluate accurate *L* flux and corresponding R_L value for carbon stars. Until now line blanketed fluxes for carbon stars have been determined by the opacity probability distribution function method (OPDF, Querci Querci and Tsuji 1974; Querci and Querci 1976) or by the opacity sampling method (Sneden, Johnson and Krupp 1976). A problem in model atmospheres for carbon stars concerns the assumption of a composition especially of C, N and O. One hypothesis is that the atmospheres of carbon stars are mainly composed of the material processed through CNO cycle, and the emergent fluxes based on this idea have been evaluated by Querci, Querci and Tsuji (1974). This type of model atmospheres is characterised by a high abundance of nitrogen and we refer to this series of models as N-rich models. Another hypothesis is that the origin of carbon stars should be due to mixing of material processed through 3α reaction, and some emergent fluxes for such models have been given by Querci and Querci (1976). These atmospheres are carbon-rich and we refer to this series of models as C-rich models.

Another problem is a possible effect of 3 μm absorption which is situated at the edge of the *L* band filter. The 3 μm absorption is now known to be due to polyatomic molecules such as C_2H_2 and HCN(Ridgway, Hall and Carbon 1978). In the model atmospheres of carbon stars noted above, the effect of these polyatomic molecules has not yet been taken into account. For our present purpose, however, we find that an empirical approach based on the observed band absorption may be sufficient. According to a detailed study of 3 μm absorption in carbon stars by Noguchi *et al.* (1977), the observed flux $F_{\rm obs}(\lambda)$ around 3 μm band can be represented by

$$F_{\rm obs}(\lambda) = F_0(\lambda) \exp[-\tau(\lambda)], \tag{4}$$

where $\tau(\lambda)$ is the optical depth of the 3 μm band and $F_0(\lambda)$ is the local pseudo continuum around the 3 μm band. These authors have further shown that

$$\tau_{\rm norm}(\lambda) = \tau(\lambda) / \tau_m \tag{5}$$

normalized by the maximum optical depth τ_m is remarkably similar for all the carbon stars observed, both in the position of the maximum depth and in the band shape (sec Figs 11-13 of Noguchi *et al.* 1977).

The problem now is to assign the value of τ_m for a model of a given effective temperature. For this purpose, we find that the 3μm band optical depths τ_m measured by Noguchi *et al.* (1977) correlate very well with the effective temperatures determined by the infrared flux method. This correlation was already found for the effective temperatures determined by R_L values which have been evaluated without the effect of 3 μm absorption. With this correlation between τ_m and τ_{eff} it is now possible to assign a value of τ_m for a model of a given effective temperature. Assuming that the normalized band shape τ_{norm} represented by a triangular dip centred at 3·07 μm (see Fig. 17 of Noguchi *et al.* 1977), the effect of 3 μm band on the emergent flux can be evaluated by equation (4) and (5). The resulting L flux and R_L values can be used to estimate the improved values of effective temperatures. After a few iterations, the values finally found are τ_{m} = 0·15, 0·3 and 0·9 for T_{eff} = 3400,3000 and 2600 K respectively. More detailed discussion on this correlation will be given in a subsequent paper (Paper II: Tsuji 1981). In Fig. 2, the solid lines are the predicted line blanketed fluxes based on OPDF opacity for CN, C_2 and CO (Querci, Querci and Tsuji 1974). As the absorption lines due to diatomic molecules are rather uniformly distributed in this spectral region, these line blanketed fluxes can be identified with the pseudo continuum F_0 (λ) defined in equation (4). Against this pseudo

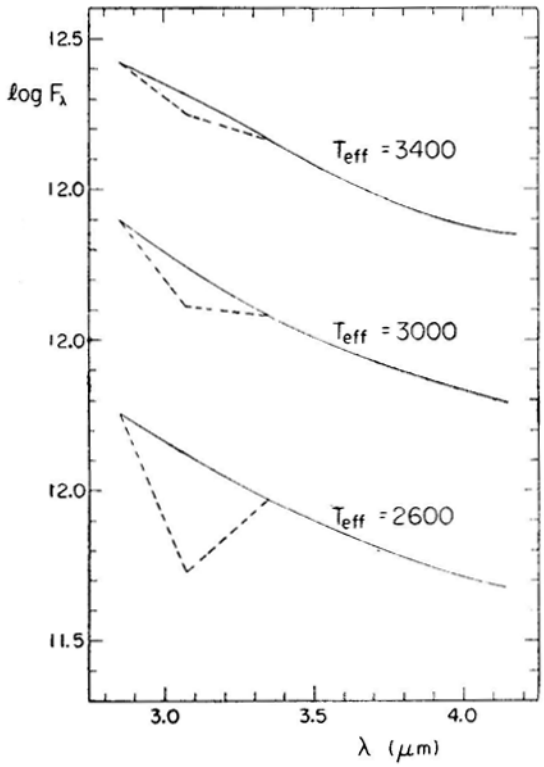

Figure 2 Spectral energy distributions between 3 and 4 μm are shown for models with T_{eff} = 3400, 3000 and 2600 K. The solid lines represent predicted line blanketed fluxes including the effect of diatomic molecules such as CN, CO and C_2, while dashed lines further include the effect of polyatomic molecules, mostly of HCN and C_2H_2, estimated by empirical method outlined in the text

continuum, the dashed line represents the polyatomic absorption estimated for each model with the corresponding values of τ_m.

Based on the emergent fluxes such as those shown in Fig. 2, integrated L fluxes are evaluated by

$$F_L = \int F_\lambda S_\lambda \, d\lambda \Big/ \int S_\lambda \, d\lambda, \tag{6}$$

where S_λ is the response function of the L filter (Johnson 1965). Then, R_L values are obtained from

$$R_L = \sigma T_{\rm eff}^4 / \pi F_L. \tag{7}$$

The resulting L fluxes and R_L values are given in Table 1, for the cases with and without 3 μm absorption. As the effect of gravity is found to be very small (the difference in log F_L is less than 0·01 for a difference of log g by 1·0), the mean value for models with different gravities is given for each effective temperature. The effect of 3 μm absorption is Δ log R = 0·020, 0·031 and 0·084 for $T_{\rm eff}$ = 3400, 3000 and 2600 K respectively. These differences in predicted R_L values give differences of $\Delta T_{\rm eff}$ = 20, 30 and 200 K in resulting effective temperatures at around $T_{\rm eff}$ = 3400, 3000 and 2600 K respectively. Thus, the effect of 3 μm absorption is not very important, except for the coolest stars. This is as expected since the 3 μm absorption is situated where the response function of the L filter is already rapidly decreasing. The effect of chemical composition is found to be of some importance only for the coolest models. In Fig. 3, values of log R_L (with the effect of 3 μm. absorption included) for C-rich and N-rich series are shown by solid and dashed lines, respectively. The effective temperatures, determined from a given value of observed log R using the predicted log R_L — $T_{\rm eff}$ relations shown in Fig. 3 may differ by about 200 K for C-rich and N-rich cases at around $T_{\rm eff}$ = 2600 K, but the difference may be less than 100 K in most of the cases with $T_{\rm eff}$ above 2800 K.

Table 1. Predicted L fluxes and R values for carbon stars.

Model atmospheres				Line blanketed flux[1]		Line blanketed flux[2]		
Series	$T_{\rm eff}$	log g	$V_{\rm tur}$	log F_L	log R_L	log F_L	log R_L	τ_m
N	4500	−1.0 ~ 1.0	5.0	12.261	−2.392	12·261	−2.392	0.0
N	4200	−1.0 ~ 1.0	5.0	12.479	−2.479	12.479	−2.479	0.0
N	3800	−1.0 ~ 1.0	5.0	12.186	−2.610	12.186	−2.610	0.0
N	3400	−1.0 ~ 1.0	5.0	12.134	−2.755	12.117	−2.735	0.15
N	3000	0.0	5.0	12.062	−2.897	12.031	−2.866	0·30
N	2600	1·0	5.0	11.949	−3.033	11.865	−2.949	0.90
C	3600	1.0	5.0	12.137	−2.656	12.137	−2.656	0.0
C	3000	0.0	5.0	12.068	−2.903	12.038	−2.872	0.30
C	2600	1.0	5.0	12.006	−3.090	11.927	−3.011	0.90

[1]Line blanketed fluxes based on the OPDF opacities for C_2, CN and CO; N-rich models by Querci, Querci and Tsuji (1974) and C-rich models by Querci and Querci (1976).
[2]With further empirical correction for the effect of 3 μm absorption; see Section 4 for details.

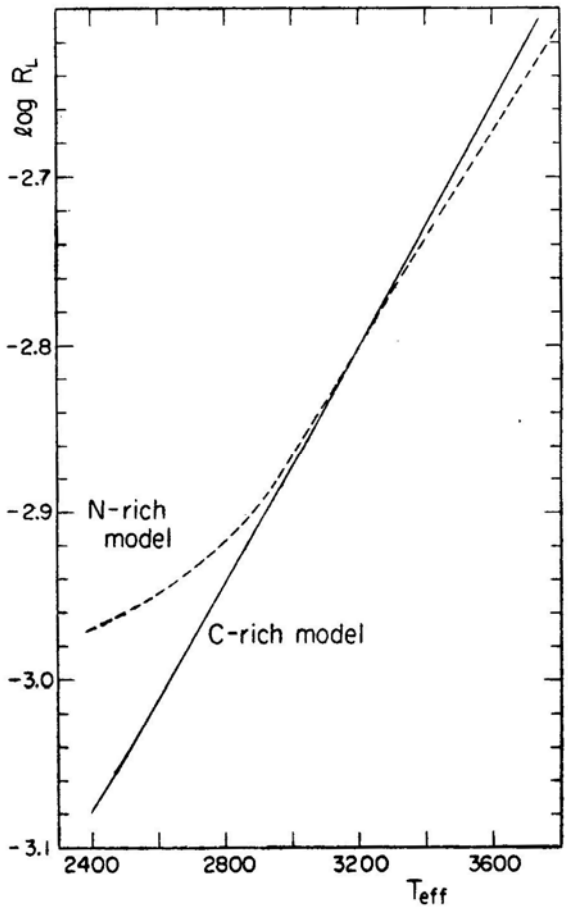

Figure 3. The values of log R_L, where R_L is the ratio of bolometric flux to L flux, are plotted against effective temperatures for C-rich models (solid line) and for N-rich models (dashed line). The effect of polyatomic absorption at 3·07 μm is taken into account in both the cases.

4. Effective temperatures of cool carbon stars

A problem one encounters in applying the infrared flux method to carbon stars is that most of these stars are variable and this fact makes it difficult to obtain a consistent set of photometric data. This difficulty, however, may not be very serious if we restrict our attention to Lb and SRb variables as defined by Kukarkin *et al.* (1969). Some characteristics of these variables were summarized by Peery (1975) who denoted these variables as N irregular variables. These variables show much smaller variabilities (typically 0·2 mag versus 1-2 mag at 1·04 μm) and smaller infrared excess (1 mag versus 1·5-2·5 mag at 11 μm), as compared with SRa and Mira variables.

The first extensive infrared photometry of carbon stars has been done by Mendoza and Johnson (1965). Further infrared flux measurements have occasionally been done by several authors and these results are summarized by Bergeat *et al.* (1976a) together

with their own observations. The spectral energy distributions given by these authors are integrated to obtain bolometric fluxes. The interstellar reddenings for these relatively bright carbon stars are generally unimportant, but they are estimated by applying Parenago's formula (Sharov 1964) or else by applying the results of FitzGerald (1968). The distances are estimated with the assumption of $M_{1\cdot04\mu m}$= —4·3 (Baumert 1974). The reddening law by Lee (1970) is applied. More recently, Walker (1980) has carried out new infrared photometry of southern carbon stars; he has also given bolometric magnitudes corrected for interstellar reddening.

Bolometric fluxes and *L* fluxes both corrected for the effect of interstellar reddening, compiled from these sources are summarized in Table 2. On the basis of these data, observational values of log R_L can be computed and the effective temperatures can be determined from Fig. 3. The predicted log R_L – $T_{\rm eff}$ relation used for determining effective temperatures is based on the model atmospheres of C-series as defined in Section 3. In fact, the recent studies (*e.g.* Kilston 1975; Querci and Querci 1976; Thompson 1977) seem to support the hypothesis that the origin of carbon stars may be due to the mixing of carbon produced by He-burning rather than by H-burning in CNO cycle. The resulting effective temperatures are also given in Table 2. For a few stars photometric data from different sources do not agree. These differences may be mostly due to variabilities of these stars. The difference in the resulting effective temperatures are generally less than 150 K, which is the estimated accuracy of our analysis as will be discussed here. Inspection of the result reveals that the effective temperatures of N-type carbon stars are generally very low, mostly below 3200 K (only exception is BL Ori with $T_{\rm eff}$ = 3420 K, which should be further examined). This is in contrast to the effective temperatures of non-Mira M-giant stars that are generally hotter than 3200 K (*e.g.* Tsuji 1978; Ridgway *et al.* 1980).

The accuracy of the resulting effective temperatures depends on the accuracies of both observed and predicted R_L values. As to the observed *RL* values, a major source of error may be the present uncertainty in absolute calibration of the infrared photometric system. Our analysis is based on the calibration by Johnson (1966) and its accuracy is estimated to be about 10 per cent. Even with the possible error of 10 per cent in observed R_L values the corresponding error in resulting $T_{\rm eff}$ is about 3 per cent (100 K) because of the high sensitivity of R_L to $T_{\rm eff}$ as noted before. On the other hand, the error due to the predicted R_L values may be of the same order as those of the observed *RL* values in most cases, since the differences in the predicted R_L values due to different assumptions on composition, gravity, line blanketing and so on are rather small so that the resulting uncertainties in $T_{\rm eff}$ are generally less than 100 K as is shown in Section 3. Only in the coolest models of $T_{\rm eff}$ near 2600 K, R_L values are more sensitive to these assumptions and the possible error may be as large as 200 K. Considering these uncertainties both in observed and predicted R_L values, the overall accuracy of our effective temperatures may be about 150 K for most cases.

Another problem to be examined is whether circumstellar dust emission has any importance to our analysis. For example, Bergeat *et al.* (1976 a, b, c) have employed a model in which dust thermal emission is of considerable importance in explaining the spectral energy distribution of carbon stars in the near infrared. They have applied such a model not only to Mira-types but also to non-Mira types covered in

Table 2. Spectral types, L fluxes, integrated fluxes, and effective temperatures of N-type carbon stars.

GCCCS	Name	Spectral types			E_{B-V}	$\log f_L$	$f_{\rm bol}$	$\log R_L$	$T_{\rm eff}$	Ref
(1)		(2)	(3)	(4)	(5)	(6)	(7)			(8)
250	T Cae	N4	C6, 3	C5 II	0.03	−3.868	−6·741	−2.873	3000	W
284	W Ori	N5	C5, 4	C6 II	0.06	−2·744	−5·749	−3.005	2620	W
					0.04	−2·727	−5·689	−2.962	2745	B
297	SY Eri	N0	C6, 3	C5 II	0.08	−3.844	−6.777	−2.933	2830	W
508	BL Ori	Nb	C6, 3	C5 II	0.03	−3·372	−6.093	−2·721	3420	B
537	UU Aur	N3	C6, 4	C5 II	0.04	−2.612	−5.546	−2.934	2825	B
1338	X Cnc	N3	C5, 4	C6 II	0·08	−3·036	−6·049	−3·013	2600	W
					0·00	−3·035	−6·000	−2·965	2735	B
1714	U Hya	N2	C6, 3	C5 II	0·01	−2·584	−5·517	−2·933	2825	B
1736	VY UMa	N0	C6, 3		0·02	−3·061	−5·984	−2·923	2855	B
2030	Y CVn	N3	C5, 5J	C7 I	0·01	−2·526	−5·493	−2·967	2730	B
2047	RY Dra	N4	C4, 5J	C7 I	0·02	−2·852	−5·900	−3.048	2500	B
2157	T Lup				0·4	−3·676	−6·613	−2·938	2810	W
2160	RS Lup				0·2	−4·363	−7·257	−2·887	2960	W
2173	Z Lup	Na	C4, 3		0·18	−3·684	−6·633	−2·949	2780	W
2219	X Tra			C5 II	0·06	−2·616	−5·601	−2·985	2680	W
2240	U Aps				0.16	−3·548	−6·545	−2·997	2640	W
2362	V Tra				0·18	−4·016	−6·837	−2·821	3140	W
2478	SZ Sgr	Nb	C7, 3	C5 II	0·21	−3·780	−6·625	−2·845	3080	W
2499	V781 Sgr				0·8	−3·420	−6·369	−2·949	2780	W
2608	T Lyr	N3	C6, 5J	C8	0·06	−2·925	−6·013	−3·088	2380	B
2620	RX Sct	N3	C5, 5	C5 II	0·8	−3·488	−6·341	−2·853	3055	W
2660	S Sct	N3	C6, 4	C5 II	0·4	−3·092	−6·001	−2·909	2895	W
2695	V Aql	N6	C5, 4	C5 II	0·25	−2·828	−5·837	−3·009	2610	W
2721	V1942 Sgr	N2	C6, 4		0·15	−3·320	−6·229	−2·909	2895	W
2744	AQ Sgr	N3	C7, 4	C5 II	0·15	−3·208	−6·210	−3·002	2630	W
2785	UW Sgr			C3 II	0·2	−4·340	−7·169	−2·829	3120	W
2882	RT Cap	N3	C6, 4	C6 II	0·10	−3·104	−6·109	−3·005	2620	W
3013	T Ind	Na	C7, 2	C5 II	0·03	−3·204	−6·065	−2·861	3030	W
3018	Y Pav				0·07	−3·056	−5·921	−2·865	3020	W
3060	V460 Cyg	N1	C6, 3	C5 II	0·06	−2·977	−5·903	−2·926	2845	B
3061	RR Ind				0·07	−4·316	−7·173	−2·857	3040	W
3202	TX PSc	N0	C7, 2	C5 II	0·00	−2·684	−5·577	−2·893	2945	W
					0·00	−2·735	−5·583	−2·848	3070	B

Notes:

(1) Stephenson(1973).
(2) N-classification (Shane 1928; Yamashita 1972, 1975a).
(3) C-classification (Keenan and Morgan 1941; Yamashita 1972, 1975a).
(4) Richer's (1971) classification.
(5) From Walker (1980) for his sample, and estimations by the method outlined in the text for other stars.
(6) $f_{\rm L}$ in unit of erg cm^{-3} per $\Delta\lambda = 1$ cm.
(7) $f_{\rm bol}$ in unit of erg cm^{-2}.
(8) Major sources of photometric data; B:Bergeat *et al.* (1976a) and references cited therein, W: Walker (1980).

the present study. Recently, however, Walker (1980) has concluded from his analysis of the two-colour diagram that there is no evidence of dust thermal emission in the near infrared for most N-type irregulars. Also, detailed photometric analysis of the infrared spectra of Y CVn that extends to 30 μm and for which Bergeat *et al.* (1976a, b, c) suggest possible importance of dust shell, reveal almost no contribution of dust thermal emission (Goebel *et al.* 1980). Furthermore, the very fact that the 3 μm absorption is very deep in some non-Mira N-type stars (Noguchi *et al.* 1977) clearly indicates that the dust thermal emission will be of little importance in the near infrared at least around the *L* band. For these reasons, we conclude that the effect of dust is not important to our analysis for the sample of stars covered in the present study. The effect of dust thermal emission, however, may be of importance in Mira-type carbon stars (*e.g.* Merrill and Stein 1976). In fact, this possibility together with the large variability and very heavy line blanketing effect in these stars make it rather difficult to apply the infrared flux method.

5. Comparisons with other temperature scales

Until recently several attempts were made to determine the temperature scale for carbon stars. The most direct method was to determine the effective temperatures from the angular diameters directly measured. Recently, angular diameter measurements by the lunar occupation method have been successfully applied to 5 carbon stars (Ridgway, Wells and Joyce 1977; Ridgway, Jacoby, Joyce and Wells 1980, personal communication; Walker, Wild and Byrne 1979), of which 4 carbon stars (TX Psc, X Cnc, AQ Sgr, SZ Sgr) are N-irregulars while one (Y Tau) is Sra variable (Table 3). For these five stars, effective temperatures and angular

Table 3. Effective temperatures for carbon stars with measured angular diameters.

Star	Lunar occultation method		Infrared flux method	
	θ_{LD}	$T_{\rm eff}$	θ_{LD}[4]	$T_{\rm eff}$[5]
	(milliarcsec)	(K)	(milliarcsec)	(K)
TX Psc	9·31 ± 0·75[1]	3080 ± 150[1]	9·38	3070
		3114 ± 150[2]	10.26	2945
X Cnc	8.79 ± 1.00[1]	2491 ± 138[1]	7·31	2735
		2385 ± 140[2]	7.65	2600
AQ Sgr	5.97 ± 0.49[2]	2684 ± 110[2]	6·21	2630
SZ Sgr	3.21 ± 0.16[3]	2776 ± 70[3]	2.81	3080
Y Tau	8.58 ± 0.40[1]	2565 ± 70[3]	8.68	2520

Notes:

(1) Ridgway, Wells and Joyce (1977).
(2) Walker, Wild and Byrne (1979).
(3) Ridgway, Jacoby, Joyce and Well (1980), personal communication.
(4) Photometric angular diameter by equation (2) with the adopted effective temperature.
(5) From Table 2 except for Y Tau. For Y Tau, photometric data by Bergeat *et al.* (1976a) are used after correction of interstellar reddening with E_B-v = 0·06, log f_L = – 2·954, log $f_{\rm bol}$ = – 5·993, and log R_L = – 3·039.

diameters by the lunar occupation method and by the infrared flux method (Table 2) are compared in Fig. 4. Agreements between the effective temperatures by the two methods are remarkably good for TX Psc, AQ Sgr and Y Tau (this star is SRa variable and therefore not included in our sample; for purposes of comparison, we tentatively apply the infrared flux method to it with the photometric data noted in Table 3). The effective temperatures by the two methods show positive correlation and the mean difference is $\Delta T_{\rm eff} = -69$ K $\pm$ 82 K (mean error) for 5 stars, where $\Delta T_{\rm eff}$ is $T_{\rm eff}$ (angular diameter method) $- T_{\rm eff}$ (infrared flux method). Thus, the infrared flux method as applied to cool carbon stars results in effective temperatures consistent with those by the lunar occupation method. However in the case of X Cnc and SZ Sgr the two methods give a temperature difference of about 10 per cent.

Other temperature scales for carbon stars have mostly been based on the infrared colour indices. In Fig. 5a, b, c and d, temperatures estimated by Mendoza and Johnson (1965), by Richer (1971), by Bergeat *et al.* (1976c), and by Walker (1980), respectively, are plotted against our effective temperatures. Mendoza and Johnson (1965) estimated their effective temperatures by applying the colour index—effective temperature calibration for K-M giant stars to carbon stars. This procedure, however, cannot be justified for two reasons; firstly the photometric properties of carbon

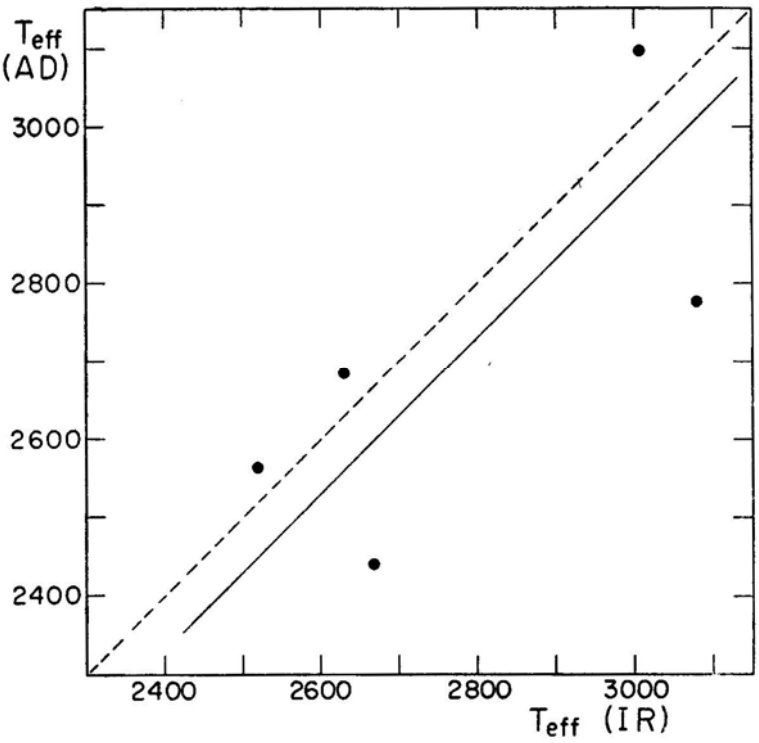

Figure 4. Comparison of the effective temperatures determined by the infrared flux method (abscissa) are compared with those by the angular diameters directly measured by the lunar occultation method (ordinate). Mean values are used when two estimates are available in Table 3. The dashed line corresponds to $T_{\rm eff}$ (AD) = T_{eff} (IR) while the solid line corresponds to the mean difference of $T_{\rm eff}$ (AD) $-T_{\rm eff}$ (IR) = – 69 K.

stars may be different from those of K-M giant stars (Paper II) and, secondly the calibration for KM giant stars which they have applied is now known to be erroneous by several hundred degrees (*e.g.* Tsuji 1978; Ridgway *et al.* 1980). For these reasons, it is possible that the apparently good agreement in effective temperature values between those obtained by Mendoza and Johnson (1965) and ours may be fortuitous. Other temperature determinations were based on the calibrations of infrared colour indices by means of blackbodies. Although some authors suggest that carbon stars radiate roughly like blackbodies and hence the colour temperatures can be good approximations to effective temperatures *(e.g.* Scalo 1976), it is difficult to justify this in view of the large line blanketing effect in carbon stars (see Fig. 1). In fact, the results of different authors which are based on different colour indices show systematic differences with our effective temperatures in different ways, as shown in Fig. 5. Also, the results of Bergeat *et al.* (1976c) are based on the assumption that dust thermal emission is of some importance, but this may probably be an overestimate as mentioned in Section 4. One important conclusion from Fig. 5, is that all the colour-temperatures show positive correlation with our effective temperatures, and that they can be used as measures of effective temperatures if properly calibrated.

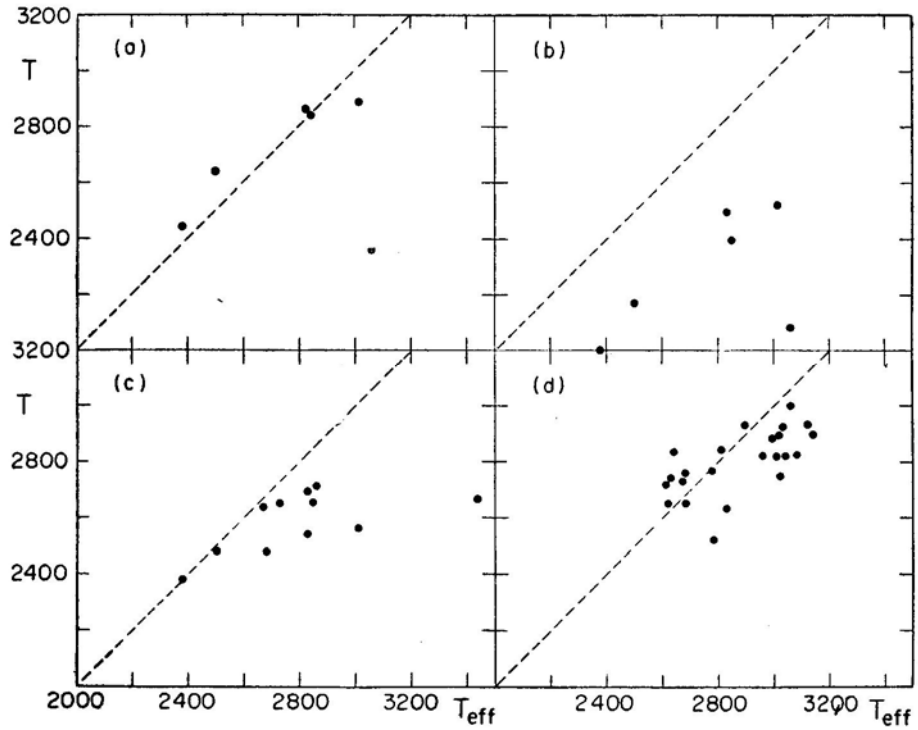

Figure 5. Colour temperatures estimated by several authors are compared with the effective temperatures based on the infrared flux method; (a) Mendoza and Johnson (1965), (b) Richer (1971), (c) Bergeat *et al.* (1976), (d) Walker (1980). One deviating star in (a) and (b) is RX Sct for which we assume large reddening of $E_{B-V} = 0{\cdot}8$, following Walker (1980), while other authors probably did not. For this reason, this star can be omitted from comparisons. In fact, this star is also included in (d) and it shows no deviation from the mean relation, because the same reddening is used.

6. Spectral classification of cool carbon stars

As compared with the normal red giant stars for which MK classification can be applied, spectral classification of carbon stars has been more difficult (Fujita 1980). Cool carbon stars have been classified as N-type in the Harvard classification, and Shane (1928) had later revised the sub-classification of N-type on the basis of the spectral gradient in short wavelengths (violet and blue). In the upper panel of Fig. 6, N-subtypes due to several authors, as summarized by Yamashita (1972, 1975a), are plotted against the effective temperatures we have derived. This plot reveals that the dependence of N-subtypes on effective temperatures is not strong. It was, however,

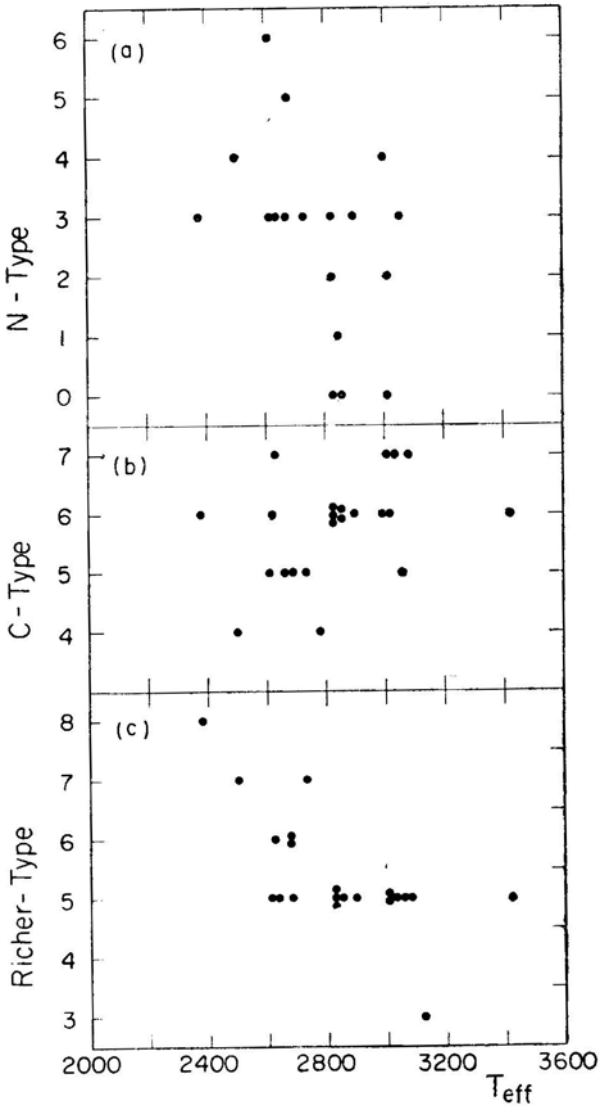

Figure 6. Spectral types are plotted against effective temperatures; (a) R -N classification (Shane 1928 (b) C-classification (Keenan and Morgan 1941; Yamashita 1972), (c) Richer's classification (1971)

noted by Shane (1928) himself that the redness of carbon stars cannot be satisfactorily related to stellar temperatures because colour temperatures based on violet-blue fluxes were too low (below 1000 K for some stars) and that some selective absorption may play an important role.

Keenan and Morgan (1941) have proposed a new classification scheme of carbon stars based on several spectroscopic features that may be sensitive to temperature. This classification is now known as the C-classification and is most commonly used in studies of carbon stars. In the middle of Fig. 6, temperature classes of C-classification by Yamashita (1972, 1975a) are plotted against our effective temperatures. Although the scatter in effective temperatures for a given spectral type is rather large, the general trend between C4 and C7 is opposite to what one might expect from the original intent of the spectral classification. This conclusion can be extended to C-classifications done by other authors, since Yamashita's classification shows good agreement with those by Keenan and Morgan (1941), by Bouigue (1954), and by Yamashita (1967) as has been shown by Yamashita (1972).

Recently, another classification scheme has been proposed by Richer (1971) on the basis of the near infrared spectra of carbon stars . In the lower panel of Fig. 6, Richer's temperature classes are plotted against our effective temperatures. Again, the dispersion in effective temperatures at a given spectral type is rather large, but this spectral classification shows better correlation with effective temperatures, as compared with the other classifications. It is also consistent with the fact that Richer's classification shows an inverse correlation with C-classification, as has been noted by Yamashita (1972).

Until recently, some questions on the validity of the C-classification as a temperature sequence have been expressed already by several authors. Especially, it was pointed out that temperatures determined from infrared colour indices generally show poor correlation, or even anti-correlation, with C-classification (*e.g.* Richer 1971; Scalo 1976; Bergeat *et al.* 1976c). However, the temperatures determined by these authors are essentially colour temperatures as has been noted in Section 5. Differential line blanketing effect by molecular bands or of interstellar reddening can complicate the problem. The validity of the C-classification as a temperature classification can still be defended, as discussed in detail by Yamashita (1975b). It is to be remembered that the values of effective temperatures we derive are almost free from the differential line blanketing effect. As shown in Section 5 the colour temperatures show a good correlation with our effective temperatures.

The possibility that the later C-type stars may have higher effective temperatures than the earlier C-type stars was also suggested on the basis of effective temperatures derived from angular diameters measured by the lunar occupation method for three stars (Ridgway, Wells and Joyce 1977). Although the number of stars covered by their analysis was too small, our analysis is now extended to a larger sample of stars so that a general conclusion can be made. Thus, we can finally confirm that it is the C-classification that is incorrect as a temperature indicator for cool carbon stars, at least between C4 and C7.

7. Discussion and conclusions

We have determined effective temperatures for a large sample of cool carbon stars

on the basis of the infrared flux method developed by Blackwell, Petford and Shallis (1980). Our analysis reveals that the majority of N-type carbon stars, which are also classified as SRb or Lb variables, are confined to the effective temperature range between 2400 and 3200 K. In contrast, M-giant stars of the spectral type between M0 and M6, the latter half of which are mostly variables of SRb and Lb types (Kukarkin *et al.* 1969), are confined to the effective temperature range between 3200 and 3900 K (Tsuji 1978, 1980; Ridgway *et al.* 1980). Thus, red variables of small amplitude (SRb and Lb types) are sharply divided at about $T_{\rm eff} \sim 3200$ K into oxygen-rich and carbon-rich giants. It is to be noted that Mira and SRa type variables are not included in our sample both for M giants and carbon stars. To extend the temperature calibration to these large amplitude variables should be a major problem to be studied in the future.

Because of the well known complexity of the spectra of cool carbon stars and, especially because of the heavy line blanketing effect in these stars, it was generally not expected that the effective temperatures of cool carbon stars can be determined by the analysis of the photometric data. The present author also expressed rather a pessimistic view that the effective temperature scale of carbon stars can be determined only if direct measurements of angular diameters can be extended to a large number of carbon stars in future (Tsuji 1979). By the infrared flux method, however, it is shown that the difficulty due to heavy line blanketing effect can be avoided to some extent, because this method utilizes the ratio of the integrated flux which is free from differential line blanketing effect, and one infrared flux that can be chosen to be free from strong line absorption. In fact, it can be confirmed that this expectation is indeed realized by the following lines of evidence. Our effective temperatures show good agreement with those based on the angular diameters measured by the lunar occultation method (Ridgway, Wells and Joyce 1977; Ridgway, Jacoby, Joyce and Wells 1980, personal communication; Walker, Wild and Byrne 1979) as is shown in Fig. 4, and colour temperatures defined by various photometric indices all show good correlations with our effective temperatures (Fig. 5). The spectroscopic as well as photometric properties of cool carbon stars can most consistently be understood on the basis of the effective temperatures we desire. We propose to show this in detail in Paper II.

Such a success in applying the infrared flux method to cooler stars with complicated spectra like carbon stars demonstrates that the infrared flux method is a truly fundamental technique in stellar astronomy. In fact, this method has already been applied not only to temperature determinations of normal stars (*e.g.* Blackwell Shallis and Selby 1979; Blackwell, Petford and Shallis 1980) but also to some peculiar stars (Shallis and Blackwell 1979) and also to the calibration of stellar radii (Shallis and Blackwell 1980). Furthermore, an important advantage of this method is its simplicity; although our analysis is presently limited to 31 carbon stars, this method can be easily applied to any individual carbon star for which the effective temperature is required. For this purpose, what is necessary is a consistent set of photometric data covering the near infrared (including the *L* band).

The accuracy of our values of effective temperature is estimated to be about 150 K for most carbon stars. For improvement in accuracy, accurate calibration of the infrared photometry is important. Recently an attempt of direct comparison between the stellar flux and a blackbody source at *K*-band has been done by Selby *et al.* (1980),

and extension of this work to other bands, now in progress at Tenerife (Blackwell 1980), should provide more accurate calibration in the near future. The accuracy of the resulting effective temperatures also depends on the accuracy of the predicted R_L values and, for this reason, the infrared flux method is model dependent. The present limitations on the model atmospheres of carbon stars have been reviewed, for example, by Carbon (1979). Especially, in view of very low effective temperatures of carbon stars, the effect of polyatomic molecular opacity should be more important in carbon stars than in M-giant stars. Certainly, model atmospheres of the coolest carbon stars should be reconsidered by taking into account the effect of opacity sources due to polyatomic molecules. In the infrared flux method, however, some uncertainties in model atmospheres may not be very important, since we have applied this to the spectral region least disturbed by line absorption and hence the predicted flux may be relatively free from some shortcomings of the model atmospheres.

Our new effective temperature scale reveals that the C-classification for carbon stars, which has widely been used in the past, can no longer be regarded as a tempe rature classification scheme, at least for most N-type stars classified as C4-C7. The reason why C-classification has failed to represent the temperature sequence of carbon stars is not clear, but some possibilities were suggested by Bergeat *et al.* (1976c); the major classification criterion of C-classification is sodium D lines, but as these lines are in the strong CN bands, the D-line index may be more sensitive to CN blanketing rather than to temperature. Also, D-line index may be susceptible to contamination by interstellar or circumstellar D lines. Scalo (1973) considered a possible effect of (C – O) /H ratio on the atmospheric structure and hence on some spectral characteristics including D lines. Certainly, these problems should be examined in more detail. On the other hand, the spectral classification scheme proposed by Richer (1971) shows better correlation with the effective temperatures and his system will provide a promising basis for future spectral classification of cool carbon stars.

In the present paper, carbon stars classified as C0-C3 or R-type stars are not discussed, but these carbon stars are intrinsically different from N-type stars; for example, these relatively hot carbon stars are much less luminous than the cool carbon stars in general and may have quite different evolutionary history. For this reason, it is probably not justified to combine R and N-type stars in a single sequence of C-classi fication. Also, carbon stars that have been classified as C8-C9 are mostly peculiar stars or Mira-type variables, and the placement of these stars in a classification scheme of carbon stars is an open question. As N-type stars are generally cooler than M-giant stars and also as R-type and N-type stars are different not only in temperature but also in luminosity and evolutionary state, the Harvard classification scheme may be better interpreted as follows:

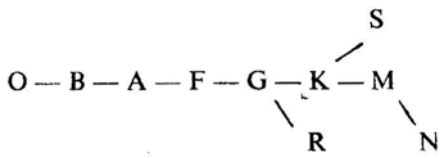

The difficulty in the spectral classification of carbon stars introduced considerable confusion in the interpretation and analysis of the spectra and other observations of

these stars in the past. We believe that the correct temperature sequence and reasonable estimation of the effective temperatures for cool carbon stars can now be given. It is hoped that these findings will provide a new background to future studies of carbon stars both observational and theoretical.

Acknowledgements

The author would like to thank D. E. Blackwell for helpful correspondence and encouragement throughout this work, to S. T. Ridgway for making available his latest preprint on angular diameter measurement of carbon stars and to Y. Yamashita for useful discussion on the spectral classification of carbon stars.

The computation has been carried out at the computer centre of the Tokyo Astronomical Observatory.

References

Baumert, J. H. 1974, *Astrophys. J.,* **190**, 85.
Bergeat, J., Sibille, F., Lunel, M., Lefevre, J. 1976a, *Astr. Astrophys.,* **52**, 227.
Bergeat, J., Lefevre, J., Kandel, R., Lunel, M., Sibille, F. 1976b, *Astr. Astrophys.,* **52**, 245.
Bergeat, J., Lunel, M., Sibille, F., Lefevre, J. 1976c, *Astr. Astrophys.,* **52**, 263.
Blackwell, D. E., Petford, A. D., Shallis, M. J. 1980, *Astr. Astrophys.,* **82**, 249.
Blackwell, D. E., Shallis, M. J. 1977, *Mon. Not. R. astr. Soc.,* **180**,177.
Blaclcwell, D. E., Shallis, M. J., Selby, M. J., 1979, *Mon. Not. R. astr. Soc.,* **188**, 847.
Blanco, B. M., Blanco, V. M.. McCarthy, M. F. 1978, *Nature,* **271**, 638.
Bouigue, R. 1954, *Ann. Astrophys.,* **17**, 104.
Carbon, D. F. 1979, *A. Rev. Astr. Astrophys.,* **17**, 513.
FitzGerald, M. P. 1968, *Astr. J.,* **73**, 983.
Fujita, Y. 1980, *Space Sci. Rev.,* **25**, 89.
Goebel, J. H., Bregman, J. D., Goorvitch, D., Strecker, D. W., Puetter, R. C., Russell, R. W., Soifer, B. T., Willner, S.P., Forrest, W. J., Houck, J. R., McCarthy, J. F. 1980, *Astrophys. J.,* **235**, 104.
Iben, I. Jr. 1975, *Astrophys. J.,* **196**, 525.
Johnson, H. L. 1965, *Astrophys. J.,* **141**, 923.
Johnson, H. L. 1966, *A. Rev. Astr. Astrophys.,* **4**, 193.
Keenan, P. C., Morgan, W. W. 1941, *Astrophys. J.,* **94**, 501.
Kilston, S.1975, *Publ. astr. Soc. Pacific,* **87**, 189.
Kukarkin, B. V. Kholopov, P. N., Efremov, Yu. N., Kukarkina, N. P., Kurochkin, N.E., Medvedeva, G. I., Perova, N. B., Fedorovich, Y. P., Frolov, M. S. 1969, *General Catalogue of Variable Stars,* Astronomical Council of the Academy of Sciences, Moscow.
Lee, T.A.1970, *Astrophys. J.,* **162**, 217.
Mendoza, V. E. E., Johnson, H. L. 1965, *Astrophys. J.,* **141**, 161.
Merrill, K. M., Ridgway, S. T. 1979, *A. Rev. Astr. Astrophys.,* **17**, 9.
Merrill, K. M., Stein, W. A. 1976, *Publ. astr. Soc. Pacific,* **88**, 285.
Noguchi, N., Maihara, T., Okuda, H., Sato, S., Mukai, T. 1977, *Publ. astr. Soc. Japan,* **29**, 511.
Peery, B. F. Jr. 1975, *Astrophys. J.*, **199**, 135.
Querci, F., Querci, M., Tsuji, T. 1974, *Astr. Astrophys.,* **31**, 265.
Querci, M., Querci, F. 1976, *Astr. Astrophys.,* **49**, 443.
Richer, H. B. 1971, *Astrophys. J.*, **167**, 521.
Ridgway, S. T., Carbon, D. F., Hall, D. N. B. 1978, *Astrophys. J.,* **225**,138.
Ridgway, S. T., Joyce, R. R., White, N. M., Wing, R. F. 1980, *Astrophys. J.,* **235**, 126.
Ridgway, S. T., Wells, D. C, Joyce, R. R. 1977, *Astr. J.,* **82,** 414.
Scalo, J. M. 1973, *Astrophys. J.,* **186**, 967.

Scalo, J. M. 1976, *Astrophys. J.,* **206,** 474.
Selby, M. J., Blackwell, D. E., Petford, A. D., Shallis, M. J. 1980, *Mon. Not. R. astr. Soc.,* **193**, 111.
Shallis, M. J., Blackwell, D. E. 1979, *Astr. Astrophys.,* **79**, 48.
Shallis, M. J., Blackwell, D. E. 1980, *Astr. Astrophys.,* **81**, 336.
Shane, C. D. 1928, *Lick Obs. Bull.,* **13**, 123.
Sharov, A. S. 1964, *Soviet Astr.,* **7,** 689.
Sneden, C., Johnson, H. R., Krupp, B. M. 1976, *Astrophys. J.*, **204**, 281.
Stephenson, C. B. 1973, *Publ. Warner Swasey Obs.,* **1**, No. **4**.
Sugimoto, D., Nomoto, K. 1974, in *IAU Symp. 66: Late Stages of Stellar Evolution,* Ed. R. J. Taylor, D. Reidel, Dordrecht, p. 105.
Thompson, R. I. 1977, *Astrophys. J.,* **212**, 754.
Tsuji, T. 1978, *Astr. Astrophys.,* **62,** 29.
Tsuji, T. 1979, *New Zealand J. Sci.,* **22**, 415.
Tsuji, T. 1980, *Astr. Astrophys.,* (in press).
Tsuji, T. 1981, In preparation.
Walker, A. R. 1980, *Mon. Not. R. astr. Soc.,* **190**, 543.
Walker, A. R., Wild, P. A. T., Byrne, P. B. 1979, *Mon. Not. R. astr. Soc.,* **189**, 455.
Yamashita, Y. 1967, *Publ. Dom. astrophys. Obs.,* **13**, 67.
Yamashita, Y. 1972, *Ann. Tokyo astr. Obs., Sec. Ser.,* **13**, 169.
Yamashita, Y. 1975a, *Ann. Tokyo astr. Obs., Sec. Ser.,* **15,** 47.
Yamashita, Y. 1975b, *Publ. astr. Soc. Japan,* **27,** 459.
Zuckerman, B. 1980, *A. Rev. Astr. Astrophys.,* **18**, 263.

J. Astrophys. Astr. (1981) **2,** 115–118

A Spectroscopic Orbit for 26 Comae

R. F. Griffin *The Observatories, Madingley Road, Cambridge, England, CB3 OHA*

Received 1981 February 3; accepted 1981 February 16

Abstract. Photoelectric radial-velocity measurements show that 26 Comae is a spectroscopic binary with a very eccentric orbit and a period of 972 days.

Key words: radial velocities—spectroscopic binaries—stars, individual

26 Comae Berenicis (HR 4815, HD 110024) is a late-type giant star near the North Galactic Pole. It has a V magnitude of 5·46, a $(B - V)$ colour of $0^{m}\cdot958$ (Häggkvist and Oja 1968) and a spectral type of G9 III (Appenzeller 1967). Its radial velocity was measured long ago at Victoria (Plaskett *et al.* 1921, 1922) and at Mount Wilson (Wilson and Joy 1950). The Victoria authors considered that their observations showed 26 Com to be a spectroscopic binary. The star narrowly escaped observation at Lick in the early years of this century. The Lick radial-velocity programme was intended to include all stars brighter than $5^{m}\cdot51$, but 26 Com was just disquali fied by being listed in the Revised Harvard Photometry (Pickering 1908) at magnitude 5·51 exactly.

In the course of a survey, whose principal results have yet to be published, of the radial velocities of all late-type stars in the Henry Draper Catalogue within 15° of the North Galactic Pole, the binary nature of 26 Com has been firmly established. The 48 observations in Table 1 are now available for a discussion of the orbit. All but three of them were made by the author with the original photoelectric radial-velocity spectrometer at Cambridge (Griffin 1967). The exceptions are the first observation, which was made by Dr G. A. Radford with the Cambridge instrument, and those of 1976 July 9 and 1978 May 23, which were made by Dr J. E. Gunn and the author with the photoelectric spectrometer at the Hale Telescope (Griffin and Gunn 1974). All photoelectric velocities in the North Galactic Pole field are measured differentially with respect to the reference star 41 Com, for which a velocity of — 14·7 km s^{-1} has been adopted (Griffin 1969).

The orbit of 26 Com has been derived from the observations in Table 1 by means of the computer programme supplied to the author by Dr Radford (Griffin 1978); it has the following elements:

$P = 972{\cdot}4 \pm 1{\cdot}4$ days	$(T)_2 = \text{MJD } 43303{\cdot}5 \pm 1{\cdot}9$
$\gamma = -20{\cdot}26 \pm 0{\cdot}08$ km s^{-1}	$a_1 \sin i = 112{\cdot}9 \pm 1{\cdot}6$ Gm
$K = 10{\cdot}46 \pm 0{\cdot}13$ km s^{-1}	$f(m) = 0{\cdot}0607 \pm 0{\cdot}0026\ M_\odot$
$e = 0{\cdot}590 \pm 0{\cdot}007$	
$\omega = 102{\cdot}5 \pm 1{\cdot}4$ degrees	rms residual $= 0{\cdot}5$ km s^{-1}

The subscript outside the parentheses enclosing the element T here indicates the cycle number of the epoch of periastron, corresponding to the cycle numbers that appear in Table 1 before the decimal point in the phase column. This particular epoch is chosen because it is the one with the smallest standard deviation, being nearest in time to the mean time of all the observations.

The computed radial-velocity curve is illustrated in Fig. 1, in which the velocities given in Table 1 are plotted against phase. Fig. 1 also shows the early Victoria and Mount Wilson observations. The Victoria velocities were all measured during a single cycle (cycle — 20 in the system of Table 1). The ' wild ' one near phase 0·5 was noted as " poor " by the Victoria authors (Plaskett *et al.* 1921, 1922) and should perhaps be disregarded. Since the standard error of the period is 1·4 days, the phases of the Victoria observations, which were made between 21 and 22 periods before the epoch of periastron determined here, are uncertain by about 30 days or 0·03 periods. It is doubtful whether the period can be further refined by incorporating the Victoria results into the orbital solution. In 0·03 periods the change in the velocity of 26 Com in the part of the orbit covered at Victoria is only about 1 km s^{-1} and because all the observations are on an almost linearly rising part of the velocity curve there is no means of distinguishing between a shift of phase and a systematic

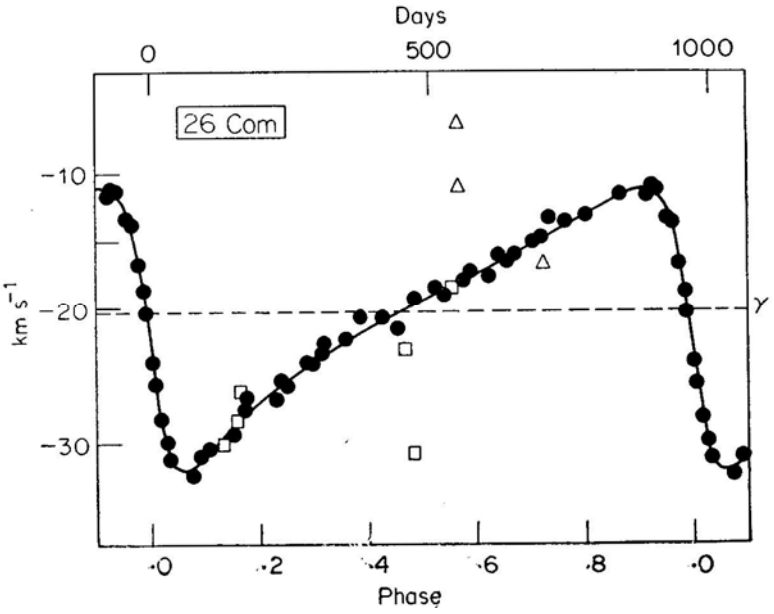

Figure 1. The computed radial-velocity curve (full line) for 26 Com. The photoelectric observations are plotted as filled circles, the photographic ones as open squares (Victoria) and open triangles (Mount Wilson). The broken line indicates the *y*-velocity.

Table 1. Photoelectric radial-velocity measurements of 26 Comae.

Date	MJD	Velocity km s^{-1}	Phase	$(O-C)$ km s^{-1}
1973 Apr 26·00	41798·00	−21·5	0.452	−1·2
1975 June 9·89	42572·89	−25·8	1·249	−0·5
1976 Jan 24·18	42801·18	−19·3	1·483	+0·4
Mar 1·09	838·09	−18·6	·521	+0·3
Apr 22·97	890·97	−18·0	·576	−0·2
June 7·90	936·90	−17·6	·623	−0·8
July 9·15	968·15	−16·6	.655	−0·4
Nov 29·22	43111·22	−13·2	·802	−0·3
1977 Jan 30·16	43173·16	−11·6	1·866	0·0
Mar 30·03	232·03	−11·0	·926	+0·4
Apr 24·99	257·99	−13·4	·953	−0·4
May 27·89	290·89	−20·4	·987	−0·6
June 10·91	304·91	−24·1	2·001	+0·2
July 5·91	329·91	−29·9	·027	+0·4
Nov 1·23	448·23	−29·4	·149	−0·6
25·29	472·29	−26·6	·174	+1·2
1978 Jan 18·20	43526·20	−26·8	2·229	−0·9
27·13	535·13	−25·5	·238	+0·1
Mar 13·09	580·09	−24·2	·284	+0·1
24·07	591·07	−24·2	.296	−0·2
Apr 12·99	610·99	−22·8	·316	+0·6
May 23·14	651.14	−22·4	·357	0·0
June 18·91	677·91	−20·8	·385	+0·1
July 26·87	715·87	−20·8	·424	+0·1
Nov 16·23	828·23	−19·1	·540	−0·6
1979 Jan 3·23	43876·23	−17·4	2·589	+0·1
Feb 25·75	929·15	−16·1	·643	+0·3
Mar 8·09	940·09	−16·3	·655	−0·1
22·00	954·00	−16·1	·669	−0·2
Apr 25·02	988·02	−15·1	·704	0·0
May 9·94	44002·94	−14·8	·719	0·0
23·92	016·92	−13·3	·734	+1·2
June 22·92	046·92	−13·7	·764	+0·1
Nov 19·24	196·24	−11·7	·918	−0·5
28·26	205·26	−11·2	·927	+0·2
Dec 4·26	211·26	−11·2	·933	+0·4
25·23	232·23	−13·6	·955	−0·4
31·18	238·18	−13·8	·961	+0·2
1980 Jan 13·20	44251·20	−16·7	2·975	−0·2
24·25	262·25	−18·8	·986	+0·7
Feb 12·13	281·13	−25·7	3·005	−0·3
23·08	292·08	−28·2	·017	+0·1
Mar 9·07	307·07	−31·2	·032	−0·3
Apr 18·90	347·90	−32·4	·074	+0·6
May 3·96	362·96	−31·0	·089	+0·3
18·93	377·93	−30·5	·105	+0·1
July 21·88	441·88	−27·6	·171	+0·3
Dec 7·24	580·24	−23·5	·313	0·0

difference in the zero-points of the velocities measured at Victoria and Cambridge respectively. It is apparent from Fig. 1 that the Mount Wilson velocities, details of which have been published by Abt (1973), are not of assistance in refining the orbit.

No evidence has been seen of the secondary star in the system. The mass function shows that, for primary masses of 1 to 4 $M_{\odot}$, the minimum mass of the secondary ranges from 0·5 to 1·2 $M_{\odot}$. Thus we have only weak constraints on the nature of the secondary, which could easily be a lower-main-sequence star or a white dwarf.

References

Abt, H. A. 1973, *Astrophys. J. Suppl. Ser.,* **26**, 365.
Appenzeller, 1.1967, *Publ. astr. Soc. Pacific,* **79**, 102.
Griffin, R. F. 1967, *Astrophys. J.,* **148**, 465.
Griffin, R. F. 1969, *Mon. Not. R. astr. Soc.,* **145**, 163.
Griffin, R.F. 1978, *Observatory,* **98**,14.
Griffin, R. F., Gunn, J. E. 1974, *Astrophys. J.,* **191**, 545.
Haggkvist, L., Oja, T. 1968, *Ark. Astr.,* **5**,125.
Pickering, E. C. 1908, *Ann. Harv. Coll. Obs.,* **50**.
Plaskett, J. S., Harper, W. E., Young, R. K., Plaskett, H. H. 1921, *Publ. Dom. astrophys. Obs.,* **2** ,1.
Plaskett, J. S., Harper, W. E., Young, R. K., Plaskett, H. H. 1922, *Publ. Dom. astrophys. Obs.,* **1**, 287.
Wilson, R. E., Joy, A. H. 1950, *Astrophys. J.,* **111,** 221.

J. Astrophys. Astr. (1981) **2,** 119–132

A Model of the Algol Type Close Binary TT Hydrae

A. G. Kulkarni* and K. D. Abhyankar *centre of Advanced study in Astronomy, Osmania University, Hyderabad 500007*

Received 1980 April 18; accepted 1981 April 29

Abstract. *UBV* photometric observations and elements of TT Hydrae obtained by Kulkarni and Abhyankar (1980) are combined with the radial velocity curve of Popper (1979, personal communication) to derive the absolute dimensions and. a model of this important Algol system. While the photometric ratios of radii in *V* and *B* are in agreement giving $k = 0{\cdot}3812$ for a limb darkening coefficient of $x = 0{\cdot}6$, application of Irwin's (1947) method gives $x = 0{\cdot}4$ for *U*. The primary is found to be a main sequence Al V star of mass $2{\cdot}61\ M_{\odot}$ and radius $2{\cdot}01\ R_{\odot}$, and the secondary is classified as a Kl III star of mass $0{\cdot}70\ M_{\odot}$ and radius $5{\cdot}33\ R_{\odot}$. The observed Fourier coefficients for the light outside the eclipse agree with those calculated from theory for the reflection and ellipticity effects. The system shows an ultraviolet excess of 0·5 to 0·6 magnitudes during primary eclipse, which is attributed to an asymmetric circumstellar distribution of matter around the primary. The evolutionary status of the secondary, which does not appear to fill its Roche lobe completely, is discussed.

Key words: close binaries—absolute dimensions—ultraviolet excess in Algols

1. Introduction

TT Hydrae (variously designated as HD 97528, CD –25° 8531, CPD –25° 4711, Gou 15354, Cord A 8686) was discovered to be an eclipsing variable of Algol type by Wood (1926) at the Union Observatory in Johannesburg. Since then it has been studied photometrically by Hertzsprung (1928), Reilly (1946) and Shapley (1927) who made the first attempt to derive the photometric orbit using Hertzsprung's observations.

*Present address: Sardar Patel Planetarium, Sayaji Baug, Baroda 390018

Systematic spectroscopic investigations were initiated by Wyse (1934) who reported that the spectrum of the secondary star of the system contains bright hydrogen lines. The first spectrographic orbit is due to Sanford (1937) who obtained 16 spectrograms spread over a period of 6 years from 1930 to 1936, all outside the primary minimum. The orbit was found to be fairly circular (e = 0·08). Sahade and Cesco (1946) also gave spectrographic orbits based on Ca II K line as well as hydrogen lines. These orbits are somewhat eccentric with e = 0·12 for the Ca II line and e = 0·24 for hydrogen lines. The third spectroscopic study is due to Miller and McNamara (1963). They obtained six spectra of the primary and one spectrum of the secondary. Their velocities from the spectra of the primary agree well with Sahade and Cesco's orbit from Ca II K line. They have obtained the mass ratio of 0·17 and hence the masses of the component stars as 13 2 $M_\odot$ and 2·3 $M_\odot$ for the primary and the secondary, respectively.

From the evolutionary point of view, the system of TT Hydrae is somewhat controversial. Kopal (1959) lists this system as one with an ' undersize subgiant secondary' under the assumption that the present secondary is less massive now after the loss of matter to the present primary in its evolutionary history. Later, Hall (1974) examined this list of systems with 'undersize subgiant secondaries' along with a few other systems, and came to the conclusion that there is no evidence to support the notion that such a subgroup of post-main sequence mass exchange remnants exists in which the subgiant is smaller than its Roche lobe. Discussing this particular system (TT Hydrae), Hall says, "If the error in the relative radius of the cooler component were ±0·02 instead of ±0·01, the computed and observed K_h (velocity amplitudes of the hotter components) will agree". The computed K_h is obtained under the assumption that the secondary fills its Roche lobe. Thus there is a need for determining the radii of the component stars with better accuracy.

We have tried to obtain the absolute dimensions and a model for TT Hydrae by combining our photometric elements (Kulkarni and Abhyankar 1980, hereafter called Paper I) with the most recent and accurate spectrographic observations of this system by Popper (1979, personal communication). He obtains the velocity curve for the primary and the secondary using the image tube spectrograms. For primary, he uses numerous lines in the photographic region and finds that the curve is not perfectly sinusoidal. The secondary appears to be showing good sinusoidal variation. Measurements for the secondary were made using the sodium D lines.

2. Photometric study

2.1 *Observations*

This binary system was observed by us in *UBV* on 63 nights during a period of four years from 1973 to 1977, with a photoelectric photometer attached to the 1·2–m reflector telescope of the Japal-Rangapur Observatory. All the observations were reduced to the standard *UBV* system of Johnson by observing several standard stars. The individual observations are already published (Kulkarni and Abhyankar, 1978) and the light curves based on them were plotted in Figs 1 and 2 of Paper I, which show that the primary eclipse is total. The $B - V$ and $U - B$ colours for the primary

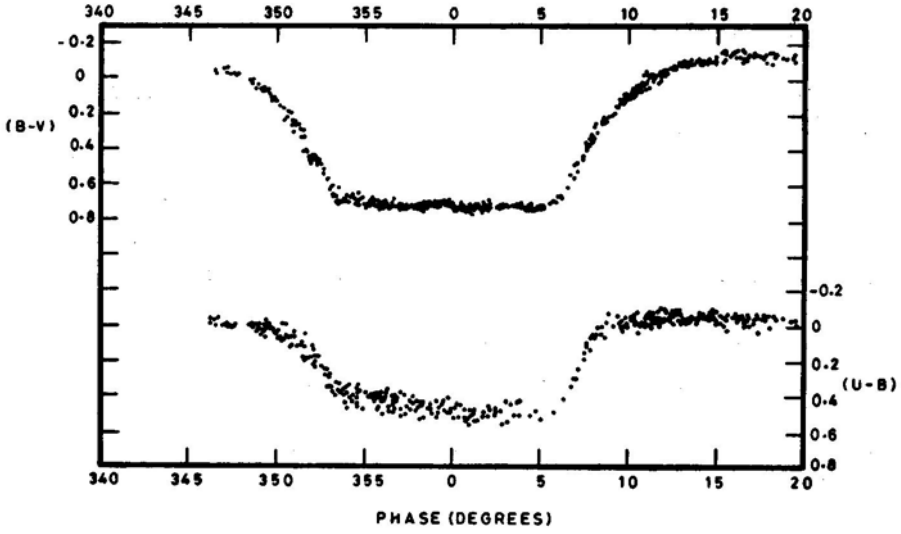

Figure 1. Primary eclipse of TT Hydare in ($B - V$) and ($U - B$) colours

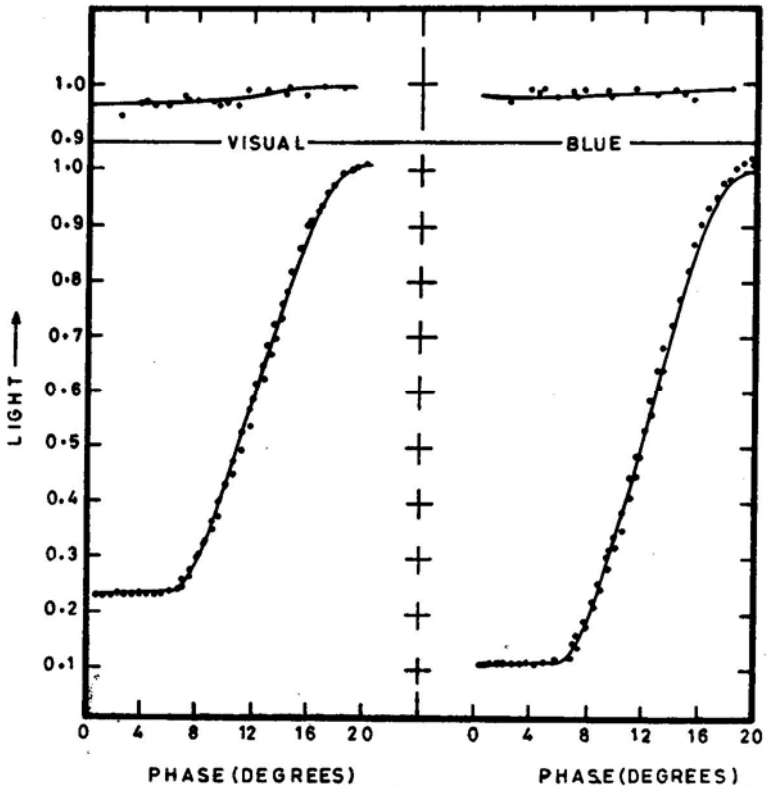

Figure 2. Fit of observed normal points (rectified) to the computed elements for primary and secondary eclipse in *V* and *B*.

eclipse phases are plotted in Fig. 1 of this paper. Eggen (1978) has published his magnitude and colour observations outside and inside the eclipse. Our values agree very closely with his values. The normal points obtained from the 931 observations in *V,* 855 observations in *B* and 761 observations in *U* as tabulated by Kulkarni (1979) are shown in Fig. 2.

2.2 *Rectification*

1. The light outside the eclipse was represented by a series of the type:

$$L = A_0 + A_1 \cos\theta + A_2 \cos 2\theta + A_3 \cos 3\theta + A_4 \cos 4\theta + \ldots . \\ + B_1 \sin\theta + B_2 \sin 2\theta + B_3 \sin 3\theta + B_4 \sin 4\,\theta \ldots . \quad (1)$$

The constants and their probable errors are listed in Table 1.

2. The Reflection constants C_0 and C_2 were obtained from the ratio of the surface brightness given by the primary and secondary depths and the tables of luminous efficiencies given by Cester (1969). For this purpose, the primary spectrum was assumed to be of type A3 and the secondary was assumed to be of type G5. All the relevant parameters are listed for each colour in Table 2.

Table 1. Fourier coefficients of the harmonic representation.

Coefficient	*V*	*B*	*U*
A_0	·95762±·00115	·97521±·00128	·97672±·00168
A_1	−·01379±·00159	−·01103±·00176	−·01479±·00241
A_2	−·03479±·00187	−·01635±·00204	−·01012±·00267
A_3	·00111±·00159	·00153±·00177	−·00202±·00240
A_4	−·00650±·00163	−·00608±·00183	−·00703±·00247
B_1	·00556±·00105	·00701±·00118	·00947±·00162
B_2	−·00237±·00094	−·00180±·00103	−·00401±·00148
B_3	−·00296±·00114	−·00330±·00127	−·00259±·00175
B_4	−·00087±·00127	−·00022±·00144	·00352±·00195
p.e.	·00142	·01037	·01378

Table 2. Parameters for rectification.

Quantities	*V*	*B*	*U*
λ_{eff} (Å) (Primary, A3)	5480	4400	3650
λ_{eff} (Å) (Secondary, G5)	5510	4500	3800
E_c/E_h	·96859	·57358	·61517
J_h/J_c	19·41	44·32	202·00
G_c/G_h	18·2095	14·5797	76·4429
x (A3)	·520	·680	·648
x (adopted)	·6	·6	·6*
N	2·6	2·6	2·6
z	·06037	·03046	·02185
C_0	·01154	·00949	·01139
C_2	·00385	·00316	·00379

*The limb darkening coefficient x for ultraviolet is computed later to be 0·42 from. Irwin's (1947) method of obtaining differential limb darkening coefficient. However, initially x was taken as 0·6 for the *U* solution as well.

3. Rectification of light curve was performed by (i) initially removing the asymmetric sine terms (B_i sin $i\theta$, i= 1, 2, 3, 4) by subtraction, (ii) adding subsequently the reflection terms ($C_0 - A_1 \cos \theta + C_2 \cos 2\theta$), (iii) further effecting the rectification for ellipticity of the stars with division by the factor ($A_0 + C_0$) +($A_2 + C_2$) cos 2θ + A_3 cos 3θ + A_4 cos 4θ and (iv) finally rectifying the phases in the customary manner with x and z given in Table 2.

3. Solution of the light curve

3.1 *Determination of the Ratio of Radii*

The light curves show that the primary eclipse is deep while the secondary eclipse is very shallow (0.07 mag in *V,* 0.02 mag in *B* and almost zero in *U*). Therefore, it was decided to solve only the primary eclipses and later use these elements to representthe light curve in the secondary eclipses. It is also evident from the totality phase that the primary eclipse is an occultation while the secondary eclipse is a transit. From the rectified light curves, the fractional light losses $\alpha = (1 - l)/(1 - l_0)$ were computed, where l_0 is the light in the total phase of the eclipse.

Kopal's (1959) first method was used to solve all the three (*V, B* and *U*) light curves. In this method, for each assumed value of *k,* the ratio of radii, the rectified phases Θ and the corresponding geometrical depths p are fitted to an equation of the type

$$y = mx + c,$$

Where

$$y = \sin^2 \Theta,\ x = (1 + kp)^2,\ m = r_g^2 \operatorname{cosec}^2 i, \text{ and } c = \cot^2 i, \tag{4}$$

by the method of least squares with the weights

$$W_i = \frac{n_i}{l_i^2 (1 + kp_i)^2 \left(\frac{dp}{d\alpha}\right)_i^2}, \tag{5}$$

where n_i is the number of observations in each normal point. It may be noted that these weights apply for the deviation in $\sin^2 \Theta$. This fit was obtained for various values of k with an initial value of 0·35, and steps of 0·025. The quantity $\Sigma\ W_i\ (O - C)_i^2$ was computed for each *k,* and plotted in Fig. 3(a). As is evident from the figure the best fit is obtained for k =0·4375, 0·4300 and 0·4575 for *V, B* and *U,* respectively. As the k values for *V* and *B* are close to each other while that for *U* is rather removed from both, we took the average of *V* and *B* results to obtain a value of k = 0·4337.

The above procedure (Kopal's first method) assumes that the observed phases (times of observation) are in error and not the observed lights. However the observed lights do have errors whereas the phases are comparatively accurately determined quantities. We proceeded to correct for this effect. For each value of *k,* the values

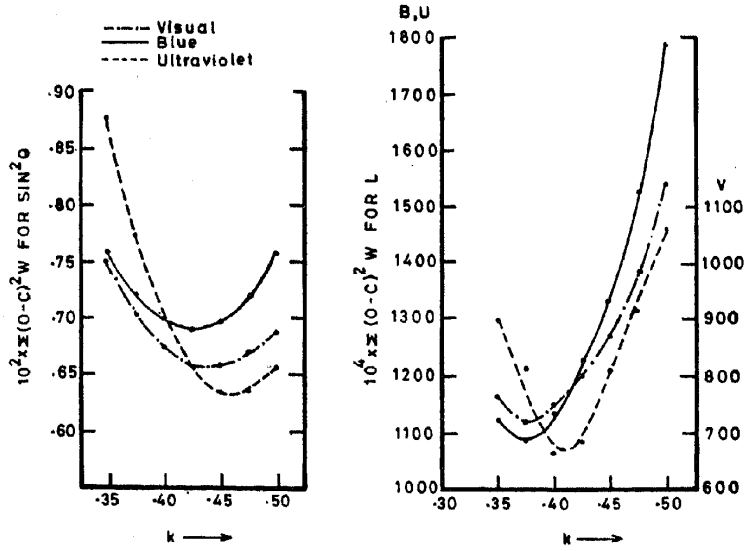

Figure 3. Sum of the weighted $(O - C)^2$ plotted against k for (a) $\sin^2\Theta$ (b) light.

of r_g, i and p (Θ) obtained from the Kopal solution were used for computing the light at the phases of each normal point. Then taking the appropriate weights for light as (n_i / l_i^2),we obtained $\sum W_i (O - C)_i^2$, for various values of k. They are shown in Fig. 3(b). We find that the best fit now occurs at k= 0·3825, 0·3800 and 0·4075 for V, B and U respectively. Again, the k value for U differs from that for V and B, so we took the mean for V and B which gave k = 0·3812. We feel this to be the correct value of k and not the earlier one where the phases were presumed to be in error.

The secondary eclipses in V and B were further represented by using the elements obtained from the primary, with k = 0·3812 and also with k = 0·4337. We find that the weighted $(O - C)^2$ are much less in the case of k = 0·3812 than in 0·4337. In the former case, $\sum W_i (O - C)_i^2$ is 68 $\times 10^{-4}$ and 85 $\times$ 10^{-4} in V and B respectively while in the latter case the corresponding values are 164 $\times$ 10^{-4} and 145 $\times$ 10^{-4}. This fact further confirms that the former (0·3812) value of k is the correct one and not the latter (0·4337).

3.2 *Elements of the Binary*

After determining the value of k, the values of i, the inclination of the orbit and r_g, the relative radius of the larger component, were obtained by interpolation from the values of these quantities derived for various values of k. They come out to be i = 83°·64, r_g = 0·2438 and therefore r_s= 0·0929 since $k = r_s/r_g$= 0·3812. All the photometric elements are given in Table 1 of Paper 1 which are reproduced in Table 3 for completeness.

Representation of the primary and the secondary eclipses using computed elements is shown by the continuous line in Fig. 2 for V and B.

Table 3. Photometric orbital elements of TT Hydrae.

Element	Present study	Shapley (1927)
θ_e	18°·55	
X_s (V, B)	0·6	
X_g (V, B)	0·8	
X_s (U)	0·4	
k	0·3812	0·30
j	83°·74	82°·6
r_g	0·2438	0·240
r_s	0·0929	0·072
L_s (V)	0·7682	
L_g (V)	0·2318	
J_s/J_g (V)	19·41	
L_s (B)	0·8858	0·895
L_g (B)	0·1142	0·105
J_s/J_g (B)	44·32	95
L_s (U)	0·9100	
L_g (U)	0·0900	
J_s/J_g (U)	~200	

3.3 *Limb Darkening in Ultraviolet*

We have already noted that the values of k for V and B are closer to each other while that for U is somewhat different. This could presumably be due to a wrong choice of limb darkening (x = 0·6) for U. Hence, we took the mean geometrical elements obtained from V and B light curves to be representative of the system and obtained the value of x_U *by* Irwin's (1947) method. In this way we find x=0·42 for U. On using this value of x and k = 0·3812 (mean for V and B) we found that the sum of weighted $(O - C)^2$ was significantly reduced (by about 40 per cent) as compared to x= 0·6. This clearly indicates that x = 0·4 is closer to the actual situation. This lowering of x can be attributed to the larger Balmer discontinuity in the Al star, with a consequent increase in the absorption coefficient in the ultraviolet. It may be pointed out here that the observed U flux may not originate entirely in the secondary (see the discussion of ultraviolet excess in Section 5).

3.4 *Spectral Types and Colours of the Component Stars*

Using the computed dimensions, observed fractional luminosities and the ratio of luminous efficiencies, the reflection corrections were computed and applied to the observed luminosities of the hotter and the cooler components. After converting these into magnitudes they were added to the brightness (in magnitudes) of the system at phases 0·25 and 0·75 quadratures. Thus we obtained the magnitudes and colours of each component given in Table 4. From the $(B - V)$ and $(U - B)$ colours for the hotter and cooler components thus obtained, the spectral types were read off from Allen's (1973) Table. The spectral type for the primary (hotter) component is A1 from both the $(B - V)$ and $(U - B)$ colours. As far as the secondary is concerned, the spectral class obtained from the $(U - B)$ colour came out to G8 III while that

Table 4. Spectral types and colours of component stars

Quantity	Primary	Secondary
Spectral type	A1	K1
Luminosity class	V	III
V	7·526	8·903
$B-V$	+·027	0·970
$U-B$	−·019	0·283
Distance to the system	157 parsecs	

from (B — V) is K3 III. We suspect that the U flux may not entirely originate in the secondary and that the gaseous radiating plasma around the primary may be contributing heavily to this band. This question is discussed in a greater detail in Section 5. For these reasons we fix the spectral class as Kl III for the secondary.

Using the derived spectral classes, new values of (E_c/E_h) were obtained applying Cester's (1969) tables. These improved values were used again for the computation of the reflection corrections to the observed fractional luminosities and further, the magnitudes and colours of the component stars. These new colours again gave the spectral types of Al V and Kl III which we had used for reading the E values from Cester's tables.

From the spectral type of the primary and using the spectral class—mass and the spectral class—radius relation (Allen 1973), the preliminary estimate of its mass is obtained as 3·0 $M_\odot$ and radius as 2·3 $R_\odot$. From the V magnitude and the colours, the distance to the binary system turns out to be about 157 parsecs.

4. Absolute dimensions and the model

4.1 *Masses and Radii of the Components*

As reported earlier in Paper I the absolute dimensions were computed in different ways under different initial assumptions

1. That Miller and McNamara's (1963) estimate of the mass ratio from one secondary spectrum is reasonably good,
2. That the primary is on the main sequence and follows the spectral type—mass relation (Allen 1973),
3. That the primary is on the main sequence and follows the spectral type—radius relation (Allen 1973),
4. That the secondary is filling its Roche lobe, giving us a mass ratio from Roche limit calculations of Plavec and Kratochvil (1964).

Each of these four assumptions were applied to the spectroscopic orbits given by Sahade and Cesco (1946) and by Sanford (1937). As pointed out in Paper I, Sanford's (1937) spectroscopic elements represent the evolutionary aspect of the system better than those given by Sahade and Cesco (1946). This conclusion is strengthened by the observations of Popper. According to him, the amplitude of the velocity curve of the secondary is 130 km s^{-1} while that of the primary appears to be about 35 km s^{-1}.

Popper has measured the sodium D lines for the secondary. This appears more definitive and less ambiguous compared to the case of the primary for which numerous lines in the blue region have been measured. Although the velocity curve of the primary shows a distortion in the phase range 0·2 to 0·7 due to the fact that the lines chosen for measurement do not originate wholly in the photosphere of the primary, the amplitude is not likely to be much different. Thus we obtain the mass ratio of the component stars as the inverse of the ratio of their amplitudes of velocity variation and obtain a value of $m_2/m_1 = 0{\cdot}269$.

Assuming the orbital eccentricity to be zero, which is borne out by our light curves as well as Popper's velocity curves, we obtained the absolute dimensions given in Table 5. A scale model of the system is shown in Fig. 4. It may be emphasised that the mass of the primary component derived from our observed colours as a main sequence star and that derived from Popper's observations are quite consistent.

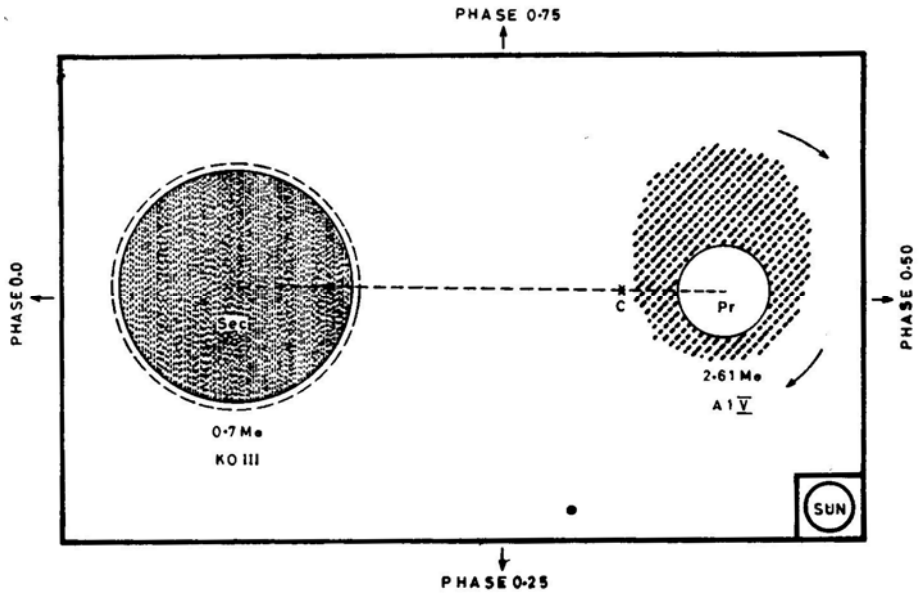

Figure 4. Scale diagram for the system of TT Hydrae based on Popper's velocity curve. The linear scale is shown by the solar diameter (7×10^5 km). C denotes the centre of mass of the system. The dashed circle around the secondary is the theoretical Roche lobe. The dimensions of the circumstellar matter around the primary is, however, not drawn to scale.

Table 5. Absolute dimensions of TT Hydrae based on Popper's* velocity curves.

mass ratio = 0·269

Physical parameter	Primary	Secondary
Mass $M_\odot$	2·61	0·70
Radius $R_\odot$	2·01	5·53
Density gm cm^{-3}	0·453	0·002
Size of the orbit (10^6 km)	3·37	12·50
Centre to centre distance (10^6 km)	15·87	

*1979, personal communication

4.2 *Comparison between the Theoretical and the Observed Fourier Coefficients*

The observed Fourier coefficients obtained by a harmonic representation of the outside eclipse normal points have contributions from the reflection effect as well as the ellipticity effect. Thus $A_i = A_i^{ell} + a_i^{ref}$ Hence we proceed as follows: (1) Using the (E_c/E_h) ratios, and the dimensions, the G_h and G_c values were computed by equation (102) of Russell and Merril (1952) which were then used to obtain C_1 C_0 and C_2 with $i = 83°.74$, obtained from the photometric analysis. This gives the reflection component of the Fourier coefficients. (2) The ellipticity components are computed using the formulae given by Merrill (1970). For this purpose, we adopted $x = 0{\cdot}6$ for V and B and $0{\cdot}4$ for U and $y = 1$ for all the three filters. The coefficients were computed for the mass ratio $m_2/m_1 = 0{\cdot}269$ for the hotter and the cooler components, and they were combined with weights proportional to the observed luminosities. (3) The ellipticity and reflection coefficients obtained from the geometrical elements and mass ratio were added and compared with the observed Fourier coefficients. As shown in Table 5 the agreement is quite good for most of the coefficients. This is an indirect proof of the validity of our solution.

The small discrepancy in computed and observed coefficients can be traced to the inclusion of sine terms in the representation of the observed light curve outside the eclipse by equation (1). In order to verify this we have calculated l (90°), the luminosity at quadrature, both from the theoretical and observed Fourier coefficients. In the first case it is given by $(A_0 - A_2 + A_4)$ while in the latter it will be equal to $(A_0 - A_2 + A_4 + B_1 - B_3)$. The computed and observed values of l (90°) are given at the bottom of Table 6, the agreement between them is remarkably good which again points to the validity of our solution.

Table 6. Comparison of theoretical and observed Fourier coefficients for TT Hydrae

$m_2/m_1 = 0{\cdot}269$

Coefficient		V	B	U
A_0	Computed	+0·97164	+0·98330	+0·98534
	Observed	+0·95762±·00115	+0·97521±·00128	+0·97672±·00168
A_1	Computed	−0·01604	−0·00961	−0·00884
	Observed	−0·01379±·00159	−0·01103±·00176	−0·01479±·00241
A_2	Computed	−0·03074	−0·01605	−0·01362
	Observed	−0·03479±·00187	−0·01635±·00204	−0·01012±·00267
A_3	Computed	+0·00087	+0·00169	+0·00217
	Observed	+0·00111±·00159	+·000153±·00177	−0·00202±·00240
A_4	Computed	−0·00635	−0·00605	−0·00703
	Observed	−0·00650±·00163	−0·00608±·00183	−0·00703±·00247
l(90°)	Computed	0·99603	0·99330	0·99193
l(90°)	Observed	0·99433	0·99579	0·99187

5. Problem of ultraviolet excess

The existence of the problem of ultraviolet excess in cool subgiant secondaries in Algol type eclipsing binaries is well known (Koch 1972, Hall and Garrison 1972, Devinney, Hall and Ward 1970). As noted in Section 3.4, the secondary component of TT Hydrae also exhibits an ultraviolet excess of 0·5 to 0·6 magnitudes. There are two hypotheses regarding the origin of the ultraviolet excess in Algol secondaries, one of which attributes it to the underabundance of metals in the secondary itself (Bond 1972, Sistero 1968, 1971) while the other places its origin in the circumstellar matter around the bright primary component that is not totally obscured by the large secondary even during the total phase of the eclipse of the primary (Hall 1969, Hall and Garrison 1972).

Our photometric observations of TT Hydrae in U and $(U- B)$ show that the ultraviolet excess is due to asymmetric circumstellar matter around the primary, in confirmation with the results of Hall and Garrison (1972). A detailed observation of the light and colour curves shows the following features.

(1) The second contact in U and $(U - B)$ is not as sharp as that in B and V filters. Moreover, it is less well defined compared to the third contact.
(2) Asymmetry in the U and $(U–B)$ curves during the primary minimum from the first to the fourth contact is noticeably large.
(3) Variation of light over a few days in the total phase of the primary minimum is observed in U, similar to the case of U Cep (Huffer and Code 1959).
(4) The ultraviolet excess manifests itself well after the first contact and is restored well before the fourth contact.

There is also supporting spectroscopic and Polarimetric evidence from earlier and recent observations.

(1) Hα-emission lines appear redshifted just before the totality begins and violet-shifted just after the totality ends (Wyse 1934; Sahade and Cesco 1946). The lines are otherwise in 'normal' position during the total phase.
(2) Distortion is present in the velocity curve of the primary component as compared to the essentially sinusoidal nature of the secondary velocity curve. Popper's velocity curve of the primary shows a blueward shift of the lines used for its measurement from phase 0·2 to 0·7.
(3) Popper also notes that the lines of Mg II and Si II are essentially absent and that the intensity of all lines shows large variations.
(4) About 1 to 2 per cent polarisation during the totality has been reported by Serkowski (1970).

We therefore propose that the extra light at the second contact in U filter, compared to that at the third contact may be due to the asymmetric distribution of matter around the primary as shown in Fig. 4. An excess which is entirely due to the secondary will not exhibit any asymmetry in the light or the colour curve. Secondly, the excess cannot vary if it were intrinsic to the secondary component. We observe a change of about 0·07 mag in the excess within a few days (our observational error is $\leqslant 0{\cdot}02$ mag). Thirdly, the excess should change continuously from the

first to the fourth contact, whereas our observations show to the contrary. The excess shows itself well after the first contact and is restored well before the fourth contact. All these photometric features lead to the conclusion that the origin of the ultraviolet excess is not intrinsic to the secondary and that it must be due to the circumstellar matter (thick ring or disk) around the primary. Further, we also conclude that the distribution of matter around the primary is asymmetric. The circumstellar matter becomes photometrically conspicuous in *U* band when most of the light from the bright primary is cut off during an eclipse. It is due to this reason that our attemped solution of the *U* light curve gave the ratio of radii as 0·4075 in comparison to 0·3812 (mean) for *B* and *V* filters (see Section 4.1 and 4.2). The overall picture is very similar to U Cep (Batten 1974) in many respects. SW Cyg (Hall and Garrison, 1972) is yet another Algol system showing similar behaviour.

The spectroscopic features also very clearly indicate that there is matter around the primary and that it is observable even during totality. The abundance analysis of the subgiant secondary of U Cep (Algol type eclipsing binary with B7 V + G8 III-IV) has been recently reported by Parthasarathy, Lambert and Tomkin (1979). They have obtained high dispersion (1·9 Å mm^{-1}) spectra in the near infrared region, which is much less contaminated by any emission from the circumstellar matter in the system. They find the composition to be normal within the limits of observational errors. However, Naftilan (1975) reports [Fe/H] = – 0·3 for TT Hya, indicating a mild underabundance. His spectra are obtained at a rather coarse dispersion of 125 Å mm^{-1} and are not good enough for abundance analysis (Parthasarathy 1979, personal communication). Parthasarathy, Lambert and Tomkin (1979) find that the cores of Ca II triplets in the infrared are very weak for the secondaries of U Cep and U Sge in comparison with the standard stars. Baldwin (1973) reported that the Ca II K lines in the spectrum of U Cep to be somewhat filled in by emission. Since the H and K line emission intensity is found to be an indicator of chromospheric activity (Wilson and Bappu 1957; Wilson 1963) and the Ca II H and K lines and the Ca II infrared triplet have the same common upper state, we conclude that the secondaries of Algols might have active chromospheres. This might explain a part of the ultraviolet excess observed in their atmospheres.

6. Discussion and conclusion

The theoretical computation of the fractional radii of the secondary for given mass ratios (Plavec and Kratochvil, 1964) is used for computing the size of the Roche lobe. For the observed ratio of 0·269, the fractional radius turns out to be 0·264 whereas the observed value given in Table 5 is 0·2438. This indicates that the secondary has not filled its Roche lobe, and thus the system is an undersize subgiant. The primary appears to be a normal main sequence star (Al V)in every respect *i.e.* from its photometric colours, the radius and the mass. However, the secondary has not filled its Roche lobe as the theory of mass transfer and the accepted theory of stellar evolution requires. Still about 10 per cent of the secondary Roche lobe remains to be filled during its evolution off the main sequence.

The above conclusion may not be valid if the derived mass ratio and radii of the components are not correct, which may very well prove to be the case. We do not really understand just where the primary lines are formed on account of their variable

intensities and clear evidence of dilution. There is also some uncertainty in the radii. We estimate that our value of $k = 0{\cdot}3812$ is fairly well determined within an error of $\pm\ 0{\cdot}0012$. The corresponding error in $r_g = 0{\cdot}2438$ will be about $\pm\ 0{\cdot}0008$. If the Roche lobe of the secondary is to be filled completely, the mass ratio should lie between 0·202 and 0·208. We do not believe that the spectroscopic data can be reconciled with such low values of mass ratio. Hence, it is quite likely that the secondary does not fill its Roche lobe. Anyway taking the values of the mass ratio and radii at their face value we may consider the possibility of TT Hydrae being a very young system with its secondary still in the pre-main sequence stage of evolution. Then using the evolutionary calculations of Iben (1965) we get a thermal contraction time of 2×10^6 years for the primary which has a mass of $2{\cdot}6\ M_\odot$. For this mass, the main sequence lifetime is 2×10^8 years, while we obtain the contraction time of 7×10^7 years for the secondary with $0{\cdot}7\ M_\odot$ Thus, we think the age of the system is of the order of about 5×10^7 years with the secondary in some sort of T Tauri phase. Further observations would be necessary to confirm these conclusions by placing more stringent limits on the radii of components.

It may be mentioned that one needs to explain the origin of the circumstellar matter around the primary if the secondary is not filling its Roche lobe and hence not transferring mass to the primary. It is not wrong to assume that the young binary may still have some remnant of the original gas cloud which is now being slowly accreted by the more massive primary component. The variation of intensities and dilution effect in the lines of the primary as well as the ultraviolet excess may be manifestations of interaction of this matter with the photosphere.

Our observations indicate that the orbit is circular. As is evident from the light curves, a better photometric confirmation for the circularity of the orbit is possible only through low frequency filters like red and infrared. Hence we recommend observations of the secondary minima in these filters. An important conclusion we draw from our studies regarding the choice of photometric bands is that any band shortward of 4000 Å is not quite representative of the orbital features of the system. Therefore one has to exercise enough caution in using *U* magnitudes for an analysis of the orbit.

In recent years, TT Hya has also been observed in the radio region. Altenhoff *et al.* (1976) place an upper limit to the radio emission as 10 mJy at 10·69 GHz on 16th June 1973. Plavec (1977, personal communication) reports the appearance of shell lines. Peters and Polidan (1976) report cyclic variation in *V*/*R* for this system. Bidelman (1976) has listed this system as an early type shell star. All this work indicates that the system is not a simple one and there are many spectroscopic peculiarities and complications.

Detailed spectroscopic investigation of the secondary is possible for this system with the use of modern detectors and techniques. The duration of totality is also fairly large (6 hours) to give uncontaminated spectra of the secondary. One can also study the spectral features of the circumstellar matter around the primary. We also suggest photometric observations of the secondary in the red and infrared in order to improve the photometric elements, particularly to confirm the circularity of the orbit. Ultraviolet observations during the primary minimum from space vehicles might give important information regarding the unstable ring/radiating plasma in the system.

Acknowledgement

We are grateful to Prof. D.M. Popper for kindly sending us his unpublished radial velocity curves of the star and for helpful comments. A.G.K. wishes to thank the University Grants Commission, New Delhi for financial assistance during the course of the work.

References

Allen, C. W. 1973, *Astrophysical Quantities,* Athlone Press, London, p. 209.
Altenhoff, W. J., Braes, L. L. E., Olnon, F. M., Wendker, H. J. 1976, *Astr. Astrophys.,* **46**, 11
Baldwin, B. W. 1973, *Publ. astr. Soc. Pacific,* **85**, 714
Batten, A. H. 1974, *Publ Dom. astrophys. Obs.,* **14**,191.
Bidelman, W. P. 1976, in *IAU Symp. 70: Be and Shell Stars,* Ed. A. Slettebak, D. Reidel, Dordrecht, p. 457.
Bond, H. E. 1972, *Publ. astr. Soc. Pacific,* **84**, 839.
Cester, B. 1969, *Mem. Soc. astr. Ital.,* **40**, 169.
Devinney, E. J., Hall, D. S., Ward, D. H. 1970, *Publ. astr. Soc. Pacific,* **82**,10.
Eggen, O. J. 1978, *Inf. Bull. Var. Stars,* No. 1426.
Hall,D. S. 1969, *Bull. Am. astr. Soc.,* **1**, 345.
Hall, D. S. 1974, *Acta Astr.,* **24**, 215.
Hall, D. S., Garrison, L. M. 1972, *Publ. astr. Soc. Pacific,* **84**, 552.
Hertzsprung, E. 1928, *Bull. astr. Inst. Netherl,* **4**, 160.
Huffer, C. M., Code, A. D. 1959, *Astr. J.,* **64**,129.
Iben, I. Jr. 1965, *Astrophys. J.,* **141**, 993.
Irwin, J. B. 1947, *Astrophys. J.,* **106**, 380.
Koch, R. H. 1972, *Publ. astr. Soc. Pacific,* **84**, 5.
Kopal, Z. 1959, *Close Binary Systems,* Chapman and Hall, London, p. 497.
Kulkarni, A. G. 1979, *PhD thesis,* Osmania Univ., Hyderabad.
Kulkarni, A. G., Abhyankar, K. D. 1978, *Contr. Nizamiah JapalRangapur Obs.,* No. 9.
Kulkarni, A. G., Abhyankar, K. D. 1980, *Astrophys. Sp. Sci.,* **67**, 205.
Merrill, J. E. 1970, *Vistas Astr.,* **12**, 43.
Miller, E. W., McNamara, D. H. 1963, *Publ. astr. Soc. Pacific,* **75,** 346.
Naftilan, S.A. 1975, *Publ. astr. Soc. Pacific,* **87**, 321.
Parthasarathy, M., Lambert, D. L., Tomkin, J. 1979, *Mon. Not. R. astr. Soc.,* **186**, 391.
Peters, G. J., Polidan, R. S. 1976, *Bull. Am. astr. Soc.,* **8**, 39.
Plavec, M., Kratochvil, P. 1964, *Bull. astr. Inst. Csl.,* **15**,165.
Reilly, E.F.1946, *Harvard Coll. Obs. Bull,* No. 918,18.
Russell, H. N., Merrill, J. E. 1952, *Contr. Princeton Univ. Obs.,* No. 26.
Sahade, J., Cesco, C. U. 1946, *Astrophys. J.,* **103**, 71.
Sanford, R. F. 1937, *Astrophys. J.,* **86**,153.
Serkowski, K. 1970, *Astrophys. J.,* **160**,1083.
Shapley, M. B. 1927, *Harvard Coll Obs. Bull,* No. 847,12.
Sistero, R. F. 1968, *Publ astr. Soc. Pacific,* **80**, 474.
Sistero, R. F. 1971, *Bull. astr. Inst. Csl.,* **22**,188.
Wilson, O. C.1963, *Astrophys. J.,* **138**, 832.
Wilson, O. C., Bappu, M. K. V. 1957, *Astrophys. J.***, 125**, 661.
Wood, H.E.1926, *Union Obs. Circ,* No. 69, 368.
Wyse, A. B. 1934, *Lick Bull,* **17**, 37.

J. Astrophys. Astr. (1981) **2,** 133–139

Time-Dependent Interaction of Granules with Magnetic Flux Tubes

P. Venkatakrishnan and S. S. Hasan *Indian Institute of Astrophysics, Bangalore 560034*

Received 1981 January 1; accepted 1981 April 20

Abstract. The time-dependent interaction of the granulation velocity field with a magnetic flux tube is investigated here. It is seen that when a magnetic field line is displaced normal to itself so as to simulate the *buffeting* action of granules, a flow of gas is initiated along the field. By choosing a lateral velocity field which is consistent with observations of granules, it is found that the resulting gas motion is a downward flow with a velocity compatible with the observed downflow in isolated photospheric flux tubes. It is therefore proposed that the observed photospheric downflow is a manifestation of the interaction of granules with flux tubes.

Key words: Sun—small scale magnetic fields—granules—downdrafts—fluid dynamics—unsteady one-dimensional flow

1. Introduction

The dynamical state of a highly conducting fluid embedded in a magnetic field can be greatly influenced by changes in the field geometry. Such changes can often result in a significant flow being set up along the field lines (Hasan and Venkatakrishnan 1980, 1981). On the Sun, there are several processes which can change the magnetic field geometry, for example, hydromagnetic or thermal instabilities, or the *buffeting* of the field lines by an externally imposed flow. This paper is a study of the interaction of granular velocity fields with magnetic flux tubes. For purposes of mathematical simplicity and also to focus our attention on the vertical flow, we solve the MHD equations in a specified stream geometry as discussed by Kopp and Pneuman (1976). By assuming a form for the velocity field normal to the magnetic field based on the observations of granular velocities, we obtain estimates for the resulting fluid velocity along the magnetic field. These velocities compare

favourably in magnitude and direction with the observed values of the fluid velocity within isolated flux tubes.

2. The model

At photospheric levels, granulation forms a velocity pattern which has a typical length scale of a few seconds of arc and a time scale of a few minutes. There are also concentrated magnetic flux elements in the photosphere which will undergo *buffeting* by the granules. A magnetic element situated in the intergranular lanes will be acted upon by these granules on its boundary. In this paper, we represent the element as a magnetic flux sheath in a plane normal to the intergranular lane. We attempt to model the result of nonlinear interaction between the velocity field of the granulation and the magnetic field of this flux sheath. As a model input, we assume a form for the motion of the magnetic field lines normal to themselves which is related to the observed form of the granular velocity field. The resulting model output is the velocity of gas parallel to the magnetic field.

When field lines are displaced normal to themselves, with a non-uniform velocity a centrifugal acceleration results along the direction of the field. This induces flow of gas along the field. The magnitude and direction of such induced flow depends on the amplitude of velocity fluctuations normal to the field lines and on the direction of positive gradient in this amplitude respectively (Hasan and Venkatakrishnan 1980, 1981). Since the granular velocity field decreases with height, when field lines are displaced with such a velocity field, the resulting flow will be a downdraft. The details of this downflow depend upon the details of the lateral velocity field like its amplitude at the base of the sheath and the scale height of its variation.

3. The basic equations

Let us assume that the flux sheath is in the *y*-*z* plane, with gravity acting in the negative z-direction. It is convenient to transform to a system of coordinates (*s, n*), where *s* is the distance measured along the sheath axis and η denotes the distance measured along a normal curve (in the same plane). Following Kopp and Pneuman (1976), we see that the unit vectors $\hat{\mathrm{S}}$ and $\hat{\mathrm{n}}$ satisfy the following geometric relations

$$\begin{pmatrix} \frac{\partial}{\partial t} \\ \frac{\partial}{\partial s} \\ \frac{\partial}{\partial n} \end{pmatrix} (\hat{\mathbf{s}}, \hat{\mathbf{n}}) = \begin{pmatrix} \frac{\partial \theta}{\partial t} \\ \frac{\partial \theta}{\partial s} \\ \frac{\partial \theta}{\partial n} \end{pmatrix} (\hat{\mathbf{n}}, -\hat{\mathbf{s}}) \tag{3.1}$$

where θ is the angle the field makes with the *z*-axis. The equation of motion along the field can now be expressed as

$$\frac{\partial V_s}{\partial t} + V_s \frac{\partial V_s}{\partial s} + V_n \frac{\partial V_s}{\partial n} = -\frac{1}{\rho} \frac{\partial p}{\partial s} - g \cos \theta + V_n \frac{\partial \theta}{\partial t} + V_n V_s \frac{\partial \theta}{\partial s} + V_n^2 \frac{\partial \theta}{\partial n} \tag{3.2}$$

where V_s is the gas velocity parallel to the field, V_n the velocity normal to the field, p the gas pressure, ρ the density and g the acceleration due to gravity. Let us now consider a frame of reference fixed to the sheath. The space and time derivatives in such a frame will be denoted as $\frac{D}{Ds}$ and $\frac{D}{Dt}$ respectively. These satisfy the following operator relationships

$$\frac{D}{Dt} \equiv \frac{\partial}{\partial t} + V_n \frac{\partial}{\partial n} \tag{3.3a}$$

and

$$\frac{D}{Ds} \equiv \frac{\partial}{\partial s}. \tag{3.3b}$$

From equations (3.2) and (3.3) we have

$$\frac{DV_s}{Dt} + V_s \frac{DV_s}{Ds} = -\frac{1}{\rho}\frac{Dp}{Ds} - g\cos\theta + V_n \frac{D\theta}{Dt} + V_n V_s \frac{D\theta}{Ds}. \tag{3.4}$$

In a similar manner the equation of continuity takes the form (Kopp and Pneuman 1976)

$$\frac{D}{Dt}(\rho A) + \frac{D}{Ds}(\rho V_s A) - \rho V_n A \frac{\partial \theta}{\partial s} = 0, \tag{3.5}$$

where A is the cross-sectional area of the flux sheath. In the above equation we have assumed the constancy of all flow variables in a direction normal to the sheath axis. The evolution of the magnetic field, assuming infinite conductivity, is given by the induction equation

$$\frac{\partial \mathbf{B}}{\partial t} = \nabla \times (\mathbf{V} \times \mathbf{B}), \tag{3.6}$$

which can be resolved into the components

$$B\frac{\partial \theta}{\partial t} = \frac{\partial}{\partial s}(V_n B) \tag{3.7a}$$

along the field and

$$B\frac{\partial \theta}{\partial t} = \frac{\partial}{\partial s}(V_n B) \tag{3.7b}$$

normal to the field respectively. Using the condition for flux conservation in a sheath (BA = constant) and the geometric relation for the rate of change of the angle

$$\frac{D\theta}{Dt} = \frac{\partial V_n}{\partial s}, \tag{3.7c}$$

we can rewrite equations (3.7a) and (3.7b) as

$$\frac{D}{Dt}(\ln A) = \frac{\partial V_n}{\partial n} \tag{3.7d}$$

and

$$\frac{D}{Ds}(\ln A) = \frac{\partial \theta}{\partial n} \tag{3.7e}$$

respectively. Eliminating A between equations (3.7d), (3.7e) and (3.5) we have

$$\frac{DV_s}{Ds} + \frac{D}{Dt}(\ln \rho) + V_s \frac{D}{Ds}(\ln \rho) + V_s \frac{\partial \theta}{\partial n} - V_n \frac{D\theta}{Ds} + \frac{\partial V_n}{\partial n} = 0 \tag{3.8}$$

We relate density and pressure by a polytropic law

$$P/\rho^{\Gamma} = \text{constant}, \tag{3.9}$$

where Γ is the polytropic index. We thus have three equations (3.4, 3.8 and 3.9) in the four unknowns p, ρ, V_s and V_n respectively. The equation of motion normal to the field (which involves the Lorentz force and all other forces acting on the sheath) supplies the means of determining the four quantities uniquely. However, we replace this equation by a prescribed form for V_n (a similar procedure was adopted by Kopp and Pneuman 1976 to model post flare reconnection of coronal loops, as well as by Hasan and Venkatakrishnan 1981 to model spicule flow). Equations (3.4), (3.8) and (3.9) form a set of hyperbolic partial differential equations. These were solved numerically using the method of characteristics. The characteristic equations are

$$\frac{D\xi_+}{Dt} = A + B/a \quad \text{along} \quad \frac{Ds}{Dt} = u + a \tag{3.10a}$$

and

$$\frac{D\xi_-}{Dt} = A - B/a \quad \text{along} \quad \frac{Ds}{Dt} = u - a\,, \tag{3.10b}$$

where

$$\xi_{\pm} = \ln \rho \pm V_s/a, \tag{3.10c}$$

$$A = -V_s \frac{\partial \theta}{\partial n} + V_n \frac{\partial \theta}{\partial s} - \frac{\partial V_n}{\partial n} \tag{3.10d}$$

and

$$B = -g \cos \theta + V_n \frac{D\theta}{Dt} + V_n V_s \frac{\partial \theta}{\partial s}. \tag{3.10e}$$

The same boundary conditions, as in Hasan and Venkatakrishnan (1981), were used.

4. The stream geometry

At $t = 0$, the magnetic field is assumed to be potential with components

$$B_y = B_0 \exp(-kz) \sin \theta, \tag{4.1a}$$

$$B_z = B_0 \exp(-kz) \cos \theta \tag{4.1b}$$

And

$$\theta = ky. \tag{4.1c}$$

Here we have assigned a zero value for k so that the flux sheath is vertical initially. At later instants of time, the sheath geometry is completely determined by V_n. The coordinates of a given point on the sheath axis at different instants of time can be determined from the following equations

$$\frac{Dy}{Dt} = V_n \cos \theta, \tag{4.2a}$$

$$\frac{Dz}{Dt} = -V_n \sin \theta, \tag{4.2b}$$

$$\frac{D\theta}{Dt} = \frac{\partial V_n}{\partial s}. \tag{4.2c}$$

We integrated equation (4.2) numerically from a time t_0 to a time $t_0 + \Delta t$ where Δt is the step size for the grid used to integrate equations (3.10) (Hasan and Venkatakrishnan 1980).

Since the magnetic field is initially potential, it exerts no force on the gas. The initial stratification of the gas was assumed to be polytropic with a polytropic index $\Gamma = 1{\cdot}064$. This polytropic index was chosen to fit the *Harvard-Smithsonian Reference Atmosphere* (Gingerich *et al.* 1971) for a height of 500 km above the photosphere.

5. The choice of the lateral velocity field

Observations of the granular velocity variation with height in the solar atmosphere (Durrant *et al.* 1979) indicate a decrease of the rms velocity with height. The scale height of the variation is of the order of 500 km. The lifetime of the granule varies between 2 to 15 minutes. The time variation of a single granulation flow can therefore be approximated by a sine function with a half period equal to the granule lifetime. More specifically, one can represent the granular velocity V_g as

$$V_g = V_0 \exp(-z/H) \sin(\pi t/T), \tag{5.1}$$

where H is the scale height of variation and T is the lifetime of the external velocity field respectively. V_0 is the amplitude of the velocity at the base. In this paper we assume the form given by equation (5.1) for the velocity V_n of the field lines normal to the sheath axis.

6. Results and discussion

Fig. 1 shows the variation of the fluid velocity component in the direction of the magnetic field with distance along the field, at different instants of time. For this

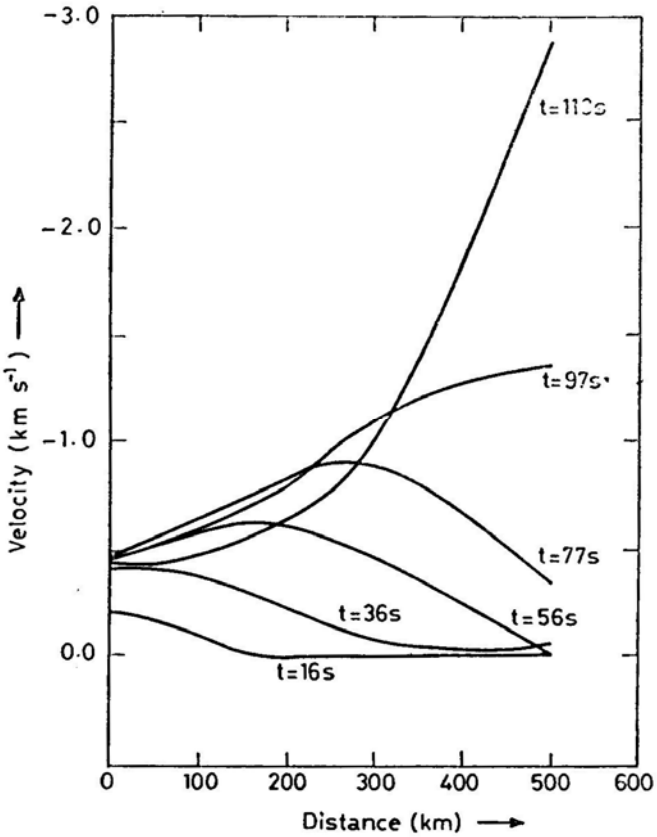

Figure 1. Variation of velocity component in the direction of the magnetic field with distance along the field at five instants of time. The scale height H of the lateral velocity field is 500 km, the half period T = 120 s, and the velocity amplitude at the base V_0 = 500m s^{-1}.

particular calculation, we chose H = 500 km, T = 120 s and V_0 = 500 m s^{-1}. The flow begins as a downflow and remains as such throughout the lifetime of the lateral velocity field. The magnitude of the velocity along the field initially decreases with height but at later instants of time, it increases with height. After $t \simeq 100$ s the velocity attains values around 1 to 2 km s^{-1} which are comparable to those observed in isolated flux tubes (Giovanelli and Slaughter 1978; Giovanelli 1980).

So far we have considered the interaction of a single granule with a flux tube. The granular buffeting can last at the most for a lifetime of a granule. Once the buffeting ceases, the downflow relaxes towards hydrostatic equilibrium, in a manner described previously (Hasan and Venkatakrishnan 1980). The relaxation time is approximately equal to the time taken for a sound wave to traverse the length of the field line participating in the lateral motion. Using a typical value of 1000 km for the size of a granule and 10 km s^{-1} for the sound speed in the photosphere, the relaxation time is of the order of 100 s. Therefore, if the tube is acted upon by a new granular velocity field within about 100 s the downflow will never decrease to zero. On the other hand, the downflow will not be stationary but will be modulated by the frequency of granular buffeting. Observations with a coarse time resolution (larger than the relaxation time of $\simeq$ 100 s) would only detect the averaged velocity field. Thus, it would be interesting to observe the downflow with a finer time resolution.

Furthermore, downflows caused by granular buffeting could, under appropriate conditions, act as seeds for the convective collapse of flux tubes (Webb and Roberts 1978; Spruit 1979; Spruit and Zweibel 1979). Such a collapse might lead to the strong downflow which is inferred by Deubner (1976) to be present in the dark intergranular lanes.

Finally, it must be mentioned that the interaction of other dominant velocity fields (for example, the five minute oscillations or supergranulation) with the tiny flux tubes would produce negligible internal motions since the horizontal length scales of these fields are much larger than that of the flux tubes. The tubes will have maximum internal response to those scales which are of comparable size. The granular velocity field is the only known dominant field which has dimensions closest to those of the flux tubes.

All computations were performed using the TDC-316 system of the Indian Institute of Astrophysics.

References

Deubner, F-L.1976, *Astr. Astrophys.,* **47,** 475.
Durrant, C. J., Mattig, W., Nesis, A., Reiss, G., Schmidt, W. 1979, *Solar Phys.,* **61,** 251.
Gingerich, O., Noyes, R. W., Kalkofen, W., Cuny, Y. 1971, *Solar Phys.,* **18,** 347.
Giovanelli, R. G. 1980, *Solar Phys.,* **67,** 211.
Giovanelli, R. G., Slaughter, C. 1978, *Solar Phys.,* **57**, 255.
Hasan, S. S., Venkatakrishnan, P. 1980, *Kodaikanal Obs. Bull. Ser. A,* **3,** 6.
Hasan, S. S., Venkatakrishnan, P. 1981, *Solar Phys.,* (in press).
Kopp, R. A., Pneuman, G. W. 1976, *Solar Phys.,* **50,** 85.
Spruit, H. C. 1979, *Solar Phys.,* **61,** 363.
Spruit, H. C., Zweibel, E. G. 1979, *Solar Phys.,* **62**, 15.
Webb, A. R., Roberts, B. 1978, *Solar Phys.,* **59,** 249.

J. Astrophys. Astr. (1981) **2,**141–159

Photographic Spectrophotometry of Selected Bright B and Be Stars

Elaine M. Hendry *Department of Physics and Astronomy, Georgia State University, Atlanta, Georgia 30303, USA*
J. D. R. Bahng* *Lindheimer Astronomical Research Center, Northwestern University, Evanston, Illinois 60201, USA*

Received 1981 January 16; accepted 1981 May 25

Abstract. Coudé spectra taken in the red region of 49 bright B and Be stars were examined for the behaviour of Hα and the He I λλ 5876 and 6678 line profiles. 51 per cent of the stars were found to show Hα emission to some degree and 22 per cent showed helium emission. Evidence is presented for the existence of drastic changes in the line profile and the radial velocity in some of the stars on a time scale of fractions of a day.

Key words: B stars—Be stars—photographic spectrophotometry

1. Introduction

There has been an accumulation of evidence in recent publications to suggest that rapid spectral changes in Be stars occur on time scales as short as minutes. Hutchings (1967), Bahng (1971, 1975a,b, 1976), Brucato (1971), McBeath (1974), and Sanyal (1974) among others have reported variations in hydrogen emission strengths. The majority of these investigations have been undertaken with low resolution photoelectric spectrum scanners and therefore, the details of the profile changes have remained largely unexplored. The present investigation has been undertaken in order to complement the earlier studies and examine a larger number of stars at a higher wavelength resolution.

*Visiting Astronomer, Kitt Peak National Observatory and Cerro Tololo Inter-American Observatory, operated by the Association of Universities for Research in Astronomy, under contract with the National Science Foundation.

2. The Observations

A total of 144 high dispersion coudé spectra of 49 B-type stars brighter than $V = 5{\cdot}47$ mag were obtained with the 1·5-m telescope of the Cerro Tololo Inter-American Observatory (CTIO) and the auxiliary coudé feed of the 2·1-m telescope of the Kitt Peak National Observatory (KPNO). The KPNO observations were carried out during the period of 1973 December 18-20 and the CTIO plates obtained during the period of 1974 February 1-3 and 11-13. Reciprocal dispersions are 25Å mm^{-1} for the KPNO plates and 18 Å mm^{-1} for the CTIO plates, both in the first order red. The usable spectrum covers the range 5600-6800 Å on Kodak 098-02 emulsion for the CTIO plates and IIa-F for the KPNO plates. The measurements and reductions of these plates were made by Bahng with the Kitt Peak facilities in Tucson.

The radial velocities of Hα, He I λλ 5876, 6678, and Na I λλ 5889, 5895 were measured whenever possible on the Grant Spectrum Comparator. The photometric measurements were made on the PDS microdensitometer at KPNO. A rectangular analyzing slit of 0·2 mm length perpendicular to the dispersion (chosen to include sufficient photographic emulsion grains while still sufficiently small with respect to the spectrum widths) and 0·02 mm width along the dispersion (chosen to approximate the projected spectrograph slit width) were used to record the densities at every 0·02 mm of the spectrum. Each stellar spectrum was scanned in two parallel overlapping strips whose centres were 0·1 mm apart, and the data for the stellar spectra refer to the averages of these two scans. The scanning speed was chosen to be sufficiently slow (approximately 50 data points per second) as to minimize inaccurate readings due to lag time effects in the microdensitometer at high density levels, as in the case of the strong emission lines seen on some of the spectra. Thus, the wavelength resolution and the separation of the adjacent data points are 0·5 Å for the KPNO plates and 0·36 Å for the CTIO plates. The spot sensitometer calibration plates, one for each night of observations, were also traced to allow the density readings to be converted into the intensity scale.

The details of the stars observed appear in Table 1.

3. Non-emission . stars

Twentyfour of the programme stars were found to evince no emission features whatsoever at Hα or the helium lines. With the exception of one star (*β* Persei, whose line profile is probably contaminated by emission from the shell of the primary), none of these stars showed any profile changes whatsoever within reasonable allowances. The range of spectral types observed was B2 through A0. These stars provided an excellent opportunity to examine the accuracy provided by photometric measures of line profiles and the equivalent widths calculated therefrom. Those B stars which showed no Hα emission are designated by X in the last column of Table 1.

Equivalent widths for selected non-emission stars as well as for those which had been observed more than once were calculated. Standard deviations about the mean values were reasonable, varying from 0·007 to 0·965 Å. To be conservative, a value of five times the largest individual deviation (*i.e.* 4·825 Å) was chosen as the discri-

Table 1. The journal of observations.

Star		No. of plates	V* mag	Sp. Type*	$v \sin i$** km s^{-1}	Hα in emission
HR 39	= γ Peg	2	2·83	B2 IV	0	X
193	= o Cas	1	4·57	B2 V	260	X
264	= γ Cas	16	2·65	B0 IV? e		
496	= ϕ Per	3	4·03	B1 III-IV? pe	450	
542	= ϵ Cas	1	3·38	B3 IV? p	24	X
936	= β Per	2	2·2 v	B8 V + G	67	X
1122	= δ Per	2	2·99	B5 III	271	X
1165	= η Tau	3	2·86	B7 III	216	
1203	= ζ Per	1	2·83	B1 Ib	72	X
1220	= ϵ Per	2	2·88	B0·5 V	150	X
1273	= 48 Per	2	4·02	B3 V pe	217	
1641	= η Aur	1	3·17	B3 V	139	X
1788	= η Ori	2	3·35	B0·5 V	47	X
1790	= γ Ori	1	1·64	B2 III	64	X
1791	= β Tau	2	1·65	B7 III	68	X
1875	= 121 Tau	1	5·16	B3 V	117	X
1899	= ι Ori	1	2·77	O9 III	122	X
1903	= ϵ Ori	1	1·70	B0 Ia	85	
1910	= ζ Tau	10	2·99	B2 IV p	310	
1956	= α Col	6	2·63	B8 V e	155	
2095	= θ Aur	1	2·69	B9·5 pv	52	X
2282	= ζ CMa	3	3·02	B2·5 V	70	X
2343	= ν Gem	1	4·15	B7 IVe	215	
2356	= β^1 Mon	1	4·60	B3 Ve	382	
2538	= κ CMa	6	3·96	B2 Ve	191†	
2781	= UW CMa	3	4·50	O7f	135	
3117	= χ Car	3	3·46	B2 IV	98	
3165	= ζ Pup	6	2·25	O4f	185	
3447	= o Vel	3	3·61	B3 III	0	X
3665	= θ Hya	4	3·88	B9·5 Vp	86	X
3734	= κ Vel	5	2·49	B2 IV	31	
3937	= ν Leo	1	5·17	B9·5 V	96	X
3982	= α Leo	1	1·36	B7 V	354	X
4037	= ω Car	5	3·31	B7 IV		
4140	= PP Car	6	3·58	B5 Ve	356	
4390	= π Cen	3	3·88	B5 Vn	350	X
4621	= δ Cen	7	2·88	B2? V? pe	215	
4638	= ρ Cen	3	3·96	B4 V	147	
4656	= δ Cru	4	2·82	B2 IV	218	X
4743	= σ Cen	3	3·90	B2 V	231	X
4773	= γ Mus	1	3·86	B5 V	278	
4787	= κ Dra	1	3·84	B7p	249	
4798	= α Mus	1	2·71	B3 IV	195	X
4844	= β Mus	2	3·04	B2·5 V	95	
5132	= ϵ Cen	4	2·30	B1 V		
5190	= ν Cen	1	3·40	B2 IV	94	
5191	= η UMa	1	1·86	B3 V	216	X
5193	= μ Cen	3	3·47	B2 V? pne	191	
5440	= η Cen	1	2·35	B1·5 V? ne	300	

Sources of data:

* Hoffleit (1964)

** Uesugi and Fukuda (1970)

† Buscombe (1967)

Table 2. Hα equivalent widths for stars whose variations are considered significant.

Star name	JD	Equivalent width (Å)
HR 264 = γ Cas	2442034·582	−40·92
	34·588	−35·92
	34·592	−43·99
	34·597	−37·17
	34·654	−35·36
	34·663	−37·26
	34·665	−37·38
	35·589	−36·89
	35·596	−38·50
	35·608	−44·09
	36·604	−31·43
	36·610	−34·97
	36·614	−32·86
		Mean: −37·44 ± 2·45
HR 496 = φ Per	2442034·718	−80·44
	35·658	−56·18
	36·634	−64·40
		Mean: −67·01 ± 6·80
HR 1910 = ζ Tau	2442034·854	−28·02
	34·864	−25·62
	34·873	−25·69
	34·881	−29·95
	35·841	−25·90
	35·852	−30·37
	36·921	−31·68
	36·938	−33·70
		Mean: −28·68 ± 1·85
HR 2538 = κ CMa	2442081·560	−26·88
	81·699	−20·53
	90·583	−28·54
	90·602	−17·13
	91·561	−23·81
	91·571	−35·10
		Mean: −25·33 ± 3·90
HR 4037 = ω Car	2442081·725	− 9·11
	90·734	−12·80
	90·750	− 0·46
	91·683	−29·76
		Mean: −13·03 ± 7·18
HR 4140 = PP Car	2442080·794	−36·67
	81·748	− 8·35
	90·825	−39·01
	91·692	−30·52
	91·699	−13·50
		Mean: −25·61 ± 8·37
HR 4 621 = δ Cen	2442081·790	−36·52
	90·844	−29·65
	91·741	−25·21
		Mean: −30·46 ± 3·14

Note: All errors quoted are proble errors.

minatory factor for significant variations in equivalent width for the analysis to follow. Only those stars with deviations from the mean larger than this value were considered to actually vary in H*α* equivalent width.

4. Emission-line B stars

Of the 49 stars observed, 25 (51 per cent) showed emission of one form or another at H*α*, the profiles of these lines, of course, differing widely. Eleven stars (22 per cent of all programme stars; 44 per cent of Hα emission stars) showed emission at either λλ 5876 or 6678 of He I or both.

Equivalent widths for all those stars which showed emission at Hα were calculated. Utilizing the criterion stated previously, it was found that 7 stars (41 per cent) of the 17 which had been observed more than once showed significant variations in equivalent width. The remaining 9 stars had been observed only once, and while they showed emission, no comment can be made on any possible changes. The stars whose variations are considered to be ‘ real’ appear in Table 2.

It is interesting to compare these results with those of Bahng (1976) who observed some of the same stars with the two-channel low-resolution spectrum scanner at both KPNO and CTIO during the same month as these spectra were obtained. He found that although the resolution was too low for a line profile study, 4 of the stars (*ζ* Tauri, α Columbae, PP Carinae, and δ Centauri) showed significant variations in the total emission strength of Hα. These observations corroborate the variations found in this study for *ζ* Tauri, PP Carinae and δ Centauri, though the magnitudes of the variations are not the same in both studies. Bahng found variations of only a few per cent with time scales of 1 to 3 minutes, α Columbae was observed but twice in this study and the data seem to suggest that variations exist, though they are smaller than the adopted criterion. It is thought that the resolution and time scale differences between the two studies account for the dissimilarity in the results, with this study providing more accurate data because of its higher resolution.

For those stars that show changes in Hα equivalent width larger than the designated limit, it is certain that large profile changes occur. However, as will be seen in the following sections, small changes in equivalent widths do not preclude small changes in the profile of Hα.

5. Individual stars

HR 264 = γ Cassiopeiae = HD 5394

As one of the brightest and most active Be stars visible from the northern hemisphere, *γ* Cas has been spectroscopically followed for some years. According to Hubert-Delplace and Hubert (1979), Hα and H*β* have been observed to be in emission since 1953 with the emission reaching maximum intensity during l973-74 at which time the authors’ plate collection was obtained. Previous investigations (Kupo 1971) have found H*β* changes on time scales of approximately 10 minutes while McBeath (1974) found no changes in the equivalent width of H*α* over four nights in

1972 October. Schoembs and Spannagl (1976) found a 10 per cent decrease in the equivalent width of Hα over the period of 1973–75 which was superposed on night-to-night variations, though no variations were found over the time scales of a few hours or less. On the other hand, Slettebak and Snow (1978) have found variations to occur on time scales as short as 100 minutes. More recent observations in the ultra-violet with the IUE Satellite indicate that sometimes there are significant and spectacular changes in the profiles of C IV, N V and Si IV resonance lines. (Doazan *et al.* 1980; Henrichs, Hammerschlag-Hensberge and Lamers 1980).

A curious feature that appears on all present plates is that Hα is a single, strong emission line, asymmetric to the red (width 17·1 Å, or 780 km s^{-1}), while the helium lines at λλ 5876 and 6678 are both double emission profiles with a central absorption core. The helium lines do undergo a drastic change; for all plates leading up to JD 2442034·597, they consist of double emission lines. Both lines reverse to absorption profiles 0·057 days after this date. They return to the double emission form after another 0·009 days, accompanied by a diminution in the strength of the Hα emission. When in double emission, both helium lines had a mean width at base intensity level of 10·1 Å (514 km s^{-1}) and a peak-to-peak separation of 5·0 Å (255 km s^{-1}). The V/R ratio in both cases was 1·5.

The mean emission profile for γ Cas appears in Fig. 2 and the deviations therefrom in Fig. 3. It can be seen that on the average, deviations from the mean profile consist of an enhancement of the central portion of the emission profile during the initial part of the observing run, and a suppression during the latter part. Cowley, Rogers and Hutchings (1976) report that Hα has been subject to *V/R* variations with an average cycle of 3·4 years, beginning in 1969 and that in 1975–76 there existed strong double emission peaks for the line. This is in marked contrast to the form of the line as it exists in these 1973 data.

It is of interest that evidence was found in our study to support Hutchings (1970) previous observations of a 0·7 day variation in the line profiles, which he assumed was

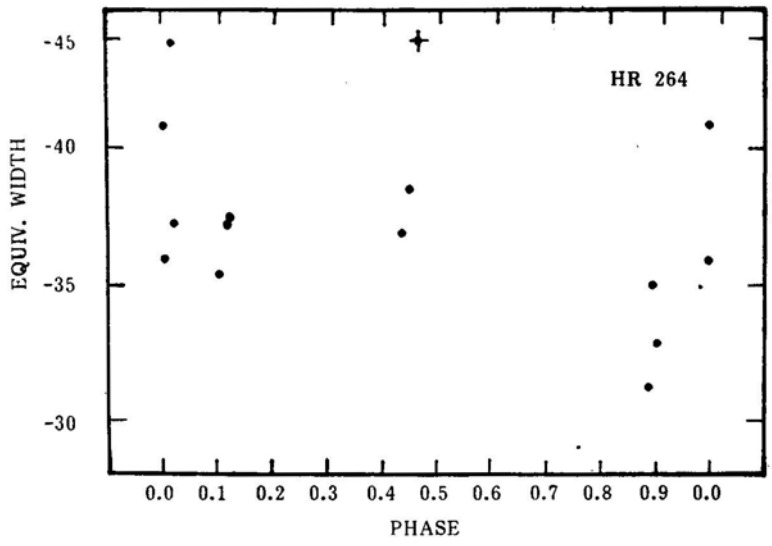

Figure 1. Variation of Hα equivalent width for γ Cas (HR 264) with a period of 0·7 days. t_0 was taken as JD 2442034·582. The cross(+) represents the sole point which does not fit the period well.

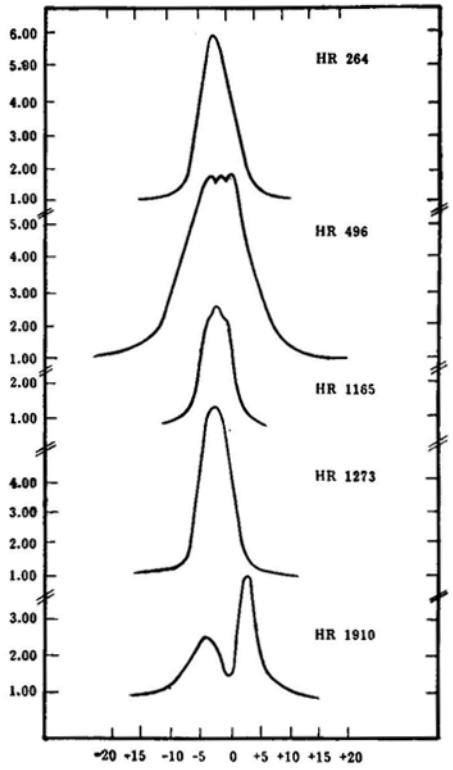

Figure 2. Mean profiles calculated for all Hα observations of γ Cas, ϕ Per , η Tau, 48 Per, and ζ Tau. The abscissa is in Å (with zero corresponding to line centre) and the ordinate is normalized intensity.

caused by inhomogeneities carried by rotation. With the exception of one value, the periodicity would seem to hold fairly well (Fig. 1).

It is possible that there also exist significant changes in the radial velocities of the helium lines. The average velocity of the Hα emission peak was + 8·3 ± 13·7 km s^{-1} (all the errors quoted henceforth are probable errors) while the average velocities for the central absorptions of the helium lines were + 29·7 ± 13·3 km s^{-1} for λ5876 and – 11·0 ± 44·15 km s^{-1} for λ6678. Velocities obtained appear in Table 3. It seems likely that these variations are real.

HR 496 = ϕ Persei = HD 10516

The width of the Hα emission is quite extraordinary, reaching nearly 35·2 Å (1610 km s^{-1}) at the beginning of the observing run and increasing to 45·3 Å (2070 km s_{-1}) at the end. There possibly exists a slight central absorption feature which would give a *V/R* value of 1·0, if real. Previous work would indicate that Hα will not develop a pronounced central absorption until phases 0·9 to 0·1 of its orbital cycle, ϕ Persei is a spectroscopic binary of period 126·696 days and the previous work of Hendry (1976) suggests that the secondary star is also an emission star. It is possible that this steady increase in the width of the Hα line is a function of the orbital motion of the system. The phase of the observations was calculated to be

Table 3. Variations in radial velocities observed in some stars.

JD	λ5876 km s^{-1}	Hα km s^{-1}	λ6678 km s^{-1}
HR 264 = γ Cas			
2442034·582	+ 37·0	− 11·5	+ 58·0
34·588	− 1·4	+ 14·9	
34·592	+ 24·8	+ 10·7	− 57·2
34·597	+ 19·5	+ 40·2	− 57·1
34·654	+ 23·3	+ 2·8	+ 50·1
34·663	+ 67·3	− 4.2	− 87·5
34·665	+ 20·8	+ 2·4	− 38·8
34·677	+ 19·0	+ 5·0	− 89·9
35·589	+ 17·2	+ 26·1	− 87·1
35·596	+ 45·8	+ 25·9	+ 55·2
35·608	+ 17·3	+ 19·2	+ 71·0
36·604	+ 66·0	+ 21·0	+ 62·5
36·614		− 44·3	
HR 3165 = ζ Pup			
2442081·559	− 46·8		+ 135·7
81·568	− 49·3	+ 60·3	+ 231·7
81·646			+ 64·9
81·713	− 65·4	+ 81·3	+ 171·2
91·638	+ 64·9	− 45·5	+ 226·3
HR 4140 = PP Car			
2442080·794		+ 15·6	
81·748		+ 25·2	
90·755		− 14·1	
91·692		− 13·8	
91·699		+ 22·1	

0·659 which is consistent with the idea that two superposed emission lines are separating in wavelength. Also in agreement with this hypothesis is the drop in intensity from the first observation to the last.

The mean emission profile of Hα for ϕ Per appears in Fig. 2 and the deviations from the mean in Fig. 3. As can be seen, the red edge of the profile is observed to be symmetrically depressed while the blue edge becomes enhanced. This is in agreement with the hypothesis that the stronger emission contribution of the primary is emerging to the blue, as is consistent with the observed radial velocity curve (Hendry 1976) for the primary star. The fainter Hα emission component of the secondary star causes a reduction of intensity on the red edge.

The average radial velocity of the central point of the Hα line is — 27·3 ±1·0km s^{-1}. This is consistent with past work that suggests that Hα does not share the systemic velocity of 0·0 km s^{-1} but instead hovers at velocity values of about — 20 km s^{-1} throughout the entire orbital cycle. Insofar as the Hα line is concerned, it seems likely that the profile and intensity changes simply reflect the changing orbital aspects of the two emission-line stars.

Both helium λλ 5876 and 6678 line profiles are of double emission, central absorption form. The central absorption falls below the continuum in both cases. The *V/R* ratio is consistent for both lines and has an average value of 0·93. Peak-to-peak separation for λ6678 is 7·6 Å (340 km s^{-1}) and the width is 12·6 Å (565 km s^{-1}). For λ5876 these values are 4·5 Å (230 km s1) and 10·1 Å (513 km s^{-1}) respectively.

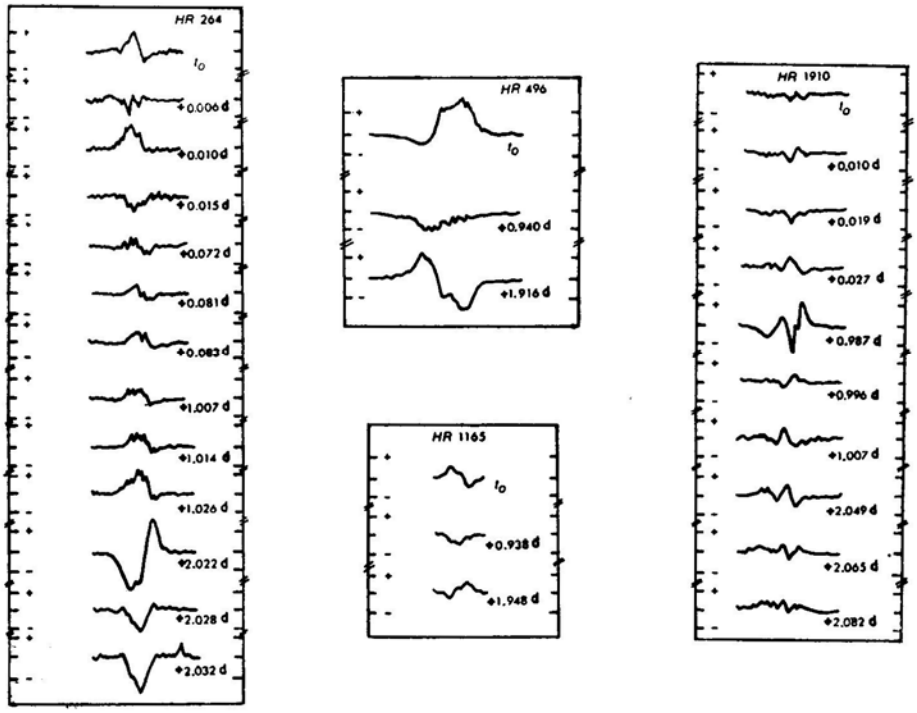

Figure 3. Deviations from mean profile for γ Cas, ϕ Per, η Tau, ζ Tau. The units of the Ordinate are + and – one intensity unit. The abscissa is in Å. t_0 corresponds in each case to the first plate obtained.

HR 1165 = η Tauri = HR 23630

Hubert-Delplace and Hubert (1979) have stated that this star did not exhibit any noticeable changes in emission at Hα during the period 1953-76, with the line being always a narrow emission of moderate intensity. This is confirmed by our observations (Fig. 2 and 3) which show little deviation from the mean profile. The mean width of the emission is 9·5 Å (434 km s^{-1}).

HR 1273 = 48 Persei = HD 25940

The only reported spectrum change for this star is a slight strengthening in emission observed to take place in 1963–68 by Hubert-Delplace and Hubert (1979). Bahng (1976) reported marginal changes in the Hα emission line which is quite quiescent (see Fig. 2) in profile in our observations, having a mean width of 12·5 Å (571 km s^{-1}).

HR 1903 = ε Orionis = HD 37128

Though only one plate was obtained of this B0 Ia star (Fig. 8), it is sufficient to show that Hα has a faint P Cygni profile, as is common with these stars. However, there exist slight changes from the Hα profile observed in 1970 November by

Rosendhal (1973), most notably the small emission component in the blue wing of the profile is absent.

HR 1910 = ζ Tauri = HD 37202

ζ Tauri has been extensively observed for decades and has been previously shown to exhibit variations in Hα emission strength. Bahng (1971) has reported extremely rapid equivalent width changes over the time scale of about 10 minutes at Hβ and Hγ. As previously mentioned, his (Bahng 1976) photoelectric observations of this star during a single observing season showed significant variations in the total Hα emission line strength, as well as a progressive increase in the emission strength over the 4 nights. It is unlikely that these changes are related to the binary motion (ζ Tau is a spectroscopic binary of period 132·91 days, according to Hynek and Struve, 1942) or to motions of the shell (Delplace 1970) but instead to smaller, more localized features. It should be mentioned that Hubert-Delplace and Hubert (1979) noted that ζ Tau reached a maximum of emission in 1973 when these observations were made.

Curiously, the Hα profile in this study was observed to be rather quiescent. The profile consisted of a markedly asymmetric double emission line with *V/R* = 1·8. Its average width was 25·2 Å (1150 km s^{-1}). Observations of Gray and Marlborough (1974) made in January 1972 on the other hand, show a substantially weaker total emission and rather symmetrical profile with *V/R* approximately 1.1. Possibly there exists a slight increase in equivalent width from the beginning to the end of the observing run.

The mean profile can be seen in Fig. 2 and the graphical depiction of the time-dependent changes from mean profile in Fig. 3. As can be seen, initial suppression of the two emission peaks gives way to an enhancement and an increase in the central absorption depth. This situation is reversed by the end of the sequence of plates.

From this small collection of data, a case can probably be made for a 0·2 day periodicity in Hα equivalent width. However, a much longer run of observations would be necessary to confirm this.

The radial velocities of the visible lines are generally disparate. The sharp, strong circumstellar D lines of Na I have an average velocity of — 25·2 ± 0·8 km s^{-1} and the quite sharp and deep helium lines are in substantial agreement, with a mean velocity of — 25·9 ± 3·8 km s^{-1}. On the other hand, the velocity of the Hα central absorption feature is +13·6 ± 2·9 km s^{-1}. Clearly, the velocity system of the helium and D lines is quite different from that of the Hα producing region, with the helium and sodium absorptions both being circumstellar in origin. Their velocities fall outside the range of velocities allowed by the observed binary motion of the ζ Tauri system.

HR 1956 = α Columbae = HD 37795

This binary star showed minor changes in Hα emission line profiles. This is in keeping with the previously mentioned photoelectric work reported by Bahng (1976) during the same observing season; The present work shows that the emission strength decreases and the central absorption feature Becomes more pronounced over a period of 0·995 days.

The average radial velocity of the emission peak is + 46·1 ± 0·7 km s^{-1} and probably does not change over the series of observations. The helium lines are essentially filled in and do not change; their radial velocities average to + 42·3 ± 28·8 km s^{-1}, which is in good agreement with the Hα emission line; however, due to their very faint nature, not much confidence should be placed in this measurement.

HR 2343 = ν Geminorum = HD 45542

McLaughlin (1932) initially reported this star to have emission confined to Hα and H*β*, with no changes of *V/R* or *E/C* occurring in the period from 1915 to 1931. More recently, Hubert-Delplace and Hubert (1979) observed that a little change had taken place in the emission strengths from 1955 to 1975, with a slight minimum in emission strength possibly taking place in 1971–72. No change was observed by Bahng (1976). Only one observation was obtained of this star and Hα shows a moderately strong emission profile (See Fig. 8), centrally bisected by a deep absorption, giving a *V/R* ratio of 1·0. The emission width is 12 Å (548 km s^{-1}).

HR 2536 = β^1 Monocerotis = HD 45725

Cowley and Gugula (1973) showed that β^1 Monocerotis undergoes a semi-periodic variation of *V/R* and radial velocity shift over an approximate period of 12·5 years. Hubert-Delplace and Hubert (1979) stated that the emission lines and shell components of the spectrum were depressed during the time it was under observation by the authors. The sole spectrum (Fig. 8) obtained by us showed a strong double emission line with *V/R* = 0·98, and an emission width of 18 Å (822 km s^{-1}).

HR 2538 = κ Canis Majoris = HD 50013

The unusual behaviour of the Hα line and the helium lines in this star's spectrum during this observing run has already been reported by Bahng and Hendry (1975). Bahng (1976) found only marginal Hα equivalent width changes at this time. Both λ5876 and λ6678 are in emission (at approximately the same intensity) with two components and no discernible central absorption in between. The Hα profile is observed to undergo radical changes during the time periods of fractions of a day, as can be seen in Fig. 4. Suppression of the emission line as a whole as well as variability of the central absorption is noted to occur.

The Hα absorption core has a velocity of + 15 ± 3 km s^{-1}, which is in good agreement with the previously published photospheric velocities (+ 14 km s^{-1}, Wilson 1953) as well as with the midpoints of the *V* and *R* components of Hα (+ 11 ± 5 km s^{-1}) and the helium lines (+ 9 ± 8 km s^{-1}).

Curiously, the width of the Hα emission line is about 400 km s^{-1}, which is nearly the same as the separation of the helium *V* and *R* components. Clearly, the helium emission is taking place in a region close to the star and does not produce appreciable absorption, while the hydrogen emission is derived from the entire circumstellar disk or ring.

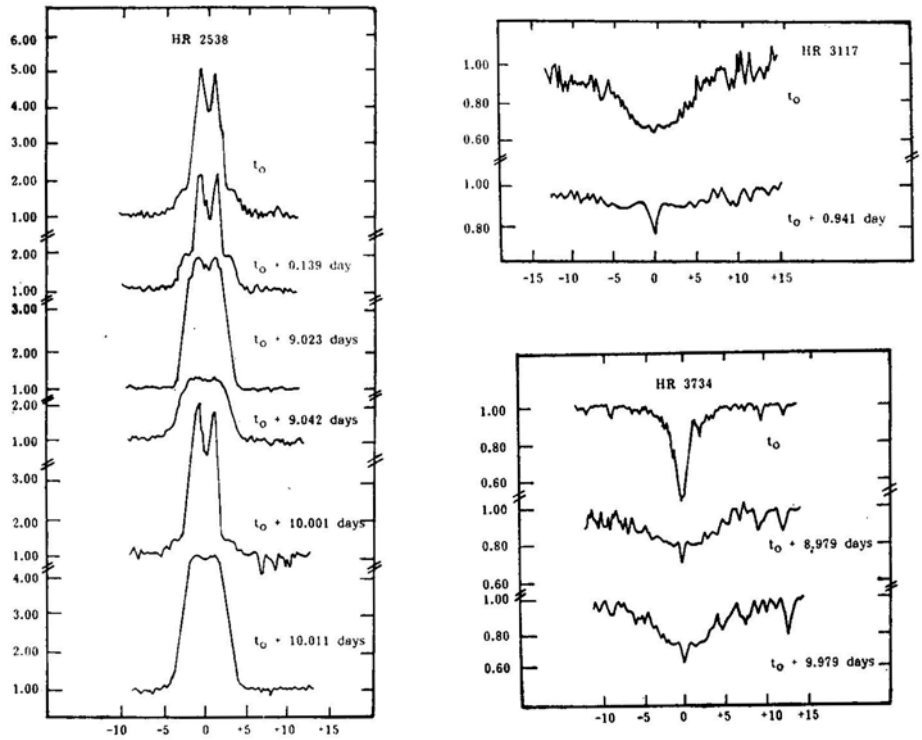

Figure 4. Hα profiles of κ CMa, χ Car and κ Vel. The abscissa is in Å and the ordinate in intensity units, with zero on the abscissa corresponding to line centre. The values of t_0 are JD 2442081·560 (κ CMa), JD 2442090·685(χ Car) and JD 2442081·678(κ V el).

HR 2781 = UW Canis Majoris = HD 57060

This massive, short period (P = 4·39341 days) binary system is thought to contain an O7f primary star and an OB secondary whose contribution to the spectrum has never been conclusively proved (Struve *et al.* 1958a). In another paper, Struve *et al.* (1958b) suggest that perhaps Hα consists of a P Cygni profile associated with the brighter star in addition to a broad, stationary emission line. They also observed dramatic spectrum changes in the regions of the helium lines, with λ5876 very conspicuous when the fainter star is approaching while barely visible with a faint, broad emission on the red side when the fainter star is receding.

Though only one plate of this interesting system was usable in the Hα region, it was sufficient to show a very unusual Hα profile (see Fig. 8). The width of the feature is 23·6 Å (1079 km s^{-1}) and a V/R ratio of 1·03. The helium lines change greatly in form. Initially (JD 2442090·635), λ6678 is filled-in while λ5876 is a deep, wide absorption feature which is either double in character or has a central single emission in the core. Struve *et al.* (1958b) have noted this line to be occasionally double. On JD 2442091·602 (the same plate from which the Hα profile is shown in Fig. 8), λ6678 remains filled-in but λ5876 has become a faint double emission line with V/R = 1 and a width of 5·4 Å (277 km s^{-1}).

The helium velocities undergo great changes beginning at — 218·2 ± 24·8 km s^{-1} and ending at — 133·4 ± 14·6. The Hα central absorption velocity is + 142·1, with the violet peak at — 162·5 and the red peak at + 364·6 km s^{-1}. The D lines of Na I exhibit a constant velocity of + 38·1 ± 1·8 km s^{-1} and are undoubtedly interstellar in origin. The observations reported upon occur at phases 0·188 for the earlier plate and 0·409 for the later one.

HR 3177 = χ Carinae = HD 65575

This star is not listed in Wackerling's (1970) catalogue as having undergone an emission episode. However, Fig. 4 shows that during this period of observation, the Hα line began to develop a dark core on an emission line, superimposed on a photospheric absorption line. The emission strengthened considerably in a period of 0·941 day. The helium lines too undergo some changes. On JD 2442090·685, both λλ5876 and 6678 are deep absorptions. 0·941 day later, λ6678 remains a deep absorption while λ5876 has become completely filled in.

The radial velocity of Hα is considered to be constant between the two plates at + 28·1 ± 7·1 km s^{-1}. Helium, on the other hand, gives values of + 22·4 ± 6·0 and + 34·5 ± 3·2 km s^{-1}, this would seem to indicate a slight change.

HR 3165 = ζ Puppis = HD 66811

This oft-studied star has proved to be very interesting in the ultraviolet region of the spectrum, showing P Cygni profiles at N V, C IV, and N IV. An extreme Of star (O4f or earlier according to Heap, 1972), it was first thought that the spectroscopic companion was a WN star, though this has now been discounted from infrared observations (Barnes, Lambert and Potter 1974). It has a previous history of short-term changes in line profiles, with Brucato (1971) having observed large scale variations in λ4686 of He II over time scales as short as ten minutes. The form of the Hα emission has been observed to be a faint double emission (asymmetrically formed) with a variable central absorption (Baschek and Scholz, 1971) and Conti and Niemela (1976) report that 1974-76 brought about a substantial change in the emission profile : a decrease in emission due to a decrease in the density of the envelope and the mass loss rate.

The present observations show a reasonable amount of activity at Hα (Fig. 5). Initially the line is of the double emission-central absorption form (V/R = 1) with a width of 9·1 Å (415 km s^{-1}), while both helium lines were filled in. 0·009 day later, the hydrogen lines were filled-in to the continuum, λ6678 was also filled-in and λ5876 barely visible. After nearly two hours, Hα showed a complex absorption profile while both helium lines were filled-in. 9·093 days from the initial observation, Hα took the form of a P Cygni profile, with λ6678 filled-in and λ5876 in slight absorption. Finally, after another 0·986 days, Hα became a sharp, slight absorption and both the helium lines were filled-in to the continuum.

As might be expected, there also exist changes in the radial velocities. Their values appear in Table 3. It is not known how significant the helium line measurements are since the lines are generally almost totally filled-in.

HR 3734= κ Velorum = HD 81188

This star is not listed in Wackerling's catalogue as having shown emission in the past years. Being a binary of period 116·65 days (Curtis 1907), it is possible that some of the observed changes are correlated with changing orbital phase. Only slight changes in the absorption profile can be seen in Fig. 4. Initially a normal absorption profile develops a perturbing emission with absoprtion core in the span of 8·979 days and one day later, this additional feature becomes slightly more pronounced. Minor changes were observed in the profiles of the helium lines, both becoming sharper and deeper at the end of the three-plate sequence.

HR 4037 = ω Carinae = HD 89080

Previous observations of this star by Bahng (1976) did not show any significant variations in Hα equivalent width. However, we find the line to be particularly active in both equivalent width and line profile (see Fig. 5). Initially, on JD 2442081·725, Hα was seen in double emission with *V*/*R*=0·94 and a width of 10·1 Å (463 km s^{-1}). After 9·009 days, the emission became stronger while maintaining the same *V*/*R* ratio. After another 0·016 days, the emission subsided dramatically and the *V*/*R* ratio became 1·0, while the width decreased to 16·3 Å (745 km S^{-1}). After another 0·933 days, the situation changed completely with Hα becoming a very strong single emission line with a slight asymmetry or possible central absorption beginning at the peak. The width of the line was 13· 8 Å (629 km s^{-1}).

HR 4140 = PP Carinae = HD 91465

This star has been observed by Bahng (1976) to undergo significant changes at Hα during the observing season of 1974, and this is corroborated by the present work

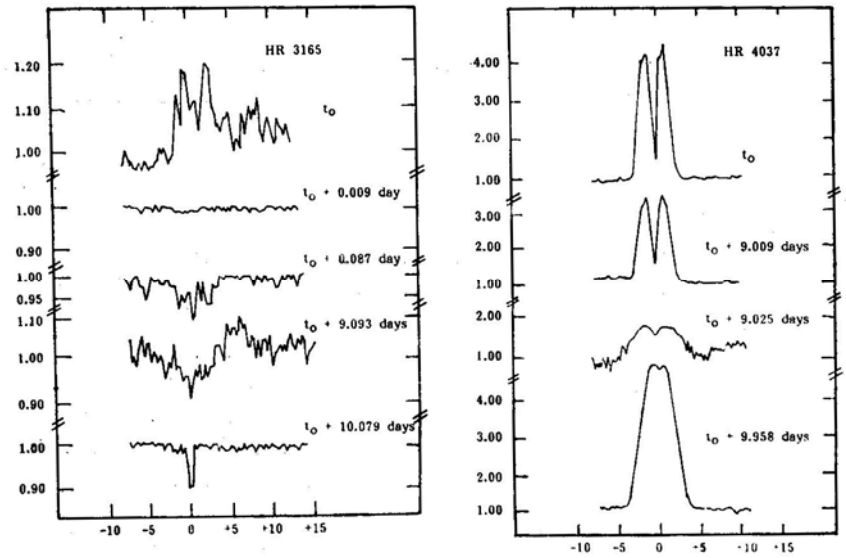

Figure 5. Ha profiles for ζ Pup and ω Car. The ordinate and abscissa are as in Fig. 4. The values of t_0 are JD 2442081.559 (ζ Pup) and JD 2442081.25 (ω Car).

(see Fig. 6). According to the General Catalogue of Variable Stars (Kukarkin *et al.* 1969), PP Carinae is an irregular variable of early spectral class.

On JD 2442080·794, Hα appeared as a single strong emission of width 25·4 Å (1158 km s^{-1}) while He I λλ5876 and 6678 were completely filled-in. 0·954 days later, the Hα emission changed into a very complex, wide feature (width= 39·9 Å, 1820 km s^{-1}). λ5876 remained filled-in but λ6678 became a very strong, narrow emission (width = 3·6 Å, 162 km s^{-1}). On JD 2442090·825, Hα became a very strong, narrow emission on broad shoulders of width 19·9 Å (910 km s^{-1}). Finally, on JD 2442091·699, Hα took the form of a double emission with V/R=1·0 and a width of 9·1 Å (414 km s^{-1}). Helium remained filled-in. It is likely that the blue edge of the Hα emission line might correspond to the high stellar wind velocities, 7201025 km s^{-1} obtained by Dachs (1980) from C IV and Si IV resonance lines.

HR 4621 = δ Centauri = HD 105435

Bahng (1976) found this star to have significant variations at Hα which is substantiated by Fig. 6. On JD 2442081·790, Hα is a wide single emission (width = 23·5 Å, 1076 km s^{-1}). This changes (on JD 2442090·844 and on 91·741) to a very strong narrow emission on broad shoulders (13·8 Å, 630 km s^{-1}). 0 · 006 days later, Hα has returned to a single wide emission (width =29·0 Å, 1324 km s^{-1}) while λλ5876 and 6678 which were filled-in so far change to wide faint absorptions.

The radial velocity of the Hα line has a mean value of — 21·3 ± 8·7 km s^{-1} which is at odds with the published velocities of the star at +9·5 and + 20·0 km s^{-1} (Abt and Biggs 1972).

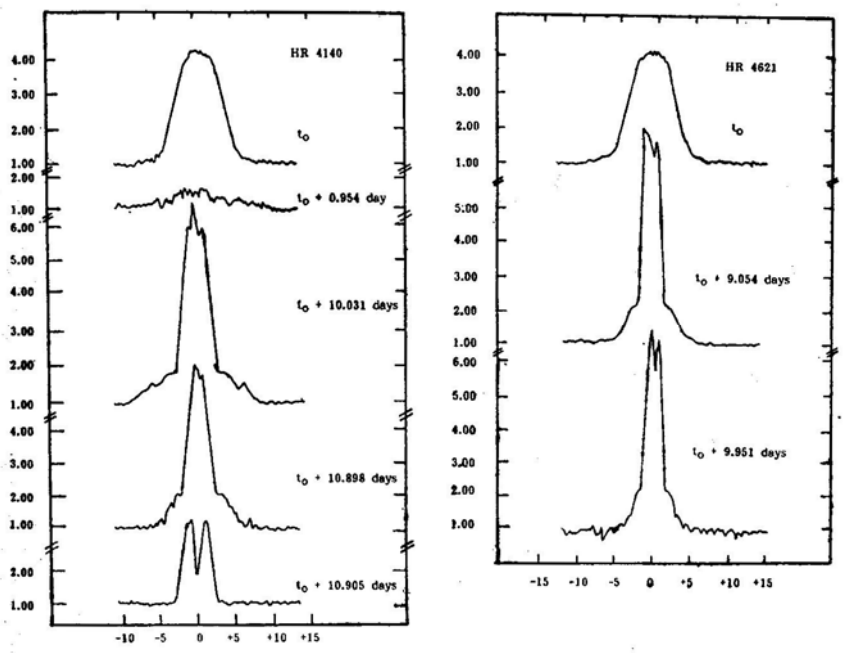

Figure 6. Hα profiles for PP Car and δ Cen. The ordinate and abscissa are as in Fig. 4. The values of t_0 are JD 2442080·794 (PP Car) and JD 2442081·790 (δ Cen).

HR 4773 = γ Muscae = HD 109026

One observation of this star was made (Fig. 8) which is sufficient only to show that the form of the Hα line is that of a photospheric absorption line nearly filled-in by double emission (*V/R* = 1) and central absorption. No previous emission episodes have been noted.

HR 4787 = κ Draconis = HD 109387

Hubert-Delplace and Hubert (1979) state that sharp, dark cores were seen as shell components on the hydrogen emission lines in 1973, when the single plate in this collection was obtained and that the cores seem to change very quickly within several days. The core of Hα appears very weak in our plate (Fig. 8) and a *V/R* = 1·08 is observed. The width of the line is 15 Å (685 km s^{-1}).

HR 4844 = β Muscae = HD 110879

It does not appear that *β* Muscae has undergone any previous emission episodes. On JD 2442081·878, Hα appears as a normal, wide absorption feature, while λ6678 was distorted and filled in with a possible double emission. λ5876 appeared normal. 9·622 days later, Hα was filled with emission to the continuum as was λ5876. λ6678 became a wide, deep absorption feature.

Radial velocities of the hydrogen and helium lines appear disparate, with the mean velocity of hydrogen being + 19·8 ± 5·5 km s^{-1} and of helium being + 58·7 ± 4.3 km s^{-1}.

HR 5132 = ϵ Centauri = HD 118716

This star does not appear to have undergone any previous emission episodes. Bahng (1976) found no Hα equivalent width changes. On JD 2442081·861, Hα appears as a very weak double emission with a pronounced central absorption (Fig. 7). The *V/R* ratio is 1·0. λ5876 is filled-in to the continuum and λ6678 possesses a wide, faint, unusual dish-like profile. 9·981 days later, the central absorption of Hα has become very faint and λ5876 has gained a faint double emission with *V/R* = 1. The mean radial velocity for Hα is — 0·1 ± 1·3 km s^{-1}.

HR 5190 = ν Centauri = HD 120307

The single plate (Fig. 8) of this star shows a filled-in Hα profile with double emission *(V/R* = 1) and a pronounced central absorption. There was an extreme disparity between the velocity measurements of this well-defined central absorption (—19·6 km s^{-1}) and λ5876 (+122·5 km s^{-1}). The Hα velocity is consistent with the velocities predicted by the orbital solution of Rajamohan (1977), who also speculates that the primary is a *β* Cephei type variable star. The high helium line velocity remains anomalous.

HR 5193 = μ Centauri = HD 120324

This star has undergone phases of strong Balmer line emission (1904,1923-31, 1940, 1953,1962, and 1967) and was found to be in a phase of declining emission by Peters (1979) during the period in which our spectra were obtained. The object is a pole-on Be star.

The profile of Hα line changed little during our observations, but its intensity varied moderately (Fig. 7). The width of this feature remained nearly constant at 8·3 Å (381 km s^{-1}). Over 0·018 days, the helium lines change from wide, near-continuum intensity features, to deep, distorted profiles. The radial velocities of hydrogen and helium would also appear to be different. The mean radial velocity for Hα is observed to be + 5·8 ± 5·6 km s^{-1}, while that of helium is + 47·8 ± 10·7.

HR 5440 = η Centauri = HD 127972

Our single observation shows a faint double emission-central absorption profile (Fig. 8). The Hα line has not changed significantly since the data obtained by Plavec (1976), though the magnitude of the double emission may have diminished slightly.

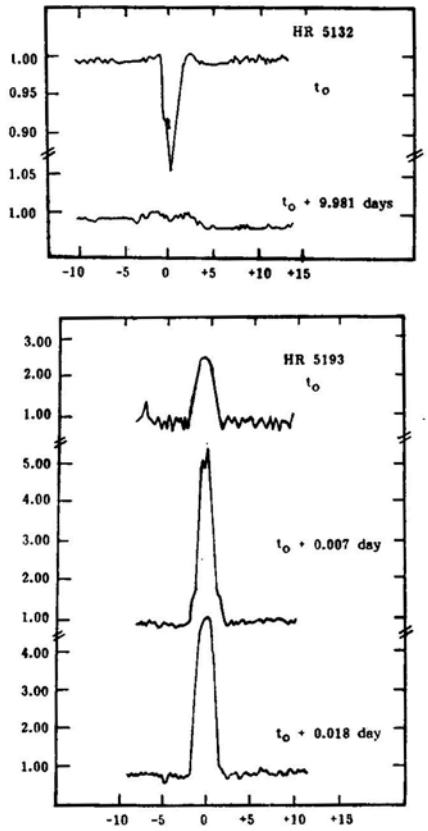

Figure 7. Hα profiles for ϵ Cen and μ Cen. The ordinate and abscissa are as in Fig. 4. t_0 for ϵ Cen corresponds to JD 2442081·861; for μ Cen, it is JD 2442091·867.

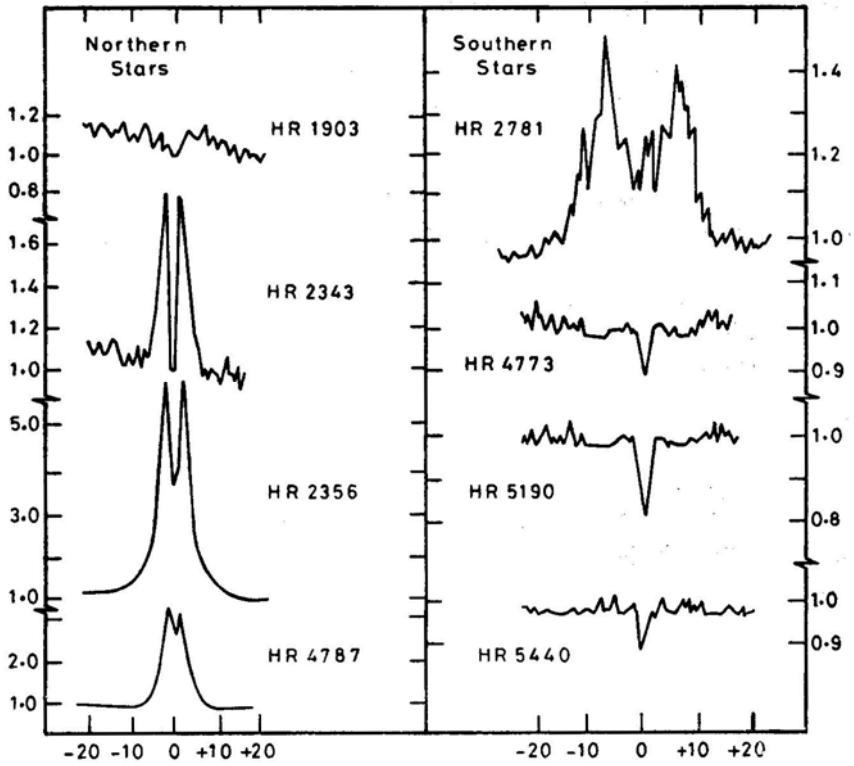

Figure 8. Hα profiles for stars which were observed only once but showed emission of some sort. The abscissae and ordinates are as in Fig. 4.

4. Conclusions

It can be seen from this study that some of those B stars which show emission at Hα line are extremely likely to be variable at that line (and also possibly at the helium lines) on time scales as short as fraction of a day.

Those stars for which changes in line profiles are demonstrated here would seem to be excellent choices for further work at high resolution (both temporal and spectral).

References

Abt, H. A., Biggs, E. S. 1972, *Bibliography of Stellar Radial Velocities,* Kitt Peak National Observatory, New York.

Bahng, J. D. R. 1971, *Astrophys. J.*, **167**, L75.

Baling, J. D. R. 1975a, *Mon. Not. R. astr. Soc,* **170**, 611.

Bahng, J. D. R. 1975b, *Astrophys. J.*, **200**,128.

Bahng, J. D. R. 1976, in *IAU Symp. 70: Be and Shell Stars,* Ed. A. Slettebak, D. Reidel, Dordrecht, p. 41.

Bahng, J. D. R., Hendry, E. 1975, *Publ astr. Soc. Pacific,* **87**,137.

Barnes, T. G., Lambert, D. L., Potter, A. E. 1974, *Astrophys. J.*, **187**, 73.

Baschek, B. Scholz, M. 1971, *Astr. Astrophys.*, **15**, 285.

Brucato, R.J. 1971, *Ph D thesis*, Northwestern University, Evanston.

Buscombe, W. 1967, *Inf. Bull. Sth. Hem.*, **11**, 29.
Conti, P. S., Niemela, V. S. 1976, *Astrophys. J.*, **209,** L37.
Cowley, A., Gugula, E. 1973, *Astr. Astrophys.*, **22,** 203.
Cowley, A. P., Rogers, L., Hutchings, J. B. 1976, *Publ. astr. Soc. Pacific*, **88,** 911.
Curtis, H. D. 1907, *Lick Obs. Bull.*, 4, 153.
Dachs, J.1980, in *Proc. Second European IUE Conf.*, ESA, Paris, p.139.
Delplace, A.-M.1970, *Astr. Astrophys.*, **7,** 459.
Doazan, V., Selvelli, P., Stalio, R., Thomas, R. N. 1980, in *Proc. Second European IUE Conf.,* ESA, Paris, p. 145.
Gray, D. F., Marlborough, J. M. 1974, *Astrophys. J. Suppl. Ser.*, **27,** 121.
Heap, S. R. 1972, *Astrophys. Lett.*, **10,** 49.
Hendry, E. M. 1976, in *IAU Symp. 70: Be and Shell Stars*, Ed.. A. Slettebak, D. Reidel, Dordrecht, p. 429.
Henrichs, H. F., Hammerschlag-Hensberge, G., Lamers, H. J. G. L. M. 1980, in *Proc. Second European IAE Conf.,* ESA, Paris, p. 147.
Hoffleit, D. 1964, *Catalogue of Bright Stars*, Yale University Observatory, New Haven.
Hubert-Deplace, A.-M., Hubert, H. 1979, *An Atlas of Be Stars*, Meudon Obs., Paris.
Hutchings, J. B. 1967, *Observatory*, **87,** 289.
Hutchings, J. B. 1970, *Mon. Not. R. astr. Soc*, **150,** 55.
Hynek, J. A., Struve, O. 1942, *Astrophys. J.*, **96**, 425.
Kukarkin, B. V., Kholopov, P. N., Efremov, Yu. N., Kukarkina, N. P., Kurochkin, N. E., Medvedeva, G. I., Perova, N. B., Fedorovich, V. P., Frolov, M. S. 1969, *General Catalogue of Variable Stars,* Astronomical Council of the Academy of Sciences, Moscow.
Kupo, I. D. 1971, *Trudy Astrofiz. Inst. Alma-Ata,* **16**, 65.
McBeath, K. R. 1974, *Ph D thesis*, Northwestern University, Evanston.
McLaughlin, D. B. 1932, *Publ. Obs. Univ. Michigan*, **4,**175.
Peters, G. J. 1979, *Astrophys. J. Suppl. Ser.*, **39,** 175.
Plavec, M. 1976, in *IAU Symp.* 70*: Be and Shell Stars,* Ed. A. Slettebak, D. Reidel, Dordrecht, p. 2.
Rajamohan, R. 1977, *Kodaikanal Obs. Bull. Ser. A,* **2***,* 6.
Rosendhal, J. D. 1973, *Astrophys. J.*, **186**, 909.
Sanyal, A. 1974, *Bull. Am. astr. Soc.*, **6,** 460.
Schoembs, R., Spannagl, Chr. 1976, *Astr. Astrophys. Suppl. Ser.*, **26,** 55.
Slettebak, A., Snow, T. P. 1978, *Astrophys. J.*, **224,** L127.
Struve, O., Sahade, J., Zebergs, V., Lynds, B. T. 1958a, *Publ. astr. Soc. Pacific,* **70,** 267.
Struve, O., Sahade, J., Huang, S.-S., Zebergs, V. 1958b, *Astrophys. J.*, **128,** 328.
Uesugi, A., Fukuda, I. 1970, *Contr. Inst. Astrophys. Kwasan Obs.*, Univ. Kyoto, No. 189.
Wackerling, L. R. 1970, *Mem. R. astr. Soc*., **73,**153.
Wilson, R. E. 1953, *General Catalogue of Stellar Radial Velocities,* Carnegie Institution of Washington.

J. Astrophys. Astr. (1981) **2,** 161–164

Anomalous Giants in Magellanic Cloud Clusters

P. W. Hodge* *Astronomy Department, University of Washington, Seattle, Washington 98195, USA*

Received 1981 February 12; accepted. 1981 March 1

Abstract. Many of the populous intermediate-age star clusters (the *blue globulars)* of the Magellanic Clouds have a few stars that occupy a 'forbidden zone' in the colour-magnitude diagrams of the clusters, where stellar evolutionary theory does not predict that stars should lie. The properties of these stars in 13 clusters are gathered in Table 1, where it can be seen that the absolute magnitudes of the stars correlate with the cluster age, lying at a mean value of 2·7 mag above the tip of the main sequence. Several hypotheses regarding their nature are discussed, and it is concluded tentatively that they represent an unpredicted advanced stage of evolution from the giant branch, though no theoretical evidence supports such a conclusion. Considerably more observational data are needed before a more positive statement can be made.

Key words: anomalous giants—blue globular clusters—Magellanic Clouds

1. Introduction

It has been pointed out (Flower and Hodge 1975; Flower *et al.* 1980) that some of the very populous star clusters of the Magellanic Clouds (MC), the *blue globular clusters,* contain stars that occupy an unexpected position in the cluster colour-magnitude diagrams. These stars are called here 'anomalous giants'. They are both conspicuous and unaccounted for. Theoretical evolutionary tracks do not predict that there should be such bright intermediate-colour giants in the clusters' colour-magnitude (CM) diagrams, which otherwise fit theoretical tracks quite well (see summaries by Gascoigne 1980 and Hodge 1981a).

The stars in question are generally located near the centres of the clusters and are unmeasurable (and often undetectable) on the usual plates taken for the purpose of

*Visiting Astronomer, Cerro Tololo Inter-American Observatory, which is supported by the National Science Foundation under contract No. AST 78-27879.

constructing a CM diagram, as the clusters are so populous that the cores are normally burnt out except on very short exposures. In our investigations, we have generally used several very lightly exposed plates (*e.g.* 30 s to 120 s exposures with the CTIO 4-m telescope), which are needed to reveal the bright stars in the cores of the cluster and to measure them. This paper presents a preliminary survey of the properties of these stars in a number of MC clusters. A detailed optical and theoretical examination of their nature is being carried out by others (Olszewski 1980, personal communication; Flower 1980).

2. Data

Very short exposure plates of 13 rich star clusters in the Magellanic Clouds have been taken with the CTIO 4-m telescope. Plates were taken in *B* (IIa O plus a GG 385 filter) and *V* (IIa D plus a GG 495 filter) and exposures ranged from 30 seconds to 2 minutes. For most clusters a photoelectric sequence was available adjacent to the cluster. The plates were examined for the presence of intermediate-colour bright stars of the type reported previously (Flower and Hodge 1975; Flower *et al.* 1980). Their magnitudes and (*B—V*) colours were determined by either astrophotometry (when the background on the plates allowed) or by eye estimates. Stars were considered to be candidates for the anomalous giant class when they were among the cluster's brightest stars and when their colours were >0·5 mag bluer than the (usually extrapolated) giant branch at that magnitude and redder than $B–V \simeq +0{\cdot}2$. In order to avoid galactic foreground stars, which are common in this colour and magnitude range, only stars in the central core of the clusters were chosen and counts of similar stars were made in the adjacent field to determine the reliability of membership.

Table 1 lists the mean M_V magnitudes for the stars chosen by these criteria. Also listed in Table 1 are the M_V magnitudes of the tip of the main sequence for the clusters. These are taken from the published CM diagrams, or are read off from preliminary CM diagrams that are presently being constructed. Identification charts are published or will be published in the references cited.

3. Discussion

Two important conclusions can be made from the data of Table 1. First, the anomalous giants are rather common in the rich intermediate-age clusters tested. Second, there is a clear correlation of the *V* magnitudes of the forbidden giants with that of the tip of the main sequence, and thus the age, of a cluster (Fig. 1). The giants lie on an average of $2{\cdot}7 \pm 0{\cdot}4$ mag (s.e.) above the main sequence.

Although it appears obvious from both the photographs and the discovered correlation that at least most of the chosen stars are members of the clusters, it is important to have some more quantitative assurance of this fact. A statistical argument, although subject to the usual concerns about *post hoc* selection of criteria, can be made from the counts of intermediate-colour stars in the LMC foreground. The cluster diameters average ~1·5 arcmin. From the field CM diagrams given by Arp (1958 a, b, c, 1959a, b), Brück and Marsöglu (1978), Westerlund (1961b) and Hodge (1981b),

Table 1. Properties of the clusters and stars.

NGC	M_V^* (MS Tip)	$\overline{M}_V$ (Anomalous Giants)	ΔM_V	Number of Anomalous Giants
152	+0·8	−2·0	2·8	2
1831	−1·0	−3·6	2·6	4
1854	−4·5			0
1856	−1·7	−4·0	2·3	1
1868	+0·2	−2·4	2·6	10
1872	+1·0	−2·5	3·5	2:
2121	+1·0			0
2133	−1·0	−3·8	2·8	2
2134	−1·0	−4·1	3·1	3
2156	−3·0	−5·3	2·3	1
2159	−3·0	−5·6	2·6	1
2164	−3·0	−5·6	2·6	4
2172	−3·0	−5·4	2·4	1
Mean			2·7±0·4	2

*We adopt the distance moduli of Sandage and Tammann (1974).

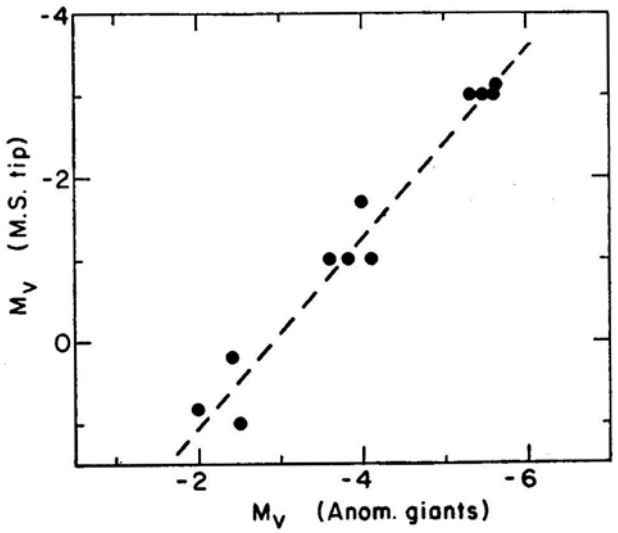

Figure 1. The relationship between the mean magnitude of the forbidden giants in a cluster and the magnitude of the tip of the main sequence in that cluster.

it is possible to estimate the expected number of candidate stars in the SMC field. Restricting attention to the colour range defined above and the magnitude range with $V < 15$, we find the expected number of candidates to be ~ 0·05 per cluster. Similarly, published CM diagrams for field stars in the LMC (Westerlund 1961a; Hodge 1965) can be used for that galaxy, and these indicate approximately 0·1 stars per cluster. The number for each Cloud is surprisingly insensitive to position in the Cloud, probably because most field stars of this colour are in the Galactic foreground. This test, though statistically very crude, clearly indicates that all or almost all of the stars in question are members of the clusters.

Several different explanations have been proposed for these stars (Flower *et al.* 1980), but only three can be considered reasonable in view of the present data; they might be multiple stars such as are found in the centre of 30 Doradus, they might be coalesced double stars whose temperatures and luminosity reflect a recent violent mixing process (Flower 1980), or they might be some late stage of stellar evolution (*e.g.* a pre-planetary nebula stage) that is not predicted by stellar evolutionary models but which occupies a significant interval in the lifetime of a star. The correlation shown in Fig. 1 seems to indicate a preference for the third hypothesis, but the data and the crudeness of the hypotheses together do not really allow a choice. Detailed spectroscopic studies such as those being carried out by Olszewski (1980, personal communication) and his colleagues may eventually solve the problem.

Acknowledgements

I am grateful to Ed Olszewski and Phillip Flower for many helpful discussions, to the Cerro Tololo Inter-American Observatory for making my observing runs there very efficient and profitable, and to the National Science Foundation for financial support under grant AST 9515148.

References

Arp, H. C. 1958a, *Astr. J.*, **63,** 118.
Arp, H. C. 1958b, *Astr. J.,* **63,** 273.
Arp, H. C. 1958c, *Astr. J.,* **63,** 487.
Arp, H. C. 1959a, *Astr. J.,* **64,** 175.
Arp, H. C. 1959b, *Astr. J.*, **64,** 254.
Brück, M. T., Marsöglu, A. 1978, *Astr. Astrophys.,* **68,** 193.
Flower, P. J. 1980, *Preprint.*
Flower, P. J., Geisler, D., Hodge, P. W., Olszewski, E. W., 1980, *Astrophys. J.*, **235,** 769.
Flower, P. J., Hodge, P. W. 1975, *Astrophys .J.,* **196,** 369.
Gascoigne, S. C. B. 1980, in *IAU Symp. 85: Star Clusters,* Ed. J. E. Hesser, D. Reidel, Dordrecht, p. 305.
Hodge, P. W. 1965, *Astrophys. J.,* **141,** 806.
Hodge, P. W. 1981a, (in press).
Hodge, P. W. 1981b, *Astrophys. J.,* **247** (in press).
Sandage, A. R., Tammann, G. A. 1974, *Astrophys. J.,* **190**, 525.
Westerlund, B. 1961a, *UppsalaAnn.,* **5,** No.1.
Westerlund, B. 1961b, *UppsalaAnn.,* **5,** No.2.

J. Astrophys. Astr. (1981) **2,** 165–169

How High Can A Mountain Be ?

P. A. G. Scheuer *Cavendish Laboratory, Cambridge, CB3 OHE, UK*

Received 1981 March 9; accepted 1981 June 3

Abstract. The possible height of a mountain on a solid self-gravitating object such as a planet or a neutron star is limited by the strength of the rock. Estimates of the limiting height and conditions for their validity are discussed.

Key words: mountains—planets—neutron stars

1. Formulation of the problem

It is obvious that a mountain of comparable height and base (Fig. 1 a, b), cannot be higher than h_1 times a numerical factor of order unity, where

$$h_1 \simeq 4Y/\rho g. \tag{1}$$

At this point the yield stress Y is reached on a diagonal plane through the mountain. Here ρ is the density of the rock and g is the acceleration due to gravity. For a mountain of square cross-section the numerical factor has a value 4. It is much less obvious what limits the height of a 'hill' (Fig. 1 c), defined as a structure with the

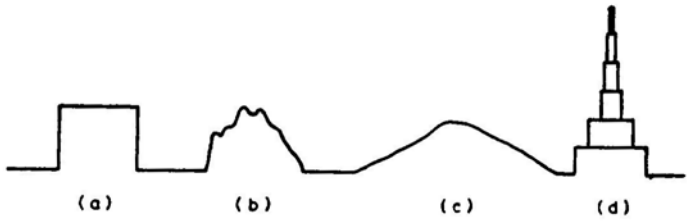

Figure 1. Profiles of four different kinds of mountains: (a) a mountain of square cross-section of comparable height and base (b) mountains of comparable height and base (e) a 'hill' with gently sloping sides (d) composite mountain of arbitrary total height.

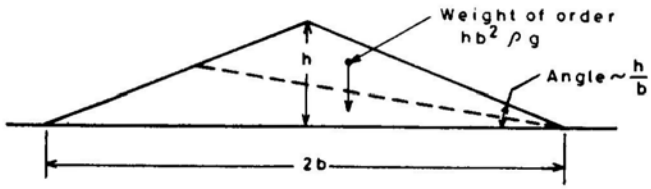

Figure 2. Diagram of a hill to illustrate the derivation of inequality (2).

base $2b$ much greater than the height h. An argument analogous to the above (*cf.* Fig. 2) shows that a solid rock will slide down the hillside if

$$h\, b^2\, \rho g\, (h/b) \gtrsim Y\, b^2$$

i.e.

$$h \gtrsim h_2 = (Y/\rho\, g)^{1/2}\, b^{1/2}. \tag{2}$$

The limiting height h_2 is thus the geometric mean of h_1 and b. Indeed, equation (2) is quoted in the literature (*e.g.* Elder 1976) and applies when the strength of a mountain is limited by a weak stratum in gently sloping sedimentary rock—a case not uncommon on earth. However, the simple argument below shows that it is not a sufficient condition in the simplest case of a mountain made of a homogeneous rock.

Consider a long hill, *i.e.* a ridge, of uniform cross section as shown in Fig. 3 and consider moments about the point P. The net couple due to gravity on the shaded section is (for $h \ll b$, and per unit length of ridge)

$$\int_0^b (x/b)\, h\, dx.\, \rho\, g.\, x = \tfrac{1}{3}\, \rho\, g h\, b^2,$$

and this must not exceed the maximum couple that can be sustained by shear stress as the boundary. $(\pi + h/b)\, b \cdot Y \cdot b \simeq \pi\, Y\, b^2$. Hence

$$h < 3\pi Y/\rho\, g = (3\,\pi/4)\, h_1 \tag{3}$$

where the numerical factor $3\,\pi\,/4$ is an upper bound to the true limit, as only one mode of fracture has been considered.

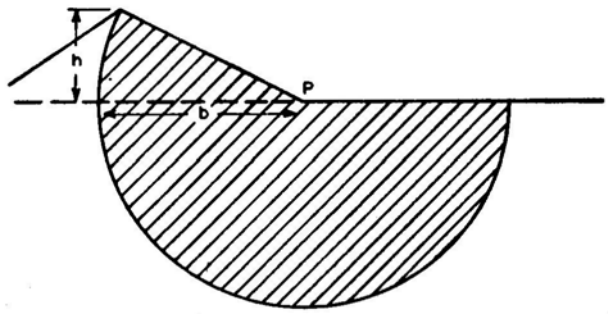

Figure 3. Diagram of a hill to illustrate the derivation of inequality (3),

Whether the same restriction applies to mountains on an inhomogeneous earth is an open question. The argument leading to condition (3) depends on homogeneity to a depth b below the plain level; in essence, it says that the underlying rock cannot support a heavier mountain. The support problem vanishes if the hill either rests on a rigid horizontal base, or (perhaps more realistically) is made of lighter rock floating in roughly isostatic conditions on a denser substrate. Yet, a fracture of the kind shown in Fig. 4(a) can still occur (implying $h \lesssim h_1$) unless the rock is firmly constrained laterally. The horizontal force due to the excess pressure of the heavier surrounding rock on a ' floating ' mountain is insufficient to prevent this type of fracture for heights much in excess of h_1; this may be illustrated using the model shown in Fig. 4(b). The weight of the triangular section ABC must equal the combined vertical components of the normal reaction P and the shear force S over BC, *i.e.*

$$\tfrac{1}{2}(d+h)^2 \rho g = (P+S)/\sqrt{2}. \tag{4}$$

Also, the magnitude of the shear force is limited by the condition

$$S \lesssim \sqrt{2}\,(d+h)\,Y. \tag{5}$$

Equating the horizontal forces on BCDE, we have

$$\tfrac{1}{2} d^2 \rho_0 g = (P-S)/\sqrt{2}, \tag{6}$$

While isostatic balance requires

$$d\rho_0 = (d + a h)\,\rho, \qquad 0 < a < 1 \tag{7}$$

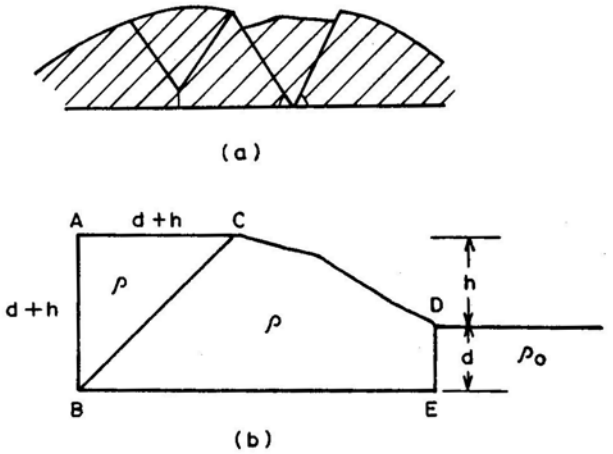

Figure 4. (a) Schematic illustration of a fracture. (b) Model of a mountain of density ρ floating on a substrate of density ρ_0. The height h above the plain level and the depth d below it are also shown. The condition for the stability of the mountain against a fracture along BC is derived in the text.

Here a is a number that depends on the shape of the hill. Subtracting equation (6) from equation (4) we find

$$\tfrac{1}{2}(d+h)^2 \rho g - \tfrac{1}{2} d^2 \rho_0 g = \sqrt{2}\, S$$

Substituting the value of ρ_0 from equation (7) the condition (5) yields

$$\tfrac{1}{2}\rho g (d+h)\left[d+h-\frac{d(d+\alpha h)}{d+h}\right] \leqslant \sqrt{2}\left\{\sqrt{2}(d+h)\, Y\right\}$$

$$h + d\frac{h(1-\alpha)}{d+h} \leqslant 4\, Y/\rho g$$

i.e. $h < h_1$ (8)

since $\alpha < 1$.

On the other hand, if the mountain is firmly glued to a rigid horizontal base, or to the underlying rock below BE in Fig. 4(b), there seems to be no reason why mountains should not form with heights up to $\sim h_2$.

While we have shown that one cannot build mountains much higher than h_1 by placing a homogeneous rock on a broad base, Dr. P. Young (personal communication) has shown that one can, in principle, build mountains of arbitrary height by making them steep enough. Young's mountain has a smooth exponential profile. The essence of the process is to pile mountains, each of height $\sim h_1$, on one another with the bases diminishing in geometric progression so that the total weight above each level is less than Y times the cross-section at that level (Fig. 1d). While such mountains are in equilibrium, the equilibrium becomes unstable if they are too slender to fulfil the Euler condition for the stability of a strut (*e.g.* Marks 1947),

$$P < \tfrac{1}{4}\pi^2 EI/L^2.$$

Here p. is the longitudinal force on a strut of length L, Young's modulus E, and moment of inertia I. If we approximate a uniform vertical bar by a light bar of square cross-section and side a and assume that the weight is equally divided between the top and the bottom, the Euler condition becomes

$$a^2 h_1^+ > (24/\pi^2)\, I^3, \tag{9}$$

where $h_1^+ = E/\rho g$. If $E \simeq Y$ (as in an ideal solid) then $h_1^+ \simeq h_1$ and the condition (9) shows that a stable mountain taller than its base cannot be taller than h_1 .For real solids $E \geqslant Y$, and the maximum height of a stable steep mountain is then roughly h_1 In $(E/Y) \simeq 5h_1$ While the Euler condition is valid only for long thin struts, the above result should give the correct order of magnitude.

2. Numerical values

Taking the shear strength of rock to be $1{\cdot}5\times 10^6$ kg m^{-2} (typical of values quoted for granite) and density $2{\cdot}65 \times 10^3$ kg m^{-3}, we obtain h_1 = 2250 m for terrestrial

mountains, 14000 m for lunar mountains, and 6000 m for Martian mountains. The highest mountains on earth, reach ~ $4h_1$*;* since isostasy is known to occur in the earth's crust, this is hardly surprising, but we note that the Tibetan plateau, for example, nowhere rises to heights comparable with the theoretical maximum $h_2 \simeq$ 45 km corresponding to its 1000 km horizontal extent. In making these comparisons we make no pretensions to serious geophysics; we merely wish to show that the simple considerations presented here lead to sensible orders of magnitude.

On the surface of a typical neutron star, the density is believed to be ~ 10^8 kg m^{-3} and the surface gravity ~10^{11} m s^{-2}. The strength of the surface material is much harder to estimate. Irvine (1978) gives a Young's modulus of ~10^{18} N m^{-2}, but more recent estimates of the binding energy are an order of magnitude below the values used by Irvine (Baym and Pethick 1979) and his estimate of Young's modulus should thus be reduced to ~10^{17} N m^{-2}. In an ideal solid the shear strength would be similar to Young's modulus, but in real terrestrial solids it is two or three orders of magnitude lower, leading to estimates of 10^{14} to 10^{15} N m^{-2}. Direct scaling from the density, chemical binding energy, and shear strength of granite gives similar results. Thus, on a neutron star, we estimate h_1 = 0·04 to 0·4 mm, with a possible upward revision if neutron star crust behaves more like an ideal solid than does terrestrial rock. We must also bear in mind that the density and other properties of neutron star crust begin to change substantially at depths ~1 m; so far as I am aware the reader is still free to speculate on possible inhomogeneities in composition (and hence possible isostasy) at lesser depths.

3. Conclusions

In a homogeneous rock stable mountains cannot rise much further than $h_1 = Y/\rho\, g$ above the level of the surrounding plains. Gently sloping 'hills' of crustal rock, 'floating' in more or less isostatic conditions on denser material, may be able to rise to greater heights of the order of $h_2 = (h_1\, b)^{½}$ where b is the base of the ' hill '.

Acknowledgements

This work originated in a discussion on the possible heights of mountains on neutron stars, and I am indebted to Drs Radhakrishnan, Vivekanand, and Rajaram Nityananda for introducing me to the problem. I am also indebted to Dr P. C. England for a very useful discussion, to Dr Peter Young for permission to quote his work on tall thin mountains, and to the staff of the C S I R O Division of Radiophysics for their help in preparing this note for publication.

References

Baym, G., Pethick, C. 1979, *A. Rev. Astr. Astrophys,* **17,** 415.
Elder, J. 1976. *The Bowels of the Earth,* Oxford University Press.
Irvine, J. M. 1978, *Neutron Stars,* Clarendon Press, Oxford.
Marks, L. S. 1941, *Mechanical Engineers' Handbook,* 4 edn, McGraw-Hill, New York.

J. Astrophys. Astr. (1981) **2,** 171–185

Current Rate of Nucleosynthesis and its Implications

D. C. V. Mallik *Indian Institute of Astrophysics, Bangalore 560034*

Received 1981 March 13; accepted 1981 May 25

Abstract. The current rate of nucleosynthesis in the solar neighbourhood is re-evaluated on the basis of Arnett's (1978) stellar yields, the mass loss models of Chiosi, Nasi and Sreenivasan (1978) and the initial mass function determined by Lequeux (1978). If massive stars are held responsible for most of the metals we observe, a higher birthrate of these stars in the past is indicated in view of the low current rate of nucleosynthesis. The intermediate mass stars may not supply the bulk of the metals unless total disruption of their carbon core takes place.

While a declining birthrate is in conflict with the result obtained from the age-metallicity relation of stars, it is supported by some galactic evolution models which interpret successfully the white dwarf mass distribution data. If the constraint of a nearly time-invariant birthrate were strictly accepted, then models of the prompt initial enrichment type are required to explain the observed abundances in terms of nucleosynthesis in massive stars.

Key words: massive stars—nucleosynthesis—stellar birthrate

1. Introduction

Massive stars are generally regarded as the principal sites of primary nucleosynthesis in galaxies. Since they are extremely shortlived, their present birthrate may be directly used to derive the rate of production of the primary synthesis species, once the stellar yields are known as a function of the stellar mass. Arnett (1978) studied the evolution of helium cores of massive stars through silicon burning, electron captures and thermal disintegration and computed the absolute yields of abundant nuclei as a function of the mass of the helium core. In several recent studies these absolute yields have been used to estimate the total yield from a generation of massive stars. These estimates are important in stellar and galactic evolution studies for a number of reasons. First, if the theory of advanced stellar evolution and nucleosynthesis were to be correct, the theoretically computed yields should follow the

observed distribution of primary abundances in the solar system. Here it is more to the point to evaluate the ratios of theoretical yields of the various elements and compare them with the observed ratios. Secondly, such a comparison can also be used to gauge the relative importance of stars in various mass intervals (*e.g.* intermediate and high) in the synthesis of various species. Lastly, if the present birthrate of massive stars were assumed to be known with some certainty, the present rate of element production in conjunction with the observed total element abundances would provide essential clues to the overall past rate of nucleosynthesis and hence to the past history of the stellar birthrate. It is this last point which has been the source of a lively debate since the publication of Arnett's singular work on bulk yields (Chiosi 1979; Wheeler, Miller and Scalo 1980).

Arnett (1978) was the first to use the stellar abundances with various choices of the initial mass function (IMF) to evaluate the elemental yield per generation of massive stars. The solar system abundances could be reproduced with reasonable choices of the slope of the IMF. Arnett varied the slope between the classical Salpeter value of 1·35 and a much steeper 3·33 and noted that the relative yields were insensitive to the choice of the slope. However, when the yields were used with the observed birthrate of massive stars according to Ostriker, Richstone and Thuan (1974, hereafter ORT), the current production rate of metals turned out to be about a tenth of the average past rate. This led Arnett to the conclusion that the present rate of nucleosynthesis, though not large, is not negligible either and that the past rate was much higher implying a higher birthrate of the massive stars in the past. This result was compatible with a class of galactic evolution models where the rate of star formation is assumed to vary as the second power of the gas density.

One of the uncertainties in Arnett's calculation was the relation between the mass of the helium core M_α and the initial main sequence mass M of the star that develops this helium core. The M–M_α transformation derived by Arnett was based on evolutionary models without mass loss. Evolutionary sequences with mass loss by stellar wind show large differences with conservative evolution of the same initial mass (Chiosi, Nasi and Sreenivasan 1978; de Loore 1979). In particular, the incorporation of mass loss in evolutionary calculations drastically changes the $M(M_\alpha)$ relation. Models computed with mass loss develop, for the same initial mass of the star, a much smaller helium core than the conservative model. The higher the mass loss rate the smaller is M_α for a given initial M. As a result the fractional mass of various species ejected from a massive star is greatly reduced. The final yields are thus much lower.

Chiosi and Cairnmi (1979), who investigated the effects of mass loss on the nucleosynthetic yields, derived a present rate of nucleosynthesis based upon the ORT birthrate which was a factor of three lower than the rate found by Arnett. Further the theoretical yields with mass loss compared favourably with the solar system abundances only if a Salpeter mass function were assumed, while IMF's with steeper slopes produced much lower yields. The implied variation of the stellar birthrate over the galactic lifetime was considerable, the average past rate derived being almost thirty times higher.

The rate of nucleosynthesis per generation of massive stars is directly dependant upon the birthrate of these stars. The birthrate is determined from observations in the solar neighbourhood of the present-day mass function of main sequence stars (PDMF). The steps to obtain the PDMF from the currently observed luminosity

function are outlined in detail in the comprehensive work of Miller and Scalo (1979, hereafter MS). Once the PDMF is obtained, the birthrate of massive stars is easily derived by dividing the PDMF by the main sequence lifetime of each star. For stars whose main sequence lifetimes are of the order of the lifetime of the Galaxy or longer, this simple procedure does not work and one has to know the history of the stellar birthrate.

The birthrate of massive stars determined by MS from the best possible evaluation of the PDMF is considerably higher than the one given in ORT. Also, the slope of the birthrate function (which is the same as the slope of the IMF for these stars) is less steep. Thus the MS birthrate coupled with Arnett's stellar yields predicts a much higher production rate of metals at the present time and to explain the observed abundances as the result of nucleosynthesis in massive stars, no great increase of the birthrate in the past is required. Several independent lines of argument suggest that the average past stellar birthrate has been no more than a factor of 2-3 different than the present one (MS; Twarog 1980). Thus the discrepancy between the predicted variation of the stellar birthrate from nucleosynthetic yields and the lack of such a variation from other evidences is apparently removed by considering the higher MS birthrate. However, when mass loss is taken into account, the discrepancy reappears and a declining birthrate has to be invoked to explain the present solar system abundance distribution (Chiosi 1979).

Observations of chemical abundances in our Galaxy show a linear relation between the helium and heavy element enrichment for a variety of objects (Peimbert 1977). The slope of this line is close to 3. The same relation is found for a large sample of external galaxies (Lequeux *et al.* 1979). In theoretical calculations it has been noted that the current stellar evolution data fail to produce this slope by a factor of 5 or more (Hacyan *et al.* 1976; Mallik 1980). However, if mass loss from the massive stars were taken into account, the agreement is much better. In the latter case, the ability of these stars to produce heavy elements is greatly reduced and the theoretical value of $\Delta Y/\Delta Z$ *is* correspondingly enhanced. Secondly, the heavy element yield p_z, defined as the ratio of heavy elements newly synthesised and ejected to the mass locked up in stars and stellar remnants per generation of stars, is observationally lower than the theoretical value when mass loss is neglected. Again a very good agreement is obtained if effects of mass loss were incorporated in the theoretical calculation. Therefore, the theoretical nucleosynthetic yields are more meaningful and closer to observational realities when computed with the M–M_α transformation obtained from mass loss models.

A new determination of the IMF of the upper main sequence stars has recently been published by Lequeux (1979). This is based on several recent catalogues, most notably the Michigan catalogue of spectral types (Houk and Cowley 1975) and the catalogue of B stars by Lesh (1968,1972). A different procedure was followed in the assignment of masses to stars of a particular spectral type and luminosity class. The observed HR diagram was superposed on a theoretical one using mass loss evolutionary sequences for massive stars ($M \geqslant 20\ M_\odot$) due to Chiosi, Nasi and Sreenivasan (1978) and Iben's (1967) tracks for intermediate mass stars ($M < 15\ M_\odot$). For each mass range on the main sequence delimited by theoretical tracks, the surface density of stars as a function of mass was directly determined. This is a better way of assessing the masses of the earliest spectral types than using the uncertain and scantily available data from massive binaries. The PDMF thus determined is

found to be quite different from the MS data. Further, the IMF is considerably steeper (slope: — 2·0) than the classical Salpeter one. While the agreement of the slope with the one derived in MS is fair for masses above 10 $M_\odot$, the Lequeux IMF is considerably steeper in the mass interval $2{\cdot}5 \leqslant M/M_\odot \leqslant 10$. The birthrate of massive stars derived from this IMF is very much lower than the MS birthrate and is closer to the ORT data although the slope of the ORT birthrate function does appear to be a bit too steep.

The Lequeux IMF should be preferred for a number of reasons. The catalogues used for its determination are the best available. This is also the first time that evolutionary sequences with mass loss have been used to obtain the masses; the flattening of the mass-luminosity relation in mass loss models affects directly the conversion of the luminosity function to the PDMF. Most importantly the Lequeux IMF has been corrected for the presence of a population of evolved O stars which have been involuntarily included in all earlier work. The presence of this population has been clearly established in the recent work of Carrasco *et al.* (1980). Thus the PDMF and hence the IMF for the massive stars are closer to the actual values.

In view of the large difference in the birthrate determined by Lequeux compared to the MS estimate it is worthwhile to have a re-evaluation of the present rate of nucleosynthesis based on the Lequeux IMF and mass loss models for the massive stars. This will then provide a better constraint on the history of the stellar birthrate. It is important to note that the Lequeux birthrate being lower, the present rate of nucleosynthesis based on it is likely to predict a large variation in the birthrate massive stars over the galactic lifetime. Alternatively, if this rate were assumed to be constant at its current value, the hypothesis of massive stars being responsible for the bulk of the nucleosynthesis should be called into question. One has to look elsewhere, possibly at the intermediate mass range ($M \lesssim 8\ M_\odot$), to locate the sites of nucleosynthesis.

In Section 2 we present a comparison of the various PDMF's and the IMF's recently determined. Section 3 describes the theoretical formalism used to calculate the current rate of nucleosynthesis. The implications of this newly derived rate are discussed in Section 4.

2. Comparison of the PDMF's and the birthrates

The PDMF $n(m)$ is defined as the number of main sequence stars in the solar neighbourhood per square parsec per unit mass interval. Here m is the mass of the star in solar units. For massive stars, the initial mass function $\phi(m)$ is directly proportional to $n(m)/\tau_m$ where τ_m is the main sequence lifetime of the star of mass m. The relation between $n(m)$ and ϕ(m) may be written as

$$\phi(m) = \frac{n(m)}{\tau_m}\,\frac{1}{\psi_1}, \tag{1}$$

where ψ_1 is the current birthrate in $M_\odot\,\mathrm{pc}^{-2}\,\mathrm{yr}^{-1}$.

In Fig. 1 the PDMF's from the work of MS and Lequeux are shown for comparison. The MS values are taken from their Table 3 and the error bars correspond to the uncertainties quoted by them in their Table 4. Lequeux (1979) has tabulated the

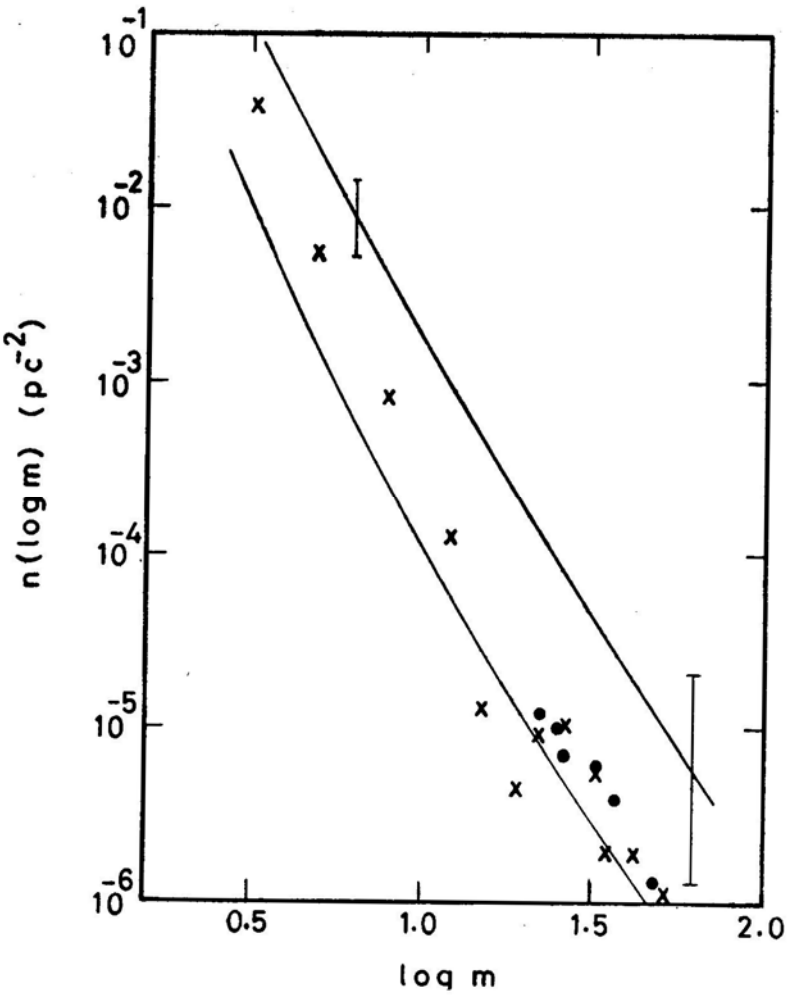

Figure 1. Comparison of the present-day mass functions. Thick solid line (upper) gives the MS data and thin solid line (lower) the Lequeux data. ×, ORT; ●,CGO. See text for details.

logarithmic surface densities (per kpc^2) as a function of mass. We have adopted the values corrected for the runaways and converted them to the same unit as in MS, namely per pc^2 per log m. The crosses in Fig. 1 show the controversial ORT data. They certainly imply a steeper birthrate function thereby reducing the fractional mass in massive stars with respect to the total mass in stars. The Lequeux data agree remarkably well with the luminosity function of O stars determined by Cruz-Gonzalez *et al.* (1974, hereafter CGO). This luminosity function includes the earliest O-type stars. We have used the spectral type-M_v calibration given by Lesh (1979) and the mass loss models of Chiosi, Nasi and Sreenivasan (1978) for the case $\alpha = 0{\cdot}90$ to convert the CGO data to the corresponding PDMF. This is shown by the filled circles in Fig. 1. It is seen that the MS data give a higher surface density of stars in each mass interval. The values obtained by Lequeux fall below the lower uncertainty limit quoted by these authors. It may be suspected that, since the mass-luminosity relation for the mass loss models is different, the implicit use of this by Lequeux has produced part of the change in his PDMF compared to the one given

by MS. However, we have done the exercise of using the mass-luminosity relation from mass loss models and the tabulated stellar densities of MS to derive the PDMF. The change is very little. Hence, the discrepancy between the two PDMF's is real. The mass-lifetime relations used by MS and Lequeux are almost the same. Thus the birthrates derived from the PDMF's have the same relationship to each other as the PDMF's themselves.

In Fig. 2 a plot of the Lequeux birthrate function in units of pc^{-2} Gyr^{-1} m^{-1} is given. The best analytical fit is a straight line with a slope of – 3·0. For the convenience of comparison we have obtained the birthrate at each mass point given in ORT from this plot and expressed the value in units of 10^{-13} pc^{-2} yr^{-1}. Table 1 shows a comparison of the various birthrates. It is to be noted that each entry in columns 3, 4 and 5 of the table is the birthrate n(m) Δm, where Δm is the mass interval centred on the mass of column 2. The Lequeux birthrate is lower than the MS birthrate. Therefore, the rate of nucleosynthesis calculated on the basis of this birthrate is expected to be much lower.

From the plot in Fig. 2 it is also possible to derive a normalised IMF if the current total birthrate in units of $M_\odot$ Pc^{-2} Gyr^{-1} were known. According to Tinsley (1979), the current birthrate has a value of $5\ M_\odot$ Pc^{-2} Gyr^{-1} which also falls almost in the

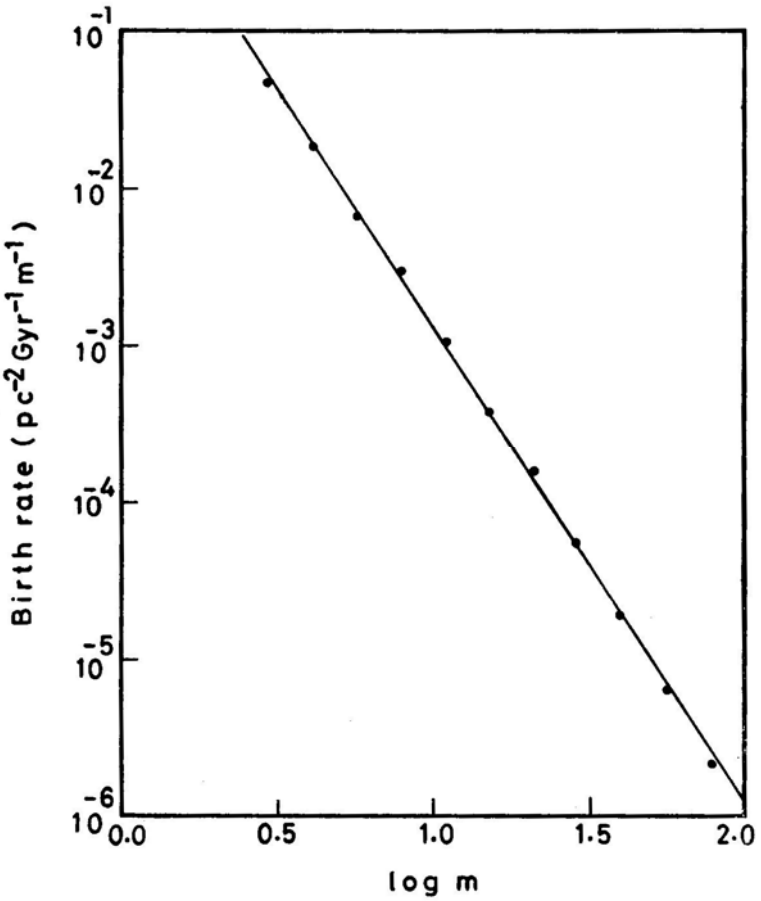

Figure 2. Birthrate function due to Lequeux in pc^{-2} Gyr^{-1} m^{-1} versus log m.

Table 1. Comparison of the current stellar birthrates.

Sp. Type	Mass ($M_\odot$)	Birthrate (10^{-13} pc^{-2} yr^{-1}) ORT	MS	Lequeux
O5	51	1·0	2·1	1·5
O6	42	2·7	4·0	2·2
O7	35	1·3	4·5	3·2
O8	32	2·8	5·4	3·8
O9	26	4·6	11·5	5·9
B0	22	2·5	14·0	8·6
B0.5	19	1·4	22·8	11·1
B1	15	3·1	47·3	18·5
	12	22·0	93.1	29.3
	8	66·0	301·0	66.3
	5	170·0	694·6	195·0

middle of the range of acceptable values suggested by MS. In the present calculations we have assumed the total present birthrate to be 5 $M_\odot$ Pc^{-2} Gyr^{-1} and written for the Lequeux IMF the analytical formula

$$\phi(m) = 0{\cdot}26\, m^{-3{\cdot}0} \tag{2}$$

for $2{\cdot}5 \leqslant m \leqslant 100$, where the masses are in solar units. This IMF is used in Section 3 to calculate the production matrix for a generation of stars and hence the production rate of the primary synthesis species.

3. Rate of nucleosynthesis in the solar neighbourhood

3.1 *Theoretical Formalism*

Following Arnett (1978), let M_j^{ej} denote the mass ejected in the form of species j from a star of initial main sequence mass M_j^{ej} The quantity M_j^{ej} may be expressed in terms of the production matrix element $Q_{ji}(M)$ as

$$M_j^{\mathrm{ej}} = M \sum_i Q_{ji}(M)\, X_i, \tag{3}$$

where i denotes the progenitor species and X_i the mass fraction abundance of species i in the stellar material. For the primary nucleosynthesis products,

$$M_j^{\mathrm{ej}} = M\, Q_j(M), \tag{4}$$

since $\sum_i X_i \simeq 1$. If $\dot{\sigma}(M)$ be the deathrate of main sequence stars in the mass interval M and $M+ dM$, the production rate of species j in the same interval is

$$d\dot{\Sigma}_j = \dot{\sigma}(M)\, M_j^{\mathrm{ej}}\, dM. \tag{5}$$

The total production rate of species j from a generation of stars is then given by

$$\dot{\Sigma}_j = \int_{M_1}^{\infty} \dot{\sigma}(M)\, M_j^{ej}\, dM. \tag{6}$$

The lower limit M_1 depends on the element in question and is larger than or equal to M_0, the present turnoff mass in the Galaxy. For the massive stars the deathrate equals the birthrate and

$$\dot{\sigma}(M)\, dM = \phi(M)\, \psi_1\, dM, \tag{7}$$

where $\phi(M)$ is the IMF and ψ_1 the total present birthrate. Thus

$$\dot{\Sigma}_j = \int_{M_1}^{\infty} \phi(M)\, \psi_1\, MQ_j\,(M)\, dM = q_j\, \psi_1, \tag{8}$$

where q_j 's are the integrated elements of the production matrix. The yield of species j is defined as

$$p_j = \frac{1}{1-f} \sum_{i \neq j} q_{ji}\, X_i \simeq \frac{q_j}{1-f}. \tag{9}$$

Here f is the total fractional mass ejected from a generation of stars and depends on the IMF and the relation between the initial mass and the mass of the stellar remnant.

Let us assume that the galactic disk behaved as a closed box after an initial epoch of enrichment. If ΔX_j were the increment of species j over the lifetime of the disk, a uniform production rate $\dot{\Sigma}_j$ acting over this period may be expressed as

$$\dot{\Sigma}_j = \frac{\Delta X_j \Sigma}{T_0}, \tag{10}$$

where Σ is the total surface density of matter participating in nucleosynthesis and T_0 the age of the disk.

However, if the rate of nucleosynthesis were higher in the past owing to a higher star formation rate, equation (10) should be modified to

$$\Delta X_j = \frac{\dot{\Sigma}_j}{\Sigma} \frac{\langle \psi \rangle}{\psi_1} T_0, \tag{11}$$

where $\langle \psi \rangle / \psi_1$ denotes the ratio of the past average birthrate to the present one. Equation (11) is the one commonly used to relate the rate of nucleosynthesis to the stellar birthrate.

3.2 *Nucleosynthetic Yields without Mass Loss*

A preliminary estimate of the nucleosynthetic yields with the Lequeux IMF has been made to compare similar estimates by Arnett (1978) and Wheeler, Miller and Scalo (1980). Here the M–M_α transformation adopted by Arnett from stellar models without mass loss has been used and the production rate of the primary synthesis species has been calculated as a function of the spectral type. Table 2 presents the results of this calculation. Columns 4–9 give $\Delta\dot{\Sigma}_j$ as defined in equation (5) for all the various species for which the stellar yields are given by Arnett (1978). The first row in the table is an addition showing the contribution to nucleosynthesis from the hottest spectral types O3-O4. The surface density of these stars is taken from CGO. The mass assignment is uncertain but close to Conti's (1975) calibration. The birthrate calculated with $\tau_m=10^{6.50}$ yr agrees very well (within 5 per cent) with the value read off Fig. 2 for M=95 $M_\odot$ Due to the rapid fall off of the birthrate function, the contribution of these most massive amongst the stars to the total nucleosynthesis is very small. As seen from the table, the present calculation gives a rate of about a factor of two higher than the one implied by the ORT birthrate and is consistently smaller than the one calculated by Wheeler, Miller and Scalo (1980). The implied variation in the birthrate is about a factor of 4 excepting for He, but He is known to be produced in a pregalactic phase. If, instead of 100 $M_\odot$ pc^{-2} for Σ, the smaller value of 35 $M_\odot$ pc^{-2} advocated by Tinsley (1980) is used, the ratio $\langle\psi\rangle/\psi_1$ is between 1–2, in excellent agreement with the result obtained from the age-metallicity relation of stars (Twarog 1980).

Table 2. Current rate of nucleosynthesis without mass loss form massive stars.

Sp. Type*	M ($M_\odot$)	$\Delta\dot{\sigma}$†	$\Delta\dot{\Sigma}_j$‡						
			He	C	O	Ne	Mg	Si+Fe	Z
O3-04	95	0·55	4·49	1·54	16·68	1·85	0·86	0·97	21·90
O5	51	1·45	7·44	3·39	17·55	2·19	0·92	1·36	26·41
O6	42	2·18	9·92	4·23	19·18	3·64	1·10	2·09	30·24
O6·5	35	3·24	13·15	5·24	20·09	4·61	1·31	5·08	36·33
O7	32	3·85	14·82	5·62	20·02	4·85	1·39	2·60	34·48
O8	26	5·92	20·25	5·68	17·76	5·62	1·72	2·31	33·09
O9·5	22	8·58	26·56	4·87	14·24	6·60	2·32	2·92	30·95
B0·5	19	11·12	31·69	4·45	14·46	6·67	2·95	3·45	31·98
B1	15	18·53	45·40	4·82	12·97	5·93	3·80	4·26	31·78
B1·5	12	29·25	59·79	5·62	4·88	1·18	1·92	2·95	16·55
$\dot{\Sigma}_j$			233·5	45·5	157·8	44·1	18·3	28·0	293·7
§$\dot{\Sigma}_j/(\dot{\Sigma}_j)_A$			2·1	1·7	1·8	2·0	2·2	2·2	1·9
+$\dot{\Sigma}_j/(\dot{\Sigma}_j)_{MS}$			0·4	0·5	0·6	0·5	0·5	0·5	0·6

*The Sp. Type-Mass calibration is approximate and adopted from ORT and MS.
† The Lequeux birthrate in units of 10^{-13} pc^{-2} yr^{-1}.
‡ The production rate in units of 10^{-13} $M_\odot$ pc^{-2} yr^{-1}.
§Ratio of the rate estimated in the present work to that of Arnett (1978).
+Ratio of the rate estimated in the present work to that of Wheeler, Miller and Scalo (1980

3.3 *Nucleosynthetic Yields with Mass Loss*

In the computation of the rate of nucleosynthesis with mass loss a slightly different procedure has been followed. In an earlier paper (Mallik 1980), we had calculated the chemical evolution coefficients using the stellar nucleosynthesis data from Iben and Truran (1978) and Arnett (1978). The Q_{ij} (M) matrix was calculated based on the M–M_α transformation of Arnett for the massive stars and the Iben and Truran scenario for the low and intermediate mass stars. While the effects of mass loss were thus included for stars of mass lower than 8 $M_\odot$, no attempt was made to do the same for the massive stars. In the present work, we have retained the Q_{ij} (M) prescription of the earlier paper for stars of $M \leqslant 8\ M_\odot$ and have modified the matrix elements for the massive stars for the mass loss case with the M–M_α transformation obtained by Chiosi (1979). The stellar abundances produced in a helium core of mass M_α are taken from the work of Arnett (1978) but each M_α now corresponds to a larger initial main sequence mass M. It is also assumed that all stars above 12 $M_\odot$ leave a remnant of mass 1·4 $M_\odot$ following a terminal explosion event.

With the IMF given in equation (2) and the new $Q_{ij}(M)$ values the production matrix per generation of stars ranging from 2·5 $M_\odot$to 95 $M_\odot$ has been calculated. In Table 3 the q_{ij} matrix is displayed. Since we are interested only in the primary nucleosynthesis products, only the relevant matrix elements are shown. For all the species, except C and He the stellar evolution data have nonzero Q_{ij} (M) values only for $M >$ l0 $M_\odot$ C and He, are produced in low and intermediate mass stars also, following the three stages of element dredge-up as enumerated by Iben (1977) and Iben and Truran (1978). The values quoted in Table 3 include the contribution of the less massive stars to the production of C and He.

In Table 4 the production rates of the various species are presented. The change is rather drastic compared to the case without mass loss as presented in Table 2. The change from the rate based on the MS birthrate function and mass loss models

Table 3. Production matrix q_{ij} for a generation of stars.

Product		Progenitor j				
i	H	He	C	O	Ne	Mg	Si+Fe
H	7·25(−2)	...	...	...	...	...	...
He	4·84(−3)	7·70(−2)	...	...	...	...	...
C	9·17(−4)	9·17(−4)	...	...	...	...	...
O	5·76(−4)	5·76(−4)	...	...	...	...	...
Ne	1·45(−4)	1·45(−4)	...	...	...	...	...
Mg	5·46(−5)	5·46(−5)	...	...	...	...	...
Si+Fe	9·95(−5)	9·95(−5)	...	...	...	...	7·84(−2)

Table 4. Current rate of nucleosynthesis with mass loss form massive stars.

$\dot{\Sigma}_j$ $(10^{-13}\ M_\odot \mathrm{pc}^{-2}\ \mathrm{yr}^{-1})$	He	C	O	Ne	Mg	Si+Fe	Z
Mass loss case	179·0	15·5	28·3	7·1	2·7	4·9	58·5
No mass loss	229·0	43·9	141·2	42·3	17·4	27·0	271·8
Chiosi (1979)	364·4	27·9	47·1	16·9	8·0	12·0	111·0
†$\dot{\Sigma}_j/(\dot{\Sigma}_j)_C$	0·49	0·56	0·60	0·42	0·34	0·41	0·53

† The ratio of row 1 to row 3

Table 5. The ratio of the average past birthrate to the current birthrate $\langle\psi\rangle/\psi_1$.

Solar system abundance	He 2·4(−1)	C 4·5(−3)	O 1·1(−2)	Ne 1·2(−3)	Mg 5·6(−4)	Si+Fe 2·0(−3)	Z 1·9(−2)
$\Sigma = 100\ M_\odot\ \mathrm{pc}^{-2}$	89·4	19·3	25·9	11·3	13·8	27·2	21·7
$\Sigma = 35\ M_\odot\ \mathrm{pc}^{-2}$	31·3	6·8	9·1	3·9	4·8	9·5	7·6

should also be noted. The latter has been taken from Chiosi (1979) and is included in Table 4. Using equation (12) we can now calculate the ratio $\langle\psi\rangle$ / ψ_1 For this we have assumed T_0 = 15 Gyr and used two values of the surface density Σ.The results are given in Table 5. The solar system abundances quoted in the table are from Cameron (1973). We find that even for the lower value of Σ, the average past birthrate has to be several times higher than the present one, if massive stars are assumed to be responsible for most of the nucleosynthesis. The lower value of Σ may indeed be the lowest surface density compatible with observations. If a significant fraction of the total mass density resides in low-luminosity dwarfs, Σ should be higher. Thus the variation in the stellar birthrate predicted from the present rate of nucleosynthesis is incompatible with some of the other evidences which suggest a more even birthrate through the galactic history.

4. Implications of the currently observed rate of nucleosynthesis

The present evaluation of the rate of nucleosynthesis casts serious doubts on some of the conclusions of Wheeler, Miller and Scalo (1980). A combination of Arnett's stellar yields for helium cores, the M–M_α transformation obtained from mass loss models and the Lequeux IMF predicts a current rate of nucleosynthesis far below the value quoted by these authors. Various observations of hot stars and interstellar matter in galaxies provide strong evidence for mass loss from massive stars. If we were to accept this fact, then the currently observed heavy element abundance could result from the nucleosynthesis in these stars with a stellar birthrate declining in time. If, on the other hand, the stellar birthrate had not varied by more than a factor of 2 over the past history of the Galaxy, the current rate of nucleosynthesis shows the inadequacy of massive stars in producing the observed metals.

One may look into the mass range 5–15 $M_\odot$, which provides the bulk of the observed supernova rate, to see if these stars also the source of the metals we observe. However, this also has problems. Weidemann (1977) has discussed the evidences of large mass loss in low and intermediate mass stars. Several pieces of observation suggest that stars larger than 5 $M_\odot$ have evolved to white dwarfs after going through an appropriate planetary nebula phase. The birthrate of planetary nebulae is insensitive to the choice of the upper mass limit and does not provide any stringent constraint. The currently observed birthrate is compatible with an upper mass limit in the range of 4–8 $M_\odot$ Abundance analysis of planetary nebulae shows that there is a population of these objects which has most likely come from stars in the intermediate mass range (Peimbert 1978). Most recently, Koester and Weidemann (1980) have analysed the data on DA white dwarfs and have found that the upper limit on stars becoming white dwarfs is higher than 5 $M_\odot$. If all stars of mass up to 8 $M_\odot$ evolve finally to planetary nebulae and white dwarfs, the ability of the

intermediate mass stars to produce elements heavier than carbon is severely limited. The entire responsibility of nucleosynthesis would then devolve on stars in the narrow mass interval 8–15 $M_\odot$ One can estimate the average metal yield per star in the mass range 5–15 $M_\odot$ assuming that they supply the bulk of the metals we observe. The result obtained in Section 3 shows that massive stars ($M \geqslant 15\ M_\odot$), at their current birthrate, produce about 5–10 per cent of the total metal abundance. If the rest were to come from 5–15 $M_\odot$ stars, the increment in metallicity over the age of the disk,

$$\Delta Z \sim \langle M_z \rangle\, \psi_1 \frac{T_0}{\Sigma} \int_5^{15} \phi\,(M)\, dM, \tag{13}$$

where $\langle M_z \rangle$ is the yield per star in $M_\odot$. With a surface density $\Sigma = 100\ M_\odot\ \mathrm{pc}^{-2}$, and the IMF given in equation (2) this leads to $\langle M_z \rangle \sim 5\ M_\odot$ which is absurd since no star in the mass interval 5–15 $M_\odot$ may develop a core so large and proceed through advanced thermonuclear burning. If instead, $\Sigma = 35\ M_\odot\ \mathrm{pc}^{-2}$, $\langle M_z \rangle \sim 1.7\ M_\odot$, and the requirement of metal production may be satisfied by some models with a total disruption of the carbon core. The present calculation shows that a stellar birthrate declining in time is perfectly compatible with the accepted idea that massive stars produce most of the observed metals. The Lequeux birthrate being lower than the MS birthrate no overproduction of metals results if $\langle \psi \rangle / \psi \geqslant 10$. There is a certain internal consistency in the present calculation which, for obvious reasons, was absent in earlier work. This is in reference to the methods used in the derivation of the IMF by Lequeux which has the mass loss evolutionary sequences already built in.

Koester and Weidemann (1980) have presented a series of models to fit the observed narrow mass distribution of DA white dwarfs. Since a large fraction of the white dwarfs comes from stars formed in the early history of the Galaxy, the white dwarf data could be a sensitive probe into certain aspects of the early galactic evolution. In particular, the mass distribution of white dwarfs depends on the IMF, the birthrate and the relation between the initial and final masses of stars becoming white dwarfs. For a time-invariant IMF of the' power-law form, it is seen that the observed data may be reproduced with only a variable birthrate function. The best fit comes from models with either the Salpeter IMF or the Larson-Tinsley IMF (Larson and Tinsley 1978) and a time-varying birthrate of the form $e^{-t/5}$ where t is expressed in Gyr. Interestingly enough with a galactic age of 15 Gyr, this amounts to a decline in the birthrate by a factor of 20 which is close to the ratio predicted in Table 5. Although the Lequeux IMF does not extend beyond 2·5 $M_\odot$ and is considerably steeper and we have made no explicit calculation of the white dwarf mass distribution with this IMF, the comparison is made because we have here an independent evidence of a birthrate varying in time.

Recently, Twarog (1980) has determined the age-metallicity relation (AMR) of stars and interpreted it in the light of models of galactic evolution. There is a remarkable discrepancy in this work with the observations of supergiants obtained by Luck and Bond (1980). The actual abundances derived by Luck and Bond are much higher, and in conflict with the AMR derived by Twarog. Twarog has put forth

strong arguments in favour of a nearly constant birthrate, the variation in no case exceeding a factor of 2. This result is incompatible with the constraint obtained from nucleosynthetic yields.

In the framework of the simple model of galactic evolution, a high star formation rate in the past implies that a large fraction in the interstellar gas has been astrated by the present time. Consequently, the pregalactic deuterium abundance should be much higher than the observed value. If deuterium were entirely of cosmological origin, this may pose problems for some of the currently accepted models of Big Bang nucleosynthesis. However, the argument favouring a low degree of astration is model dependant and may not be relevant at all, if part of the deuterium were of noncosmological origin, or if the Big Bang nucleosynthesis calculations were wrong in some ways so as to underproduce deuterium (Audouze and Tinsley 1976). The upper limit to the degree of astration is set by the density of visible matter in the universe and a variation of a factor of thirty in the deuterium abundance can be accommodated within this limit (Reeves 1975). The degree of astration implied in the present work does not violate this.

The discussion, so far, is based on the assumption that the IMF is constant through the history of the Galaxy. There is no strong argument for or against the variation of the IMF with time. If the IMF varied any time in the past and were, for example, flatter, the nucleosynthetic yields would be significantly affected. It is conceivable that a flatter IMF in the early history of the Galaxy resulted in a large production of metals and that the IMF steepened later to assume its present form. The birthrate, in this case, need not show any variation. There is some observational evidence that this may have been the case. The analysis of oxygen abundance in metal-poor stars by Sneden, Lambert and Whitaker (1979) shows a substantial overabundance in the [O/H] versus [Fe/H] plot, while the carbon abundance in the same stars follow the line [C/Fe] = 0. The carbon and iron yields from stars are relatively constant over the entire stellar mass spectrum, while the oxygen yield increases dramatically at the higher mass end. The overabundance of oxygen in the old stars suggests that oxygen was produced faster in the early epoch than carbon and iron and may be explained in terms of a flattening of the mass function in the first 2·5 Gyr. Freeman (1977) has shown that the young globular clusters in the Large Magellanic Cloud have remarkably flat IMF's and has argued that their present environment may be similar to the one prevailing in the Galaxy in the early epoch. In case a flat IMF truly represents the situation in the first few billion years of the Galaxy, the metal production rate during the time should have been very high. As the IMF steepened, the mass fraction in massive stars decreased preventing overcooking of the galactic medium. This solution is of the same nature as some of the others invoked to solve the ' G dwarf' problem. The prompt initial enrichment (PIE) model of Truran and Cameron (1971) and the two-component galactic evolution model of Ostriker and Thuan (1975) give similar solutions to the abundance distribution, successfully accounting for the paucity of metal-poor dwarfs (Pagel and Patchett 1975). It may as well be that the present rate of nucleosynthesis indirectly leads us to the same picture, if we accept that the stellar birthrate has been relatively constant during the evolution of the disk.

In conclusion, the current rate of nucleosynthesis is compatible with the idea of massive stars producing most of the metals only if the stellar birthrate decreased with time. The current stellar evolution data as well as observations do not support

the premise that intermediate mass stars are the source of the bulk of the nucleosynthesis in the Galaxy. One has to go beyond the purview of the Simple Model and invoke prompt initial enrichment, if the stellar birthrate were to be constant and yet the metals had to come from the massive stars.

References

Arnett, W. D. 1978, *Astrophys. J.,* **219**, 1008.

Audouze, J., Tinsley, B. M. 1976, *A. Rev. Astr. Astrophys.,* **14,** 43.

Cameron, A. G. W. 1973, *Space Sci. Rev.,* **15,** 121.

Carrasco, L., Bisiacchi, G. F., Cruz-Gonzalez, C, Firmani, C, Costero, R. 1980, *Astr. Astrophys.,* **92,** 253.

Chiosi, C. 1979, *Astr. Astrophys.*, **80,** 252.

Chiosi, C, Caimmi, R. 1979, *Astr. Astrophys.*, **80,** 234.

Chiosi, C., Nasi, E., Sreenivasan, S. R. 1978, *Astr. Astrophys.*, **63,** 103.

Conti, P. S. 1975, in *HII Regions and Related Topics,* Eds T. L. Wilson and D. Downes, Springer-Verlag, Berlin, p. 207.

Cruz-Gonzàlez, C, Recillas-Cruz, E., Costero, R., Peimbert, M., Torres-Peimbert, S. 1974, *Rev. Mexicana Astr. Astrofis.*, **1,** 211 (CGO).

de Loore, C. 1979, in *IAU Symp. 83: Mass Loss and Evolution of O-Type Stars,* Eds P. S. Conti and C. de Loore, D. Reidel, Dordrecht, p. 313.

Freeman, K. C. 1977, in *The Evolution of Galaxies and Stellar Populations,* Eds B. M. Tinsley and R. B. Larson, Yale University Observatory, New Haven, p. 133.

Hacyan, S., Dultzin-Hacyan, D., Torres-Peimbert, S., Peimbert, M. 1976, *Rev. Mexicana Astr. Astrofis.,* **1,** 355.

Houk, N., Cowley, A. P. 1975, *The University of Michigan Catalogue of Two-Dimensional Spectral Types for the HD Stars,* **1,** University of Michigan.

Iben, I. jr. 1967, *A. Rev. Astr. Astrophys.,* **5,** 571.

Iben, I. jr. 1977, in *Advanced Stages of Stellar Evolution,* Eds P. Bouvier and A. Maeder, Geneva Observatory, p. 3.

Iben, I. jr., Truran, J. W. 1978, *Astrophys. J.*, **220,** 980.

Koester, D., Weidemann, V. 1980, *Astr. Astrophys.*, **81,** 145.

Larson, R. B., Tinsley, B. M. 1978, *Astrophys. J.*, **219,** 46.

Lequeux, J. 1979, *Astr. Astrophys.,* **80,** 35.

Lequeux, J., Peimbert, M., Rayo, J. F., Serrano, A., Torres-Peimbert, S. 1979, *Astr. Astrophys.* **80,**155.

Lesh, J. R. 1968, *Astrophys. J. Suppl. Ser.,* **17,** 371.

Lesh, J. R. 1972, *Astr. Astrophys. Suppl. Ser.*, **5,** 129.

Lesh, J. R, 1979, in *IAU Coll. 47: Spectral Classification of the Future,* Eds M. F. McCarthy, A. G. D. Phillip, G. V. Coyne, Vatican Observatory, p. 81.

Luck, R. E., Bond, H. E. 1980, *Astrophys. J.*, **241,** 218.

Mallik, D. C. V. 1980, *Astrophys. Sp. Sci.*, **69,** 133.

Miller, G. E., Scalo, J. M. 1979, *Astrophys. J. Suppl Ser.,* **41,** 513 (MS).

Ostriker, J. P., Richstone, D. O., Thuan, T. X. 1974, *Astrophys. J.*, **188,** L87 (ORT).

Ostriker, J. P., Thuan, T. X. 1975, *Astrophys. J.*, **202,** 353.

Pagel, B. E. J., Patchett, B. E. 1975, *Mon. Not. R. astr. Soc.*, **172,** 13.

Peimbert, M. 1977, in *Topics on Interstellar Matter*, Ed. H. van Woerden, D. Reidel, Dordrecht, p. 249.

Peimbert, M. 1978, in *IAU Symp. 76: Planetary Nebulae*, Ed. Y. Terzian, D. Reidel, Dordrecht, p. 215.

Reeves, H. 1975, in *Atomic and Molecular Physics and the Interstellar Matter*, Eds R. Balian, P. Encrenaz, J. Lequeux, North Holland, Amsterdam, p. 591.

Sneden, C, Lambert, D. L., Whitker, R. W. 1979, *Astrophys. J.*, **234,** 964.

Tinsley, B. M. 1979, *Astrophys. J.,* **229,**1046.

Tinsley, B. M. 1980, *Astr. Astrophys.*, **89,** 246.
Truran, J. W., Cameron, A. G. W. 1971, *Astrophys. Sp. Sci.,* **14,** 178.
Twarog, B. A. 1980, *Astrophys. J.*, **242,** 242.
Weidemann, V. 1977, *Astr. Astrophys.*, **59,** 411.
Wheeler, J. C, Miller, G. E., Scalo, J. M. 1980, *Astr. Astrophys.*, **82,** 152.

J. Astrophys. Astr. (1981) **2,** 187–199

Intersteller Masers: The Influence of the Geometrical Shape on the Radiation Properties

Erich Bettwieser *Universitats-Sternwarte, Geismarlandstr. 11, D-3400 Göttingen, W. Germany*

Received 1981 April 4; accepted 1981 May 28

Abstract. The relation between the minimum and the maximum of the energy density of the microwave field is important in determining the internal physical conditions in a maser source and is directly connected with the size of the emission spot. This relation is investigated for models of homogeneous maser clouds for three different geometries: a thin tube, a thin disk and a sphere.

For substantial degrees of saturation, an approximate analytical calculation scheme is presented. The radiation properties found satisfy the transfer and the rate equations well. As expected, the analysis supports the long standing view that the active medium is 10 to 100 times larger than the interferometer size. Here the real purpose is to provide some insight into the dependence of the radiation characteristics on the geometrical shape of the emission region. The luminosity is only slightly affected by the shape of the emitting region (for the same volume). However, the angular variation of the intensity and the peak intensity of the rays reflect sensitively on the geometrical shape.

Key words: cosmic masers—radiative transfer—influence of geometry

1. Introduction

It is a well established fact that the angular size of some OH and H_2O emitting regions is very small; one of the smallest being 0·0003 arcsec for a H_2O maser in the H II region W49. Therefore the brightness temperature is very high, reaching 10^{15} K in an extreme case (for a general review *cf.* Goldreich 1975 or Cook 1977).

One model for a cosmic maser consists of a spherical region in which an inverted population is created in a two level atom. The pump is described in a phenomenological way. Even this simple model allows us to gain a general insight into the

properties of cosmic masers (*cf* . Litvak 1971; Goldreich and Keeley 1972; Litvak 1973; Lang and Bender 1973; Bettwieser and Kegel 1974; Keeley 1974; Bettwieser 1976).

In general the differential equations describing the transfer of maser photons can not be solved analytically, since they present a non-local and non-linear two point boundary problem even in the simplest approximation. On the other hand, numeri cal solutions are difficult to construct since within the model the stimulated emission process enhances not only the physical signal but also the numerical errors. The total enhancement can be quite large (intensity = 10^{10} times the source function) and is highly non-linear; therefore one is faced with the real computational problem of extreme non-LTE (*cf.* Jefferies 1968; Lang and Bender 1973; Bettwieser and Misselbeck 1977; Kegel 1979). We note that even the idea of an Aitken or Steffensen-transformation seems to be of restricted use.

A model which can be discussed analytically is very useful, even if the model is not entirely realistic. This is especially true if the stimulated emission rate dominates over the pumping and relaxation rates. This situation is called the saturation of the masing medium. In saturated masers the amplification coefficient depends on the value of the intensity and on its frequency and directional dependence (Bettwieser and Kegel 1974). In the following, we neglect the effect of saturation by signals of different frequencies travelling in different directions. We use an isotropic induced transition rate which is proportional to the mean intensity J_ν. This is the correct expression in the limiting case of an extremely anisotropic, *i.e.* unidirectional radiation field. Therefore it is a good approximation for filamentary-type amplifiers as well as in the outer parts of a spherical maser, provided most of the radiation is concentrated in a very small solid angle.

In the next two sections we consider and intercompare saturated radiation transfer for three different geometrical shapes. We note that the strictly one-dimensional homogeneous maser is an exception. All its radiation properties can be studied completely in terms of the solution of a transcendental equation (*cf.* Maeda and Yariv 1973). In this case our results can be checked with this exact solution.

The notation and the microscopic model used are the same as in Bettwieser (1976). The general approximations are similar to the ones used by the authors cited above.

2. Radiation properties

We consider the radiative transport in a spectral line corresponding to a transition between a lower level 1 and upper level 2. The masing matter (H_2O, OH, SiO molecules) interacts with the line radiation field through the induced emission [$B_{21}N_2$ $(4\pi/c)\,J_\nu$] and with the heat bath in which the matter is embedded, through a collisional transition from level 2 to level 1 ($C_{21}\,N_2$); it also interacts with all matter levels m different from m = 1, 2. To take the last interaction into account we introduce the quantities R_1, R_2, C_1 and C_2. C_1 is the probability for transitions from level 1 to all states n $\neq$ *2;*R_1 is the rate of transitions from all states $n \neq 2$ to level 1; C_2 and R_2 are similar quantities for the level 2. The population densities N_i are determined from the steady state rate equations for balancing the population and depopulation of the two levels with an energy difference of $h\nu_0$.

In the approximation discussed in the introduction, the rate equations can be written as

$$R_1 + R_2 = C_1 N_1 + C_2 N_2 \tag{1a}$$

$$\dot{N}_1 = 0 = \left(A_{21} N_2 + B_{21} N_2 \frac{4\pi}{c} J_\nu - B_{12} N_1 \frac{4\pi}{c} J_\nu \right)$$

$$+ (C_{21} N_2 - C_{12} N_1) + (R_1 - C_1 N_1). \tag{1b}$$

The solution of equations (la) and (lb) provides the number densities N_i in the states $i = 1, 2$ which are needed in the field equation. The variation of the intensity I_ν along a line of sight in the direction e (unit vector) may be written as usual

$$(\mathbf{e} \cdot \nabla)\, I_\nu = - k_\nu I_\nu + k_\nu S_\nu. \tag{2}$$

Our fundamental equations do not describe quantum coherence effects which might be important in cosmic masers (Rosen 1974). Thus we assume that the electric field is the sum of several independent fields which yields Gaussian statistics by the central limit theorem. The observed radiation field shows indeed a Gaussian statistics (Evans *et al.* 1972) and furthermore the most probable signal amplified in saturated masers is the (noise-like) spontaneous emission. (In Appendix A it is shown that the radiation properties do not depend on the background signal provided the optical depth is large).

Due to the matter equation, k_ν and S_ν depend on the average line intensity. These dependences are characterized by certain threshold intensities I_s and I_m respectively (compare Bettwieser and Kegel 1974). The numerical difference of I_s and I_m is small, but the maser condition $k_\nu < 0$ (and $S_\nu < 0$) is equivalent to $I_\mathrm{s} < I_\mathrm{m}$.

Strong natural masers seem to favour saturated situations (*cf.* Goldreich, Keeley and Kwan 1973; Goldreich and Kwan 1974). In this case the interaction rate of the molecule with the line radiation field is larger than the interaction with the heat bath and with the pump. This can be written as $J_\nu > I_\mathrm{s}$. In the extremely saturated situation ($J_\nu \gg I_\mathrm{s}$) we have

$$k_\nu = (k_\nu^0 I_s) / J_\nu \quad ; \quad k_\nu^0 = \lim_{J_\nu \to 0} (k_\nu) \tag{3}$$

The same relation between the absorption coefficient k_ν and the average line intensity J_ν in the radio line applies in the general n-level system (Appendix B); but k_ν^0 and I_s depend on the line intensities of the connected infrared lines, too (*cf.* Bettwieser 1981). We note that equation (3) is a direct consequence of the conservation of energy. From the matter equations we take the result (*cf.* Bettwieser and Kegel 1974)

$$4\pi\, k_\nu^0\, I_s = h\nu\, \phi(\nu)\, [\{(A_{21} + C_{21}\, (\exp(\Delta\chi_{12}/kT) - 1))\, (R_1 + R_2)\}$$

$$+ \{R_1\, C_2\, g_2/g_1 - R_2\, C_1\}]/[C_1 + C_2\, g_2/g_1] \tag{4}$$

Here we have made use of the detailed balance assumption for the collisional relaxation (Δx_{12} is the energy separation of the two levels); $\phi(\nu)$ is the unsaturated profile of the absorption coefficient under the assumption that the profile is the same for stimulated absorption as well as emission. We have assumed $A_{iJ} \ll C_{ij}$ (compare numerical example preceding equation 15).

The rate of the effective energy thermalisation is represented by the first curly bracket of equation (4). If the second curly bracket is negative, it represents the rate of the energy which can in principle be pumped into the radiation field. The result expressed in equation (3) is now understandable: the total average stimulated emission ($-k_\nu J_\nu$) is limited by the pump effectivity ($-k_\nu^0 I_s$)

The luminosity of any extremely saturated maser source simply follows from the conservation of energy. For the sake of simplicity let us consider homogeneous configurations of high symmetry: a sphere (n = 3 for short), a thin disk (n = 2) and a narrow tube (needle) (n = 1). The diameter of the first two configurations as also the length of the needle is denoted by 2 R; the thickness of the disk and the radius of the needle is denoted by p ($p \ll R$); the Eddington flux integral is denoted as usual by H_ν. Then the luminosity $\sim R^{n-1}\, p^{3-n}\, H_\nu\,(R)$ is limited by the product of the pumped volume ($\sim R^n\, p^{3-n}$) and the rate of the energy density (erg cm^{-3} s^{-1} Hz^{-1}) generated by the pump ($-4\pi\, k_\nu^0\, I_s$). The emitted flux from the surface with its normal in the direction of the largest optical depth is found to be

$$H_\nu\,(R) \xrightarrow[\text{extremely saturated}]{} \frac{1}{n}(-k_\nu R)\, I_s \tag{5}$$

for n = 1, 2, 3. The H_ν moment of equation (2) yields the same result. We note that for $J_\nu \lesssim I_s$ the emitted flux is smaller by a factor $(1 + I_s/J_\nu)^{-1}$

The restriction to a *thin* disk (*needle*) is necessary in order to be sure that most of the energy flows outwards in the symmetry plane of the disk (along the needle axis). On the other hand a saturated *thick* disk would almost look like a sphere (see Section 3 for further discussion).

Extremely saturated masers are self-excited, since the line source function S_ν increases with increasing line intensity and is amplified, but any background signal is only amplified and the optical depth is limited (see below). In the extremely saturated limit the spontaneous generation of incoherent photons from the upper maser level is determined by

$$k_\nu S_\nu \xrightarrow[\text{extremely saturated}]{} (k_\nu^0\, I_s)\,(S_\nu^0/I_m) \tag{6}$$

which does not depend on J_ν. Here $I_m/(-S_\nu^0)$ is the relative pump strength, since it is given by the induced emission divided by the spontaneous emission, both quantities taken in the saturated limit. The stationary rate equations yield (*cf.* Bettwieser and Kegel 1974)

$$\frac{I_m}{-S_\nu^0} = \left[\frac{R_2 C_1 - R_1 C_2\, g_2/g_1}{R_1 + R_2} - C_{12}\left(\exp\left(\frac{\Delta\chi_{12}}{kT}\right) - 1\right)\right]\left(\frac{1}{A_{12}}\right). \tag{7}$$

We note that in the case of very strong pumping into the upper level ($R_2 \to \infty$)the relative pump strength is proportional to C_1/A_{21} This shows the importance of

the depopulation of the lower maser level in this context. Changing the gain, changes the luminosity, increasing the loss; the relative pump strength increases and drives the mean intensity gradient to a higher value. This changes the optical appearance of the source, too.

The solution of the radiation transport problem defined above is in general quite complicated. In order to elucidate the effects just noted we make use of an approximation. We start with the following expression for the average intensity J_ν at the radial coordinate r for each n

$$[J_\nu (r)]^2 = [H_\nu (R)]^2 [\Theta^2 + (r/R)^2]. \tag{8}$$

In principle this expression can be obtained from moment equations. However, the latter do not provide any possibility of calculating the quantity Θ. This can only be done by a self-consistent procedure (*cf.* Bettwieser 1976).

Equations (3) and (8) allow us to calculate the optical depth τ. We are specially interested in the optical depth for a ray passing through the centre of the emission region. τ (0) and τ (R) are the depths for matter at the centre (r=0) and at the end ($r = R$) of the region, respectively. From equation (5) we find the surprising result that τ does not depend on the value of the absorption coefficient *(cf.* Bettwieser 1976 in the n=3 case)

$$\tau(0) = -n \ln [\Theta^{-1} + (1+\Theta^{-2})^{\frac{1}{2}}] \quad ; \quad \tau(R) = 2\tau(0). \tag{9}$$

In the extremely saturated case we expect $\Theta \ll 1$, since we have $J(0) = H(R)\ \Theta$ by equation (8). This yields

$$\exp [-\tau(R)] \simeq (2/\Theta)^{2n}. \tag{10}$$

Introducing relative coordinates along the rays of integration in the transport equation (i.e. replacing (e.∇) by $.R\ \partial_z$ along the ray) one can see that the intensity has to be proportional to ($k_\nu^0\ I_s\ R$) (S_ν^0 / I_m) in the case of a self-excited emission region (background signal = 0). Thus a rough estimate of the intensity emitted in the radial direction (θ=0) is

$$I_\nu (R, \theta = 0) = (k_\nu^0\ R\ I_s) (S_\nu^0/I_m) (2/\Theta)^{2n}. \tag{11}$$

In Appendix A we discuss a more rigorous treatment which justifies the present approximation.

Since $\Theta \ll 1$ we expect the emitted intensity to be confined to a very narrow solid angle. In the n = 2, 3 geometries the polar angle between e and the radial direction is denoted by θ. Using the definitions of J and H we obtain, after linearisation

$$H_\nu (R)^2 \simeq [J_\nu (R)]^2 (\mathbf{e}.\mathbf{e}_r)^2 \simeq [J_\nu (R)]^2 (1-\theta^2). \tag{12a}$$

Combining equation (12a) and equation (8) we get $\theta = \Theta$. Thus the quantity Θ is a measure of the characteristic width of the centre to limb variation of the emitted intensity. If we compare the present result with a rigorous treatment (equation 4.17

in Bettwieser 1976) the implicitly used definition of the *apparent size* Θ in equation (12a) is

$$I_\nu^+ (R, \theta=\Theta) = \tfrac{1}{8}\, I_\nu^+ (R, \theta=0) \tag{12b}$$

According to equations (3) and (8) the population inversion peaks at the centre of the emission region (r =0), and Θ describes the average variation of the saturated inversion. Since rays going through the centre experience an extra amplification, the apparent size and Θ are directly connected; this interprets the formal proof for $\theta = \Theta$ given above.

The phenomenon just discussed is known to occur in laboratory lasers too (*cf.* Haken 1970). The amount of gain achieved in a neodym-glass laser is limited by 'super-radiance'. The latter is the stimulated emission driven by spontaneous emission within the laser rod. In view of equation (9) the matter near the end of the emission region sees a large radiation field since spontaneous emission from the other end is amplified by exp $(-\tau(R))$. The matter near the centre sees spontaneous emission amplified by $[\exp(-\tau(R))]^{1/2}$, but the amplified radiation field is seen from a larger solid angle. For a high gain maser or laser the different gain dominates over the geometrical factor and the saturated population difference is a decreasing function of the radial coordinate *r*. The self consistent solution is obtained as follows. We calculate J_ν(r=0), make use of the fact that I_ν (r=0) is isotropic and demand that the calculated central mean intensity be equal to $\Theta\, H_\nu(R)$

$$J(0) = I(0) \simeq (k_\nu^0\, R\, I_s)\,(S_\nu^0/I_m)\frac{1}{n+1}\exp(-\tau(0)) = \Theta\, H_\nu(R). \tag{13}$$

The additional factor $(n+1)^{-1}$ is derived in Appendix A. With the aid of equations (5) and (9) we find *(cf.* equation A10)

$$\Theta = \left\{2^n \frac{n}{n+1}(-S_\nu^0/I_m)\right\}^{\frac{1}{n+1}}. \tag{14}$$

This important result of our analysis connects the relative pump strength (equation 7) with (i) the saturated optical depth (equation 10), (ii) the intensity emitted in the radial direction (equation 11) and (iii) the apparent size of the emission region (equation 14). Since our definition of the apparent size leads in a sense to an apparent size which is too broad, the condition $H_\nu(R) \simeq I_\nu^+ (R, \Theta)\,\Theta^2/2$ dictated by self consistency turns out to be of restricted numerical accuracy though acceptable (see Bettwieser 1976 for a more accurate treatment of the spherically symmetric case).

We close this section with some remarks on the simple two level model we have adopted. The phenomenological pump rate R_i and the depopulation probability C_i can be interpreted within the scheme of a given multilevel system (compare Appendix B). In this way some ideas on the processes by which population inversion is produced can be obtained (Goldreich and Kwan 1974). A detailed analysis requires, of course, a solution for the radiative transfer and for lines other than the maser line itself. This new situation is however very simple if cold dust of high density

is present, since an internal heat sink for the (infrared) photons limits the energy density within the other lines. Therefore the microscopic description is modified (equations (4) and (7), depend on the infrared and dust properties). However our main results in equations (4), (8), (10) and (14) are still valid (Bettwieser 1981) at least in regions which are optically thick in the infrared lines.

3. Discussion

We have found that the apparent size of the emitting region is determined by the relative pump effectivity equation (7). Thus the apparent size can be much smaller than the physical size. Our results are in good agreement with those of Goldreich and Keeley (1972) or Lang and Bender (1973). These authors considered uniformly pumped spherical regions (n = 3). Goldreich and Keeley considered tube-shape geometries too.

The assumption of a particular geometrical configuration is still open to question. Cook (1968), for example, has discussed long and thin emitting regions. In this case we can only see the radiation if the axis is pointed roughly towards the earth. The commonly observed velocity differences of ~10 km s^{-1} among the individual masers in a maser 'nest', suggest that long amplification paths may be confined to small solid angles.

Litvak (1973) included in his analysis effects of inhomogeneous pumping and of bydrodynamic motion. He considered a spherical region which is expanding or contracting with the pump rate increasing towards the edge. This results in a shell like structure. In the case of the source complexes W3–OH and W49–H_2O the increase of 10 km s^{-1} in radial velocity along a line of sight of 10^{17} cm is interpreted as a rotating disk seen nearly edge-on (Litvak 1971).

In general the radiation characteristics of a model will depend sensitively on the geometry assumed. In the unsaturated case the intensity emitted mainly reflects the geometrical shape, the latter is even amplified by a factor of exp ($|\tau|$).The high brightness temperatures of the stronger H_2O and OH lines can only be reached in saturated masers. In the saturated case the emitted flux $4\pi H_\nu(R)$ (equation 5) is almost independent of the geometrical shape. This has been pointed out by others too. For example, Lang and Bender (1973), while discussing the case of an ellipsoidal maser, find that saturation tends to make it look more spherical than it really is.

In the unsaturated case the apparent size reflects again the geometry, *i.e.* it depends on the size of the emission region ($\Theta \sim R^{-1/2}$). In the saturated case the apparent size Θ is mainly determined by the relative pump strength. The latter is the ratio of the input signal $\int dv\ (k_\nu S_\nu)$ to the amplification power provided by the pump $\int dv\ (-k_\nu^0 I_s)$. The observed value of the apparent size Θ and a certain knowledge of the geometrical shape (*i.e.* the parameter n) determine the relative pump strength (equation 14).

For comparison of the different geometries we adopt the following parameters. For the Einstein A-coefficient we choose $A_{21} = 2 \times 10^{-9}$ s^{-1} which is appropriate for the $6_{12} - 5_{23}$ microwave transition in water. We assume $\Delta\nu/\nu = 10^{-6}$, $R_1 + R_2 = 0.1\ N_{H_2O}$, $R_1 - R_2 = -10^{-3}\ N_{H_2O}$ s^{-1} and for the losses $C_1 = C_2 = 1.0$ s^{-1}; $C^{12} = 0{\cdot}1$ s^{-1}. To be specific we assume the maser emission to stem from a cocoon around

a newly born star (*cf.* Yorke 1979, 1980 and Bettwieser 1981); therefore we adopt $R = 10^{17}$ cm, $T = 10^3$ *K*, $N_{H_2} = 10^9$ cm^{-3} and $N_{H_2O} = 10^4$ cm^{-3}. The chosen parameters and the relations given above yield

$$\left.\begin{aligned} &\int d\nu\, k_\nu^0 I_s = 5 \times 10^{-25}\ \text{erg cm}^{-3}\ \text{s}^{-1}, \\ &I_m / |S^0| = 5 \times 10^6, \\ &-k_{\nu_0}^0 R = 6 \times 10^3. \end{aligned}\right\} \tag{15}$$

The energy density at the centre of the cloud $(4\pi/c)\, J_\nu(0)\, \Delta_\nu$ is, according to equation (14), a factor of 2236 for $n = 1$, 123 for $n = 2$ and 30 for n = 3 smaller than the energy density at the edge. The ratio of the apparent to the physical size of the cloud changes with the geometrical shape in the same manner.

The first point we wish to make concerning this result is that the degree of saturation increases with n (compare Fig. 1 and Fig. 2). We therefore combine equation (14) with equation (13). By rearrangement of the expression $J(0)/I_s > 1$ we find

$$(-k_\nu^0 R) \geqslant (2n/2^{n+1})^{\frac{n}{n+1}} \left(\frac{I_m}{-S_\nu^0}\right)^{\frac{1}{n+1}}. \tag{16}$$

Inserting the values given above this relation is true in the $n = 2, 3$ cases but only marginally fulfilled for the $n = 1$ geometry. A partial or unsaturated core would make the source look broader.

We interpret the strong dependence of $J(R)/J(0)$ on the geometrical configuration by the following thought of experiment. Deform a sphere of radius R to a disk of radius R and thickness p ($p \ll R$). Since the disk is very thin, saturated emission occurs only perpendicular to the symmetry axis. In the extremely saturated limit the

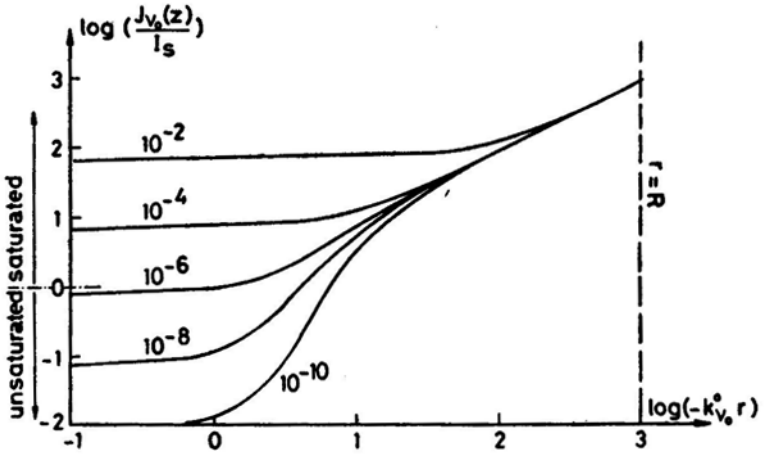

Figure 1. For the $n = 1$ case (see text) the variation of the mean intensity J_ν as a function of the radial coordinate r is shown. J_ν is in units of the saturation intensity and r in units of the unsaturated amplification length $(k_{\nu_0}^0)^{-1}$ at the line centre $\nu = \nu_0$. The unsaturated optical depth is $k_{\nu_0}^0 R = -10^2$ and the inverse of the relative pump efficiency $(-S_\nu^0/I_m)$ varies from 10^{-2} to 10^{-10} Note that the region where $J_\nu(r)$ is almost constant varies as $(-S_\nu^0/I_m)^{1/2}$

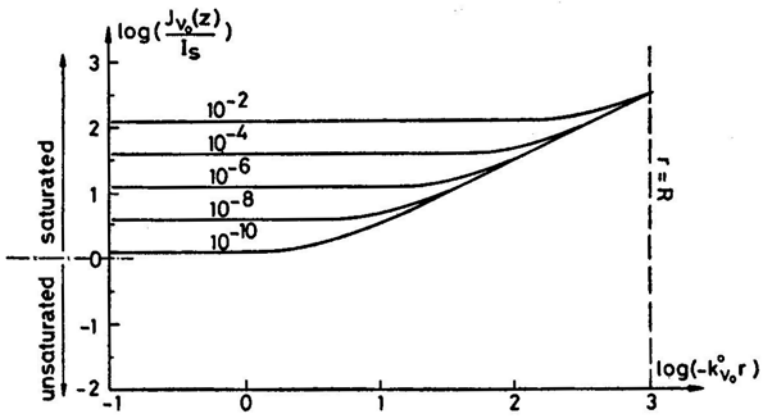

Figure 2. Same as Fig. 1 for the spherically symmetric case (n = 3) adopting the same parameters. Note that $J_\nu(R)$ decreased by a factor of 3 and the central isotropic region varies now like $(-S^0_\nu/I_m)^{1/4}$.

stimulated emission of radiation eats up the energy delivered by the pump. Therefore the radial flux increases by $n = 3 \rightarrow n = 2$ transition (*cf.* equation 5). We note that the luminosity decreases during this transition simply because the emitting surface area decreases. The increase of the flux is small. However, the angular dependence of the photon field and the value of the radial beam is very different *(cf.* equations 11 and 14). I_ν (R, $\theta = 0$) increases by a factor larger than $I_m/(-S^0_\nu)$! The formal reason for this dramatic behaviour is of course the sensitive dependence of exp ($|\tau|$) on n (equation 10), which rests on equation (8). The latter is almost exact in he n = 1 case and proves to be a very good approximation in the n = 3 case (Bettwieser 1976).

The models discussed above are of course very different from the emission regions found in nature. One emission spot may consist of many cloudlets each of them having a different fractional Brownian surface. Nevertheless, as long as our geometrical description is right on the average and if the whole region is saturated, the irregularity of the geometry does not play an important role. The emitted radiation reflects the radial variation of its own energy density, which has to be rather smooth in the saturated limit. This aspect is particularly intuitive, but might be proved at least for a certain class of Hausdorff Besicovitch dimensions (*cf.* Mandelbrot 1978) characterizing the structure of the foam-like emission region.

Appendix A

Integration of the Line Transfer Equation

We introduce a relative coordinate z along a central ray (p = 0) which varies from $z = -1$ to $z = +1$ and consider the intensity $I^+_\nu(z)$ propagating in the positive z direction. Using equations (8), (3), (5) and (6) we find for our transport problem (equation 2)

$$\frac{\partial}{\partial z} I^+_\nu(z) = \frac{n}{(z^2 + \Theta^2)^{1/2}} I^+_\nu(z) + nH_\nu(R)\,(-S^0_\nu/I_m). \tag{A1}$$

The optical depth $\tau_\nu(z)$ is defined by

$$|\tau_\nu(z)| = \int_{-1}^{z} \frac{n}{(z^2+\Theta^2)^{1/2}}\,dz \tag{A2}$$

and turns out to be

$$\exp\left(|\tau_\nu(z)|\right) = \left\{[(z^2+\Theta^2)^{1/2}+z]/[(1+\Theta^2)^{1/2}-1]\right\}^n. \tag{A3}$$

We assume symmetric boundary conditions on the intensity

$$I_\nu^+(z=-1) = I_\nu^-(z=+1) = J_b. \tag{A4}$$

The formal solution of equation (A1) is then given by

$$I_\nu^+(z) = \left[J_b + nH_\nu(R)\,(-S_\nu^0/I_m)\int_{-1}^{z} e^{-|\tau|}\,dz\right] e^{|\tau(z)|}. \tag{A5}$$

The integral in equation (A5) can be calculated analytically, but the result is opaque. Therefore we do this integration in an approximate way assuming $\Theta \ll 1$. Our aim is to calculate $J_\nu(0)$ and to construct a self consistent solution (*cf.* equation 13).

First we consider $-1 \leqslant z \lesssim -\Theta$. To a fairly good approximation we can write for the z dependent part of equation (A3)

$$(\Theta^2+z^2)^{1/2} - |z| \simeq \frac{1}{2}\frac{\Theta^2}{|z|}. \tag{A6}$$

Accordingly we find

$$\int_{-1}^{-\Theta} \exp\left(-|\tau(z')|\right) dz' \simeq \frac{(-\Theta)^{n+1}+1}{n+1}. \tag{A7}$$

Next we consider $-\Theta \leqslant z \leqslant 0$. In this range the left hand side of equation (A6) varies from $(\sqrt{2}-1)\,\Theta$ to Θ. Therefore one can write

$$\int_{-\Theta}^{0} \exp\left(-|\tau(z')|\right) dz' \simeq \left(\frac{\Theta}{2}\right)^n \Theta\,. \tag{A8}$$

Inserting equations (A3), (A7) and (A8) into the formal solution equation (A5) we find the following result

$$I_\nu^+(0) = \left[J_b + nH_\nu(R)\,(-S_\nu^0/I_m)\left(\frac{1+(-\Theta)^{n+1}}{n+1} + \frac{\Theta^{n+1}}{2^n}\right)\right]\left(\frac{2}{\Theta}\right)^n. \tag{A9}$$

In the present approximation ($\Theta \ll 1$) the integral in equation (A5) contributes to the result (equation A9) only a factor $(n + 1)^{-1}$ (compare with equation 13). Our ansatz equation (8) demands that $I^{+}_{\nu}(0)$ is equal to $\Theta\, H_{\nu}(R)$. This yields

$$\Theta^{n+1} = \left\{ \frac{J_b}{H_\nu(R)} + \left(\frac{n}{n+1} \right) (-S^0_\nu / I_m) \right\} 2^n. \tag{A10}$$

Equation (5) and $I_s \simeq I_m$ imply that the results in the main text apply as long as

$$J_b \ll \left(\frac{-k^0_\nu R}{n+1} \right) | S^0_\nu |. \tag{A11}$$

Since any background signal may be of the order S^0_ν he maser is self-excited if the unsaturated optical depth ($-k^0_\nu R$) is large.

We note that the unsaturated parts of the spontaneous emission neglected in equation (Al) contribute in the same way as J_b (*i.e.* replace J_b by $(J_b - S^0_\nu)$)

Concerning the frequency dependence of Θ we observe that in the self-excited limit $\Theta(\nu)$ does not vary over the line, but since $k^0_\nu \sim \phi\ (\nu) \sim \exp\ [-(\Delta^\nu/\Delta^\nu D)^2]$ ($\Delta^\nu D$ being the Doppler width), the limiting case of equation (All) is not fulfilled in the wings of the line. Only the core of the line is self-excited.

Appendix B

The Multilevel Rate Equations and its Two Level Interpretation

The purpose of this appendix is to interpret the phenomenological pump model introduced in the main text. To keep matters simple we consider the general transition rate t_{kl} which contains all radiative and nonradiative transitions from level k to level l. The maser levels are the $l = 1$ (lower) and $l = 2$ (upper) and the t_{k1}, t_{1k}, t_{k2}, t_{2k} do not, by definition, include the radiative transitions between the two maser levels. The latter are described in the approximation discussed in the introduction. For convenience we introduce $\beta_{12} = (4\pi/c)\ B_{12}$. Then, for the levels participating directly in the maser process, the rate equations read (*cf.* Haken 1970)

$$\dot{N}_1 = \sum_{l \neq 1} t_{l1}\, N_l - N_1 \sum_{l \neq 1} t_{1l} + \beta_{12}\, J_\nu\, (N_2 - N_1), \tag{Bl}$$

$$\dot{N}_2 = \sum_{k \neq 2} t_{k2}\, N_k - N_2 \sum_{k \neq 2} t_{2k} - \beta_{12}\, J_\nu\, (N_2 - N_1). \tag{B2}$$

The levels which participate in the pump process but do not couple directly to the levels 1 and 2 are populated according to

$$\dot{N}_l = \sum_{m \neq l} t_{ml}\, N_m - N_l \sum_{n \neq l} t_{ln}. \tag{B3}$$

The above equations are not independent of each other, since the total occupation number N_0 is a conserved quantity

$$N_0 = (N_1 + N_2) + \Big(\sum_{l \neq 1,2} N_l \Big). \tag{B4}$$

Due to the latter equation we can omit *e.g.* equation (B2). We replace N_1 and N_2 by the new variables $(N_1 + N_2)$ and $\Delta N = N_1 - N_2$, and consider a stationary situation $N_i = 0$. The resulting inhomogeneous set of linear equations $Ax = b$ with $x = (N_1 - N_2, N_3, N_4 ...)$ is solved by Cramer's rule. On account of this general theorem we can write

$$(N_1 - N_2) = (\det A_1)/(\det A) \tag{B5}$$

The term $\beta_{12} J_\nu (N_2 - N_1)$ occurs only in one single equation, *e.g.* the first one. In the matrix A_1, the first column of A is replaced by the inhomogenity introduced through equation (B4). Therefore A_1 and its determinant does not depend on J_ν. The total determinant det A depends linearly on J_ν. Therefore the absorption coefficient $k_\nu \sim (N_1 - N_2)$ must have the following structure

$$k_\nu = \frac{h\nu}{c} B_{12} \phi(\nu) (\Delta N^0)/(1 + J_\nu/I_s). \tag{B6}$$

Here ΔN^0 and I_s do not depend on the maser line intensity J_ν. They are determined by the transition rates t_{em}. The latter contain (i) collisions (C_{ij}-probabilities), (ii) spontaneous radiative transitions (A_{ij}-Einstein coefficient) and (iii) induced radiative transitions [B_{ij} $(4\pi/C)$ J_{ij}]. We rediscover the structure of the two level system, especially the saturation behaviour of equation (3).

Our phenomenological pump rates R_j and the depopulation probabilities C_j can be interpreted in a complete induction process (*i.e.* consider ρ levels and then $\rho + 1$ levels). To keep matters simple we consider a 3-level system, where the lower maser transition is maser-active (*cf.* Bettwieser 1981). If the upper transition in the 3-level system is maser-active a cyclic permutation of the level numbers ($1 \to 2$, $2 \to 3$, $3 \to 1$) allows us to apply the former result too. In any case det A of equation (B5) is a positive definite quantity, but det A_1 is not! Thus ΔN^0 describes some conditions specified by the transition rates t_{em} for maser action to occur (*i.e.* $\Delta N^0 < 0$). We denote by $n(\Delta N^0)$ the numerator of ΔN^0 (the denominator of ΔN^0 is a part of det A). In the three level systems we have

$$n(\Delta N^0) = \Big[(t_{31} + t_{32}) \Big\{ A_{21} + C_{21} \Big(\exp\Big(\frac{\Delta \chi_{12}}{kT} \Big) - 1 \Big) \Big\} + (t_{31}\, t_{23} - t_{32}\, t_{13}) \Big] N_0. \tag{B6}$$

The comparison with equation (4) shows that $R_1 \sim t_{31}$, $R_2 \sim t_{32}$, $C_2 \sim t_{23}$, $C_1 \sim t_{13}$. By a complete induction one might prove more general relations.

The principle physics of three and four level systems has been discussed by Maiman (1961), Haken (1970) and Bettwieser (1981) among others.

References

Bettwieser, E. 1976, *Astr. Astrophys.*, **50,** 231.
Bettwieser, E. 1981, *Astr. Astrophys.*, **93,** 8.
Bettwieser, E., Kegel, W. H. 1974, *Astr. Astrophys.*, **37,** 291.
Bettwieser, E., Misselbeck, G. 1977, *Astr. Astrophys.*, **61,** 567.
Cook, A. H. 1968, *Mon. Not. R. astr. Soc.*, **140,** 299.
Cook, A. H. 1977, *Celestial Masers,* Cambridge University Press.
Evans, N. J., Hills, R. E., Rydbeck, O.E.H., Kollberg, E. 1972, *Phys. Rev.,* **A6,** 1643.
Goldreich, P. 1975, in *Atomic and Molecular Physics and the Interstellar Matter,* Eds R. Balian, P. Encrenaz, J. Lequeux, North Holland, Amsterdam, p. 409.
Goldreich, P., Keeley, D. A. 1972, *Astrophys. J.*, **174,** 517.
Goldreich, P., Keeley, D. A., Kwan, J. Y. 1973, *Astrophys. J.*, **179,** 111.
Goldreich, P., Kwan, J. 1974, *Astrophys. J.,* **191,** 93.
Haken, H. 1970, in *Encyclopedia of Physics*, **XXV/2C,** Ed. L. Genzel, Springer-Verlag, Berlin.
Jefferies, J. T. 1968, *Spectral Line Formation*, Blaisdell, Waltham.
Keeley, D. A. 1974, *Astrophys. J.*, **192,** 601.
Kegel, W. H. 1979, *Astr. Astrophys. Suppl. Ser.*, **38,** 131.
Lang, R., Bender, P. L. 1973, *Astrophys. J.*, **180,** 647.
Litvak, M. M. 1971, *Astrophys. J.*, **170,** 71.
Litvak, M. M. 1973, *Astrophys. J.*, **182,** 711.
Maeda, H., Yariv, A. 1973, *Phys. Lett.*, **43A,** 383.
Maiman, T. H., 1961, *Phys. Rev.*, **123,** 1145.
Mandelbrot, M. M. 1978, *Form*, *Chance and Dimension*, Freeman, San Francisco.
Rosen, R. A. 1974, *Astrophys. J.*, **190,** L73.
Yorke, H. W. 1979, *Astr. Astrophys.,* **80,** 308.
Yorke, H. W. 1980, *Astr. Astrophys.*, **85,** 215.

J. Astrophys. Astr. (1981) **2,** 201–212

Long Term Variations in Solar Flare Activity

J. N. Goswami, R. Jha and D . Lal *Physical Research Laboratory, Ahmedabad 380009*

Received 1981 April 4; accepted 1981 June 8

Abstract. A statistical analysis of the contemporary (1954–1975) solar flare particle events has been made for the parameters F (integrated, proton fluence in cm^{-2} in an event with kinetic energy above 10 MeV) and R_0 (the characteristic rigidity). These data are compared with the long-term averaged values determined from stable- and radio-nuclide measurements of lunar samples. The analysis shows that the ancient solar flare proton spectrum was harder (higher R_0 values) compared to that observed in contemporary flares. A similar analysis can not be made for the mean long-term averaged flux ($\bar{J}$, cm^{-2} s^{-1}), since the contemporary averages suffer from an uncertainty due to the statistics of a single event. However, the average flux estimates for time durations $\langle T \rangle$ exceeding 10^3 yr, are free from such uncertainties. The long-term averaged $\bar{J}$ values obtained over different time scales (10^4 – 10^6 yr) suggest a possible periodic variation in solar flare activity, with enhanced flux level during the last 10^5 yr. The available data rule out the occurrence of giant flares, with proton fluence exceeding 10^{15} cm^{-2} during the last million years.

Key words: solar flares—solar activity—long term variations

1. Introduction

The variability in the solar output of matter and radiation as also in the magnetic fields associated with solar active regions is of considerable importance in the studies of aeronomy, meteorolgy, atmospheric physics as well as stellar land solar physics. The most commonly used indicators of solar activity are sunspots, flares, plages and related phenomena. These phenomena, in one way or the other, are related to solar magnetic fields and hyperthermal processes. Our knowledge of the basic processes involved is still poor in spite of the facts that the 11 yr sunspot cycle was recognized

about a hundred and fifty years ago, that the corroborating records exist from the seventeenth century and that the solar flare events have been studied in great detail during the last three decades (Schwabe 1843; Webber *et al.* 1963; McDonald, Fichtel and Fisk 1974; Eddy 1976). An important supplement to direct observations is a study of the behaviour of the Sun over long periods of time. This would be of great importance for the following reasons. First, the sunspot activity itself has been recognised as exhibiting a multiple periodicity over and above the 11 yr cycle, which extends to the duration of the record itself. Second, direct observations of solar electromagnetic processes are restricted to only a few sunspot cycles. Besides the 11 and 22 yr cycles, periodicities of 55 and 90 yr seem to be well established (Wittmann 1978). In the absence of direct observations extending over long periods of time, a near constancy of the sun has been assumed although theoretical models and scanty experimental data have questioned this off and on. Only recently, Eddy was able to bring forth a rather conclusive evidence that even on the time scale of three centuries for which sufficient direct solar measurements and indirect evidence relating to solar phenomena exist, the Sun can not be called a constant star (Eddy 1976,1977). He showed that the envelope of the 11 yr solar activity has been fluctuating considerably. He was able to extend the studies to variations in solar activity over time periods of about 7000 yr B P by tying on to the ^{14}C tree ring chronology (Eddy 1977). He hypothesised that the Sun has had sustained periods of high and low activities of duration of the order of a century, back to 7000 yr B P. These periods have been designated by him as Grand Maxima and Grand Minima. An example of the latter is the Maunder minimum during 1645–1715 A D. How can a variation in the solar activity change the ^{14}C tree ring record? This question was recently considered in detail by Castagnoli and Lal (1980) and it could be shown that Eddy's hypothesis is tenable since changes in solar activity produce modulation in galactic cosmic ray intensity which is adequate to account for the observed ^{14}C deviation in tree rings. Thus although there seems to exist a strong case for Maunder minimum type of solar minima, one must look for additional evidence.

In this paper, we present an intercomparison between the contemporary flare data (1956-1973) based on rocket and spacecraft experiments and the long term ($> 10^4$ yr) averaged solar flare data, based on stable- and radio-nuclide studies of lunar samples.

2. Contemporary solar flare data

Direct measurements at high altitudes and latitudes provided the first insight into the composition and the energy spectrum of solar flare radiation. Pioneering work in this field was carried out by the Goddard group (Biswas and Fichtel 1965; McDonald Fichtel and Fisk 1974) which exposed nuclear emulsion detectors using rockets and balloons over a decade (1960–1972). For other investigations contributing to information about solar flare events, reference is made to Webber *et al.* (1963), McDonald (1963), Weddel and Haffner (1966), Crawford *et al.* (1975) and Biswas (1972). In the present paper we make use of these basic data which also allow one to make cumulative estimates for each event. Such estimates have been made by Webber *et al.* (1963) and Weddel and Haffner (1966) for events during solar cycle 19 (1954–1964). For solar cycle 20(1965-1975) much more reliable information is available based on the counting rate data obtained by the Solar Proton Monitor Experiment (SPME)

on the satellites IMP-4, 5, and 6 (Bostrom *et al.* 1967–1973). An intercomparison was made between the four sets of data and a mutual consistency in event integrated fluxes found to be better than 25 per cent (King 1972).

All available information on solar flare events, some of which has been briefly summarised above, was carefully considered by Reedy (1977) who has compiled fluences (F) of all solar events during solar cycles 19 and 20, for events with total proton fluence exceeding 10^7 cm^{-2} and kinetic energies exceeding 10 MeV. He has also given fluence data separately for energies above 30 MeV and 100 MeV, and above 30 MeV and 60 MeV respectively for solar cycles 19 and 20. We will use these data as a representative sample of contemporary solar flare events. We will also confine ourselves to the method of representing the differential energy spectrum on an exponential rigidity basis

$$d\,N/dR = K \exp(-R/R_0), \tag{1}$$

where R is the rigidity in MV and R_0 the characteristic rigidity in MV. Here dN/dR denotes the omni-directional (4π) differential rigidity flux and K is a constant. Such a representation describes the energy spectrum fairly well in the interval 5-100 MeV n^{-1} for both singly and multiply charged particles (Lal 1972). Typical values of R_0 lie between 50 and 100 MV.

3. Ancient solar flare data

There are not many ways of studying long term (prehistoric) characteristics of solar flares. For this study one has to find some vestigial records of flare particles of which nuclear effect is the only known example. Fortunately, there exist extensive studies of two flare particle-induced nuclear effects in extraterrestrial samples: (i) Production of isotopes in the target matrix, both stable and radioactive, due to nuclear interactions, and (ii) solid state damage of the crystalline structure of the constituents in the target matrix as a result of ionisation losses suffered by charged particles.

In the case of the former, stable products *e.g.* He and Ne isotopes, and radioactive isotopes, *e.g.* ^{14}C, ^{26}A1, ^{53}Mn, ^{59}Ni and ^{81}Kr, have been detected. In the case of the latter, etch tracks and thermoluminescence effects have been studied. Although these flare effects could be detected in meteorite samples (Amin *et al.* 1969; Lal and Rajan 1969; Pellas *et al.* 1969) quantitative studies of flare effects began only after the acquisition of the first lunar samples (Shedlovsky *et al.* 1970; Lai *et al.* 1970; Crozaz *et al.* 1970). For a review of the studies of extraterrestrial rock samples conducted with a view to determining prehistory of cosmic radiation, both galactic and solar, reference is made to Lal (1972).

In this paper we concern ourselves only with the long term averaged proton fluxes and spectra, based on the studies of radionuclides ^{14}C, ^{26}A1,^{53}Mn and ^{81}Kr (Wahlen *et al.* 1972; Boeckl 1972; Bhattacharya and Bhandari 1976; Kohl *et al.* 1978; Yaniv, Marti and Reedy 1980) and stable nuclide ^{3}He (Venkatesan *et al.* 1980) in lunar samples. The radioactive isotopes provide flux and energy spectra of protons, averaged over time periods (10^4 yr to ~ 5 Myr) comparable to their mean lives. The presently available ^{3}He data also cover a similar range since the exposure ages of the two rocks studied are about 1 Myr.

A convenient way to express the solar proton spectrum is to characterise it by two parameters: (i) characteristic rigidity R_0, and (ii) the integrated omni-directional (4π) flux above 10 MeV kinetic energy J (> 10 MeV).

The long term averaged values for J (> 10 MeV) and R_0, inferred from lunar data, lie in the range of 70 to 200 cm^{-2} s^{-1} for J, and 100-150 MV for R_0.

4. Comparison of contemporary and ancient flare data

We will now compare the ancient and the contemporary flare data. However, before we proceed, we will evaluate the general features in the distribution of the flare particle energy spectra and fluences in different events for the contemporary data. Such an analysis is necessary because the contemporary data are limited to the past three decades, and it is important to evaluate the nature of fluctuations between the events to assess the meaning of possible differences between the two sets of data.

A number of useful analyses of contemporary flare data have been made earlier with a view to assessing the effects of solar flare radiation due to exposures near Earth as well as during interplanetary flights on both man and hardware (Webber *et al.* 1963; Modisette, Vinson and Hardy 1965; Weddel and Haffner 1966, Divine 1973; King 1974; Kolomenskii *et al.* 1978). Primary emphasis in these investigations has been on deducing the probability of getting a total fluence which exceeds a certain specified value during a mission of specified duration. We will however be more concerned with the details of the distribution of fluence F, and characteristic rigidity R_0, and the relationship between them in order to deduce expected long term averaged flare spectra. Analyses reported here is more detailed than those of the earlier workers; the gross features are however similar to those obtained earlier.

4.1 *Statistical Analysis of Contemporary Solar Flare Data*

As mentioned earlier, we adopt the compilation of Reedy (1977) for solar flare events during 1954–1975, encompassing solar cycles 19 and 20. This compilation lists 65 flare events with fluence exceeding 10^7 cm^{-2} for protons of kinetic energy above 10 MeV. A statistical analysis of these events leads to three important conclusions.

1. The F and R_0 values both follow a lognormal distribution. As an illustration, we show in Figs 1 and 2 the observed distribution and the log-normal fits for F and R_0 respectively.
2. Flare events of the solar cycles 19 and 20 are all statistically very similar with respect to the R_0 values (Table 1). The F values are however appreciably different (Table 2). This difference may be genuine, but in view of the difference of three orders of magnitude in the measured F values, the difference in μ_n and σ_n values may not be statistically significant (μ_n = mean of In x's and σ_n = standard deviation of In x's; Aitchison and Brown 1957). The imprecise determination of the statistical parameters for F, however, is not of any serious consequence as discussed later.
3. Non-parametric test shows that there is no correlation between F and R_0 in individual events *i.e.* in any given event of a particular fluence F_1, all values of R_0 are equally probable. We checked by setting up a contingency table the null-

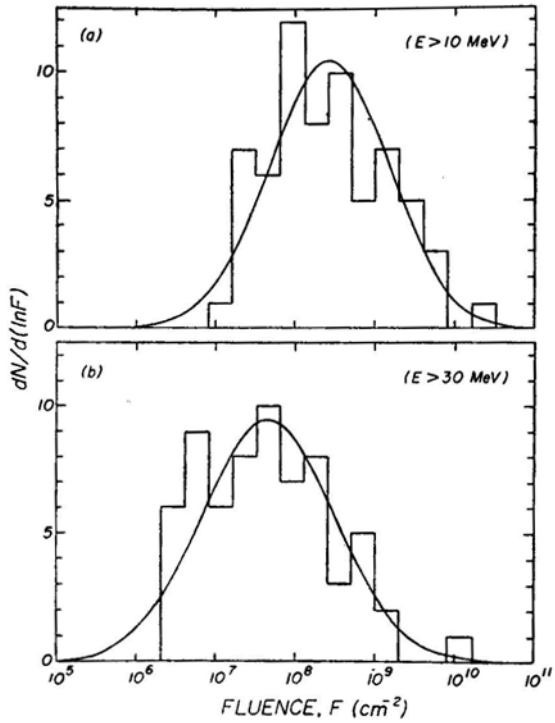

Figure 1 Frequency distribution of cumulative omni-directional (4π) proton fluence (cm^{-2}) in 65 solar flare events (during 1954–1975) for protons of kinetic energy above 10 MeV (a), and 30 MeV (b) All events of fluence above 10^7 protons cm^{-2} of $E > 10$ MeV are considered. Data are from compilation by Reedy (1977). The smooth curve represents the best fit log-normal distribution to the data.

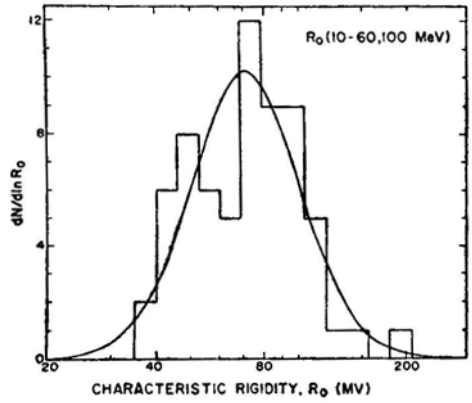

Figure 2 Frequency distribution of the characteristic rigidity (R_0) values for all events considered in Fig. 1 for the energy interval (10-60, 100) MeV. R_0 values were calculated from the data on proton fluence above different energies. The smooth curve represents the best fit log-normal distribution to the data.

hypothesis that R_0 and F values in individual events are correlated. The probability that R_0 and F are correlated was calculated to be less than 0·3 per cent.

Table 1. Statistical analysis of the characteristic rigidity R_0 (MV), in contemporary solar flare events.

Parameter	Solar cycle 19		Solar cycle 20		Solar cycles 19 + 20
	10-30 (MeV)	10-100 (MeV)	10-30 (MeV)	10-60 (MeV)	10-(60, 100) (MeV)
$\mu_n^{\dagger}$	1·81	1·89	1·76	1·8	1·85
$\sigma_n^{\dagger}$	0·14	0·14	0·18	0·16	0·15
$\bar{R}_0$	68	82	63	68	75
σ_{R_0}	22	26	28	25	27
$\sigma_{\bar{R}_0}$	3·7	4·5	4·7	4·2	3·2

† Mean and standard deviation for the best fit log R_0 distribution

The above results, consistent with, the earlier analyses, are extremely significant for the present analysis since they allow us to estimate the expected values for long-term averages if the solar cycles 19 and 20 are considered representative. In particular, we would like to stress here the importance of the third result, namely the statistically independent R_0 and F values in individual events. This has an important bearing on the physics of particle acceleration in flares. Both a harder spectrum (larger R_0 value) and a higher F value imply larger energy in the flare particles, but their statistical independence indicates that a highly variable mechanism is operative which controls the fraction of particles which leave the Sun. In order to accelerate particles efficiently to higher energies (events with larger R_0 values) more energy must initially be available. Implicit here is the assumption of equivalence between the observed solar flare spectra (at 1 AU) and the source spectra. This equivalence may not be exact due to the interplanetary propagation effects, resulting in some deviations in the observed spectra from the source spectra. However, in the case of *event-integrated* spectra, in the energy region of interest (10-100 MeV), both the observed spectra and the deduced source spectra show similar characteristics. Both of them can be represented either on exponential rigidity basis (dN=const × e^{-R/R_0} dR) or as power law in kinetic energy (dN=const×$E^{-\gamma}$ dE). In the former representation the source spectrum has a slightly higher characteristic rigidity R_0, while in the kinetic energy representation it is characterized by a slightly lower value for the power law exponent γ, compared to the values of these parameters for the observed spectrum (Krimigis 1965; Wibberenz 1979 and references therein). Thus the assumed equivalence of the source and the observed spectra can be considered to be valid.

In view of the statistical independence of R_0 and F values in individual events, we can write down the following expression for the fluence in an *average flare event* above energy E (or rigidity R)

$$F(>R) = \int_0^{\infty}\int_0^{\infty} F(R, R_0, F')\, p(R_0)\, p(F')\, dR_0\, dF', \tag{2}$$

where $p(F')$ and $p(R_0)$ are respectively the probability (log-normal distribution) of obtaining a specified value of F' or R_0 in an event. The function $F(R, R_0, F')$ gives the fluence above rigidity R in an event of total fluence F' (> 137 MV), and characteristic rigidity R_0, and is given by

$$F(R, R_0, F') = F'\ (>137\ \text{MV})\ \exp\ [(137-R)/R_0] \tag{3}$$

Equation (2) can now be rewritten as

$$F(>R) = \bar{F}(>137\ \text{MV}) \int_0^\infty \exp\ [(137-R)/R_0]\ p(R_0)\ dR_0$$

where $\bar{F}$ (> 137 MV) is the time-averaged fluence per event above a kinetic energy of 10 MeV. Taking $\bar{F}$(> 137 MV) = 1·2 × 10^9 cm^{-2} based on contemporary data (Table 2), we obtain values of $F(>R)$ and deduce the effective characteristic rigidity (R_0) values. These estimates, separately or together for the solar cycles 19 and 20, are in good agreement with the effective R_0 values deduced from $F(>R)$ values obtained by directly summing up the fluences above different rigidities.

4.2 *J and R_0 Values in Contemporary and Ancient Solar flares*

The integral flux of protons above energy E as well as the R_0 values for solar cycles 19 and 20 along with the long term averages based on radio-nuclide studies of lunar samples are given in Table 3.

Table 2. Statistical analysis of fluence, $F_{>10\ \text{MeV}}$ (cm^{-2}), in contemporary solar flare events.

Parameter	Solar cycle 19 1954–1964	Solar cycle 20 1965–1975	Solar cycles 19 + 20 1954–1975
μ_n†	8·8	8·1	8·4
σ_n†	0·6	0·75	0·75
$\bar{F}$	1·5 × 10^9	5·4 × 10^8	1·2 × 10^9
σ_F	3·7 × 10^9	2·3 × 10^9	5·0 × 10^9
$\sigma_{\bar{F}}$	3·7 × 10^8	1·7 × 10^8	2·5 × 10^8

† Mean and standard deviation for the best fit log F distribution.

Table 3. Integral flux (cm^{-2} s^{-1})* and the characteristic rigidity (MV)* in solar flares averaged over different time scales

Period	J(>10 MeV)	J(>30 MeV)	J(>60 MeV)	J(>100 MeV)	R_0(10−100)
(i) Contemporary					
Cycle 19 (1954–64)	143	41	12	3	82 (68)+
Cycle 20 (1965–75)	51	11	3	1	68 (63)+
Cycles 19 + 20 (1954–75)	114	28	8	2	75 (65)+
(ii) Long term average					
10^4 yr (^{14}C)[a]	200	72	26	9	100
3 × 10^5 yr (^{81}Kr)[b]	154†	52†	18	6	95
10^6 yr (^{26}Al)[c]	70 (125)§	25 (55)§	9 (24)§	3 (11)§	100 (125)§
5 × 10^6 yr (^{53}Mn)[c]	70	25	9	3	100
~ 10^8 yr (^{3}He)[d]	80	29†	10†	4†	100

*J (> 10 MeV) and R_0 for solar cycles 19, 20 and their composite has been obtained from the lognormal distribution fit to data compiled by Reedy (1977). The values of $J(>E)$ were computed using the values of J(> 10 MeV) and R_0.

+The numbers within parentheses refer to R_0 values for the energy interval 10-30 MeV.

†Extrapolated values assuming exponential rigidity spectrum.

§The numbers within parentheses are from the revised data of Bhattacharya and Bhandari (1976); Bhandari (1981, personal communication).

[a]Boeckl (1972); [b]Yaniv, Marti and Reedy (1980); [c]Kohl *et al.* (1978); [d]Venkatesan *et al.* (1980)

The marked difference in the J values between cycles 19 and 20 can be easily understood since the average fluence for short durations can be drastically affected by the occurrence of one or two large events. This becomes evident from the raw data. In the solar cycle 19, about fifty per cent of the total fluence was due to 4 out of 32 events, whereas seventy per cent of the total fluence in cycle 20 was due to the 1972 August 4 event. The long term average fluxes are, however, expected to be free from such statistical uncertainty. This is easily seen from Fig. 3 where we have considered the effect of occurrence of an extra event with fluence exceeding F. Figure 3(a) gives the resulting time averaged $\bar{F}$ values per event due to the occurrence of this one event, as a function of F for different time periods $\langle T \rangle$ over which the averages are taken. Also shown in Fig 3(b) is the probability of occurrence per event of an event with fluence $\geqslant F$. These calculations are based on the lognormal distribution parameters for F, for contemporary flares (Table 2).

It becomes apparent that the short duration averages are prone to statistical uncertainties due to statistics of single event and therefore they may not have much significance. But the average flux estimates for long durations are free from such uncertainties. For example, due to the occurrence of a single event, the probabilities of the time averaged fluxes being doubled are about 10^{-7} and 10^{-14} for $\langle T \rangle = 10^4$ and 10^6 yr respectively. Consequently any measured variations in the long term averaged flux values for different durations should reflect real changes in the ancient solar flare intensity. For a critical assessment of the long term averaged flux values given in Table 3, reference is made to the recent work of Reedy (1980).

In contrast to the case for $\bar{F}$, the much smaller spread in the case of R_0 values leads to a reasonably good estimate from data of short duration. The calculated change in the time averaged R_0 value due to the occurrence of an extra event of high rigidity even during a short period of 20 years is less than four per cent. Because of this, the effective R_0 value based on the contemporary data alone (1954-1975) is expected to be quite reliable.

Thus the time averaged R_0 values for different integrating periods (10-10^6 yr) would be expected to be similar within 5 per cent. The expected trend is reflected by

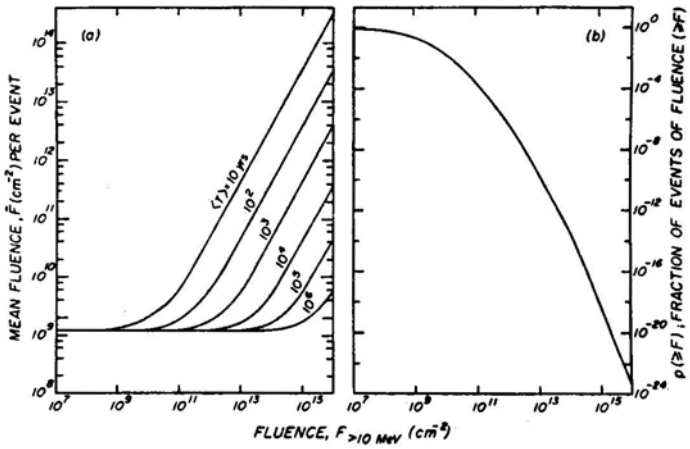

Figure 3. (a) The effective $\bar{F}$ values (mean fluence per event) due to the occurrence of an extra event of fluence $\geq F$, plotted against F for different time periods over which the averages are taken. (b) The theoretical values of ρ ($\geq F$), the fraction of events having fluence $\geq F$, are plotted as a function of F.

the fact that in spite of a significant difference in the average proton fluxes in solar cycle 19 and 20, the average R_0 is similar in both the cycles (Table 3).

Based on the above discussions and data in Table 3, we observe:

1. There exists a definite difference between the time averaged R_0 values for contemporary and ancient flares ($\langle T \rangle = 10^4$–10^6 yr). The ancient solar flares are characterised by a spectrum harder than that of the contemporary. As discussed above, this conclusion is free from sampling uncertainties.
2. The long term and recent time averaged J values differ by a factor of about 2 to 3. However, considering statistics of a single event, no meaningful conclusion can be drawn about possible differences between the contemporary and long term average J values.
3. Out of the different long term averaged flux values, those obtained from ^{14}C ($\langle T \rangle = 10^4$ yr) and ^{81}Kr ($\langle T \rangle = 3 \times 10^5$ yr) are distinctly higher. If this result is taken at its face value, it would imply a higher solar flare activity (by about a factor of two) in the past 10^4 or 10^5 years, compared to that in the earlier epoch of a few million years.

Considering the stability of the $\bar{J}$ value based on the long term averages, we consider a $\bar{J}$ value of ~ 100 cm^{-2} s^{-1} for $\langle T \rangle = 10^6$ yr to be a good representative of the average solar proton flux. This value can be appreciably affected only due to the occurrence of a large flare with fluence F exceeding 10^{16} cm^{-2}. It is also interesting to note here that the integrated fluence over 10^6 yr, with $\bar{J} = 100$ cm^{-2} s^{-1}, is 3×10^{15} cm^{-2}, which by itself rules out the occurrence of a single flare with fluence exceeding a few times 10^{15} cm^{-2}.

A number of solar cycle periodicities ranging between 20 to 250 yr (besides the 11 yr cycle) have been suggested from an analysis of sunspot numbers and ^{14}C tree ring data (Bonov 1972; Cohen and Lintz 1974; Eddy 1976; Wittmann 1978). The possibility of longer term periodicity cannot be ruled out since the above values were obtained from short duration data extending upto a few thousand years in the past. For the present purpose, we will assume that the prominent variations in the solar activity are restricted to cycles of durations $< 10^3$ yr, and thus any variation in $\bar{J}$ values for $\langle T \rangle$ exceeding 10^3 yr should result from the occurrence of a single or a few large flares. Thus, the higher values of $\bar{J}$ for $\langle T \rangle = 10^4$ and 10^5 yr, based on ^{14}C and ^{81}Kr data (Table 3) are suggestive of the occurrence of a few large flares with fluence $F(> 10$ MeV) of $\geqslant 10^{13}$ cm^{-2} during the last 10^4 yr and of $\geqslant 10^{14}$ cm^{-2} during the time interval between last 10^4 to 10^5 yr. Based on the ^{14}C tree ring data Lingenfelter and Hudson (1980) ruled out the possibility of the occurrence of such large flares during the ^{14}C mean lifetime scale ($\sim 10^4$ yr). However, in view of the large attenuation of amplitude in tree rings compared to that in solar flare production, this conclusion must be checked carefully. An alternative explanation for the variations in the long term averaged $\bar{J}$ values will be to postulate a longer term solar activity cycle of period lying between 10^5–10^6 yr.

Since we are dealing with solar flare spectral parameters averaged over a large number of events, the effect of interplanetary propagation on the time averaged spectral parameters are expected to be similar both for the contemporary and for the ancient solar flares. Thus the differences in the time averaged spectral parameters

for contemporary and ancient solar flares observed at 1 AU should represent differences in their source spectra as well. Therefore the higher value for the characteristic rigidity R_0 in ancient solar flares averaged over $\langle T \rangle \geqslant 10^4$ yr indicates the availability of larger amount of energy during particle acceleration compared to flares occurring in the last two solar cycles. It may be reiterated here that the variation in $\bar{J}$ between the contemporary and ancient flares lies within a factor of three. The prob lem before us is to deduce the average R_0 value during earlier epochs of high rigidity. This calculation can only be made if we have an *a priori* knowledge of the variations in $\bar{J}$ values during high and low rigidity period. We have, therefore, deduced working values of $\bar{R}_0$ during the active periods by assuming (i) equal duration of high and low activity period (quite consistent with the deduction of Eddy for the duration of Grand Maxima and Minima) and (ii) ratio of mean $\bar{J}$ (maxima)/$\bar{J}$ (minima) to be in the range 1 to 5. The values of $\bar{R}_0$ (Maxima epoch) thus obtained are in the range 130 to 300 MV.

We now wish to make some general remarks about the sources of variation of solar activity. We are basically dealing with a short enough time scale that whatever the process, it must be related to periodicities in the observed solar surface phenomena, such as variations in the sunspot numbers. Although there is no consensus yet on the solar flare models, it is clear that during periods of sustained solar minimum or maximum, the energy available for particle acceleration may be quite different, being larger during active periods such as the Eddy maxima. For recent discussions and review on storage and conversion of magnetic energy see Akasofu (1981); Schussler (1980); Brown and Smith (1980) and Mullan (1975).

It is generally believed that solar flares depend for their energy source on the toroidal magnetic field created inside the Sun by the action of the solar differential rotations on the poloidal field. The internal toroidal field is like a wound-up spring. Following Mullan and Kent (1979), one may imagine that the spring gets more and more tightly wound up as the cycle progresses and the effects may be appreciable for cycles of 100-250 yr periodicity. Evidence for subsurface storage of energy has recently been provided for the Sun by Glencross (1979). In order to see the validity of the hypothesis that higher energy may become available during the progression of a solar cycle, we have analysed the data for solar cycles 19 and 20 Indeed one does observe a fairly good positive correlation between R_0 in individual events with $F \geqslant 5 \times 10^8$ cm^{-2} and ΔT, the time elapsed since the beginning of the cycle. It may be noted that no such correlation could be found for the F values of the individual events.

The present work thus provides clear evidence for a long term variation in solar activity. The high value of the characteristic rigidity in ancient flares can be understood only if the past solar activity was higher than that observed in the last 25 years. This variation can be understood in terms of Eddy's hypothesis of periodic maxima and minima in solar activity. The changes in the mean flux values averaged over different durations in the past also indicate either the occurrence of one or a few large solar flares ($F \geqslant 10^{13}$ cm^{-2}) during the last 10^5 years or a long term solar activity cycle with periods lying between 10^5 to 10^6 yr.

References

Aitchison, J., Brown, J. A. C. 1957, *The Log-normal Distribution with Special Reference to its Use in Economics*, Cambridge University Press.

Akasofu, S. I. 1981, *Preprint.*

Amin, B. S., Lai, D., Lorin, J. C, Pellas, P.,Rajan, R. S., Tamhane, A. S., Venkatavaradan, V.S. 1969, in *Meteorite Research*, Ed. P. M. Millman, D. Reidel, Dordrecht, p. 316.

Bhattacharya, S. K., Bhandari, N. 1976, *Proc. Seventh Lunar Sci. Conf: Geochim. Cosmochim. Acta*, *Suppl.*, **7***,* 1901.

Biswas, S. 1972, *Indian J. Radio Sp. Phys.*, **1**,19.

Biswas, S., Fichtel, C. E. 1965, *Space Sci. Rev.*, **4,** 709.

Boeckl, R. S. 1972, *Earth Planet. Sci. Lett.*, **16,** 269.

Bonov, A. D. 1972, in *Proc. First European astronomical Meeting*, Ed. J. Xanthakis, Springer-Verlag, Berlin, p. 83.

Bostrom, C. O., Williams, D. J., Arens, J. F., Kohl, J. W. 1967-1973, *Solar Geophys. Data,* Nos 282–341

Brown, J. C, Smith, D. F. 1980, *Rep. Prog. Phys.*, **43**, 125.

Castagnoli, G., Lai, D. 1980, *Radiocarbon*, **22,** 133.

Cohen, T. J., Lintz, P. R. 1974, *Nature*, **250,** 398

Crawford, H. J., Price, P. B., Cartwright, B. G., Sullivan, J. D. 1975, *Astrophys. J.*, **195,** 213.

Crozaz, G., Haack, U., Hair, M., Hoyt, H., Kardos, J., Maurette, M., Miyajima, M., Seitz, M., Sun, S., Walker, R., Wittels, M., Woolum, D. 1970, *Science*, **167,** 563.

Divine, N. 1973, *JPL Quarterly Technical Review*, **3, 37**.

Eddy, J. A. 1976, *Science*, **192,** 1189.

Eddy, J. A. 1977, *Clim. Change*, **1,** 173.

Glencross, W. M. 1979, *Mon. Not. R. astr. Soc.*, **186,** 305.

King, J. H. 1972, *NSSDC,* 72-14, NASA, Greenbelt.

King, J. H. 1974, *J. Spacecr. Rockets*, **11,** 401.

Kohl, C. P., Murrell, M. T., Russ, G. P. III., Arnold, J. R. 1978, *Proc. Ninth Lunar Planet. Sci. Conf: Geochim. Cosmochim. Acta, Suppl.,* **10,** 2299.

Kolomenskii, A. V., Petrov, V. M., Zil, M. V., Eremkina, T. M. 1978, *Kosmicheske Issledovaniya*, **16,** 698.

Krimigis, S. M. 1965, *J. Geophys. Res.*, **70,** 2943.

Lal, D. 1972, *Space Sci. Rev.*, **14,** 3.

Lal, D., MacDougall, D., Wilkening, L., Arrhenius, G. 1970, *Proc. Apollo Eleven Lunar Sci. Conf: Geochim. Cosmochim. Acta, Suppl.*, **1,** 2295.

Lal, D., Rajan, R. S. 1969, *Nature*, **223,** 269.

Lingenfelter, R. E., Hudson, H. S. 1980, in *Proc. Conf. Ancient Sun*, Pergamon Press, New York, p. 45.

McDonald, F. B. 1963, *Solar Proton Manual*, NASA TR R-169, NASA, Greenbelt.

McDonald, F. B., Fichtel, C. E., Fisk, L. A. 1974, in *High Energy Particles and Quanta in Astrophysics,* Eds F. B. McDonald and C. E. Fichtel, MIT Press, Cambridge, p. 212.

Modisette, J. L., Vinson, T. M., Hardy, A. C. 1965, *NASA Report*, TN D-2746, NASA, Greenbelt.

Mullan, D. J. 1975, *Astrophys. J.*, **200,** 641.

Mullan, D. J., Kent, D. W. 1979 in *Proc. Sixteenth Int. Cosmic Ray Conf*, 5, University of Tokyo, Japan, p. 323.

Pellas, P., Poupeau, G., Lorin, J. C, Reeves, H., Audouze, J. 1969, *Nature*, **223,** 272.

Reedy, R. C. 1977, *Proc. Eighth Lunar Sci. Conf: Geochim. Cosmochim: Acta, Suppl.,* **8,** 825.

Reedy, R. C. 1980, in *Proc. Conf Ancient Sun*, Pergamon Press, New York, p. 365.

Schwabe, H. 1843, *Astr. Nachr.*, **20,** 495.

Schussler, M. 1980, *Nature*, **288**, 150.

Shedlovsky, J. P., Honda, M., Reedy, R. C, Evans, J. C. Jr., Lai, D., Lindstrom, R. M., Delany, A. C, Arnold, J. R., Loosli, H., Fruchter, J. S., Finkel, R. C. 1970, *Proc. Apollo Eleven Lunar Sci. Conf: Geochim. Cosmochim. Acta*, *Suppl*, **1,**1503.

Venkatesan, T. R., Nautiyal, C. M., Padia, J. T., Rao, M. N. 1980, *Proc. Eleventh Lunar Planet Conf: Geochim. Cosmochim. Acta*, *Suppl.,* **12,** 1271

Wahlen, M., Honda, M., Imarnura, M., Fruchter, J. S., Finkel, R. C, Kohl, C. P., Arnold, J. R., Reedy, R. C. 1972, *Proc. Third Lunar Sci. Conf: Geochim. Cosmochim. Acta*, *Suppl.*, **8,** 1719.

Webber, W. R., Benbrook, J. R., Thomas, J. R., Hunting, A., Duncan, R. 1963, *The Boeing Company Report*, D2-90469.

Weddel, J. B., Haffner, J. W. 1966, *North American Aviation Report*, SID 66-421.

Wibberenz, G. 1979, in *Proc. Sixteenth Int. Cosmic Ray Conf.*, **14,** University of Tokyo, Japan, 234.

Wittmann, A. 1978, *Astr. Astrophys.*, **66,** 93.

Yaniv, A., Marti, K., Reedy, R. C. 1980, in *Proc. Eleventh Lunar Planet. Sci. Conf: Geochim Cosmochim. Acta*, *Suppl* **12,** p. 1291.

Corrigenda

'The Structure of Integrated Pulse Profiles ' by M. Vivekanand and V. Radhakrishnan was published in *Journal of Astrophysics and Astronomy*, Volume 1, Number 2, December 1980.
The last equation on page 123 should read

$$\left(1+2\frac{\Delta\lambda_{ph}}{G}\right)^{60} = (1+0{\cdot}06)^{60} \simeq 30.$$

In line 6 on page 124, ' $\approx 10^3$' should read '10.'

'Intrinsic Properties of Carbon Stars. I. Effective Temperature Scale of N-type Carbon Stars ' was published in *Journal of Astrophysics and Astronomy*, Volume 2, Number 1, March 1981.

Equation (1) on page 97 should read

$$T_{\rm eff} = (4f_{\rm bol}/\sigma\theta^2_{LD})^{1/4} \qquad (1)$$

and equation (3) on page 98 should read

$$f_{\rm bol}/f_\lambda = T^4_{\rm eff}/\sigma F_\lambda(T_{\rm eff}, g, \ldots) = R_\lambda(T_{\rm eff}, g, \ldots). \qquad (3)$$

On page 98 line 11, for ' R_λ varies as $T_{\rm eff}$' read 'R_λ varies as $T^3_{\rm eff}$'.
On page 100 line 6, for '$\tau_{\rm eff}$' read '$T_{\rm eff}$'
On page 104 Table 2 Column 8, for '$f_{\rm bol}$' read 'log '$f_{\rm bol}$'.
On page 110 line 31, for 'we desire' read 'we derived'.

'A Spectroscopic Orbit for 26 Comae' by R. F. Griffin was published in *Journal of Astrophysics and Astronomy*, Volume 2, Number 1, March 1981. Table 1 on page 117 has three typographical errors. The relevant lines after correction are reproduced here.

Date	MJD	Velocity km s^{-1}	Phase	$(O-C)$ km s^{-1}
1978 June 18·91	43677·91	−20·8	2·385	+1·0
1979 Feb 25·15	43929·15	−16·1	2·643	+0·3
1980 Apr 18·90	44347·90	−32·4	3·074	−0·6

Corrigenda

'The Structure of Integrated Pulse Profiles ' by M. Vivekanand and V. Radhakrishnan was published in *Journal of Astrophysics and Astronomy*, Volume 1, Number 2, December 1980.
The last equation on page 123 should read

$$\left(1+2\frac{\Delta\lambda_{ph}}{G}\right)^{60} = (1+0{\cdot}06)^{60} \simeq 30.$$

In line 6 on page 124, ' $\approx 10^3$' should read '10.'

'Intrinsic Properties of Carbon Stars. I. Effective Temperature Scale of N-type Carbon Stars ' was published in *Journal of Astrophysics and Astronomy*, Volume 2, Number 1, March 1981.

Equation (1) on page 97 should read

$$T_{\rm eff} = (4f_{\rm bol}/\sigma\theta^2_{LD})^{1/4} \qquad (1)$$

and equation (3) on page 98 should read

$$f_{\rm bol}/f_\lambda = T^4_{\rm eff}/\sigma F_\lambda(T_{\rm eff}, g, \ldots) = R_\lambda(T_{\rm eff}, g, \ldots). \qquad (3)$$

On page 98 line 11, for ' R_λ varies as $T_{\rm eff}$' read 'R_λ varies as $T^3_{\rm eff}$'.
On page 100 line 6, for '$\tau_{\rm eff}$' read '$T_{\rm eff}$'
On page 104 Table 2 Column 8, for '$f_{\rm bol}$' read 'log '$f_{\rm bol}$'.
On page 110 line 31, for 'we desire' read 'we derived'.

'A Spectroscopic Orbit for 26 Comae' by R. F. Griffin was published in *Journal of Astrophysics and Astronomy*, Volume 2, Number 1, March 1981. Table 1 on page 117 has three typographical errors. The relevant lines after correction are reproduced here.

Date	MJD	Velocity km s^{-1}	Phase	$(O-C)$ km s^{-1}
1978 June 18·91	43677·91	−20·8	2·385	+1·0
1979 Feb 25·15	43929·15	−16·1	2·643	+0·3
1980 Apr 18·90	44347·90	−32·4	3·074	−0·6

Corrigenda

'The Structure of Integrated Pulse Profiles ' by M. Vivekanand and V. Radhakrishnan was published in *Journal of Astrophysics and Astronomy*, Volume 1, Number 2, December 1980.
The last equation on page 123 should read

$$\left(1+2\frac{\Delta\lambda_{ph}}{G}\right)^{60} = (1+0{\cdot}06)^{60} \simeq 30.$$

In line 6 on page 124, ' $\approx 10^3$' should read '10.'

'Intrinsic Properties of Carbon Stars. I. Effective Temperature Scale of N-type Carbon Stars ' was published in *Journal of Astrophysics and Astronomy*, Volume 2, Number 1, March 1981.

Equation (1) on page 97 should read

$$T_{\rm eff} = (4f_{\rm bol}/\sigma\theta^2_{LD})^{1/4} \qquad (1)$$

and equation (3) on page 98 should read

$$f_{\rm bol}/f_\lambda = T^4_{\rm eff}/\sigma F_\lambda(T_{\rm eff}, g, \ldots) = R_\lambda(T_{\rm eff}, g, \ldots). \qquad (3)$$

On page 98 line 11, for ' R_λ varies as $T_{\rm eff}$' read 'R_λ varies as $T^3_{\rm eff}$'.
On page 100 line 6, for '$\tau_{\rm eff}$' read '$T_{\rm eff}$'
On page 104 Table 2 Column 8, for '$f_{\rm bol}$' read 'log '$f_{\rm bol}$'.
On page 110 line 31, for 'we desire' read 'we derived'.

'A Spectroscopic Orbit for 26 Comae' by R. F. Griffin was published in *Journal of Astrophysics and Astronomy*, Volume 2, Number 1, March 1981. Table 1 on page 117 has three typographical errors. The relevant lines after correction are reproduced here.

Date	MJD	Velocity km s^{-1}	Phase	$(O-C)$ km s^{-1}
1978 June 18·91	43677·91	−20·8	2·385	+1·0
1979 Feb 25·15	43929·15	−16·1	2·643	+0·3
1980 Apr 18·90	44347·90	−32·4	3·074	−0·6

J. Astrophys. Astr. (1981) **2,** 215–244

Mass Segregation in Globular Clusters

K. K. Scaria and M. K. V. Bappu *Indian Institute of Astrophysics, Bangalore 560034*

Received 1980 December 3; accepted 1981 August 27

Abstract. Photoelectric aperture-photometry of ω Cen in *U, B, V, R* and *I* bands has established that the cluster is bluer between 2 arcmin and 4 arcmin from the centre, than it is elsewhere. The difference in $B - I$ colour between the centre and this blue zone is $\simeq 0{\cdot}45$ mag. The core radius is found to be dependant on the wavelength band chosen for observation, the smallest core radius being for the *I* band. Equidensitometry of ω Cen in *B, V* and infrared bands shows a wavelength dependence with the cluster being nearly spherical in the infrared band. It shows a maximum ellipticity around 3 arcmin from the cluster centre. The blue contribution in this zone comes from both a diffuse background of unresolved stars and an increase in the relative abundance of horizontal branch (HB) stars. The similarity between the diffuse background and the HB stars has been demonstrated. A photographic subtraction technique is used to study the distribution of HB stars in the cluster.

Results of equidensitometry of the cluster 47 Tuc, obtained in the present study, are compared with the earlier results of photoelectric photometry. Here too an increase in ellipticity is associated with an increase in the blueness of the cluster. All globular clusters studied so far for ellipticity show a similarity in the dependence of the ellipticity on the distance from the centre. The ellipticity has small values near the centre and in the outer regions, with the maximum value in between. We suggest that the red stars in globular clusters have a nearly spherical distribution. The blue stars form a bulge around the core with a more elliptical distribution and a different orientation. A similarity between the ellipticity aspects of both the globular clusters and rotation in the nucleus of M 31 is pointed out; the M 31 nucleus may thus show a bluer colour and smaller UV excess around the region where the rotation curve shows a peak.

Key words: globular clusters—ω Centauri—photoelectric photometry of globular clusters—equidensitometry—horizontal branch stars

1. Introduction

Relaxation times in globular clusters are short compared to their ages and hence these objects must be in a state of dynamical equilibrium. Hence the equipartition of energy in these clusters will cause a stratification of stars; the large mass stars would be concentrated towards the centre and the low mass stars predominate the outer regions. In an old stellar system, stars of larger mass are the red stars and a concentration of these stars towards the centre will make the system look redder at the centre. Evidence of this kind is available. Gascoigne and Burr (1956) have shown that 47 Tuc is redder at the centre by $P - V = 0{\cdot}17$ mag. Chun and Freeman (1979) find that 47 Tuc becomes bluer beyond 2 arcmin from the centre. They have made concentric aperture observations of 24 globular clusters and find that 8 of them show an increase in reddening towards the centre. King (1962) has pointed out the importance of relaxation, in very old stellar systems following mass loss, due to stellar evolution. Martin (1938) observed the RR Lyr stars in ω Cen to be less concentrated towards the centre of the cluster. The clusters M 3, M 5 and M 15 also show similar characteristics in the distribution of RR Lyr stars. Oort and van Herk (1959) have tried to explain this feature on the basis of mass loss during the evolution from the tip of the giant branch to the horizontal branch. The loss of mass at these phases of evolution gives these stars a higher velocity dispersion and hence a larger spatial distribution. An alternative interpretation can be that a radial colour gradient may indicate an abundance gradient, since the morphology of the horizontal branch is sensitive to abundance.

In a rotating cluster the segregation effect may cause different degrees of flattening for the groups of large mass and low mass stars. Many of the globular clusters are found to be elliptical in form. Dickens and Woolley (1967) have shown that the flattening of ω Cen can be explained by its rotation. The segregation effects are best seen in the inner regions of the cluster, since stellar encounters are more frequent in this region. It is impossible to study such segregation effects near the centre in a globular cluster, because of the large density of stars. But it is possible that these effects may produce changes in colour depending on the location in the cluster. We have used the photoelectric and the photographic techniques to study the colour changes indicative of these effects over the cluster ω Cen and also over 47 Tuc.

2. Photoelectric photometry of ω Centauri

The bulk of photoelectric measurements available in the literature for globular clusters are in the *U*, *B* and *V* bands. For old stellar systems like globular clusters, there is a predominance of light in the longer wavelengths and hence the *R* and *I* bands would be valuable sources of information. We have therefore employed the five colour *UBVRI* photometry for this study.

The cluster ω Cen is a very good candidate for a study of the colour gradient, because it is the most massive cluster in our galaxy. It has the largest core radius among the brightest galactic globular clusters. There is no evidence of non-uniform reddening over the cluster, even though it is only 15° above the galactic plane. Star counts of Lindsay (1956) and the observations on the horizontal and the giant branches of the cluster by Freeman and Rodgers (1975) and Norris and Bessell (1975)

show that there is no large scale differential interstellar reddening across the cluster. We also find from the equidensitometry of photographs obtained in different wavelength bands, that there is no asymmetric absorption over the cluster. The major axis of the cluster is inclined by 10° to the east-west direction. There is also some evidence to the fact that the axis of rotation is perpendicular to the line of sight (Poveda and Allen 1975). Hence, we take the east-west scan as representative of the intensity gradient along the major axis and the north-south scan as indicative of the gradient along the minor axis. The relaxation time of the cluster is quite long; but since the cluster age is greater than one relaxation time (Peterson and King 1975), it has had enough time to reach a state of dynamical equilibrium.

2.1 *The Observations*

Spot measurements of brightness over the cluster were made on four consecutive nights in the month of May 1979. On each night one scan was obtained along both the east-west and north-south directions. The photometry on the cluster was done with the 102-cm reflector at Kavalur. A dry-ice cooled EMI 9558 B tube was used as the detector at the (*f*/13) Ritchey-Chrétien focus. This was followed by a pulse counting equipment and an on-line computer. Since ω Cen has an appreciable ellipticity, concentric aperture measures are not likely to yield a correct gradient of brightness in the cluster. Hence, the aperture photometry was planned along two directions in the cluster. The aperture used for the spot measurements has a diameter of 40 arcsec. The star-changing device on the telescope is a programmable facility that moves the telescope in a and δ by known amounts from a reference point, with an accuracy of 1 arcsec. The backlash in the system is less than 1 arcsec. Thus the aperture can be positioned quite accurately over the cluster, with reference to a star in the field. The star P in Fig. 14 is used as the reference star for scanning the cluster in the east-west direction while the star Q functioned as the reference star for north-south direction. The counts had a high degree of stability; the values were consistent on all the nights for each scan location. The nights used for observations were of high photometric quality. Due to the large declination, the cluster was observed every day for only about two hours around the time of culmination. The filter combination is similar to that used by Fernie (1974) except for the fact that in the *R* combination, RG 8 was used in place of RG 6. The *UBVRI* filter system was calibrated using 20 standard stars from the list of Iriarte *et al.* (1965). The comparison stars used in the cluster are marked B and D in Fig. 14. They have also been used as standard stars earlier by Arp (1958), Geyer (1967) and Dickens and Woolley (1967). Extinction coefficients and transformation coefficients for conversion to the standard Johnson *UBVRI* system, were derived for each night. Sky corrections become more and more important as we go to the outer regions of the cluster. Hence much care has been taken to make accurate measurements of the sky brightness. A relatively star-free region near the standard star D was chosen from a well exposed plate of ω Cen; the telescope was moved to this starfree region to get the sky brightness in *U, B, V, R* and *I* bands before and after a set of 3 to 4 measurements over the cluster. The sky correction applied in each band is the mean of the values obtained before and after the measurements over the cluster.

The cluster centre has been determined by the equidensitometric technique with reference to the stars T and M. The photoelectric scan paths are 10 arcsec to the west and 5 arcsec to the south of the centre thus defined. Since the diaphragm used for the scans is 40 arcsec in size, we do not consider the error, in the location of origin, to cause any inaccuracy.

2.2 *Evaluation of Errors in Photometry*

The problem of errors involved in surface photometry of globular clusters is explained in detail by King (1966b), Illingworth and Illingworth (1976), Da Costa (1979) and Chun and Freeman (1979). These authors show that the sampling and the centering errors are the most important errors encountered in surface photometry. In the case of bright globular clusters like ω Cen, the principal contribution is likely to be from sampling errors and hence we consider these in detail.

An unavoidable source of error in surface photometry of globular clusters arises from the statistical fluctuations in the number of stars of a given luminosity contained in the finite sample selected by the aperture (King 1966b). The mean relative error (σ/L) is proportional to $L^{-1/2}$ where L is the total luminosity given by $L = \Sigma\, L_i\, N_i$. Illingworth and Illingworth give the formula for the sampling errors in log f_V, where f_V is the surface brightness in the V band, as

$$E_{\rm sa} = 0{\cdot}4343\ (\sigma/L)_V \left[\frac{\text{dex } 0{\cdot}4\ (10 - m_{\rm er})}{L_{\rm obs}}\right]^{1/2}. \tag{1}$$

Here $(\sigma/L)_V$ is the sampling error for the model corresponding to the total integrated magnitude M_V, $m_{\rm er} = (m - M)_{{\rm app},V} + M_V$ *and* $L_{\rm obs}$ is the total brightness in the aperture used for the scan expressed in units of $V = 10{\cdot}0$ mag.

Illingworth and Illingworth (1976) give a value of 0·023 for $(\sigma/L)_V$ *at* $M_V = -8{\cdot}5$ and 0·020 for $(\sigma/L)_B$ at $M_B = -7{\cdot}8$ based on the M 3 model of Sandage (1957).

When sampling errors are calculated in magnitudes, these values are to be multiplied by 2·5. If the surface brightness profile is folded at the centre to give a mean surface brightness over the cluster, then the errors obtained as above should be divided by $\sqrt{2}$.

Sampling errors in colour are calculated from Sandage's (1957) luminosity function of M 3 by Chun and Freeman (1979) using the equation

$$\sigma_c^2 = (1{\cdot}085)^2 \sum N_i \left[\frac{L_{vi}}{L_v} - \frac{L_{bi}}{L_b}\right]^2 \tag{2}$$

where L_{vi} is the visual luminosity of the stars of class i, and L_v the total visual luminosity *etc.* Chun and Freeman give values of 0·46 $(\sigma/L)_B$ and 0·51$(\sigma/L)_B$ for σ_{U-B} and σ_{B-V} respectively. The sampling error in the magntiude units is calculated as

$$E_c = 1{\cdot}086 \times 10^{-2}\, \sigma_c\ (L_{\rm obs})^{-1/2} \tag{3}$$

where L_{obs} is the total blue brightness in the aperture expressed in the units of $B = 10{\cdot}0$ mag.

Since our photometry is in the *U*, *B*, *V*, *R* and *I* bands, we need the estimates of sampling errors for the *R* and *I* bands also. Instead of taking the luminosity function of a fairly metal rich cluster like M 3, we have chosen the luminosity function of the metal poor cluster M 92. This cluster compares well with ω Cen in both the metal abundance and the geometrical form. The *V* luminosity function for M 92 has been published by Hartwick (1970). Sandage (1970) has published the *UBV* photometry of stars in M 92 in the range from $V = 16{\cdot}26$ to $V = 22{\cdot}26$. Cathey (1974) has published the *UBVR* observations from $V = 12{\cdot}19$ to $V = 15{\cdot}41$ and Rusev (1974) has listed *BVI* magnitudes in the range $V = 12{\cdot}16$ to $V = 14{\cdot}19$. Using the above data, we have estimated the sampling errors as explained in the following.

Hartwick's (1970) luminosity function has a step size of 0·1 mag between $V = 11{\cdot}9$ to $V = 21{\cdot}1$. We have calculated the sampling errors in *V* directly by using the equation

$$\sigma/L = \sum_i (L_i^2\, N_i)^{1/2} \Big/ \sum_i (L_i\, N_i). \tag{4}$$

In order to estimate the sampling errors in the rest of the bands, we have treated each step in the *V* magnitudes as a box consisting of identical stars with constant colours. For each of these boxes, we estimate the mean colours *U* — *V*, *B* — *V*, *V* — *R* and *V* — *I* using the photometric data cited above. Due to the limitation in the published photometry, we could obtain the colours *V* — *R* only for $V \leqslant 15{\cdot}5$ and *V* — *I* only for $V \leqslant 14{\cdot}5$ while *U* — *V* and *B* — *V* colours are available for the entire range of $V \leqslant 21{\cdot}1$. These colours are used in estimating the luminosity in *U*, *B*, *V*, *R* and *I* bands for stars in each box with a given *V* magnitude to the limits of the available photometry. The sampling errors are then derived using equation (4) to these limits. The errors in colours are also derived similarly using equation (2). The limits of available photometry, which have forced us to truncate the luminosity function in each band or colour are enumerated below.

Case A: *U*, *B*, *V* band and *U* — *B*, *B* — *V* colours for the full range of $V \leqslant 21{\cdot}1$
Case B: *R* band and *V* — *R* colour for stars with $V \leqslant 15{\cdot}5$
Case C: *I* band and *R* — *I* colour for stars with $V \leqslant 14{\cdot}5$

In order to estimate the sampling error in *R*, *I*, *V* — *R* and *R* — *I* for the full range ($V \leqslant 21{\cdot}1$), we have studied the effect of truncating the luminosity function at $V \leqslant 15{\cdot}5$ and $V \leqslant 14{\cdot}5$ in the case of *U*, *B*, *V*, *U* — *B* and *B* — *V*. Table 1(a) lists the value of (σ/L) for these three cases while Table 1(b) lists the values of $\sigma_c/(\sigma/L)_B$. The ratios of Case A and Case B, and of Case A and Case C are shown in the last two columns. The values for *U*, *B*, *V*, *U* — *B* and *B* — *V* are computed directly in all the three cases. The values corresponding to *R* and *V* — *R* are computed directly only for the Cases B and C. The values for *I* and *R* — *I* are computed only for Case C. A comparison of (σ/L) in *U*, *B* and *V* shows that the ratios A/B and A/C gradually increase towards longer wavelengths. This is due to the relative increase in the contribution of the brighter stars to the total luminosity, without a

comparable increase in σ. One can infer thereby that the relative contribution of fainter stars to the total (σ/L) increases with wavelength· However, the rate of increase in A/B and A/C slows down as one moves to longer wavelengths. We assume an estimated value of A/B = 0·58 and A/C = 0·43 for the bands *R* and *I*. These are shown in parentheses in Table 1. The resultant estimates of the total (σ/L) in *R* and *I* bands are also shown in parentheses.

The corresponding ratios A/B and A/C do not vary appreciably between $U - B$ and $B - V$ colours. Hence we assume the values of A/B = 1·3 and A/C = 1·7 for the colours $V - R$ and $R - I$. These values as well as the estimates of errors in $V - R$ and $R - I$ appear in parentheses in coloumns 5 and 6 in Table 1.

The values of σ/L and $\sigma_c/(\sigma/L)_B$ computed by us may be compared with the values derived by previous investigators for M 3. Illingworth and Illingworth (1976) derive a value of $(\sigma/L)_V$ = 0·023 for an integrated absolute magnitude M_V = — 8·5. The apparent magnitude of our model, integrated over all the stars considered in the evaluation of (σ/L) is equal to 8·17 mag. With a distance modulus of 14·50, this gives the model an absolute magnitude M_V = — 6·33. Our value for $(\sigma/L)_V$ at this magnitude is 0·071. Similarly the absolute magnitude in the *B* band is M_B = —5·7 and the corresponding $(\sigma/L)_B$ = 0·053. When sampling errors are calculated using the above constants, we get errors which are 13 per cent larger in the *V* band and 1 per cent larger in the *B* band, as compared to the errors calculated using the M 3 luminosity function. These differences are indicative of errors introduced by using different luminosity functions. Table 2 gives sampling errors calculated on the basis of both the M 3 and M 92 models. For $V - R$ and $R - I$ colours, only our estimates of errors from the M 92 model above are given.

2.3 *Results of the Photometry*

We list separately in Table 2 the results of the aperture scans for the east-west and north-south directions. Column 1 gives *r*, the distance of the aperture from the cluster centre in minutes of arc. The letter E or W with the numbers indicates

Table 1. (a) (σ/L).

Band	Case A $V \leq 21{\cdot}1$	Case B $V \leq 15{\cdot}5$	Case C $V \leq 14{\cdot}5$	A/B	A/C
U	0.035	0.087	0.140	0.402	0.250
B	0.053	0.103	0.155	0.514	0.342
V	0.071	0.126	0.176	0.563	0.403
R	(0.084)	0.143	0.195	(0.580)	(0.430)
I	(0.090)	(0.155)	0·209	(0.580)	(0.430)

(b) $\sigma_c/(\sigma/L)_B$.

Colour	Case A $V \leq 21.1$	Case B $V \leq 15.5$	Case C $V \leq 14{\cdot}5$	A/B	A/C
$U - B$	0·49	0·39	0·31	1.3	1.6
$B - V$	0·48	0·38	0·28	1·3	1·7
$V - R$	(0·35)	0·26	0·20	(1·3)	(1·7)
$R - I$	(0·50)	(0·38)	0·29	(1·3)	(1·7)
$B - I$	(0·50)	(0·38)	0·29	(1·3)	(1·7)

whether the location is to the east or west of the centre of the cluster for the major axis scan. Similarly the letters N or S for the scan along the minor axis denote the locations to the north or south of the centre. Columns 2, 5, 8, 10, 12 and 15 give the $U - B$, $B - V$, $V - R$ and $R - I$ colours and the V and B magnitudes respectively. In columns 3, 6, 13 and 16, the sampling errors are listed for $U - B$, $B - V$ colours and V, B bands calculated from the $(\sigma/L)_V$, $(\sigma/L)_B$, σ_{U-B} and σ_{B-V} values derived

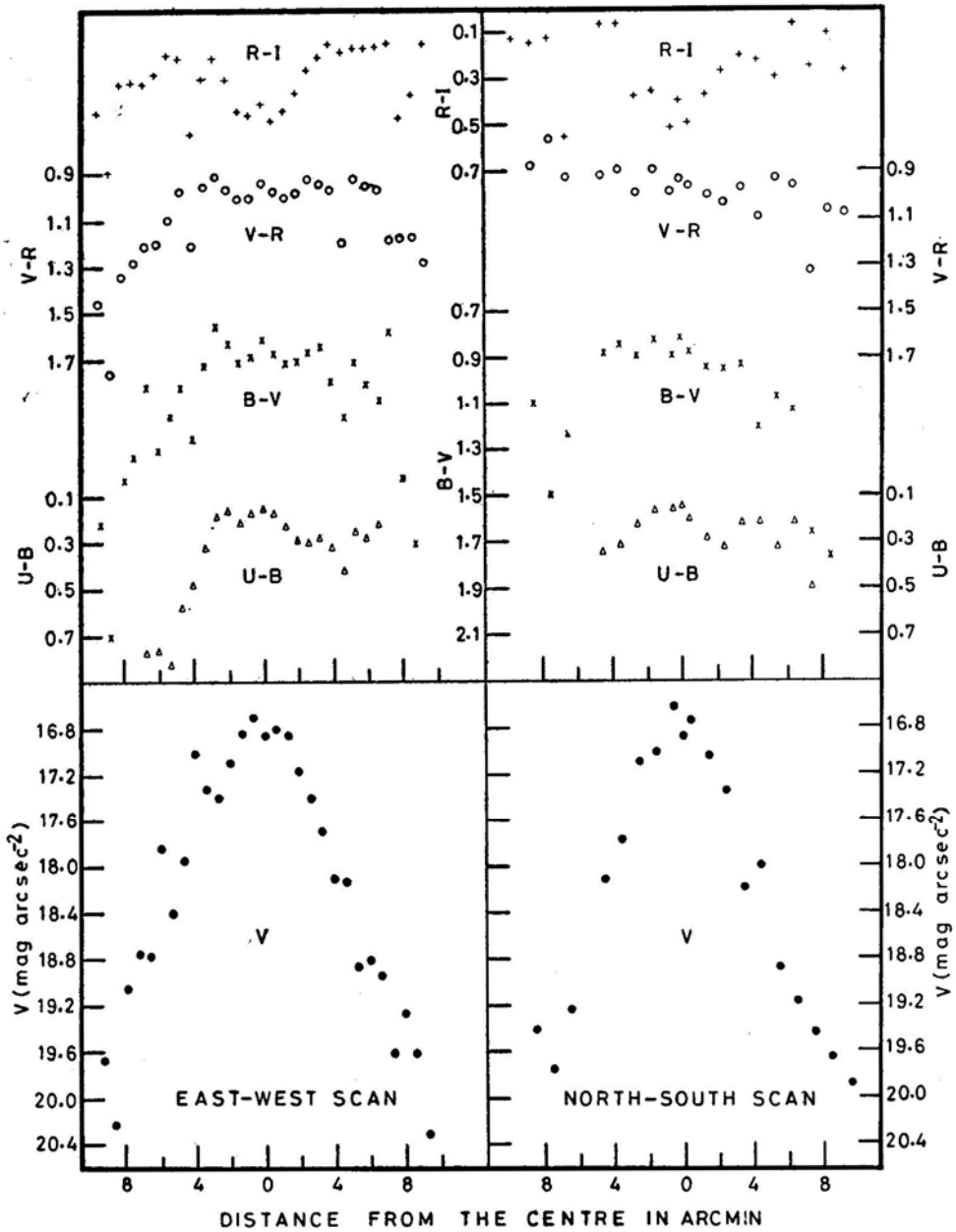

Figure 1. Results of spot measurements over the cluster ω Centauri. $U - B$, $B - V$, $V - R$ and $R - I$ colours and V magnitudes obtained for the east-west scan and the north-south scan are plotted separately.

Table 2. Values of surface brightness and colours at different locations over the cluster.

r	$U-B$	σ_{U-B} (M 3)	σ_{U-B} (M 92)	$B-V$	σ_{B-V} (M 3)	σ_{B-V} (M 92)	$V-R$	σ_{V-R} (M 92)	$R-I$	σ_{R-I} (M 92)	V	σ_V (M 3)	σ_V (M 92)	B	σ_B (M 3)	σ_B (M 92)
1	2	3	4	5	6	7	8	9	10	11	12	13	14	15	16	17
							East-West scan									
9·33W				1·62	0·31	0·29	1·46	0·21	0·44	0·30	19·67	0·46	0·52	21·29	0·61	0·61
8·67W				2·11	0·51	0·48	1·76	0·35	0·70	0·50	20·23	0·59	0·67	22·34	0·99	1·00
8·00W	1·60	0·19	0·21	1·43	0·21	0·20	1·34	0·15	0·32	0·21	19·06	0·35	0·39	20·49	0·42	0·42
7·33W	0·77	0·16	0·17	1·33	0·18	0·17	1·28	0·12	0·31	0·18	18·76	0·30	0·34	20·09	0·35	0.35
6·67W	0·76	0·14	0·15	1·02	0·16	0·15	1·21	0·11	0·32	0·16	18·78	0·30	0·34	19·80	0·31	0.31
6·00W	0·83	0·11	0·11	1·30	0·12	0·11	1·20	0·08	0·28	0·12	17·84	0·20	0·22	19·14	0·23	0·23
5·33W	0·58	0·12	0·13	1·15	0·14	0·13	1·10	0·09	0·20	0·14	18·41	0·26	0·29	19·56	0·27	0·27
4·67W	0·37	0·10	0·10	1·02	0·11	0·10	0·98	0·07	0·21	0·11	17·95	0·21	0·24	18·97	0·21	0·21
4·00W	0·48	0·07	0·07	1·25	0·08	0·07	1·21	0·05	0·53	0·08	17·02	0·14	0·15	18·27	0·15	0·15
3·33W	0·32	0·07	0·07	0·93	0·08	0·07	0·96	0·05	0·30	0·08	17·32	0·16	0·18	18·25	0·15	0·15
2·67W	0·18	0·06	0·07	0·76	0·07	0·07	0·92	0·05	0·21	0·07	17·40	0·16	0·18	18·16	0·14	0·14
2·00W	0·16	0·06	0·06	0·84	0·07	0·06	0·97	0·05	0·30	0·07	17·10	0·14	0·16	17·94	0·13	0·13
1·33W	0·21	0·06	0·06	0·91	0·06	0·06	1·01	0·04	0·44	0·06	16·85	0·13	0·14	17·76	0·12	0·12
0·67W	0·17	0·05	0·05	0·89	0·06	0·05	1·01	0·04	0·50	0·06	16·71	0·12	0·13	17·60	0·11	0·11
0·00	0·15	0·06	0·06	0·82	0·06	0·06	0·94	0·04	0·40	0·06	16·87	0·13	0·14	17.69	0·12	0.12
0·67E	0·17	0·06	0·06	0·88	0·06	0·06	0.98	0·04	0·48	0·06	16·81	0·13	0·14	17·69	0·12	0·12
1·33E	0·23	0·06	0·06	0·92	0·06	0·06	1·01	0·04	0·44	0·06	16·87	0·13	0·14	17·79	0·12	0·12
2·00E	0·29	0·06	0·06	0·91	0·07	0·07	0·99	0·05	0·36	0·07	17·18	0·15	0·17	18·09	0·14	0·14
2·67E	0·30	0·07	0·07	0·88	0·08	0·07	0·93	0·05	0·26	0·08	17·41	0·16	0·18	18·29	0·15	0·15
3·33E	0·28	0·08	0·08	0·85	0·09	0·08	0·95	0·06	0·21	0·09	17·70	0·19	0·21	18·55	0·17	0·17
4·00E	0·32	0·10	0·11	1·00	0·11	0·11	0·98	0·08	0·15	0·11	18·11	0·22	0·25	19·11	0.22	0·22
4·67E	0·42	0·11	0·12	1·16	0·12	0·12	1·20	0·08	0·18	0·12	18·14	0·23	0·26	[19·30	0·24	0·24
5·33E	0·25	0·14	0·15	0·92	0·16	0·15	0·93	0·11	0·17	0·15	18·87	0·32	0·36	19·79	0·31	0.31
6·00E	0·28	0·14	0·15	1·01	0·16	0·15	0·96	0·11	0·17	[0·15	18·82	0·31	0·35	19·83	0·31	0·31

6·67E	0·22	0·16	0·17	1·08	0·17	0·16	0·98	0·12	0·16	0·17	18·95	0·33	0·37	20·03	0·34	0.34
7·33E				0·79	0·21	0·20	1·19	0·14	0·15	0·21	19·62	0·45	0·51	20·41	0·41	0·41
8·00E				1·42	0·24	0·22	1·18	0·16	0·47	0·23	19·28	0·38	0·43	20·70	0·46	0·46
8·67E				1·71	0·32	0·30	1.16	0·22	0·37	0·31	19·63	0·45	0·51	21·34	0·62	0·62
9·33E							1·29		0·15		20·32	0·62	0·68			
							North-South scan									
9·5N				0·07	0·03	0·03	0·23	0·02	0·13	0·03	16·21	0·09	0·10	16·28	0·06	0·06
8·5N				1·10	0·22	0·21	0·88	0·15	0·15	0·22	19·43	0·41	0·47	20·53	0·43	0·43
7·5N				1·50	0·31	0·29	0·76	0·21	0·13	0·30	19·77	0·48	0·55	21·27	0·60	0·60
6·5N				1·24	0·19	0·20	0·93	0·15	0·56	0·21	19·26	0·38	0·43	20·50	0·42	0·42
4·5N	0·35	0·10	0·11	0·89	0·11	0·10	0·92	0·07	0·07	0·11	18·13	0·23	0·26	19·02	0·21	0·21
3·5N	0·32	0·08	0·09	0·85	0·11	0·09	0·90	0·06	0·07	0·09	17·79	0·19	0·44	18·64	0·18	0·18
2·5N	0·23	0·06	0·06	0·90	0·06	0·06	1·00	0·05	0·38	0·07	17·11	0·14	0·16	18·01	0·13	0·13
1·5N	0·12	0·06	0·06	0·83	0·06	0·06	0·90	0·05	0·36	0·07	17·03	0·14	0·16	17·86	0·13	0·13
0·5N	0·16	0·05	0·05	0·90	0·05	0·05	0·99	0·04	0·52	0·06	16·64	0·11	0·13	17·54	0·11	0·11
0·5S	0·21	0·06	0·06	0·88	0·05	0·05	0·97	0·04	0·50	0·06	16·85	0·13	0·15	17·73	0·12	0·12
1·5S	0·29	0·06	0·06	0·95	0·06	0·06	1·01	0·05	0·38	0·07	17·06	0·14	0·16	18·01	0·13	0·13
2·5S	0·33	0·07	0·07	0·96	0·08	0·08	1·04	0·06	0·27	0·08	17·36	0·16	0·18	18·32	0·16	0·16
3·5S	0.22	0·11	0·12	0·94	0·12	0·11	0·98	0·08	0·21	0·12	18·21	0·23	0·26	19·15	0·23	0·23
4·5S	0·22	0·11	0·12	1·21	0·12	0·11	1·10	0·08	0·23	0·12	18·01	0·21	0·24	19·22	0·23	0·23
5·5S	0·33	0·15	0·16	1·08	0·17	0·16	0·93	0·12	0·30	0·17	18·89	0·32	0·36	19·97	0·33	0·33
6·5S	0·22	0·18	0·19	1·13	0·20	0·19	0·97	0·14	0·07	0·20	19·19	0·37	0·42	20·32	0·39	0·39
7·5S	0·50	0·26	0·28	1·67	0·29	0·27	1·33	0·20	0·25	0·28	19·45	0·41	0·47	21·12	0·56	0·56
8·5S				1·77	0·33	0·31	1·07	0·23	0·11	0·33	19·67	0·46	0·52	21·44	0·65	0·65
9·5S				2·35	0·48	0·45	1·08	0·33	0·27	0·47	19·89	0·51	0·58	22·24	0·94	0·94
10·5S				1·71	0·39	0·37	0·83	0·27	0·00	0·39	20·09	0·56	0·64	21·80	0·77	0·77

from the M 3 model. In columns 4, 7, 9, 11, 14 and 17, we have listed the sampling errors in $U - B$, $B - V$, $V - R$, $R - I$ colours and V, B bands respectively, as derived from the M 92 model.

We find that the sampling errors obtained from both the models are comparable. Sampling errors for the region within 4 arcmin from the centre of the cluster vary from 0·06 mag to 0·09 mag. Since the colour is symmetric with respect to the centre of the cluster, this value may be divided by $\sqrt{2}$ and hence the average sampling error in this region is of the order of 0·05 mag.

Fig. 1 shows the variation of colours $U - B$, $B - V$, $V - R$ and $R - I$ and the brightness in V along both the east-west and north-south directions. In Fig. 2 we plot the individual V magnitudes and $B - V$ colours in the east-west direction obtained on two consecutive nights. These points indicate the reproducibility of our measurement from night to night. The bumps in the wings of the brightness profile are inherent in the cluster. Similar bumps have been seen by Gascoigne and Burr (1956) for both ω Cen and 47 Tuc. Such abrupt changes in intensity are often asso-

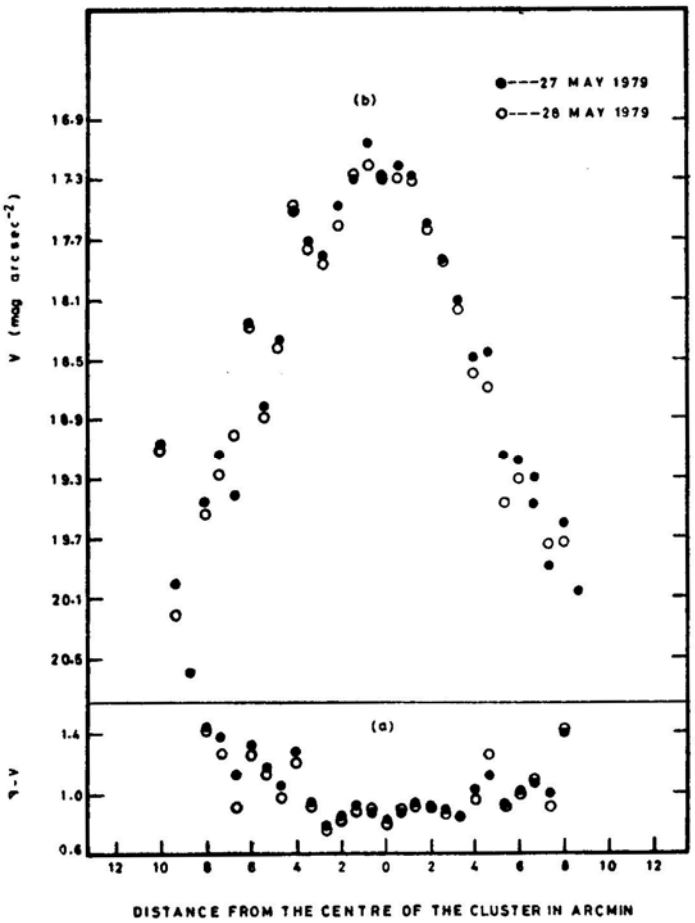

Figure 2. V magnitudes and $B - V$ colours obtained on two consecutive nights by an aperture scan of ω Cen in the east-west direction. The stability of the counts proves the accuracy of positioning the aperture over the cluster.

Table 3. Log f values for the two scan directions.

East-West Scan

log r	log f				
	U	B	V	R	I
−0·176	−3·116	−3·048	−2·692	−2·296	−2·100
0·125	−3·195	−3·103	−2·739	−2·335	−2·160
0·301	−3·294	−3·206	−2·854	−2·462	−2·330
0·426	−3·383	−3·287	−2·961	−2·591	−2·500
0·523	−3·480	−3·360	−3·004	−2·624	−2·520
0·602	−3·637	−3·477	−3·027	−2·589	−2·453
0·669	−3·813	−3·657	−3·219	−2·785	−2·705
0·727	−4·037	−3·873	−3·457	−3·053	−2·977
0·778	−4·017	−3·797	−3·333	−2·901	−2·813
0·824	−4·160	−3·968	−3·546	−3·108	−3·012
0·865	−4·344	−4·100	−3·676	−3·184	−3·092
0·903		−4·236	−3·668	−3·164	−3·008
0·938		−4·536	−3·972	−3·388	−3·176
0·970			−3·998	−3·448	−3·332

North-South Scan

log r	log f				
	U	B	V	R	I
−0·303	−3·116	−3·044	−2·688	−2·296	−2·092
0·176	−3·251	−3·171	−2·815	−2·431	−2·283
0·398	−3·378	−3·262	−2·894	−2·482	−2·354
0·544	−3·663	−3·559	−3·199	−2·823	−2·767
0·653	−3·760	−3·648	−3·228	−2·824	−2·764
0·740	−4·121	−3·989	−3·557	−3·185	−3·065
0·813	−4·217	−4·165	−3·689	−3·309	−3·185
0·875	−4·649	−4·477	−3·845	−3·625	−3·549
0·929		−4·597	−3·821	−3·429	−3·381
0·978		−4·897	−3·956	−3·524	−3·417
1·021		−4·720	−4·036	−3·704	−3·704

ciated with changes in colour. The bumps are barely noticeable in a *U* scan; they are striking in either *R* or *I*. Table 3 gives the mean surface brightness log *f* in the *U*, *B*, *V*, *R* and *I* bands expressed in units of 10·0 mag arcsec^{-2}. Column 1 gives log *r* where *r* is the distance from the centre in arcmin. Columns 2, 3, 4, 5 and 6 give the values of log *f* in the *U*, *B*, *V*, *R* and *I* bands. These are the means around the centre, separately evaluated for the east-west and the north-south scans. In evaluating the mean variation of surface brightness, the values at the locations of bumps in the profile have not been included. The log *f* values given here have been corrected for aperture smoothing, using an approximate equation similar to the one used by Illingworth and Illingworth (1976) for concentric aperture measures. In Fig. 3, we have plotted log *f* against log *r* (*r* in arcmin) along the major axis for the *U*, *B*, *V*, *R* and *I* bands. For the *V* band, the measures of Gascoigne and Burr as well as those of Da Costa (1979) uncorrected for the ellipticity of the cluster, are also plotted together with our results. The plot gives the values of log f_0 = 2·700 where f_0 is the surface brightness at r = 0 (King 1962) and is expressed in units of V = 10·0 mag arcsec^{-2}. From the measured $U - B$, $B - V$, $V - R$ and $R - I$ colours for the centre of the

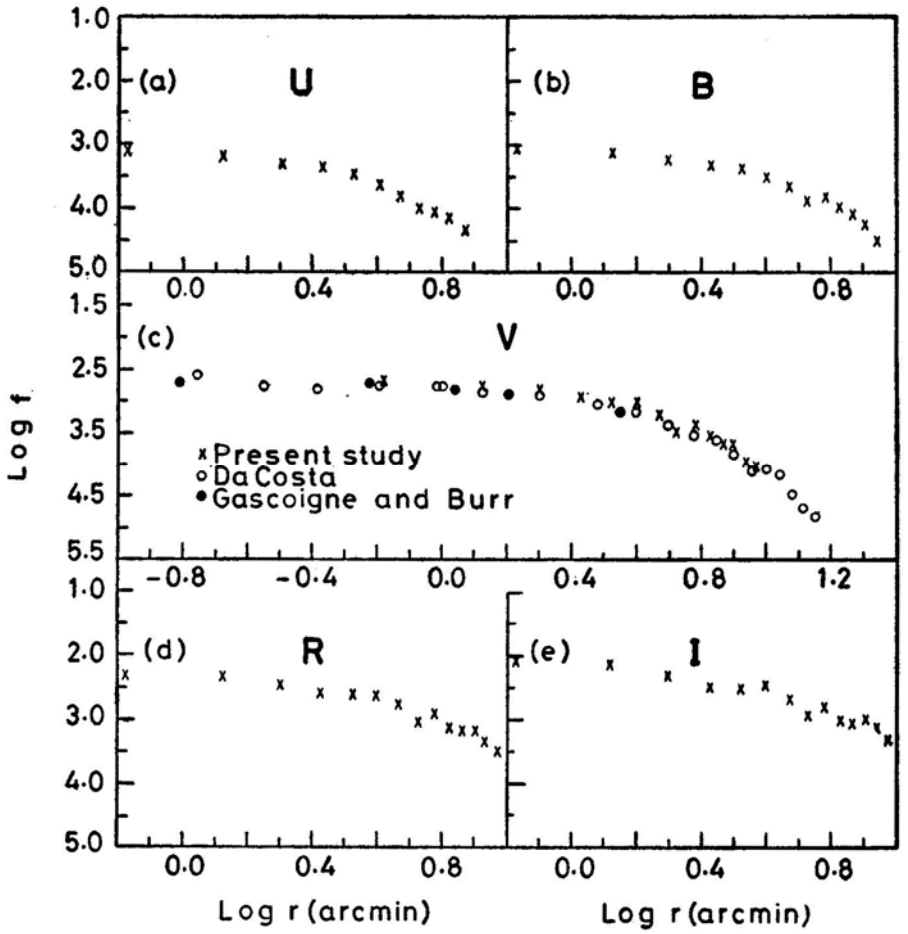

Figure 3. Variation of surface brightness over the cluster ω Centauri in *U*, *B*, *V*, *R* and *I* bands in the direction of the major axis. The central frame (c) has the measures of Gascoigne and Burr (1956), Da Costa (1979) as well as the results of the present study for the *V* band.

cluster, we have calculated the values of log f_0 for the remaining wavelength bands. Table 4 gives the mean values of cluster brightness and colour at the centre in the U, B, V, R and I bands.

The variation of log f with distance from the centre of the cluster along both the major and minor axes is shown in Fig. 4 for the five wavelength bands of observation. The continuous lines in each figure show the best fitting model of King (1966a).

Table 4. log f_0 values for different wavelength bands.

Wavelength band	log f_0
U	−3·112
B	−3·048
V	−2·700
R	−2·312
I	−2·128

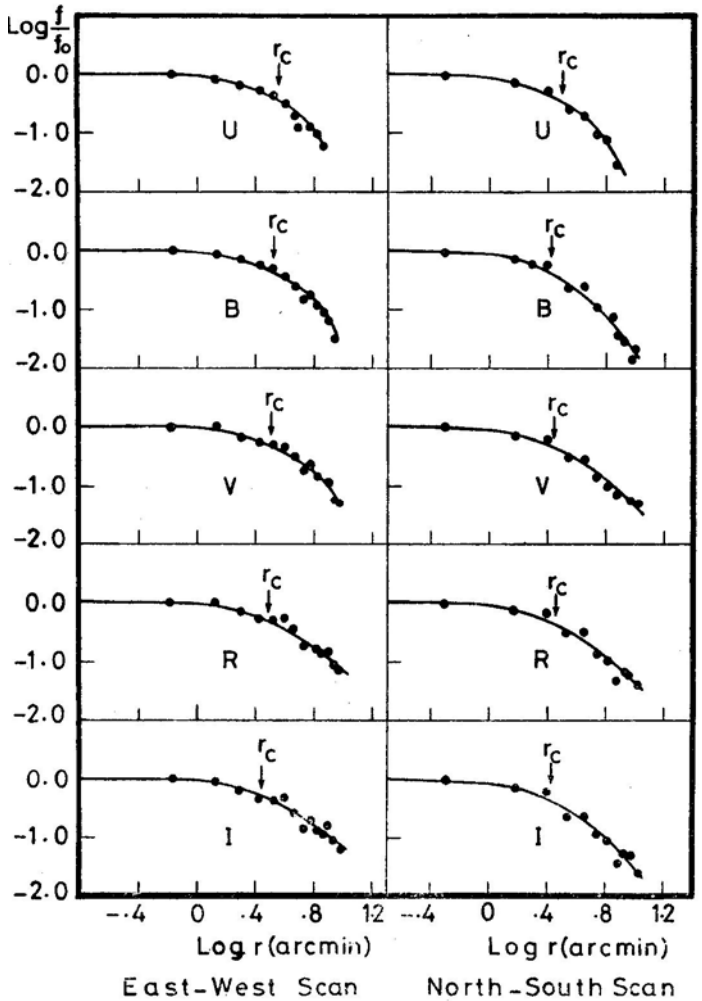

Figure 4. Surface brightness profiles in *U*, *B*, *V*, *R* and *I* bands, of ω Cen, along the major and minor axes. Continuous lines in each figure show the best fitting model of King (1966a). Core radii r_c are marked.

The core radius r_c and the concentration factor $C = \log (r_t / r_c)$ for the curves fitted to the five wavelength bands are given in Table 5. The last column in Table 5 gives the ratio of the core radius along the minor axis to that along the major axis, in the respective bands. Three aspects of the colour variation over the cluster are of interest. These are the dependence of the cluster ellipticity, the derived core radii and the values

Table 5. Core radii and concentration factors for different wavelength bands.

Wavelength band	East-West scan		North-South scan		$\frac{r_c \text{ (minor)}}{r_c \text{ (major)}}$
	log r_c	log (r_t/r_c)	log r_c	log (r_t/r_c)	
U	0·55	0·75	0·50	0·75	0·89
B	0·52	1·00	0·42	1·00	0·79
V	0·50	1·25	0·44	1·25	0·87
R	0·48	1·50	0·45	1·25	0·93
I	0·44	1·75	0·42	1·25	0.96

of the concentration factor on wavelength. The cluster appears more elliptical in the short wavelength bands than at the longer wavelengths. The values of core radii are greater in the ultraviolet or blue than in the red and near infrared. If the distribution of blue star experiences a peak, before it falls with increasing radial distance from the centre, the contribution of these stars to the intensity in the blue will be such as to give a larger value of the core radius. It is of interest to recall that Dickens and Woolley (1967) have observed a larger concentration of bright horizontal branch (HB) stars in the major axis sectors than in the minor axis sectors. This is further corroborated by the study of Strom, Strom and Goad (1976) who have observed colour gradients in E and S0 galaxies to be the greatest along the minor axis. As seen in a later section of this paper our counts of HB stars show a preponderance along the major axis than in a direction perpendicular to it. This feature also explains how the values of r_c along the minor axis do not show a striking dependence on colour. The variation in radial gradient of the blue component of stars along the minor axis is insufficient to modify the light distribution significantly. Also, the values of the concentration factor (C) show a gradual increase from short wavelength bands to the long wavelength bands. This could be because of a faster decrease of the number density of the stars contributing to the surface brightness in the blue band compared to that of the red stars which contribute most of the light in the I band. The core radius and the concentration factor C obtained by us in the visual band are comparable in magnitude to the values obtained by King (1966a) and Da Costa (1979), even though the technique employed is different and the data covers only a limited region of the cluster.

Fig. 5 shows the distribution of $B - I$ colour along the major and minor axes. The curve is fairly symmetrical around the centre. The region between A_1 and A_2 has a diameter of about 3·5 arcmin with $B - I \simeq 2{\cdot}45$ mag. Beyond this region the cluster gets bluer and reaches a maximum blueness at B_1 and B_2. The difference in $B - I$ colour between the centre and this zone is 0·45 mag. The width of this zone is about 1·5 arcmin. Beyond B_1, B_2 the cluster becomes redder again. The change in colour is rather sharp. The arrows in the figure show the regions where the cluster has a discontinuity in the trend. The effect of these three zones on the equidensity contours is discussed later.

Fig. 6(a) shows the ($U - B$, $B - V$) relation for the observed regions of the cluster.

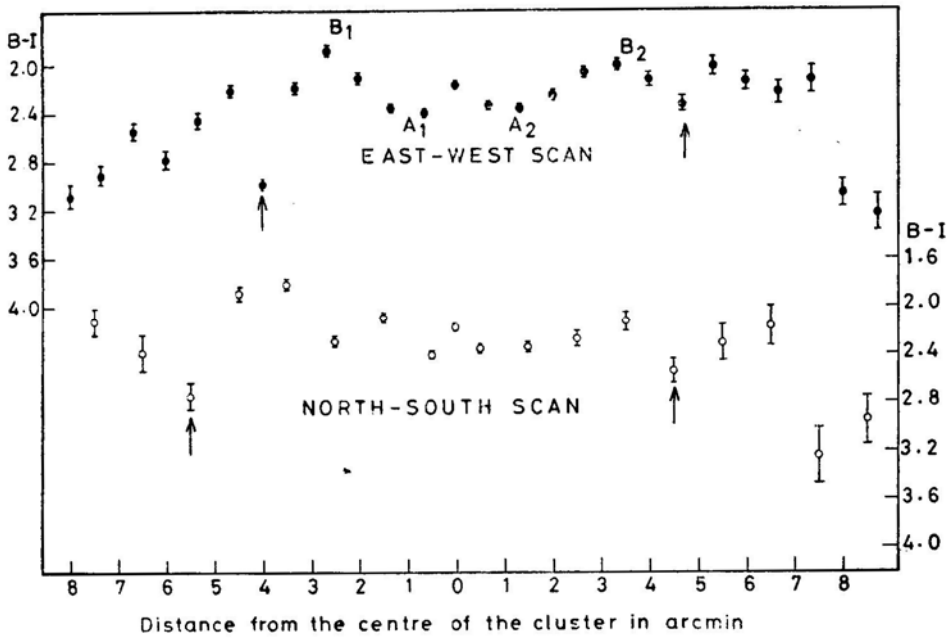

Figure 5. Distribution of B — I colour along the major and minor axes of ω Cen. The scale for the east-west (major axis) scan is at the left while the scale at the right corresponds to the north-south (minor axis) scan.

The points on the minor and major axes can be easily discerned. A number adjacent to each point indicates its distance in minutes of arc from the cluster centre. The continuous line is the intrinsic (U — B, B — V) relation (Eggen and Sandage 1965) for the main sequence, shifted by E_{B-V} = 0·11 mag and E_{U-B} = 0·08 mag for space reddening. In Fig. 6(b) we have plotted the values of δ (U — B), the ultraviolet(UV) excess, for each point. This excess is the difference between the Hyades standard relation and the observed U — B for each observed B — V point. The abscissa shows the distance r of the point from the cluster centre. We note that from r = 0 to r = 1·7 arcmin the UV excess values range between 0·2 and 0·3 mag. Of considerable intererst is the fact that the UV excess right at the centre is only 0·2 mag. Beyond r = 4 arcmin, the UV excess keeps increasing with increasing distance from the cluster centre. Between r = 1·7 arcmin and r = 4 arcmin, the UV excess shows a decrease with a minimum value around 3 arcmin. This is also the region where the cluster has become bluer in B — I by about 0·45 mag over its value at the cluster centre.

The presence of a large number of red stars around the cluster has been observed by Dickens and Woolley (1967). The total counts for the region from 3·5 arcmin to 5·5 arcmin from the cluster centre, are 917 for the red and 298 for the blue stars. Most of these red stars are much brighter than the blue stars in the cluster and hence the contribution to surface brightness by these red stars is much more than what the counts show. The kinks seen in the B — I versus r curve located in Fig. 5 by arrows, are the result of the presence of these red stars. Almost all the globular clusters observed by Strauss (1978) show similar kinks in B — I colour. The stars at the centre and the stars that give rise to the kinks have similar B — I colours and UV excesses. The

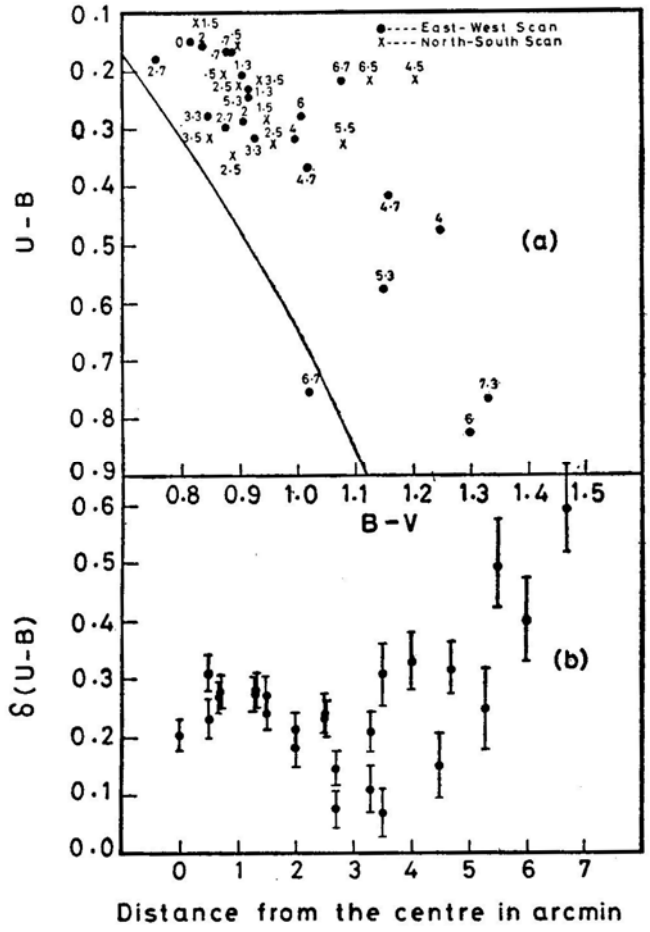

Figure 6. (a) U — B, B — V relation for the observed regions of the cluster ω Cen. The number marked against each point is the distance in minutes of arc from the centre of the cluster. (b) The dependence of the UV excess of these regions on their distance from the centre. The sampling error in U — B is shown by vertical bars.

zone between these two regions is different in that it has a bluer colour and a smaller UV excess.

Three colour photometry by Sandage and Walker (1966) on M 92 shows that the stars belonging to the subgiant sequence can be separated from the asymptotic giant branch (AGB) stars in a (U — B, B — V) diagram. *UBV* photometry on M 3 by Johnson and Sandage (1956) and on ω Cen by Geyer (1967) show the same effect. But this photometric difference is not seen in the spectral features of the stars belonging to these groups. A moderate resolution spectrophotometric survey of M 92 by Strom and Strom (1971) revealed no difference in the spectral energy distribution except for wavelengths below the Balmer jump. Strom and Strom find that the differences in δ (U — B) between the red giants and the AGB stars have a weak dependence on distance of the star from the cluster centre. For the red giants in M 92, they get a UV excess of 0·24 mag. This matches well with our value of 0·26 mag for the region around the centre of ω Cen. Strom and Strom also get a UV excess value of 0·04 mag for the AGB stars which compares well with our value of 0·10 for the

intermediate region in the cluster ω Cen. Any attempt to seek a one-to-one correspondence between the $\delta(U - B)$ behaviour of individual stars and that in the integrated light of the different regions of the cluster, is perhaps not justified because of the contribution of the blue horizontal branch (BHB) stars to the *UBV* light of the cluster. But the similarity in the range of $\delta(U - B)$ values gives an indication of the kind of stars which dominate the surface brightness in any of the different regions of the cluster studied.

We now search for a similar distance dependence of UV excess in M 3 from published data by Sandage (1953). Stars measured by him from Series I plates cover a magnitude range of $12{\cdot}7 \leqslant m_{pv} \leqslant 17{\cdot}5$ and are selected from an annulus with the inner and outer radii of 100 arcsec and 600 arcsec respectively. In Fig. 7 we have plotted the UV excess of these stars against their distance from the cluster centre. Stars which belong to the giant branch, subgiant branch, horizontal branch, asymptotic giant branch and the blue extension of the horizontal branch are plotted with different symbols in the figure. All the stars measured within 2·75 arcmin from the centre of the cluster show UV excess much lower than what is seen outside this zone. It is apparent that all stars located within 2·75 arcmin of the cluster centre have small values of UV excess, regardless of their position in the HR diagram. The giant branch (GB) stars have large UV excess only when they are located outside the 2·75 arcmin zone. The AGB stars for which the photometric data are available fall within the 2·75 arcmin zone and show small UV excess. The BHB stars are the stars with a UV deficit and these are within the 2·75 arcmin zone. The range in δ $(U - B)$ is very large for the giants. The BHB stars in the cluster form a homogeneous group having similar brightness and colour. If we consider the mean UV excess of the BHB stars within 2·75 arcmin from the cluster centre and also outside 2·75 arcmin from the centre, we find that the BHB stars in the inner region have UV excess smaller by 0·05 mag when compared to the UV excess of BHB stars in the outer region. This difference in UV excess should be definitely coming from a diffuse background radiation, affecting the photometry of individual stars. The fact that the BHB stars nearer to the centre have a smaller UV excess when compared to the outer stars, shows the similarity of the radiation from the BHB stars and the diffuse background.

The small UV excess in the intermediate region in ω Cen can be due to (i) the contribution from a diffuse background which has properties similar to the HB stars, (ii) an increase in the number density of HB stars and (iii) a decrease in the number of bright red giants. The results of the photometry of individual stars in M 92 and M 3 show the effect of the background on the UV excess of the stars very clearly. The increase in the density of HB stars in the intermediate region of the cluster ω Cen (from 1·7 arcmin to 4 arcmin) and also its correlation with the ellipticity derived from equidensity contours of the cluster are demonstrated in a later section. A region with numerous HB stars will therefore show, in integrated light, the effects of a small UV excess. The core of the cluster is abundant in closely packed bright red stars and hence the disturbing effects of the radiation from the diffuse background and HB stars are not very apparent. Right at the centre there is a zone of 40 arcsec diameter where the bright red stars are few; this region is found to show a smaller UV excess as seen in Fig. 6. There is an increase in the number of HB stars with increasing distance from the centre. This results in a bluer colour and smaller UV excess in integrated light that originates from the intermediate zone in ω Cen.

Wherever the aperture comes across bright red stars during the scan, 'kinks' are produced in the colour curve as seen in Fig. 5 and 'bumps' in the surface brightness profiles as seen in Fig. 1. Gascoigne and Burr (1956) have shown that these bumps are seen not only in the profiles of ω Cen on both sides of the cluster centre, but also in 47 Tue at a distance of about 2 to 2·5 arcmin from the centre. This becomes significant when we consider the fact that 47 Tuc also becomes bluer beyond 2 arcmin from the centre.

A large range in δ (U — B) for the giant branch and the main sequence stars of M 3 has been pointed out by Johnson and Sandage (1956). Despite the scatter in these values, as seen in Fig. 7, at large distances from the cluster centre, the dependence of δ (U — B) on distance from the centre is obvious and this aspect seems best ascribed to a background contribution similar to the BHB stars of low UV excess.

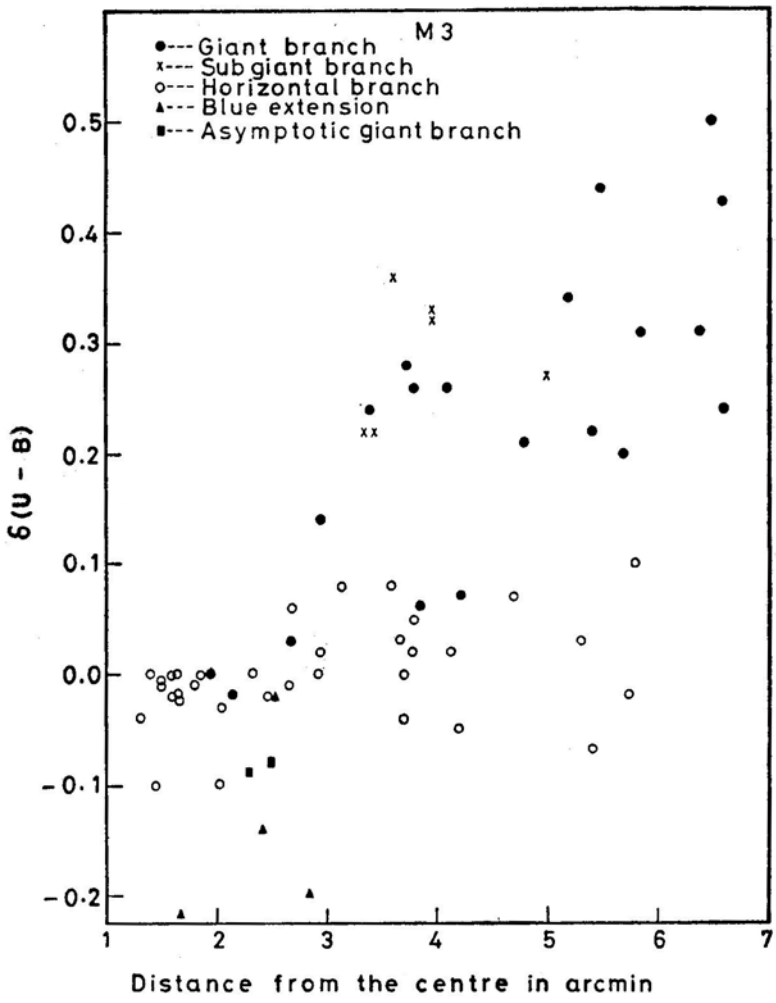

Figure 7. Plot of UV excess δ (U — B) of stars in M 3 measured by Sandage (1953) from series I plates, against the distance from the centre. The effect of the blue diffuse background is found to be maximum within 2.75 arcmin from the centre.

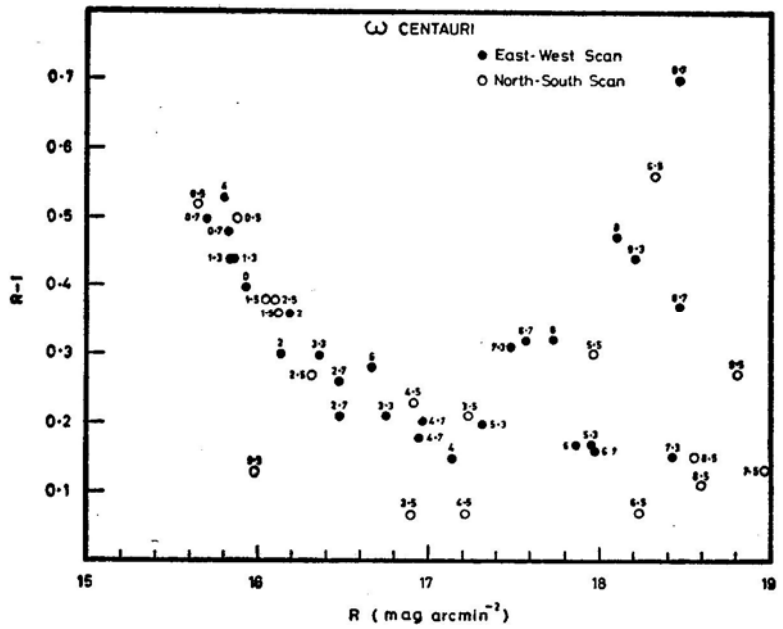

Figure 8. *R, R — I* relation for the observed regions of the cluster ω Cen. The number marked against each point shows the distance from the centre in minutes of arc.

2.4 *R, R– I Relation*

Fig. 8 is a plot of *R*, the surface brightness in mag arcsec^{-2} against *R — I* colour over the cluster ω Cen along the major and minor axes. Major axis locations are shown by filled circles and those on the minor axis by open circles. The number marked near each point shows its distance from the centre of the cluster in minutes of arc. The diagram shows the cluster to be the reddest near the centre, and becoming blue away from the centre. Since the contribution to the surface brightness of the red stars is decreasing and that from the bluer stars is increasing we can expect to see the colour of the cluster becoming bluer as we go outwards from the centre with normalcy in redness restored in the outer regions. The change appears to be the same for the major and minor axes. The large scatter at faint values of brightness can be caused by the sporadic appearance within the diaphragm of a red or blue star either belonging to the cluster or to the background field. Of particular interest is the fact that right at the centre the cluster is bluer than the region at its immediate vicinity (0·5 arcmin away). This aspect is also similar to the pattern seen in the $\delta(U — B)$ variation.

In the next section, we will show how this change in the distribution of colour affects the equidensity contours of the cluster.

3. Equidensitometry of ω Centauri and 47 Tucanae

Aperture photometry carried out by us and the photometric observations of individual stars made by other authors show an increase in the population of giants towards the

centre of ω Cen. We have seen in an earlier section, evidence for a blue bulge of resolved and unresolved stars around the central regions. The effect of this peculiar distribution of blue and red stars will be apparent in the results of multicolour equidensitometry of the cluster. The segregation effects are best seen in the dense inner regions of the cluster. In these regions of high star density, only equidensitometry can be used to study the ellipticity and colour gradients. We have used the well known Sabattier technique to obtain equidensity contours of the cluster. The Sabattier technique has been employed earlier on globular clusters, for a determination of the axial ratios and the position angles of the major axes. Kadla (1966) and Sistero and Fourcade (1970) used the technique with success on M 13 and ω Cen respectively. These results on the degree of ellipticity of the two clusters are in conformity with the results of star counts. Kadla *et al.* (1976) made a detailed study of the dependence of the axial ratio b/a and the position angle of the major axis, on the distance from the centre of the clusters M 3, M 5, M 13, M 15 and M 92 in *UBV* and *R* bands. In all these clusters the ellipticity reaches a maximum at a certain distance from the cluster centre, depending on the cluster. In some clusters like M 92 and M 5, the curves show well defined regions of minimum ellipticity close to the centre and again at some distance away from the cluster centre. The position angle of the major axis of this inner region is, however, different from that of the outer region in both these clusters.

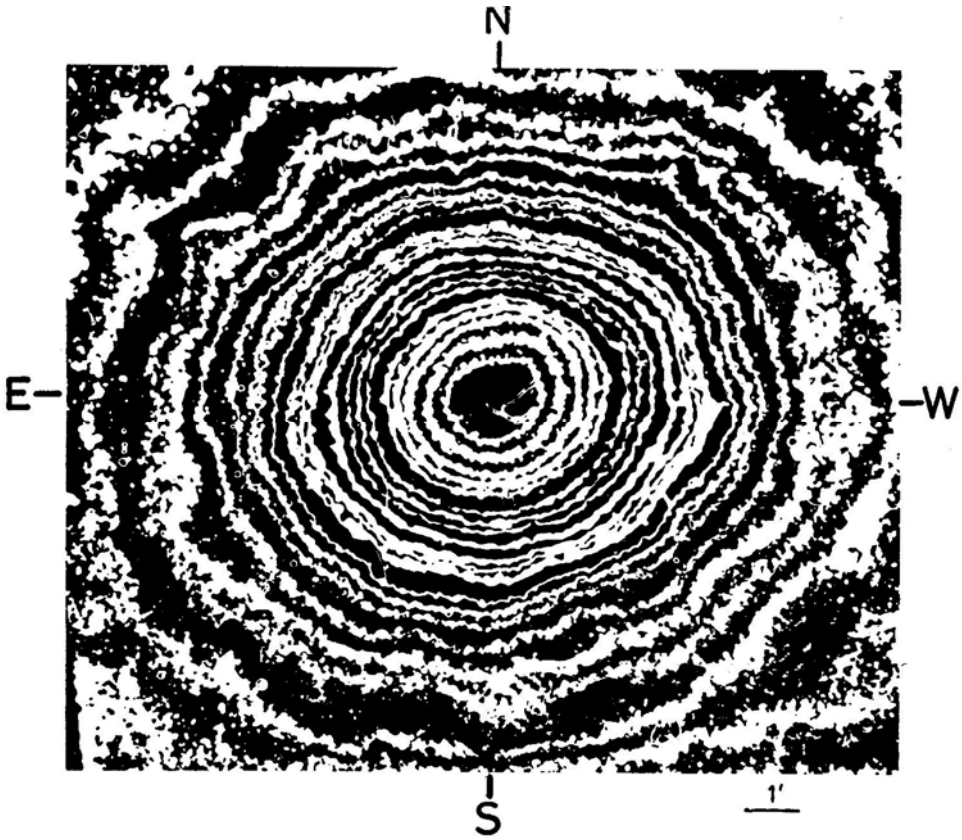

Figure 9. Equidensity contours of ω Cen in the *V* band.

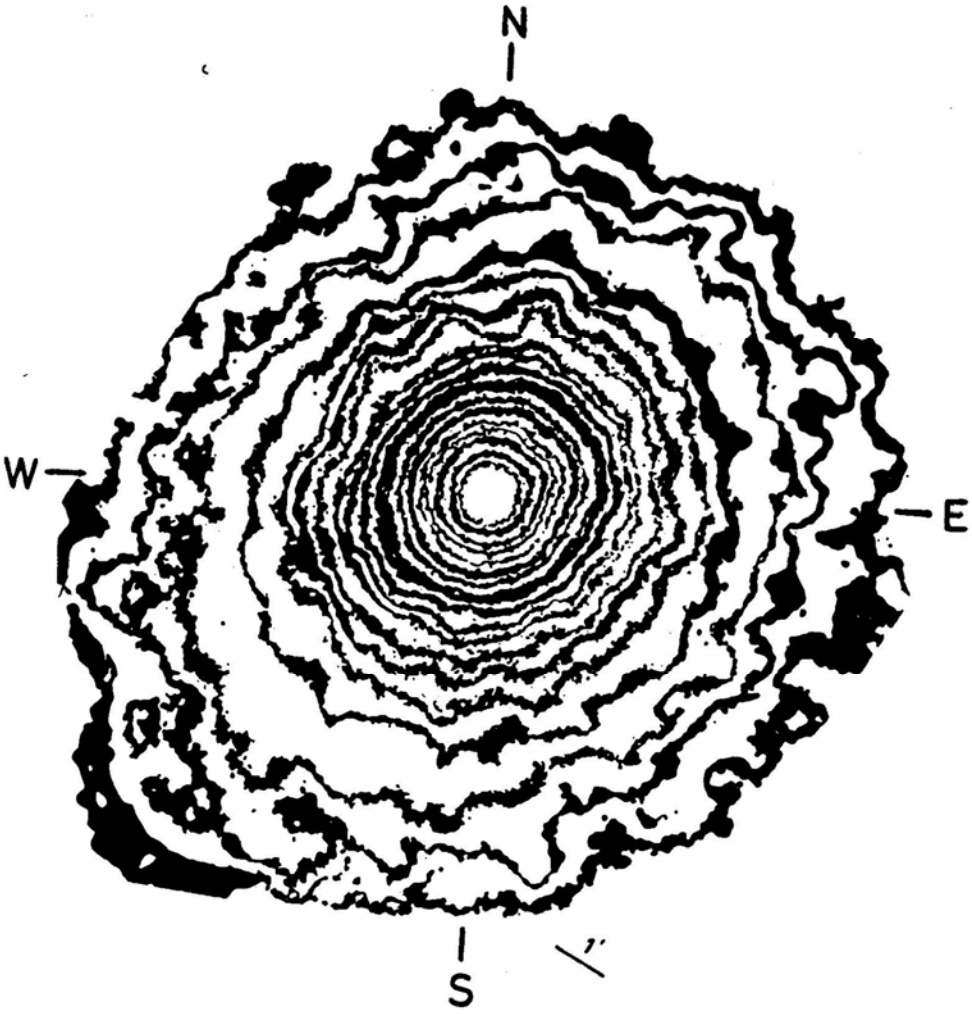

Figure 10. Equidensity contours of 47 Tuc in the *V* band.

3.1 *The Equidensity Contours*

We have derived equidensity contours of ω Cen from photographs taken through the filter and emulsion combinations of the standard *B*, *V* system, together with an infrared band isolated by the combination of hypersensitized I-N and an RG 8 filter. The equidensity contours of 47 Tuc were also obtained from a *V* photograph kindly supplied by Dr Martha Liller. A diffuser was introduced between the photographic film and the cluster photograph while taking the initial graded exposures. Outlying stars on the plate are used to match the contours while making the isophote maps. Equidensity contours of ω Cen and 47 Tuc in *V* band are shown in Figs 9 and 10 respectively. For each contour, we have measured *x*, *y* coordinates for 72 points on the contour at 5° intervals along with the *x*, *y* coordinates of 2 reference stars of the cluster. A computer program is used to derive the axial ratio *b/a*, position angle ϕ,

area within each contour, (x, y) coordinates of the centre of each contour and the respective errors. The origin of the coordinate system is the star marked T in Fig. 14 and the x-axis is the line joining T to the second reference star M. Since all the distances are normalised to the distance TM on every plate, the small differences in the scales of the plates taken in B, V and infrared bands will not cause any error in the results. Detailed measures are published elsewhere (Scaria 1980).

In Fig. 11(d) we note the change of axial ratios with distance from the centre in the B and the infrared bands. The contour 1·7 arcmin distant from the centre along the major axis is the closest to a circle in shape. Beyond this location the ellipticity increases and reaches a maximum around 3 arcmin from the centre. As one continues outward, the ellipticity decreases to a minimum given by an axial ratio of 0·88 before

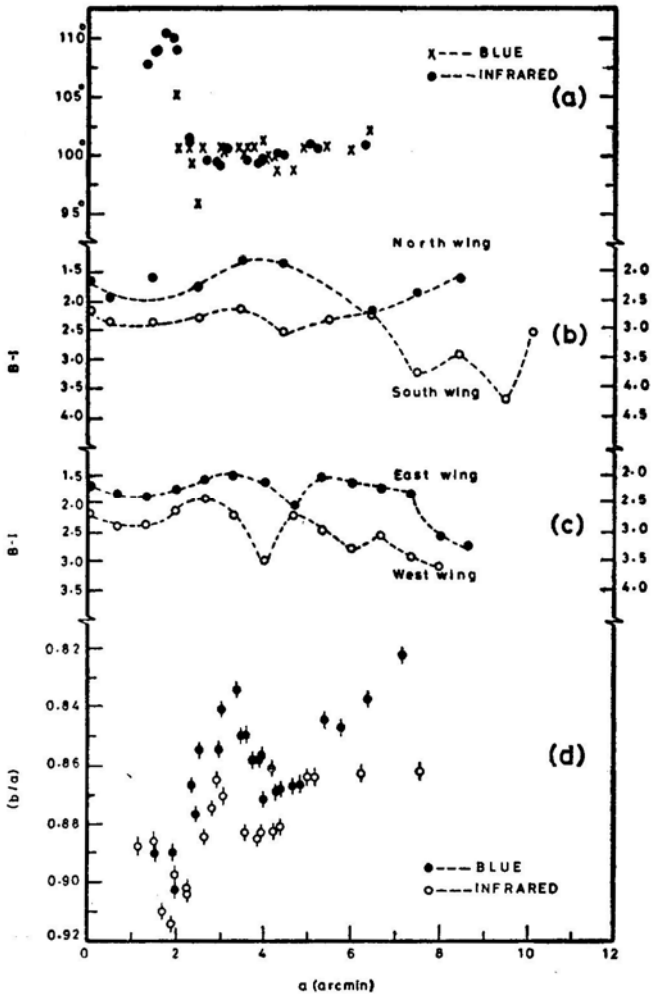

Figure 11. (a) The variation of position angle of the major axis of the equidensity contours of ω Cen as a function of the semi major axis (a). (b) The variation of B — I colour along the minor axis of ω Cen. The north wing (scale at right) and the south wing (scale at left) are separately shown. (c) The variation of B — I colour along the major axis of ω Cen. The east wing (scale at right) and the west wing (scale at left) are separately shown. (d) The variation of the axial ratio (b/a) of the equidensity contours of ω Cen as a function of the semimajor axis (a).

it increases again in the outermost regions. It should be noted that the cluster is definitely less elliptical in the infrared band than it is in the blue band. This difference is very pronounced everywhere beyond 2 arcmin from the centre. We plot in Fig. 11 (a) the position angle ϕ against a the semimajor axis. A change in position angle is quite striking between 1·7 arcmin and 2·5 arcmin. Beyond this there is little change in the outer regions.

Fig. 12 is a plot of b/a against a for the clusters M 92 and ω Cen in the B band. Data for M 92 is taken from Högner *et al.* (1973). The values of a for M 92 have been normalized to the distance of ω Cen. The great similarity between the two curves shows that whatever dynamical conditions prevail in ω Cen are also found in M 92. Plots of similar data for M 5 obtained by Kadla *et al.* (1976) are also alike. All these clusters show a minimum in b/a at 3·2 arcmin from the centre, with low values appearing again in the outer regions. There is also a sudden change in the position angle of the major axis in the vicinity of the location of the first minimum.

Figs 11 (b) and (c) show the change in the $B - I$ colour across the cluster. The $B - I$ colour along the east, west, north and south wings are plotted separately. The most striking feature in the figure is that the change in ellipticity is connected with a change in colour. The core, which can be identified in the colour curve, matches with the first minimum in ellipticity. As we go outwards, we come across the bluer region in the cluster where the ellipticity reaches the highest value seen in the cluster. The

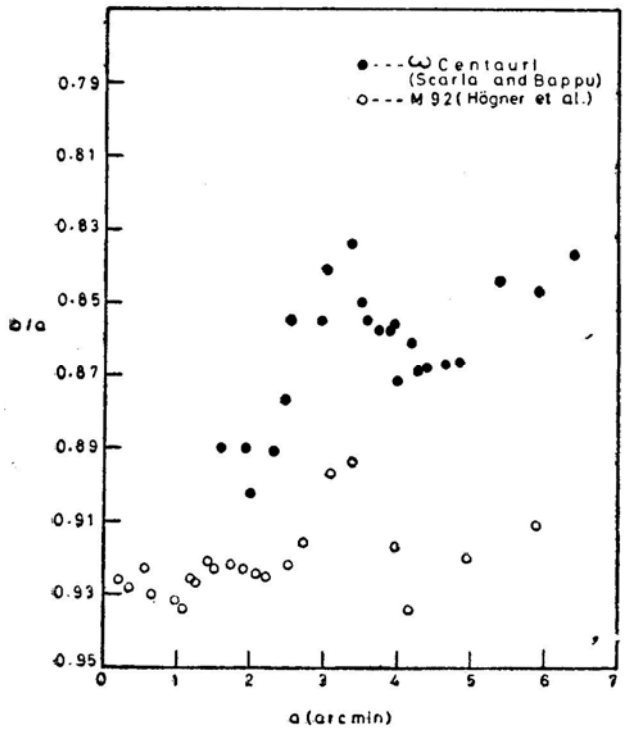

Figure 12. The relationship between b/a and a for the clusters ω Cen and M 92. Values of semimajor axis a for M 92 have been normalized to the distance of ω Cen. The data for M 92 is taken from Högner *et al*. (1973).

second minimum in the ellipticity curve falls in the region of the colour curve where the cluster is becoming redder with distance from the centre. This is the region where Dickens and Woolley (1967) get larger counts for red stars as compared to the blue ones. Thus, wherever the red stars predominate, the cluster ellipticity is small. The blue stars appear as a bulge around the core and this system shows a distribution more elliptical than the system of red stars. This blue bulge is between 1·7 arcmin and 4·0 arcmin from the centre.

Fig. 13 shows the relationship between the ellipticity curve and the colour curve of 47 Tuc. The colour curve is obtained from the photometry of Chun and Freeman (1979). The ellipticity curve was obtained by us in the *V* band through the same procedure as explained earlier. Our conclusion that the cluster ellipticity increases where the cluster is becoming bluer, is found to be valid here also. The diaphragm used by Chun and Freeman is too large to demonstrate strikingly a differential colour

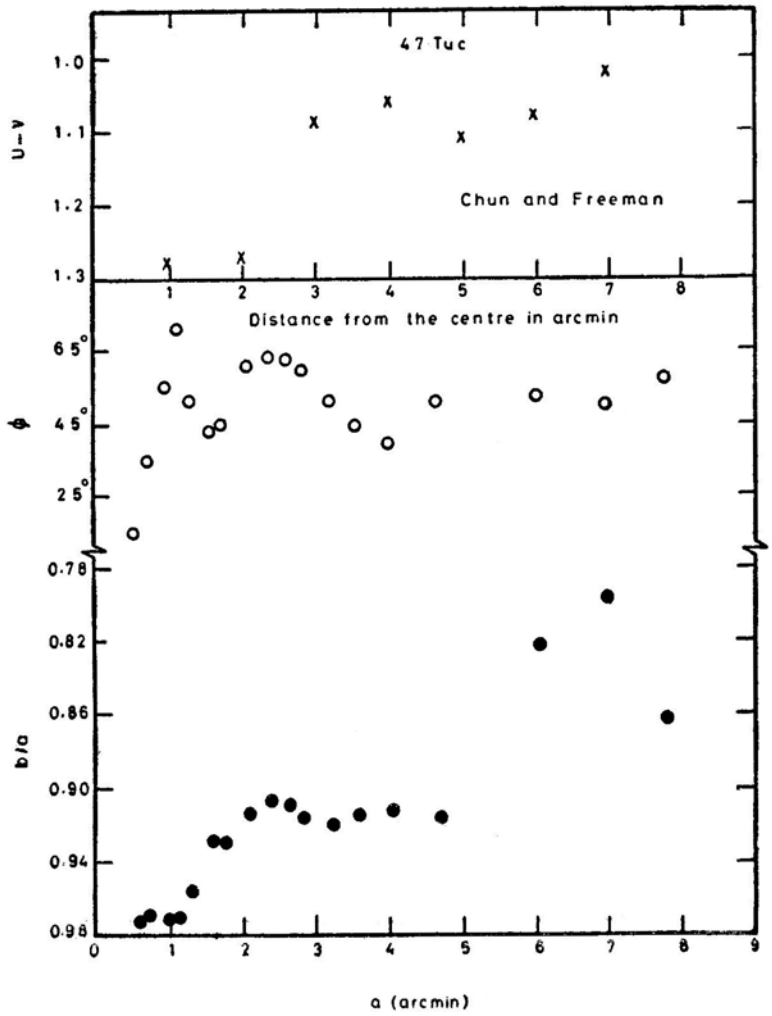

Figure 13. Variation of $U - V$ colour, position angle of the major axis (ϕ) and the ellipticity (b/a) for the cluster 47 Tuc as a function of distance from the centre.

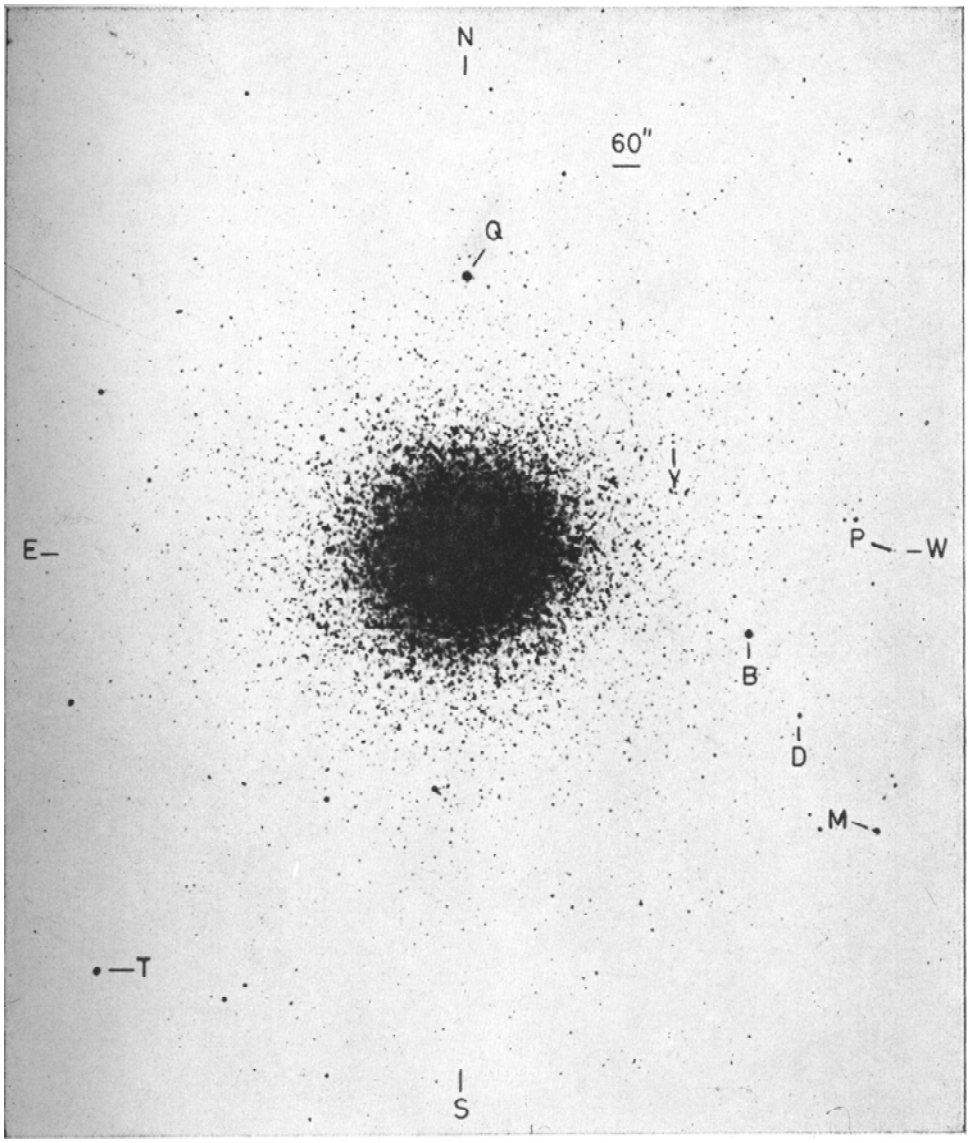

Figure 14. ω Cen in *B* band taken with the 102-cm reflector at Kavalur. Stars marked T and M are the reference stars for the equidensitometry of the cluster. Star P is the reference star for the scan in the east- west direction and star Q is the reference star for the north-south scan. Stars B and D are the two photoelectric standards. Star Y has been identified in Fig. 15(b).

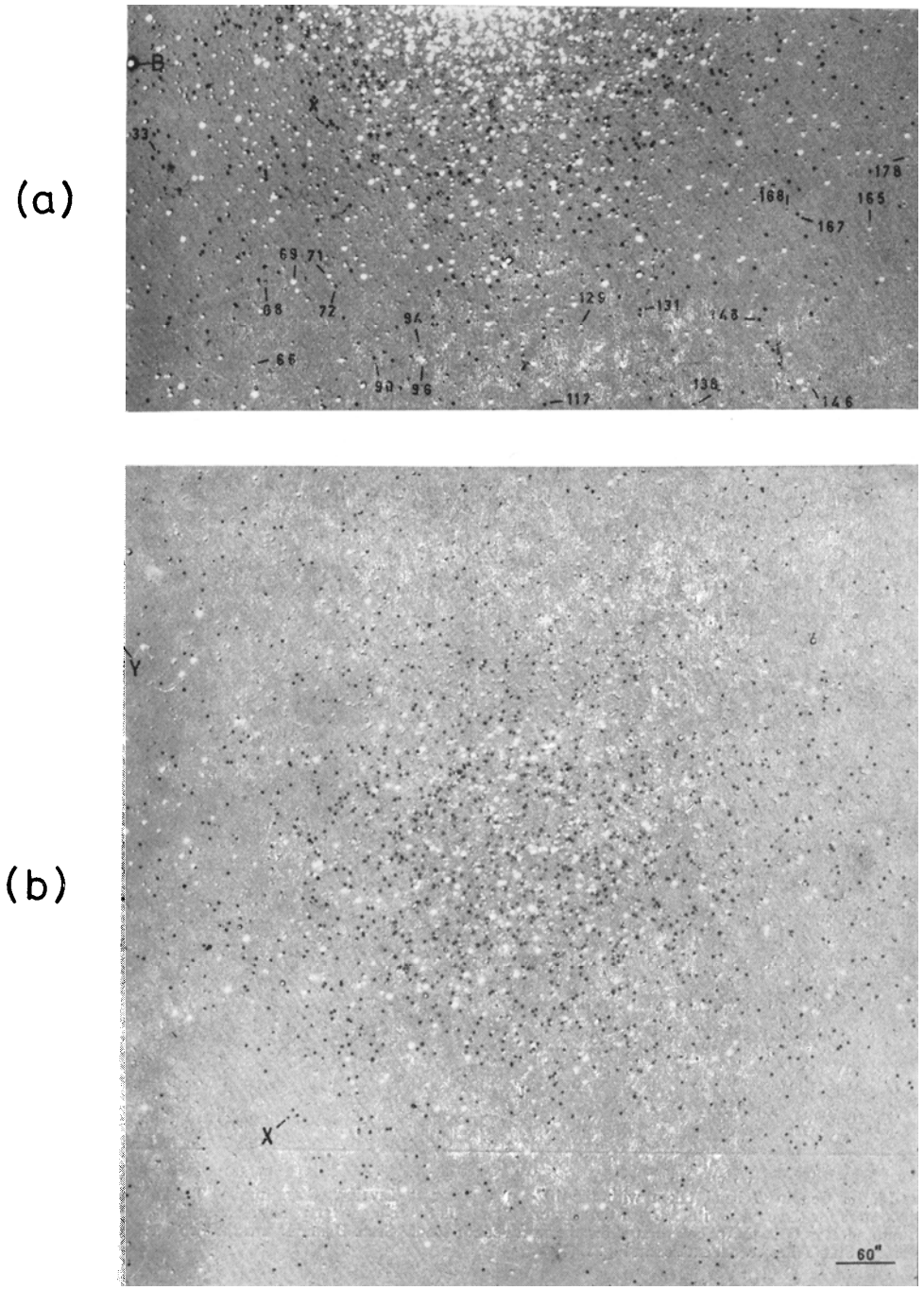

Figure 15. Distribution of Horizontal Branch stars in ω Cen. (a) Outer region: 20 stars with *UBV* photometry by Geyer (1967) are identified. Stars having colour $B - V < 0.4$ mag are seen as dark points while redder stars are seen as white points. (b) Inner region: Star X is marked to allow an easy comparison of the two figures.

change for a cluster with, such a small core radius; hence the exact location of the colour change cannot be determined from their observations.

In Section 2·3 we have pointed out the indirect evidence available for the presence of a bluer continuous background in the case of M 92 and M 3. Kadla *et al.* (1976) give the change in the ellipticity of these clusters from the inner to the outer regions. For M 92, the ellipticity increases from a = 100 arcsec to a maximum between 100 and 160 arcsec. This is also the region where the difference in the UV excess of AGB and GB stars is maximum as shown by Strom and Strom (1971). Hence we see that, even in this cluster, the background contribution has a relationship with the sudden increase in ellipticity of the cluster. Fig. 7 shows that the background effect is maximum within 2·8 arcmin from the centre of M 3. From Kadla *et al.* (1976) we find the ellipticity for M 3 increases from about 1·4 arcmin and reaches a maximum value around 2·7 arcmin. The red stars in the outer regions like those near the centre of the cluster, show a more spherical distribution as indicated by the decrease in the ellipticity of the cluster.

4. The Stars of the horizontal branch

In an earlier section we have shown the close association between the colour gradient across the cluster and the change in ellipticity with distance from the centre. We have also shown that a part of the contribution to the colour gradient is from a blue diffuse bulge of unresolved stars and that this bulge is characterised by a small UV excess. The main contribution to the colour gradient must be coming from the BHB stars. In this section, we describe the use of composite photography to separate out the blue and red stars in a globular cluster and study their distribution to explain the observed colour distribution over the cluster.

We know that ω Cen has a populated horizontal branch that is well separated in B — V colour, from the giant and the subgiant branch. All the HB stars have a colour B — V < 0·40 mag and the giant stars have B — V < 0·60 mag. Since it is a metal poor cluster, the asymptotic branch is not well populated and hence the blue stars are well separated from the red stars in the HR diagram. It is therefore easy to isolate them by photographic subtraction. In the case of horizontal branch stars, we have the added advantage that these stars are within a very small magnitude range and appear as stars with almost equal image diameters in the composite photograph. To avoid the main sequence, which is at best a minor contributor to the total brightness of the cluster, we have to control the exposure times of the original plates.

The blue plates are taken on 103a-O emulsion through a GG 11 filter. The infrared plates are on I-N emulsion through an RG 8 filter. Two kinds of composites are possible. In one case the negative of the blue plate is matched with the positive of the infrared plate ($B^{-}I^{+}$) and in the other case the negative of the infrared plate is matched with the positive of the blue plate ($B^{+}I^{-}$). Fig. 15 is a positive of a $B^{+}I^{-}$ composite photograph of ω Cen. In such a picture, stars bluer than 0·40 mag are seen as black dots. Fig. 15(a) shows the blue stars in the outer regions of the cluster while in Fig. 15(b) we see the blue stars in the central regions of the cluster. Table 6 gives a list of stars taken from Geyer (1967) for which *UBV* magnitudes have been determined. These have been marked in Fig. 15(a). Star X is marked in both the pictures to allow an easy comparison. It is very clear that all stars bluer than 0·40

Table 6. Geyer numbers of stars identified in Fig. 15(a).

Geyer Number	V	$B-V$	$U-B$
B	8·78	−0·01	−0·12
33	15·34	−0·04	−0·31
66	13·90	1·01	0·10
68	14·95	−0·03	0·05
69	12·26	1·29	0·83
71	12·92	1·23	0·20
72	15·01	0·05	−0·17
90	15·07	−0·08	−0·12
94	15·06	−0·19	−0·03
96	13·48	0·94	0·08
117	14·97	−0·05	0·03
129	14·04	1·03	0·01
131	14·57	0·15	0·02
138	13·52	0·49	−0·05
146	13·05	0·56	0·06
148	14·75	−0·08	0·18
165	13·39	0·98	0·37
167	14·78	0·03	0·02
168	14·66	0·83	−0·06
178	15·02	0·60	−0·11

mag appear as black dots in the picture. We have counted these blue stars with the aid of a grid of the kind shown in Fig. 16. The total counts per unit area in each annular ring of width 34 arcsec provides an idea of the density distribution. The values marked outside the outermost ring in Fig. 16 are the total counts in each sector. These values show the cluster ellipticity very well. The position angle of the major axis is about 70° which is much smaller than the value obtained for the cluster in V band equidensitometry. Thus the position angle is about 110° for the cluster core, about 100° for the region between 2 arcmin and 6 arcmin and about 70° for the system of blue stars.

In Fig. 17(a) we have compared the distribution of the HB stars in ω Cen with its surface brightness in the I and U bands. Fig. 17 (b) shows log N_{HB} against r_e where N_{HB} is the number of HB stars per arcmin^2 and r_e is the effective distance of the annular zone given by $r_e = \{[\frac{1}{2}\ (r_1^2 + r_2^2)]\}^{1/2}$, r_1 and r_2 being the inner and the outer radii of the annulus. The data for Fig. 17(a) are taken from Table 3. Since the contribution from the blue stars to the I band is negligible, we may assume that the I band surface brightness is indicative of the distribution of the GB stars in the cluster. From Fig. 17(a), the GB stars can be seen decreasing in density from the centre. The number density of the HB stars exhibits a general drop with distance from the centre; the striking feature is an enhancement over the normal gradient between 1·5 arcmin and 4·5 arcmin. It is this relative increase in the number of HB stars over the bright red giants in the 2 arcmin to 4 arcmin zone that gives much of the blue colour to the cluster seen in Fig. 5 between 1·5 arcmin and 4·5 arcmin. The system of HB stars shows a more elliptical distribution when compared to the system of red stars and also has a different position angle for the major axis. Thus all the; available, evidence shows the presence of a blue bulge of resolved and

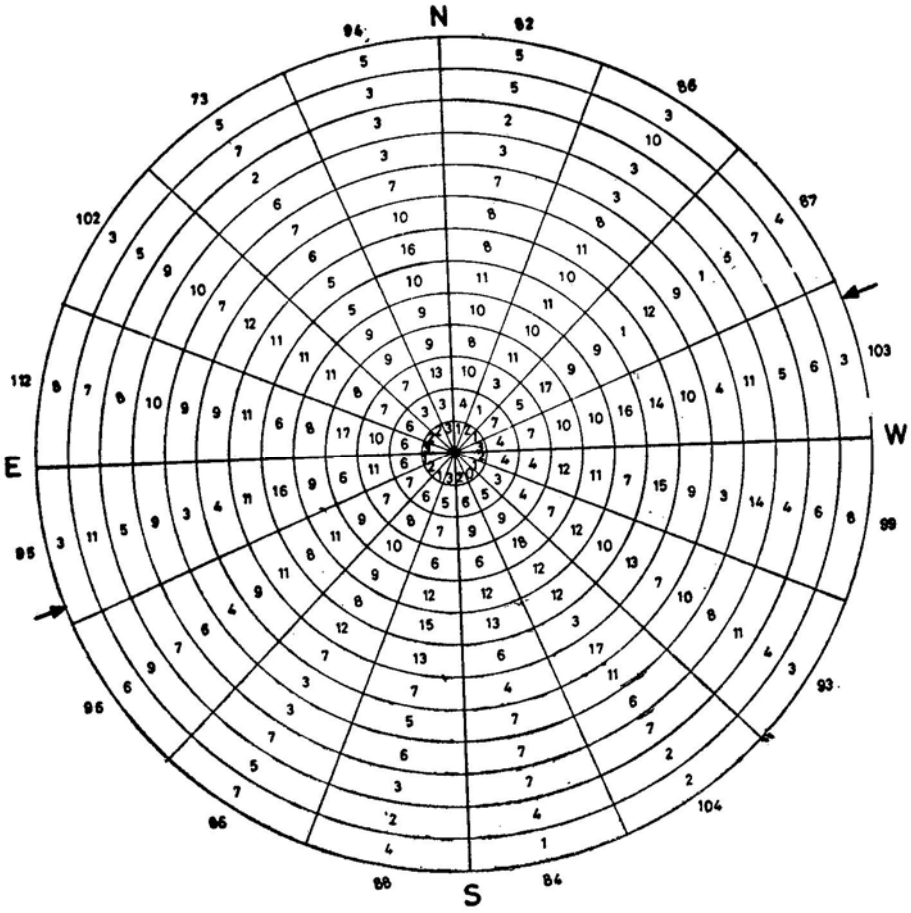

Figure 16. Counts of the horizontal branch stars in the inner regions of the cluster ω Cen. The grid shown in the figure is the kind used for counting the stars. The east-west line is marked on the grid, the centre of which is exactly superposed on the centre of the cluster determined from equi-densitometry. The numbers marked outside the outermost ring are the total counts for each sector. Also marked in the figure (arrows) is the position angle of the inner region of the cluster.

unresolved stars with a distribution different from that of the giant stars in the cluster.

The horizontal branch stars show a larger number density in the region between 1·7 arcmin and 4 arcmin in ω Cen. This cluster is well known for its wide giant branch which is indicative of a large range in metal abundance in the GB Stars. Norris (1980) has reported that the H and K lines of singly ionised Calcium and also the CN features vary greatly in strength from one giant to another in ω Cen. The colour-abundance corelation is so well established for the giants that the colour of a giant at a given magnitude is taken as a measure of its abundance. Freeman and Rodgers (1975) find that there is a large spread in the [Ca/H] values for the 25 RR Lyrae stars they observed. This indicates a primordial abundance variation in the gaseous cloud which formed ω Cen. Globular clusters are very old stellar systems and hence we should expect mass segregation in them. Theoretical considerations show that a metal rich main sequence star takes much longer to reach the giant stage than a metal

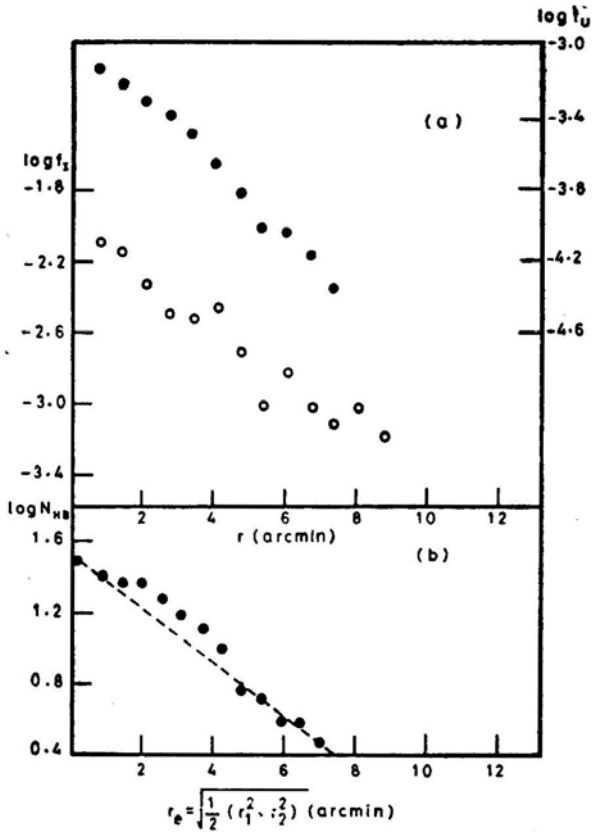

Figure 17. (a) The surface brightness profiles for ω Cen in U and the infrared bands. The filled circles represent log f values in U (scale at right) while the open circles denote the infrared values (scale at left). (b) The variation of the number of HB stars (N_{HB}) per arcmin^2 as a function of distance from the centre.

poor star. If two stars-one metal poor and the other metal rich-reach the giant stage at the same time, then the metal rich star should have started with a larger mass, so that the increase in the evolution time from the main sequence to the giant branch is compensated by the decrease in it due to a larger initial mass. Hence, at any time, a metal poor giant branch star is less massive than a metal rich giant branch star. For stars of mass close to that of the Sun and lower, the evolution time from the main sequence to the giant stage is much longer than the relaxation time at the centre of the cluster. Hence the metal poor giants can have a larger spatial distribution in be confined to the core. Thus, in ω Cen, giant stars which are metal poor compared to the red giants forming the core of the cluster, should find themselves at larger distances from the centre. These stars, when they evolve to the HB stage will continue to have the same distribution, since the evolution time from GB to HB is much shorter than the relaxation time of the cluster. This can explain the presence of a larger BHB to GB ratio and the resultant bluer colour for the intermediate region in ω Cen. It is difficult to speculate on the nature of the diffuse background Similar to the HB stars, the stars forming the background also have a small UV

excess. The contribution of white dwarfs to this background would also be very significant.

5. Nucleus of M 31 and ω Centauri

Using Stratoscope pictures of M 31, Light, Danielson and Schwarzschild (1974) have shown that the nucleus of M 31 is a separate and distinct feature of the Galaxy. It is found to be elliptical (1 arcsec × 1·6 arcsec) with its major axis lying in a position angle of 63° ± 5°. The position angle of M 31 is 38° (Johnson 1961). Light, Danielson and Schwarzschild find a sharp discontinuity of the nucleus from the nuclear bulge. They suggest that, as the nucleus and bulge are separate features, they would exhibit different velocity dispersions, colour, metallicity *etc.* which can be detected from ground based observations.

Walker's (1974) rotation curve of the nucleus of M 31 peaks with V_r= 100 km s^{-1} at r = 2·2 arcsec. The rotation curve falls in a Keplerian manner beyond r = 2·2 arcsec. Peterson (1978) has measured the rotation in the nuclear region of M 31 and obtained a peak velocity of V_r= 60 km s^{-1} at r = 1·5 arcsec. He finds that the velocity drops to zero between 3 arcsec and 6 arcsec before increasing once again. This rotation curve is explained using a two-component dynamical model, one component representing the nucleus and the other representing the nuclear bulge. The bulge component which dominates the surface brightness beyond 2 arcsec ($\simeq$ 6·5 pc) has a major axis luminosity profile with a core radius of 20 arcsec (from a fit of King's model).

In the case of ω Cen we have seen that the values of core radii are larger at shorter wavelengths than in the near infrared. We have also pointed out the correspondence between the locations of a blue bulge and the change in ellipticity of the isophotes. This bulge seems to contain a large number of AGB and HB stars as derived from their δ (U — B) characteristic. If we assume that a larger ellipticity is the result of a higher velocity of rotation, then the bulge in ω Cen should be rotating faster than the core. In the results obtained by Walker, the region of maximum rotational velocity falls well outside the nucleus. The core size of ω Cen in the light of the B band is about 2·5 pc in radius, whereas for the nucleus of M 31 the value is $\simeq$ 5 pc. The maximum ellipticity in ω Cen is at 6 pc and the maximum rotational velocity in the nucleus of M 31 is at 7·5 pc (Walker 1974). Peterson (1978) shows a dip in the velocity of nuclear rotation in M 31 between 10 pc and 20 pc from the centre. For ω Cen also we see a decrease in ellipticity between 6 pc and 8 pc. Beyond this region the ellipticity in the globular cluster and the rotation in the nucleus of M 31 show a gradual increase.

The similarity between the nucleus of M 31 and ω Cen in the photometric aspects of behaviour seems real and not fortutious. Dynamical causes, as yet unknown, may be responsible for the existence of sub-systems with characteristics that are subtly revealed by some aspects of integrated photometry. As we are on the threshold of high resolution studies of such galactic nuclei, the similarities seen over a range of stellar aggregates with a range of masses would undoubtedly contribute greatly to their elucidation.

References

Arp, H. C. 1958, *Astr. J.*, **63**, 118.
Cathey, L. R. 1974, *Astr. J.*, **79**, 1370.
Chun, M. S., Freeman, K. C. 1979, *Astrophys. J.*, **227**, 93.
Da Costa, G. S. 1979, *Astr. J.*, **84** , 505.
Dickens, R. J., Woolley, R. v.d. R. 1967, *R. Obs. Bull*, No. 128.
Eggen, O. J., Sandage, A. R. 1965, *Astrophys. J.*, **141**, 821.
Fernie, J. D. 1974, *Publ. astr. Soc. Pacific*, **86**, 837.
Freeman, K. C., Rodgers, A. W. 1975, *Astrophys. J.*, **201**, L71.
Gascoigne, S C. B., Burr, E. J. 1956, *Mon. Not. R. astr. Soc.*, **116**, 570.
Geyer, E. H. 1967, *Z. Astrophys.*, **66**, 16.
Hartwick, F. D. A. 1970, *Astrophys. J.*, **161**, 845.
Högner, W., Kadla, Z. I., Richter, N., Strugatskaya, A. A. 1973, *Soviet Astr.*, **16,** 843.
Illingworth, G., Illingworth, W. 1976, *Astrophys. J. Suppl. Ser.*, **30,** 227.
Iriarte, B., Johnson, H. L., Mitchell, R. I., Wisnieswski, W. 1965, *Sky Telesc.*, **30,** 21.
Johnson, H. L., Sandage, A. R. 1956, *Astrophys. J.*, **124,** 379.
Johnson, H. M. 1961, *Astrophys. J.*, **133,** 309.
Kadla, Z. I. 1966, *Soviet Astr.* **10,** 97.
Kadla, Z. I., Richter, N., Strugatskaya, A. A., Högner, W. 1976, *Soviet Astr.*, **20,** 49.
King, I. R. 1962, *Astr. J.*, **67,** 471.
King, I. R. 1966a, *Astr. J.*, **71,** 64.
King, I. R. 1966b, *Astr. J.*, **71,** 276.
Light, E. S., Danielson, R. E., Schwarzschild, M. 1974, *Astrophys. J.*, 1**94,** 257.
Lindsay, Ë. M. 1956, *in Vistas in Astronomy*, Ed. A. Beer, Pergamon Press, New York, p. 1057.
Martin, W. Chr. 1938, *Ann. Sterrew. Leiden*, XVII, Part 2.
Norris, J. E. 1980, in *Globular Clusters*, Ed. D. Hanes and B. Medore, Cambridge University Press, P. 113.
Norris, J., Bessell, M. S. 1975, *Astrophys. J.*, **201,** L76.
Oort, J. H., van Herk, G. 1959, *Bull. astr. Inst. Netherl.* **14,** 299.
Peterson, C. J. 1978, *Astrophys. J.*, **221,** 80.
Peterson, C. J., King, I. R. 1975, *Astr. J.*, **80,** 427.
Poveda, A., Allen, C. 1975, *Astrophys. J.*, **197,** 155.
Rusev R. M. 1974, *Sov. Astron.*, **18,** 71.
Sandage, A. R. 1953, *Astr. J.*, **58,** 61.
Sandage, A. 1957, *Astrophys. J.*, **125,** 422.
Sandage, A. 1970, *Astrophys. J.*, **162,** 841.
Sandage, A., Walker, M. F. 1966, *Astrophys. J.*, **143,** 313.
Scaria, K. K. 1980, *Kodaikanal Obs. Bull*, (in press).
Sistero, R. F., Fourcade, C. R. 1970, *Astr. J.*, **75,** p. 34.
Strauss, F. M. 1978, *Astr. Astrophys. Suppl. Ser.*, **33,** 315.
Strom, S. E., Strom, K. M. 1971, *Astr. Astrophys.*, **14,** 111.
Strom, S. E., Strom, K. M., Goad, J. W. 1976, *Astrophys. J.*, **204,** 684.
Walker, M. F. 1974, *Publ. astr. Soc. Pacific*, **86,** 861.

J. Astrophys. Astr. (1981) **2,** 245–252

Effects of Redistribution with Dipole Scattering on Line Source Functions

A. Peraiah and K. E. Rangarajan *Indian Institute of Astrophysics, Bangalore 560034*

Received 1981 March 20; accepted 1981 August 27

Abstract. The partial frequency redistribution function for zero natural line width with dipole scattering ($R_{\rm I}$) has been considered in obtaining the simultaneous solution of the statistical equilibrium and line transfer equations in the comoving frame of the expanding gas. We have considered a non-LTE two level atom in an expanding spherical medium whose outer radii are 3, 10 and 20 times the stellar radius with a total optical depth $T \simeq 2 \times 10^3$. In all the cases, we have calculated the population ratio of the two levels N_2/N_1 and compared these results with those obtained by using different expansion velocities and geometrical extensions. Initially, the upper level population (N_2) is set equal to zero. The converged simultaneous solution shows that the upper level population is enhanced considerably from the initial value. Variation in velocity gradients seem to have little effect on the ratio N_2/N_1 when the geometrical thickness of the medium is 3 or 10 times the stellar radius. However, when the thickness is increased to 20 times the central radius, the velocity gradients change the ratio N_2/N_1 considerably in the region where $\log T \leqslant 2$. The effect of variation of geometrical thickness is to reduce the N_2/N_1 ratio at $\tau = 0$.

Key words: partial frequency redistribution—dipole scattering—statistical equilibrium equation—line transfer equation in the comoving frame.

1. Introduction

In an earlier paper (Peraiah 1980b, hereafter referred to as Paper I), we have investigated the simultaneous solution of the equation of radiative transfer and the statistical equilibrium equation. In this paper, we have treated the complete redistribution in a resonance line. Convergence was achieved within a small number of iterations. Complete redistribution was used for the sake of simplicity and to test the

capabilities of the method of obtaining the solution by direct iteration between the two equations. A considerable amount of work was done in calculating the lines in a fast expanding atmosphere using partial frequency redistribution in the comoving frame (see Mihalas, Kunasz and Hummer 1976; Peraiah 1980a). However, these calculations do not give a simultaneous solution of radiative transfer equation and Statistical equilibrium equation. It is important that one must obtain a consistent solution for correct estimation of the line profiles. This becomes particularly obvious in the light of the calculations of Shine, Milkey and Mihalas (1975a, b) who simulated the centre to limb variation of solar Ca II H and K lines.

We intend to obtain a consistent solution using partial frequency redistribution with zero natural line width. We have considered isotropic and dipole scattering. The results of isotropic scattering are published elsewhere and the results of the calculations with dipole scattering are presented here. We have assumed a highly scattering medium with no continuum emission.

2. Outline of the computational procedure

The method is described in Paper I and we shall repeat the main points of the procedure. The Statistical equilibrium equation for a two level atom is written as,

$$N_1 \left[B_{12} \int_{-\infty}^{+\infty} dx\, \phi(x)\, J_x + C_{12}\right] = N_2 \left[A_{21} + C_{21} + B_{21} \int_{-\infty}^{+\infty} dx\, \phi(x)\, J_x\right] \tag{1}$$

where N_1, N_2 are the number densities in the lower and upper levels, and B_{12}, B_{21} and A_{21} are the Einstein coefficients. C_{12} and C_{21} are the rates of the collisional excitation and de-excitation respectively. We have estimated these quantities for Hydrogen Lyman alpha line using the equations given by Jefferies (1968). J_x is the mean intensity at the normalized frequency, x ($\equiv (\nu - \nu_0)/\Delta_s$,. Δ_s being a standard frequency interval). $\phi(x)$ is the profile function given by

$$\phi(x) = \int_{-\infty}^{+\infty} R\,(x, x')\, dx' \tag{2}$$

where $R\,(x, x')$ is the angle averaged partial redistribution function. In the case of zero natural line width (R_{I}) and dipole scattering, R is given by (see Hummer 1962, Peraiah 1978)

$$R_{\text{I-}AD}\,(x, x') = \frac{3}{8}\left\{\frac{1}{\sqrt{\pi}} \int_{|x|}^{\infty} \exp(-t^2)\, dt\, [3 + 2\,(x^2 + x'^2) + 4\, x^2\, x'^2] - \frac{\exp(-\bar{x}^2)}{\sqrt{\pi}} |\bar{x}|\,(2\,|\underline{x}|^2 + 1)\right\}, \tag{3}$$

where $\bar{x}$ and $\underline{x}$ are the maximum and minimum values of x and x'. The profile is normalised such that

$$\int_{-\infty}^{\infty} \phi(x)\, dx = 1. \tag{4}$$

The statistical equilibrium equation will supply N_1 and N_2 and these are used to calculate the absorption at the line centre given by

$$K_L(r) = \frac{h\,\nu_0}{4\pi\ \Delta_s}\,(N_1\,B_{12} - N_2\,B_{21}). \tag{5}$$

The absorption coefficient given above is used in the calculation of J_x from the radiative transfer equation in the comoving frame

$$\mu\frac{\partial I(x,\mu,r)}{\partial r} + \frac{1-\mu^2}{r}\,\frac{\partial I(x,\mu,r)}{\partial \mu}$$

$$= K_L(r)\,[\beta + \phi(r)]\,[s(x,r) - I(x,\mu,r)]$$

$$+ \left\{(1-\mu^2)\frac{V(r)}{r} + \mu^2\frac{d\,V(r)}{dr}\right\}\frac{\partial I(x,\mu,r)}{\partial x} \tag{6}$$

and

$$-\mu\frac{\partial I(x,-\mu,r)}{\partial r} - \frac{1-\mu^2}{r}\,\frac{\partial I(x,-\mu,r)}{\partial \mu}$$

$$= K_L(r)\,[\beta + \phi(r)]\,[S(x,\mu) - I(x,-\mu,r)]$$

$$+ \left\{(1-\mu^2)\frac{V(r)}{r} + \mu^2\frac{d\,V(r)}{dr}\right\}\frac{\partial I(x,-\mu,r)}{\partial x} \tag{7}$$

where $I(x,\ \mu,\ r)$ is the specific intensity making an angle $\cos^{-1}\mu$ with the radius at r. β is the ratio of absorption per unit frequency interval in the continuum to that in the line centre. $V(r)$ is the velocity of the gas at the radial point r. $S(x,\ r)$ is the source function given by

$$S(x,r) = \frac{\phi(x)}{\beta + \phi(x)}\,S_L(r) + \frac{\beta}{\beta + \phi(x)}\,S_C(r). \tag{8}$$

Here $S_C(r)$ is the continuum source function and $S_L(r)$ the line source function given by

$$S_L(r) = \frac{(1-\epsilon)}{\phi(x)}\int_{-\infty}^{+\infty} R(x,x')\,J(x')\,dx' + \epsilon\,B(r) \tag{9}$$

Where $B(r)$ is the Planck function and ε is the probability per scattering, that a photon is lost by collisional de-excitation. The line source function can also be calculated from the level populations and is given by the formula

$$S_L(r) = \frac{A_{21}\, N_2(r)}{B_{12}\, N_1(r) - B_{21}\, N_2(r)}. \tag{10}$$

We have set β=0 and $S_C(r) = B(r)$ the Planck function, the initial radius to be 10^{12} cm and the geometrical extension is put equal to 3×10^{12} cm, 10^{13} cm and 2×10^{13} cm. The electron density is chosen to be varying as $1/r^3$ and initially at $r = 10^{12}$ cm, it is taken to be 10^{12} cm^{-3}. A constant temperature of 30,000 K is assumed in all the cases. We started the first iteration by assuming that all the neutral atoms are in the level 1 (*i.e.* $N_2 = 0$). This enables us to calculate the absorption coefficient in equation (5) with which we solve the line transfer given in equations (6) and (7). This solution is used to calculate the mean intensities J_x which can be inserted in equation (1) to obtain the new ratio of N_2/N_1. This process is repeated until convergence is obtained within 1 per cent of N_2/N_1 in two successive iterations at each radial point.

We have considered the variation of density and velocity so that the equation of continuity is always satisfied in a spherically symmetric steady state flow. The velocity is changing with a negative gradient with respect to the optical depth. As we have divided the medium into 30 shells of equal geometrical thickness, the velocity gradient becomes a function of the absorption characteristics of the shell in question.

3. Discussion of the results

As we are calculating the solution of radiative transfer in the comoving frame, we need to calculate the partial frequency redistribution function only once. In Fig. 1,

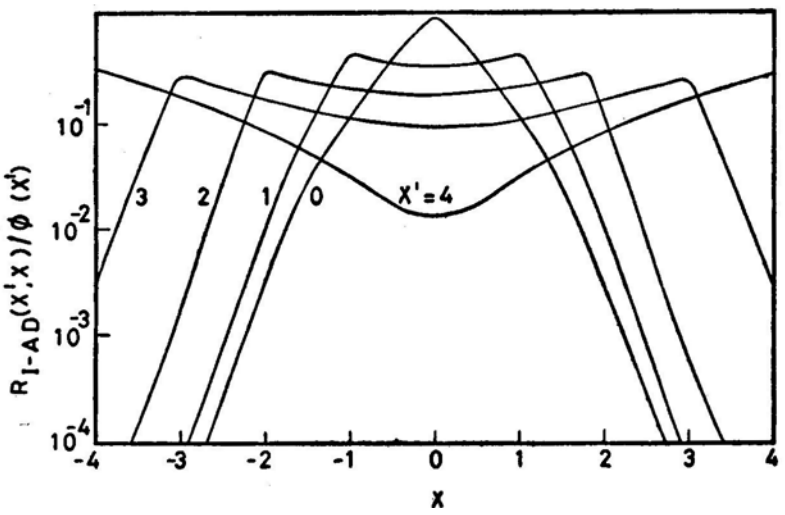

Figure 1. The probability of emission at frequency x per absorption at x', $R_{\text{I–AD}}$ $(x'; x)/\phi(x')$ is given against x.

we have plotted R_{I-AD} $(x', x)/\phi(x')$ for x', where the numerator is given by equation (3) and the denominator by equation (2). If we compare the probability of emission/absorption curves in this figure with those of Mihalas (1978, Figure 13-2, page 428) it becomes immediately obvious that there are important differences between these

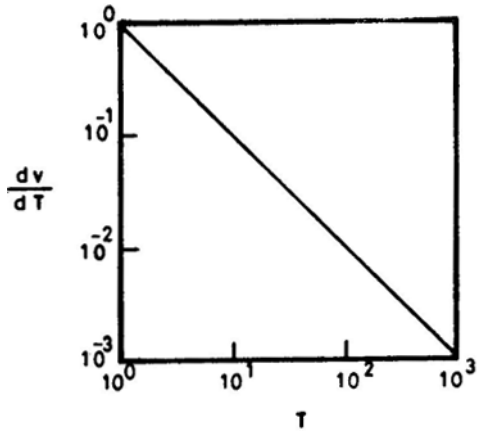

Figure 2. $dV/d\tau$, the velocity gradient with respect to optical depth is plotted against optical depth T.

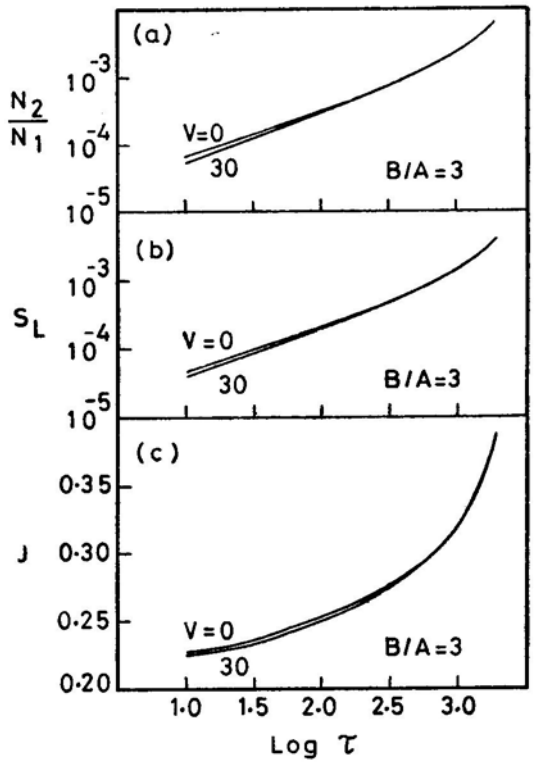

Figure 3. (a) The ratio of number densities of upper to lower level N_2/N_1, (b) the line source function S_L and (c) the total mean density J are plotted against optical depth T for $B/A = 3$.

two results. These differences are mainly due to the type of scattering we have considered. Mihalas (1978) has used the expression for isotropic scattering whereas we have considered dipole scattering. For $x' = 0$, we note that the probability of finding a photon at $x = 0$ is nearly 1 in both the cases. As x' is increased, the probability flattens and becomes constant around $x = 0$ for isotropic scattering. However, the probability of finding the scattered photon around $x = 0$ reduces considerably for dipole scattering and at $x' = 4$, there is a clear dip in the curve. This difference between isotropic scattering and dipole scattering is quite important when we calculate the redistribution of photons from the line centre to the wings and vice versa in spherically symmetric expanding media.

In Fig. 2, we have given the velocity gradient versus the total optical depth. The velocity gradient is proportional to the total optical depth T, the optical depth being measured 0 at $r = r_{max}$. This means that the velocity will be increasing with radius starting with $V(\tau = T) = 0$ and $V(\tau = 0) = V_{max}$. We have set $V_{max} = 0$, 5, 10, 30 mean thermal units (hereafter we need not mention mean thermal units).

In Fig. 3 (a, b, c) we have plotted the ratio N_2/N_1 the line source function S_L and the total mean intensity J versus the total optical depth. The curves for various V_{max} (= 0, 5, ….30) cannot be resolved graphically and, therefore, we have presented results only for $V_{max} = 0$ and 30. In this figure we have considered $B/A = 3$ (the ratio

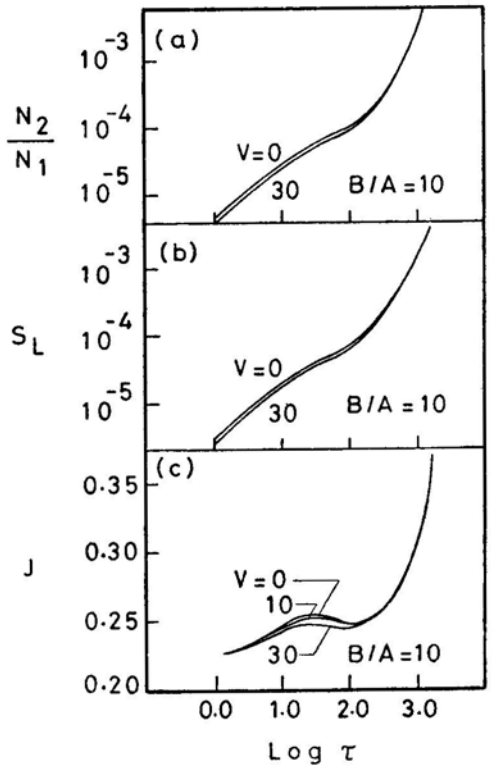

Figure 4. (a) The ratio of number densities of upper to lower level N_2/N_1, (b) the line source function S_L and (c) the total mean intensity J are plotted against optical depth T for $B/A = 10$.

of outer to inner radii of the medium). We see that at $\tau = T$, the variation in velocity makes no difference either in the ratio N_2/N_1 or S_L or J. The changes in the above quantities are noticed only from log $T \leqslant 2{\cdot}5$. The change in N_2/N_1 from B to A is nearly two orders of magnitude whereas the source functions do not fall as rapidly. The ratio N_2/N_1 is much less than the equilibrium value even at the point $\tau = T$. The line source function and the ratio N_2/N_1 are reduced considerably mainly because of the fact that we have set $\beta = 0$ (*i.e.* no continuum emission) and the quantity ε is of the order of 10^{-6} to 10^{-8}. All the photons incident at $\tau = T$ are being scattered several times inside the medium. In particular at $\tau = T$, many of these are back scattered and consequently we notice that the source functions reduce at $\tau = 0$. These results look quite similar to those obtained in Paper I, in which we have employed complete redistribution (CRD). The fall in the ratio N_2/N_1 and S_L is more rapid in the case of partial frequency redistribution (PRD) than in the case of CRD. We needed a maximum velocity of 60 to obtain any graphically distinguish–able results in the case of CRD whereas in PRD a maximum velocity of 30 is enough to get graphically resolvable results from those of $V_{\max} = 0$. We have plotted the ratio N_2/N_1, S_L and J in Figs. 4 and 5 for $B/A = 10$ and 20 respectively. These are quite similar to those described in Fig. 3. The changes in N_2/N_1 for $B/A = 10$ are quite substantial. The changes in N_2/N_1 and S_L between the points A and B

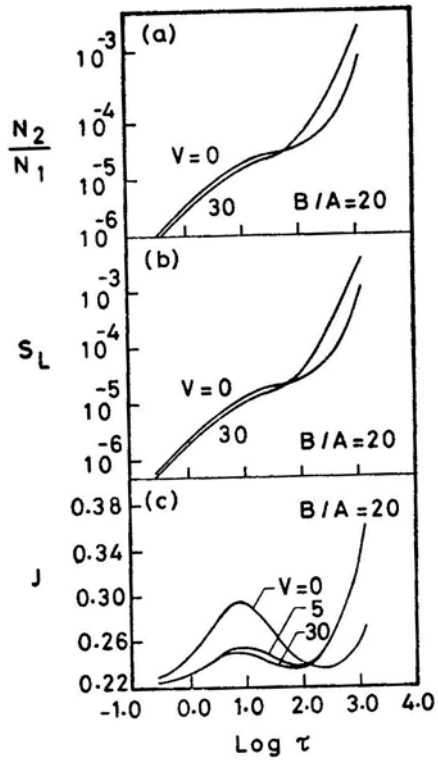

Figure 5. (a) The ratio of number densities of upper to lower level N_2/N_1, (b) the line source function S_L and (c) the total mean intensity J are plotted against optical depth T for $B/A = 20$.

are as large as 4 to 5 orders of magnitudes. Most of the photons are involved in the multiple scattering at $\tau = T$ and consequently the radiation field is much more diluted than in the case of the medium with $B/A = 3$ or 10.

References

Hummer, D. G. 1962, *Mon. Not. R. astr. Soc.*, **125,** 21.
Jefferies, J. T. 1968, *Spectral line formation*, Blaisdel, Waltham.
Mihalas, D. 1978, *Stellar Atmospheres*, 2nd edn., Freeman, San Francisco.
Mihalas, D., Kunasz, P. B., Hummer, D. G. 1976, *Astrophys. J.*, **210,** 419.
Peraiah, A. 1978, *Kodaikanal Obs. Bull. Ser. A.*, **2,** 115.
Peraiah, A. 1980a, *J. Astrophys. Astr.*, **1,** 3.
Peraiah, A. 1980b, *J. Astrophys, Astr.*, **1,** 101, (Paper I).
Shine, R. A., Milkey, R. W., Mihalas, D. 1975a, *Astrophys. J.*, **199,** 724.
Shine, R. A., Milkey, R. W., Mihalas, D. 1975b, *Astrophys. J.*, **201,** 222.

J. Astrophys. Astr. (1981) **2,** 253–276

Intrinsic Properties of Carbon Stars. II. Spectra, Colours, and HR Diagram of Cool Carbon Stars

Takashi Tsuji *Tokyo Astronomical Observatory, University of Tokyo, Mitaka, Tokyo, 181 Japan*

Received 1981 April 3; accepted 1981 August 26

Abstract. On the basis of the effective temperature scale proposed previously for cool carbon stars (Paper I), other intrinsic properties of them are examined in detail. It is shown that the major spectroscopic properties of cool carbon stars, including those of molecular bands due to polyatomic species (SiC_2, HCN, C_2H_2 *etc*.), can most consistently be understood on the basis of our new effective temperature scale and the theoretical prediction of chemical equilibrium. Various photometric indices of cool carbon stars also appear to be well correlated with the new effective temperatures. Furthermore, as effective temperatures of some 30 carbon stars are now obtained, the calibration of any photometric index is straightforward, and some examples of such a calibration are given. In general, colour index-effective temperature calibrations for carbon stars are quite different from those for K–M giant stars. It is found that the intrinsic $(R - I)_0$ colour is nearly the same for N-irregular variables in spite of a considerable spread in effective temperatures, and this fact is used to estimate the interstellar reddening of carbon stars.

An observational HR diagram of red giant stars, including carbon stars as well as K–M giant stars, is obtained on the basis of our colour index-effective temperature calibrations and the best estimations of luminosities. It is shown that carbon stars and M giant stars are sharply divided in the HR diagram by a nearly vertical line at about $T_{\rm eff}$ = 3200 K (log $T_{\rm eff}$ = 3·50) and the carbon stars occupy the upper right region of M giant stars (except for some high luminosity, high temperature J-type stars in the Magellanic Clouds; also Mira variables are not considered). Such an observational HR diagram of red giant stars shows rather a poor agreement with the current stellar evolution models. Especially, a more efficient mixing process in red giant stars, as compared with those ever proposed, is required to explain the formation of carbon stars.

Key words: carbon stars—HR diagram—stellar evolution—molecular spectra—photometric indices

1. Introduction

Red giant stars include a variety of objects such as carbon stars, S stars and others which, show fascinating spectroscopic characteristics, in addition to the more normal constituent represented by K–M giant stars. One of the major problems in current theory of stellar evolution is to clarify the relationship among various types of red giant stars. Also, red giant stars should be important probes of the structure and evolution of extragalactic systems as well as of our Galaxy because of their high luminosities and prevalent existence. For these purposes, intrinsic properties of red giant stars should be accurately specified from observations.

Although this problem of determining the intrinsic properties of red giant stars has been deemed difficult for a long time, considerable progress has recently been done. For example, the effective temperature scale for K–M giant stars has been determined consistently by angular diameter measurements and by the model atmosphere analysis of observed spectral energy distributions (*e.g.* Tsuji 1978; Ridgway *et al.* 1980a). Analogous problem in other types of red giant stars has been more difficult than in the case of K–M giant stars. However, recently, we have found that the infrared flux method for determining the stellar effective temperatures (Blackwell, Petford and Shallis 1980) can be applied to cool stars including carbon stars, and thus succeeded in determining effective temperature scale for cool carbon stars (Tsuji 1981a, hereafter referred to as Paper I) as well as for K–M giant stars (Tsuji 1981b).

We recall that the infrared flux method originates from the idea of estimating the stellar angular diameter by a comparison of the observed and the emergent stellar fluxes. Although an estimate of the emergent stellar flux depends on the model atmospheres used, it is relatively insensitive to the details of the model atmosphere in the infrared. Hence the idea noted above can be best applied in the infrared (Blackwell and Shallis 1977). In the case of cool carbon stars, we have found that the *L*-flux ($\lambda_{\rm eff}$ =3·4 μm) is relatively free from the effects of strong molecular bands. This fact, together with an empirical correction for the effect of polyatomic molecular absorption at 3·1 μm, makes it possible to estimate the emergent stellar fluxes of cool carbon stars with a reasonable accuracy, even with the present uncertainties in the model atmospheres of cool carbon stars. Our estimate of the error in the effective temperatures resulting from the uncertainties of model atmospheres is 100–200 K while the error due to the present uncertainties in absolute calibration of the infrared flux is about 100 K (Paper I). In fact, our effective temperatures for cool carbon stars based on the infrared flux method showed reasonable agreement with those by the direct measurements of angular diameters (Ridgway, Wells and Joyce 1977; Walker, Wild and Byrne 1979; Ridgway *et al.* 1980b), within the limits of our error estimations noted above.

Our effective temperatures for cool carbon stars, however, showed anti-correlation with the temperature classes of C-classification. As most interpretations of obser–vations on carbon stars have been done in the past on the basis of C-classification, the anti-correlation noted implies that our understanding on the atmospheres of carbon stars should radically be reconsidered. For this purpose, major observational data on cool carbon stars are re-examined on the basis of the new effective temperature scale. As the physical and chemical characteristics of stellar atmospheres are largely determined by their temperatures, it is hoped that this analysis will clarify

the physical properties of cool carbon stars which have been rather confusing till now. Also, the effective temperature itself is one of the basic stellar parameters. Combined with the best estimate of luminosity, it is expected that the HR diagram for cool carbon stars can be discussed on a better observational basis than before.

2. Spectroscopic properties of carbon stars

The spectra of carbon stars have been more enigmatic as compared with those of other red giant stars. Till now, definite identification is not yet given to some spectral features such as selective ultraviolet absorption which has been discovered half a century ago. More recent discovery of 3 μm absorption in carbon stars has provided another challenge; extensive survey of large number of carbon stars by Noguchi *et al.* (1977) revealed that the 3 μm absorption shows no correlation with the known spectral types nor with other major physical properties of carbon stars. Some correlations they have found were with ultraviolet colour index and with CN/C_2 ratio. Also, Faÿ and Ridgway (1976) showed that the 3 μm absorption increases with the strength of Na D lines but this correlation seems to be not very significant.

In Fig, 1(a), the 3 μm band depths measured by Noguchi *et al.* (1977) are plotted against our effective temperatures determined in Paper I (Table 2). This plot reveals that the 3 μm absorption shows a very good correlation with the effective temperature, and shows a rather steep increase at effective temperatures below 3000 K. It is now known that the 3 μm absorption is due to CH characteristic vibration of HCN and C_2H_2 (Ridgway, Carbon and Hall 1978). The abundances of these polyatomic molecules are highly sensitive to temperatures (Tsuji 1964; Morris and Wyller 1967) and the correlation shown in Fig. 1(a) can be reasonably understood as a temperature effect (see Appendix). For comparison, the same 3 μm. band depths are plotted

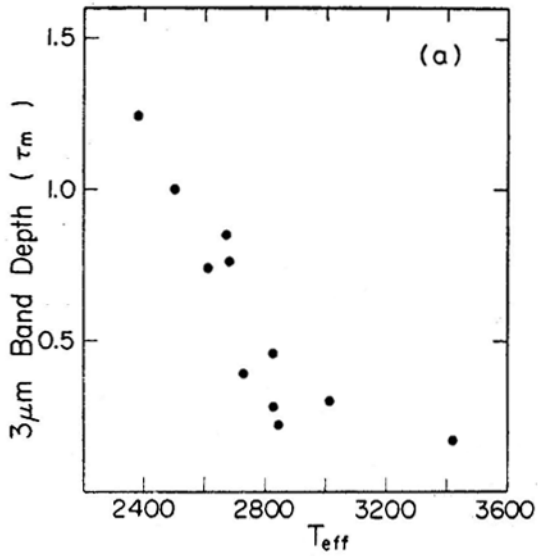

Figure 1. (a) The 3 μm band depths observed by Noguchi *et al.* (1977) are plotted against effective temperatures. Note that the 3μm absorption band depths increase at cooler temperatures especially below 3000 K.

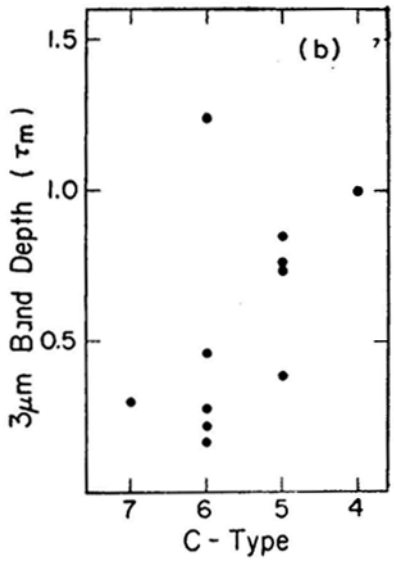

Figure 1. (b) The 3 μm absorption depths are plotted against the temperature classes of C-classification. Note that 3μm absorption, now known to be due to HCN and C_2H_2, is stronger at earlier C-types than at later C-types.

against temperature classes of C-classification in Fig. 1(b). This plot clearly shows that the 3 μm absorption is more stronger in earlier C-types than in later C-types. As it is unlikely that stable polyatomic molecules such as HCN and C_2H_2 are more abundant in hotter stars than in cooler stars, this plot gives the most clear demonstration that the temperature index of C-classification is negatively correlated with stellar temperature. The previous failure to find this anti-correlation of the 3 μm absorption with the C-classification (*e.g.* Noguchi *et al.* 1977) may be due to the inclusion of Mira and dusty carbon stars in their sample, while our sample includes only N-irregular types.

Another polyatomic species known to exist in cool carbon stars is SiC_2. The strengths of Merrill-Sanford bands due to SiC_2 show rather disordered behaviour if plotted against the temperature types of the C-classification. In fact, SiC_2 bands are very strong in some stars of C4–C5 but they are not observed at all in other stars of the same spectral types (Yamashita 1972). To explain this fact within the framework of C-classification, a large luminosity effect (Tsuji 1964), a large variation in Si abundance (Yamashita 1972), or a difference in Si/S ratio (Tsuji 1973) had to be postulated. In Fig. 2(a), the observed strengths of SiC_2 bands (Yamashita 1972; Walker 1976) are plotted against our effective temperatures. This plot reveals that SiC_2 bands also show good correlation with effective temperatures and show steep temperature dependence quite similar to that of the 3 μm absorption. Again, this behaviour of SiC_2 bands can be reasonably understood by high temperature sensitivity of abundances of polyatomic molecules (see Appendix). It is true that the computation of chemical equilibrium in carbon stars showed that SiC_2, unlike the more stable polyatomic species such as HCN or C_2H_2, does not increase monotonically to very cool temperatures. However, the concentration of SiC_2 attains a maximum at about 2000 K (Tsuji 1973), and accordingly SiC_2 can still increase throughout the tempera-

ture range considered in Fig. 2(a) as can actually be confirmed from Fig. 13 (Appendix). In Fig. 2(b), the same SiC_2 data as used in Fig. 2(a) are plotted against the C-types. Here again, the SiC_2 absorption is larger at earlier types than in later types of C-classification, and this is quite difficult to understand from the viewpoint of chemical equilibrium theory as noted above. Thus, the origin of the previous confusion concerning the Merrill-Sanford bands is that the stars classified as C4–C5 show strong SiC_2 bands while they are actually cooler than the stars classified as C6–C7. Also, the large scatter of SiC_2 abundance at the same C-type may be simply due to insensitivity of C-classification to detect some temperature differences among these stars.

Another prominent feature that may be due to polyatomic molecules is the selective ultraviolet absorption. Although not definite, this feature is tentatively identified with C_3 (*e.g.* Goebel *et al.* 1978). In Fig. 3, $(U - V)_0$ colour indices (Mendoza and Johnson 1965; Richer 1971; Walker 1979) are plotted against our effective temperatures. The correction for the interstellar reddening is made using the colour excesses given in Table 2 of Paper I. Again, $(U - V)_0$ colour index is highly sensitive to temperature and this fact implies that the selective absorption in the ultraviolet is due to species that increase rapidly with decreasing temperature.

It has long been known that the observed strengths of diatomic molecules such as C_2 and CN show maxima at about C4–C5 if plotted against the temperature classes of C-classification (Keenan and Morgan 1941; Yamashita 1972). However, if C-classification is no longer a temperature sequence, such a correlation should be re-examined. For this purpose, C_2 and CN indices measured by a photoelectric scanner (Gow 1977) are plotted against our effective temperatures in Fig. 4, in the lower and middle panels, respectively. These plots show no clear maximum in the temperature range considered, but the C_2 band intensity continues to increase to the effective

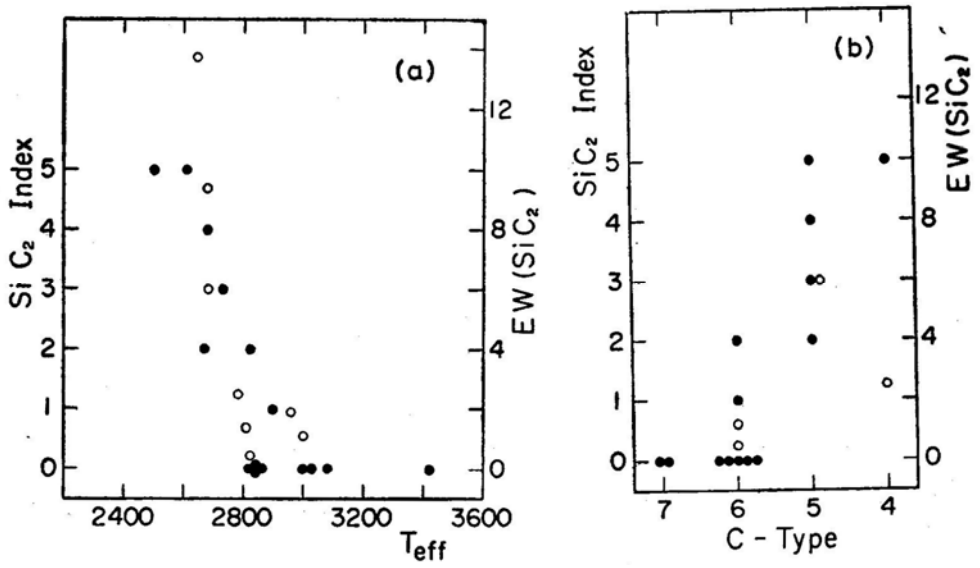

Figure 2. (a) The intensities of Merrill-Sanford bands due to SiC_2 are plotted against the effective temperatures. Filled circles are SiC_2 indices estimated by Yamashita (1972, 1975) and should be referred to the left scale. Open circles are equivalent widths measured by Walker (1976) and should be referred to the right scale, (b) The same data for Merrill-Sanford bands are plotted here against temperature classes of C-classification.

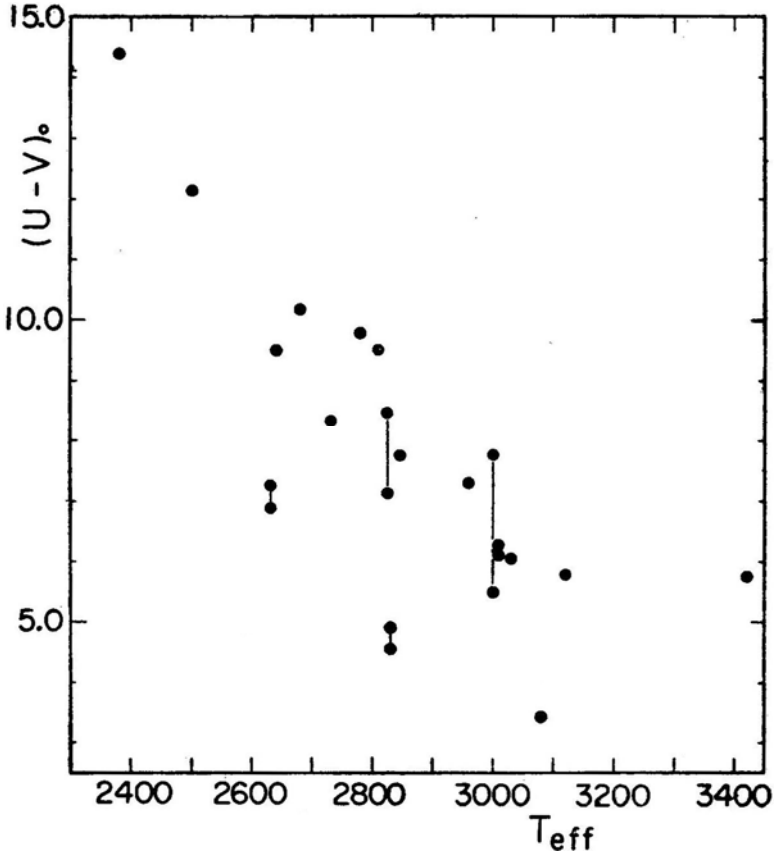

Figure 3. $(U - V)_0$ colour indices are plotted against effective temperatures. Different observations for the same star are connected by a thin line.

temperatures as low as 2500 K. Previously, the maximum of C_2 band intensities at about C4–C5 subclasses was interpreted by the possible depletion of free carbon atoms due to the formation of more stable polyatomic molecules at the cooler temperatures in carbon stars later than C5 (Tsuji 1964). However, from the facts that C-type is anti-correlated with effective temperature (Paper I) and that C_2 intensity increases towards lower temperatures (Fig. 4, lower panel), we now realize that the maximum C_2 intensity for those stars previously classified as C4–C5 is because these stars are actually cooler than the stars classified as later subtypes. It is to be noted that stars classified as C0–C3 may actually be hotter than those classified as C4–C9, and C-type–effective temperature relationship may have a discontinuity at C4–C5. Then, the maximum of C_2 at C4–C5 is a result of this discontinuity in temperature scale and should not be confused with the maximum of C_2 predicted by the chemical equilibrium computation noted above.

It is true that the theory of chemical equilibrium predicts a maximum abundance of C_2 at about 2500 K for low gas pressure (Tsuji 1964), but the predicted band intensities still continue to increase at a model of $T_{\rm eff}$ = 2600 K (see Appendix). This result can be understood if we consider the decrease of continuous opacity at lower temperatures and the stratification effects. However, it can reasonably be expected that C_2 band intensity may decrease in very cool carbon stars. Probably, the sample

of carbon stars covered by the present analysis may not be cool enough, to attain the maximum C_2 concentration. Only one star of $T_{\rm eff} \simeq 2380$ K (T Lyr) shows an indication of decreasing C_2 intensity in Fig. 4. It is to be noted that the Mira type carbon stars, which may be the coolest carbon stars, are not included in our sample.

It appears from Fig. 4 that CN bands show almost no change with temperature. Although CN band intensity shows slight increase as the temperature decreases down to $T_{\rm eff} \sim 2500$ K, this increase of CN band intensity is very slow as compared with the increase of C_2 band intensity discussed above. This difference is qualitatively consistent with the prediction shown in Fig. 13 in which increase of CN band intensity is relatively slow as compared with that of C_2 (see Appendix). Also, one possible

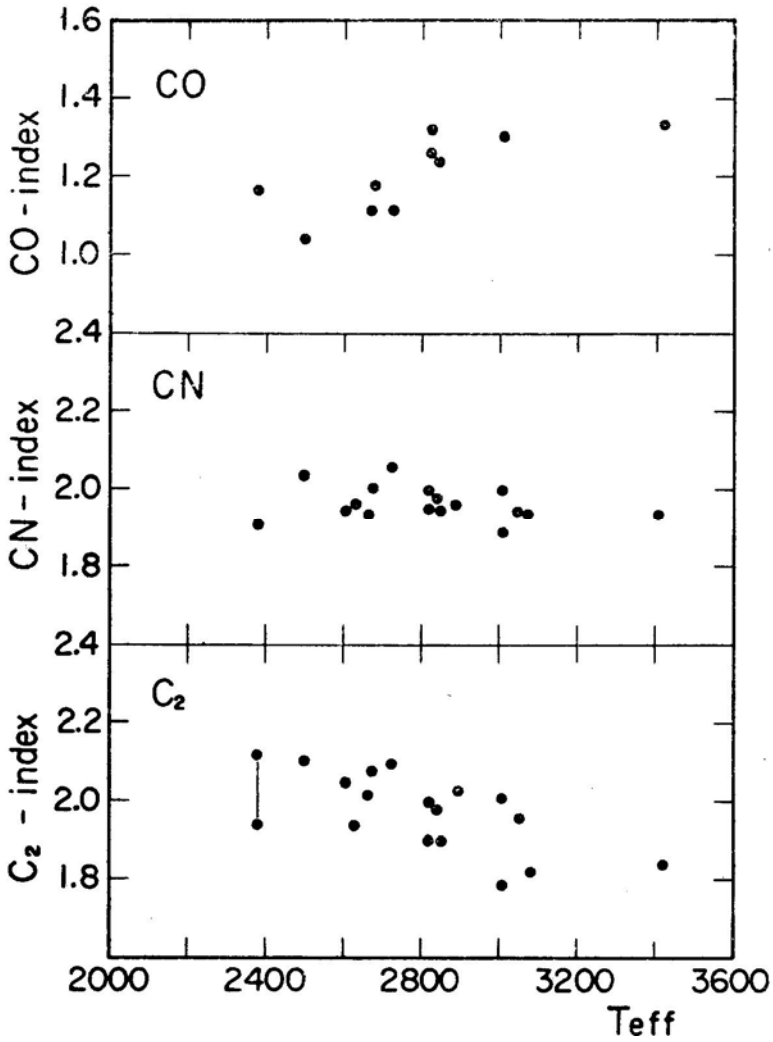

Figure 4. CO, CN, and C_2 indices given by Gow (1977) are plotted against the effective temperatures at the top, middle and bottom, respectively. Each molecular index is defined by 100 ($m_{\rm Mol}$-$m_{\rm BB}$) where $m_{\rm Mol}$ is the observed magnitude at the molecular band while $m_{\rm BB}$ is the magnitude calculated from the black-body curve at a given wavelength.

explanation for the near constancy of CN bands in all the carbon stars shown in Fig. 4 could be the saturation effect in strong CN bands.

Now, with the new effective temperature scale for carbon stars, the observed behaviour of diatomic as well as polyatomic molecules can be understood better than before on the basis of chemical equilibrium computations. In fact, we now have a direct evidence that the stable polyatomic molecules such as HCN and C_2H_2 continue to increase to a temperature as low as 2500 K (Fig. 1a), and this fact implies that the free carbon atoms should still be available to a temperature as low as 2500 K. This fact is quite consistent with the behaviour of unstable free radicals such as C_2 whose abundances are still increasing to temperature as low as 2500 K (Fig. 4). Only below 2500 K where the concentrations of stable polyatomic molecules may level off, the abundances of unstable free radicals may decrease, and this prediction should be confirmed by observations of the coolest carbon stars.

Another diatomic molecule that has been observed rather recently is CO. Observed values of CO-index, which is a measure of CO first overtone band at 2·3 μm (Gow 1977), are plotted against our effective temperatures in the upper panel of Fig. 4. This plot reveals that CO absorptions are apparently weaker in cooler carbon stars than in hotter carbon stars. Observations of CO bands by Frogel and Hyland (1972) and by Bergeat *et al.* (1976) also show similar behaviour if plotted against our effective temperatures. As CO is quite stable, its abundance will be almost independent of temperature for cool carbon stars. The column density and hence the band intensity of CO increase towards cooler stars because of the decrease of continuous opacity (see Appendix). Thus, the observed behaviour of CO bands shown in Fig. 4 is difficult to understand by a simple model.

It has already been pointed out by Frogel and Hyland (1972) that the first overtone bands of CO are weaker in Mira type carbon stars than in non-Miras, and they have suggested that this may be caused by the veiling effect due to the thermal emission by dust in Mira type carbon stars. This interpretation, however, cannot be applied to our sample, because there is no reason to believe that the thermal emission by dust may be important in our sample (Paper I). Especially, the very fact that the 3 μm absorption is still increasing towards cooler temperature in our sample (Fig. 1a) clearly indicates that the veiling effect by the dust thermal emission at 2·3 μm is of little importance if any. Then, another possibility may be that the CO-index defined above is essentially a measure of other absorptions underlying the CO bands rather than of CO band absorption itself. For example, CN bands due to the red system (Δv = — 2 sequence) are strong just around the CO first overtone bands and they should have some effect upon the measured CO band intensities. Also, if opacity due to unresolved polyatomic molecules such as HCN ($\nu_2 + \nu_3$) and C_2H_2 ($\nu_1 + \nu_5$) are important, the plot shown in Fig. 4 (upper panel) can be reasonably understood as the effect of such a pseudo-continuous opacity in and around the CO bands. In fact, abundances of polyatomic molecules are just increasing at the temperature where CO index is decreasing (Figs 1–3).

Finally, equivalent widths of Na D lines (Bouigue 1954) are plotted against the effective temperatures in Fig. 5. This plot reveals that D line equivalent widths show rather poor correlation with effective temperatures. In C-classification, D-line intensity is the major classification criterion. Accordingly, it is supposed that the correlation between D-line intensity and effective temperature may be essentially the same as that between temperature index of C-classification and effective temperature (Fig. 6

of Paper I). In fact, if any correlation exists in Fig. 5, it is positive in Consistency with this expectation. This behaviour of D-line intensity, however, is against general expectation that D lines should be stronger at cooler temperatures. One possible explanation is that the D lines are embedded in strong CN bands, especially of (7, 2) red system, as shown by Wyller (1960). In view of such a complication, D-line intensity may anyhow not be a good indicator of temperature.

3. Photometric properties of carbon stars

Interpretation and analysis of photometric data on carbon stars are generally difficult because of the heavy line-blanketing effect in these stars. However, once the effective temperature is determined by another method, we can calibrate any colour index against the effective temperature. Some examples of such a calibration for colour indices in Johnson system are given below on the basis of the effective temperatures for carbon stars listed in Table 2 of Paper I, and those for K–M giant stars which have also been determined by the infrared flux method (Tsuji 1981b). Photometric data are mostly taken from Johnson *et al.* (1966), Lee (1970), Glass (1974), and Ridgway *et al.* (1980a) for K–M giant stars, and from Mendoza and Johnson (1965) and Walker (1980) for carbon stars. The correction for the interstellar reddening

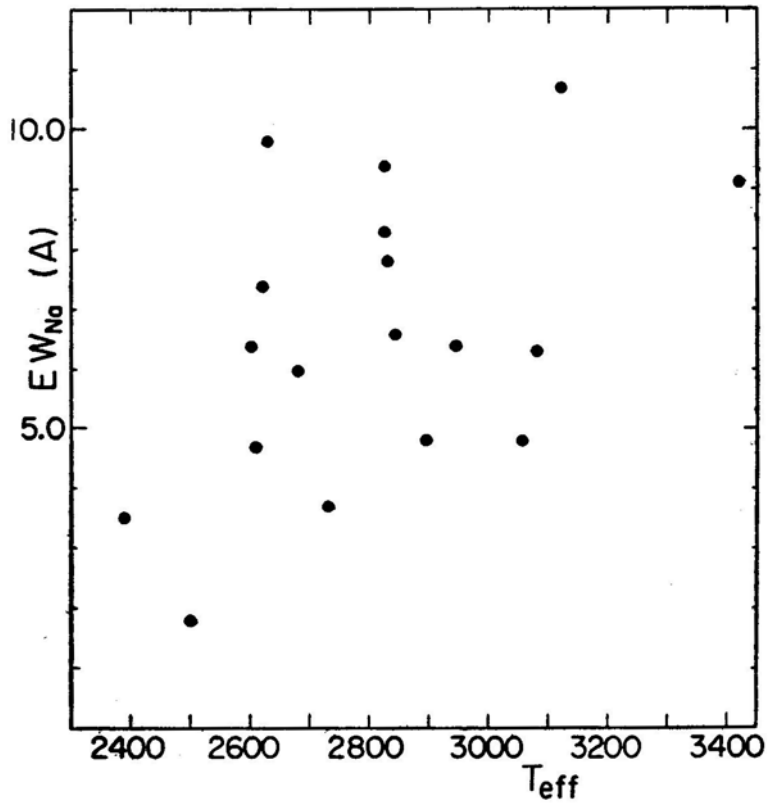

Figure 5. Equivalent widths of Na D line plotted against the effective temperatures of cool carbon stars.

is made for the carbon stars with the colour excesses given in Table 2 of Paper I using the reddening law of Lee (1970).

In Fig. 6, $V - L$ colour indices are plotted against the effective temperatures both for carbon stars (filled circles) and for K–M giant stars (open circles). In this diagram, carbon stars and K–M giant stars are clearly separated, which is expected from the differences in line-blanketing effect for different types of stars. In spite of the heavy line-blanketing effect, however, the colour index such as $V - L$ that is based on a long baseline in wavelength should primarily be sensitive to effective temperature. Thus, the reasonably tight correlation between $V - L$ colour index and the effective

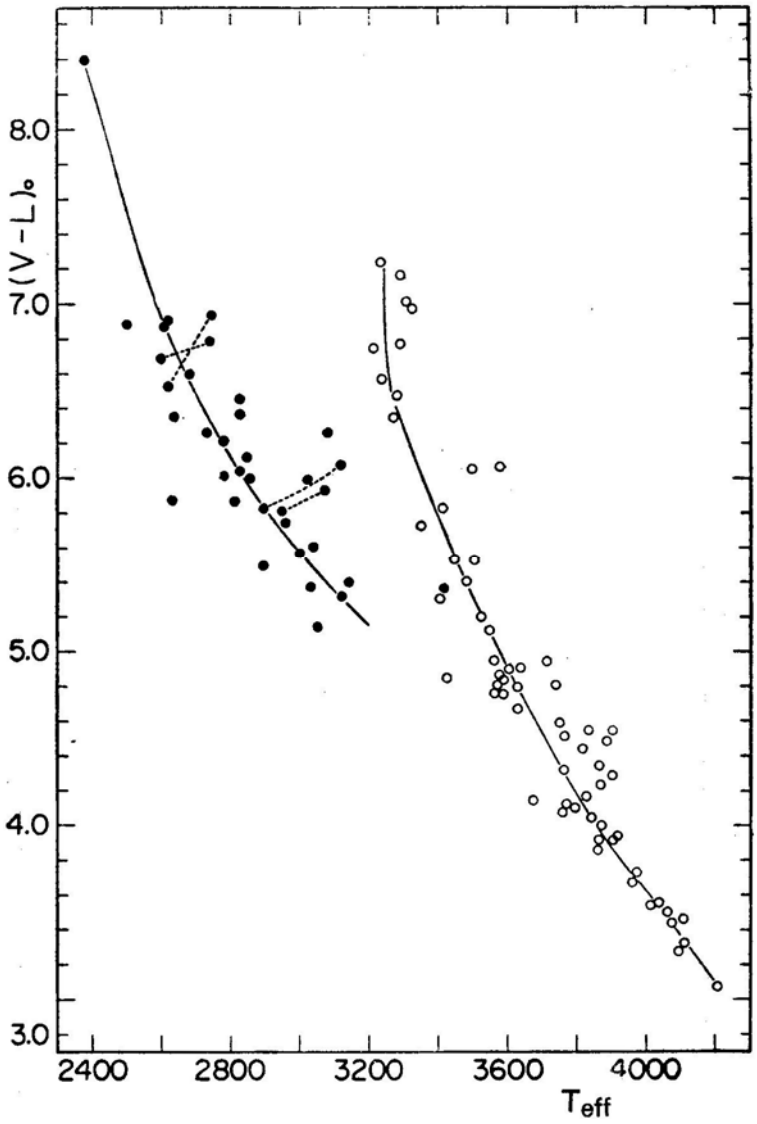

Figure 6. $(V—L)_0$-effective temperature calibration for carbon stars (filled circles) and for K–M giant stars (open circles). Results due to different photometric data for the same star are connected by a dashed line.

temperature for carbon stars shown in Fig. 6 can be regarded as a supporting evidence to our effective temperature scale for carbon stars.

In Fig. 7, V — I and V — R colour indices are calibrated against the effective temperatures. For some carbon stars, R, I photometric data in Kron-Cape system are transformed to R, I photometry in Johnson system (Walker 1979) by using the transformation equations given by Cousins (1976). The applicability of these equations for carbon stars is ascertained by using the stars that have been observed in both the systems. These plots again show that the photometric properties of carbon stars (filled circles) are quite different from those of K–M giant stars (open circles). However, these colour indices that can easily be observed by the current photo-

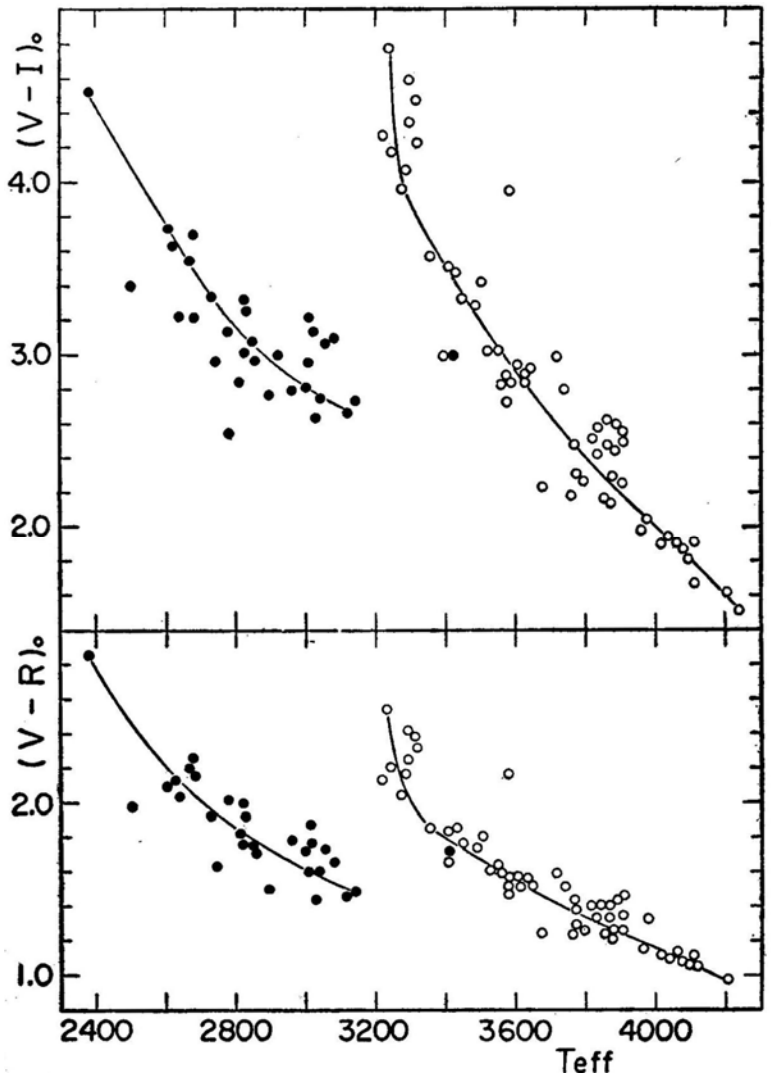

Figure 7. $(V - 1)_0$ and $(V - R)_0$ are calibrated against the effective temperature for carbon stars (filled circles) and for K – M giant stars (open circles).

electric photometers are reasonably sensitive to effective temperatures; therefore they can be used for the practical purposes of determining the effective temperatures of carbon stars.

In Fig. 8, R — I and I — L colour indices are plotted against our effective temperatures. Unlike other colour indices, the I — L colour index-effective temperature calibration follows a single relationship for carbon stars as well as for K–M giant stars, although the effective temperature range of these two types of stars are rather sharply divided at about $T_{\rm eff} \simeq 3200$ K. This fact suggests that the I — L colour index should be the best parameter for the comparative studies of different types of red giant stars. In contrast, R — I colour index also shows quite different characteristics for carbon stars and for K–M giant stars. R — I colour index is generally used as a good indicator of effective temperature for K–M giant stars. It is often used also as a temperature indicator in carbon stars. For example, Scalo (1976) has recommended blackbody calibration of infrared colour indices including R — I using the arguments that the two angular

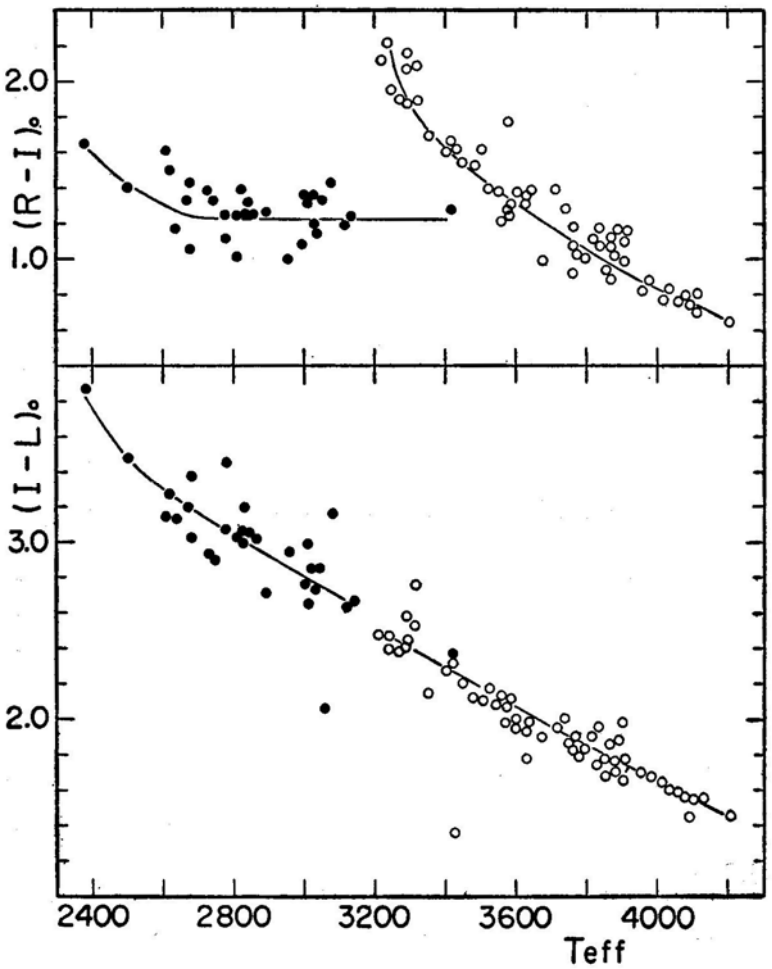

Figure 8. $(R-I)_0$ and $(I-L)_0$ are calibrated against effective temperatures for carbon stars (filled circles) and K–M giant stars (open circles) at the top and bottom, respectively. Note that $(R—I)_0$ is nearly the same for most of the carbon stars.

diameters of carbon stars which, were available to him at that time were consistent with blackbody temperatures and that the carbon stars followed blackbody curves in various infrared two-colour diagrams. Perhaps, because of the calibration by effective temperatures based on angular diameters, the effective temperatures of carbon stars by this method cover nearly the same range as our effective temperatures. However, as is shown in Fig. 8, the R — I colour index is almost insensitive to effective temperature in carbon stars and can not be used for an accurate calibration.

The property that the R — I colour index is nearly the same for carbon stars was previously recognized by Eggen (1972), but he interpreted this fact as an indication that the effective temperatures as well as luminosities of most carbon stars are almost the same. With this interpretation, it was suggested that most N-type stars that appear in a sharply defined gap at $(R - I)_K \sim 0{\cdot}9$ (this correspond to $(R - I)_J \sim 1{\cdot}2$ in agreement with Fig. 8) represent a very transient stage in the evolution of old disk population stars of masses about $1{\cdot}25\ M_\odot$ (Eggen 1972). Such a conclusion, however, should be reconsidered in view of the present result that the photometric properties of carbon stars and those of M giant stars are very different in general.

As examples of the infrared colour indices, H — K and J — K indices are plotted against effective temperatures in Fig. 9. As expected, the infrared colour indices

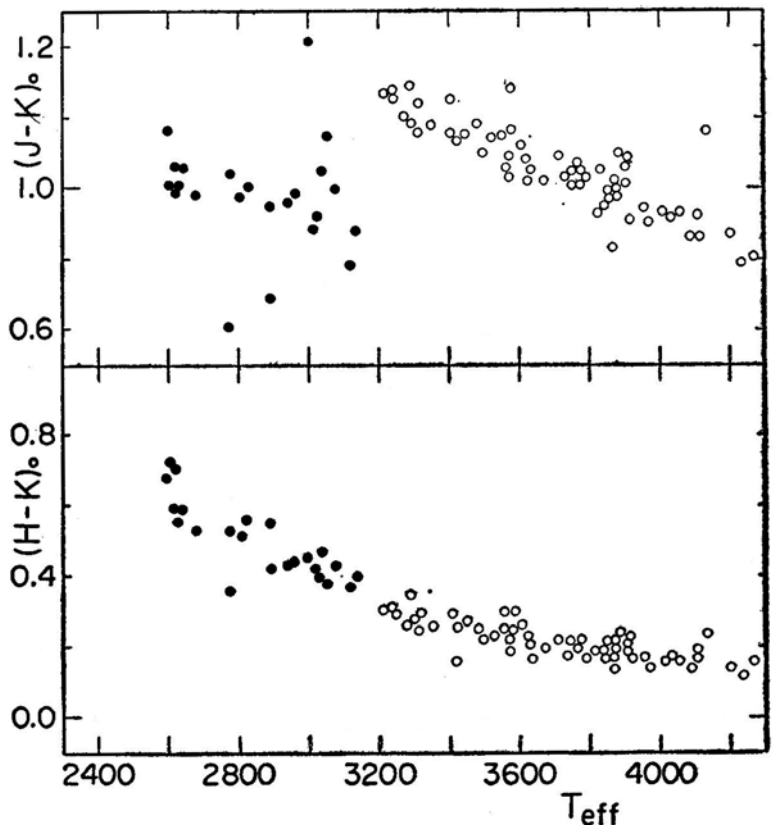

Figure 9. $(H - K)_0$ and $(J - K)_0$ are plotted against effective temperatures for K–M giant stars (open circles) and carbon stars (filled circles). Photometric data for carbon stars are due to Walker (1980).

defined in Rayleigh-Jeans region are rather insensitive to effective temperatures (note that Ordinate scales are exaggerated by a factor of 2 in Fig. 9 as compared with Figs 6–8), and the infrared colour indices are not necessarily very useful in temperature determination. If infrared photometric data are available, the best way is to determine the effective temperatures directly the infrared flux method of Blackwell, Petford and Shallis (1980).

4. Interstellar reddening of carbon stars

The fact that the intrinsic R — I colour index is almost the same for N-type irregular variables (Section 3) provides a new possibility of determining interstellar reddening for carbon stars. In fact, the near constancy of intrinsic B—V colour index in M giant stars has been used in the determination of the interstellar reddening for these stars (*e.g.* Johnson 1967), and R — I colour index can play a similar role for carbon stars. Also, Peery (1975) has applied a similar technique to carbon stars using a narrow band index defined by $m_{0\cdot78}$ — $m_{1\cdot08}$. He has assumed that stellar temperatures are the same for all the N-irregular variables and hence the intrinsic colour may also be the same. This assumption was criticized by Walker (1980) who found that stellar temperatures may differ by about 500 K among N-irregular variables. We have shown, however, that R — I is nearly the same for almost all the N-irregular variables,

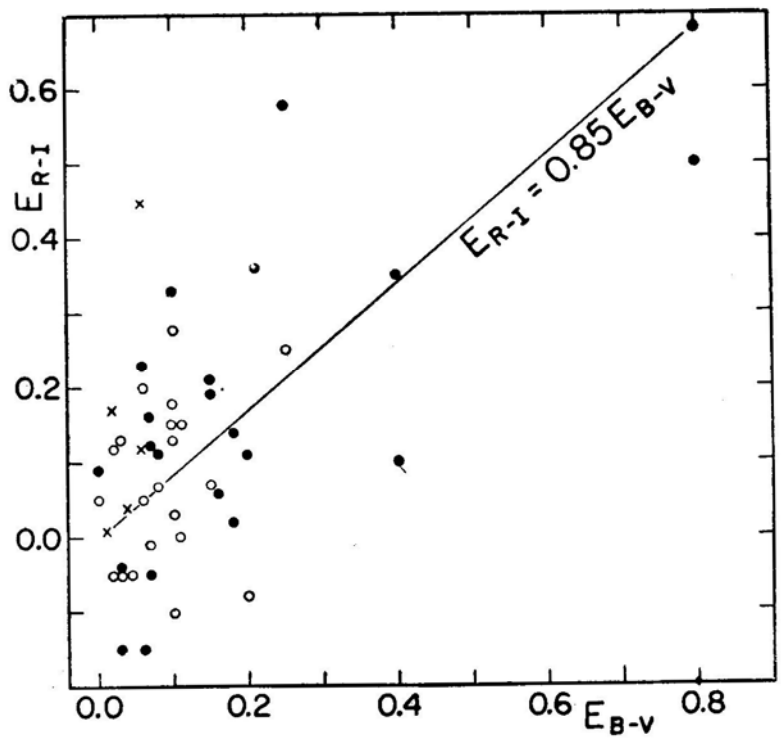

Figure 10. colour excess E_{R-I} based on the assumption of $(R–I)_0$ = 1·26 are plotted for N-irregular variables against E_{B-V} based on other methods. The straight line represents predicted realtion between E_{R-I} and E_{B-V} based on the reddening law of Lee (1970); E_{R-I} = 0·85 E_{B-V}.

in spite of the difference of effective temperatures by more than 500 K (this fact, however, does not necessarily warrant the constancy of $m_{0\cdot78} - m_{1\cdot08}$ index).

With the assumption that $(R - I)_0$ index is 1·26 (this is a mean value for the stars in Fig. 8, excluding a few of the coolest stars) for all the N-irregular variables, we obtain E_{R-I} for carbon stars for which interstellar reddening has been estimated by other methods. The observed values of $R - 1$ are taken from Mendoza and Johnson (1965), Eggen (1972), and Walker (1979), after being transformed to the Johnson system when necessary. In Fig. 10, the resulting values of E_{R-I} are compared with E_{B-V} estimated by Eggen (1972, open circles), by Walker (1980, filled circles), and by the author (Paper I, crosses). The correlation between E_{R-I} and E_{B-V} is reasonably good in general. However, intrinsic colours for the coolest stars with $T_{\rm eff}$ below 2600 K may be somewhat large (see Fig. 8) and E_{R-I} for these stars may be somewhat overestimated.

Also, the intrinsic colour of $R - I$ in Kron-Cape system is found to be nearly constant at 1·04 except for a few of the coolest stars. The colour excesses E_{R-I} in Kron-Cape system are obtained for 70 carbon stars (SRb and Lb variables) observed by Walker (1979) and the results are plotted against the galactic latitudes in Fig. 11. This plot shows that the interstellar reddening estimated from E_{R-I} are statistically larger at lower galactic latitudes.

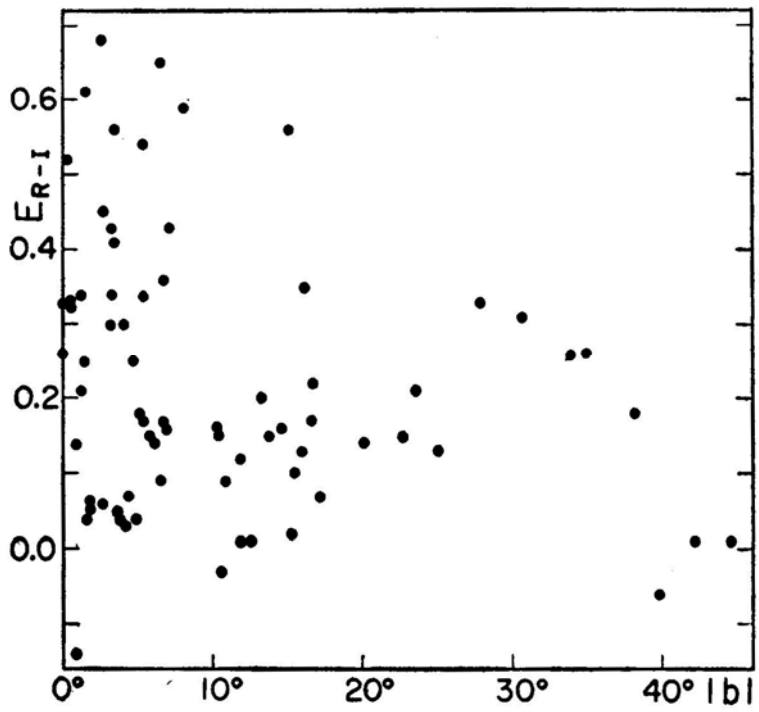

Figure 11. Colour excesses E_{R-I} based on the assumption of $(R–I)_0$ = 1·04 for all the SRb and Lb variables observed by Walker (1979) are plotted against the galactic latitudes. Here, $R – 1$ index is on Kron-Cape system.

5. Luminosity and HR diagram

For cool carbon stars, neither spectroscopic nor photometric parallax is established. Although Statistical parallax is evaluated by several authors (Baumert 1974, Mikami 1975), estimation of the absolute magnitude for an individual carbon star is very difficult in general. However, some carbon stars are found in binary systems and their absolute magnitudes can be estimated if the spectroscopic parallaxes of the companions are known (Gordon 1968, Richer 1972, Olson and Richer 1975). At present, these absolute magnitudes are probably the best estimates available for carbon stars in our Galaxy, and we have selected several stars that have been given high weights by Olson and Richer (1975). Among these, only SZ Sgr has been observed by infrared photometry and therefore a direct determination of effective temperature was possible (Table 2 of Paper I). For other stars (UV Aur, BD—26°2983, W CMa, MSB 64), effective temperatures are estimated by the use of $(V - R)_0 - T_{\rm eff}$ calibration (Fig. 7). Also, absolute magnitude of one carbon star in our sample (V Aql, Table 2 of Paper I) was estimated by interstellar absorption of Na D lines (Utsumi and Yamashita 1971). All these results are plotted in Fig. 12 by filled circles.

We must recall, however, that the estimations of absolute magnitudes by the methods mentioned above are not very accurate. As another possibility, carbon stars in well defined systems such as clusters or nearby galaxies are very useful if their membership is well established and consistent photometry is available. In this respect, recent discovery of a large number of carbon stars in the Magellanic Clouds is of great importance. Especially, the recent study by Richer, Olander and Westerlund (1979) has provided photometric data in *V*, *R* and *I* for a large sample of carbon stars in the Large Magellanic Cloud (LMC). For these carbon stars, bolometric magnitudes have been estimated from $(V - R)_0 - (m_{\rm bol} - I)$ relation established from the data of Mendoza and Johnson (1965), and effective temperatures from $(V - R)_0 - T_{\rm eff}$ calibration in Fig. 7 (a few LMC stars with $V - R < 1{\cdot}5$ are not included because these lie outside our range of calibrations). The results are plotted in Fig. 12 by filled triangles. Similar attempt has been made by Crabtree, Richer and Westerlund (1976) and by Richer, Olander and Westerlund (1979), but they have used $R - 1$ as a temperature indicator. Although $R - 1$ colour index for LMC carbon stars are confined to a rather narrow range (see Fig. 1 of Richer, Olander and Westerlund 1979), this fact does not necessarily imply that effective temperatures of these stars are also confined to a narrow range (reason noted in Section 3). This fact, however, implies that interstellar reddening may be not important for these carbon stars, since the observed values of $R - I$ are mostly close to the intrinsic colour of $(R - I)_0 = 1{\cdot}26$. Spectral observations on the LMC carbon stars by Richer, Olander and Westerlund (1979) revealed that these carbon stars have essentially the same properties as the Galactic carbon stars. This conclusion is also consistent with Fig. 12 where the Galactic carbon stars and the LMC carbon stars occupy essentially the same region in HR diagram.

More recently, infrared photometry of the reddest stars in the LMC clusters has been done by Frogel, Persson and Cohen (1980). This sample includes both carbon stars and M giant stars. For these stars, effective temperatures are obtained from *H*—*K* or *J*—*K* colour indices by the calibrations of Fig. 9 and the absolute magnitudes are taken from Frogel, Persson and Cohen (1980). The positions of these stars in $\log T_{\rm eff} - M_{\rm bol}$ plane are shown in Fig. 12 by open and filled squares for M giants and

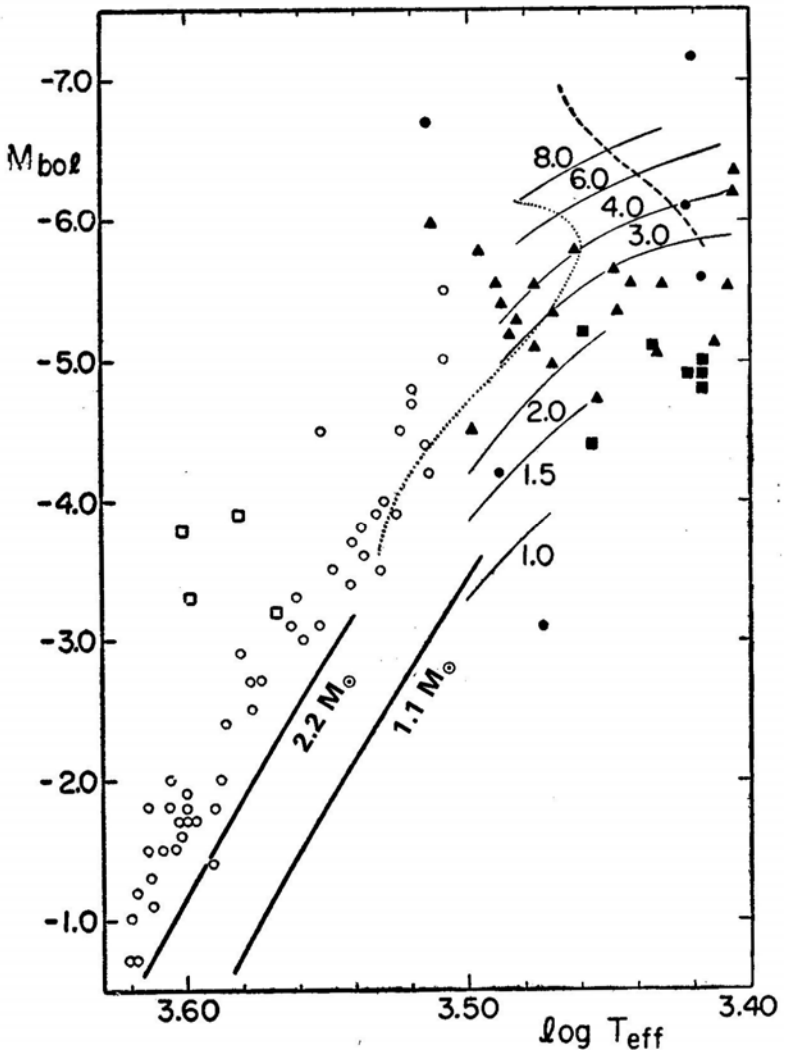

Figure 12. An observational HR diagram of red giant stars including K–M giant stars and carbon stars. Mira variables and SRa variables, however, are not included. Nearby K–M giant stars of old disk population are represented by open circles while carbon stars of binary pair in our Galaxy by filled circles. Carbon stars in the LMC (Richer, Olander and Westerlund 1979) are represented by filled triangles. Also, M giant stars and carbon stars in the LMC clusters (Frogel, Persson and Cohen 1980) are represented by open and filled squares, respectively. Evolutionary tracks for models of 1.1 and $2.2M_{\odot}$ with Z= 0·01 and Y = 0·2 (Sweigart and Gross 1978) are shown by heavy solid lines. Also, 'carbon star formation curve' (Iben and Truran 1978) are shown by dashed line and the evolutionary tracks in asymptotic giant phase are shown by thin solid lines with masses indicated in solar units. The locus of the onset of He-shell flash (Scalo, Despain and Ulrich 1975) is shown by a dotted line.

carbon stars, respectively. This result confirms the HR diagram of these stars presented by Frogel, Persson and Cohen (1980).

In comparison with carbon stars, it is interesting to see the positions of normal red giant stars in log $T_{\rm eff}$ – $M_{\rm bol}$ plane for a larger sample. For this purpose, we have used a sample of red giant stars of old disk population compiled by Tinsley and

Gunn (1976). We have simply transformed the values of $R - I$ colour index listed in Tables A1–A2 of Tinsley and Gunn (1976) to effective temperatures by the use of our calibration given in Fig. 8. The resulting positions of these old disk K–M giant stars in log $T_{\rm eff}$–$M_{\rm bol}$ plane are shown by open circles in Fig. 12. Theoretical evolutionary tracks of Sweigart and Gross (1978) for population I stars are shown for comparison by heavy solid lines. It is generally believed that old disk giant stars may have masses of about 1 $M_\odot$ (Eggen 1973). Recently, masses of red giant stars have been examined in detail by Scalo, Dominy and Pumphrey (1978) and they have shown from a statistical analysis of binary pairs with red giant primary that the initial mean mass of red giant stars should be between 0·8–1·2 $M_\odot$. They have further shown that some selection effects may increase the upper limit of the initial mean mass; however 1·4 $M_\odot$ is a fairly secure upper limit. Our comparison between an observational HR diagram and the theoretical evolutionary tracks, however, reveals that most K–M giant stars of old disk moving groups do not appear on the theoretical evolutionary tracks for stars with expected masses. The theoretical evolutionary tracks shown in Fig. 12 are for Z = 0·01 and Y = 0·2. It is unlikely that any reasonable change in these parameters could account for the discrepancy of more than 1 mag (or the corresponding difference in effective temperature) between the observed positions of M giant stars and the theoretical evolutionary tracks. Thus, something is still wrong in our understanding of these rather normal red giants and substantial re-evaluations of a single star evolution at the red giant stage should be necessary. For example, more realistic treatments of the surface conditions, especially of surface convective zone are indispensable. These conclusions confirm the result of a similar analysis based on a somewhat different stellar sample (Tsuji 1981b).

A comparison of carbon stars and M giant stars in HR diagram of Fig. 12 reveals that these two types of stars are sharply divided into two regions; carbon stars clearly having lower effective temperatures and higher luminosities as compared with M giant stars. This result is quite consistent with the HR diagrams of Mould and Aaronson (1980) for SMC and LMC clusters. These authors have shown that the transition from M to C stars occurs at $M_{\rm bol} \simeq -4{\cdot}4$ and $T_{\rm eff} \sim 3100$ K in both Clouds. It is to be noted that their effective temperatures of carbon stars were calibrated using the scale of Mendoza and Johnson (1965). This may give nearly correct results even though rather fortuitously (Paper I). The fact that carbon stars may have a sharp blue boundary in HR diagram has previously been shown for carbon stars in LMC by Crabtree, Richer and Westerlund (1976) and by Richer, Olander and Westerlund (1979). Similar result has been shown for field red giant stars by Scalo (1976), but M giant stars and carbon stars were rather mixed in the same portion of his HR diagram, in marked contrast to our result. This difference is largely due to the differences between his effective temperatures and ours for M giant stars while his effective temperatures for carbon stars cover the same range as ours by the reason noted in Section 3. It is to be remembered, however, that there is a small number of high luminosity, high temperature carbon stars in LMC (Richer, Olander and Westerlund 1979). Although these stars are not included in Fig. 12 for the reason noted before, it is clear that these carbon stars appear to the left of the blue boundary of carbon stars noted above. These carbon stars are mostly J-type stars with strong ^{13}C-features and some characteristics of these carbon stars have been discussed by Crabtree, Richer and Westerlund (1976) and by Richer,

Westerlund and Olander (1978). It is especially interesting to note that J-type stars in LMC occupy such a particular position in HR diagram while J-type stars in our Galaxy do not show such a clear separation from N-type stars. Also, these authors suggested that these stars may be high mass stars. It is interesting to note that such high mass and high luminosity stars show strong ^{13}C-features in LMC.

It is to be noted that the HR diagram of Fig. 12 is composed of rather heterogeneous samples of stars that may belong to different populations. For this reason, discussions of stellar evolution based on such a diagram should be done with some caution. Nevertheless, the result on stars in the globular clusters of the Magellanic Clouds (Frogel, Persson and Cohen 1980; Mould and Aaronson 1980) indicates that a clear division of carbon stars and M giant stars in HR diagram may have a genetic meaning. Similar result is also shown for the Fornax dwarf spheroidal galaxy by Aaronson and Mould (1980). It is interesting to see that carbon stars in different stellar systems occupy such a well defined portion in HR diagram in spite of the considerable difference in metallicity. In Fig. 12, the dashed line represents 'carbon star formation curve' predicted by Iben and Truran (1978); as a consequence of thermal pulses in He-shell burning and convective dredge-up mechanism, oxygen-rich giants will eventually be converted to carbon stars during the ascent of the asymptotic giant branch (shown by thin solid lines with masses indicated in solar units). It is clear that carbon stars exist well below the 'carbon star formation curve'. Iben and Truran (1978) suggested that the 'carbon star formation curve' becomes nearly vertical at log $T_{\rm eff}$ = 3·45, if less conservative 'dredge-up' mechanism can be assumed. This is somewhat more consistent with our observational HR diagram, but it is to be noted that the dividing line between M giant stars and carbon stars is nearly vertical at log $T_{\rm eff}$ = 3·50 in our observational HR diagram rather than at log $T_{\rm eff}$ = 3·45. On the other hand, the dotted line in Fig. 12 represents the locus where He-shell flash begins (Scalo, Despain and Ulrich 1975). Inspection of Fig. 12 reveals that the boundary between M giant stars and carbon stars does not necessarily coincide with the locus of the onset of He-shell flash, in contrast to a previous conclusion by some authors (*e.g.* Crabtree, Richer and Westerlund 1976, Scalo 1976, Richer, Olander and Westerlund 1979). This may partly be due to the inaccuracy of the temperature calibration based on $R - I$ index by these authors. However, if we consider some uncertainties both in observations and in theory, it is difficult to conclude that carbon stars may or may not be produced just after the onset of He-shell flash. Anyhow, there should be more efficient mechanism of mixing to convert atmospheric C/O ratio above unity in red giant stars than those we have just examined.

6. Discussion and conclusions

n the present paper, we first show that the spectroscopic properties of cool carbon stars can consistently be understood on the basis of the new effective temperature scale determined in Paper I. In fact, several prominent spectral features of cool carbon stars can most reasonably be understood on the basis of our effective temperature scale (Section 2) and this fact shows marked contrast to the confusing situation when these spectral features are interpreted on the basis of C-classification. Second, photometric properties of cool carbon stars are well understood on the basis of our effective

temperature scale. In fact, our effective temperatures show good correlations with most of the colour indices (Section 3) and with colour temperatures based on different photometric systems (Paper I). These results in turn can be regarded as supporting evidences to the effective temperature scale of cool carbon stars proposed in Paper I.

A conclusion of Paper I that the C-classification is anti-correlated with stellar temperatures is finally confirmed by a detailed re-examination of the major spectroscopic characteristics of cool carbon stars. This analysis reveals that the spectra of most diatomic molecules and atoms do not show very clear correlations with stellar temperatures, but those of polyatomic molecules do. This fact may explain, at least partly, why spectral classification of carbon stars has been so difficult. In fact, among the polyatomic molecules that are sensitive to temperature, only SiC_2 can be accessible by the classical spectroscopy. Certainly, Merrill-Sanford bands should be considered as a classification criterion in future spectral classification of carbon stars. Also, estimation of excitation temperature from the line ratios is generally difficult for carbon stars and this fact makes the spectral classification further difficult. However, it has already been shown in an early work by Wyller (1960) that C-classification is not compatible with the vibration temperatures determined from CN bands. Some considerations on vibrational excitation have been included in the original idea of C-classification by Keenan and Morgan (1941), but it has been difficult to utilize such a criterion in actual spectral classification of carbon stars possibly because vibrational excitations are generally too small.

Also, the C-classification by Keenan and Morgan (1941) designated a second parameter that may characterize carbon abundance. This was based on the large variation of C_2 band intensities at the same temperature class. However, if C_2 band intensities measured by the modern photometer are plotted against our effective temperatures (Fig. 4), the dispersion in C_2 band intensity is not very large and it is difficult to assign abundance classes from such an analysis. Probably, as in the case of SiC_2 noted before, the large variation of C_2 band intensities plotted against C–types may be due to the insensitivity of C-classification for small differences in temperature. In fact, we are rather surprised to find that many spectroscopic features as well as various photometric indices of cool carbon stars show a tight correlation with the effective temperatures (Sections 2 and 3), in spite of a large variety in the spectra of these stars. This fact implies that the major parameter that characterizes the spectra of carbon stars, at least at the classification level, is the effective temperature and it is not necessary to introduce other parameters, except for distinguishing some peculiar stars.

In contrast to the difficulty in the spectral classification of carbon stars, various photometric indices of carbon stars turn out to be good temperature indicators (Section 3). Until the present, possible but unknown effect of differential line-blanketing severely limited the use of these photometric indices for the practical purpose of temperature calibration. It is to be emphasized again that this difficulty is mostly avoided in our effective temperatures based on the infrared flux method and, as effective temperatures of some 30 stars are now determined (Table 2 of Paper I), any photometric index can be calibrated against effective temperatures. Some examples of such a calibration are given in Section 3, and their application in determining an observational HR diagram of red giant stars in Section 5.

One major property of cool carbon stars that remains uncertain is the intrinsic luminosity of these stars. As photometric properties of carbon stars are now well

understood, we had hoped that their photometric parallax can be established. However, this hope is not sustained by Fig. 12 where carbon stars are not necessarily confined to a narrow strip. In the past, there has been a general belief that the effective temperatures of. red giant stars are extremely uncertain and luminosities are more reliable (Tinsley and Gunn 1976). This situation has radically been changed, and the major uncertainty in determining an observational HR diagram for red giant stars is now in luminosity (or parallax) rather than in effective temperature. It can now be hoped that an observational HR diagram of red giant stars such as shown in Fig. 12 could provide some further constraints on the theory of stellar evolution at the late stages. For example, although the luminosity function for old-disk red giant stars was shown to be consistent with the present theory of stellar evolution (Tinsley and Gunn 1976), our HR diagram for the same sample of stars fails to match with the present theoretical prediction (Fig. 12). This fact implies that our understanding of red giant stars is far from satisfactory even for the normal red giant stages. The available theoretical predictions (*e.g.* Fujimoto, Nomoto and Sugimoto 1976, Iben and Truran 1978) seem to be still not efficient enough to account for the formation of the more advanced stages represented by carbon stars (Section 5). Baschek (1979) has shown that the mixing processes in actual stars might be more efficient than what the current theory of stellar evolution can account for. Carbon stars too can not escape from this general tendency.

Another major property of carbon stars that remains unclear is the chemical composition, especially of H, C, N and O. This information will be vital in clarifying the details of evolution of carbon stars, since an HR diagram alone does not necessarily provide sufficient constraint on the theory of stellar evolution, if positions of red giant stars in HR diagram are largely determined by the stellar surface condition (Hayashi and Hoshi 1961). In fact, very low effective temperatures of carbon stars can largely be explained by the high atmospheric opacity due to carbon and related molecules. Such an effect of carbon-to-oxygen ratio on HR diagram of red giant stars has actually been shown for some models by Scalo and Ulrich (1975). In quantitative analyses of stellar spectra for determining chemical composition, one important prerequisite is to have a good knowledge on the temperature structures of stellar atmospheres and effective temperature is the most important parameter for this purpose. This requirement is now met for cool carbon stars, and it is hoped that the abundance determination for these stars can be done with better accuracy than before.

In conclusion, we believe that the intrinsic properties of cool carbon stars can be made clear on the basis of the new determination of effective temperatures by the infrared flux method of Blackwell, Petford and Shallis (1980). With this effective temperature scale for cool carbon stars, many a confusion in the interpretation of the spectra and photometric data of carbon stars based on the C-classification can be cleared. Furthermore, the evolutionary status of carbon stars can be made clear on the basis of an observational HR diagram of red giant stars based on our new effective temperature scales for these stars. Accurate determination of effective temperatures of carbon stars is also an important initial step towards a detailed analysis of the spectra and abundance determination in these stars.

Appendix

To have a better understanding of the observed behaviour of molecular bands, some predictions of the molecular band intensities are needed. For this purpose, we define molecular band intensity by

$$\log (W_{v'v''}/\lambda_{v'v''}) = \log g_e f_{v'v''} + \log \Gamma_{\text{band}},$$

where

$$\Gamma_{\text{band}} = \frac{\pi e^2}{mc^2} \int_0^\infty G_\nu (\tau_\nu) P_\nu (\tau_\nu) d\tau_\nu,$$

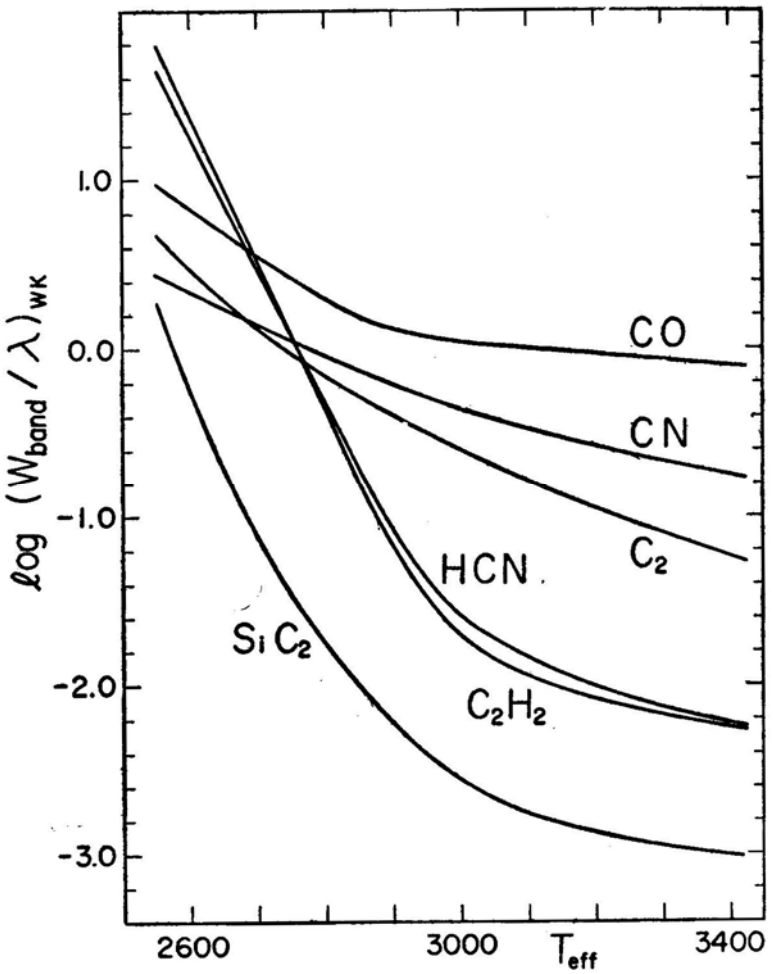

Figure 13. The predicated band intensities are plotted against the effective temperatures of model atmospheres.

in which

$$G_\nu(\tau_\nu) = \frac{2}{F_{\text{cont}}} \int_{\tau_\nu}^{\infty} \frac{dS_\nu}{dt_\nu} E_2(t_\nu)\, dt_\nu$$

is the weighting function and

$$P_\nu(\tau_\nu) = \frac{P_{\text{mol}}}{P_g} \frac{Q_R(T)}{Q_{\text{int}}(T)} \exp\left[-(T_e'' + G_v'')\, hc/kT\right] \left[1 - \exp(h\nu/kT)\right] \frac{1}{\mu m_{\text{H}} k_\nu}$$

gives the population in the lower vibrational levels. The notations have their usual meanings. The values of $W_{v'v''}$ obtained in this way represents the saturation-free equivalent width for a molecular band (for details, see Tsuji 1978). The model atmospheres are based on the carbon rich case (PL03 models with log g = 0·0; of Querci and Querci 1975). Some molecular bands are selected so that they may correspond to the observations discussed in Section 2 and the molecular data used are summarized in Table 1. The resulting molecular band intensities are shown in Fig. 13.

Table 1. Molecular data for band intensity.

Molecule	Transition	$\lambda_{v'v''}$ (μm)	$f_{v'v''}$	Ref
CO	VR band (2, 0)	2·3	$8{\cdot}2 \times 10^{-8}$	(1)
C_2	Swan band (0, 1)	0·5635	$6{\cdot}6 \times 10^{-3}$	(2)
CN	Red System (6, 1)	0·5760	$1{\cdot}0 \times 10^{-4}$	(3)
C_2H_2	ν_3, $\nu_2+\nu_4+\nu_5$	3·1	$1{\cdot}4 \times 10^{-5}$	(4)
HCN	ν_3	3·1	$1{\cdot}1 \times 10^{-5}$	(5)
SiC_2	Merrill-Sanford band	0·4977	$2{\cdot}0 \times 10^{-2}$	(6)

References

(1) Roux, Effantin and D'Incan (1972).
(2) Curtis, Engman and Erman (1976).
(3) Arnold and Nicholls (1972).
(4) Varanasi and Bangaru (1974).
(5) Braslawski and Ben-Aryen (1969).
(6) *f*–value is assumed.

References

Aaronson, M., Mould, J. 1980, *Astrophys. J.*, **240,** 804.
Arnold, J. O., Nicholls, R. W. 1972, *J. quantit. Spectrosc. radiat. Transfer*, **12,** 1435.
Baschek, B. 1979, in *International astrophys. Coll. 22: Les Elements et Leurs Isotopes dans l'Univers*, University of Liege, p. 327.
Baumert, J. H. 1974, *Astrophys. J.*, **190,** 85.
Bergeat, J., Sibille, F., Lunel, M., Lefevre, J. 1976, *Astr. Astrophys.*, **52**, 227.
Blackwell, D. E., Petford, A. D., Shallis, M. J. 1980, *Astr. Astrophys.*, **82,** 249.
Blackwell, D. E., Shallis, M. J. 1977, *Mon. Not. R. astr. Soc.*, **180,** 177.
Bouigue, R. 1954, *Ann. Astrophys.*, **17,** 104.
Braslawski, J., Ben-Aryen, Y. 1969, *J. molec. Spectrosc.*, **30,** 116.
Cousins, A. W. J. 1976, *Mem. R. astr. Soc.*, **81,** 25.
Crabtree, D. R., Richer, H. B., Westerlund, B. E. 1976, *Astrophys. J.*, **203,** L81.

Curtis, L., Engman, B., Erman, P. 1976, *Phys. ScrIipta*, **13,** 270.
Eggen, O. J. 1972, *Astrophys. J.*, **174,** 45.
Eggen, O. J. 1973, *Publ. astr. Soc. Pacific*, **85,** 542.
Faÿ, T. D., Ridgway, S. T. 1976, *Astrophys. J.*, **203,** 600.
Frogel, J. A., Hyland, A. R. 1972, in *International astrophys. Coll. 17: Les Spectres des Astres dans l'Infrarouge et les Microondes, Mem. Soc. R. Sci. Liège, Ser.* 6, **3,** 111.
Frogel, J. A., Persson, S. E., Cohen, J. G. 1980, *Astrophys. J.*, **239,** 495.
Fujimoto, M. Y., Nomoto, K., Sugimoto, D. 1976, *Publ. astr. Soc. Japan*, **28,** 89.
Glass, I. S. 1974, *Mon. Notes astr. Soc. Sth. Afr.* **33,** 53.
Goebel, J. H., Bregman, J. D., Strecker, D. W., Witteborn, F. C., Erickson, E. F. 1978, *Astrophys. J.*, **222,** L129.
Gordon, C. P. 1968, *Publ. astr. Soc. Pacific*, **80,** 597.
Gow, C. E. 1977, *Publ. astr. Soc. Pacific*, **89**, 510.
Hayashi, C., Hoshi, R. 1961, *Publ. astr. Soc. Japan*, **13,** 442.
Iben, I. Jr., Truran, J. W. 1978, *Astrophys. J.*, **220,** 980.
Johnson, H. L. 1967, *Astrophys. J.*, **149,** 345.
Johnson, H. L., Mitchell, R. I., Iriarte, B., Wisniewski, W. Z. 1966, *Commun. lunar planetary Lab.*, **4,** 99.
Keenan, P. C., Morgan, W. W., 1941, *Astrophys. J.*, **94,** 501.
Lee, T. A. 1970, *Astrophys. J.*, **162,** 217.
Mendoza, V. E. E., Johnson, H. L. 1965, *Astrophys. J.*, **141,** 161.
Mikami, T. 1975, *Publ. astr. Soc. Japan*, **27,** 445.
Morris, S., Wyller, A. A. 1967, *Astrophys. J.*, **150,** 877.
Mould, J., Aaronson, M. 1980, *Astrophys. J.*, **240,** 464.
Noguchi, K., Maihara, T., Okuda, H., Sato, S., Mukai, T. 1977, *Publ. astr. Soc. Japan*, **29,** 511.
Olson, B. I., Richer, H. B. 1975, *Astrophys. J.*, **200,** 88.
Peery, B. F. 1975, *Astrophys. J.*, **199,** 135.
Querci, F., Querci, M. 1975, *Astr. Astrophys.*, **39,** 113.
Richer, H. B. 1971, *Astrophys. J.*, **167,** 521.
Richer, H. B. 1972, *Astrophys. J.*, **172,** L63.
Richer, H. B., Olander, N., Westerlund, B. E. 1979, *Astrophys. J.*, **230,** 724.
Richer, H. B., Westerlund, B. E., Olander, N. 1978, *Astrophys. J.*, **219,** 452.
Ridgway, S. T., Carbon, D. F., Hall, D. N. B. 1978, *Astrophys. J.*, **225,** 138.
Ridgway, S. T., Jacoby, G. H., Joyce, R. R., Wells, D. C. 1980b, *Astr. J.*, **85,** 1496.
Ridgway, S. T., Joyce, R. R., White, N. M., Wing, R. F. 1980a, *Astrophys. J.*, **235,** 126.
Ridgway, S. T., Wells, D. C., Joyce, R. R. 1977, *Astr. J.*, **82,** 414.
Roux, F., Effantin, C., D'Incan, J. 1972, *J. quantit. Spectrosc. radiat. Transfer.*, **12,** 97.
Scalo, J. M. 1976, *Astrophys. J.*, **206,** 474.
Scalo, J. M., Despain, K. H., Ulrich, R. K. 1975, *Astrophys, J.*, **196,** 805.
Scalo, J. M., Dominy, J. F., Pumphrey, W. A. 1978, *Astrophys. J.*, **221,** 616.
Scalo, J. M., Ulrich, R. K. 1975, *Astrophys. J.*, **200,** 682.
Sweigart, A. V., Gross, P. G. 1978, *Astrophys. J. Suppl. Ser.*, **36,** 405.
Tinsley, B. M., Gunn, J. E. 1976, *Astrophys. J.*, **206,** 525.
Tsuji, T. 1964, *Ann. Tokyo astr. Obs.*, 2nd Ser., **9,** 1.
Tsuji, T. 1973, *Astr. Astrophys.*, **23,** 411.
Tsuji, T. 1978, *Astr. Astrophys.*, **62,** 29.
Tsuji, T. 1981a, 7. *Astrophys. Astr.*, **2,** 95 (Paper I).
Tsuji, T. 1981b, *Astr. Astrophys.*, **99,** 48.
Utsumi, K., Yamashita, Y. 1971, *Publ. astr. Soc. Japan*, **23,** 437.
Varanasi, P., Bangaru, B. R. P. 1974, *J. quantit. Spectrosc. radiat. Transfer.*, **14,** 839.
Walker, A. R. 1976, *Mon. Not. R. astr. Soc.*, **174,** 609.
Walker, A. R. 1979, *South Africa astr. Obs. Circ.*, **1,** 112.
Walker, A. R. 1980, *Mon. Not. R. astr. Soc.*, **190,** 543.
Walker, A. R., Wild, P. A. T., Byrne, P. B. 1979, *Mon. Not. R. astr. Soc.*, **189,** 455.
Wyller, A. A. 1960, *Astrophys. norv.* **7,** 13.
Yamashita, Y. 1972, *Ann. Tokyo astr. Obs.*, 2nd Ser., **13,** 169.
Yamashita, Y. 1975, *Ann. Tokyo astr. Obs.*, 2nd Ser., **15**, 47.

J. Astrophys. Astr. (1981) **2,** 277–284

Optical Depth Effects on the Formation of Spectral Lines in Rotating and Expanding Spherical Atmospheres

A. Peraiah, G. Raghunath and K. N. Nagendra *Indian Institute of Astrophysics, Bangalore 560034*

Received 1981 April 15; accepted 1981 August 27

Abstract. We have investigated the effects of increasing optical depths on spectral lines formed in a rotating and expanding spherical shell. We have assumed a shell whose outer radius is 3 times the inner radius, with the radial optical depths equal to 10, 50, 100, 500. We have employed a constant velocity with no velocity gradients in the shell. The shell is assumed to be rotating with velocities varying as $1/\rho$, where ρ is the perpendicular distance from the axis of rotation, implying the conservation of angular momentum. Two expansion (radial) velocities are treated: (1) $V = 0$ (static case) and (2) $V = 10$ mean thermal units. The maximum rotational velocities are $V_{\rm rot} = 0$, 5, 10 and 20. In the shell where there are no radial motions, we obtain symmetric lines with emission in the wings for $V_{\rm rot} = 0$ and 5 while for $V_{\rm rot} \geqslant 10$ we obtain symmetric absorption lines. In the case of an expanding shell, we obtain lines with central emission.

Key words: spectral lines—rotating and expanding shells

1. Introduction

In an earlier paper (Peraiah 1980, henceforth called Paper I) we have investigated how rotation affects the line profiles formed in radially expanding atmospheres. There we have treated small rotational velocities with a constant optical thickness and found out that there are substantial changes introduced by rotation and radial expansion. However, in reality, there are stars whose atmospheres rotate faster and simultaneously expand radially (Slettebak 1979). Here we intend to study how high optical depths and large rotational velocities change the spectral lines observed at infinity in a shell of varying optical thickness.

2. The model and the computational procedure

First, we shall give a brief account of the model we have chosen. The main purpose of this investigation is to study the effects of a rotating and radially expanding shell on the formation of lines in it. Therefore, we have chosen a shell whose inner and outer radii are

r_{in} = 2 6 X 10^{11} cm,

r_{out} = 3 X 10^{11} cm

while the radius of the star is

r_* = 10^{11} cm.

The intermediate space between the shell and the star is assumed to have a continuous distribution of matter, *i.e.* there is no discontinuity in density. The density is adjusted in such a way that most of the matter is concentrated in the shell. Here we should realize that the equation of continuity need not apply for a spherically symmetric steady-state flow, because of the time dependancy. Due to this uncertainty, we assumed densities in the shell which would give us radial optical depths of 10, 50, 100 and 500. We have shown the shell in Fig. 1. We have divided the medium of 4 X 10^{10} cm into a large number of shells smaller in size so that it is convenient to calculate the solution. The emergent rays are calculated along the line of sight. The emergent intensity in each shell is obtained from the formal solution of radiative transfer and is given by (see Mihalas 1978)

$$I(\tau_1, \mu, x) = I(\tau_2, \mu, x) \exp[-(\tau_2 - \tau_1)/\mu] + \int_{\tau_1}^{\tau_2} S(t) \exp[-(t - \tau_1)/\mu]\, dt/\mu, \quad (1)$$

where x is the normalized frequency given as x (ν — ν_0)/Δ_s (Δ_s being a standard frequency interval), τ_1 τ_2 are the optical depths (at the boundaries of a small shell) along the line of sight, τ_2 being away from the observer (see Fig. 1). In general, μ is the cosine of the angle made by the ray with the line of sight and $S(t)$ is the source function. Here we are considering the rays along the line of sight and therefore μ is kept equal to 1. I is the specific intensity. Hence equation (1) becomes

$$I(\tau_1, x) = I(\tau_2, x) \exp[-(\tau_2 - \tau_1)] + \int_{\tau_1}^{\tau_2} S(t) \exp[-(t - \tau_1)]\, dt. \quad (2)$$

We have assumed a source function that varies as $1/r^2$. The optical depths in equations (1) and (2) are calculated along the line of sight. The difference τ_2 — τ_1 is calculated as this is the quantity that enters the calculation of emergent intensities. This is given by

$$\tau_2 - \tau_1 = K_0 N \exp(-x'^2)\, \Delta Q, \quad (3)$$

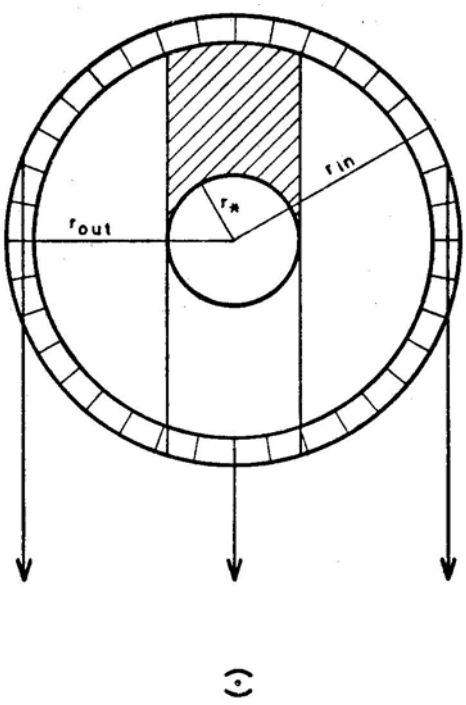

Figure 1. Schematic diagram of the shell.

where ΔQ is the geometrical distance along the line of sight between two consecutive shell boundaries. N is the density of the atoms in the shell. K_0 is the absorption coefficient. This quantity is chosen in such a way that the radial optical depths are 10, 50, 100 and 500. The quantity x' is the normalized frequency which is given by

$$x' = x + \mathbf{V}_{\text{rot}} \cdot 1 + \mathbf{V}_{\text{rad}} \cdot 1, \tag{4}$$

where 1 is the unit vector in the line of sight and $\mathbf{V}_{\text{rot}}$ and $\mathbf{V}_{\text{rad}}$ are the rotational and radial velocities. $\mathbf{V}_{\text{rot}}$ and $\mathbf{V}_{\text{rad}}$ are normalized in terms of mean thermal velocity units (mtu). The integral in equation (2) has been evaluated by assuming that the source function S changes linearly with respect to $(\tau_2 - \tau_1)$ between the two successive shell boundaries along the line of sight (radial variation of S should not be misunderstood with its variation along the line of sight). No incident radiation has been given from outside the shell. The emergent intensities are calculated for each of the smaller shells by employing equation (2) and this process is repeated until the emergent intensity at the final shell is obtained. The flux is calculated by the relation

$$F_x = 2\pi \int_{r_*}^{r_{\text{out}}} I(h, x)\, h\, dh, \tag{5}$$

where h is the perpendicular distance from the centre of the star to the ray parallel to the line of sight.

3. Discussion of the results

The results are presented in Figs 2–9. We have considered two cases; (1) a rotating but static shell and (2) a rotating and expanding shell. The velocity of expansion in the second case is taken to be equal to 10 mtu (all velocities are measured in mtu and henceforth we omit the units). The rotational velocities are assumed to vary according to the principle of conservation of angular momentum. Therefore, we set them to change proportionately according to $1/\rho$ where ρ is the perpendicular distance from the rotation axis. Essentially, we calculate the flux in the cylindrical tubes with the line of sight as axis which is parallel to the rotation axis. The maximum rotational

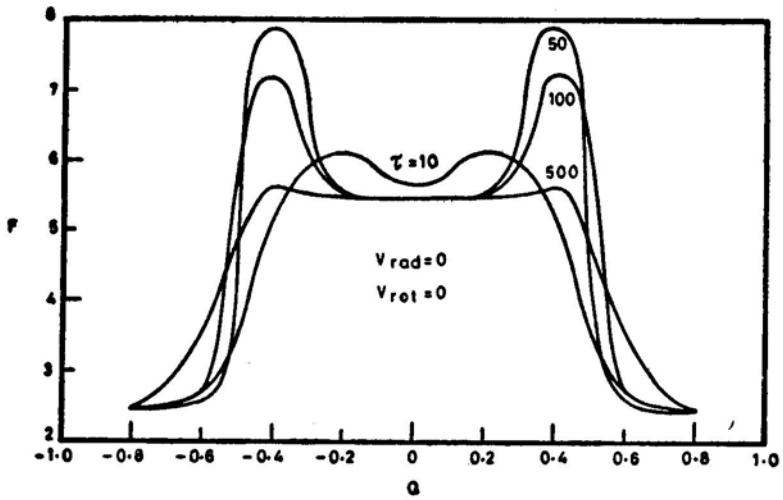

Figure 2. Line profiles for $V_{rad} = 0$, $V_{rot} = 0$; $F = F(x)/F(x_{max})$; $Q = x/x_{max}$.

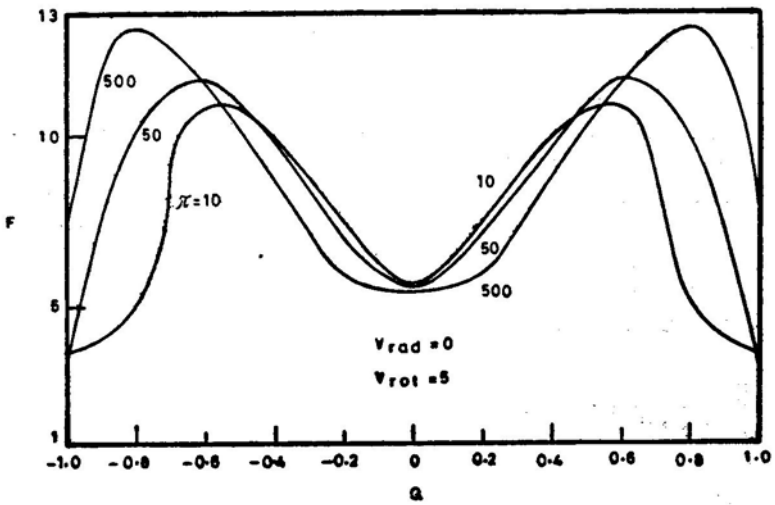

Figure 3. Line profiles for $V_{rad} = 0$, $V_{rot} = 5$.

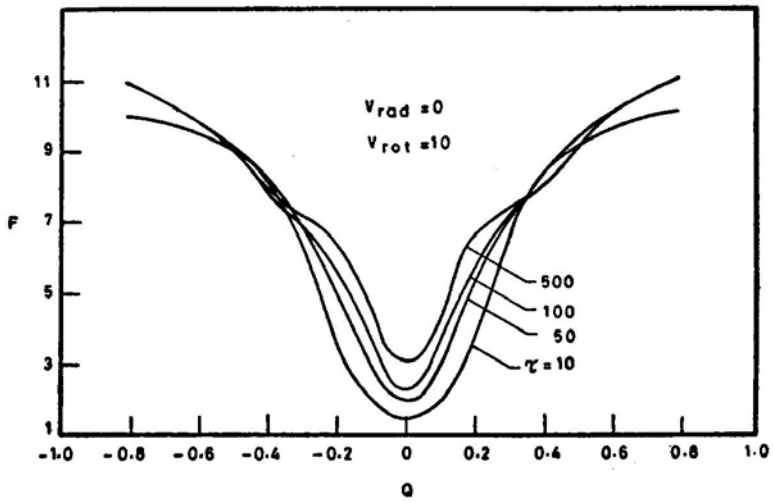

Figure 4. Line profiles for $V_{rad} = 0$, $V_{rot} = 10$.

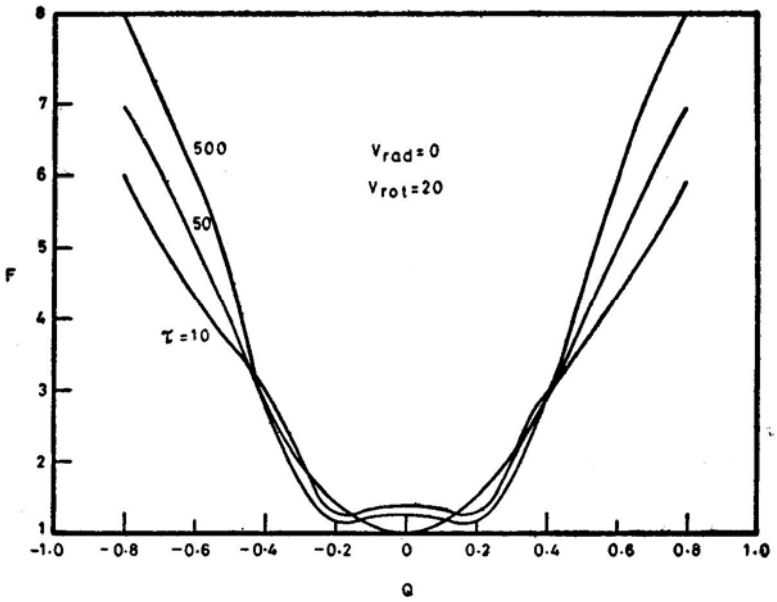

Figure 5. Line profiles for $V_{rad} = 0$, $V_{rot} = 20$.

velocity at r_* is taken to be 0, 5, 10 and 20 corresponding to Figs 2, 3, 4 and 5 respectively. We have plotted in these figures the ratio of $F = F(x)/F(x_{max})$ to $Q = x/x_{max}$. The profiles in Fig. 2 are in emission and symmetrical about the centre of the line with central absorption. As the, optical depth increases the emission in the wings also increase with almost a proportionate decrease in the central absorption. In Fig. 3, we present results for $V_{rad} = 0$ and $V_{rot} = 5$. As one would expect, the lines become broader, but exhibit essentially the same profile. In Fig. 4, the lines

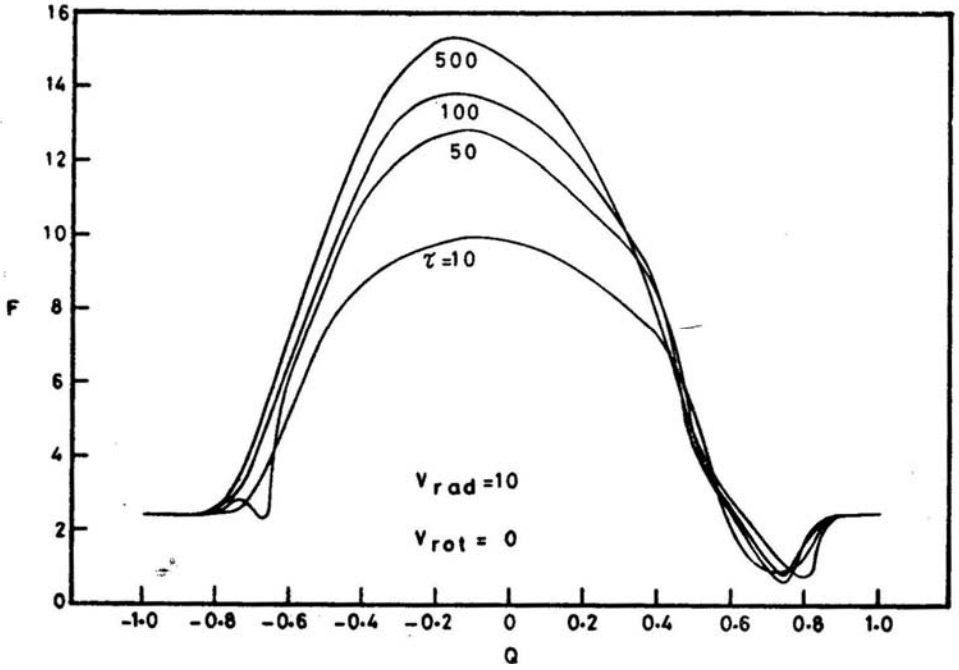

Figure 6. Line profiles for $V_{rad} = 10$, $V_{rot} = 0$.

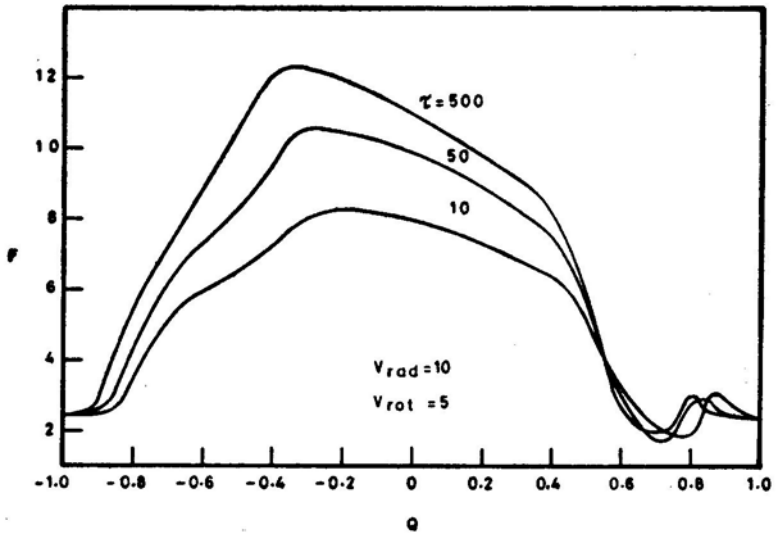

Figure 7. Line profiles for $V_{rad} = 10$, $V_{rot} = 5$.

are given for $V_{rad} = 0$ and $V_{rot} = 10$. There is a dramatic change in the profiles. The emission from the wings disappears completely and a pure symmetric absorption line appears. When V_{rot} is further increased to 20, symmetric absorption lines appear with broadened profiles (see Fig. 5).

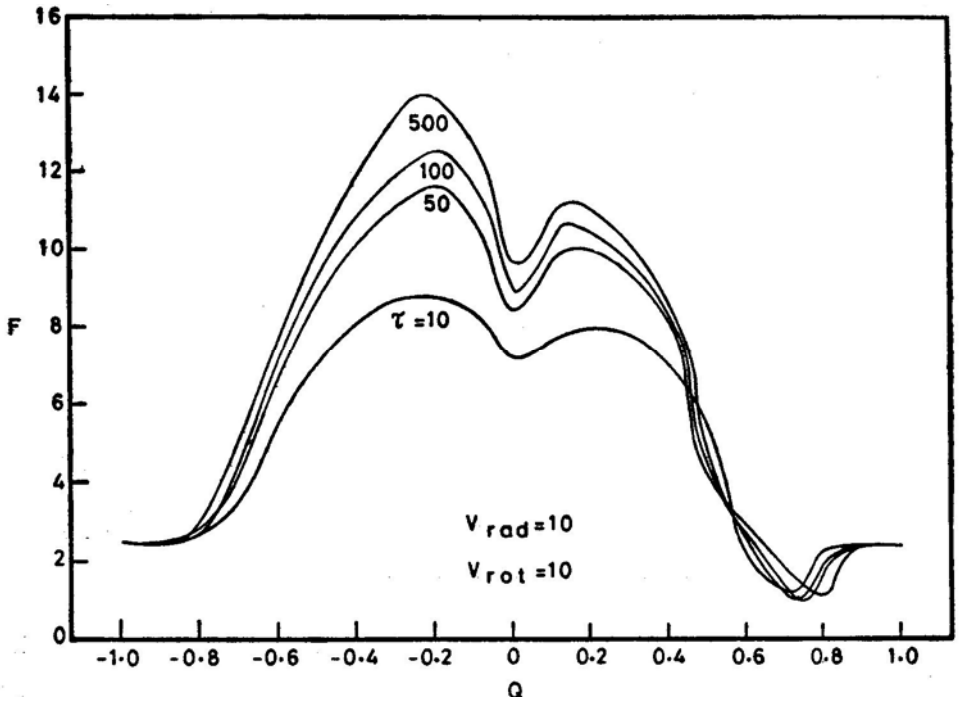

Figure 8. Line profiles for V_{rad} = 10, V_{rot} = 10.

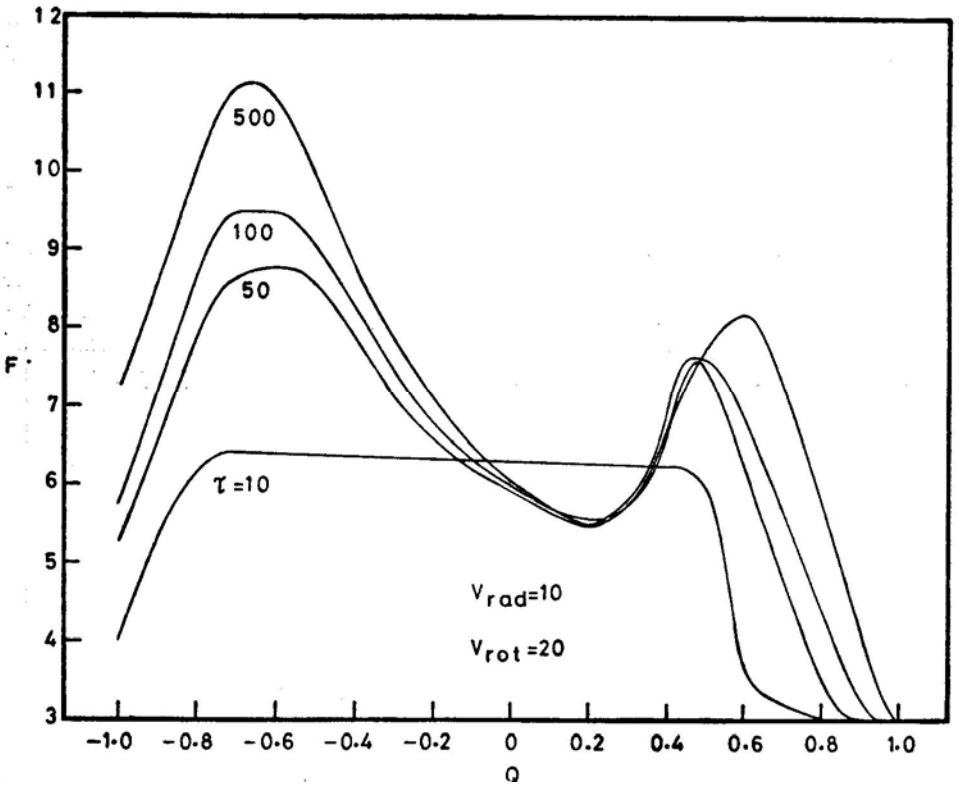

Figure 9. Line profiles for V_{rad} = 10, V_{rot} = 20.

Table 1. Equivalent widths for $V_{rad} = 0$.

V_{rot} \ τ	10	50	100	500
0	− 6·6283	− 8·2914	−7·799	−7·7712
5	−37·2515	−16·1857	−5·944	−2·4224
10	− 2·702	3·2478	3·1773	2·8508
20	5·2665	5·2844	5·24	4·8836

Note: Negative equivalent widths mean that the lines are in emission.

Table 2. Equivalent widths for $V_{rad} = 10$.

V_{rot} \ τ	10	50	100	500
0	−40·6318	−55·603	−60·1595	−66·7998
5	−37·2515	−50·3248	−54·5	−60·75
10	−33·9622	−44·7707	−42·7826	−53·43
20	−10·5504	− 7·3345	− 5·982	− 1·3147

Note: Negative equivalent widths mean that the lines are in emission.

A constant velocity of V_{rad} 10 and V_{rot} = 0, 5, 10 and 20 were introduced into the shell and these results are presented in Figs 6 to 9 respectively. The line profiles shown in Fig. 6 show emission and a small absorption in the blue side (about 7 per cent). The lines are asymmetric because of the expansion velocities. When the rotational velocity is increased to 5 then the asymmetry in the profiles increases. With V_{rot} = 10, again we note that there is a central absorption whose minimum is exactly at $Q = 0$ (see Fig. 8). A further increase in the rotational velocity to 20, changes the line profiles to those with asymmetric emission wings. It is interesting to note how the optical depths change the profiles. Although the optical depths do not change the profiles of the lines substantially, the equivalent widths are affected considerably (see Tables 1 and 2).

These results do show that the rotation, expansion and the number of absorbing atoms (through the changes in the optical depth) give rise to considerable changes in the line profiles. Therefore, one has to incorporate all such effects mentioned above in simulating the observed line profiles. One might obtain erroneous estimates of mass losses if one does not take these physical effects into account properly.

Acknowledgement

The authors thank the referees for pointing, out a few conceptual discrepenciaes.

References

Mihalas, D. 1978, *Stellar Atmospheres*, 2nd edn, Freeman, San Francisco.
Peraiah, A. 1980,. *J. Astrophys. Astr.*, **1,** 17 (Paper I).
Slettebak, A. 1979, *Space Science Rev.*, **23,** 541.

J. Astrophys. Astr. (1981) **2,** 285-288

On the MgH Oscillator Strengths

K. Sinha *Uttar Pradesh State Observatory, Manora Peak, Naini Tel 263129*

Received 1981 April 27; accepted 1981 July 24

Abstract. The theoretical estimates of the oscillator strengths by Kirby, Saxon and Liu (1979) for the $A\ ^2\Pi$ — $X\ ^2\Sigma$ system of the MgH molecule are compared with the solar photospheric results. It is found that the two results are in reasonable agreement.

Key words: oscillator strengths—photospheric spectrum—MgH molecules

1. Introduction

Due to an increase in laboratory data and the availability of refined solar photospheric models, studies are being undertaken to have reliable estimates of elemental abundances for the solar atmosphere (Tsuji 1977; Lambert 1978; Lambert and Luck 1978). However, reliable laboratory estimates of the MgH oscillator strengths are still lacking and hence Lambert and Luck (1978) could not use the *A*–*X* transition of this molecule observed in the photospheric spectrum for a similar analysis. They used Mg I and Mg II lines to derive the solar magnesium abundance.

Recently, Kirby, Saxon and Liu (1979) have presented a set of theoretical estimates of oscillator strengths for the MgH transition under consideration. Naturally, one would like to use them in order to interpret the MgH line intensities.

In the present paper, the results of Kirby, Saxon and Liu (1979) are compared with our solar photospheric results obtained using the latest magnesium abundance. The KPNO Atlas (Brault and Testerman 1972) and Liege Solar Atlas (Delbouille, Roland and Neven 1973) were used in this analysis.

2. Calculations

Four photospheric models were used to compute the ratio of the equivalent width (W) to the oscillator strength of the 0–0 band (f_{0-0}) for a fairly large number of MgH lines. Dividing the corresponding observed photospheric equivalent width by this ratio yields an average value of f_{0-0}. The results presented by Sinha (1981) for

unblended MgH lines of good quality present in the KPNO Atlas (Brault and Testerman 1972), were used to determine the observed equivalent widths. The Liege tracings due to Delbouille, Roland and Neven (1973) were used as a check.

For the model calculations of W/f_{0-0} the standard procedure for equivalent width calculations of weak lines (Sotirovski 1971) was used under the assumption of LTE. The lines were assumed to be unsaturated and Doppler broadened. The photospheric models considered were HSRA-71 (Gingerich *et al.* 1971), AC-72 (Altrock and Cannon 1972), HM-74 (Holweger and Müller 1974) and VAL-76 (Vernazza, Avrett and Loeser 1976). The reason for selecting these models is given in a paper by Sinha, Shukla and Tripathi (1979). The magnesium abundance was taken to be 7·62 (Lambert and Luck 1978) for each photospheric model. The dissociation constants due to Tripathi and Gaur (1979) were used to evaluate the partial pressure of magnesium. The calculations are based on D_0^0 (MgH) = 1 27 eV (Balfour and

Table 1. (0–0) band of the MgH ($A - X$) system in the photospheric spectrum.

Wavelength	Branch (N'')	Equivalent width (mÅ)					Ratio
					Present analysis		Liege
(Å)		MMH	S	LMP	KPNO	Liege	KPNO
5209·567	P_1 (19)	1		1·4	3·6	4·8	1·3
5207·625	P_1 (21)	4·5	3		5·7	8·2	1·4
5207·29	P_2 (10)	2	2	1·5	3·1	4·2	1·4
5207·073	P_2 (21)	1·5		1·7	3·6	5·0	1·4
5203·477	P_1 (7)	3·5			3·7	4·6	1·2
5202·985	P_1 (24)	2·5	3	1·9	2·1	3·2	1·5
5200·822	P_2 (6)	3	1·5	1·8	3·7	3·7	1·0
5198·326	P_2 (26)	2	2	1·5	2·4	3·9	1·6
5193·865	P_1 (28)	2	2	3·8	3·7	5·4	1·5
5193·358	P_2 (28)	3	2·5	2·2	3·7	7·9	2·1
5190·561	P_2 (29)	7	2	1·0	3·2	3·2	1·0
5178·464	Q_2 (8)	5·5	4·6		8·3	12·1	1·5
5159·790	Q_2 (16)	4	6	4·1	7·7	6·8	0·9
5157·006	Q_1 (17)	7		4·5	5·9	7·7	1·3
5124·367	R_2 (13)	3·5			3·5	5·0	1·4
5121·237	Q_1 (26)				3·2	4·5	1·4
5118·311	R_2 (14)				4·3	3·4	0·8
5106·848	R_2 (16)	4·5	3·5	3·7	5·1	5·3	1·0
5106·206	Q_2 (29)				4·3	4·8	1·1
5096·151	Q_1 (31)	3	3		5·3	7·5	1·4
5090·367	Q_2 (32)	2·5	3·5		2·1	3·2	1·5
5088·724	R_2 (19)	3	3		3·7	4·5	1·2
5085·178	Q_1 (33)		3·5		4·2	8·7	2·1
5063·519	R_1 (23)	2·5	3		1·8	3·7	2·1
5061·536	Q_2 (37)	3·5	2·5	2·9	3·7	4·8	1·3
5055·405	Q_2 (38)	1·5	1·5	1·0	1·6	2·6	1·6

Code:

MMH : Moore, Minnaert and Houtgast (1966).
S : Schadee (1964).
LMP : Lambert, Mallia and Petford (1971).
KPNO : Brault and Testerman (1972).
Liege : Delbouille, Roland and Neven (1973).

Lindgren 1978). The opacity sources listed by Tsuji (1966) were included in the opacity calculations.

3. Results and discussion

The MgH-line intensities as measured from the KPNO and the Liege tracings are given in Table 1. Similar results by Moore, Minnaert and Houtgast (1966), Schadee (1964) and Lambert, Mallia and Petford (1971) are also presented for the sake of comparison. In the present analysis, the wings of each line were traced to the near by true continuum marked in the atlas and the area under the curve was evaluated by counting the square millimetres on a transparent graph paper placed above the tracing (Moore, Minnaert and Houtgast 1966). Due to a higher placement of continuum, the Liege equivalent widths are higher by 40 per cent on an average.

Table 2 summarises the results of our oscillator strength calculations. The Liege results are again higher than the KPNO result, but agree within the standard deviations.

The mean result for the HSRA-71, AC-72 and VAL-76 is about the same. This is so because these models vary only slightly from one another. Model HM-74 differs substantially in structure and hence the result based on it is different. A higher value of oscillator strength for HM-74 is an indicator of the fact that this model needs a higher magnesium abundance, because a hotter model leads to lesser molecule formation. To keep the HM-74 result close to the VAL-76 result, the magnesium abundance may have to be increased by about 0.16 dex.

The result f_{0-0} = 0·161 ± ·03 obtained by Kirby, Saxon and Liu (1979) is in perfect agreement with the KPNO result. Hennekar and Popkie (1971) found f_{0-0} = 0·250. The dissociation energy used by them is not known to us. Lambert, Mallia and Petford (1971), Grevesse and Sauval (1973) and Balfour and Cartwright (1976) give f_{0-0} as 0·055, 0·035 and 0·257 respectively. These results appear to differ from our results presented in Table 2, because a different elemental abundance and/or a different dissociation energy was used in their evaluation.

For the photospheric MgH molecules, Hinkle and Lambert (1975) remarked that there is practically no difference in the results obtained for scattering and for pure absorption hypotheses. So the assumption of pure absorption used here is probably satisfactory.

Table 2. Oscillator strength for the *A–X* system of MgH deduced from the solar spectrum.

Model	Oscillator strength for the (0–0) band	
	KPNO	Liege
HSRA-71	0·19 ± 0·08	0·25 ± 0·11
AC-72	0·21 ± 0·09	0·28 ± 0·12
HM-74	0·28 ± 0·13	0·37 ± 0·16
VAL-76	0·19 ± 0·08	0·26 ± 0·11

Code:
KPNO : Brault and Testerman (1972).
Liege : Delbouille, Roland and Neven (1973).

In conclusion it may be remarked that the results of oscillator strength calculations due to Kirby, Saxon and Liu (1979) are in agreement with the solar result. They may serve as the lower limit on MgH oscillator strengths; the only experimental result (f_{0-0} <0·002) due to Main, Carlson and DuPuis (1967) is too low.

References

Altrock, R. C., Cannon, C. J. 1972, *Solar Phys.*, **26**, 21.
Balfour, W. J., Cartwright, H. M. 1976, *Astr. Astrophys. Suppl. Ser.*, **26**, 389.
Balfour, W. J., Lindgren, B. 1978, *Can. J. Phys.*, **56**, 767.
Brault, J. W., Testerman, L. A. 1972, *Preliminary Edition of Kitt Peak Solar Atlas,* Arizona.
DeIbouille, L., Roland, G., Neven, L. 1973, *Photometric Atlas of the Solar Spectrum from λ3000 to λ10000,* Institut d'Astrophysique de l'Université de Liège, Belgium.
Gingerich, O., Noyes, R. W., Kalkofen, W., Cuny, Y. 1971, *Solar Phys.*, **18**, 347.
Grevesse, N., Sauval, A. J. 1973, *Astr. Astrophys.*, **27**, 29.
Hennekar, W. H., Popkie, H. E. 1971, *J. chem. Phys.*, **54**, 1963.
Hinkle, K. H., Lambert, D. L. 1975, *Mon. Not. R. astr. Soc.*, **170**, 447.
Holweger, H., Muller, E. A. 1974, *Solar Phys.*, **39**, 19.
Kirby, K., Saxon, R. P., Liu, B. 1979, Astrophys. J., **231**, 637.
Lambert, D. L. 1978, *Mon. Not. R. astr. Soc.*, **182**, 249.
Lambert, D. L., Luck, R. E. 1978, *Mon. Not. R. astr. Soc.*, **183**, 79.
Lambert, D. L., Mallia, E. A., Petford, A. D. 1971, *Mon. Not. R. astr. Soc.*, **154**, 265.
Main, R. P., Carlson, D. J., DuPuis, R. A. 1967, *J. quantit. Spectrosc. radiat. Transfer, **7**,* 805.
Moore, C. E., Minnaert, M. G. J., Houtgast, J. 1966, *The Solar Spectrum 2935*Å to *8770*Å*: Second Revision of Rowland's Preliminary Table of Wavelengths,* NBS, Washington.
Schadee, A. 1964, *Bull. astr. Inst. Netherl.*, **17,** 311.
Sinha, K. 1981, *In preparation.*
Sinha, K., Shukla, D. S., Tripathi, B. M. 1979, *Bull astr. Soc. India,* **7**, 38.
Sotirovski, P. 1971, *Asir. Astrophys.*, **14**, 319.
Tripathi, B. M., Gaur, V. P. 1979, *J. quantit. Spectrosc. radiat. Transfer,* **22,** 407.
Tsuji, T. 1966, *Publ. astr. Soc. Japan,* **18**, 127.
Tsuji, T. 1977, *Publ. astr. Soc. Japan,* **29**, 497.
Vernazza, J. E., Avrett, E. H., Loeser, R. 1976, *Astrophys. J. Suppl. Ser.,* **30,** 1.

J. Astrophys. Astr. (1981) **2**, 289–307

A Doppler Theory of Quasars

J. V. Narlikar *Tata Institute of Fundamental Research, Homi Bhabha Road, Bombay ,400005*
M. G. Edmunds *Department of Applied Mathematics and Astronomy, University College, Cardiff, UK*

Received 1981 April 28; accepted 1981 July 16

Abstract. We examine a Doppler theory of quasars in which it is assumed that a fraction of the total population of quasars are fired from centres of explosion with moderate cosmological redshifts. It is argued that the substantial part of the redshift of a typical high redshift quasar could be of Doppler origin. If Hoyle's recent hypothesis that quasars emit the bulk of their radiation in a narrow backward cone is given a quantitative form, it is shown that the kinematic and emission parameters of this model can explain the observed features of the four aligned triplets of quasars discovered by Arp and Hazard (1980) and by Saslaw (personal communication). The model predicts a small but nonzero fraction of quasars with blueshifts. Further observational tests of the model are discussed.

***Key words*:** quasar alignments—non cosmological redshifts of quasars

1. Introduction

Doppler theories of quasars have been in the astronomical literature since the early days of the discovery of quasars. The first of these was proposed by Terrell (1964) who argued that quasars are small stellar mass objects ejected from our own Galaxy. On a somewhat larger scale, Hoyle and Burbidge (1966) suggested that quasars were ejected in violent explosions in nearby galaxies, citing NGC 5128 as a likely source. For many years Arp has been presenting evidence in support of the point of view that high redshift quasars are physically associated with low redshift galaxies (Arp 1966). Recently one of us (Narlikar and Das 1980) was concerned with explaining the existing data on quasar–galaxy associations in. terms of a cosmology of variable particle masses in which the quasars are considered as eject a from nearby galaxies.

We do not wish to enter into the debate on quasar redshifts; we simply wish to examine whether a Doppler model can be excluded on the, basis of current observations.

With this view we investigate here in some detail a variation on the theme proposed by Hoyle and Burbidge (1966)— a variation based on. Hoyle's recent hypothesis that quasars emit most of their radiation in a narrow *backward* cone as they travel through the intergalactic medium (Hoyle 1980).

In Section 2 we outline the essential features of Hoyle's hypothesis. Although Hoyle assumed that the entire redshift of the quasar is due to the Doppler effect we will suppose that a small component of the redshift may be due to the expansion of the universe. As we discuss in Sections 3 and 4, it then becomes possible to introduce additional inputs into the theory which can be tested by observations already available. In Section 5 we discuss limitations of this theory and outline ways in which it can be tested further.

2. Hoyle's hypothesis

The main objection to the Burbidge-Hoyle theory was that it predicted a preponderance of blueshifted, quasars over redshifted ones. According to a calculation made by Strittmatter (1967) if quasars are emitted isotropically from exploding nuclei of galaxies within a cosmologically nearby region (*i.e.* up to 10–100 Mpc), then in a flux limited survey the number of blueshifted quasars (N_b) is related to the number of redshifted quasars (N_r) by the formula

$$N_b/Nr = (1+Zm)^4, \tag{1}$$

where z_m is the maximum redshift observed in the survey. This calculation makes the following assumptions.

(1) Each quasar emits radiation isotropically in its rest frame.
(2) Quasars are emitted with the same speed from their respective sources.
(3) All quasars have the same luminosity.
(4) The cosmological redshift of a source of explosion is zero.
(5) The sample is complete.

For a characteristic value of $z_m = 2$, equation (1) gives 81 times as many blueshifted quasars as the redshifted ones. The fact that *no* blueshifted quasars have been observed to date, effectively disposes of the theory.

Burbidge and Burbidge (1967) have discussed possible reasons for the non-observance of blueshifts. Among the various causes, they mention that blueshifts could be avoided if each quasar emits in backward direction with respect to its motion, so that a quasar moving towards us would be invisible and no blueshift would be seen from it.

Hoyle (1980) has calculated the precise angle of the backward cone within which a quasar must emit its radiation in order not to exhibit a blueshift to *any* observer. The angle, as Hoyle pointed out, does not depend on where the observer is located provided he is at rest relative to the intergalactic medium. The angle depends *only* on the speed V of the quasar relative to the intergalactic medium and is given by $2\theta_{\mathrm{H}}$ where

$$\theta_{\mathrm{H}} = \cos^{-1}\left[\frac{1-(1-V^2)^{1/2}}{V}\right] \text{ (speed of light } c = 1\text{).} \tag{2}$$

We will refer to θ_{H} as the Hoyle-angle and the backward cone of semi-vertical angle θ_{H} with its axis along the line of motion as the Hoyle-cone.

The Hoyle-angle tends to zero as $V \rightarrow$ the speed of light. However, even for substantial relativistic speeds θ_{H} is fairly large. Thus for $V = 0{\cdot}8$, $\theta_{\mathrm{H}} = 60°$ and for $V = 0{\cdot}95$, $\theta_{\mathrm{H}} \simeq 43°$. Hence even for such high speeds the ejection does not have to be confined to a very narrow beam. Hoyle did not discuss the type of emission mechanism which would be confined in such a fashion, beyond pointing out that a quasar moving rapidly through the intergalactic medium may tend to pile up gas in the forward direction and leave a relatively rarefied region in the backward direction. Thus the opacity of gas in the forward direction will be high and in the backward direction low. While this argument supplies a qualitative basis for Hoyle's hypothesis, only a detailed investigation of relativistic plasma physics may tell us how, if at all, radiation is allowed to escape only in a specified backward cone. Before such an investigation could be undertaken it is desirable first to see whether observations provide any support for Hoyle's hypothesis.

The observational motivation which led Hoyle to resurrect the Doppler theory was provided by the discovery of two perfectly aligned triplets of quasars by Arp and Hazard (1980). These quasars designated (B, A, C) and (X, Y, Z) by Arp and Hazard lie in adjacent areas of the sky at $11^{\mathrm{h}}\,30^{\mathrm{m}} + 10°{\cdot}6$. In each triplet a bright central quasar is flanked by fainter ones of larger redshifts. The striking feature about each triplet is that the three quasars lie on a straight-line within the observational accuracy (claimed to be $\sim$1 arcsec). In addition to these triplets Saslaw (personal communication) found two more in another field studied by Arp and Hazard (1980) at $11^{\mathrm{h}}\,46^{\mathrm{m}} + 11°{\cdot}1$. These triplets also show similar characteristics as (B, A, C) and (X, Y, Z). We will refer to these four triplets by I, II, III and IV respectively.

Are these triplets cases of chance projection on the sky in our frame of reference? If the cosmological hypothesis is to survive this is the conclusion one must come to; for in each triplet the vastly different redshifts of the member quasars imply (according to this hypothesis) that they are at very, different distances from us. If the probability of chance projection is moderately large (say $\gtrsim 10$ per cent) then such observations pose no threat to the cosmological hypothesis. If the probability is small (say $\lesssim 1$ per cent) then we must conclude that the members of a triplet form a part of the same physical system. The problem of estimating this probability is not simple and it requires the specification of the selection procedure as well as an accurate knowledge of the quasar surface density at a given magnitude. We do not wish to enter into the arguments for and against the cosmological hypothesis based on probability estimates. We simply refer the reader to Hoyle (1980) and Arp and Hazard (1980) who have argued that the chance probability is low and to Edmunds and George (1981) who have argued that the probability is moderately large.

Hoyle took the view that the probability of chance alignment is low, and argued further that triplets like these present *prima facie* examples of ejection of the three quasars from a central explosion, in a straight-line Thus in Hoyle's theory the redshifts of A, B and C are entirely of Doppler origin and in the centre of mass frame A, B and C are moving in a straight-line. Would this alignment be pre-

served in the rest frame of any other observer? The answer is in the negative. As shown by one of us (Narlikar 1981) the angle between the lines joining the end quasars to the middle one is given by

$$\chi = \frac{n}{(1-f^2)^{1/2}} \frac{V \sin\theta}{(1-V^2)^{1/2}} \frac{\theta_{AB} + \theta_{AC}}{2}. \tag{3}$$

The notation in formula (3) is explained in Fig. 1. The above formula is valid for small χ. Although χ could in principle be as high as 90° in the most extreme case, the smallness of θ_{AB} and θ_{BC} make χ small. For the example worked out by Hoyle (personal communication) the angle χ is on the borderline of the alignment accuracy claimed by Arp and Hazard. Thus in. future more accurate positional measurements may provide a good observational test of Hoyle's theory.

In this paper we take a middle-of-the-road point of view. There is considerable observational evidence for a moderate cosmological redshift ($z < 0{\cdot}5$) for at least some quasars *e.g.* 3C 273 (Stockton 1978, 1980; Wyckoff *et al.* 1980). We assume that there might be another population of quasars, ejected with large speeds from centres of explosion which have moderate cosmological redshifts. We consider whether such quasars may have a large Doppler component in their redshifts which may substantially exceed the redshifts of the centres of explosion. For a non-cosmological theory we expect the cosmological component of the redshift of any such ballistic quasar not to exceed $z \sim 1$ which is the limit to which galaxies are being observed today.

In a typical quasar triplet we will assume that the redshift of the middle quasar is wholly cosmological. This could happen either by the firing of the end quasars with large speeds and the middle one with a small speed in a single explosion, or by the middle quasar itself acting as a source of explosion. In either case the three quasars will appear well aligned to us provided they were so in the rest frame of the middle quasar. Such alignment-preserving ejections are not unknown in high energy astrophysics: the double radio sources appear to show the same pattern.

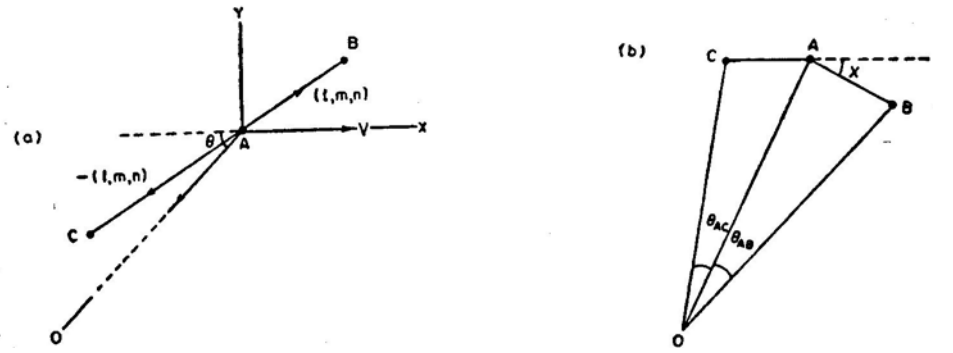

Figure 1. (a) The quasar A moves with speed V, relative to the observer O, in the direction shown by the arrow. θ is the angle measured by A between its backward direction of motion and, the direction AO along which it must emit radiation reaching O. Take rectangular axes AXYZ in the rest frame of A with AX along A's direction of motion, AY in the plane OAX and AZ (not shown) perpendicular to the plane OAX. ± (l, m, n) are the direction cosines of AB and AC. $F \equiv l \cos\theta + m \sin\theta$ is the projection of the unit vector (l, m, n) on the line OA.

(b) As seen from O the line CAB of (a) appears bent with an angle χ between the segments CA and AB. (Figure not drawn to scale).

This assumption enables us to calculate the kinematic parameters of each of the four triplets uniquely. We will outline the calculation in Section 3. The uniqueness of the solution enables us to test an emission function which gives a quantitative form to Hoyle's hypothesis that quasars emit their radiation preferentially backwards.

To avoid confusion with the notation of Arp and Hazard we will denote a triplet by (L, M, N), of which M is the middle quasar with wholly cosmological redshift.

3. The kinematics of triplets

We will assume that in a typical triplet (L, M, N) the end quasars L and N were fired at relativistic speeds in *opposite* directions from the central quasar M. We will denote the redshifts of L, M and N by z_L z_M and z_N respectively; z_M is cosmological in origin. Our calculations can also be applied to quasars ejected from galaxies although so far no linear alignment as good as those discussed in Section 2 is known in which the middle member is a galaxy. If, however, more than two quasars are ejected in a single explosion from M, as Arp has suggested, then linear alignments would not be expected.

We will assume that the cosmological component in the redshift of L or N is also z_M and define the non-cosmological components in their redshifts by Z_L and Z_N respectively where

$$1+Z_L=\frac{1+z_L}{1+z_M}, \qquad 1+Z_N=\frac{1+z_N}{1+z_M}. \tag{4}$$

To determine the kinematic parameters of the triplets we will assume that the large scale properties of spacetime are determined by the Robertston-Walker metric

$$ds^2=dt^2-S^2(t)\left[\frac{dr^2}{1-kr^2}+r^2\left(d\theta^2+\sin^2\theta\, d\phi^2\right)\right], \tag{5}$$

where k = 1, 0 or—1 and $S(t)$ is the scale factor of expansion.

Since the angular separation of L or N from M is small in a typical triplet ($< 10^{-2}$) we are able to make several simplifying assumptions in our calculations. To begin with, we can assume that L and N are moving in the locally inertial coordinate system in which M is at rest. Fig. 2 illustrates the geometry of the problem.

The circled region at M is where the locally inertial coordinates operate and where special relativity can be used. The passage of light from M to the observer O (*i.e.* ourselves) is across the curved spacetime of equation (5). Through M draw the line JMK perpendicular to MO. The quasars L and N are fired along a line making angle α with OM. The light ray from L to O crosses JK at a point E. In the rest frame of M, denoted by $\mathfrak{T}$, the line LE is parallel to MO because of the smallness of the angle MOL. Let V_L and V_N be the velocities with which L and N were fired from M, at the cosmic time $t = \bar{t}$. Suppose t_L and t_N are the times in the locally inertial frame when light signals left L and N respectively in order to arrive simultaneously at O at the cosmic time t_0.

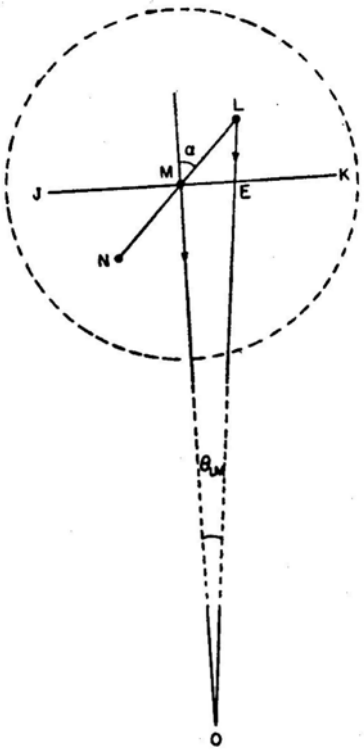

Figure 2. The circled region is local to the system LMN wherein the spacetime may be taken as flat. Cosmological effects arise when observations are made from O lying well outside the circle. (Figure not drawn to scale).

Let the Robertson-Walker space coordinates of M be $r = r_M$, $\theta = \theta_M$, $\phi = \phi_M$, the origin of the coordinates being at O. Suppose light leaving M at $t = t_M$ arrives at O at $t = t_0$ then

$$\int_0^{r_M} \frac{dr}{(1-kr^2)^{1/2}} = \int_{t_M}^{t_0} \frac{dt}{S(t)}. \tag{6}$$

The light tracks from L and N towards O are small variations on the light track from M to O. For motion or light propagation in the circled region it is a sufficiently good approximation to freeze $S(t)$ at a typical value, say $S(t_M)$.

In $\mathfrak{T}$, the distances of interest are

$$\mathrm{ML} = V_L(t_L - \bar{t}), \qquad \mathrm{ME} = V_L(t_L - \bar{t}) \sin \alpha,$$

$$\mathrm{LE} = V_L(t_L - \bar{t}) \cos \alpha. \tag{7}$$

In terms of the Robertson-Walker metric we have

$$\mathrm{LE} \simeq S(t_{\mathrm{M}}) \int_{r_{\mathrm{E}}}^{r_{\mathrm{L}}} \frac{dr}{(1-kr^2)^{1/2}} \simeq S(t_{\mathrm{M}}) \int_{r_{\mathrm{M}}}^{r_{\mathrm{L}}} \frac{dr}{(1-kr^2)^{1/2}}, \tag{8}$$

$$\mathrm{ME} \simeq r_{\mathrm{M}}\, S(t_{\mathrm{M}})\, \theta_{\mathrm{LM}} \tag{9}$$

Here θ_{LM} and θ_{NM} are the angles subtended by the segments LM and NM at O.

Light propagation from L to O can be split into two parts: first from L to E in the local region of M and then from E to O in the expanding universe

$$\int_0^{r_{\mathrm{L}}} \frac{dr}{(1-kr^2)^{1/2}} = \int_{t_{\mathrm{L}}}^{t_0} \frac{dt}{S(t)},$$

i.e.

$$\int_0^{r_{\mathrm{M}}} \frac{dr}{(1-kr^2)^{1/2}} + \frac{V_{\mathrm{L}}\,(t_{\mathrm{L}} - \bar{t}) \cos\alpha}{S(t_{\mathrm{M}})} = \int_{t_{\mathrm{M}}}^{t_0} \frac{dt}{S(t)} + \frac{t_{\mathrm{M}} - t_{\mathrm{L}}}{S(t_{\mathrm{M}})}. \tag{10}$$

In view of equation (6) we get

$$t_{\mathrm{M}} - t_{\mathrm{L}} = V_{\mathrm{L}}\,(t_{\mathrm{L}} - \bar{t}) \cos\alpha, \tag{11}$$

which can be rewritten in the form

$$(t_{\mathrm{L}} - \bar{t})\,(1 + V_{\mathrm{L}} \cos\alpha) = t_{\mathrm{M}} - \bar{t} \equiv T. \tag{12}$$

By symmetry we get a similar relation for quasar N by changing α to $\alpha + \pi$

$$(t_{\mathrm{N}} - \bar{t})\,(1 - V_{\mathrm{N}} \cos\alpha) = T. \tag{13}$$

A variation of the propagation relation for light from L to O gives us the redshift of L seen by O

$$1 + z_{\mathrm{L}} = \frac{1 + V_{\mathrm{L}} \cos\alpha}{(1 - V_{\mathrm{L}}^2)^{1/2}} (1 + z_{\mathrm{M}}) \tag{14}$$

and a similar equation is obtained for N.

Next, from equations (7), (9) and (12) we get

$$\theta_{LM} = \frac{V_L T \sin \alpha}{(1 + V_L \cos \alpha) r_M S(t_M)} \tag{15}$$

and a similar relation for θ_{NM}.

From the above we have three equations relating the observable quantities θ_{LM}, θ_{NM}, Z_L and Z_N to the three unknowns V_L, V_N and α

$$\frac{1 + V_L \cos \alpha}{(1 - V_L^2)^{1/2}} = 1 + Z_L, \tag{16}$$

$$\frac{1 - V_N \cos \alpha}{(1 - V_N^2)^{1/2}} = 1 + Z_N, \tag{17}$$

$$\frac{V_L (1 - V_N \cos \alpha)}{V_N (1 + V_L \cos \alpha)} = \frac{\theta_{LM}}{\theta_{NM}} \equiv k. \tag{18}$$

These equations can be solved with the help of a little algebra. It is convenient to define the known quantities

$$\lambda_L = (1 + k)^{-1} (1 + Z_L)^{-1}, \quad \lambda_N = (1 + k^{-1})^{-1} (1 + Z_N)^{-1}. \tag{19}$$

We then. have

$$V_L = \left[1 - \left(\frac{2\lambda_L}{1 + \lambda_L^2 - \lambda_N^2}\right)^2\right]^{1/2}, \tag{20}$$

$$V_N = \left[1 - \left(\frac{2\lambda_N}{1 + \lambda_N^2 - \lambda_L^2}\right)^2\right]^{1/2}, \tag{21}$$

and

$$\cos \alpha = \frac{(1 - k)/(1 + k) + \lambda_N^2 - \lambda_L^2}{\{[1 - (\lambda_N + \lambda_L)^2]\ [1 - (\lambda_N - \lambda_L)^2]\}^{1/2}}. \tag{22}$$

The angle made by the light ray leaving quasar L with the backward direction of motion of L as measured in the rest frame of L, is $\tilde{\alpha}_L$ where

$$\cos \tilde{\alpha}_L = \frac{\cos \alpha + V_L}{1 + V_L \cos \alpha}. \tag{23}$$

Similarly,

$$\cos \tilde{\alpha}_N = \frac{V_N - \cos \alpha}{1 - V_N \cos \alpha}. \tag{24}$$

The corresponding Hoyle-angles are $\tilde{\alpha}_{LH}$ and $\tilde{\alpha}_{NH}$ where

$$\cos \tilde{\alpha}_{LH} = \left[\frac{1-(\lambda_L+\lambda_N)}{1+(\lambda_L+\lambda_N)} \times \frac{1-(\lambda_L-\lambda_N)}{1+(\lambda_L-\lambda_N)}\right]^{1/2} \tag{25}$$

$$\cos \tilde{\alpha}_{NH} = \left[\frac{1-(\lambda_N+\lambda_L)}{1+(\lambda_N+\lambda_L)} \times \frac{1-(\lambda_N-\lambda_L)}{1+(\lambda_N-\lambda_L)}\right]^{1/2} \tag{26}$$

Table 1 gives the values of all the kinematic parameters for the four triplets mentioned in Section 2. (Of these, I and II are the triplets of Arp and Hazard and III and IV are Saslaw's triplets.)

Note that all end quasars are emitting within their Hoyle-cones, even though we have now added the complication of a cosmological redshift for the central quasar. This is hardly surprising, however, since our general calculation above gives

$$\cos \tilde{\alpha}_L - \cos \tilde{\alpha}_{LH} = \frac{1 - V_L^2}{V_L (1 + V_L \cos \alpha)} Z_L > 0, \tag{27}$$

$$\cos \tilde{\alpha}_N - \cos \tilde{\alpha}_{NH} = \frac{1 - V_N^2}{V_N (1 - V_N \cos \alpha)} Z_N > 0. \tag{28}$$

So long as the end quasars in a triplet have higher redshifts than the middle quasar, the property of emission within the Hoyle-cone will always hold. This property applies not only in the local special relativistic case considered by Hoyle but also in the 'mixed' case where the quasar has been fired from a source which itself has a significant cosmological redshift with respect to the observer.

It is necessary to make this distinction between Hoyle's purely local theory and the mixed theory being discussed here. In Hoyle's theory the intergalactic medium in

Table 1. The kinematic parameters of quasar triplets I, II, III and IV.

Triplet	Observed quantities					Computed quantities						
No.	z_M	z_L	z_N	$\theta_{LM}\times10^3$	$\theta_{MN}\times10^3$	α^0	V_L	$\tilde{\alpha}^0_{LH}$	$\tilde{\alpha}^0_L$	V_N	$\tilde{\alpha}^0_{NH}$	$\tilde{\alpha}^0_N$
I	0·51	2·15	1·72	1·66	3·08	73·8	0·80	59·8	27·9	0·91	50·1	32·4
II	0·54	2·12	1·61	0·83	2·08	66·6	0·76	62·3	27·0	0·93	47·5	32·8
III	1·01	2·22	1·93	3·64	3·58	88·8	0·77	61·8	38·6	0·74	63·9	43·3
IV	1·01	1·67	2·12	5·03	1·01	125·2	0·94	45·8	38·0	0·54	73·1	31·8

which the quasar moves is also the medium in which the observer is at rest. In the present theory, however, the intergalactic medium against which the quasars move has its standard of rest redshifted (cosmologically) relative to the observer. The Hoyle-cone for a quasar is therefore determined by the speed of the quasars relative to its local intergalactic medium and not relative to the intergalactic medium of the observer.

4. Constraints on quasar emission

We now try to test the hypothesis that quasars emit preferentially within their backward Hoyle-cone. Until a quasar emission mechanism has been worked out in detail (in the lines indicated at the end of Section 2, we do not have a precise theory to test. Nevertheless an empirical approach can still be useful, and we outline it here.

In this approach we postulate an *ad hoc* anisotropic emission pattern in the rest frame of a typical quasar and then test it against the data on the four triplets discussed above. To this end we first outline the emission pattern and then discuss how the relative brightness of the end quasars would appeal to a remote observer.

If a quasar were emitting isotropically, then its total luminosity $\mathscr{L}$ would be evenly distributed over the solid ankle 4π so that the luminosity $\mathscr{L}$ across a solid angle $d\,\Omega$ would be simply $\mathscr{L}\,d\,\Omega/4\pi$. In the case of anisotropic emission we have to modify this expression to

$$\mathscr{L}\,Q\,(\tilde{\theta})\,d\,\Omega/4\pi = (\mathscr{L}/4\pi)Q\,(\tilde{\theta})\sin\tilde{\theta}\,d\tilde{\theta}\,d\phi, \tag{29}$$

where $\tilde{\theta}$ measures the angle with the *backward* direction of motion in the rest frame of the quasar. Although $Q\,(\tilde{\theta}) \neq$ constant indicates anisotropic emission, it still preserves axi-symmetry about the direction of motion.

We now give quantitative expression to Hoyle's hypothesis that a quasar emits preferentially within $\theta \leqslant \tilde{\theta}_{\mathrm{H}}$. It is of course possible to choose a function $Q\,(\tilde{\theta})$ which vanishes beyond this range. However, a very sharp cut-off is unlikely to arise in a physical theory of light propagation from a rapidly moving source, so we prefer an exponential form which would tend to damp out beyond $\tilde{\theta} = \theta_{\mathrm{H}}$. A form for $Q\,(\tilde{\theta})$ which naturally suggests itself is

$$Q\,(\tilde{\theta}) = Q_0 \exp\left[-\frac{(1-\cos\tilde{\theta})}{2n^2\,(1-\cos\tilde{\theta}_{\mathrm{H}})}\right], \tag{30}$$

where Q_0 and n are constants. The similarity of equation (30) with the Gaussian form is more apparent if we write it as

$$Q\,(\tilde{\theta}) = Q_0 \exp\left[-\frac{\sin^2(\tilde{\theta}/2)}{2n^2\sin^2(\tilde{\theta}_{\mathrm{H}}/2)}\right]. \tag{31}$$

In a crude sense the above expression suggests that the damping at $\tilde{\theta} = \tilde{\theta}_H$ corresponds to an attenuation of the Gaussain profile at a distance σ/n from its mean. This comparison is, however, not exact since the apparent Gaussian form of equation (31) is with respect to sin $\tilde{\theta}/2$ and not with respect to $\tilde{\theta}$. Thus the damping for $\tilde{\theta} > \tilde{\theta}_H$ is not as rapid as it would have been in a Gaussian profile with respect to $\tilde{\theta}$.

The constant Q_0 is determined by integrating Q ($\tilde{\theta}$) over all solid angles and requiring the integral to be unity. Assuming that n is large enough to ensure that

$$\exp\left[-\left\{n^2\,(1-\cos\tilde{\theta}_H)\right\}^{-1}\right] \ll 1 \tag{32}$$

we get

$$Q_0 = \frac{1}{4\pi n^2\,(1-\cos\tilde{\theta}_H)}\,. \tag{33}$$

Note that at this empirical level it is equally possible to postulate anisotropic emission which is preferentially in the *forward* direction. This would correspond to $n^2 < 0$. While the form favouring backward emission (equation 30) is

$$Q(\theta) = Q_B(\tilde{\theta}) = \frac{1}{4\pi n^2\,(1-\cos\tilde{\theta}_H)} \exp\left[-\frac{(1-\cos\tilde{\theta})}{2n^2\,(1-\cos\tilde{\theta}_H)}\right], \quad n^2 > 0\,, \tag{34}$$

a preferentially forward emission function would look like

$$Q(\theta) = Q_F(\tilde{\theta}) = \frac{1}{4\pi\,|\,n^2\,|\,(1-\cos\tilde{\theta}_H)} \exp\left[\frac{1+\cos\tilde{\theta}}{2n^2\,(1-\cos\tilde{\theta}_H)}\right], \quad n^2 < 0. \tag{35}$$

We will consider both Q_B and Q_F.

Our testing procedure is now as follows. We make the assumption that the two quasars L and N are ejected from M with equal luminosities and that their emission functions satisfy the form given by equation (34) with the same value of n^2. The Hoyle angles for the two quasars are however different, as are their speeds of ejection and redshifts. Their apparent brightness at O will not therefore be the same. Since the apparent magnitudes of all quasars in the four triplets are given we can use them to determine n^2. If the underlying assumptions of high velocity and backward emission are correct, we expect n^2 to be positive and small ($n^2 < 1$). If the quasars are emitting preferentially in the forward direction then n^2 should come out negative and equation (35) should provide the correct fit to the data.

A few kinematic corrections are needed before the emission functions can be compared directly with the data. Strittmatter (1967) has discussed, within the framework of a purely local quasar ejection theory how the flux densities are modified by the relativistic Doppler effect and aberration. His calculation has to be modified to include the effect on the flux densities by the expansion of the universe. The calcul-

ation is straightforward, though somewhat tedious. We quote the answer in the following form.

Suppose the emission function of quasar L in its rest frame has the form

$$f(\tilde{a}_L, \nu) = \mathscr{L} Q(\tilde{a}_L) J(\nu), \tag{36}$$

where $J(\nu)d\nu$ is the fraction of energy emitted in the frequency range $(\nu, \nu + d\nu)$. Thus

$$\int_0^\infty J(\nu)\, d\nu = 1. \tag{37}$$

Then the flux density at O in the frequency range $(\nu_0, \nu_0 + d\nu_0)$ is given by $S_{L,}(\nu_0)\, d\nu_0$ where

$$S_L(\nu_0) = \frac{\mathscr{L}}{r_M^2 S_0^2} Q(\tilde{a}_L) J[\nu_0(1+z_L)] \frac{(1+z_M)^2}{(1+z_L)^3}. \tag{38}$$

Therefore we have

$$\frac{S_L(\nu_0)}{S_N(\nu_0)} = \frac{1-\cos\tilde{a}_{NH}}{1-\cos\tilde{a}_{LH}} \exp\left[\frac{-1}{2n^2}\left\{\frac{1-\cos\tilde{a}_L}{1-\cos\tilde{a}_{LH}} - \frac{1-\cos\tilde{a}_N}{1-\cos\tilde{a}_{NH}}\right\}\right]$$

$$\times \frac{J[\nu_0(1+z_L)]}{J[\nu_0(1+z_N)]} \frac{(1+z_N)^3}{(1+z_L)^3}. \tag{39}$$

To fix ideas we have taken

$$J(\nu) \propto \nu^{-\beta}, \quad 0 \leqslant \beta \leqslant 1 \tag{40}$$

in the relevant frequency of observation. Since the V_{5000} magnitudes of L and N are known from the work of Arp and Hazard for the four triplets, it is now a simple matter to compute n^2 from the formula (40). Table 2 gives the values of n^2 for the three cases $\beta = 0$, $\beta = 0{\cdot}5$ and $\beta = 1$ for each of the four triplets.

Table 2. Emission parameters of quasar triplets I, II, III and IV.

Triplet No.	Observed apparent magnitude			Attenuation parameter n^2		
	M	L	N	$\beta=0$	$\beta=0{\cdot}5$	$\beta=1$
I	17·6	19·4	19·0	0·27	0·23	0·20
II	16·9	19·0	19·9	0·075	0·075	0·07
III	19·5	18·9	18·9	0·16	0·135	0·115
IV	18·9	18·2	18·1	0·17	0·165	0·155

Note that the expectations of the model are borne out in all cases. We have $n^2 > 0$ and $n^2 < 1$. If ballistic, the quasars *are* preferentially emitting backwards within their Hoyle-cones. If we try to fit equation (35) to the data we do not get a similar consistent picture.

If we further assume that the quasar emission mechanism recognizes a universal value of n^2, then we can use the least square method to determine the 'best fit' value of n^2 for all four triplets taken together. Such an analysis assigns different weights to the different triplets depending on residual errors and leads to the value

$$n^2 \simeq 0\,125. \tag{41}$$

Recalling our interpretation of n from the pseudo-Gaussian form in equation (31) we note that the damping at the Hoyle-angle is as at $\sim 3\sigma$ away from the mean of $\sin(\theta/2)$.

It would be interesting to apply the above analysis to any other triplet that might be discovered in future and to see whether n^2 does vary around the value given by equation (41). In what follows we will use the value of 0·125.

5. **The possibility of observing blueshifts**

Since the model holds good so far, it is worth considering its further consequences. The most important of these is whether we are likely to observe any blueshifted quasars. In Section 1 we had mentioned that the original Burbidge-Hoyle ballistic model predicted an embarrassingly large preponderance of blueshifted quasars over the redshifted ones. The possibility of seeing blueshifted quasars can be entirely eliminated in Hoyle's new model by assuming that quasars do not emit at all outside their Hoyle-cone. However, we will consider the emission function of Section 4 in which radiation outside the Hoyle-cone is permitted but with damped intensity.

First we note that if a quasar L has been ejected out of a source M which itself has cosmological redshift z_M, then in order for us to see L as blueshifted, its Doppler blueshift must be larger than the redshift of M. More precisely, from equation (14) we must have

$$\frac{1 + V_L \cos\alpha}{(1 - V_L^2)^{1/2}}(1 + z_M) < 1. \tag{42}$$

In order to be seen blueshifted, L must therefore emit well outside its Hoyle-cone. The exponential damping may therefore render such a quasar too faint to be readily observable.

This raises an interesting possibility. Suppose a case where the factor multiplying $(1 + z_M)$ in the expression (42) is less than unity but not small enough to satisfy the inequality. In this case L may be seen with a redshift smaller than z_M. Now in the case of a triplet, α the direction of ejection could have any value between 0 and π. What is the probability that α lies in a small enough range so that

$$(1 + z_M)^{-1} < \frac{1 + V_L \cos\alpha}{(1 - V_L^2)^{1/2}} < 1\ ? \tag{43}$$

A simple calculation shows the answer to be

$$\rho(Z_M, V_L) = \frac{(1 - V_L^2)^{1/2}}{2V_L}\left[1 - \frac{1}{1 + Z_M}\right]. \tag{44}$$

For the triplet I of Table 1, this value is $\sim$ 1/8. Similarly for quasar *N* of triplet I this value is $\sim$ 4/27. Since the cos α values in, the two ranges do not overlap the total probability that one or the other end quasar will have a lower redshift than the middle quasar is $\sim$ 0·28. However, if the triplet arose out of accidental projection of three quasars on a straight-line the probability that the middle quasar will have a larger redshift than at least one end quasar would be simply 2/3. Thus, provided a large number of photographic plates are examined for such triplets, the distribution of quasar redshifts will provide a test between this theory and the cosmological hypothesis. On the basis of this theory the expected proportion of cases with $z_M > z_L$ or $z_M > z_N$ should be significantly *less* than 2/3.

Since the observation of *net* blueshifts is easier for small z_M, let us first set $z_M = 0$. We are then following Hoyle in considering quasars ejected in our local region of space. Hoyle and Burbidge (1966) had considered sources of quasars lying within a distance of $\lesssim$ 100 Mpc. Arp's claim of observations of anomalous redshifts usually relate to the presence of high redshift quasars near low redshift (NGC) galaxies. Thus setting $z_M = 0$ will give a good approximation of such scenarios.

Suppose from such a source M a quasar L is fired in an arbitrary direction making angle α with the radial direction OM. Let *V* be the speed of the quasar L relative to M, and $\tilde{\alpha}$ denote the angle with the backward direction of motion of L made by the light ray from L to O, as measured in the rest frame of L. α and $\tilde{\alpha}$ are related by the equation

$$\cos\tilde{\alpha} = \frac{\cos\alpha + V}{1 + V\cos\alpha}, \tag{45}$$

and the redshift/blueshift factor 1 + *z* is given by

$$1 + z = \frac{1 + V\cos\alpha}{(1 - V^2)^{1/2}} = \frac{(1 - V^2)^{1/2}}{1 - V\cos\tilde{\alpha}}. \tag{46}$$

For blueshift, $z < 0$. The maximum redshift (z_{max}) is obtained in the case $\alpha = 0$ and the maximum blueshift (z_{min}) in the case $\alpha = \pi$. Let us compare the flux density $S(z)$ for different values of *z*. Thus if we fix *z* we know $\tilde{\alpha}$: from equation (46). Then from equations (38) and (40) we can compute $S(z)$. It is convenient to express $S(z)$ as the fraction of the flux level $S(z_{max})$ corresponding to the maximum redshift. We get

$$\frac{S(z)}{S(z_{max})} = \exp\left[-\frac{(1 - \cos\tilde{\alpha})}{2n^2(1 - \cos\tilde{\alpha}_H)}\right]\frac{(1 + z_{max})^{3+\beta}}{(1 + z)^{3+\beta}}. \tag{47}$$

The above result can be expressed in the form

$$\frac{S(z)}{S(z_{\max})} = \left(\frac{1+z_{\max}}{1+z}\right)^{3+\beta} \exp\left[-\frac{(z_{\max}-z)}{2n^2\, z_{\max}\,(1+z)}\right]. \tag{48}$$

The magnitude difference corresponding to equation (48) is plotted in Fig. 3 against $(1 + z)$, for $z_{\max} = 1, 2, 3$ (*i.e.* for $V = \cdot 6, \cdot 8, \cdot 88$), $\beta = 1$ for a range of values of n^2. It is easy to verify that $S(z)$ has a maximum at $\bar{z}$ given by

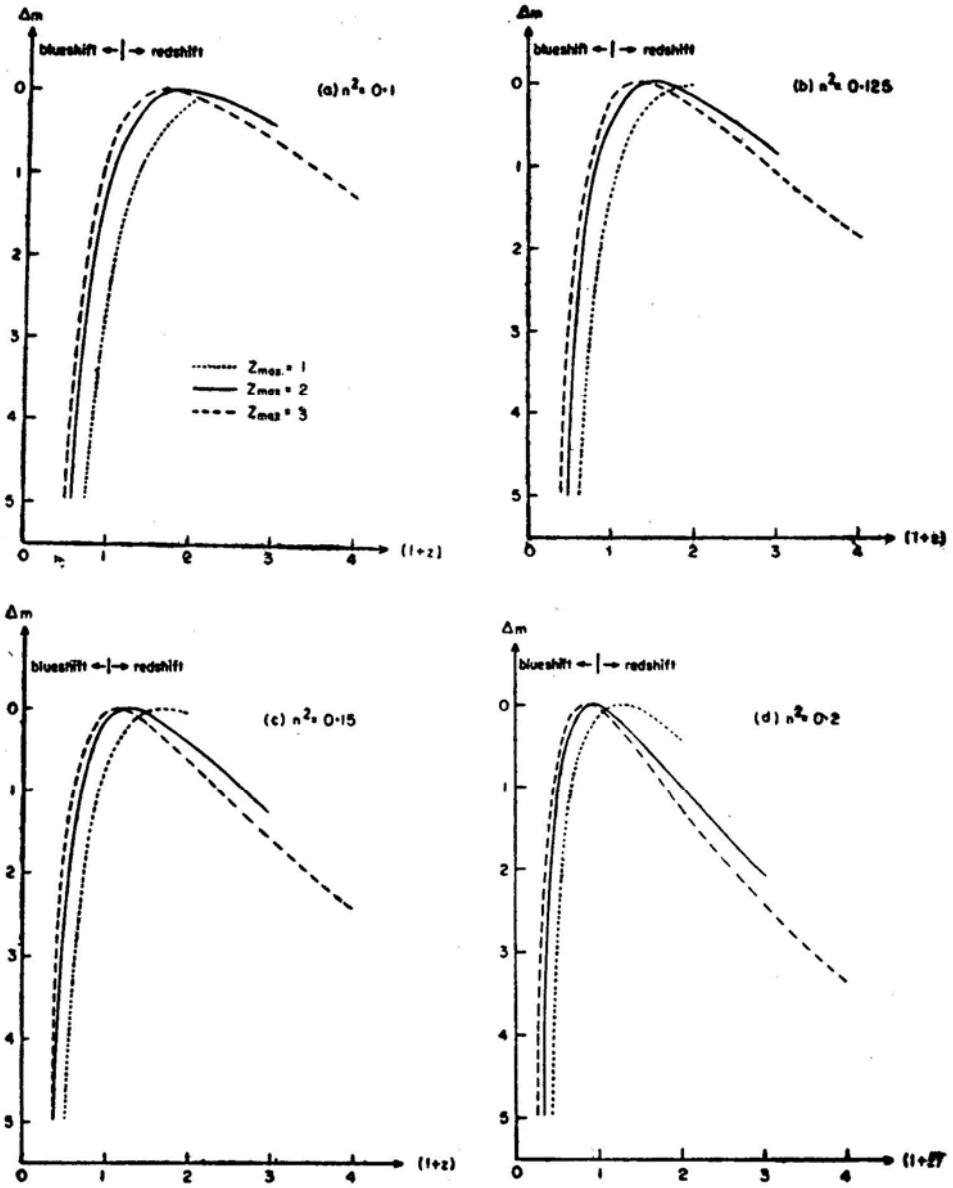

Figure 3. Redshift-apparent magnitude curves for different values of the parameters $z_{\max}$ and n^2. The zero magnitude for each curve is arbitrarily set at the maximum value of $S(z)$.

$$1 + \bar{z} = \frac{1 + z_{\max}}{2n^2 (3 + \beta) z_{\max}}. \tag{49}$$

For $\beta = 1$, the maximum flux is in the blueshift range ($\bar{z} < 0$) if

$$n^2 > \frac{1 + z_{\max}}{8 z_{\max}}.$$

Thus small values of n^2 make it easier to observe redshifted objects than blueshifted ones. For our canonical value of $n^2 = 0{\cdot}125$, and for $z_{\max} = 2$, $\bar{z} = 0{\cdot}5$; *i.e.* redshifted-quasars are generally brighter.

Note further that from equation (48)

$$\frac{S(z_{\max})}{S(\bar{z})} = \left[\frac{e}{2n^2 (3 + \beta) z_{\max}}\right]^{3+\beta} \exp\left[-\frac{1}{2n^2 z_m}\right]. \tag{50}$$

Thus as the ejection speed is increased, the flux level at maximum redshift decreases in relation to the maximum flux level. We have therefore an. effect working against the observation of very large redshift quasars. We will return to this point in our final discussion.

If the quasar L is ejected randomly in any direction with a given velocity V, the probability that z lies in a range dz is

$$P(z) = \frac{dz}{z_{\max} - z_{\min}}, \quad (z_{\min} \leqslant z \leqslant z_{\max}).$$

The probability of observing redshift is, however, higher than this because the life-time of a redshifted quasar is higher in the rest frame of O. The appropriate weighting factor is $(1 + z)$, as was pointed out by Strittmatter (1967).

If we consider Strittmatter's calculation, the ratio of the number of redshifted quasars to the number of blueshifted quasars is now modified to

$$\frac{N_r}{N_b} = \frac{\phi\,[1 + z_{\max}, 1]}{\phi\,[1, 1 + z_{\min}]}, \tag{51}$$

where

$$\phi(z_1, z_2) = \int_{z_2}^{z_1} (1 + z)^{-(3{\cdot}5 + 1{\cdot}5\beta)} \exp\left[-\frac{(z_{\max} - z)}{4n^2 z_{\max} (1 + z)}\right] dz. \tag{52}$$

It is now easy to estimate the ratio N_b/N_r in a given flux limited sample. The ratio is given in Table 3, column 2 for various values of n^2. Table 3 also gives the ratio

Table 3. The ratio of blueshifted to redshifted quasars in a flux-limited quasar sample calculated for ejection speed $V = 0{\cdot}8$.

Attenuation parameter n^2	Maximum redshift of the ejecting source $z = 0$	$z = 0{\cdot}2$	$z = 0{\cdot}5$
0·1	0·008	0·005	0·003
0·125	0·03	0·02	0·01
0·15	0·08	0·04	0·02
0·20	0·27	0·145	0·07
0·25	0·58	0·32	0·15

Notes: (1) Zero redshift corresponds to local ejection of quasars.
(2) The ratios N_b/N_r for redshifts 0·2 and 0·5 have been computed for the Friedmann model with $q_0 = 0$.

N_b/N_r, for our mixed theory in which the ejection centre has a nonzero cosmological redshift z. The values of N_b/N_r given in each column represent those expected in a flux-limited sample with the maximum value of z given at the top of the column. We have used the empty Friedmann model ($q_0 = 0$) for making these estimates.

It is immediately clear that the ratio N_b/N_r is dramatically reduced from the high value of equation (1). Further, the larger the value of z and smaller the value of n^2 the smaller is the value of N_b/N_r. Thus the theory no longer predicts a preponderance of blueshifts.

However, so long as the radiation outside the Hoyle-cone is allowed, the possibility of observing blueshifted quasars exists. The calculations presented here therefore provide a potential test of this theory. The following points may be made.

(a) From equation (42) it is clear that relative blueshifts can be seen in triplets with $z_M > z_L$ or z_N. Arp (personal communication) has reported that he has found one such triplet.

(b) If z is very small say, $z \simeq 0$, then $N_b/N_r \simeq 0{\cdot}03$ for $n^2 = 0{\cdot}125$ (Table 3). Corresponding to a total of $\sim$ 1500 redshifted quasars listed by Hewitt and Burbidge (1980), we should be seeing $\sim$ 45 blueshifted quasars. This number drops to $\sim$ 30 for z=0·2 and to $\sim$ 15 for $z = 0{\cdot}5$. On the other hand all these numbers increase if n^2 increases above the canonical value of 0·125. For example, for $n^2 = 0{\cdot}2$, the number of blueshifted quasars in a purely local theory ($z = 0$) should be as high as $\sim$ 400.

(c) The above estimates in (b) are reduced if we assume that a substantial part of the quasar population has only cosmological redshift. Thus if only a fraction $f(<1)$ of all quasars have large Doppler components then the numbers estimated in (b) must be multiplied by f. Although a small value of f may help in explaining why no blueshifted quasars are found, this alternative is not attractive if the theory is claimed to offer a serious alternative to the cosmological hypothesis.

(d) Although increasing z reduces N_b/N_r, there is a limit on how high z can be. This limit arises from the V/V_m test of radio quasars made by Wills and Lynds (1978). These authors find that the V/V_m test is consistent with an entirely local theory of

quasars ($z = 0$). As z is increased the average value of V/V_m calculated for the quasars in the Wills and Lynds samples rises above 0·5, thus implying evolution. However, for $z \lesssim 0{\cdot}2$ the departure from 0·5 may be statistically insignificant. Taking $z = 0{\cdot}2$ we find from Table 3, $N_b/N_r = 0{\cdot}02$ for $n^2 = 0{\cdot}125$. Thus corresponding to the 226 quasars in Wills and Lynds analysis, we should be seeing ~5 blueshifted quasars.

(e) For calculations of Table 3 the velocity of ejection was taken as $V = 0{\cdot}8$. Larger values of V can lead to larger N_b/N_r. However, if V is large, the maximum redshift observed also increases. In a purely local theory, the least value of V which can generate a redshift of 3·5 is $\sim 0{\cdot}905$. If, however, z can be as high as 0.5, $V \lesssim 0{\cdot}8$. Thus the paucity of redshifts higher than 3·5 sets limits on z and V. We have already seen in equation (50) how the very high redshift quasars become relatively faint and difficult to observe.

(f) Finally we consider the old question again: 'Why are no blueshifts seen?' Although this question can be answered by following Hoyle's hypothesis strictly and permitting no radiation beyond the Hoyle-cone, we find it more attractive to take the more vulnerable option of Section 4**.** Apart from the indirect evidence of the type mentioned in (a) it is tempting to speculate whether some of the lineless objects might not in fact be blueshifted quasars. The BL Lac objects listed in the Hewitt-Burbidge catalogue contain a large fraction for which no spectral lines are known. We end this section with the provocative conjecture that although we have no reason to believe that the line spectrum of blueshifted quasars would be radically different from that of redshifted ones, it remains possible that some of the lineless objects could be blueshifted.

6. Conclusion

Having applied the available data on aligned triplets of quasars to a Doppler theory of quasars we find that a self-consistent solution emerges. In a typical triplet, the middle quasar is assumed to have a wholly cosmological redshift while the end quasars have substantial Doppler redshift components. Hoyle's hypothesis that quasars emit predominantly backwards is quantified by the assumption of an exponential drop off in emission outside the Hoyle-cone. The parameters of the model can be fitted uniquely to the four triplets known.

We have investigated the implications of our model for the detection of blueshifted quasars. Unlike the original Doppler theory of Burbidge and Hoyle, the theory predicts only a small (but nonzero) number. of observable blueshifted quasars. If a Doppler theory is to survive, examples of at least a few of these blueshifted quasars must be found.

Acknowledgement

One of us (J**.** V. N.) thanks the Science Research Council for a Senior Visiting Fellowship and the Department of Applied Mathematics and Astronomy, University College, Cardiff for hospitality which made this work possible. We also thank Sir Fred Hoyle for critical comments.

References

Arp, H. 1966, *Science*, **151**, 1214.
Arp, H., Hazard, C. 1980, *Astrophys. J.*, **240**, 726.
Burbidge, G., Burbidge, M. 1967, *Quasi-Stellar Objects*, Freeman, San Francisco, p. 173.
Edmunds, M. G., George, G. H. 1981, *Nature*, **290**, 481.
Hewitt, A., Burbidge, G. 1980, *Astrophys. Suppl. Ser.*, **43**, 57.
Hoyle, F. 1980, *Preprint.*
Hoyle, F., Burbidge, G. R. 1966, *Astrophys. J.*, **144**, 534.
Narlikar, J. V. 1981, *Preprint.*
Narlikar, J. V., Das, P. K. 1980, *Astrophys. J.*, **240**, 401.
Stockton, A. 1978, *Astrophys. J.*, **223**, 747.
Stockton, A. 1980, in *IAU Symp. 92: Objects of High Redshift*, Eds G. O. Abell and P. J. E. Peebles, D. Reidel, Dordrecht, p. 89.
Strittrnatter, P. 1967 in *Quasi-Stellar Objects*, G. Burbidge and M. Burbidge, Freeman, San Francisco, p. 164.
Terrell, J. 1964, *Science*, **145**, 918.
Wills, D., Lynds, R. 1978, *Astrophys. J. Suppl. Ser.*, **36**, 317.
Wyckoff, S., Wehinger, P. A., Gehren, T., Morton, D. C., Boksenberg, A. Albrecht, R. 1980, *Astrophys. J.*, **242**, 159.

J. Astrophys. Astr. (1981) **2**, 309–313

A Spectroscopic Orbit for HD 115968

R. F. Griffin *The Observatories, Madingley Road, Cambridge, England, CB3 0HA*

Received 1981 June 9; accepted 1981 July 24

Abstract. Photoelectric radial-velocity measurements show that the eighth-magnitude star HD 115968 is a spectroscopic binary with a period of 16·195 days. The star has a large proper motion, and is unlikely to have the luminosity corresponding to the spectral type of G8 III favoured by Zaitseva. It is most probably a late-G dwarf.

Key words: radial velocities—spectroscopic binaries—stars, individual

HD 115968 is an eighth-magnitude late-type star in the constellation Canes Venatici, near the North Galactic Pole. Its position was first determined by Lalande (Delalande 1801; Baily 1847), and its large proper motion, amounting to about 0·41 arcsec per annum in position angle 259°, became apparent during the nineteenth century (Robinson and Dreyer 1886). This led to the object's inclusion in many catalogues· of proper-motion stars as well as in the more general catalogues; in particular, its position was repeatedly measured at Cincinnati. In Table 1 are collected its designations in some of the more important catalogues.

The spectral type of HD 115968 is given in the *Henry Draper Catalogue* (Cannon and Pickering 1920) as K0, and Joy (1947) gives it as dG6. Zaitseva (1973), on the basis of objective-prism spectra at a dispersion of 166 Å mm^{-1} at Hγ, found an MK type (Morgan, Keenan and Kellman 1943) of G8 III. Such a luminosity seems improbable, because at the implied distance modulus of about 7 magnitudes, corresponding to a distance of 250 pc, the transverse velocity required by the proper motion is almost 500 km s^{-1}. The catalogue compiled by Buscombe (1980) of MK classifications includes a type of K0 V and magnitudes of V = 8·00 and (B—V) = 0·69 for HD 115968, but unfortunately (Griffin 1981) it does not give any references. The dwarf luminosity classification is almost certainly correct, but the (B—V) colour corresponds to a main-sequence type of G5 rather than K0. Evidently the last word has not yet been said on the spectral type of HD 115968; but for the moment it appears that the type of dG6 suggested by Joy is as likely as any, and is moreover in excellent accord with the parallax of 0·025 ± 0·007 arcsec given in the *General Catalogue of Stellar Parallaxes* (Schlesinger 1935).

Table 1. Aliases for HD 115968.

Catalogue	Number	Reference	Date
Lalande	24760-1	Baily	1847
Bonner Durchmusterung	38°2431	Argelander	1861
Second Armagh Catalogue	1554	Robinson and Dreyer	1886
Cincinnati 12	765	Porter	1892
Cincinnati 13	1173	Porter	1895
A. G., 35°–40° zone	5733	Dunér, Engström and Psilander	1902
Cincinnati 18	1720	Porter, Yowell and Smith	1916, 1918
Cincinnati 19	2520	Smith and Porter	1922
Cincinnati 20	772	Porter, Yowell and Smith	1930
Albany Catalogue	10967	Boss, Roy and Varnum	1931
Second Greenwich Catalogue	5360	Dyson	1935
Parallax Catalogue	4007	Schlesinger	1935
Eigenbewegungs-Lexicon	38°2431	Schorr	1936
General Catalogue	18040	Boss	1937
Cincinnati 22	1218	Smith and Herget	1946
Radial Velocity Catalogue	7926	Wilson	1953
AGK 2	38°1259	Schorr and Kohlschütter	1953
Luyten	LTT 13873	Luyten	1961
SAO Catalogue	63483	Smithsonian.....	1966
Lowell Proper Motion Survey	G164-067	Giclas, Burnham and Thomas	1971
North Galactic Pole Catalogue	38°209	Zaitseva	1973
AGK 3	38°1259	Heckmann and Dieckvoss	1975

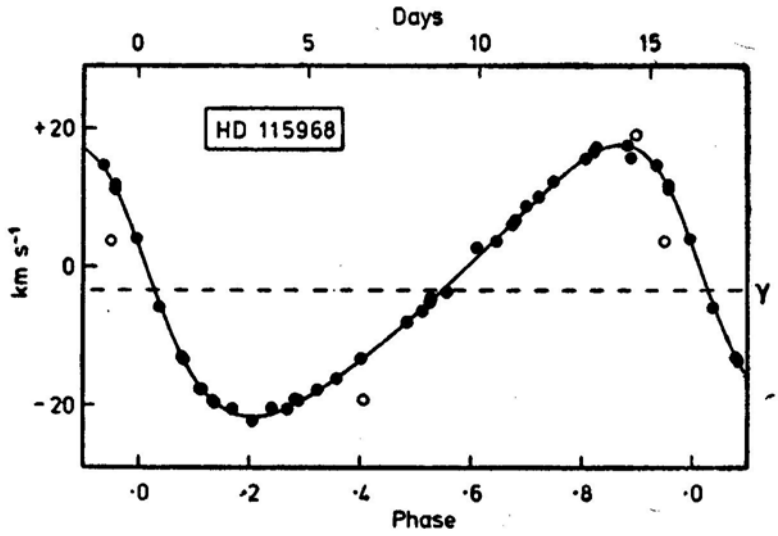

Figure 1. The computed radial-velocity curve (full line) for HD 115968. The photoelectric observations are plotted as filled circles, the Mount Wilson photographic ones as open circles.

Table 2. Photoelectric radial-velocity measurements of HD 115968.

Date			MJD	Velocity km s^{-1}	Phase	$(O-C)$ km s^{-1}
1968	Apr	11·07	39957·07	−19·7	0·138	−0·1
1976	July	2·96	42961·96	+6·7:	185·680	0·0
1977	Jan	30·18	43173·18	+10·0	198·723	0·0
	Mar	30·06	232·06	−16·2	202·358	−0·2
	Apr	26·98	259·98	−13·5	204·082	+0·1
	May	27·98	290·98	+4·0	205·996	+0·3
1978	Jan	23·18	43531·18	+17·3	220·828	+0·6
	Mar	24·09	591·09	−5·1	224·527	−0·2
		26·03	593·03	+3·7	·647	−0·4
		31·05	598·05	+11·0	·957	−0·2
	Apr	15·06	613·06	+17·5	225·884	0·0
	May	23·24*	651·24	−20·5	228·241	+0·5
	June	18·95	677·95	+15·8	229·891	−1·5
	Nov	16·25	828·25	−20·6	239·171	+0·5
1979	Jan	3·26	43876·26	−19·5	242·136	0·0
		13·22	886·22	+12·3	·751	+0·2
	Feb	25·17	929·17	−13·2	245·403	+0·2
	Mar	8·12	940·12	−13·1	246·079	−0·1
		12·09	944·09	−17·8	·324	+0·1
		22·01	954·01	+14·6	·936	+0·5
	Apr	25·04	988·04	−5·9	249·038	−0·6
		29·04	992·04	−19·2	·285	+0·4
	May	3·01	996·01	−4·6	·530	+0·1
		9·94	44002·94	+11·8	·958	+0·7
		13·98	006·98	−22·3	250·207	−0·8
		14·99	007·99	−20·6	·270	−0·4
		18·94	011·94	−6·3	·513	−0·4
		21·99	014·99	+8·7	·702	+0·3
		23·96	016·96	+16·6	·823	+0·1
	June	22·95	046·95	+6·1	252·675	−0·2
	Dec	25·25	232·25	−17·7	264·117	+0·2
		31·22	238·22	−7·9	·485	0·0
1980	Jan	2·27	44240·27	+2·7	264·612	+1·3
		13·26	251·26	−19·3	265·291	+0·1
	May	9·94	368·94	−3·7	272·557	−1·0
		14·02	373·02	+15·6	·809	−0·2
		18·94	377·94	−17·6	273·113	−0·1

*Observed, in collaboration with Dr J. E. Gunn, with the 200-inch telescope (Griffinand Gunn 1974).

Joy (1947) obtained three radial-velocity measurements of HD 115968 from the same 36 Å mm^{-1} Mount Wilson spectrograms that he used to classify it, and he showed it to be a spectroscopic binary. The three velocities were subsequently published individually by Abt (1973). In the course of radial-velocity observations in the North Galactic Pole field, the star came under observation with the photoelectric spectrometer at Cambridge (Griffin 1967) several years ago, and its binary nature was confirmed. The 37 photoelectric observations now available are listed in Table 2, and yield the orbit plotted in Fig. 1 and having the following elements:

$P = 16{\cdot}1952 \pm 0{\cdot}0004$ days	$(T)_{234} = \text{MJD } 43760{\cdot}70 \pm 0{\cdot}06$
$\gamma = -3{\cdot}30 \pm 0{\cdot}09$ km s^{-1}	$a_1 \sin i = 4{\cdot}19 \pm 0{\cdot}03$ Gm
$K = 19{\cdot}58 \pm 0{\cdot}13$ km s^{-1}	$f(m) = 0{\cdot}0112 \pm 0{\cdot}0002\ M_\odot$
$e = 0{\cdot}274 \pm 0{\cdot}006$	
$\omega = 75{\cdot}4 \pm 1{\cdot}5$ degrees	rms residual $= 0{\cdot}5$ km s^{-1}

The Mount Wilson velocities were not taken into account in the orbital solution; they are, however, plotted in Fig. 1, where they are seen to be in fully satisfactory agreement with the computed orbit.

The secondary star is not apparent in the radial-velocity traces; it is likely to be a main-sequence star much fainter than the primary.

References

Abt, H. A. 1973, *Astrophys. J. Suppl. Ser.*, **26**, 365.

Argelander, F. W. A. 1861, *Astronomische Beobachtungen,* Adolph Marcus, Bonn, **4**, 317.

Baily, F. 1847, *A Catalogue of Those Stars in the Histoire Celeste Francaise.....*, R. Taylor and J. E. Taylor, London, pp. 619, 620.

Boss, B. 1937, *General Catalogue of 33342 Stars for the Epoch 1950,* Carnegie Institution of Washington, **4**, 64.

Boss, B., Roy, A. J., Varnum, W. B. 1931, *Albany Catalogue of 20811 Stars for the Epoch 1910,* Carnegie Institution of Washington, p. 220.

Buscombe, W. 1980, *Fourth General Catalogue of MK Spectral Classifications,* Northwestern University, Evanston.

Cannon, A. J., Pickering, E. C. 1920, *Ann. Harv. Coll. Obs.*, **95**, 126.

Delalande, J. 1801, *Histoire Celeste Francaise,* Imprimerie de la Republique, Paris, pp. 58, 339.

Dunér, N. C., Engström, F., Psilander, A. A. 1902, *Catalog von 11446 Sternen,* Engelmann, Leipzig, p. 116.

Dyson, F. 1935, *Second Greenwich Catalogue of Stars for 1925.0,* HMSO, London, p. 153.

Giclas, H. L., Burnham, R., Jr., Thomas, N. G. 1971, *Lowell Proper Motion Survey,* Lowell Observatory, Flagstaff, p. 74.

Griffin, R. F. 1967, *Astrophys. J.*, **148**, 465.

Griffin, R. F. 1981, *J. Brit. astr. Assoc.*, **91**, 297.

Griffin, R. F., Gunn, J. E. 1974, *Astrophys. J.*, **191**, 545.

Heckmann, O., Dieckvoss, W. 1975, *AGK3,* Hamburger Sternwarte, Hamburg-Bergedorf, **4**, 59.

Joy, A. H. 1947, *Astrophys. J.*, **105**, 96.

Luyten, W. J. 1961, *A Catalogue of 7127 Stars in the Northern Hemisphere with Proper Motions Exceeding 0″.2 Annually,* Lund Press, Minneapolis.

Morgan, W. W., Keenan, P. C., Kellman, E. 1943, *An Atlas of Stellar Spectra with an Outline of Spectral Classification,* University of Chicago Press.

Porter, J. G. 1892, *Cincinnati Publ.*, No. 12, pp. 133, 243.

Porter, J. G. 1895, *Cincinnati Publ.*, No. 13, 35.

Porter, J. G., Yowell, E. I., Smith, E. 1916, *Cincinnati Publ*, No. 18, Part II, 88.
Porter, J. G., Yowell, E. I., Smith, E. 1918, *Cincinnati Publ*, No. 18, Part IV, 33.
Porter, J. G., Yowell, E. I., Smith, E. S. 1930, *Cincinnati Publ.*, No. 20, 18.
Robinson, T. R., Dreyer, J. L. E. 1886, *Second Armagh Catalogue of 3300 Stars for the Epoch 1875*, Thom, Dublin, p. 70.
Schlesinger, F. 1935, *General Catalogue of Stellar Parallaxes*, Yale University Observatory, New Haven, p. 74.
Schorr, R. 1936, *Bergedorfer Eigenbewegungs-Lexicon*, 2 ed-n, Hamburger Sternwarte, Bergedorf, **1**, 126.
Schorr, R., Kohlschütter, A. 1953, *Zweiter Katalog der Astronomischen Gesellschaft*, Hamburger Sternwarte, Bonn, **7**, 181.
Smith, E. S., Herget, P. 1946, *Cincinnati Publ.*, No. 22, 25.
Smith, E., Porter, J. G. 1922, *Cincinnati Publ.*, No. 19, 57.
Smithsonian Astrophysical Observatory Star Catalog, 1966, Smithsonian Institution, Washington, Part 1.
Wilson, R. E. 1953, *General Catalogue of Stellar Radial Velocities*, Carnegie Institution of Washington, p. 159.
Zaitseva, E. I. 1973, *Abastumani Bull*, No. 44, 55.

J. Astrophys. Astr. (1981) **2**, 315–337

A New Look at Pulsar Statistics—Birthrate and Evidence for Injection

M. Vivekanand and R. Narayan *Raman Research Institute, Bangalore 560080*

Received 1981 July 3; accepted 1981 September 30

Abstract. We make a statistical analysis of the periods P and period-derivatives $\dot{P}$ of pulsars using a model independent theory of pulsar flow in the P–$\dot{P}$ diagram. Using the available sample of P and $\dot{P}$ values, we estimate the current of pulsars flowing unidirectionally along the P-axis, which is related to the pulsar birthrate. Because of radio luminosity selection effects, the observed pulsar sample is biased towards low P and high $\dot{P}$. We allow for this by weighting each pulsar by a suitable scale factor. We obtain the number of pulsars in our galaxy to be $6.05^{+3\,32}_{-2\,80} \times 10^5$ and the birthrate to be $0{\cdot}048^{+0\,014}_{-0\,011}$ pulsars yr^{-1} galaxy^{-1}. The quoted errors refer to 95 per cent confidence limits corresponding to fluctuations arising from sampling, but make no allowance for other systematic and random errors which could be substantial. The birthrate estimated here is consistent with the supernova rate. We further conclude that a large majority of pulsars make their first appearance at periods greater than 0·5 s. This 'injection', which runs counter to present thinking, is probably connected with the physics of pulsar radio emission. Using a variant of our theory, where we compute the current as a function of pulsar 'age' ($\frac{1}{2}P/\dot{P}$), we find support for the dipole braking model of pulsar evolution upto 6×10^6 yr of age. We estimate the mean pulsar braking index to be $3.7^{+0\,8}_{-0\,8}$.

Key words: pulsar statistics—birthrate—injection

1. Introduction

Neutron stars are widely believed to be born in supernova explosions (Baade and Zwicky 1934). The matter in the envelope of the star forms the expanding supernova remnant (SNR) while the core of the progenitor star is compressed into the

highly magnetised and rapidly rotating neutron star which, is believed to manifest itself as a pulsar (Gold 1968). If the above scenario is true, one expects to find a strong association between pulsars on the one hand and Supernovae and SNRs on the other. However, observations have failed to bring this out. On the contrary, there seem to be two important discrepancies:

(a) The birthrates of pulsars and Supernovae in the galaxy are apparently in disagreement. Pulsars are believed to be born once every six to eight years (Taylor and Manchester 1977; Phinney and Blandford 1981). On the other hand, estimates of the birthrate of Supernovae, while varying over a wide range of values (Ilovaisky and Lequeux 1972; Tammann 1974; Clark and Caswell 1976), seem to be converging to one supernova every thirty years (Clark and Stephenson 1977; Srinivasan and Dwarakanath 1981).

(b) Among the 300 or more pulsars and 120 SNRs known, positional associations have been reliably established only in two cases (the Crab and Vela pulsars).

In this paper, the main thrust of our calculations is towards obtaining a more reliable pulsar birthrate. Usually, the birthrate of pulsars is computed by the simple argument that, in steady state conditions, the total number of pulsars $\mathcal{N}$ in our galaxy should be equal to the birthrate B multiplied by the mean lifetime of pulsars τ_m. $\mathcal{N}$ is obtained by using the inferred space density of potentially observable pulsars in our galaxy, and multiplying it by a 'beaming-factor' K which accounts for those pulsars which are not beamed towards the earth. It is believed (Taylor and Manchester 1977) that $\mathcal{N} \simeq 5 \times 10^5$ pulsars. By assuming the dipole model for pulsar braking (Ostriker and Gunn 1969), τ_m can be estimated through the relation $\tau = \frac{1}{2} P/\dot{P}$ where τ is the present age of a pulsar, P is its period and $\dot{P}$ is its (dimensionless) period derivative. Alternatively, τ_m can also be estimated by dividing the mean height $\langle z \rangle$ of pulsars above the galactic plane by their mean z–velocity $\langle V_z \rangle$ ($\langle V_z \rangle$ can be obtained indirectly from the proper motions which have been measured for a few pulsars). This 'kinematic' age has the advantage of being independent of errors in pulsar distances. By using a combination of both values of τ_m, Taylor and Manchester (1977) computed a birthrate of one pulsar every six years in our galaxy.

In this paper, we have adopted an entirely different approach to the birthrate calculation. We use the concept of pulsar current in the P–$\dot{P}$ diagram which has been recently introduced by Phinney and Blandford (1981) and Narayan and Vivekanand (1981). We show that the birthrate can be related to the component of current J_P parallel to the P axis. J_P can be estimated from pulsar data *independently of any model of pulsar evolution.* This is a powerful advantage in our calculations since, as mentioned above, previous attempts usually require postulating the dipole model for pulsar braking. The second new feature in our analysis is that we have treated luminosity selection effects in detail. All earlier calculations assumed that selection effects could be handled with a single scale factor from the observed pulsars to the total population in the galaxy. However, it is known (Lyne, Ritchings and Smith 1975) that the luminosities L of pulsars are correlated with P and $\dot{P}$ (hence τ also). Consequently, the necessary scale factor differs from one pulsar to the other (Taylor 1981, personal communication). We have carried out this more detailed analysis and find that it makes a significant difference to the answers. We now obtain a mean pulsar birthrate of one pulsar every 21 years which is in comfortable agreement with current estimates of supernova explosion rates.

The paper is divided into two parts (Sections 2 and 3). In Section 2, our analysis is model free and we make very few approximations. The numbers we obtain from these calculations are therefore unbiased. Unfortunately, in the process, we lose in Statistical significance (as anticipated by Phinney and Blandford 1981) and the expected errors on the estimated quantities are very large. A preliminary version of these results was recently published (Narayan and Vivekanand 1981).

Section 3 deals with an 'improved' analysis whose main attempt is to reduce the statistical errors. This we have achieved by modelling the dependence of radio luminosity upon P and $\dot{P}$ by the following functional form (first used by Lyne, Ritchings and Smith 1975)

$$L'(P, \dot{P}) \propto P^{\alpha} \dot{P}^{\beta} \tag{1}$$

where L' is the 'mean' luminosity of pulsars of a given P and $\dot{P}$. By making certain further approximations, which are discussed in Section 3.2, we have computed the scaling factor as a function of P and $\dot{P}$ alone. Using a fairly stringent statistical test, we have verified that equation (1) and the approximations made are a fair and unbiased representation of the data. Furthermore, the pulsar birthrate we compute with the new scales is statistically consistent with the result in Section 2, thus increasing our confidence in the new results. As anticipated, there is a significant improvement in the confidence limits of our results, the error bars being reduced by more than a factor of three.

The results of Section 3 are sufficiently accurate to enable us to investigate in coarse detail the variation of J_P s a function of P. Surprisingly, we find that J_P is quite low at small values of P and picks up significantly at $P > 0{\cdot}5$ s. The startling implication of this is that a number of pulsars are 'born' in the P–$\dot{P}$ diagram with fairly large periods. This is totally contrary to the current belief that most neutron stars, and therefore pulsars, are born with periods of the order of a few milliseconds. We therefore conclude that although neutron stars may be born with very short periods (which seems to be suggested by angular momentum considerations), many of them probably turn on as pulsars only somewhat later in their life. Apart from explaining the 'injection' of pulsars at higher periods, this suggestion would also naturally account for the lack of many pulsar-SNR associations, which is the second discrepancy mentioned earlier. Of course, we also need to assume that neutron stars cool quickly after birth to explain the lack of X-ray emission from the (hot) surface.

Lastly, we have computed an average value for the 'braking-index' n. By comparing J_P with the current J_T parallel to τ, we estimate the braking index to be $n \simeq 3.7^{+0\,8}_{-0\,8}$. This result, which is not inconsistent with the dipole model for pulsar braking ($n = 3$), is important because all earlier studies on pulsar evolution have neglected selection effects as well as pulsar injection and could therefore be seriously in error.

2. Model-free approach

2.1 *Introduction*

In this section we present the basic theory of pulsar current J_P parallel to the P-axis and its connection with pulsar birthrate. We introduce the scale factor $S(L)$, which

gives the ratio of all potentially observable pulsars of luminosity L in the galaxy to those observed, and describe how it is computed. We apply the theory to the P, $\dot{P}$ and L data of 210 pulsars (Although more than 300 pulsars have been detected so far, we have 'pruned' the data to 210 pulsars for reasons that are given later). Using the theory, we estimate the number of pulsars in our galaxy and also make a model-independent estimation of pulsar birthrate. Finally, we calculate the current J_τ parallel to τ and find that the dipole model for pulsar braking is a reasonable description of 'young' pulsars.

2.2 *Theory of Pulsar Current*

We make the following two postulates:

(a) The distribution of pulsars in the Galaxy is in a steady state. This is reasonable since the lifetimes of pulsars, believed to be a few million years, are much smaller than the lifetime of our galaxy.

(b) The period of a pulsar always increases with age. In support of this is the fact that every observed $\dot{P}$ is positive.

Let $\rho(P, \dot{P}, L)\, dP\, d\dot{P}\, dL$ be the number of pulsars in our galaxy in the period range P to $P + dP$, period derivative range $\dot{P}$ to $\dot{P} + d\dot{P}$, and radio luminosity range L *to* $L + dL$. Since $\dot{P}$ is the component of pulsar 'velocity' parallel to the P-axis, the 'current' of pulsars (number per unit time) at any P moving from lower values of P to higher values is evidently given by

$$J_P(P) = \int\int \rho(P, \dot{P}, L)\dot{P}d\dot{P}dL \ \text{ pulsars s}^{-1}\ \text{galaxy}^{-1}. \tag{2}$$

It turns out that the statistics are too poor for us to compute the function J_P with any reliability from the available data. Hence we consider an average of J_P over a range of period from $P_{\min}$ to $P_{\max}$

$$\bar{J}_P\,(P_{\min}, P_{\max}) = \frac{1}{(P_{\max} - P_{\min})} \int_{P_{\min}}^{P_{\max}} J_P(P)\, dP\,. \tag{3}$$

Fig, 1 illustrates the relation between J_P and B, the birthrate of pulsars. Since all $\dot{P}$ are positive, the continuity equation implies that J_P (P) is identically equal to the total birthrate of pulsars in the period range 0 to P, minus the death rate in the same

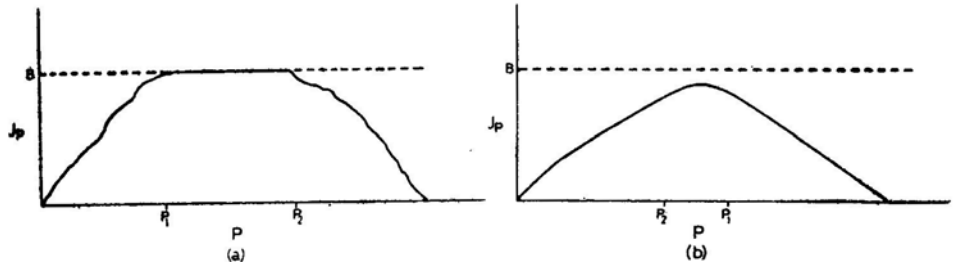

Figure 1. Qualitative plot of pulsar current J_P against period P. B *is* the total birthrate of pulsars. All births occur for $0 < P < P_1$ while all deaths occur for $P > P_2$. (*a*) $P_2 > P_1$; (*b*) $P_2 > P_1$.

range. Let all births occur between 0 and P_1 and all deaths occur beyond P_2. If, as in Fig. 1(a), $P_2 > P_1$, then there is a plateau in J_P between P_1 and P_2 where the function is equal to the total birthrate B. However, if there is an overlap of births and deaths as in Fig. 1 (b) (*i.e.* $P_2 < P_1$), then J_P is less than B at all P. By the above arguments, it is clear that $\bar{J}_P$ ($P_{\min}$, $P_{\max}$) defined in equation (3) is always a lower bound on B whatever $P_{\min}$ and $P_{\max}$ we may choose. In practice, we closely examine the noisy J_P calculated from experimental data and compute $\bar{J}_p$ for values of $P_{\min}$ and $P_{\max}$ selected at the two edges of the apparent plateau. It is then reasonable to expect that the value of $\bar{J}_P$ so obtained is a close estimate of B itself and not just a lower bound.

The total pulsar density $\rho(P, \dot{P}, L)$ is not directly available. It is related to the observed density function $\rho_0 (P, \dot{P}, L)$ by two factors:

(a) There is a 'beaming-factor' K which arises because many pulsars may not be beamed towards us. K *is* generally assumed to be 5 (Taylor and Manchester 1977).

(b) There is a scale factor $S(L)$ which arises because pulsars of a given L can be detected only upto a certain maximum distance by the instruments currently available. $S(L)$ also allows for those parts of the sky which have not been searched by the various surveys. We discuss $S(L)$ in further detail in the next section.

Therefore,

$$\rho(P, \dot{P}, L) = K\, S(L)\, \rho_0\, (P, \dot{P}, L). \tag{4}$$

The observed density function $\rho_0(P, \dot{P}, L)$ is not known as a continuous function. Instead we have P, $\dot{P}$ and L values for N pulsars. We therefore approximate equation (4) by the following expression

$$\rho(P, \dot{P}, L) \simeq \sum_{i=1}^{N} KS(L_i)\, \delta\, (P - P_i)\, \delta\, (\dot{P} - \dot{P}_i)\, \delta\, (L - L_i) \tag{5}$$

where $\delta\,(x)$ is the Dirac delta function at $x = 0$. We may point out that $\bar{J}_P$ is evaluated as an integral over P, $\dot{P}$ and L and therefore the δ-functions in equation (5) are always integrated out in the quantities of interest to us. Substituting equation (5) in equation (3), we obtain an estimate of $\bar{J}_P$ in the form

$$\bar{J}_{P,\,\mathrm{est}}\,(P_{\min}, P_{\max}) = \frac{K}{(P_{\max} - P_{\min})} \sum_{i=1}^{N} S(L_i)\, \dot{P}_i, \quad P_{\min} \leqslant P_i \leqslant P_{\max}\,. \tag{6}$$

In Appendix A, we have shown that the variance of this estimator is

$$\sigma_J^2 = \frac{K^2}{(P_{\max} - P_{\min})^2} \sum_{i=1}^{N} S^2\,(L_i)\, \dot{P}_i^2, \quad P_{\min} \leqslant P_i \leqslant P_{\max}\,. \tag{7}$$

Equation (7) allows for errors arising from fluctuations in the observed sample but does not take into account possible errors in K and $S(L_i)$.

As mentioned before, $\bar{J}_{P,\,\mathrm{est}}$ would be an unbiased estimator of the birthrate B if $P_{\min}$ and $P_{\max}$ correspond to the true plateau region of J_P and if the birth and death domains are non-overlapping as in Fig. 1(a). If not, $\bar{J}_{P,\,\mathrm{est}}$ is, in any case, an estimator of a rigorous lower bound on B.

Before closing this section, we briefly discuss the convergence of the integral in equation (2). Phinney and Blandford (1981) claim (i) that the observed distribution of pulsars is free of selection effects (*i.e.* in our notation, $\rho(P, \dot{P}, L) \equiv K \langle S \rangle \rho_0(P, \dot{P}, L)$ where $\langle S \rangle$ is a constant scale for all pulsars), (ii). that at large $\dot{P}$, $\rho_0(P, \dot{P}) \propto \dot{P}^{-1/2}$, (iii) that therefore the integral in equation (2) is divergent. On these grounds they expect 'kinematic approaches' such as ours to be 'doomed to failure' and have instead attempted a 'dynamical approach'. We, however, find a systematic variation of L over the P–$\dot{P}$ plane (see Section 3.2). Therefore our scale factors $S(L)$ are a necessary and important input for the evaluation of the integral in equation (2). Very roughly, $S(L)$ is seen to vary as $\dot{P}^{-1/2}$. While this anticorrelation of $S(L)$ with $\dot{P}$ does not remove the apparent divergence noted by Phinney and Blandford (1981), it certainly improves matters. Moreover, we show in Section 3.4 that there is a cut-off value of $\dot{P}$ above which pulsars apparently do not function. Such a cut-off will obviously cure all divergence problems. Finally, in the event that there really is a long tail in the distribution of pulsars at high values of $\dot{P}$, we are left with the implication that there are many unseen pulsars in the top region of the P–$\dot{P}$ diagram. If so, all forms of analysis including the dynamical approach are bound to be incomplete.

2.3 *Scale Factors*

We have computed the scale factors, $S(L)$, using the parameters of the three major pulsar surveys *viz.* the Jodrell Bank survey (Davies, Lyne and Seiradakis 1972,1973), the Arecibo survey (Hulse and Taylor 1974, 1975) and the II Molonglo survey (Manchester *et al.* 1978). We used the following equation for $S(L)$

$$S(L) = \frac{\int\int\int \rho_{R_g}(R_g)\, \rho_z(z)\, R_g\, dR_g\, d\theta\, dz}{\int\int\int \rho_{R_g}(R_g)\, \rho_z(z)\, \eta(L, R_g, \theta, z)\, R_g\, dR_g\, d\theta\, dz} \tag{8}$$

where ρ_{R_g} describes the variation of pulsar density with galactocentric radius R_g and ρ_z describes the density as a function of height z above the galactic plane, θ is the polar angle defined with respect to the galactic centre. The parameter $\eta(L, R_{g,}, \theta, z)$ is set to the value 1 if a pulsar of luminosity L at coordinates R_g, θ, z can be detected by any of the three surveys. Otherwise, it is set to zero. Therefore, the denominator of equation (8) is proportional to the number of pulsars of radio luminosity L which can be detected by the three reference surveys while the numerator is proportional to all potentially observable pulsars in the galaxy with luminosity L. In computing $S(L)$ through equation (8), we have adopted an exponential form for ρ_z with a scale height of 350 pc (Manchester 1979). For ρ_{R_g}, we have fitted the experimental histo

gram of number of pulsars against R_g given by Manchester (1979) to obtain the following gaussian form

$$\rho_{R_g}(R_g) \propto \exp\,[-(R_g/10{\cdot}9)^2], \tag{9}$$

where R_g is measured in kpc. It is interesting that the scale length of 10·9 kpc is close to the radial distance of the sun from the galactic centre. This illustrates the well-known fact that the density of pulsars falls off rapidly with galactocentric radius in the solar neighbourhood. The function (9) is probably incorrect in the range $0 \leqslant R_g \leqslant 4$ kpc where observations seem to suggest a deficit of pulsars. However, this region is only about 10 per cent of the volume of the galaxy and can cause a systematic error of at most 20 per cent in our calculations.

$S(L)$ was calculated at a number of selected values of L using a Monte Carlo method to evaluate the integrals in equation (8). The luminosities of the observed pulsars were calculated from their radio fluxes and estimated distances. Following the convention of Taylor and Manchester (1977), we have evaluated L in units of mJy kpc^2. Distances were calculated from the observed dispersion measures, assuming the interstellar electron density n_e in the plane of the galaxy to be 0·03 cm^{-3} and taking a scale height of 1 kpc for decay of n_e in the z direction (Taylor and Manchester 1977). We have corrected for intervening H II regions using a modification of the Prentice and ter Haar (1969) correction, which is discussed in Appendix B. For some pulsars, independent estimates of distance are available (Manchester and Taylor 1977), and these have been adopted in preference to the distances derived from the dispersion measure.

Out of the total of 302 pulsars detected, we have selected a 'pruned' list of 210 pulsars so as to obtain a uniform sample of pulsars consistent with the scale factors $S(L)$. The pruning was done on the basis of two criteria:

(a) The pruned list should contain only those pulsars which were detected by the three reference surveys. This precaution is necessary since we have computed $S(L)$ using only these three surveys.

(b) In computing $S(L)$ we have used the published parameters (such as sensitivity, sky coverage *etc.*) of the three surveys. Since the data base should also be consistent with these parameters, we have omitted those pulsars whose radio fluxes were below the quoted minimum flux detection levels of the surveys. At this stage, it would have been ideal to take into account the intrinsic intensity variations displayed by many pulsars. This would further affect the observability of pulsars by the three surveys, thereby affecting the computation of $S(L)$. However, this would require detailed information such as the phase of the intensity variation of each pulsar at the time of search. For lack of information, we have chosen to ignore this complication.

After pruning, we were left with 210 pulsars, of which we knew the $\dot{P}$ values of 185 pulsars and L values of 207 pulsars. Individual scale factors $S(L)$ were then computed for all the pulsars with known L values by suitably interpolating in the table of $S(L)$ values which we had calculated earlier.

2.4 *Number of Pulsars in the Galaxy*

The total number of pulsars in the galaxy is given by

$$\mathcal{N} = \iiint \rho(P, \dot{P}, L)\, dP\, d\dot{P}\, dL \tag{10}$$

which can be written in terms of the observed ρ_0 as

$$\mathcal{N} = K \iiint S(L)\, \rho_0(P, \dot{P}, L)\, dP\, d\dot{P}\, dL\,. \tag{11}$$

Using equation (5) for ρ_0, we obtain the following estimate for $\mathcal{N}$.

$$\mathcal{N}_{\rm est} = K \sum_{i=1}^{N} S(L_i). \tag{12}$$

The standard deviation $\sigma_{\mathcal{N}}$ of $\mathcal{N}_{\rm est}$ can be shown to be given by (Appendix A)

$$\sigma^2_{\mathcal{N}} = K^2 \sum_{i=1}^{N} S^2(L_i). \tag{13}$$

Using the data on 210 pulsars, we obtain $\mathcal{N}_{\rm est}$ to be 6·05 (± 1·88) × 10^5 pulsars. Now, the error limits specified by $\pm\,\sigma_{\mathcal{N}}$, $\pm\,2\sigma_{\mathcal{N}}$, *etc.*, have well defined meanings only if the distribution of $\mathcal{N}_{\rm est}$ is gaussian. This is not so in the present case because $S(L)$ is spread over five orders of magnitude. The bulk of $\mathcal{N}_{\rm est}$ in equation (12) is actually contributed by only a few of the highest values of $S(L)$. We can therefore expect the distribution of $\mathcal{N}_{\rm est}$ to be highly asymmetric and non gaussian. Consequently, a more meaningful concept in the present case is the confidence limit. We have derived the following upper and lower bounds on $\mathcal{N}_{\rm est}$ at a 95 per cent confidence level (the method of calculating these confidence limits is briefly given in Appendix C).

$$\mathcal{N}_{\rm est}\,|\,95\text{ per cent, lower} = 3{\cdot}19 \times 105 \text{ pulsars}, \tag{14}$$

$$\mathcal{N}_{\rm est}\,|\,95\text{ per cent. upper} = 9.{\cdot}37 \times 10^5 \text{ pulsars}. \tag{15}$$

The limits in equations (14) and (15) are formal estimates of fluctuations arising from the Poissonian nature of the observed sample of pulsars. In addition, there could be significant errors in $S(L_i)$, arising from uncertainties in the distances of pulsars (n_e is not known reliably) and in K. It should be remembered that these unestimated errors could be comparable to if not larger than the formal errors quoted here and in all subsequent sections of the paper. Arnett and Lerche (1981) have, in fact, concluded that the uncertainties in K and n_e are so large and certain other details, not relevant in our analysis, are so poorly understood that any statistical analysis of pulsar data is meaningless. We take a more optimistic view.

Our results for $\mathcal{N}$ are in good agreement with the currently accepted value (Taylor and Manchester 1977) of $\mathcal{N} \simeq 5 \times 10^5$. This is an independent check on our analysis and, in particular, on our values of $S(L)$.

2.5 *Pulsar Birthrate*

We estimate the birthrate by the 'plateau-value' of $\bar{J}_{P,\,\rm est}\,(P_{\rm min}, P_{\rm max})$ as described in Section 2.2. Fig. 2 shows the values of $\bar{J}_{P,\,\rm est}$ in various 0·5 s bins of period. The

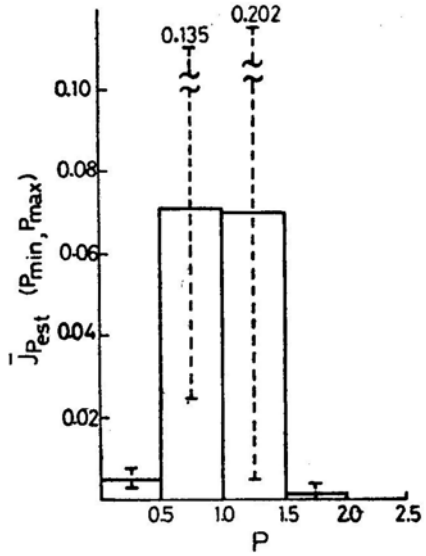

Figure 2. Plot of estimated mean pulsar current $\bar{J}_{P,\,\mathrm{est}}$ against period P. Error limits are specified at a 95 per cent confidence level. J_P has been averaged over period intervals of 0·5 s. However, the qualitative nature of the histogram remains unchanged under finer binning in period. Scale values $S(L)$ (derived from observed luminosities) have been used.

bin size was selected so as to have the best combination of good resolution in period and good error estimates. It would appear from Fig. 2 that a plateau exists from $P_{\min} = 0{\cdot}5$ s to $P_{\max} = 1{\cdot}5$ s. We thus estimate the birthrate of pulsars to be

$$B \simeq \bar{J}_{P,\,\mathrm{est}}\,(0{\cdot}5,\ 1{\cdot}5) = 0{\cdot}07^{+0{\cdot}07}_{-0{\cdot}05}\ \text{pulsars yr}^{-1}\ \text{galaxy}^{-1} \tag{16}$$

or one pulsar born every 14^{+33}_{-7} years, where the error limits correspond to the lower and upper bounds at 95 per cent confidence. The above result is slightly different from, but consistent with, the value we had published earlier (Narayan and Vivekanand 1981). The difference arises because $P_{\min}$ was earlier taken to be 0s. Keeping in mind that the error bounds refer to the 95 per cent confidence limits, and that the present analysis is approximation free and model independent, we consider the results satisfactory. However, we obtain tighter estimates in Section 3

2.6 *Birthrate on the Basis of α Dipole Model of Braking*

We briefly discuss a modification of our theory which permits us to estimate the birthrate assuming the dipole braking model of pulsar evolution.

Let $\rho'_0\,(\tau, L)\,d\tau dL$ be the observed density of pulsars with radio luminosity between L and $L + dL$ and age ($\tau = \frac{1}{2}P/\dot{P}$) between τ and $\tau + d\tau$. If τ is true age, then the 'velocity' of pulsars along the τ axis is $\dot{\tau} = 1$. Therefore, the current J_τ of pulsars at an age τ parallel to the τ-axis is given by

$$J_\tau(\tau) = \int KS(L)\,\rho'_0\,(\tau, L)\,dL. \tag{17}$$

As before J_τ is equal to the birthrate of pulsars in the age range from 0 to τ *minus*

the deathrate in the same range. Once again, for better statistics, we average J_τ from $\tau_{\min}$ to $\tau_{\max}$.

$$\bar{J}_\tau(\tau_{\min}, \tau_{\max}) = \frac{K}{(\tau_{\max} - \tau_{\min})} \int_{\tau_{\min}}^{\tau_{\max}} J_\tau(\tau)\, d\tau. \tag{18}$$

An estimator of this quantity is

$$\bar{J}_{\tau,\,\mathrm{est}}(\tau_{\min}, \tau_{\max}) = \frac{K}{(\tau_{\max} - \tau_{\min})} \sum_{i=1}^{N} S(L_i), \quad \tau_{\min} \leqslant \tau \leqslant \tau_{\max}. \tag{19}$$

Equation (19) is similar to the birthrate formula of Davies, Lyne and Seiradakis (1977) except that we use individual scales for the pulsars and also introduce finite $\tau_{\min}$ which is 0 in their analysis.

In Fig. 3 we have shown $\bar{J}_{\tau,\,\mathrm{est}}$ in bins of 3×10^6 years. Since the error bars on $\bar{J}$, est are rather large, it is difficult to locate the plateau region with any confidence. If we take the plateau to extend from 0 to 6 million years, we obtain a birthrate of $0{\cdot}04^{+0\,04}_{-0\,02}$ pulsar yr^{-1} galaxy^{-1}, or one pulsar every 25^{+45}_{-14} years. This result is consistent with our earlier result (Section 2.5), suggesting that young pulsars upto 6 million years of age may be evolving according to the dipole braking law. Fig. 3 shows a

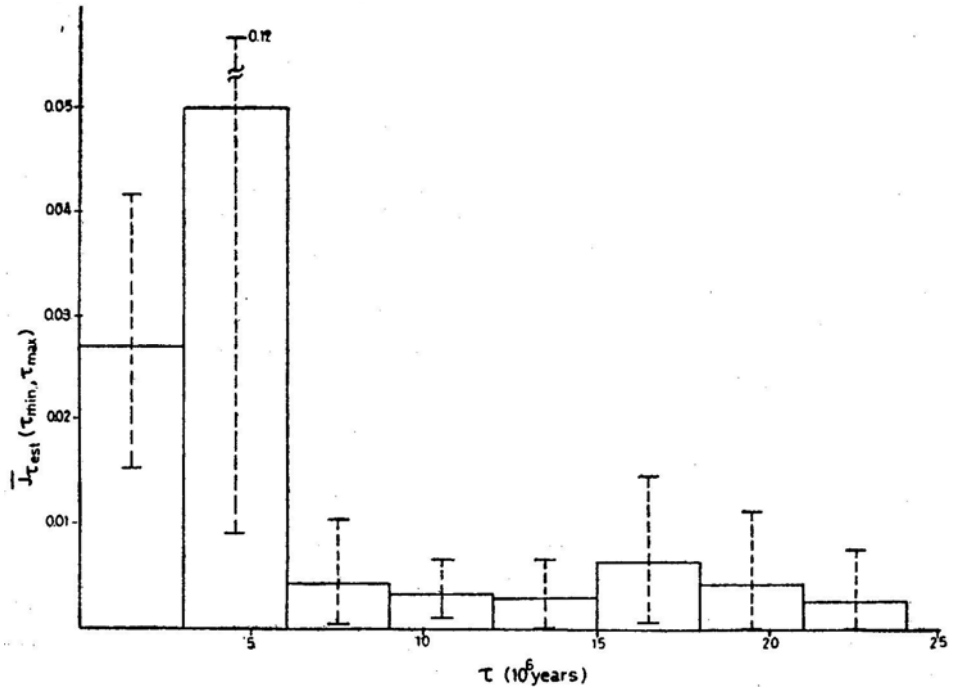

Figure 3. Plot of estimated mean pulsar current $\bar{J}_{\tau,\,\mathrm{est}}$ against apparent pulsar age $\tau = \frac{1}{2}P/\dot{P}$. J_τ has been averaged over age intervals of 3 million years. Error limits are specified at a 95 per cent confidence level. J_τ definitely drops from the first to the third bin, although J_τ in the second bin is not determined clearly. There is no detectable change in J_τ for bins of higher apparent ages. Scale values $S(L)$ have been used.

significant drop in the value of $\bar{J}_{\tau,\ \mathrm{est}}$ after 6 million years. This suggests that, beyond 6 million years, either pulsars could be dying or the relation, age $\equiv \frac{1}{2}P/\dot{P}$, may no longer be valid (say, due to magnetic field decay).

2.7 *Importance of Radio Luminosity Selection Effects*

Is the radio luminosity selection effect important for the computation of the birthrate? We can answer this by comparing the birthrate of Section 2.5 with a second calculation where all pulsars are weighted by a *single average* scale $\langle S(L)\rangle$. Equation (6) would then become

$$\bar{J}_{P,\ \mathrm{est}}\,(P_{\min}, P_{\max}) = \frac{K\,\langle S(L)\rangle}{(P_{\max} - P_{\min})} \sum_{i=1}^{N} \dot{P}_i, \quad P_{\min} \leqslant P_t \leqslant P_{\max}. \tag{20}$$

We have made a thorough statistical comparison of the currents calculated by equations (6) and (20) on the basis of which we can state with greater than 80 per cent confidence that the two quantities are not the same. The analysis of Section 3 reinforces this statement with much greater confidence. We are therefore quite certain that radio luminosity selection effects are vitally important and should not be neglected. This calls for a re-examination of all earlier analyses of pulsar data.

3. Luminosity model approach

3.1 *Introduction*

In Section 2, we computed the pulsar birthrate from $\bar{J}_{P,\ \mathrm{est}}$ (equation 6) using the scale factors $S(L)$ derived from the observed radio luminosities. Since the values of L are spread over four to five orders of magnitude, $S(L)$ is spread over a similar range. This results in a high variance for $\bar{J}_{P,\ \mathrm{est}}$. In this section we have used new scales whose variance is smaller. This we have achieved by modelling the dependence of radio luminosity upon P and $\dot{P}$ as specified in equation (1). We have thus derived 'mean' radio luminosities L' which have a 'smooth' dependence upon P and $\dot{P}$, in contrast to the old L values. Furthermore, we have allowed for the fact that, at a given P and $\dot{P}$, there is a *distribution* of L around L'. Using this distribution we calculate a mean scale value $S'(P, \dot{P})$ at any P and $\dot{P}$. The scatter in these new scales is reduced from five to three orders of magnitude. Consequently, there are much smaller statistical errors in the new estimates for the birthrate and other quantities. On the other hand, the assumed luminosity model could lead to systematic errors.

From a detailed analysis of the pulsar current J_P, we reach the important conclusion that a significant fraction of pulsars are 'born' in the period range 0·5 s to 1·0 s. This result, which we describe as 'injection', could have strong implications for theories concerning the birth of pulsars, their radiation mechanism and their evolution in the P–$\dot{P}$ diagram. We have approximately identified the area of the P–$\dot{P}$ diagram where injection is the strongest, and have suggested a possible explanation.

Finally, we have derived a mean value for the braking index of pulsars. We find it not inconsistent with the values in current use.

3.2 *Model for Luminosity Correlations*

We have fitted a least squares plane to the data of log L against log P and log $\dot{P}$ available for 242* pulsars to obtain the 'mean' luminosity L' (see equation 1) in the form

$$L'(P, \dot{P}) \propto P^{-0.86(\pm 0.2)}\, \dot{P}^{0.38(\pm 0.08)} \tag{21}$$

where the numbers in brackets represent 1σ errors, computed in the usual way for correlated parameters. Lyne, Ritchings and Smith (1975) did a similar exercise and obtained $L' \propto P^{-1.8}\, \dot{P}^{0.88}$. However, they did not fit a least-squares plane but instead arrived at their result by maximizing a correlation coefficient between L and a known function of P and $\dot{P}$. This may explain the discrepancy between their results for the exponents and ours. To check this we fitted a least squares plane to the data of 84 pulsars used by them and obtained $L' \propto P^{-79(\pm 30)}\, \dot{P}^{.36(\pm 11)}$ which is consistent with our result in equation (21).

We now make the crucial approximation that the observed density distribution of pulsars $\rho_0\,(P, \dot{P}, L)$ can be separated into the product of two functions in the form

$$\rho_0(P, \dot{P}, L) = \rho_1(P, \dot{P})\, \rho_2\,(\log L - \log L'\,(P, \dot{P})) \tag{22}$$

where ρ_1 is the density of pulsars in the P–$\dot{P}$ plane, ρ_2 is normalized to 1 and $L'(P, \dot{P})$ is defined in (21). We are thus assuming that the distribution of log L is the same at all points in the P–$\dot{P}$ plane except for the shift given by log $L'(P, \dot{P})$. We have made the following sensitive statistical test of this hypothesis. We divided the P–$\dot{P}$ plane into four quadrants, each containing approximately the same number of pulsars. In each quadrant we separately tabulated the values of [log L — log $L'(P, \dot{P})$] of the observed pulsars. Taking five bins in this variable, we carried out a χ^2-test to verify that the distributions in the four quadrants are the same. We obtained a χ^2 value of 13·6 while the number of degrees of freedom of the test is 12. There is thus very good statistical evidence for supporting the hypothesis in equation (22).

Equation (22) can be written in the equivalent form

$$\rho_0(P, \dot{P}, L) = \rho_1(P, \dot{P})\, \rho_2'(L/L'\,(P, \dot{P})) \tag{23}$$

where again ρ_2' is normalized to 1. The mean scale factor $S'(P, \dot{P})$ at a given $(P, \dot{P})$ is then obviously given by

$$S'(P, \dot{P}) = \int_0^\infty \rho_2'\,(L/L'\,(P, \dot{P}))\, S\,(L)\, dL \tag{24}$$

*To date, $\dot{P}$ values have been measured for 256 pulsars. But L values are not available for 14 of them.

where $S(L)$ is the old scale factor defined in Section 2.2. $S'(P, \dot{P})$ can be approximately calculated in terms of the data on the 242 pulsars (for which P, $\dot{P}$ and L are available) by means of the expression

$$S'(P, \dot{P}) = \frac{1}{242} \sum_{j=1}^{242} S(\xi_j(P, \dot{P})) \tag{25}$$

where

$$\xi_j(P, \dot{P}) = L'(P, \dot{P})\, L_j / L'(P_j, \dot{P}_j). \tag{26}$$

We have computed $S'(P_i, \dot{P}_i)$ for each of the 185 pulsars in the pruned list (of 210 pulsars) for which $\dot{P}_i$ are available and these have been used in the calculations discussed in the rest of Section 3.

To summarize, in this section we calculate the scale factor of a pulsar, not in terms of its *observed luminosity* but in terms of the *expected distribution of luminosity* at the particular values of P and $\dot{P}$. At the heart of this approximation is the basic assumption (equations 21 and 22) that the luminosity distribution is the same at all P and $\dot{P}$ except for the scaling by $L'(P, \dot{P})$. We are convinced of the validity of this assumption on the basis of the statistical test that we have conducted. With the new scales $S'(P_i, \dot{P}_i)$ we are able to make a much more thorough analysis of the data than was possible in Section 2 with the old scales $S(L_i)$.

3.3 *Pulsar Birthrate*

Using the new scales, equation (6) becomes

$$\bar{J}'_{P,\,\mathrm{est}}(P_{\min}, P_{\max}) = \frac{K}{(P_{\max} - P_{\min})} \sum_{i=1}^{N} S'(P_i, \dot{P}_i)\, \dot{P}_i, \quad P_{\min} \leqslant P_i \leqslant P_{\max}. \tag{27}$$

We have plotted $\bar{J}'_{P,\,\mathrm{est}}$ in Fig. 4. Comparison with Fig. 2 shows that the new scales have significantly improved the error limits. The plateau appears to extend from P = 0.5s to P = 1·5s. The mean value of $\bar{J}'_{P,\,\mathrm{est}}$ in this range is $0.048^{+0\,014}_{-0\,011}$, giving a birthrate of one pulsar every 21^{+6}_{-5} years in the galaxy. This is consistent with the number derived in Section 2.5, but has much smaller error limits. It now becomes meaningful and interesting to compare our estimated pulsar birthrate with the supernova rate.

Unfortunately, a reliable estimate of the supernova rate is not available. It is obtained both from direct observations of supernova explosions in external galaxies and from a study of historical Supernovae and SNRs in our galaxy. Estimates from studies of external galaxies range right from one explosion in 359 years (Zwicky 1962) to one every 11 years (Tammann 1977). Studies of historical Supernovae in our galaxy have yielded one explosion every 30 years (Katgert and Oort 1967; Clark and Stephenson 1977). Studies of SNRs in our galaxy have given one explosion every 60 years (Poveda and Woltzer 1968; Milne 1970; Downes 1971)

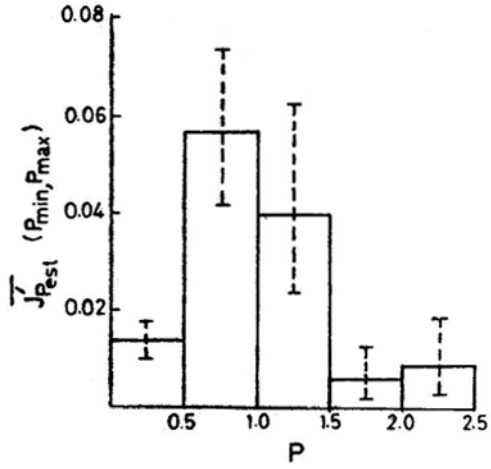

Figure 4. Same as Fig. 2, but with improved scale values $S'(P, \dot{P})$ derived from P and $\dot{P}$. J_P increases in the second bin, drops only marginally in the third, and drops significantly in the fourth bin, closely following Fig. 1 (a).

However, a recent work (Srinivasan and Dwarakanath 1981) on SNRs has estimated that supernova explosions in the Galaxy occur once every 25 years. If we accept this number, there is no significant discrepancy between the birthrates of pulsars and Supernovae.

The dramatic reduction in the error limits from equation (6) to equation (27) is easily understood. Both $S(L_i)$and $\dot{P}_i$ in (6) vary over many orders of magnitude (almost independently). On the other hand, as a consequence of the luminosity model which we have introduced, $S'(P_{i,}\ \dot{P}_i)$ varies approximately as $\dot{P}^{-1/2}$ and is therefore anticorrelated with $\dot{P}$. Thus the range of values in the summation in equation (27) is several orders of magnitude less than in equation (6), leading to much improved Statistical significance. Another way of stating it is that the effective number of pulsars contributing, to equation (16) [computed by the approximate. expression $(B/\sigma_B)^2$] is only 6 while it is nearly 60 for equation (27)

3.4 *Injection*

We now discuss a very important result of our analysis. We see in Fig. 4 that $\bar{J}'_{P,\ \mathrm{est}}$ is significantly higher in the second bin, compared to the first. The mean value is four times higher and even the 95 per cent lower limit in bin 2 is higher than the 95 per cent upper limit in bin 1. It is clear that such a situation can arise only if some pulsars make their appearance in bin 2 without 'flowing' through bin 1. In other words, some radio pulsars are apparently being 'born' in the period range of 0·5 to 1·0 s. We have verified that this 'injection' is not sensitive to the particular choice of bin size. It is also not an artifact of the new analysis with $S'(P, \dot{P})$ since there is compelling evidence for injection even in the rigorous analysis of Section 2 (see also Fig. 1 of our earlier publication, Narayan and Vivekanand; 1981).

In order to understand the details of injection, we have subdivided each bin in Fig. 4 into three further bins in $\dot{P}$. The estimated: mean current $\bar{J}'_P$ in. the various bins are shown in Table 1, along with the 95 percent confidence limits in some cases.

Table 1. Estimated mean, pulsar, current $\bar{J}'_{P,\,\mathrm{est}}$ .in various bins of the P–$\dot{P}$ diagram. The 95 per cent upper and lower limits to the current are also specified in the important bins. P is in units of seconds, and $\dot{P}$ in units of seconds per second.

	$0{\cdot}0 \leqslant P < 0{\cdot}5$	$0{\cdot}5 \leqslant P < 1{\cdot}0$	$1{\cdot}0 \leqslant P < 1{\cdot}5$	$1{\cdot}5 \leqslant P < 2{\cdot}0$
$1 \times 10^{-14} \leqslant \dot{P} < 1 \times 10^{-11}$	$\cdot0042^{+\cdot0031}_{-\cdot0022}$	$\cdot0275^{+\cdot0139}_{-\cdot0117}$	$\cdot0169^{+\cdot0176}_{-\cdot0124}$	$\cdot0027$
$1 \times 10^{-15} \leqslant \dot{P} < 1 \times 10^{-14}$	$\cdot0067^{+\cdot0016}_{-\cdot0018}$	$\cdot0120^{+\cdot0052}_{-\cdot0053}$	$\cdot0133^{+\cdot0061}_{-\cdot0057}$	$\cdot0025$
$1 \times 10^{-19} \leqslant \dot{P} < 1 \times 10^{-15}$	$\cdot0013$	$\cdot0028$	$\cdot0037$	$\cdot0018$

There seems to be strong evidence that injection occurs at *high* values of $\dot{P}$ in the period range 0·5 s to 1·0 s and possibly even in the 1·0 s to 1·5 s range. We have outlined this high injection region by means of the box in Fig. 5.

The injected pulsars are unlikely to be the 'recycled' pulsars formed in massive close binary systems (de Loore, de Greve and de Cuyper 1975), because of the following reasons.

(a) Even if all pulsars are born in massive close binary systems, the recycled pulsars cannot be more than 50 per cent of the total population. A more realistic estimate based on the actual number of such binary systems (van den Heuvel 1977) would be a few per cent. But the 95 per cent lower bound of $\bar{J}'_{P,\,\mathrm{est}}$ in bin 2 (Fig. 4) is more than twice the 95 per cent upper bound of $\bar{J}'_{P,\,\mathrm{est}}$ in bin 1, indicating that much more than 66 per cent of the pulsars are injected.

(b) There is no compelling reason to expect predominantly high values of $\dot{P}$ in such pulsars. On the contrary, low values of $\dot{P}$ are likely to occur if the magnetic field of pulsars decays on a time scale of $\simeq 5 \times 10^6$ years, which is the estimated time between the two explosions (de Loore, de Greve, de Cuyper 1975). Injection, on the other hand, occurs at high values of $\dot{P}$ as shown by Table 1.

Having rejected the 'recycled' pulsars, another possibility is that neutron stars may be born with large periods of the order of 0·5 s. However, it is widely believed (see, for example, Manchester and Taylor 1977) that there are some theoretical difficulties in getting stars to shed most of their angular momentum either before, during, or shortly after collapse (into a neutron star). Therefore we may expect neutron stars to be born with periods of the order of tens of milliseconds. There appears to be some observational support for this, in that at least a certain category of pulsars (*i.e.* those which are not injected) are born with small periods, *viz.* the Crab and Vela pulsars*. Therefore, we may expect the injected pulsars also to start their careers with low periods, say 10 ms. Now, the dipole model of pulsar braking would predict (in the absence of magnetic field decay) that the pulsars in the injection box in Fig. 5 would have had initial $\dot{P}$ values $\simeq 5 \times 10^{-12}$ s s^{-1} which is an order of magnitude more than the $\dot{P}$ of the Crab pulsar. It is therefore surprising that we do not see more pulsars with small values of P and high values of $\dot{P}$.

*Incidentally, since the injected pulsars form the hulk of the pulsar population, the Crab and Vela pulsars are by no means prototypes of young pulsars.

A close examination of Fig. 5 shows that there is apparently an abrupt cut-off of pulsars above a certain value of $\dot{P}$. We have made the following statistical test to determine whether the scarcity of pulsars at high values of $\dot{P}$ is indeed significant. We tentatively placed the cutoff line at log $\dot{P}$ = — 12·5 (Fig. 5). We assumed a dipole braking model without field decay (which is reasonable for this part of the P–$\dot{P}$ diagram), and a pulsar ' death' line of the form $\dot{P}\,P^{-5}$ = constant (Ritchings, 1976 has shown that at small values of $\dot{P}\,P^{-5}$, pulsars spend increasing lengths of time in the nulled state, apparently as a prelude to death). Assuming the period at birth to be 10 ms, we computed the birthrate of pulsars in various bins of $\dot{P}$ using the observed sample of pulsars and the scale factors $S(P, \dot{P})$. We then evolved the pulsars according to the dipole braking model and computed the number of pulsars we *should have observed* above the cut-off line. This turns out to be 6·6 pulsars. Since some of these might have been missed by the various pulsar surveys due to their having very low periods, we also computed the expected number of pulsars above the cut-off line with P > 100 ms. Our calculations show that we ought to have seen 2·9 pulsars in this region whereas we actually see none. We can therefore state with

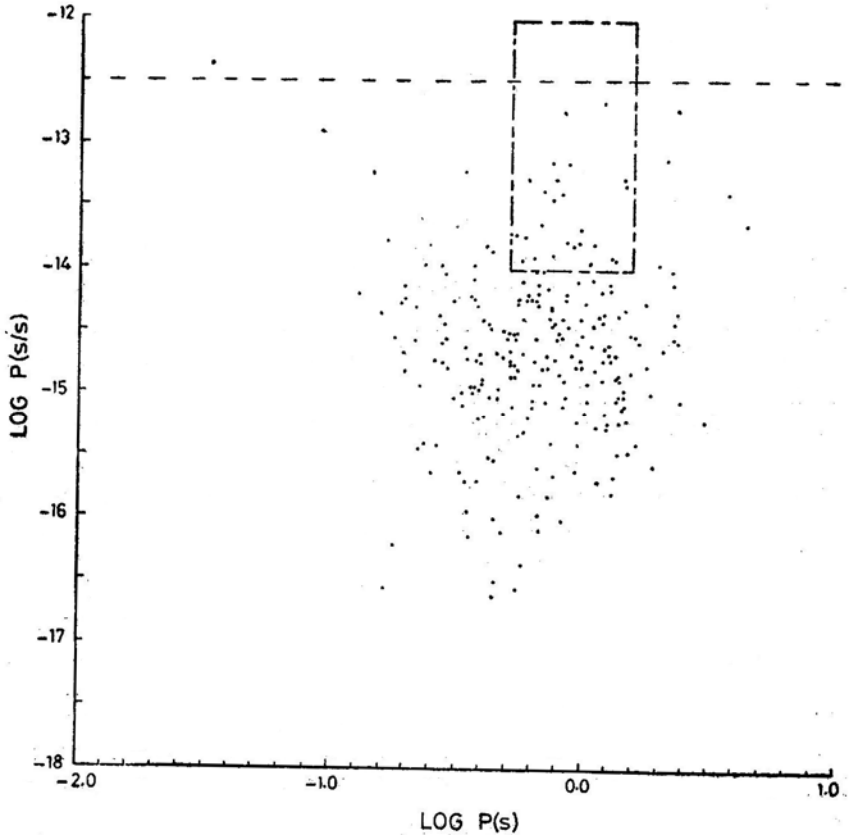

Figure 5. P and $\dot{P}$ plotted on log-log scale for 256 pulsars. Pulsars appear to be missing above a critical value of $\dot{P}$, tentatively represented by the dashed 'cut-off' line. Pulsars are born in the top left part of the diagram (the majority, being born apparently above the cutoff line), and evolve towards the bottom right of the diagram. Most of the pulsar injection occurs in the box at the top of the diagram.

94·5 per cent confidence (100 {1 — exp (— 2·9)}) that there is a genuine deficit of pulsars above the cut-off line in Fig. 5. We have verified that the above results are not very sensitive to the exact location of either the cut-off line or the death line. However, we cannot reject the possibility that the injection line is actually a more complicated curve than a single horizontal line. For instance, the distribution of points in Fig. 5 might suggest a line with negative slope in the period range from 0 to ~ 0·3 s and a second line with positive slope beyond 0·3 s at the top of the P–$\dot{P}$ diagram; there could also be an injection line with negative slope at the left of the P–$\dot{P}$ diagram. Some of these possibilities have been discussed by Radhakrishnan (1981) on the basis of an interesting model.

We would like to offer the following tentative explanation of injection. It is possible that neutron stars do not radiate in the radio region immediately on birth but do so later in their life. We suggest that neutron stars with $\dot{P}$ greater than the critical value are unable to radiate in the radio. They switch on as pulsars when their $\dot{P}$ decreases to the appropriate value. Therefore, neutron stars with initial $\dot{P}$ values above the cut-off line will 'enter' the pulsar P–$\dot{P}$ diagram at higher periods, thereby giving rise to injection. At present, we have no theory or mechanism of pulsar radiation which could explain an upper cut-off line in $\dot{P}$. This is currently under investigation.

The above scenario also explains why there are so few pulsar-SNR associations. Our data suggests that pulsars could spend ~ 10^4 year or more above the cut-off line. If SNRs dissolve into the interstellar medium on time scales comparable to the switching-on times of pulsars (there is good evidence for this in the work of Srinivasan and Dwarakanath 1981), there would be very few observable associations between pulsars and SNRs. As mentioned earlier, in this picture we also require that neutron stars should cool rapidly after birth to avoid radiating thermal X-rays.

3.5 *Braking Index*

The braking index n is defined by the equation

$$\dot{\boldsymbol{\Omega}} \propto -\boldsymbol{\Omega}^n \tag{28}$$

where the angular velocity $\boldsymbol{\Omega} = 2\pi/P$. In the dipole braking theory, $n = 3$. The age τ of a pulsar, assuming the initial period to be 0 s, can be expressed in terms of the braking index as

$$\tau = \frac{1}{(n-1)}\frac{P}{\dot{P}} = \frac{\tau'}{(n-1)} \tag{29}$$

where τ' is the characteristic time, $P/\dot{P}$ The 'velocity' of a pulsar parallel to τ' is $\tau' = (n - 1)$. Hence, the mean pulsar current parallel to τ' can be written, as in earlier sections, as

$$\bar{J}_{\tau',\,\mathrm{est}}(\tau'_{\min}, \tau'_{\max}) = \frac{K}{(\tau'_{\max} - \tau'_{\min})} \sum_{i=1}^{N} (n_i - 1)\, S'(P_i, \dot{P}_i),\ \tau'_{\min} \leqslant P_i/\dot{P}_i \leqslant \tau'_{\max}. \tag{30}$$

If we define $\langle n \rangle$ as the mean braking index of the pulsars in the τ' range defined in equation (30), then the equation can be written as

$$\bar{J}_{\tau', \text{ est}}(\tau'_{\min}, \tau'_{\max}) = \frac{K(\langle n \rangle - 1)}{(\tau'_{\max} - \tau'_{\min})} \sum_{i=1}^{N} S'(P_i, \dot{P}_i)$$

$$= (\langle n \rangle - 1)\, X(\tau'_{\min}, \tau'_{\max}), \quad \tau'_{\min} \leqslant P_i/\dot{P}_i \leqslant \tau'_{\max}. \qquad (31)$$

We have plotted X ($\tau'_{\min}$, $\tau'_{\max}$) in bins of 2 million years in Fig. 6. The curve appears to be essentially constant (barring the fluctuation in bin 3) up to about 12×10^6 yr, and falls thereafter. If we assume the dipole model and take the age as $\tau'/2$, then it would appear that up to about 6×10^6 yr, the current is constant. Incidentally, in terms of τ', injection occurs below 10^5 yr and can therefore be neglected in the discussion here.

Since the histogram in Fig. 6 does not change from $\tau' = 0$ to $\tau' = 12 \times 10^6$ yr, this strongly suggests that the mean braking index $\langle n \rangle$ is essentially constant in this range. Moreover, one can further conclude that there are probably no significant pulsar births or deaths. By an argument similar to that in Section 2.2 one therefore arrives at the interesting result that $\bar{J}'_{\tau', \text{ est}}$ (0, 12×10^6 yr) should be comparable to the birthrate B of pulsars. Since we have an independent estimate of B in Section 3.3, we can therefore use quotation (31) to obtain an estimate of $\langle n \rangle$. We obtain $\langle n \rangle = 3.7^{+0.8}_{-0.8}$ where the error limits are the 95 per cent confidence limits. It is interesting that our independent estimate of $\langle n \rangle$, based only on observational

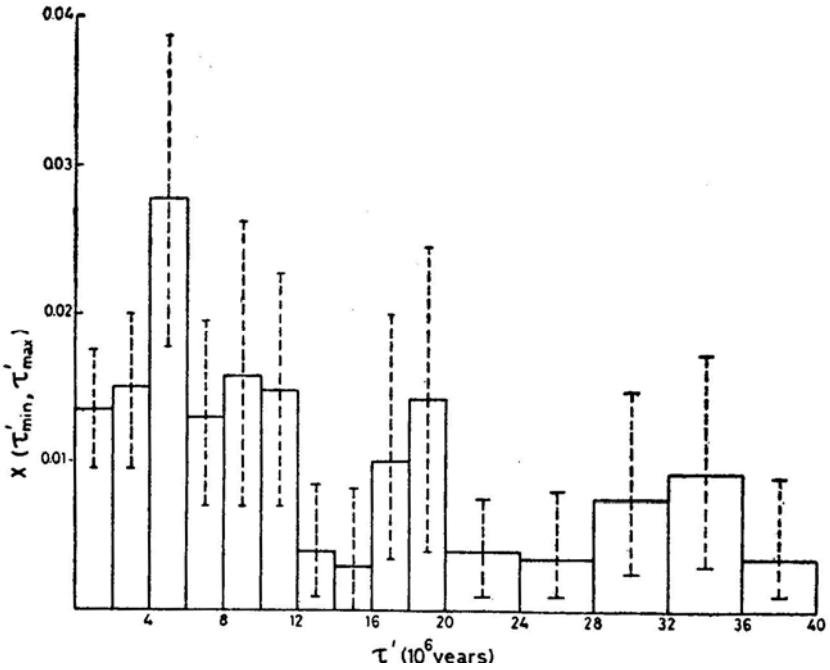

Figure 6. Plot of modified pulsar current X against apparent age $\tau' = P/\dot{P}$. X has been averaged in ' intervals of 2×10^6 yr upto $\tau' = 20 \times 10^6$ yr, and in intervals of 4×10^6 yr thereafter. There appears to be no apparent change in the current upto 12×10^6 yr.

data, is fairly consistent with, the dipole model value of $n = 3$. Incidentally, if we assume the death line of Ritchings (1976), it will be seen that some of the high magnetic field pulsars would die at τ' values smaller than 12×10^6 yr. In that case $\bar{J}_{\tau',\mathrm{est}}$ (0, 12×10^6 yr) would be smaller than B and the above value of $\langle n \rangle$ would be an overestimate. This strengthens the argument in favour of dipole braking in young pulsars (with ages upto 6×10^6 yr).

The braking index has been measured independently only for the Crab pulsar (Groth 1975), yielding the value 2·515. We do not consider this to be inconsistent with our $\langle n \rangle$ because, by our results, the Crab belongs, to a minority class of un-injected pulsars. Further, we have estimated only the *mean* braking, index for the whole pulsar population. We have no information on the individual variations in n from one pulsar to the other.

4. Conclusions

We may identify the following important sources of error in our calculations.

(a) All our results are based on the observed pulsars. Since the observed sample could differ from the true distribution due to sampling fluctuations, there are statistic-cal uncertainties associated with our numerical results. We have estimated these on a Poissonian assumption and quoted them as 95 per cent confidence limits wherever applicable.

(b) We have assumed the beaming factor K to have a value 5. However, the true value could be significantly different (*e.g.* Kundt 1981).

(c) We have taken the mean interstellar electron density n_e to be 0·03 electrons cm^{-3}. Since this is used in all distance calculations, it is a highly important input. There could be some uncertainty in the value of n_e though the value we have adopted is generally accepted as a good estimate over a large portion of the galaxy. Fluctuations in n_e in different parts of the galaxy could also contribute to the error.

(d) The calculations in Section 3 critically depend on the luminosity model, equations (21) and (22). This could introduce some error in the results. However, since all the major conclusions of Section 3 are consistent with the results of Section 2 where no model is assumed, we believe this error is quite small.

(e) There may be some errors in the computed scaling factors $S(L_i)$ and also in the manner of pruning the data, arising from possible faulty interpretations of the parameters and selection effects of the three pulsar surveys.

Of the above, errors (d) and (e) are probably not very significant. Errors of the type (a) can be calculated and have been quoted throughout. Errors (b) and (c) have not been estimated though they could be quite large. These errors are present in all earlier analyses, of pulsar data as well. It is also important to note that among our major conclusion listed below, errors (b) and (c) affect only our estimate of pulsar birthrate and have little or no bearing on the rest.

The main conclusions of our study are:

(a) A significant fraction of pulsars are born with initial periods > 500 ms. Therefore the conventional picture of pulsar evolution in the P–$\dot{P}$ diagram may require significant modifications. The injection of pulsars at high periods should be related to the physics of pulsar radio emission. We suggest that neutron stars probably

switch on as pulsars only when $\log \dot{P} < -12{\cdot}5$. This hypothesis would also explain the lack of SNR—pulsar associations. Our demonstration of injection is based on the rigorous, *model independent* calculations of Section 2 (see Fig. 2), Section 3 serving as a confirmation. Moreover, the result is independent of the particular choice of K and n_e.

(b) The birthrate of pulsars is estimated to be $0{\cdot}048^{+0\,014}_{-0\,011}$ (one pulsar every 21^{+6}_{-5} yr), which appears to be consistent with the rate of supernova explosions if (i) every explosion results in a neutron star, and (ii) every neutron star becomes a pulsar sometime in its life. Our estimate is really a lower bound, but we expect it to be close to the actual birthrate because the 'plateau' in Fig. 4 shows some resemblance to Fig. 1(a). However, it should be noted that our result depends upon the values chosen for K and n_e, neither of which is known with great precision.

(c) The number density of pulsars in the P–$\dot{P}$ diagram is significantly affected by radio luminosity selection effects which cannot, therefore, be neglected in studies of pulsar evolution in the P–$\dot{P}$ diagram, birthrate studies, *etc.* This, coupled with the injection which we have demonstrated, would cast doubts on earlier analyses of pulsar data. A complete re-examination is called for.

(d) The mean braking index of pulsars is estimated to be $3{\cdot}7^{+0\,8}_{-0{\cdot}\,8}$ this value being probably an overestimate. Hence the dipole braking model value of $n = 3$ is probably close to the truth. Also, $\tau = \frac{1}{2}P/\dot{P}$ appears to be a good indicator of pulsar age upto 6×10^6 yr, which might be a lower limit for the decay time of the magnetic field or possibly the age at which pulsars begin dying. These results do not depend upon our choice of K and n_e.

Acknowledgements

We are thankful to Rajaram Nityananda for numerous helpful discussions and suggestions, to V. Radhakrishnan for suggesting the possibility of injection, to J. H. Taylor for drawing our attention to the importance of luminosity selection effects, and to R. N. Manchester for providing in preprint form half of the data that we have used in this analysis. We also thank both our referees for many valuable suggestions.

Appendix A

In various sections of this paper, we are interested in evaluating quantities of the form

$$Q = \int x\, p(x)\, dx \tag{32}$$

where x is some property of pulsars and $p(x)\,dx$ is the probability of observing a pulsar having a value of this property in the range x to $x + dx$. For instance, in Section 2(b), $x = \dot{P}S(L)$, in Section 2·4, $x = S(L)$, *etc.* We estimate Q by means of the following sum over the X_i of the observed pulsars

$$Q_{\text{est}} = \sum_{i=1}^{N} X_i. \tag{33}$$

Now, the probabilities of observing pulsars in different ranges of x are independent of one another. Hence, Q in equation (32) is the weighted integral over independent Poisson variables (of mean $p(x)\,dx$). The variance of Q is then clearly given by

$$V = \int x^2\, p(x)\, dx. \tag{34}$$

This can be estimated in terms of the observed pulsars by means of

$$V_{\text{est}} = \sum_{i=1}^{N} X_i^2 \tag{35}$$

which is the formula used throughout the present paper.

The form of V in equation (34) is different from the following more usual form

$$\begin{aligned} V' &= \int (x - \bar{x})^2\, p(x)\, dx \\ &= \int x^2\, p(x)\, dx - \bar{x}^2 \int p(x)\, dx \end{aligned} \tag{36}$$

The difference arises because the variance in the present case (equation 34) has two contributions.

(a) There is one contribution arising from the distribution of values of x, giving an expression exactly of the form equation (36).

(b) Secondly, being a Poisson process, the total number of observed pulsars

$$N = \int p(x)\, dx \tag{37}$$

can itself fluctuate *i.e.* there can be fluctuations in the number of terms in equation (33). It is easily verified that this contribution cancels the second term in equation (36), leading to equation (34).

Appendix B

If an H II region lies along the line of sight to a pulsar, it contributes to the dispersion measure (DM), Since pulsar distances are derived using DM, the H II region contributions must be subtracted. Prentice and ter Haar (1969) have given a scheme for estimating the corrections. However, their results might be inaccurate because of unknown parameters, such as the Strömgren radii and electron densities of the H II regions. The inaccuracies could be particularly serious if the H II region contribution is a major fraction of the pulsar's DM. Therefore, we have 'softened' the Prentice-ter Haar correction using the following scheme.

We postulate that the dispersion measure correction of an H II region has a rectangular probability distribution as shown in Fig. 7 where H is the correction given by Prentice and ter Haar. We average the calculated distance to the pulsar over this probability distribution and use the averaged distance in our studies. Let d be the

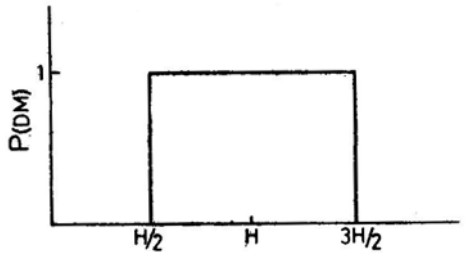

Figure 7. Assumed probability distribution of the dispersion measure correction (H) due to H II regions.

DM left to be accounted for just at the front face of the H II regions. It is easy to see that whenever $d \geqslant 3H/2$ or $d \leqslant H/2$, the present scheme gives practically the same distance as the old scheme (which directly used the single value of H). For the case $H/2 < d < 3H/2$, the new scheme gives a larger estimate for the pulsar distance than the old. A larger distance implies a larger estimate for the pulsar luminosity L and hence a smaller estimate of the scale factor $S(L)$. We are thus, in a sense, being conservative and erring on the side of slightly underestimating the quantities of interest.

Appendix C

As already mentioned in the text, we expect the distribution of Q_{est} (equation 33) to be asymmetric, with a long tail, because only a few top values of X_i usually contribute to the result. Therefore we prefer to use confidence limits rather than the Standard deviation. In computing the confidence limits, we assume that our estimator $Q_{est} = \sum_{i=1}^{N} X_i$ is the sum of N random Poisson variables (v_i) of mean equal to 1, each weighted by the respective X_i

$$Q_{est} = \sum_{i=1}^{N} v_i X_i. \tag{37}$$

By numerically generating N random variables between 0 and 1, we generate N ran dom Poisson variables with mean 1 and therefore a random value of Q_{est}. By gene rating many random values of Q_{est}, we then estimate the probability distribution of Q. The confidence limits are then easily marked off .by measuring areas under this probability curve.

References

Arnett, W. D., Lerche, I.1981, *Astr. Astrophys.*, **95**, 308.
Baade, W., Zwicky, F. 1934, *Proc. nat. Acad. Sci.*, **20**, 254.
Clark, D. H., Caswell, J. L. 1976. *Mon. Not. R. astr. Soc.*, **174**, 267.
Clark, D. H, Stephenson, F. R. 1977, *Mon. Not. R .astr. Soc.*, **179**, 89p.
Davies, J. G., Lyne, A. G., Seiradakis, J. H. 1972, *Nature*, **240**, 229.
Davies, J. G., Lyne, A. G., Seiradakis, J. H. 1973, *Nature Phys. Sci.*, **244**, 84.
Davies, J. G., Lyne, A. G., Seiradakis, J. H. 1977, *Mon. Not. Roy. astr. Soc.*, **179**, 635.

de Loore, C., de Greve, J. P., de Cuyper, J. P. 1975, *Astrophys. Sp. Sci.*, **36,** 219.
Downes, D. 1971, *Astr. J.*, **76,** 305.
Gold, T., 1968, *Nature*, **218,** 731.
Groth, E. J., 1975, *Astrophys. J. Suppl. Ser.*, **29,** 453.
Hulse, R. A., Taylor, J. H. 1974, *Astrophys. J.*, **191**, L 59.
Hulse, R. A., Taylor, J. H. 1975, *Astrophys. J.*, **201**, L 55.
Illovaisky, S. A., Lequeux, J. 1972, *Astr. Astrophys.*, **20**, 347.
Katgert, P., Oort, J. H. 1967, *Bull. astr. Inst. Netherl.*, **19**, 239.
Kundt, W. 1981, *Nature*, **292**, 865.
Lyne, A, G., Ritchings, R. T., Smith, F. G. 1975, *Mon. Not. Roy. astr. Soc.*, **171**, 579.
Manchester, R. N., Taylor, J. H. 1977, *Pulsars*, Freeman, San Francisco.
Manchester, R. N., Lyne, A. G., Taylor, J. H., Durdin, J. M., Large, M. I., Little, A. G. 1978, *Mon. Not. R. astr. Soc.*, **185**, 409.
Manchester, R. N. 1979, *Austr. J. Phys.* **32**, 1.
Milne, D. K. 1970, *Austr. J. Phys.*, **23**, 425.
Narayan, R., Vivekanand, M. 1981, *Nature*, **290**, 571.
Ostriker, J. P., Gunn, J. E., 1969, *Astrophys. J.*, **157**,1395.
Phinney, E. S., Blandford, R. D. 1981, *Mon. Not. R. astr. Soc.*, **194**,137.
Poveda, A., Woltzer, L., 1968, *Astr. J.*, **73**, 65.
Prentice, A. J. R., ter Haar, D. 1969, *Mon. Not. R. astr. Soc.*, **146**, 423.
Radhakrishnan, V. 1981, *Preprint.*
Ritchings, R. T. 1976, *Mon. Not. R. astr. Soc.* **176**, 249.
Srinivasan, G., Dwarakanath, K. S. 1981, *Preprint.*
Tammann, G. A. 1974, in *Supernovae and Supernova Remnants*, Ed. C. B. Cosmovici, D. Reidel, Dordrecht.
Tammann, G. A. 1977, *Ann. N.Y. Acad. Sci.*, **302**, 61.
Taylor, J. H., Manchester, R. N. 1977, *Astrophys. J.*, **215**, 885.
van den Heuvel, E. P. J. 1977, *Ann. N.Y. Acad. Sci.* **302**, 14.
Zwicky, F. 1962, in *IAU Symp. 15; Problems of Extragalactic Research*, Ed. G. C. Mevittie, Macmillan, New York.

J. Astrophys. Astr. (1981) **2**, 339–347

The Structure of the Cygnus Loop at 34.5 MHz

Ch. **V.** Sastry, K. S. Dwarakanath and R. K. Shevgaonkar
Indian Institute of Astrophysics, Bangalore 560034 and Raman Research Institute, Bangalore 560080

Received 1981 July 7; accepted 1981 August 27

Abstract. We have observed the large supernova remnant Cygnus Loop at 34·5 MHz with the low frequency radio telescope at Gauribidanur, India. A radio map of the region with a resolution of 26 arcmin × 40 arcmin ($\alpha \times \delta$) is presented. The integrated flux density of the Cygnus Loop at this frequency is 1245 ± 195 Jy. The radio fluxes of different parts of the nebula at this frequency were also measured and used to construct their spectra. It is found that the spectrum of the region associated with the optical nebulosity NGC 6992/5 is not flat at low frequencies, and also exhibits a break at a frequency around 400 MHz. The spectrum of the region associated with NGC 6960 also shows a break but around 1000 MHz, while the spectrum of the region associated with NGC 6974 is straight in the entire frequency range 25 to 5000 MHz. The implication of these results on the basis of existing theories of the origin of radio emission from supernova remnants is discussed.

Key words: supernova remnants, individual—radio continuum

1. Introduction

The large supernova remnant Cygnus Loop, has been studied extensively in the radio frequency domain in the range 200 MHz and above, with high resolution. It was found from these studies that the association between optical and radio features of the object is quite close in some parts. It was suggested that the spectrum of the total integrated flux density steepens above 1 GHz and also that the spectrum varies over different parts of the source (Kundu and Becker 1972; DeNoyer 1974). In order to study the variations in the radio structure of the nebula and the spectra of different parts over a wider frequency range it is necessary to extend the high resolution observations to lower frequencies. Such studies may be expected to yield information on the physical conditions and evolution of different parts of the Cygnus Loop. Here we report a study of the structure of this object at 34·5 MHz with a resolution of 26 arcmin × 40 arcmin. The only other high resolution observation at a low frequency (25 MHz) is due to Abranin, Bazelyan and Goncharov (1977).

2. Observations

The observations reported here were made with the low frequency radio telescope at Gauribidanur (Latitude 13°36′12″ N and Longitude 77°26′07″ E). The telescope can be operated in the frequency range 25 to 35 MHz. The antenna system of the telescope consists of two broad-band arrays arranged in the form of a 'T'. The half power beam widths at 34·5 MHz are 26 arcmin and 40 sec ($\delta - 14°{\cdot}1$) arcmin in the EW and NS directions respectively. The collecting area is approximately 250 λ^2. The telescope is of the transit type and the beam can be pointed anywhere along the meridian instantaneously, in the zenith angle range ± 45°, using remotely controlled diode phase shifters. A time-multiplexing system is used to point the beam to eight different declinations sequentially. The smallest time interval necessary to change the beam from one direction to another is of the order of a few milliseconds. The receiving system extracts the in-phase (cos) and the quadrature (sin) correlations between the two arms for each one of the eight beam positions. Predetection bandwidths of 30 and 200 KHz and post-detection time constants ranging from 1 to 30s are available. The output of the receiving system is recorded in both analog and digital forms. Full details of the telescope will be published elsewhere.

The observations of the Cygnus Loop were carried out with 30 KHz bandwidth and a 10s time constant. Drift scans were taken in R. A. from 20^h20^m to $21^h\ 20^m$ in the dec range 28° to $33^o{\cdot}5$ in steps of 24 arcmin. The entire Cygnus Loop was thus covered in a period of two days. As is well known, observations at low frequencies are plagued by various difficulties such as interference due to radio, broadcast stations and changing ionospheric conditions. We have found that the broadcast interference is intermittent and has no directional dependence making it very difficult to choose any particular direction or time for observations. The changing ionospheric conditions make it imperative that the observations of a given source be completed in as short a time as possible. We made repeated observations on Cygnus Loop to obtain a consistent set of data with minimum possible effects of ionosphere like scintillation and refraction. A total time of nearly eight months was required to obtain these observations due to the problems mentioned above.

3. Reductions

Each Right Ascension drift scan was calibrated with a standard noise source. The noise source in turn was calibrated using the sources 3C433, 3C436 and sometimes also 3C84. Appropriate corrections for the variation of the gain of the antenna system due to the different declinations of the calibrating sources and the Cygnus Loop were applied. The calibration sources were observed with each observation of the Cygnus Loop. The assumed flux densities of the three sources 3C433, 3C436 and 3C84 are 140 Jy, 62 Jy and 351 Jy respectively; These are obtained by extrapolating the 178 MHz flux densities of Kellermann, Pauliny-Toth and Williams (1969) using the low frequency spectral indices of Roger, Bridle and Costain (1973). Using the calibrated Right Ascension scans, a raw map of the nebula was constructed. The side lobe effects due to the uniform grading of the antenna system were removed by 'cleaning' the map using the technique suggested by Hogbom (1974). The two dimensional beam of the telescope is obtained by observing several point sources

and also calculated using the measured phase and amplitude distribution across the arrays. The observed and calculated beams agreed to within twenty per cent. This beam was used to 'clean' the map with a dynamic range of about 25. The final map was obtained, by convolving the 'cleaned' map with a gaussian beam of 26 arcmin × 40 arcmin, and is shown in Fig. 1. The map is divided into regions A, B and C, as shown in the figure.

The total flux density of the Cygnus Loop was obtained by numerical integration of the entire map. It was pointed out by Moffat (1971) and Dickel and Willis (1980) that there are several point sources within the above field. Most of these sources are believed to be extragalactic. If one assumes a spectral index of – 0·8 then the total estimated flux density due to all these sources turns out to be 40 Jy. The total flux density of the Cygnus Loop after subtracting that due to the extragalactic point sources is 1245 ± 195 Jy. The integrated flux density from each one of the regions designated as A, B and C in Fig, 1 was also found by numerical integration within the appropriate boundaries. The measured values are 660 ± 100 Jy, 469 ± 70 Jy, and 116 ± 18 Jy for the regions A, B and C respectively.

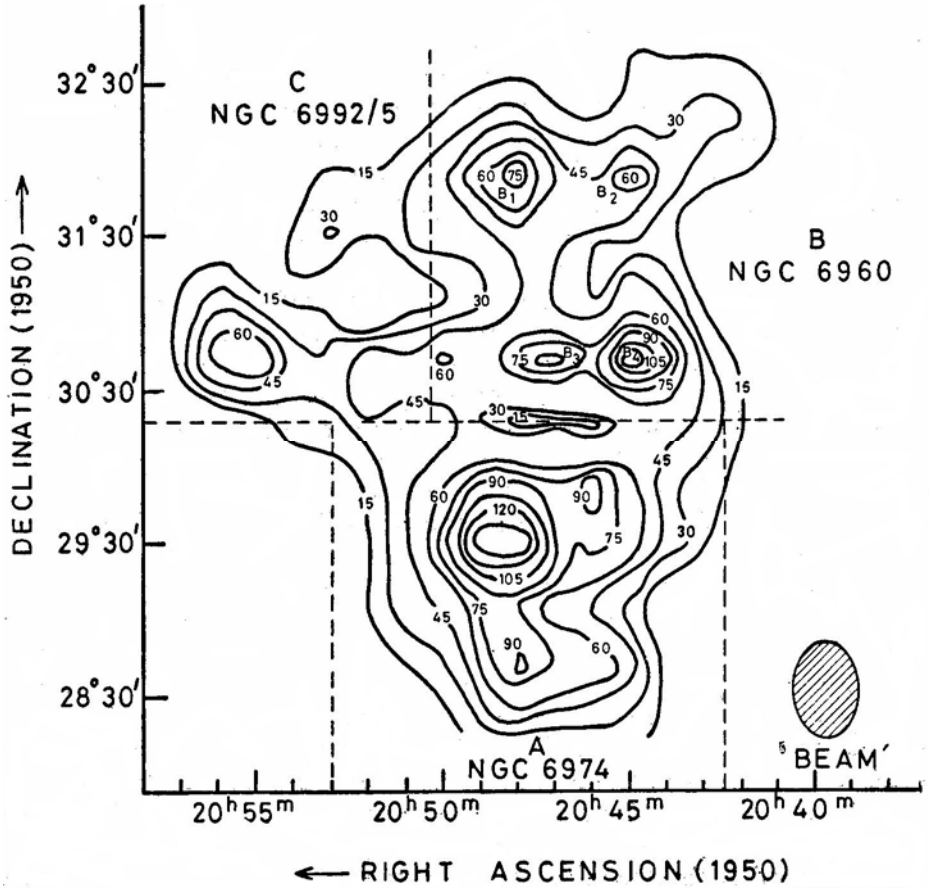

Figure 1. Radio Map of Cygnus Loop at 34.5 MHz Regions A, B and C are marked with dashed lines: The contour interval is 15·Jy. To get the brightness temperature T_b, multiply the numbers indicated by 620

4. Radio structure

It can be seen from Fig. 1 that the brightness distribution across the nebula remains quite complex even at low frequencies and shows several maxima of differing intensities. Although there is a broad similarity between our map and that of Kundu and Velusamy (1967) at 195 MHz with similar resolution there are some differences. The intensity variations seem more pronounced in our map. A similar effect was also noticed by Abranin, Bazelyan and Goncharov (1977) at 25 MHz with a resolution of 30 arcmin. The positions and fractional fluxes of the maxima around region C are similar at 34·5 and 195 MHz. The minimum between the two maxima in region C is very clearly seen in our map, and also in most of the high frequency maps, but not in the map of Abranin, Bazelyan and Goncharov (1977). In region B, there are four pronounced maxima in our map. The source B is also very prominent in the 430 MHz map of Kundu and Velusamy (1967). In the map of Abranin, Bazelyan and Goncharov (1977) the maxima in the region B are not clear excepting the one corresponding to our B_4 which is designated as E in their map. The radio emission in the region B extends much beyond the optical nebulosity, to the western side. The structure of region A is similar at all frequencies up to 600 MHz. In this frequency range there is a clear maximum near $\delta = +29^{o}\cdot5$ and $\alpha = 20^{h}\ 49^{m}$. In the maps observed at frequencies above 1 GHz (Moffat 1971; Kundu and Becker 1972; Keen *et al.* 1973), the radiation is diffused and confined to the boundaries and there is no clear maximum at the above position.

5. Discussion of the spectra

The spectrum of the total integrated flux of the Cygnus Loop is shown in Fig. 2. In constructing this plot, all available data in the literature were used. The spectral index in the frequency range 25 to 960 MHz including our measured value of 1245 ± 195 Jy at 34·5 MHz, is — 0·44 ± 0·09. As already pointed out by Kundu and Becker (1972) and DeNoyer (1974) the spectrum is steeper in the range 1 to 5 GHz with a spectral index of — 0·75 ± 0·23. More measurements of the integrated flux density are necessary to reduce the errors in the spectral indices.

Amongst the many models proposed to explain the radio emission from supernova remnants, the one due to van der Laan (1962) is generally assumed to be applicable to the case of the Cygnus Loop. In this model, the synchrotron radio emission from the remnant is from an enhanced volume emissivity of the interstellar medium due to the compression from the supernova shock. Based on van der Laan's equations, the integrated flux density expected at 34·5 MHz from a thin shell resulting from the compression of the interstellar medium originally in a sphere of 35 pc (the diameter of the Cygnus Loop) is about 600 Jy. We have assumed in the above calculations that the ratio of shell radius to shell thickness is 18 (Moffat 1971), the distance to the nebula is 770 pc (Minkowski 1958) and the average volume emissivity of galactic background is 20×10^{-41} WM^{-3} Hz^{-1} Sr^{-1} (Jones 1973). However, as pointed out by DeNoyer (1974), this method overestimates the compression factor and hence the volume emissivity; this is because one assumes that all the interstellar matter swept up in the lifetime of the supernova remnant is now contained within the thin radiating shell, and that the compression factor can be determined from the observed

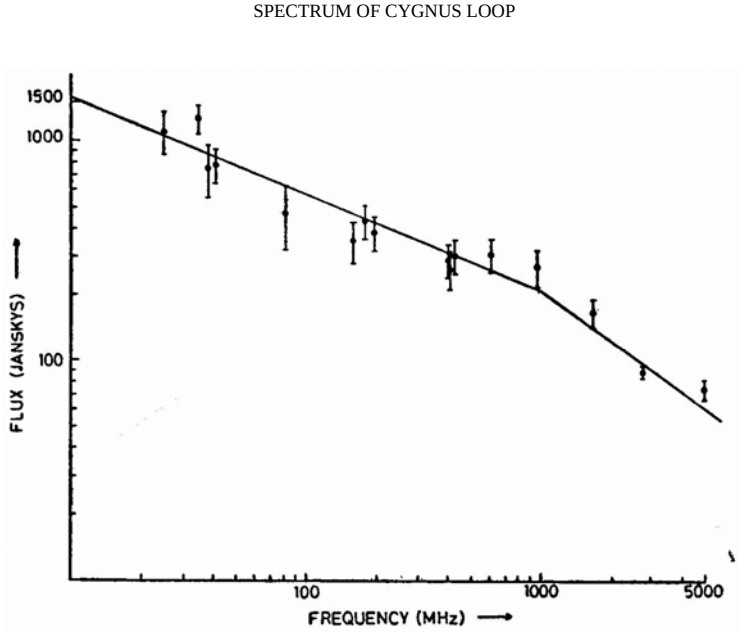

Figure 2. Spectrum of the integrated flux of Cygnus Loop.

shell thickness. It is also possible to estimate the compression factor from the observed ratio of ν_B/ν_s where ν_B and ν_s are the break frequencies in the spectra of the background radio emission and the radio emission from the supernova remnant. DeNoyer (1974) has derived relations between ν_B/ν_s and the compression behind shock, and hence the volume emissivity. The expected integrated flux density on this basis amounts to only 200 Jy at 34·5 MHz.

According to Dickel and Willis (1980) the material in the Cygnus Loop is still being heated by shocks and progressively cooling away from the shocked region by radiation of excited atomic lines. In order to maintain the pressure equilibrium within the shell the gas will contract and this compression will enhance both the magnetic field strength and the particle energies causing an increase in the radio emission as suggested by Duin and van der Laan (1975). Based on the observed densities and temperatures from optical and X-ray measurements, Dickel and Willis (1980) derived a total density enhancement due to the shock plus cooling of about 100, and the consequent increase in the volume emissivity in the filaments as 2×10^5 times the galactic background. In this case the observed integrated flux density at 34 MHz can be accounted for even if the volume occupied by the filaments is about one hundredth of the total volume of Cygnus Loop. Thus, it appears that unless one takes into account the compression due to cooling, the observed integrated flux density from the Cygnus Loop at 34·5 MHz can not be explained on the basis of enhanced volume emissivity of the interstellar medium.

The spectrum of the radio emission from region C is shown in Fig. 3. It can be seen that the slope of the spectrum changes at a frequency around 400 MHz. The spectral index is — 0·24 ± 0·10 in the frequency range 25 to 400 MHz and increases

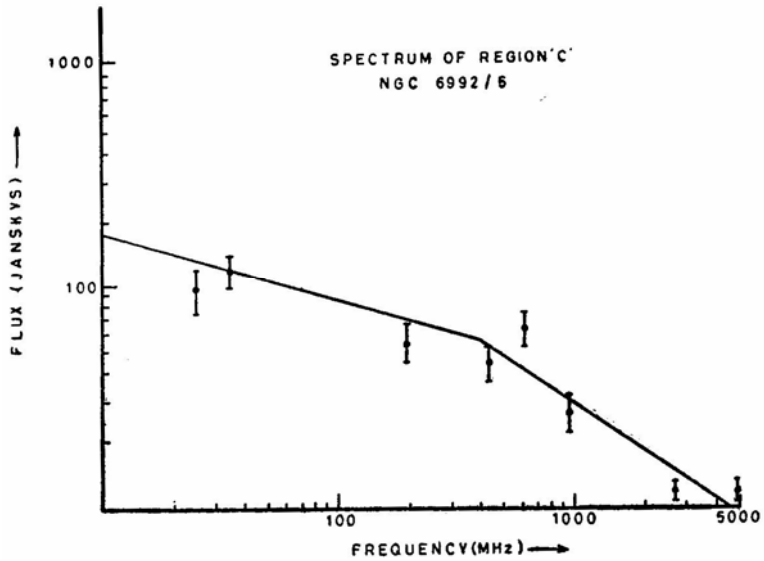

Figure 3. Spectrum of Region C (NGC 6992/5).

to — 0·75 ± 0·15 in the range 400 to 5000 MHz. The radio emission from this region is closely associated with the optical nebulosities NGC 6992/5. This close association suggests that the radio emission may be produced by free-free transitions in the ionized gas. The absence of any polarization at wavelengths above 11 cm (Kundu 1969; Moffat 1971) supports this point of view. However, as already shown by Moffat (1971), there is no evidence for any flattening of the spectrum at high frequencies which would occur if a significant part of the radiation were thermal; the emission must therefore be synchrotron radiation. Kundu and Becker (1972) detected strong polarization at 6 cm from this region and interpreted the lack of polarization at longer wavelengths as due to large and variable rotation measure. Kundu and Velusamy (1967) concluded that the spectrum of this region is flat between 38 MHz and 408 MHz. This result depended on an uncertain value of flux density at 38 MHz measured by Kenderdine (1963). A recent measurement of the flux density from this region by Abranin, Bazelyan and Goncharov (1977) showed that the spectral index is – 0·31 between 25 MHz and 1000 MHz. As shown above we find that the spectral index is – 0·24 ± 0·10 in this range if we include our measurement and that of Abranin, Bazelyan and Goncharov (1977) but omit the 38 MHz point due to Kenderdine (1963). It is now clear that the low frequency spectrum of region C is not flat below 200 MHz.

The radio emission from region B is associated with the optical nebulosity NGC 6960. Here the correspondence between the optical and the radio features is not very close as shown by the high frequency maps. The radio spectrum of this region is shown in Fig. 4 and it is similar to that of region C. The change in the slope of the spectrum occurs at a frequency around 1 GHz. The spectral index in the low frequency range is – 0·45 ± 0·10 and that in the high frequency range is – 0·84 ± 0·23. The shape of the spectrum of the region A where the radio emission is associated with the optical nebulosity NGC 6974 shown in Fig. 5 is different from that of the above

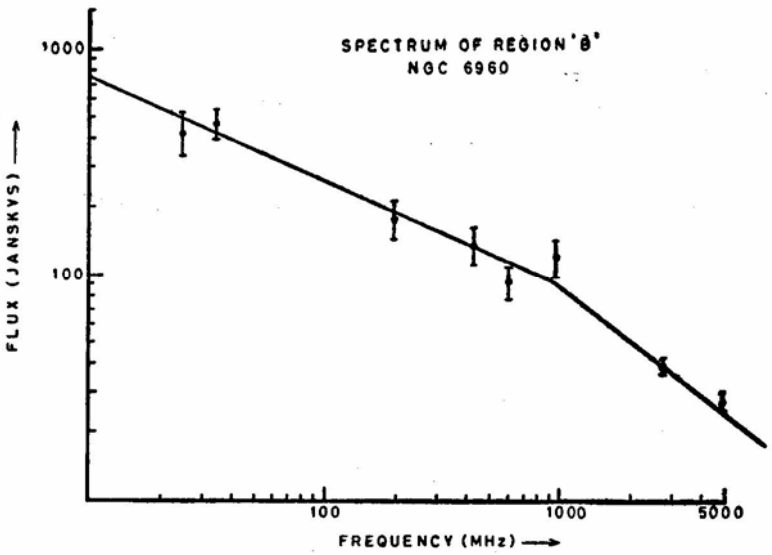

Figure 4. Spectrum of Region B (NGC 6960).

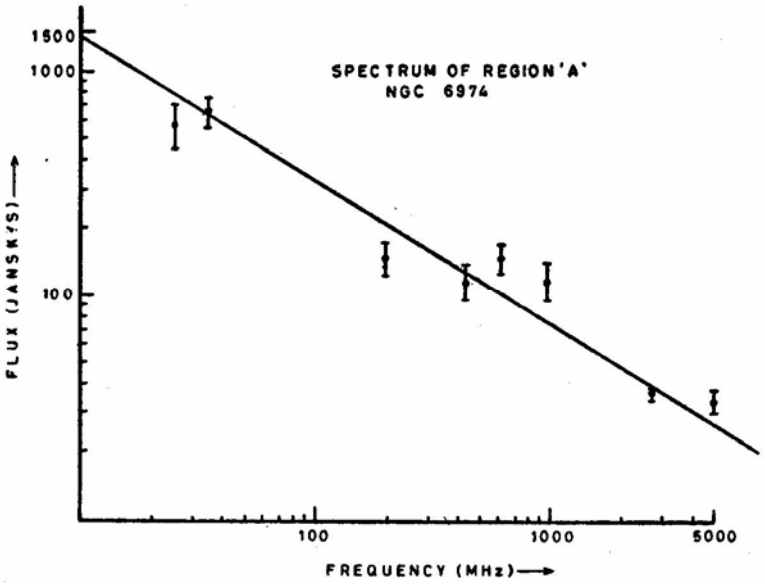

Figure 5. Spectrum of Region A (NGC 6974).

two regions. Here, it is straight without a break in the entire frequency range of 25 MHz to 5000 MHz with a spectral index of – 0·59 ± 0·05. As noted previously, the radio structure of this region appears to be different at high and low frequencies. It is interesting to note that in the region C where there is a well formed shell, the break frequency (≃ 400 MHz) and the spectral index (– 0·24) are both small. In

the region B where the shell is broken, the break frequency moves to a higher value ($\simeq$ 1000 MHz) and the spectrum is steeper with an index of – 0·45.

In the region A where there is no evidence for shell structure, the spectrum is straight without a break in the entire frequency range. This might imply that the radio emission from regions B and C have a common origin, and could be due to compressed cosmic ray electrons and the interstellar magnetic fields. The radio emission from region A on the other hand might be due to the relativistic electrons produced in the supernova remnant itself. It is interesting to note that strong polarization of about 15–25 per cent was detected in the region A by Kundu (1969), Moffat (1971) and Kundu and Becker (1972). The difference in break frequencies in the regions B and C can be attributed to the differing magnetic field strengths. The breaks in the spectra can also be attributed to synchrotron radiation losses. In this case it is possible to estimate the age of the nebula using the expressions derived by Kardashev (1962) relating the break frequency to the magnetic field strength and time. According to Dickel and Willis (1980) the compressed magnetic field strength is about 2×10^{-4} gauss in the filaments. For a break frequency of 1 GHz, this gives a time scale of 2×10^5 yr which is several times the age of the Cygnus Loop. Dickel and Willis (1980) propose that after compression, different parts of the shell can encounter interstellar media of varying densities. If parts of the shell encounter a less dense medium, they may then re-expand reducing the particle energy quickly. Such a process would predict that the spectral breaks would occur at different frequencies for different positions in the remnant. The difference in break frequencies of regions B and C could be due to this reason.

6. Conclusions

(1) The enhanced volume emissivity of the interstellar medium resulting from the compression by the supernova shock alone is not adequate to explain the observed integrated flux density at 34·5 MHz. One has to consider the additional compression due to the cooling of the material heated by the shocks.

(2) The low frequency spectrum of region C (NGC 6992/5) is not flat below 200 MHz.

(3) Both the regions B (NGC 6960) and C (NGC 6992/5) exhibit breaks in their spectra around 1000 MHz and 400 MHz respectively while the spectrum of region A (NGC 6974) is straight in the entire frequency range 25 to 5000 MHz.

(4) The difference in the break frequencies in the regions B and C can be due to different magnetic field strengths in these regions if their spectra are just a reflection of the background radio spectrum of our galaxy. Alternatively, if the breaks in the spectra are due to synchrotron radiation losses, then their difference in the two regions implies dissimilar ambient interstellar densities.

Acknowledgement

The low frequency Radio Astronomy Project at Gauribidanur owes its existence to the keen interest and continuous support of M. K. V. Bappu and V. Radhakrishnan. We would also like to thank V. Radhakrishnan for advice and criticism.

References

Abranin, E. P., Bazelyan, L. L., Goncharov, N.Yu. 1977, *Soviet. Astr.*, **21,** 441.
DeNoyer, L. K. 1974, *Astr. J.*, **79**, 1253.
Dickel, J. R., Willis, A. G. 1980, *Astr. Astrophys.*, **85,** 55.
Duin, R. M., van der Laan, H., 1975, *Astr. Astrophys.*, **40**, 111.
Högbom, J. A. 1974, *Astr. Astrophys. Suppl. Ser.*, **15**, 417.
Jones, B. B. 1973, *Ph D Thesis*, University of Sydney, Australia.
Kardashev, N. S. 1962, *Soviet Astr.*, **6**, 317.
Keen, N. J., Wilson, W. E., Haslam, C. G. T., Graham, D. A., Thomasson, P. 1973, *Astr. Astrophys.*, **28**, 197.
Kellermann, K. I., Pauliny-Toth, I. I. K., Williams, P. J. S. 1969, *Astrophys. J.*, **157**,1.
Kenderdine, S. 1963, *Mon. Not. R. astr. Soc.*, **126**, 55.
Kundu, M. R. 1969, *Astrophys. J.*, **158**, L103.
Kundu, M. R., Becker, R. H. 1972, *Astr. J.*, **77,** 459.
Kundu, M. R., Velusamy, T. 1967, *Ann. Astrophys.*, **30**, 723.
Minkowski, R. 1958, *Rev. mod. Phys.*, **30**,1048.
Moffat, P. H. 1971, *Mon. Not. R. astr. Soc.*, **153**, 401.
Roger, R. S., Bridle, A. H., Costain, C. H. 1973, *Astr. J.*, **78**,1030.
van der Laan, H. 1962, *Mon. Not. R. astr. Soc.*, **124**,125.

J. Astrophys. Astr. (1981) **2**, 349–363

Changes in Sizes and Shapes of Spherical Galaxies in Head-on Collisions

*Farooq Ahmed *Indian Institute of Astrophysics, Bangalore 560034 and Centre of Advanced Study in Astronomy, Osmania University, Hyderabad 500007*
Saleh Mohammed Alladin *Centre of Advanced Study in Astronomy, Osmania University, Hyderabad 500007*

Received 1981 March 9; accepted 1981 October 11

Abstract. Head-on collisions of two identical spherical galaxies are studied for two initial velocities (1) nearly equal to and (2) greater than the capture velocity. Orbits of about 500 representative stars are computed taking into account the effects of dynamical friction in the motion of the galaxies. From the computer studies the changes in the structure of the galaxies are deduced. The galaxies contract at closest approach and expand as they recede from each other. When the initial velocity is nearly equal to the capture velocity, the mean radius expands to almost double its size and the galaxies have a prolate structure until the closest approach with the longer axis in the direction of motion. The prolate structure is destroyed as the galaxies recede. For larger collision velocity ($V \sim 1{\cdot}5\ V_{\rm cap}$), the mean radius expands by 50 per cent and the galaxies are prolate until the closest approach and distinctly oblate after the collision. The fractional increase in the binding energy is 0·46 in the first case and 0·30 in the second case.

Key words: stellar dynamics—galaxy collisions—tidal interaction

1. Introduction

A study of the dynamics of head-on collisions of galaxies is of interest for several reasons. A head-on collision provides useful upper limits for the effects of tidal forces. The symmetry of the galaxies with respect to the direction of motion, reduces the computations. Recent cosmological N-body simulations carried out by Aarseth and Fall (1980) show that the merging of galaxies occurs mainly from marginally bound galaxies in nearly head-on collisions.

*Present address: Department of Physics, Kashmir University, Srinagar 190006

In an earlier paper (Ahmed and Alladin 1981, hereafter referred to as Paper I) we discussed the energy transfer from the translational motion of the galaxies to the internal motions of the stars in head-on collisions of two identical spherical galaxies with the initial velocities equal to and not much greater than the capture velocity (defined as in Alladin, Potdar and Sastry 1975), assuming that the stars remain stationary during the encounter (impulsive approximation). It was noted that most of the energy transfer took place close to the position of closest approach, the effect in the second half of the orbit being double that of the first. It has been shown by other workers that for smaller velocities, dynamical friction leads to a rapid merger of the two galaxies (Toomre 1974; Van Albada and Van Gorkom 1977; White 1978). Tremaine (1981) reviews the work on galaxy mergers.

In the present paper we shall obtain deeper insight into the changes in the structure of colliding galaxies from a study of the orbits of stars. As in Paper I, we shall restrict ourselves to velocities of collisions that are not too small to result in a rapid merger of the two galaxies and yet not too large so as to produce negligible tidal effects. In particular it will be our aim to investigate how a change in the collision velocity of the galaxies would affect the sizes and shapes of initially spherical galaxies.

Because of the symmetry of the galaxies with respect to the direction of motion in a head-on collision we should expect spherical galaxies to become either prolate or oblate but not triaxial. It can be seen qualitatively from a consideration of the shapes of the zero velocity surfaces in the restricted three body problem that in the limiting case of negligible collision velocity, the spherical galaxies would first become prolate with the major axis along the direction of motion. Finally the galaxies would merge. Simulations of galaxy mergers by White (1978) and Villumsen (1980) indeed show that merger remnants resulting from head-on collisions are prolate in shape. On the other hand for large collision velocities, one can get an idea of the shapes of the galaxies after the collision from the impulsive approximation, which indicates that the velocity increment of a star over the entire collision is in a direction perpendicular to the direction of relative motion of the galaxies, and consequently after the collision, the galaxies become oblate with the minor axis along the direction of motion of the galaxies. The final shapes would be quite complicated in detail, and the description of the final structures in terms of prolateness and oblateness is therefore a rather crude one.

We obtain the equations of motion for a star in a galaxy belonging to a double galaxy system, taking into account the effects of dynamical friction in reducing the translational velocity of the galaxies and use these equations to compute the orbits of about 500 stars chosen as representative of the test galaxy. From the stellar orbits, the changes in mass distribution and shape of the galaxies during the collision are obtained. The subsequent dynamical evolution of the colliding galaxies is deduced from the virial theorem.

2. Equations of motion of a star in a system of colliding galaxies

We represent the density distribution of each of the colliding galaxies by that of a polytropic sphere of index $n=4$, and radius R, and we derive the forces between them by assuming that it is unchanged during the encounter. The potential $\mathscr{V}$ and

the interaction potential energy W for these cofigurations have been given by Limber (1961) and Potdar and Ballabh (1974) respectively. We consider the tidal effects of the perturbing galaxy of mass M_1 on the test galaxy of mass M_2 Let the origin of the coordinate system be chosen at the centre of M_2. Let r (x, y, z) denote the position of the centre of M_1 and r' (x' y' z') the position of a representative star in M_2. Let r″=r —r′. The motion of a star in M_2 is given by

$$\ddot{\mathbf{r}}' = -\nabla' \mathscr{V}_2 + \nabla'' \mathscr{V}_1 - \frac{1}{M_2}\nabla W \tag{1}$$

where the first term on the right hand side represents the gravitational attraction of the parent galaxy M_2 on the star while the second and third terms together give the tidal force due to the perturbing galaxy M_1 . $\mathscr{V}$ and W may be expressed in terms of the functions Φ and X respectively as in Paper I. The equations of motion of a star in Cartesian co-ordinates for a head-on collision in the z-direction hence become

$$\ddot{x}' = \frac{GM_2}{R_2^3}\left(\frac{x'}{s'}\frac{d\Phi_2}{ds'}\right) + \frac{GM_1}{\epsilon^3 R_2^3}\left(\frac{x'}{s''}\frac{d\Phi_1}{ds''}\right), \tag{2}$$

$$\ddot{y}' = \frac{GM_2}{R_2^3}\left(\frac{y'}{s'}\frac{d\Phi_2}{ds'}\right) + \frac{GM_1}{\epsilon^3 R_2^3}\left(\frac{y'}{s''}\frac{d\Phi_1}{ds''}\right), \tag{3}$$

$$\ddot{z}' = \frac{GM_2}{R_2^3}\left(\frac{z'}{s'}\frac{d\Phi_2}{ds'}\right) - \frac{GM_1}{\epsilon^3 R_2^3}\left(\frac{z-z'}{s''}\frac{d\Phi_1}{ds''}\right) + \frac{GM_1}{R_2^3}\left(\frac{z}{s}\frac{dX}{ds}\right) \tag{4}$$

where $s'=r'/R_2$, $s'' = r''/R_1$, $s = r/R_2$, and $\in = R_1/R_2$.

The equation of the relative motion of the two galaxies with separation r is given by

$$V = \frac{dr}{dt} = \left[\frac{2}{\mu}\{E_i - W(r) - \Delta U_1(r) - \Delta U_2(r)\}\right]^{1/2} \tag{5}$$

where μ is the reduced mass and E_I is the initial translational energy $\Delta U_1(r)$ and $\Delta U_2(r)$ are changes in the internal energies of the two galaxies. Equation (5) takes into account the deceleration of the translational motion of the galaxies due to dynamical friction. Equation (5) is solved as discussed in Paper I. The above treatment takes into account the changes in the force fields due to superposition effects arising from the overlap of galaxies but not due to changes in the structures of galaxies arising from tidal distortion. A more accurate treatment of the problem should also take the latter into account.

3. Initial conditions

We study head-on collisions between two identical spherical galaxies. Let M_1 approach M_2 from $z = -3R$. As shown in Paper I the integrated tidal effects of the

galaxies on each other are very small beyond this distance. As in Paper I we choose the units of distance, mass and gravitational constant so that R= 1, M = 1, G = 0·04302 respectively. For $M = 10^{11}\ M_{\odot}$, R=10 kpc, the unit of time is 1.0×10^7 years and the unit of velocity is 1000 km s^{-1}.

Numerical calculations are performed for two values of relative velocities of the galaxies, namely 0·7 and 1·0. V_t — 0·7 is nearly the capture velocity of the galaxies, while V_t = 1·0 is a case wherein the galaxies recede to infinite distance with significant change in their structure after the encounter. We shall refer to the collisions with these two initial velocities as 'slow' and 'fast' collisions, Models S and F respectively. It is assumed that initially all stars move in circular orbits and their directions of motion have circular symmetry. Representative stars are chosen at median radius a = 0·135 and at distances a = 0·1, 0·2, 0·3, 0·4, 0·5 and 0·6. We assign to these shell numbers 1, 2, 3, 4, 5 and 6. In our model (polytrope n = 4) the mass beyond 0·6 is less than 0.1 per cent. Hence R_0 = 0·6 may be regarded as a reasonable outer radius of the galaxy. At each distance a we chose 72 stars. Because of the symmetry properties of a head-on collision about the direction of motion, orbits of only 25 stars at each distance a have to be computed and those of the remaining stars can be obtained from the symmetry considerations.

The positions and the velocities of the stars in the galaxy are obtained by integrating the differential equations (2), (3) and (4) numerically. We however stop the orbit computations when z = + 2. At this stage the fractional change in the potential energy of the galaxy is nearly 0.3 which implies that the mass distribution of the galaxies can no longer be well represented by that of a polytrope of index n=4.

4. Changes in the forms of galaxies

The positions of the stars initially moving in the x–y plane at various separations of the two galaxies are shown in Figs 1 and 2, for the two collision velocities 0·7 and 1·0 respectively. It can be seen that the shape of the galaxy does not change much until the galaxies are at their closest approach, but a noticeable contraction in the galaxy is clearly discernible soon after the closest approach. The contraction is less in the case of the faster collision. The results of N-body simulations of van Albada and van Gorkom (1977), White (1978), Miller and Smith (1980) also show that galaxies momentarily contract just after the closest approach and then expand. As galaxies recede the contraction is followed by expansion, and some of the kinetic energy is converted into potential energy.

Another note-worthy point is that the various shells of stars expand at different times; the inner shells expand first and the outer shells later giving rise to fluctuations in the original density distribution of the galaxy. In Model S when z = +1, a zone of avoidance separating the stars originally at less than or equal to the median radius from the remaining stars is very conspicuous. When z = + 2, the stars originally at less than or equal to 0·2 are well separated from those at 0·3 and beyond, while stars at 0·3, 0·4, 0·5 and 0·6 crowd together at the same distance from the centre. In Model F the expansion is smaller. The oscillations in the positions of the stars in the case of the slow collision are illustrated in Fig. 3. Lynds and Toomre (1976) have studied the effects of a head-on collision on a disk galaxy and have concluded that a ring galaxy such as II Hz 4 could be formed in this manner. The remarkable

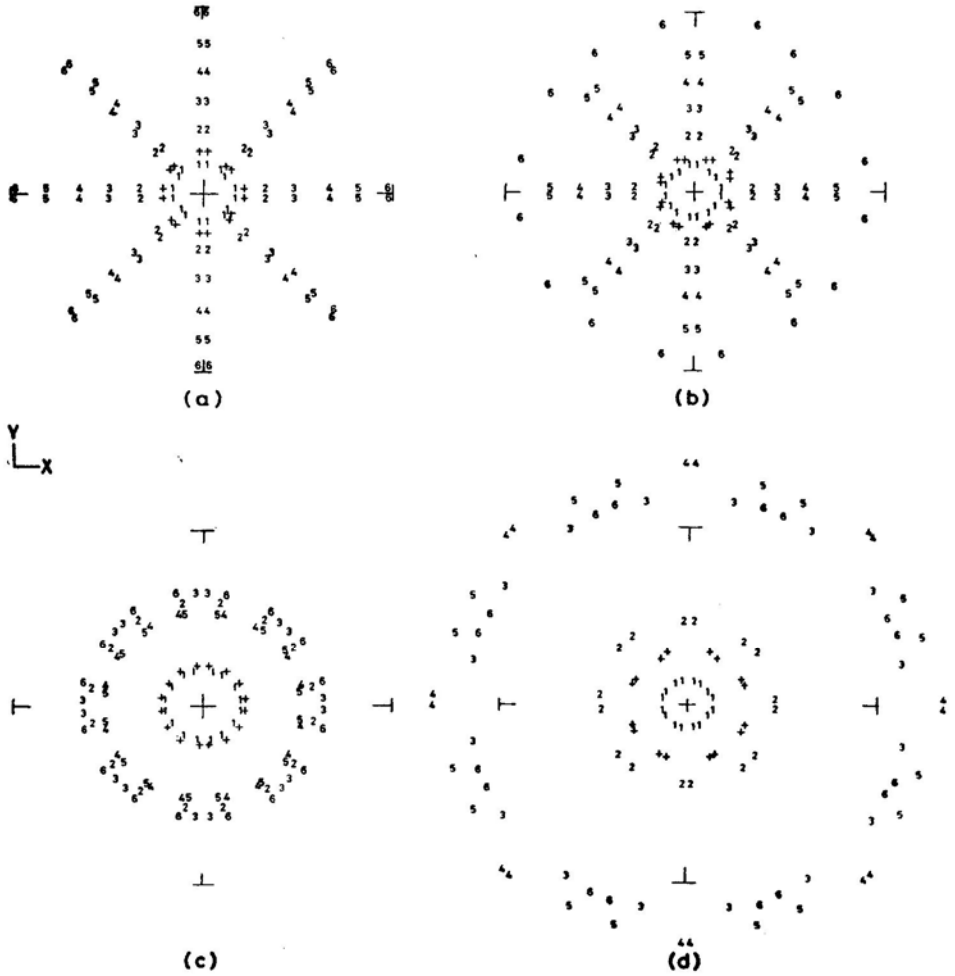

Figure 1. Positions of stars originally moving in the *x–y* plane in Model S (a) $z = -3$ ($t = 0$) (b) $z = 0$ (t=3·9) (c) $z = +1$ ($t = 5{\cdot}5$) (d) $z = +2$ ($t = 8{\cdot}5$). The numbers 1, 2 ... 6 represent stars initially at 0.1, 0·2 ... 0·6 shells respectively, and + denotes stars at median radius 0.135.

Cartwheel galaxy (A0035) was probably formed as a result of a nearly head-on collision between a disk galaxy and a spherical galaxy (Toomre 1978). In the sphere-sphere collision considered here, stars crowd together in shells (instead of rings) which are separated by regions wherein the number density of stars is small.

Figs 4 and 5 show the positions of stars originally moving in the *x–z* plane at various times. The positions of the stars in the *y–z* plane would be similar (because of the symmetry about the *z*-axis). In Fig. 6 we show the projections of all the stars in the *x–z* plane after the collision for $V_t = 0{\cdot}7$. It may be noted that until the instant of closest approach the galaxies get elongated in the *z*-direction, the maximum effect being for the outermost stars. The galaxies thus become prolate. As the galaxies recede after the closest approach, they expand appreciably

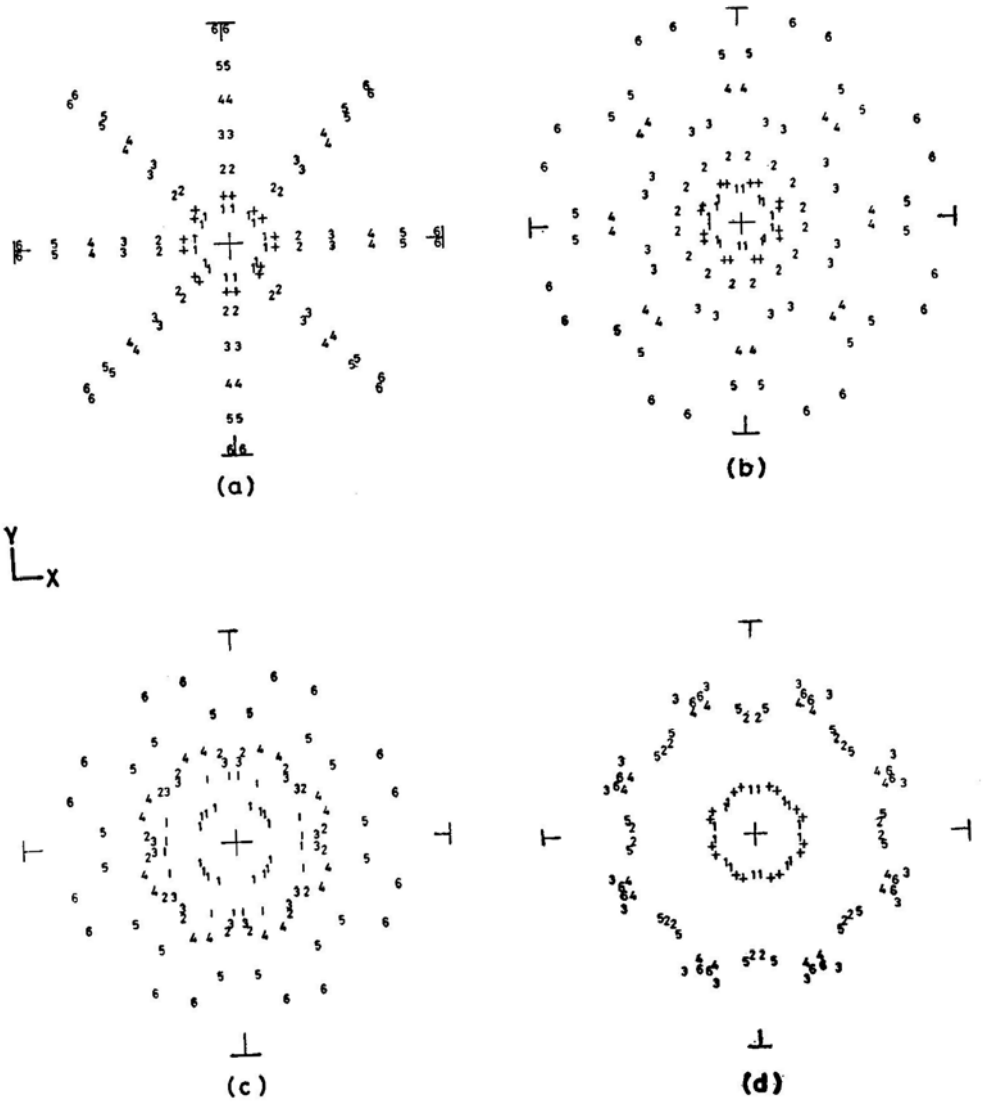

Figure 2. Positions of stars originally moving in the *x-y* plane in Model F (a) $z = -3$ ($t = 0$) (b) $z = 0$ ($t = 2{\cdot}8$) (c) $z = +1$ ($t = 3{\cdot}8$) (d) $z = +2$($t = 4.9$).

in the directions perpendicular to the *z*-axis, so that the prolate structure is destroyed and the galaxies tend to become oblate. Spherical galaxies undergoing a head-on collision would be prolate until the closest approach and, if they do not merge, they would generally be oblate after the collision. It appears from observations that elliptical galaxies have a preference for oblate structure (Marchant and Olson 1979).

An idea of the differential expansion of the galaxy can also be obtained by calculateing the average expansion of the orbits of stars at various distances from the centre. We have divided the stars into seven groups depending upon their initial distance from the centre. In Tables 1 and 2 the mean coordinates of each of these groups are given at various separations of the two galaxies for two velocities 0·7 and 1·0

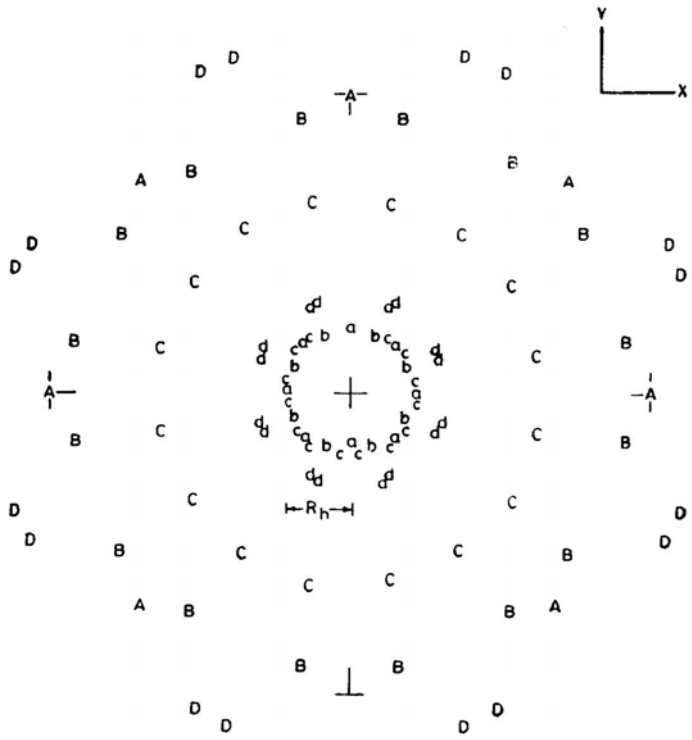

Figure 3. Positions of stars initially moving in the *x–y* plane at median radius and full radius at various separations in Model S. Capital letters, A, B, C, D denote the positions of stars initially at R_0 = 0·6 at separations z = – 3 (t = 0), z = 0 (t = 3·9), z = +1 (t = 5.5), z = + 2 (t = 8·5). Small letters a, b, c, d denote the corresponding positions of stars at median radius R_h.

respectively. Since $\langle \mid x' \mid \rangle = \langle \mid y' \mid \rangle$ by symmetry, only $\langle \mid x' \mid \rangle$ is listed. The mean position $\langle r' \rangle$ is a good measure of the over-all expansion of each group and the ratio $\langle |z'| \rangle \mid \langle |x'| \rangle$ is a useful measure of the departure from the spherical symmetry. Our results indicate that galaxies become prolate (or rather pear-shaped) until the closest approach. The ratios $\langle \mid z' \mid \rangle \mid \langle \mid x' \mid \rangle$ for the shell averaged over the whole system are 1·35 and 1·15 for slow and fast collisions respectively. At the end of the collision the corresponding ratios are 0.96 and 0.79. It can be seen from the table that the slow collision gives rise to rather large fluctuations in the oblateness. The results also show that the post-collision oblateness of the galaxies increases with the speed of the collision.

The prolate structure of the galaxies acquired in the first half of the collision tends to get destroyed in the second half of the collision because the z-component of the tidal acceleration on a star gets reversed. It can be deduced from the analysis given by Toomre (1977) that the velocity increment of a star in the z direction, V_{II}, would, be zero for the entire orbit.

As we go from the case of a head-on collision to the case of an off-centre collision, the prolate or the oblate structures would pass over to triaxial structures. Our slow collision case may be compared with the corresponding slow off-centre

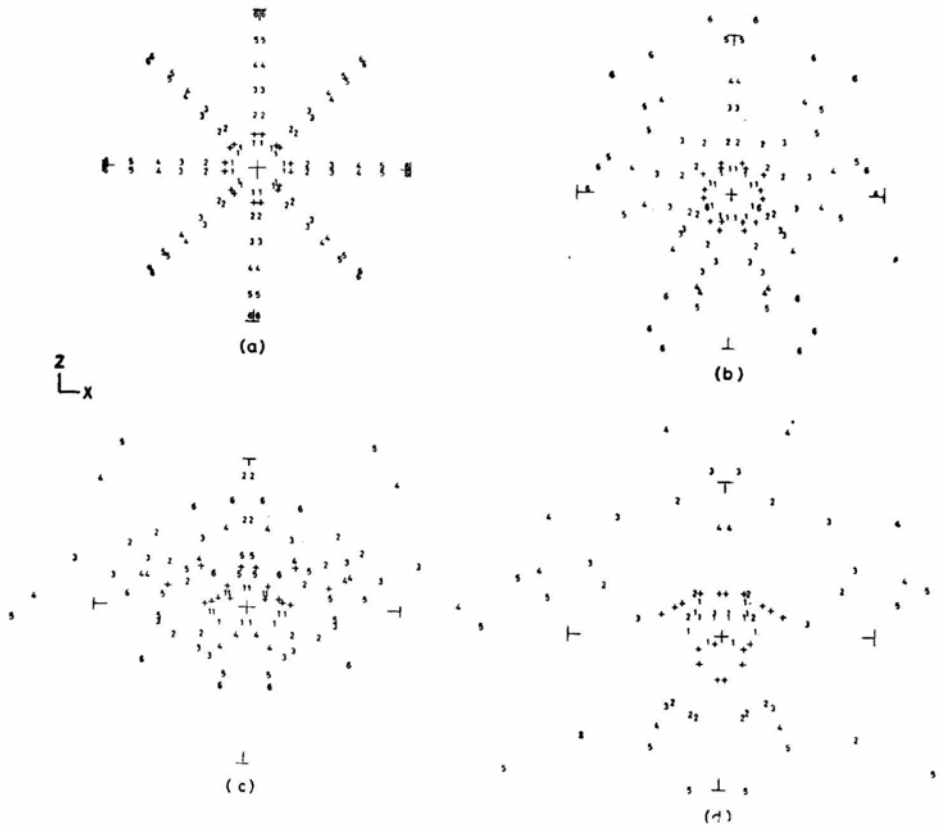

Figure 4. Positions of stars originally moving in the *x*-*z* plane, in Model S (a) $z = -3$ ($t = 0$), (b) $z = 0$ ($t = 3{\cdot}9$), (c) $z = +1$ ($t = 5.5$), (d) $z = +2$ ($t = 8{\cdot}5$).

Table 1. The mean co-ordinates of stars at various separations in Model S.

z	Initial shell No.	$\langle\|x'\|\rangle$	$\langle\|z'\|\rangle$	$\langle r\rangle$	$\langle\|z'\|\rangle/\langle\|x'\|\rangle$
−3	1	0·042	0·042	0·074	1·00
	2	0·085	0·085	0·147	1·00
	3	0·128	0·128	0·220	1·00
	4	0·170	0·170	0·295	1·00
	5	0·213	0·213	0·368	1·00
	6	0·255	0·255	0·442	1·00
0	1	0·032	0·047	0·063	1·46
	2	0·064	0·092	0·126	1·44
	3	0·099	0·131	0·225	1·32
	4	0·137	0·173	0·254	1·26
	5	0·202	0·283	0·400	1·40
	6	0·231	0·254	0·438	1·10
+2	1	0·050	0·043	0·070	0·86
	2	0·141	0·204	0·281	1·45
	3	0·314	0·249	0·507	0·79
	4	0·438	0·325	0·697	0·74
	5	0·308	0·346	0·554	1·12
	6	0·378	0·299	0·610	0·79

collision case (Model D) of White (1978). In the slow head-on collision studied by us, the galaxies are neither prolate nor distinctly oblate after the collision. White's Model D also does not show much departure from spherical shape, the final

Table 2. The mean co-ordinates of stars at various separations in Model F.

z	Initial Shell No.	$\langle\|x'\|\rangle$	$\langle\|z'\|\rangle$	$\langle r\rangle$	$\langle\|z'\|\rangle/\langle\|x'\|\rangle$
−3	1	0·042	0·042	0·074	1·00
	2	0·085	0·085	0·147	1·00
	3	0·128	0·128	0·220	1·00
	4	0·170	0·170	0·295	1·00
	5	0·213	0·213	0·368	1·00
	6	0·255	0·255	0·442	1·00
0	1	0·043	0·049	0·063	1·14
	2	0·083	0·128	0·167	1·54
	3	0·119	0·130	0·209	1·09
	4	0·170	0·214	0·317	1·26
	5	0·181	0·197	0·319	1·09
	6	0·232	0·280	0·428	1·21
+2	1	0·050	0·049	0·077	0·98
	2	0·160	0·111	0·248	0·69
	3	0·208	0·128	0·319	0·61
	4	0·194	0·141	0·304	0·73
	5	0·163	0·136	0·264	0·83
	6	0·190	0·182	0·324	0·96

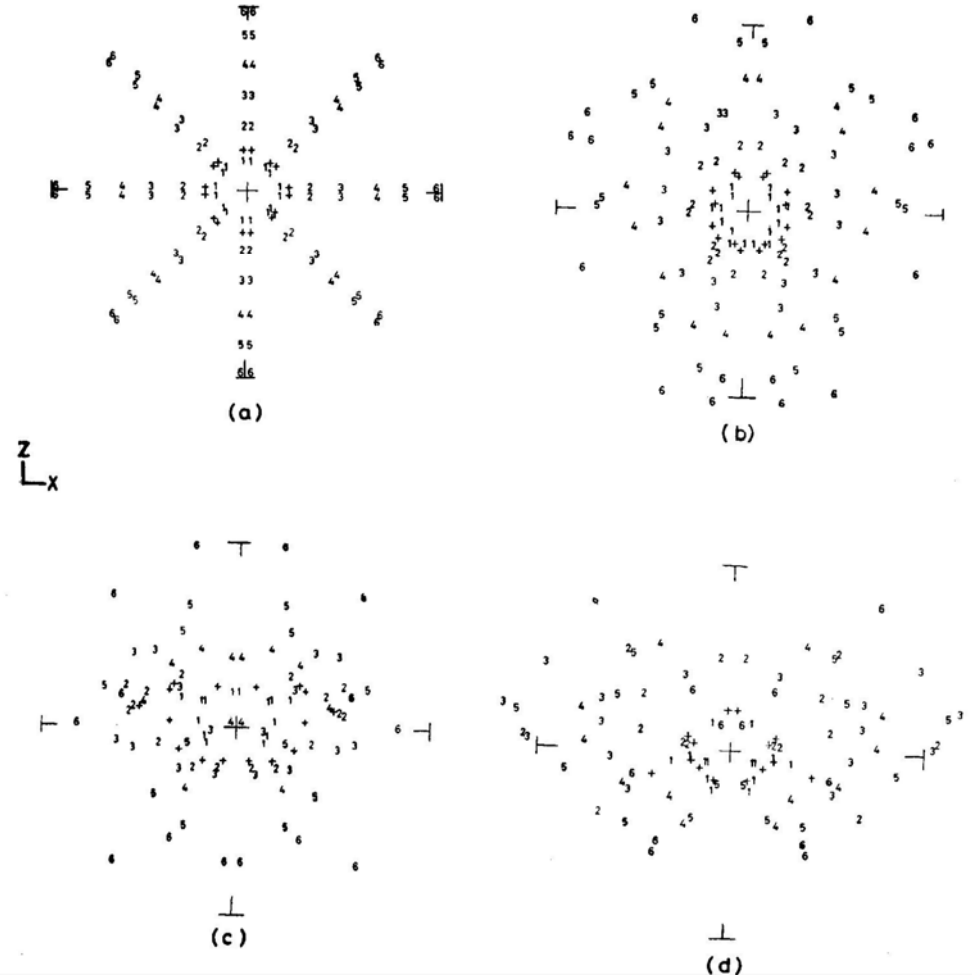

Figure 5. Positions of stars originally moving with the *x*-*z* plane, in Model F (a) $z = -3 (t = 0)$ (b) $z = 0$ ($t = 2{\cdot}8$), (c) $z = +1$ ($t = 3{\cdot}8$), (d) $z = +2$ ($t = 4.9$).

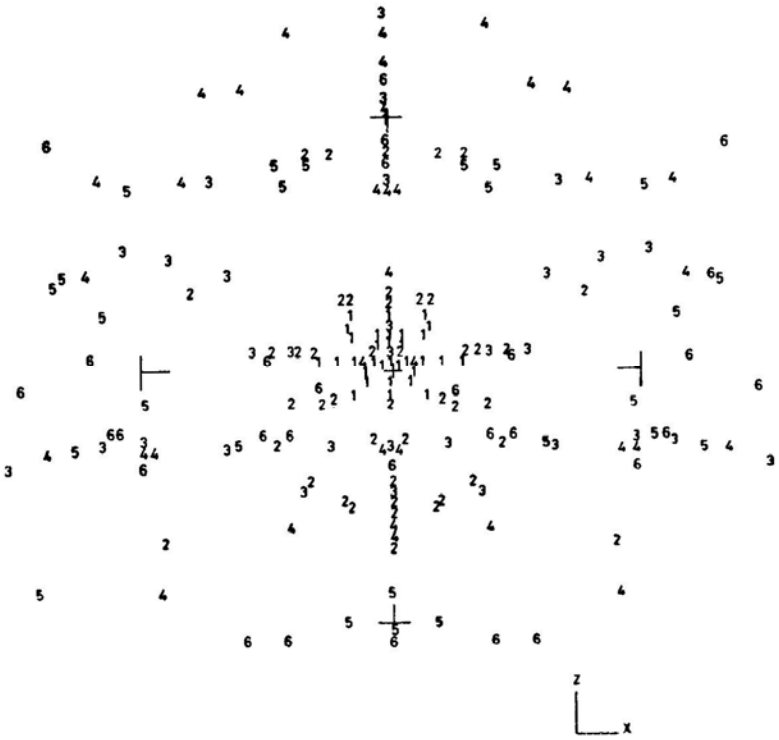

Figure 6. Projection of all the stars in the x–z plane at $z = +2$ ($t = 8{\cdot}5$) in Model S.

structures being ellipsoidal with the axes in the ratio 1:1.05:0.89 the smallest axis being perpendicular to the orbital plane and the biggest being perpendicular to the direction of the initial separation of the two galaxies in the orbital plane.

5. Changes in mass distribution during the encounter

During the encounter the distribution of stars is drastically changed as shown in Tables 3 and 4. Each star is assigned a weight equal to the mass of the shell divided by the number of stars in the shell. The mass distribution of the galaxy after the encounter is obtained from the distribution of stars shown in Tables 3 and 4. The mass within a radius 0.05 for our model is 0·0576. The results of orbit computations show that this sphere contains the same mass throughout the encounter. The mass distribution is essentially unchanged until the closest approach of the two galaxies, but there is a considerable change afterwards particularly in the outer parts. In the slow collision, the median radius changes during the collision from 0·135 to 0·160, the radius containing 75 per cent of the mass changes from 0·20 to 0·32 and the radius containing 95 per cent of the mass expands from 0·35 to 0·85. The subsequent expansion of the galaxies is discussed in Section 8.

Table 3. Distribution of star in a galaxy at z = + in model S.

Shell radii Inner — Outer	Initial Shell No.					
	1	2	3	4	5	6
< 0·05	—	—	—	—	—	—
0·05 — 0·15	60	—	—	—	—	—
0·15 — 0·25	12	12	—	—	—	—
0·25 — 0·35	—	44	8	—	—	—
0·35 — 0·45	—	—	4	8	—	—
0·45 — 0·55	—	12	—	—	8	—
0·55 — 0·65	—	—	20	—	4	2
0·65 — 0·75	—	4	16	—	8	30
0·75 — 0·85	—	—	—	40	32	12
> 0·85	—	—	20	12	4	12
Escaping Stars	—	—	4	12	16	16

Table 4. Distribution of stars in a galaxy at z = + 2 in Model F.

Shell radii Inner — Outer	Initial Shell No.					
	1	2	3	4	5	6
< 0·05	—	—	—	—	—	—
0·05 — 0·15	68	8	—	—	8	4
0·15 — 0·25	4	5	—	12	4	4
0·25 — 0·35	—	24	4	4	16	16
0·35 — 0·45	—	24	40	36	28	28
0·45 — 0·55	—	8	8	12	4	—
0·55 — 0·65	—	4	12	—	—	—
0·65 — 0·75	—	—	—	—	—	8
0·75 — 0·85	—	—	—	—	—	—
> 0·85	—	—	—	—	—	—
Escaping Stars	—	—	8	8	12	12

6. Mass escape and formation of halo

The mass escape from the galaxies during a collision is an important aspect of the study. We find that after the encounter about 1·5 per cent of the mass escapes in Model S and less than 1 per cent in Model F. Dekel, Lecar and Shaham (1980) performed N-body simulations of colliding galaxies which also includes the case of head-on collisions. Their model is less centrally concentrated than ours. Their results for identical spherical galaxies with collision velocity slightly greater than the capture velocity and with circular stellar orbits (B7 model) give 3 per cent for the fractional mass escape. This compares well with our result. Our results are also in good agreement with those of van. Albada and van Gorkom (1977), who obtained about 1 per cent of mass escape from the galaxies (represented by a polytrope n = 3) during a head-on collision with $V_i \simeq 1$ (in our units). Using isothermal model for galaxies, White (1978) also finds that only a small fraction of the total mass escapes in a head-on collision. In our model we have considered only circular motions of the stars. Models of galaxies consisting of elongated orbits of stars give greater mass loss (Gallagher and Ostriker 1972; Richstone 1975; Dekel, Lecar and Shaham 1980).

Stars having negative energies close to zero are flung into large orbits and contribute to the formation of the halo. The energy of the most loosely bound stars before the collision is – 0·036 (in our units). In Model S stars with energies in the range

0 to – 0.036 have 5·4 per cent of the total mass, while in Model F the percentage is 1·4. These stars will form the halo of the galaxy after the encounter.

7. Change in binding energy

The kinetic energy of a galaxy is given by

$$T = T_0 + \frac{M}{2} \sum_{K=1}^{S} \sum_{J=1}^{N} W_K \, V'^2_{JK} \tag{6}$$

where V'_{JK} is the velocity of the Jth star in the Kth shell, W_K is its weight, S and N are the total number of shells and the total number of stars in the shell respectively. T_0 is the kinetic energy of stars lying within the radius 0·05 and is given by

$$T_0 = \frac{G}{2} \int_0^{0.05} \frac{M(r')}{r'} \left(\frac{dM}{dr'}\right) dr'. \tag{7}$$

This is less than 0.001, and is not changed during the encounter.

The self potential energy of a spherical stellar system is obtained from the mass distribution and is given by the relation (Chandrasekhar 1943)

$$\Omega = -G \int_0^{R} \frac{M(r')}{r'} \left(\frac{dM}{dr'}\right) dr'. \tag{8}$$

The binding energy of the galaxy is obtained from

$$U = T + \Omega. \tag{9}$$

The values of the kinetic, potential and binding energies of the galaxy initially and after the encounter (z = + 2) are given in Table 5. The corresponding values of binding energy U_I, obtained in Paper I are also given. Dekel, Lecar and, Shaham (1980) estimate fractional change in internal energy $\Delta U/|U|$ (For B7 model) as 0·56, which agrees well with our value of 0.46 for Model S. The

Table 5. Energies of galaxies before and after the encounter

Energies	Initial $z = -3$	$z = +2$ Model S	$z = +2$ Model F
T	0·063	0·057	0·046
Ω	−0·126	−0·091	−0·090
U	−0·063	−0·034	−0·044
$(\Delta U/\|U\|)$	0	0·460	0·301
U_I	−0·063	−0·009	−0·030
$(\Delta U/\|U\|)_I$	0	0·851	0·522

comparison of these results with, those obtained in Paper I with the assumption that the stars remain stationary but the velocity of the galaxies is reduced due to dynamical friction indicates that the latter treatment overestimates the fractional increase in the internal energy by a factor of 1·8 in Model S and 1·7 in Model F. If the effect of dynamical friction in decelerating the galaxies is neglected in the impulsive approximation and the galaxies are assumed to move with constant relative velocity equal to that at the closest approach, the prediction of the impulsive approximation is quite accurate (Toomre 1977). Miller and Smith (1980) who carried out N-body simulations with 50,000 stars in each galaxy indicate that the impulsive approximation cannot be expected to be valid for velocities less than 1000 km s^{-1} for typical galaxies.

8. Subsequent evolution

It is seen from the preceeding sections that when the separation of the galaxies becomes + 2, the structure has changed considerably. Therefore, we shall not use the potentials of a polytrope $n = 4$ to compute the orbits of stars beyond this separation. A more accurate treatment of the problem would require the use of potentials changing with time. However, we shall confine ourselves to making a crude estimate of the evolution of the galaxies after the encounter, by using the virial theorem.

The initial self potential energy of the galaxy may be written (Chandrasekhar 1943) as

$$\Omega = -\frac{GM^2}{2\bar{R}}. \tag{10}$$

Since the internal potential energy of a sphere of polytrope $n = 4$ is given by

$$\Omega = -\frac{3GM^2}{R} \tag{11}$$

we get on comparing equations (10) and (11)

$$\bar{R} = R/6. \tag{12}$$

If the galaxies do not merge, in the new equilibrium established after the collision the potential energy and the binding energy are related by the virial theorem as

$$2U_f = \Omega_f, \tag{13}$$

where U_f is the binding energy of the galaxy at separation $z = +2$ which is conserved after the collision and Ω_f is the potential energy when the galaxy has attained the new equilibrium. From equations (10) and (13) we obtain

$$\bar{R}_f = \frac{GM^2}{4U_f}. \tag{14}$$

Initially the galaxies (n= 4) have an average radius $\overline{R}_t$ = 0.167. Using the values of U_f obtained from the orbit computations we find that after the collision the galaxies have radii $\overline{R}_f$= 0.316 and 0.250 for slow and fast collisions respectively. This indicates that the mean radius expands to almost double its initial value in the case of slow collision and increases by about 50 per cent in the case of fast collision. Thus the final dimensions of the galaxies depend much on the velocity of the encounter. Dekel Lecar and Shaham (1980) have obtained from N-body simulations for their B-7 model the fractional increase in the median radius $\Delta R_h/R_h$ = 1.42, which indicates that the median radius expands to more than double its initial value. This may be compared with our result for the slow collision.

We stopped the numerical integrations when the galaxies were separated by a distance equal to about 15 times the median radius. As shown in Paper I, the tidal action of the perturbing galaxy practically ceases by this time. Further evolution of the shapes of the galaxies would, therefore, be determined by the self-gravity of the galaxies. Chandrasekhar and Elbert (1972) studied dynamical evolution of stellar systems with the aid of the tensor virial theorem. Their results show that a homogeneous oblate spheroidal system with negative total energy becomes more oblate and a prolate system with negative energy becomes more prolate.

9. Conclusions

It has been the main purpose of this work to study the dependence of the sizes and shapes of post-collision galaxies on the collision velocity in a head-on collision. If $V_t < V_{\rm cap}$, where V_t and V_{cap} are the initial and capture velocities respectively, the galaxies perform damped oscillations about the centre of mass of the system and finally become a single system. The results of N-body simulations show that in a head-on collision the final merged product has a prolate structure with the longer axis along the direction of the relative motion of the galaxies, while off-centre collisions lead to oblate structures flattened along the initial orbital plane (Tremaine 1981).

In the case of the slow collision with V_t slightly greater than V_{cap} the mean radius expands to about twice its size. The galaxies are prolate structures before the collision with the longer axis along the direction of motion. They lose their prolateness during the collision but do not become distinctly oblate.

In the case of the fast collision, $V_t \simeq 1{\cdot}5V_{\rm cap}$, the mean radius expands by about 50 per cent of its initial value. The galaxies are prolate before the collision and distinctly oblate after the collision. Thus the tendency of the post-collision galaxies to be oblate rather than prolate increases with the velocity of the collision. For faster collision velocities, the final mean radius of the galaxies may be deduced from the impulsive approximation as in Alladin, Sastry and Ballabh (1974).

Acknowledgements

We are thankful to Professors M. K. V. Bappu and K. D. Abhyankar for their encouragement and to G. Som Sunder for helpful discussions. One of us (S. M. A.)

benefited by visiting International Centre for Theoretical Physics, Trieste and thanks Professor Abdus Salam, the International Atomic Energy Agency and the UNESCO for hospitality. He also thanks Professor Bappu for providing hospitality at the Indian Institute of Astrophysics, Bangalore. We are grateful to the referees whose comments helped to improve the paper.

References

Aarseth, S. J., Fall, S. M. 1980, *Astrophys. J.*, **236**, 43.
Ahmed, F., Alladin, S. M. 1981, *Bull. astr. Soc India*, **9**, 40 (Paper I).
Alladin, S. M., Potdar, A., Sastry, K. S. 1975, in *IAU Symp. 69: Dynamics of Stellar Systems*, Ed. A. Hayli, D. Reidel, Dordrecht, p. 167.
Alladin, S. M., Sastry, K. S., Ballabh, G. M. 1974, in *Galaxies and Relativistic Astrophysics*, Eds B. Barbanis and J. D. Hadjidemetriou, Springer-Verlag, Berlin, p. 129.
Chandrasekhar, S. 1943, *Principles of Stellar Dynamics*, Dover, New York, p. 200.
Chandrasekhar, S., Elbert, D. D. 1972, *Mon. Not. R, astr. Soc*, **155**, 435.
Dekel, A., Lecar, M., Shaham, J. 1980, *Astrophys. J.*, **241**, 946.
Gallagher, J. S., Ostriker, J. P. 1972, *Astr. J.*, **77**,288.
Limber, D. N. 1961, *Astrophys. J.*, **134**, 537.
Lynds, R., Toomre, A. 1976, *Astrophys. J.*, **209**, 382.
Marchant, A. B., Olson, D. W. 1979, *Astrophys. J.*, **230**, L157.
Miller, R. H, Smith, B. F. 1980, *Astrophys. J.*, **235**, 421.
Potdar, A., Ballabh, G. M. 1974, *Astrophys. Sp. Sci*, **26**, 353.
Richstone, D. O. 1975, *Astrophys. J.*, **200**, 535.
Toomre, A. 1974, in *IAU Symp. 58: The Formation and Dynamics of Galaxies*, Ed. J. R. Shakeshaft, D. Reidel, Dordrecht, p. 347.
Toomre, A. 1977, in *The Evolution of Galaxies and Stellar Populations*, Eds B. M. Tinsley and R. B. Larson, Yale University Observatory, New Haven, p. 401.
Toomre, A. 1978, in *IAU Symp. 79: The Large Scale Structure of the Universe*, Eds M. S. Longair and J. Einasto, D. Reidel, Dordrecht, p. 109.
Tremaine, S. D. 1981, in *The Structure and Evolution of Normal Galaxies*, Eds S. M. Fall and D. Lynder-Bell, Cambridge University Press, p. 67.
van Albada, T. S., van Gorkom, J. H. 1977, *Astr. Astrophys.*, **54**,121.
Villumsen, J. V. 1980, *Preprint.*
White, S. D. M. 1978, *Mon. Not. R. astr. Soc*, **184**, 185.

J. Astrophys. Astr. (1981) **2**, 365–377

The Two Components in the Distribution of Sunspot Groups with Respect to their Maximum Areas

M. H. Gokhale and K. R. Sivaraman *Indian Institute of Astrophysics, Bangalore 560034*

Received 1981 April 7; accepted 1981 November 23

Abstract. From an analysis of the distribution of sunspot groups with respect to their maximum areas we find that this distribution consists of two distinct components. One component contributes to spot groups of all possible values of A_* with a distribution density varying as ~ exp $(-b_1 A_*^{1/2})$ with b_1 nearly constant from cycle to cycle and having a mean value $\sim 10^{-4}$ km^{-1}. The other component is predominantly responsible for spot groups with $A_* \lesssim 30 \times 10^{-6}$ hemisphere but may provide a few spot groups even above 50×10^{-6} hemisphere. This component may follow a distribution density ~ exp $(- b_2 A_*)$. We also determine the widths of the latitude zones over which spot groups in various intervals of A_* appear and study their variation with time. These widths and their variations indicate that the two statistical samples of spot groups may be produced by two families of flux-tube clusters as suggested earlier in a phenomenological model. Very thin flux-tube clusters in the statistical samples seem to be related to the ephemeral active regions and X-ray bright points.

Key words: sunspots, distribution of areas—solar activity—solar cycle—solar magnetic field

1. Introduction

Studies of the distributions of sunspot groups with respect to their physical properties provide valuable guidelines for the development of models of solar activity and solar magnetic cycle. The distribution of spot groups with respect to the maximum values of their individual areas is especially important for making models based on emergence of magnetic flux tubes or flux ropes. Mandrykina (1974) examined this distribution and showed that the relative frequency of small spot groups is larger during solar minimum than during solar maximum. Lopez Arroyo (1965) and

recently Kuklin (1980) have attempted to fit mathematical expressions for the observed distribution. Motivation for our present study of this distribution is provided by a phenomenological model of the solar cycle proposed earlier by one of us (Gokhale 1977, 1979). According to this model the solar activity during each cycle is provided by two topologically distinct sets of magnetic flux-tube clusters. One set consists of newly formed deep-rooted compact magnetic structures and the other consists of shredded, thin remnants of the 'older' fields in the shallower parts of the convection zone. This model can account for the main qualitative features of the two 'peaks' detected by Gnevyshev (1977) in various parameters of the solar activity (Gokhale 1979). However, a direct verification for the presence of two distinct sets of flux ropes should be sought in the distribution of active regions with respect to the cross-sections of the flux ropes (or flux-tube clusters) that produce the active regions. In the case of conventional active regions, *viz.* those which produce observable pores and spots, the maximum area $A_{\max}$ reached by a spot group during its evolution may be taken as a satisfactory measure of the sub-photospheric cross-section of the flux rope responsible for the active region. The maximum area $A_{\max}$ may be further approximated by the maximum value A_* among the appropriately corrected observed values of the spot group area. We have studied the frequency distribution $f(A_*)$ of spot groups during each of the last eight solar cycles (1889–1976), using the data from the Greenwich Photoheliographic Results. We find (Section 2) that during each of these eight cycles, the distribution $f(A_*)$ has two components. The first component $f_1(A_*)$ contributes spot groups with all possible values of A_*, whereas the second component $f_2(A_*)$ contributes predominently spot groups of A_*, $\lesssim$ 30 millionths of hemisphere (henceforth expressed as mh).

To examine whether the ensembles of spot groups represented by f_1 (A_*) and f_2 (A_*) have different physical behaviours, we determine the widths of the latitude zones over which spot groups belonging to different intervals of A_* emerge. The variations of these widths in the solar cycle suggest that the statistical ensembles do correspond to two sets of magnetic flux ropes which differ both in the latitudinal distribution and in the epochs at which they start emerging above the photosphere.

2. The two components in the distribution

2.1 *Method of Analysis*

In Ledgers I and II of the Greenwich Photoheliographic Results, areas (A) of important spot groups as observed from day to day and corrected for foreshortening are given for all non-recurrent and recurrent groups observed for two or more days during the years 1894 to 1955. From these we noted down the maximum values A_* of A for each of these spot groups. For each recurrent spot group the highest value of A during its entire life was taken for A_*. For the years 1889 to 1893, when Greenwich Photoheliographic Results do not contain a separate ledger for recurrent spot groups, the identification was done following the well known rotation periods appropriate for the latitudes concerned. For spot groups whose evolution is not included even in Ledger I (and in the case of *all* spot groups from 1956 onwards when Greenwich discontinued providing separate ledgers) the value

of A_* was determined by following the evolution of each spot group from the day-to-day records. For one-day spot groups the area A_0 at the time of observation itself was taken as A_*. Thus values *of* A_* were noted down for all spot groups for each year from 1889 to 1976.

The values of A_* so obtained from photoheliograms taken once a day are bound to be different from the true maximum, values ($A_{\max}$) of the area which may be reached in-between two successive observations. However, the difference ($A_{\max} - A_*$) can be ignored so long as it is small compared to the width of the interval dA_* chosen for defining the frequency of the distribution. This is ensured by choosing the intervals dA_* at least as large as the magnitude of the typical variation of spot group area during a day. Obviously this requires different widths for dA_* corresponding to the different ranges of A_* values as described later in this paper.

In the case of short-lived spot groups lasting for less than a day, the approximation of $A_{\max}$ by the observed value A_0 would be satisfactory if ($A_{\max} - A_0$) $\lesssim$ 5 mh which is the halfwidth of the interval dA_* chosen for defining the frequency of small spot groups. This condition will be satisfied in the majority of such spot groups as they are observed in their phase of decay and the average decay rate of solar magnetic features is $\sim 10^{15}$ Mx s^{-1} (Stenflo 1976), *i.e.* $\sim$ 3 mh day^{-1}. Thus the uncertainty in taking A_0 as $A_{\max}$ may be tolerated except for 'too small' groups (those with $A_0 \lesssim 10$ mh). A greater uncertainty arises in the counts of small spot groups because they are short-lived and hence some of them will be totally missed in the observations made only once a day. The number of spot groups so missed might even be larger than the observed number for $A_* \lesssim 10$ mh, but for $A_* > 10$ mh the number of 'missed' spot groups may be ignored.

From the yearly values of A_*, frequencies of occurrence $N(A_*, dA_*)$ in intervals of sizes dA_* centred on prescribed values of A_* are now determined. The intervals chosen are as follows.

0–10, 10–20, … 90–100	in the range of 0–100 mh,
75–100, 100–125, … 175–200	in the range 75–200 mh, and
100–200, 200–300, … 900–1000	in the range 100–1000 mh,

All 'closed' at the upper extremity for the sake of definiteness. Number of spot groups with $A_* > 1000$ mh were classified separately. For each interval, the total frequency for each solar cycle was determined by summing up the yearly frequencies for all the years in the cycle.

2.2 *The Distribution Density Function*

The observed values

The observed frequencies $N(A_*, dA_*)$ were divided by widths dA_* of the respective intervals to derive the 'observed values' of the distribution density $f(A_*)$ corresponding to the midpoints A_* of the prescribed intervals. For each solar cycle, the values of $f(A_*)$, were plotted against A_*. These plots are all similar in appearance. Fig. 1 shows $f(A_*)$ for the cycle 1965–1976 as a typical sample. Each plot shows

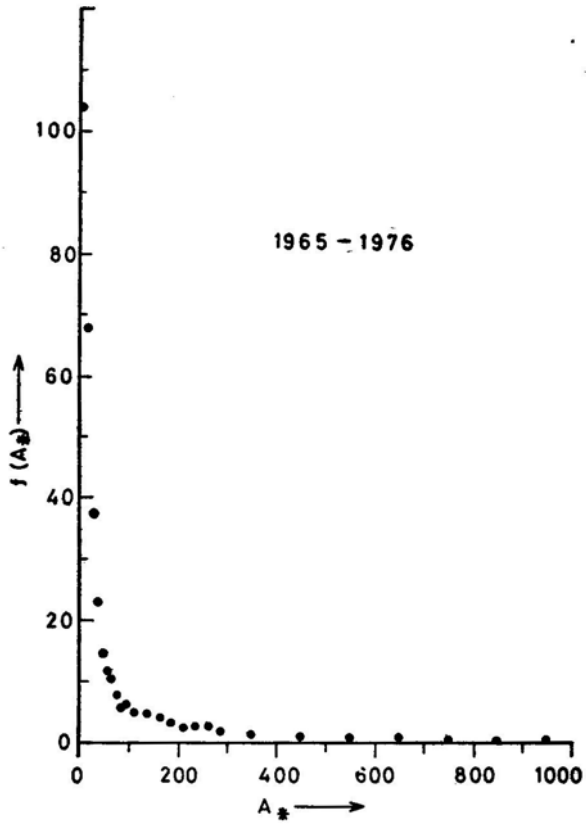

Figure 1. Observed distribution density $f(A)$ mh^{-1} as a function of A_* mh during the cycle 1965–1976.

a 'vertical branch' in the range A_*< 50 mh and a 'horizontal branch' for A_*> 300 mh which becomes irregular for A_* > 1000 mh. All attempts to fit both the branches by a single mathematical term involving a few parameters have failed.

Fit for the 'horizontal branch'

Omitting the frequencies for A_* > 1000 mh which are too small for statistical analysis, the horizontal branch fits the expression

$$f_1(A_*) = D_1 \exp(-b_1 A_*^{1/2}) \tag{1}$$

to a high level of confidence. The same expression continues to hold in the range A_* < 300 mh and past A ~ 100 mh. We calculated the weighted least square fits for the data in the range 100–1000 mh using formula (1). The values of D_1 and b_1, and the values of the coefficient of correlation $|R_1|$ between In $[N(A_*, DA_*)]$ and A_* are presented in Table 1. In the same table we have also given the probabilities of χ^2 for each fit. Values outside the brackets correspond to statistical weight based on uncertainties ~ $N^{1/2}$ in the observed frequencies N. Values within the brackets cor-

Table 1. Properties of the component $f_1(A_*)$. Values of D_1 and b_1 and their uncertainties $\sigma(D_1)$, $\sigma(b_1)$ are derived from weighted least-square fits assuming values of A_* to be exact and uncertainties of $\sim N^{1/2}$ in the values of N. Corresponding values of the coefficient of correlation ($|R_1|$) between $[\ln f_1(A_*)]$ and $A_*^{1/2}$ are also given for each cycle. Values in brackets correspond to weighted least-square fits assuming the values of N to be exact and uncertainties of $\sim dA_*/2$ in A_* values. The probabilities of χ^2 are derived from the calculated and the observed values of $N(A_*, d_{A_*})$, and happen to be the same for both methods of fitting.

First component	1889–1901	1902–1913	1914–1923	1924–1933	1934–1944	1945–1954	1955–1964	1965–1976
$D_1 \pm \sigma(D_1)$ mh^{-1}	2287 ± 3	1819 ± 5	2827 ± 7	1858 ± 7	2781 ± 4	2900 ± 4	3573 ± 4	3098 + 4
	(2309 ± 4)	(1967 ± 4)	(2987 ± 5)	(2004 ± 4)	(2780 ± 5)	(2845 ± 3)	(3598 ± 6)	(3724 ± 5)
$b_1 \pm \sigma(b_1)$ mh$^{-1/2}$	0·1608	0·1663	0·1795	0·1626	0·1521	0·1556	0·1589	0·1686
	± 0·0031	± 0·0062	± 0·0070	± 0·0074	± 0·0031	± 0·0033	± 0·0035	± 0·0031
	(0·1623	(0·1705	(0·1835	(0·1659	(0·1627	(0·1559	(0·1607	(0·1700
	± 0·0009)	± 0·0012)	± 0·0012)	± 0·0011)	± 0·0011)	± 0·0007)	± 0·0010)	± 0·0010)
$\|R_1\|$	0·998	0·994	0·993	0·992	0·998	0·997	0·998	0·998
	(0·997)	(0·991)	(0·994)	(0·995)	(0·998)	(0·998)	(0·997)	(0·997)
χ^2 probability (per cent)	99	82	65	81	59	96	85	92

respond to statistical weights based on uncertainties ~ $dA_*/2$ in A_*. It is interesting to note that the values of b_1 are roughly constant from cycle to cycle, with a mean value $\simeq$ 0·1643 $mh^{-1/2}$ *i.e.* ~ 10^{-4} km^{-1} and a root mean square deviation $\simeq 0{\cdot}0069\ mh^{-1/2}$.

Comparison with the log-normal law of distribution

Lopez Arroyo (1965) attempted to fit the cumulative frequencies of spot groups by the log-normal law of distribution. The fits obtained by him are rather unimpressive. The χ^2 probabilities exceeded 50 per cent for only five out of fourteen data sets. This is probably because he ignored the large uncertainties in the determination of frequencies for $A_* < 50$ mh and $A_* > 1000$ mh, which could lead to wrong values for percentages of cumulative frequencies. The relative values of cumulative frequencies in the domain 100–1000 mh may not be seriously affected by these uncertainties. We, therefore, fitted the log-normal law of distribution to the values of $f(A_*)$ in this domain. We find that the fit of the log-normal distribution over this range is still poor. However, over the shorter range 300–1000 mh the χ^2 probabilities are 96, 88, 60, 45, 83, 80, 70 and 75 per cent respectively. These probabilities show that the lognormal distribution might at best provide an approximate description of the distribution in the domain 300–1000. It is obvious that the formula (1) is decidedly better both in the coverage of A_* and in χ^2 probabilities.

The second component

In the domain $A_* < 50$ mh the frequencies $N_1(A_*, dA_*)$ calculated from formula (1) fall appreciably below the observed frequencies $N(A_*, dA_*)$. For $A_* \lesssim 30$ mh the difference $N(A_*, dA_*) - N_1(A_*, dA_*)$ is larger than $N_1(A_*, dA_*)$ and keeps increasing as A_* decreases. This indicates that the distribution function $f(A_*)$ must contain another term $f_2(A_*)$ which contributes substantially for $A_* \lesssim 50$ mh and very little for $A_* > 50$ mh.

We estimated the values of $f_2(A_*)$ for each cycle from the expression

$$f_2(A_*) = N_2(A_*, dA_*)/dA_*$$

where

$$\begin{aligned} N_2(A_*, dA_*) &= N(A_*, dA_*) - N_1(A_*, dA_*) \\ &= N(A_*, dA_*) - f_1(A_*)\, dA_*, \end{aligned}$$

and using formula (1) with appropriate values of D_1 and b_1 from Table 1. We find that $f_2(A_*)$ becomes the dominant component of $f(A_*)$ for $A_* \lesssim 30$ mh (Fig. 2).

We are aware of the unavoidable uncertainties in estimating $f_2(A_*)$ especially for $A_* < 10$ mh. However, we can get an insight into the nature of $f_2(A_*)$ from the three data points corresponding to the intervals 10–20, 20–30 and 30–40 mh. We find that there is a negative linear correlation between In $f_2(A_*)$ and A_* which suggests that $f_2(A_*)$ may be of the form,

$$f_2(A_*) = D_2 \exp(-b_2 A_*). \qquad (2)$$

Table 2. Properties of the component $f_2(A_*)$ with notations similar to those in Table 1.

Second component	1889–1901	1902–1913	1914–1923	1924–1933	1934–1944	1945–1954	1955–1964	1965–1976
$D_2 \pm \sigma(D_2)$ mh^{-1}	920 ± 4	833 ± 3	1536 ± 1	1400 ± 14	1300 ± 4	1255 ± 7	1636 ± 5	1306 ± 2
	(932 ± 2)	(836 ± 1)	(1536 ± 1)	(1468 ± 4)	(1306 ± 1)	(1278 ± 2)	(1643 ± 2)	(1310 ± 1)
$b_2 \pm \sigma(b_2)$ mh^{-1}	0·0712 ± 0·0059	0·0869 ± 0·0032	0·1096 ± 0·0780	0·1031 ± 0·1401	0·0844 ± 0·0037	0·0821 ± 0·0077	0·0797 ± 0·0048	0·0688 ± 0·0025
	(0.07164 ± 0·00008)	(0·03706 ± 0·00004)	(0·109596 ± 0·000006)	(0·1049 ± 0·0001)	(0·08451 ± 0·00004)	(0·08281 ± 0·00009)	(0·07994 ± 0·00006)	(0·06887 ±0·00004)
$\lvert R_2 \rvert$	0·997	0·999	1·00	0·991	0·999	0·996	0·998	0·999
	(0·997)	(0·999)	(1·00)	(0·991)	(0·999)	(0·996)	(0·998)	(0·999)
χ^2 probability (per cent)	58	72	92	25	75	48	68	79

From weighted least-square fits to this relation we determine the values of D_2 and b_2, the coefficient of correlation | R_2 | between In f_2 (A_*) and A_*, and probabilities of χ^2. These are presented in Table 2. These χ^2 probabilities are not as high as those for f_1 (A_*) obviously due to the uncertainties in estimating the values of N_2. However, the values of the correlation coefficient show that the form of the function f_2 (A_*) as given by equation (2) may be essentially correct.

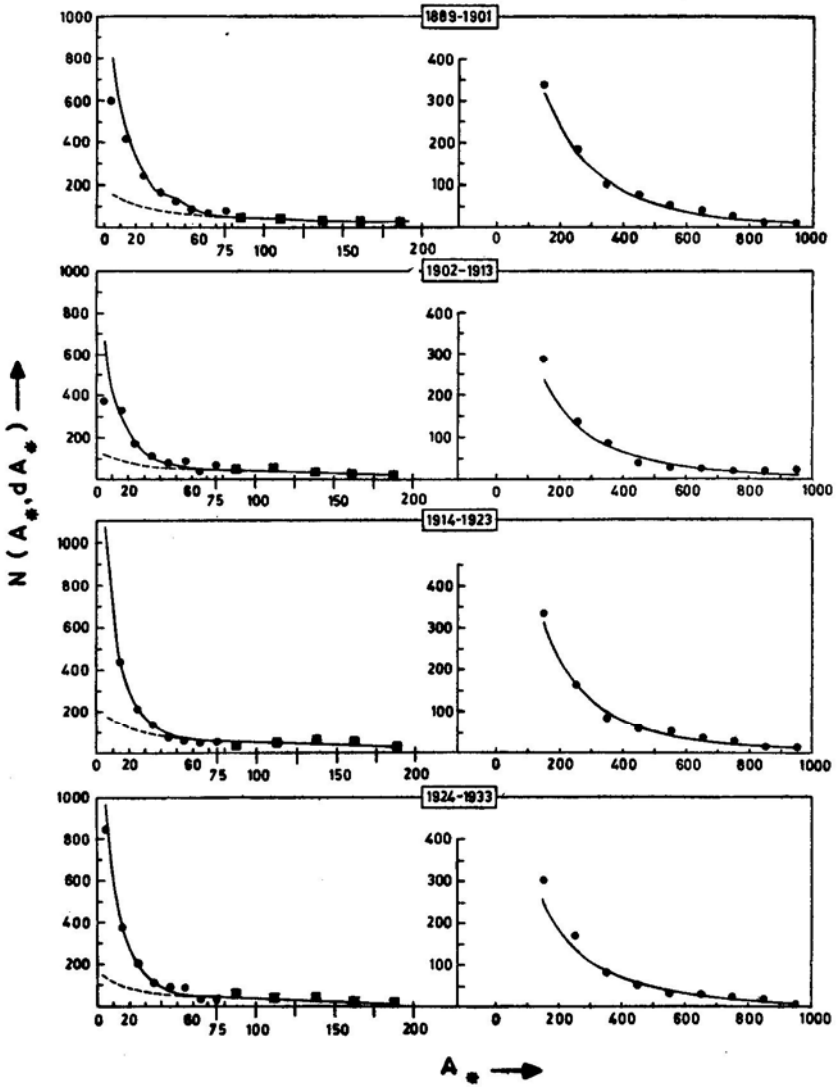

Figure 2. Comparison of theoretical and observed frequencies during the eight cycles. The continuous curve represents the formula N (A_*, dA_*) = $f_1(A_*)dA_*$ in the range 100–1000 mh. For A_* < 200 mh it represents N (A_* , dA_*) = [f_1(A$_*$) + $f_2(A_*)$] dA_*, The broken curve shows the value of $f_1(A_*)dA_*$ for A_* < 80 mh. The filled circles and squares denote the observed values of $N(A_*$, dA_*) with dA_* = 10 mh. Filled squares have been introduced only to indicate the longer (25) interval used for determining $N(A_*$, dA_*) in the range A_* = 75–200 mh before rescaling it to dA_* = 10 mh.

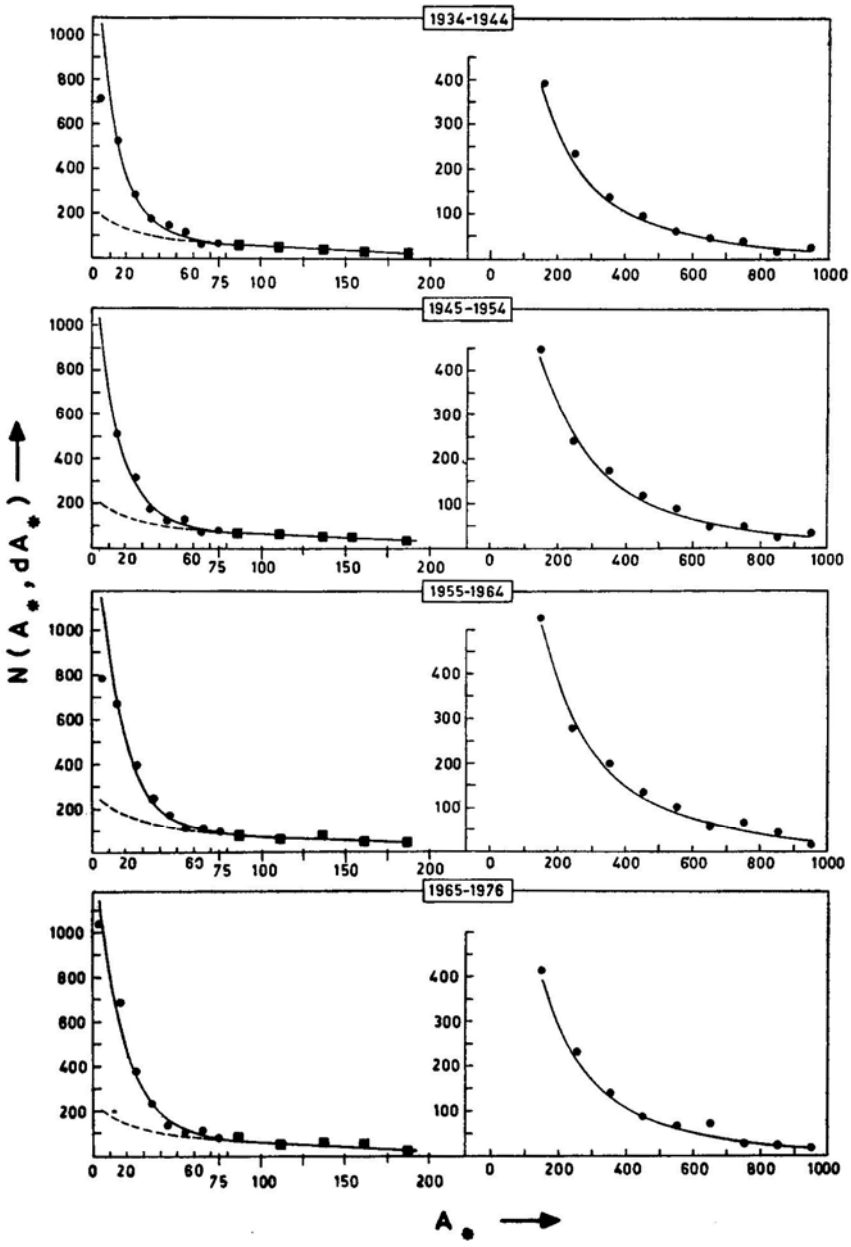

Figure 2. (Continued).

We notice that the values of b_2 –like those of b_1—are roughly constant; the mean is 0·0893 mh^{-1} and the rms deviation is $\simeq$ 0·0106 mh^{-1}. This suggests that formula (2) must have some physical reality associated with it.

Summarising Section 2, we conclude that during each solar cycle the distribution $f(A_*)$ has contributions from two distinct components. The component f_1 (A^*) contributes spot groups with all possible values of A_* and may be represented by

equation (1) to a high level of confidence in the domain 100–1000 mh. Although this contribution keeps increasing as A_* decreases, it becomes smaller than that of the second component f_2 (A_*) for $A_* \lesssim 30$ mh and for very small values of A_* it becomes negligible compared to f_2 (A_*). The second component seems to follow the formula given by equation (2).

It must be emphasized that our definition of the two components is different from that of the ' two populations ' described by Kuklin (1980) who has assumed the presence of two ' populations ', both represented by log-normal distribution, and has determined their proportion by placing their modes on the ' observed peaks ' in the density distribution function.

3. Difference in the physical behaviour of the two statistical components

3.1 *Variation of the Widths of the Latitude Zones*

The presence of two terms of distinct forms in $f(A_*)$ suggests that the two corresponding statistical samples of spot groups may be generated by two independent sets of flux ropes, differing in some physical or topological property related to the distribution of magnetic flux. One should, therefore, look for a significant difference in some physical property (other than area) or behaviour of the two statistical samples. The presence or absence of penumbra cannot be taken as the differentiating factor between the spot groups of the two categories, since spots of both kinds, with and without penumbra, can be found in any single large spot group belonging to either category.

It is logical to look for the difference in the *geometrical extent* over which the spot groups in the two components are distributed on the solar surface. This could be determined from the rms spread in the latitudes of spot groups in the two components. However, we have determined the actual extent from the span between the highest and the lowest latitudes at which spot groups in different specified intervals of A_* emerge during each year. In Fig. 3, we plot the total width W (sum of the latitude spans in the two hemispheres) as a function of time t in years, for spot groups in the intervals of A_*, 0–25, 25–100,100–200,200–500 and 500–1000 mh. From these W–t diagrams we find the following interesting features.

1. Throughout the period of the eight cycles, the W–t curve for $A_* \leqslant 25$ mh remains highest and often quite distinct from the other curves. Thus the family of flux ropes (say family II) which provides spot groups in the sample $f_2(A_*)$ must be more widely distributed in latitudes than the family of flux ropes (family I) providing the spot groups in $f_1(A_*)$

2. Near the ends of the cycles, the latitude zone for $A_* \leqslant 25$ mh suddenly expands while the latitude zones for large spot groups continue to narrow down. (Notice the horizontal arrows in Fig. 3). This illustrates the well known fact that each new cycle begins with the appearance of small spot groups at high latitudes before the end of the earlier cycle.

The narrowing of latitude zones for big spot groups represents depletion of flux ropes of family I of the old cycle. The associated sudden expansion of the latitude

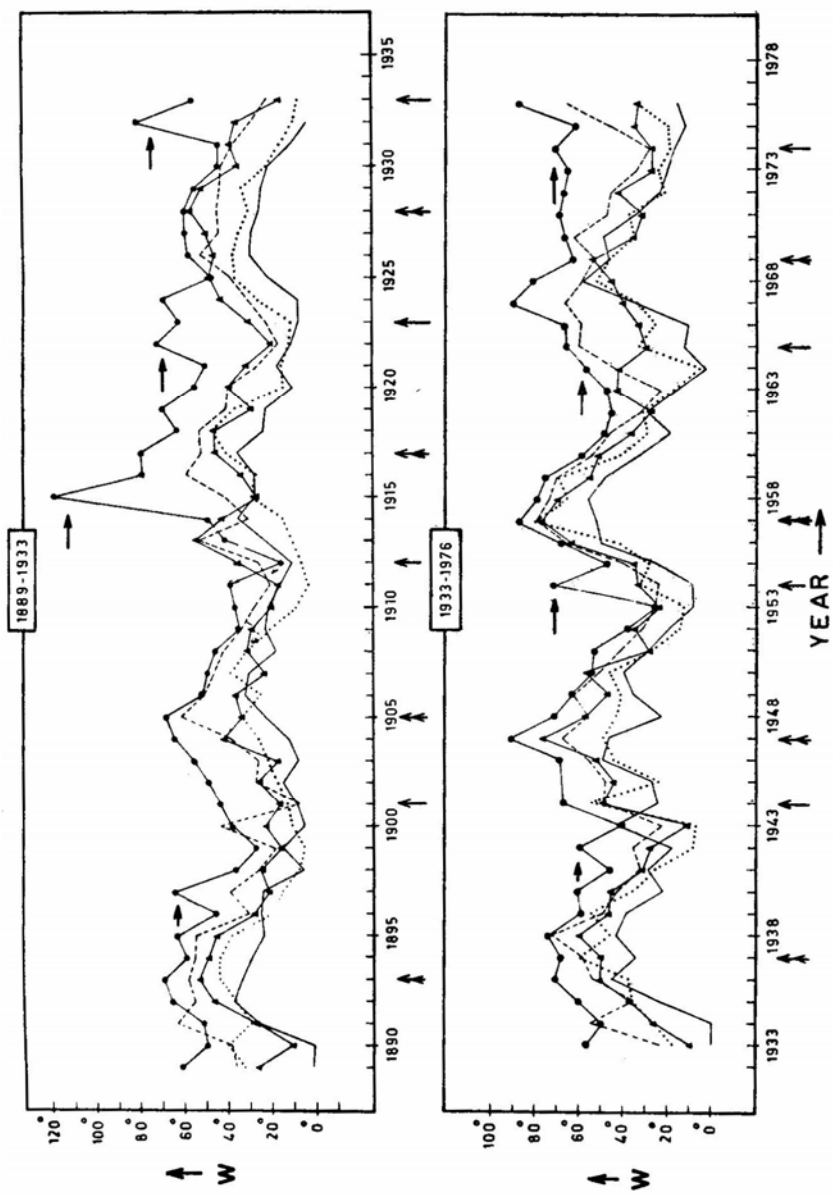

Figure 3. Total width (W) of the latitude zone corresponding to different intervals of A_*. The arrows indicate the increase of W for $A_* \leqslant 25$ mh with simultaneous decrease for high values of A_*. —●— $A_* \leqslant 25$ mh, ------ 25–100 mh, —▲— 100–200 mh, ... 200–500 mh, —— $A_* > 500$ mh. Double arrows ↑↑ represent years of sunspot maximum, single arrows ↑ represent years of sunspot minimum.

zone for small spot groups represents the beginning of the emergence of family II flux ropes of the new cycle. The emergence of family I flux ropes of the new cycle may be seen to begin, as represented by expansion of the latitude zones for large spot groups, one or two years later.

3. During considerable parts of most cycles, the *W–t* curves are ‘ bunched ’ in two groups and the value of A_* at which the two bunches separate vary from cycle to cycle and sometimes even within a cycle. This indicates that $f_2(A_*)$ does contribute a few spot groups to the intervals with $A_* > 25$ mh and the largest value of A_* up to which it contributes varies from cycle to cycle.

The *W–t* diagrams thus support the concept of the two families of flux ropes differing in latitudinal distribution and its variation.

3.2 *Relation to the Ephemeral Activity and X-ray Bright Points*

Another striking feature of the *W–t* curves is that in general the width of the latitude zone varies inversely as the value of A_*. Extrapolating this behaviour of *W* with decreasing A_*we may expect that flux tubes which are too thin even to produce

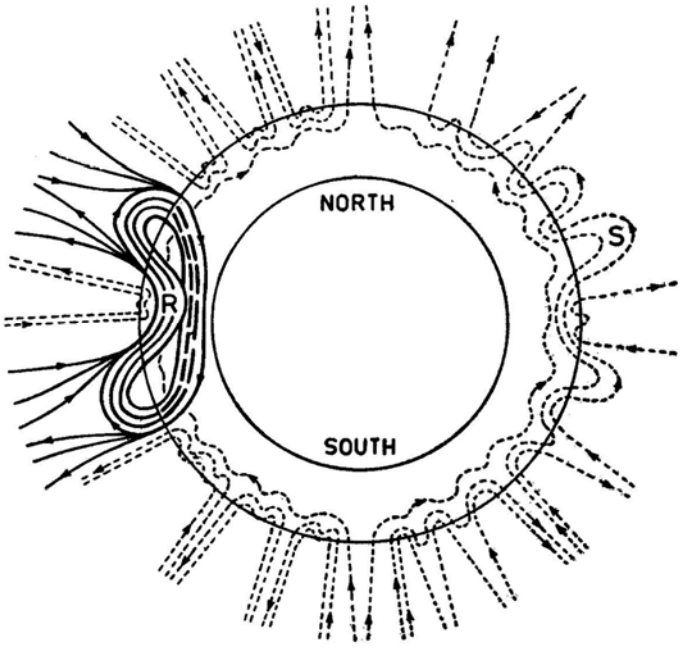

Figure 4. A schematic illustration of the phenomenological model. Thick continuous lines represent ‘R family’ flux ropes of the prevailing cycle provided by the faster rising parts of the newly created strong magnetic flux loops. Thick broken lines represent the slower rising parts of the same flux loops. These parts will provide the reversed global field of the next cycle. Thin dashed lines represent ‘S family’ flux ropes formed from the weak global field. This field is provided by the slower rising parts of the flux loops of the *previous* cycle which have diffused and dispersed all over within the convection zone while their leading parts were emerging during that cycle.

For convenience of illustration the new flux loop at only one nodal longitude is shown and the effects of the differential rotation are also omitted.

small ‘ pores’ during their emergence, will have their latitude zone wider than that for $A_* \lesssim 25$ mh. Latitude zone of sufficiently thin flux tubes might cover even the entire sun. Ephemeral active regions and X-ray bright points provide observational evidence for the existence of such flux tubes and their emergence over the whole sun (Martin and Harvey 1979). It is interesting to note in this context that the correlation between the ephemeral activity and the annual sunspot numbers (Martin and Harvey, 1979) is consistent with the year-to-year variation of the abundance of such thin flux tubes. However, it is at present premature to seek relations of the components f_1 (A_*) and f_2 (A_*) with the ephemeral activity and X-ray bright points.

4. Comparison with the phenomenological model

We illustrate in Fig. 4 the phenomenological model that motivated the present study. The main aspects of the model are:

(i) the presence of two families of flux-tubes, S and R, both contributing to the activity of the same solar cycle (note the polarity orientations),
(ii) a wider latitude distribution for flux tubes of family S and
(iii) a time delay in the emergence of flux tubes of family R.

The present study brings out the existence of the two families (I and II) from observations and enables us to identify these with the families S and R of the model.

Acknowledgements

We are thankful to Messrs M. Jayachandran, U. S. Bhat and K. M. Hiremath for their assistance in carrying out the analysis. We also thank an anonymous referee for the valuable comments which led to a considerable improvement in the presentation of this paper.

References

Gnevyshev, M. N. 1977, *Solar Phys.*, **51**, 175.
Gokhale, M. H. 1977, *Kodaikanal Obs. Bull. Ser. A.*, ***2***, 19.
Gokhale, M. H. 1979, *Kodaikanal Obs. Bull Ser. A.*, ***2***, 217.
Kuklin, G. V. 1980, *Bull. astr. Inst. Csl.*, **31**, 224.
Martin, S. F., Hervey, K. L. 1979, *Solar Phys.*, **64**, 93.
Lopez Arroyo, M. 1965, *Bull. astr. Inst. Csl*, **16**, 244.
Mandrykina, T. L. 1974, *Circ. astr. Obs. Lvov Univ.*, **49**,24.
Stenflo, J. O. 1976, in *IAU Symp. 71: Basic Mechanisms of Solar Activity*, Eds V. Bumba and J. Kleczek, D. Reidel, Dordrecht, p. 69.

J. Astrophys. Astr. (1981) **2**, 379–385

Plasma Heating in a Sheared Magnetic Field

V. Krishan *Indian Institute of Astrophysics, Bangalore 560034*

Received 1981 April 13; accepted 1981 September 15

Abstract. The mechanism of spatial resonance of Alfven waves for heating a collisionless plasma is studied in the presence of a twisted magnetic field. In addition to modifying the equilibrium condition for a cylindrical plasma, the azimuthal component of the magnetic field gives extra contribution to the energy deposition rate of the Alfven waves. This new term clearly brings out the effects associated with the finite lifetime of the Alfven waves. The theoretical system considered here conforms to the solar coronal regions.

Key words: Alfven waves—plasma heating—solar corona

1. Introduction

The magnetohydrodynamic waves are believed to be the potential candidates for heating a plasma. Since these waves are known to exist in great abundance in the solar atmosphere, they present themselves as the natural choice for heating the coronal plasma and the chromosphere-coronal transition regions. The magnetohydrodynamic waves, for example acoustic waves, Alfven waves and their other modified equivalents could be generated through the Lighthill mechanism *i.e.* direct generation by the turbulent convective motions, for example in the photospheric layers. The low frequency acoustic waves may lose major portion of their energy in the photosphere through radiative damping. On the other hand, the steepening of the wave front of the acoustic waves, as they propagate, results in shock formation, in which case, they deposit their energy over larger spatial scale. Alfven waves, as suggested by Alfven (1947), may lose their energy by ohmic losses due to the finite electrical conductivity. Piddington (1956) proposed viscous damping to be more important than Joule heating in the corona. Uchida and Kaburaki (1974) invoked the decay of slow MHD waves—produced through nonlinear coupling of Alfven waves—in order to explain the excessive heating of the active regions. The coupling of the waves has been studied using quantum field theoretical methods (Kaburaki and Uchida 1971). The coupling of Alfven waves and the fast mode waves in a stratified

medium and its significance in heating the solar corona has been discussed by Melrose (1977). Plasma heating by spatial resonance between shear Alfven waves has been proposed by Chen and Hasegawa (1974). Ionson (1978) and Wentzel (1979) applied this resonance absorption mechanism for heating the coronal loops. The terms—energy deposition rate of the waves and the plasma heating rate have been used synonymously in the literature. Actually, in the fluid treatment usually performed, there is no provision for the transfer of this deposited energy to the particles. A wave-particle interaction has to be invoked to calculate the heating rate of the plasma particles. In this paper, we calculate the energy deposition rate of the Alfven waves in an inhomogeneous plasma in a twisted magnetic field. The inhomogeneous coronal density model is derived in a cylindrical geometry from the equilibrium condition in the presence of the twisted magnetic field. We find that the results in a cylindrical geometry are qualitatively different from the ones in a planar geometry considered previously. In addition to an extra contribution to the dissipation rate, we find that an arbitrarily small value of the parameter β = ratio of the gas pressure to the magnetic pressure, is not allowed in the present analysis.

2. Dissipation rate

We consider a plasma system with mass density $p(r)$ in a magnetic field $B = [0, B_\theta(r), B_z(r)]$ where $B_\theta = Bar$ and $B_z = B$, a being a constant. This represents a uniformly twisted magnetic field with the pitch of the field given by $2\pi/\alpha$. The radio evidence for the existence of the twisted magnetic fields in the corona has been presented by McLean and Sheridan (1972). The equilibrium gas pressure $P(r)$ and the magnetic field $B(r)$ satisfy the condition

$$\frac{\partial}{\partial r}\left[P(r) + \frac{B^2}{2\mu}\right] + \frac{B_\theta^2}{\mu r} = 0. \tag{1}$$

Making use of the adiabatic equation of state, one finds the spatial variation of the mass density $p(r)$ in the limit $ar \ll 1$ to be

$$\begin{aligned} \rho(r) &= \rho_0 \exp\left(-B_\theta^2/\mu P\gamma\right) \\ &= \rho_0 \exp\left(-\alpha^2 r^2/4\beta_0\gamma\right) \end{aligned} \tag{2}$$

Where, $\beta_0 = \left.\dfrac{\mu P}{B^2}\right|_{r=0}$

and γ is the adiabatic index. Using the standard magnetohydrodynamic equations, relaxing the conditions of incompressibility, we find the equations for the radial component of the plasma displacement vector ξ_r and the total perturbed pressure p to be:

$$\frac{d^2}{dr^2}\xi_r + \frac{d}{dr}\xi_r\left[\frac{d}{dr}\left(\frac{\alpha_1 \epsilon B^2}{\alpha_1 k_\perp^2 B^2 - \epsilon}\right) + \frac{(k_\parallel B) B_\theta^2 \epsilon (\alpha_1 - 1)}{r\gamma\beta (k_\perp B)}\right]$$

$$\times\left(\frac{a_1 k_\perp^2 B^2-\epsilon}{(a_1\epsilon B^2)}\right)+\xi_r\left[\frac{d}{dr}\left(\frac{(k_\parallel B) B_\theta^2 \epsilon (a_1-1)}{r\gamma\beta (k_\perp B)}\right)-\epsilon\right]\left(\frac{a_1 k_\perp^2 B^2-\epsilon}{a_1\epsilon B^2}\right)=0 \quad (3)$$

And

$$p = -\xi_r\frac{dP}{dr}-\gamma P(\nabla\cdot\xi)+\mathbf{b}\cdot\mathbf{B}/\mu$$

$$=\xi_r\left[\frac{B_\theta^2}{\mu r}+\frac{\gamma P k_\parallel^2 B^2 B_\theta^2}{r\epsilon_1 B^2}\right]+\frac{d}{dr}\xi_r\left[-B^2(1+\gamma\beta)/\mu-\gamma^2 P k_\parallel^2 B^2/\epsilon_1\right]$$

$$+\xi_\perp\left[-i k_\perp B^2(1+\gamma\beta)/\mu - i\gamma^2 P k_\parallel^2 k_\perp B^2\beta/\epsilon_1\right], \quad (4)$$

$$\xi_\perp=\frac{i a_1 k_\perp B^2}{(a_1 k_\perp B^2-\epsilon)}\frac{d}{dr}\xi_r+\frac{i k_\parallel B_\theta^2(a_1-1)}{r\gamma\beta(a_1 k_\perp^2 B^2-\epsilon)}\xi_r \quad (5)$$

where,

$$a_1 = 1+\frac{\gamma\beta\mu\rho\omega^2}{\mu\rho\omega^2-k_\parallel^2 B^2\gamma\beta},$$

$$\epsilon = \mu\rho\omega^2-(k_\parallel B)^2,$$

$$\epsilon_1 = \mu\rho\omega^2-(k_\parallel B)^2\gamma\beta,$$

$$k_\parallel B = k_z B_z + k_\theta B_\theta, \qquad k_\theta=\frac{l}{r},$$

$$k_\perp B = k_\theta B_z - k_z B_\theta,$$

$$\mathbf{b} = (\mathbf{B}\cdot\nabla)\xi-\mathbf{B}(\nabla\cdot\xi)-(\xi\cdot\nabla)\mathbf{B} \quad (6)$$

and all perturbed quantities vary according to exp $[i(k_z z + l\theta - \omega t)]$, l is an integer. Equation (3) describes the coupling of the shear Alfven waves, the magnetosonic waves and the acoustic waves in an inhomogeneous magnetoplasma system. The singularity in the solution of equation (3), at the point where the phase velocity of a given Alfven wave propagating in the inhomogeneous plasma becomes equal to that of the local Alfven wave, has been discussed by Chen and Hasegawa (1974), Ionson (1978) and Wentzel (1979). We wish to study the effect of this particular magnetic field geometry on the singular solution and hence on the dissipation rate. An expression for the dissipation rate can be found from the relation

$$\frac{dW}{dt}=\tfrac{1}{2}\,\mathrm{Re}\int \mathbf{J}\cdot\mathbf{E}^*\,d^3r$$

where

$$\mathbf{J} = \frac{\nabla \times \mathbf{b}}{\mu} \text{ and } \mathbf{E} = i\,\omega\,\boldsymbol{\xi} \times \mathbf{B}. \tag{7}$$

Substituting for all the perturbed quantities in terms of ξ_r, one finds

$$\frac{dW}{dt} = \pi L_z r_0 \,\mathrm{Re}\left[\frac{i\omega}{\mu}\left\{\frac{B^2\,\epsilon}{\alpha_1 k_\perp^2 B^2 - \epsilon}\,\xi_r^*\,\xi_r' + \left(\frac{(k_\parallel B)(k_\perp B) B_\theta^2 (\alpha_1 - 1)}{r\gamma\beta(\alpha_1 k_\perp^2 B^2 - \epsilon)} - BB'\right)\xi_r^*\,\xi_r\right\}\right]_{r_0-\eta}^{r_0+\eta} \tag{8}$$

where L_z is the extent of the system in z direction and $\xi_r' = d\xi_r/dr$. One can solve equation (3) around the regular singular point $r = r_0$ by Frobenius' method to get

$$\xi_r = c_1 a_0 + \sum_{n=1}^{\infty} (c_1 a_n + c_2 b_n) x^n + c_2 \ln|x| \sum_{n=0}^{\infty} a_n x^n \tag{9}$$

Where $x = r - r_0 + i\,\delta$, such that $|r - r_0 \mid \eta| \gg |\delta|$,

$$\epsilon(r) = \left.\frac{d\epsilon_r}{dr}\right|_{r=r_0} (r - r_0) + i\,\epsilon_i$$

And

$$\delta = \frac{\epsilon_i(r_0)}{\left.\frac{d\epsilon_r}{dr}\right|_{r=r_0}}, \tag{10}$$

ϵ_r and ϵ_i being the real and imaginary parts of ϵ. Substituting equation (9) in equation (8) and evaluating at the upper and the lower limits, one finds

$$\frac{dW}{dt} = -\pi^2 L_z r_0 \frac{\omega}{\mu} |c_2 a_0|^2 \left\{\frac{B^2 \left.\frac{d\epsilon_r}{dr}\right|_{r=r_0}}{(\alpha_1 k_\perp^2 B^2)_{r=r_0}} + \frac{2 B_\theta^2(r_0)}{r_0}\left[\frac{k_\parallel B}{k_\perp B}\,\frac{1}{(1 - \gamma\beta)} - 1\right]\ln|\eta|\right\} \tag{11}$$

In equation (11), the first term is the familiar contribution obtained by earlier workers in a planar geometry. In arriving at the first term, though the condition that $|\eta| \gg |\delta|$ has been made use of, the quantity η does not figure explicitly. The second term, which is a direct consequence of the different equilibrium condition (1) for a cylindri-

cal plasma in a helical magnetic field, clearly shows the finite life time effects. The presence of this term forbids the wave to approach the resonance point infinitely close and η is a measure of the closest distance of approach. Thus, whereas the first term allows the energy deposition in the limit $\eta \to 0^+$, the second term makes its contribution little away from the resonance point. This could result in giving a finite width to the absorption region.

3. Application to the solar corona

Resonant Alfven wave heating mechanism has been applied to the heating of coronal loops by Ionson (1978). In view of the recent observations, where a highly inhomogeneous nature of the chromospheric-coronal transition region and that of the dense corona has been emphasized, this mechanism could be operative over large portions of the solar corona (Feldman, Doschek and Mariska 1979). These authors, from the *skylab* data, propose that the transition zone and the corona may be confined to small structures of high plasma density. The regions in between these structures would contain a negligibly small amount of plasma relative to the plasma within these structures. In such a case, one could envisage a model where the source of Alfven waves—which could be a magnetic filament or a current sheet—lies outside these high density coronal structures. We assume a cylindrical geometry where the half cylinder is filled with the high density plasma in a helical magnetic field and the source of Alfven waves is situated outside in a relatively low density region. This facilitates to relate the constant ($c_2 a_0$) of equation (11) to the energy density of the Alfven waves produced external to the region to be heated. To be able to do this, one has to determine the solution of equation (3) at the boundary *i.e.* at $r = 0$. Then, by satisfying the boundary conditions, one can relate the solution of equation (3) at the point $r \sim r_0$ to that at $r = 0$, which in turn is related to the external source of Alfven waves. We observe that in the present system $r = 0$ is a regular singular point and by Frobenius method, we can find a series solution only for $r > 0$ and $r < 0$. Therefore, this forbids a sharp boundary at $r = 0$ and one has to take the finite thickness of the boundary into account. In this piece of work, we make a simplifying assumption and solve equation (3) for $l = 0$ *i.e.* $k_\theta = 0$. In this case, we can find a general solution of equation (3) in the interval $0 \leqslant r < r_0$ in the form of a series

$$\xi_r = \sum_{n=0}^{\infty} d_n (r - r_1)^n \tag{12}$$

where r_1 is an ordinary point in the interval. The coefficients d_n can be determined by substituting solution (12) into equation (3) and comparing the coefficient of equal powers of r on both sides. Another simplifying assumption we make is to consider the low density medium as vacuum. We can decompose the magnetic field **b** of the wave into two components $\mathbf{b} = \mathbf{b_1} + \mathbf{b_2}$, where $\mathbf{b_1}$ corresponds to the external driving field. One can find an expression for these fields, satisfying the equations

$\nabla \times \nabla\, b_2 = \nabla \cdot b_2 = 0,$

$$\mathbf{b}_2 = \psi_2 \nabla e^{i(k_z z - i k_r r - \omega t)},$$

$$\mathbf{b}_1 = \psi_1 \nabla e^{i(k_z z + i k_r r - \omega t)}. \tag{13}$$

In arriving at equation (13), solution on a planar geometry has been assumed since this may be a good approximation for mode number $l = 0$. The first boundary condition is the continuity of the radial component of the magnetic field at $r = 0$, *i.e.*

$$\psi_2 = [i k_{\|}(0) B(0) \xi_r(0) - b_{1r}(0)]/k_r. \tag{14}$$

The second boundary condition is the pressure balance condition

$$\mu p(0) = \mathbf{B}_v (\mathbf{b}_1 = \mathbf{b}_2) \mid_r = 0 \tag{15}$$

where $\mathbf{B}_v$ is the vacuum magnetic field. Substituting for $p(0)$ and $\mathbf{b}_1$, $\mathbf{b}_2$, one finds

$$2 b_{1r}(0) = i k_{\|}(0) B(0) \left[\xi_r(0) - \frac{1}{k_z} \xi_r'(0) \left(1 + \gamma \beta_0 + \frac{\gamma^2 \beta_0^2}{\epsilon_1(0)} k_z^2 B_z^2\right)\right]. \tag{16}$$

Matching the solutions of equation (3), we find $\xi_r(0) = -(c_2\ a_0)$ and $\xi_r'(0) = 2c_2\ a_0/r_0$ for $r_1 = r_0/2$ and $d_0 = 0$. Here we have checked that the higher order terms (for $n \geqslant 2$) in equation (12) are small. In a more general case, the treatment has to be done numerically. From equation (16), we determine $(c_2\ a_0)$ and substitute in equation (11) to get

$$\frac{dW}{dt} = \pi^2 L_z \frac{|b_{1r}(0)|^2 \omega}{k_z^2 \mu} \frac{1}{\left[1 + \frac{2}{k_z r_0}\left(1 + \gamma \beta_0 + \frac{\gamma^2 \beta_0^2}{\epsilon_1(0)} k_z^2 \beta_z^2\right)\right]^2}$$

$$\times \left[\frac{2}{a_1 \beta_0 \gamma \left(1 - \frac{a^2 r_0^2}{4\beta_0 \gamma}\right)} + \frac{a^2 r_0^2}{2}\left(\frac{2}{a r_0 (1 - \gamma \beta_0)} + 1\right) \ln |\eta|\right] \tag{17}$$

where $(a^2 r_0^2)/(4\beta_0 \gamma) < 1$.

One must remember that in the present treatment, an arbitrary small value of the parameter $(\beta_0\ \gamma)$ is not allowed because of the assumption $a^2 r^2 < \beta_0 \gamma$ made while deriving the plasma density profile from the equilibrium condition (1). As a matter of fact, in the solar coronal conditions this number $\gamma\beta$ is not vanishingly small. The second term, as has been mentioned earlier, brings out the finite lifetime effects. A comparison of the resonant absorption dissipation rate and that of the Joule heating rate shows, for the same energy density of the Alfven waves, the latter to be much smaller than the former. The a dependent term in equation (17) could be positive or negative depending on whether the magnetic field pitch is in the positive or in the negative direction. This will give the dissipation rate to be more for one direction of twist than for the other direction. The present treatment suffers from various

assumptions and approximations. The first thing, which we plan to include in our future work is the effect of finite k_θ in the solution. In fact, the assumption of $k_\theta = 0$ may not be bad in the case of solar corona, since one desires the waves to propagate throughout the plasma, unlike in the laboratory plasma. The second improvement could be to replace the vacuum by a low density plasma, in which case the contribution from the displacement current needs to be taken into account. This investigation could be done in a nonuniformly twisted magnetic field. This would be in line with Kuperus (1965) who has stressed the need to include more realistic magnetic field configurations while studying the heating problem.

4. Conclusion

The energy dissipation rate of the Alfven waves in an inhomogeneous plasma by spatial resonance absorption mechanism is calculated in a uniformly twisted magnetic field. The physical significance of the additional contribution to the energy dissipation rate is to stress on a finite distance of the closest approach to the resonance point by the Alfven wave. In the present model, arbitrarily small values of $\gamma\beta_0$ are not allowed. The smallness of $\gamma\beta_0$ is controlled by the ratio of the azimuthal component of the magnetic field to its axial component.

References

Alfven, H. 1947, *Mon. Not. R. astr. Soc.*, **107**,211.
Chen, L., Hasegawa, A. 1974, *Physics Fluids*, **17**, 1399.
Feldman, U., Doschek, G. A. Mariska, J. T. 1979, *Astrophys. J.*, **229**, 369.
Ionson, J. A. 1978, *Astrophys. J.*, **226,** 650.
Kaburaki, O., Uchida, Y. 1971, *Publ. astr. Soc. Japan*, **23**, 405.
Kuperus, M. 1965, *The Transfer of Mechanical Energy in the Sun and the Heating of the Corona*, D. Reidel, Dordrecht.
McLean, D. J., Sheridan, K. V. 1972, *Solar Phys.*, **26**,176.
Melrose, D. B. 1977, *Austr. J. Phys.*, **30,** 495.
Piddington, J. H. 1956, *Mon. Not. R. astr. Soc.*, **116,** 314.
Uchida, Y., Kaburaki, 0.1974, *Solar Phys.*, **35**, 451.
Wentzel, D. G. 1979, *Astrophys. J.*, **233**,756.

J. Astrophys. Astr. (1981) **2**, 387–403

Rotation and Luminosity Variations in Post-Main Sequence Stars

Paul J. Wiita* *Theoretical Astrophysics Group, Tata Institute of Fundamental Research, Bombay 400005*

Received 1981 June 26; accepted 1981 September 15

Abstract. Previous first-order analytic treatments of rotation acting upon stellar equilibria are extended to include later, post-Helium burning, stages of stellar evolution. Strong differential rotation is capable of substantially increasing the photon luminosities of post-main sequence stars, and thus accelerating their evolution. On the other hand, uniform rotation reduces the photon flux for a wide range of stellar interior types and conditions. Similar conclusions are drawn regarding the effects of rotation on the emission of neutrinos in pre-collapse phases of evolution. A brief discussion of the gravitational radiation emitted during these phases is also given.

Key words: rotating stars — post-main sequence evolution — neutrino emission — gravitational radiation

1. Introduction

Rotation is recognized as playing a very important role in the life of a star, and many aspects of the subject have been extensively examined. Much theoretical work has been done on the possible effects of rotation in star formation (e.g. Boss 1980; Wiita, Schramm and Symbalisty 1979) and on its ramifications for the appearance of main sequence stars (for reviews see Fricke and Kippenhahn 1972; Tassoul 1978) and white dwarfs (Tassoul 1978). Spurred on by the discovery of pulsars, the final stages of the collapse of rotating stars have also received considerable attention recently (*e.g.* Saenz and Shapiro 1979).

Still, the number of investigations into the effects of rotation in post-main sequence stars before the onset of collapse is quite small. Of course this is understandable: the great difficulties encountered in computing the evolution of

*Permanent address: Department of Astronomy and Astrophysics, University of Pennsylvania, Philadelphia 19104, USA

complex, multi-layered spherical stars are considerably compounded by the introduction of angular momentum distributions as additional independent variables. Also, any uncertainties that arise during the calculations of rotating main sequence stellar models are amplified when one tries to go further, since various thermal, dynamical and secular timescales all change, sometimes dramatically (Fricke and Kippenhahn 1972). Because detailed numerical calculations have just recently been attempted in this regime (Endal and Sofia 1976, 1978), and because the physics involved in the transport of angular momentum is so uncertain (Kippenhahn 1974; Huppert and Spiegel 1977), it is clear that there is room for some simple analytical calculations that may point out a few basic conclusions and indicate directions for future numerical work. A useful beginning along these lines was made by Maeder (1974) when he used homology arguments to investigate the evolutionary tracks of the centres of rotating stars in the temperature-density plane.

The bulk of this paper is essentially an extension of Maeder's approach to later stages of stellar evolution. In Section 2 the approximations employed are summarized and the resulting equations relating rotation to temperatures and densities for various types of stars are presented. This technique is applied in Section 3 to the calculation of the photon and neutrino luminosities as functions of the amount and type of rotation present. Implications for evolution are outlined by considering some specific stellar structures. Finally, in Section 4, conclusions are drawn, and the great uncertainties still remaining are summarized.

2. An analytical approach

2.1 *Basic Equations and Approximations*

Following Schwarzschild (1958) and Maeder (1974) we average the effects of rotation and use a spherical approximation. Then the equation of hydrostatic equilibrium is

$$\frac{dP}{dM_r} = -\frac{GM_r}{4\pi r^4}(1-\chi), \tag{1}$$

where

$$\chi = \frac{2}{3}\frac{\Omega^2 r^3}{GM_r}, \tag{2}$$

And Ω is the angular velocity at point r. Maeder shows that if homologous contraction takes place in a star below a radius r_0, then for a radius $r \ll r_0$, we have (assuming local conservation of angular momentum)

$$\frac{1}{P}\frac{\partial P}{\partial t} = -\frac{(4-5\bar{\chi})}{(1-\bar{\chi})}\frac{1}{r}\frac{\partial r}{\partial t} \tag{3}$$

where the average effect of rotation is

$$\bar{\chi} = \left(\int_{M_r}^{M_{r_0}} \frac{GM_r}{4\pi r^4} \chi \, d\, M_r \right) \left(\int_{M_r}^{M_{r_0}} \frac{GM_r}{4\pi r^4} \, dM_r \right)^{-1}. \tag{4}$$

Other basic results are that during such a homologous contraction

$$d \ln \rho = -3 \, d \ln r \tag{5}$$

and

$$d \ln \bar{\chi} = \tfrac{1}{3} \, d \ln \rho. \tag{6}$$

Maeder (1974) uses these relations to argue (among other things) that if the contraction in the core is homologous and if angular momentum is conserved locally, that the mass of stars when carbon burns non-degenerately, M_{CD} may be raised from about 8 $M_\odot$ to as high as $20M_\odot$, while the mass limit for He flashes may be raised considerably from around $2M_\odot$ This is because, under these assumptions, a rotating star of a given mass would evolve to a lower central temperature at a given density. But some more recent calculations (Endal and Sofia 1978) show that local angular momentum conservation is probably not a good approximation in these regimes, and, since mixing tends to increase the duration of helium burning, a rotating star actually may have a higher central temperature near helium exhaustion. Later on, the pure rotational effects do start to dominate and eventually rotating models do evolve at lower central temperatures than their non-rotating counterparts. But Endal and Sofia find this effect to be smaller for more massive stars; therefore M_{CD} is unlikely to be increased very much, and we estimate that it is under 10 $M_\odot$. This question ought to be investigated more thoroughly because the numbers of Type II and Type I Supernovae, as well as the amount of heavy element enrichment they produce, may depend significantly upon this mass (Arnett and Schramm 1973; Hainebach, Norman and Schramm 1976).

We now come to the main topic of this paper, the effects of rotation upon stars in post-main sequence, but pre-collapse, phases. Several important approximations are made, and we shall mention most of them now.

First, we neglect magnetic fields completely; this is a somewhat dangerous simplification, and may be a major shortcoming, especially in the last phases of evolution (LeBlanc and Wilson 1970). Magnetic coupling between the core and the mantle could be the most efficient way to transfer angular momentum (Kippenhahn 1974) but magnetic energy is unlikely to be comparable to rotational energy, and very simple calculations show that under most circumstances the ratio of magnetic to rotational energy decreases as the core of the star contracts. Thus we join the vast majority of previous workers and shall henceforth ignore magnetic fields.

Second, we assume homology relations do hold, at least below a certain level in the star, and that any energy generation or neutrino losses outside of that zone are negligible. Homology relations do start to fail at temperatures around 10^9 K,

when neutrino emission really dominates over photons, but the numerical calculations done so far do not yet allow us to set firm bounds on the errors so introduced.

A third limiting factor is our assumption that the star behaves spherically (equation 1). Once $\bar{\chi}$ grows too large the surface temperature and most other properties will vary considerably with latitude, but as long as we restrict $\bar{\chi}$ to less than 0·187, crudely corresponding to the secular stability limit for Maclaurin spheroids (see Section 2·4 below), we can hope that these changes do not vitiate our results.

Under these assumptions the basic equations of stellar structure are

$$\frac{dM_r}{dr} = 4\pi r^2 \rho, \tag{7}$$

$$\frac{dP_r}{dr} = -\frac{GM_r \rho}{r^2}(1-\chi), \tag{8}$$

$$\frac{dL_r}{dr} = 4\pi r^2 \rho \epsilon \tag{9}$$

and

$$\frac{dT_r}{dr} = -\frac{3}{4ac}\frac{\kappa\rho}{T_r^3}\frac{L_r}{4\pi r^2} \tag{10a}$$

for a radiative zone, or

$$\frac{dT_r}{dr} = \frac{\Gamma_2 - 1}{\Gamma_2}\frac{T_r}{P_r}\frac{dP_r}{dr} \tag{10b}$$

for a convective zone, and the notation is standard.

2.2 *The Core*

For most of the post-main sequence phases of stellar evolution the star can be thought of as an inert core, covered with a shell, or multiple shells, of 'burning' material, and wrapped with a diffuse envelope. The core is usually degenerate, and this degeneracy will be assumed for the rest of this paper. As proportionalities between quantities are the only things of interest to us at this point, we can let the subscript *c* denote ' core ' values of quantities, so that

$$\rho_c \simeq M_c R_c^{-3}, \tag{11}$$

$$\frac{dP}{dr} \propto -M_c^2 R_c^{-5}(1-\bar{\chi}). \tag{12}$$

But when assume a fixed polytropic index for the core,

$$P \propto \rho^{\Gamma} \propto M_c^{\Gamma} R_c^{-3\Gamma}, \tag{13}$$

We find (Meader 1974)

$$\frac{dP}{dr} \propto -M_c^{\Gamma} R_c^{-(3\Gamma+1)}. \tag{14}$$

Combining equations (12) and (14) leads to

$$R_c \propto M_c^{(2-\Gamma)/(4-3\Gamma)} (1-\bar{\chi})^{1/(4-3\Gamma)} \tag{15}$$

and

$$\rho_c \propto M_c^{-2/(4-3\Gamma)} (1-\bar{\chi})^{-3/(4-3\Gamma)}. \tag{16}$$

This last relation can be used to show how effective rotation is in supporting additional mass, for under our linear treatment of rotation, and assuming homology we have, for a given p_c.

$$M_c \propto (1-\bar{\chi})^{-3/2}$$

Independent of the value of Γ in the core.

2.3 *The Burning Shell*

To obtain constraints on the temperature and luminosity we now generalize the approach of Refsdal and Weigert (1970) and Maeder (1974). In the shell, assumed to be thin relative to the core in both mass and radial co-ordinates, the basic parameters essentially depend on M_c (Refsdal and Weigert 1970), and including rotation (Maeder 1974) we can write

$$\rho \propto M_c^{\alpha} (1-\tilde{\chi})^{\alpha_1}, \quad P \propto M_c^{\beta} (1-\tilde{\chi})^{\beta_1},$$
$$T \propto M_c^{\gamma} (1-\tilde{\chi})^{\gamma_1} \text{ and } L \propto M_c^{\delta} (1-\tilde{\chi})^{\delta_1} \tag{18}$$

where we have used the average density weighted rotational support in *the shell* defined via

$$\tilde{\chi} = \int_{\text{shell}} \rho \chi \, d(1/r) \Big/ \int_{\text{shell}} \rho \, d(1/r). \tag{19}$$

In order to determine the exponents in equations (18) we must introduce an equation of state and the constitutive equations. For simplicity, we shall assume that the

opacity does not vary substantially across the shell; also, because the shell is assumed to be (and usually is) thin, we take $M_r = M_c$, a constant, within the shell. While the bulk of the energy is carried off by photons, the great majority of the energy is generated by nuclear fusion, and we can approximate

$$L_r \propto \rho^u T^n r^2 dr, \tag{20}$$

Where u and n depend on the dominant type of nuclear reaction (*cf.* Clayton 1968). We are then led to distinguish different cases determined by the physical conditions in the shell.

Case 1: *Gas pressure dominated, radiative transport*

In this case, the only one considered by Maeder (1974), we take

$$P \propto \rho T, \tag{21a}$$

$$dP \propto -M_c \rho \frac{dr}{r^2}(1-\chi) \tag{21b}$$

and

$$dT^4 \propto \rho L \frac{dr}{r^2} \tag{21c}$$

for the shell and the region above it. Comparing equations (18), (20) and (21) leads to the relations

$$\beta = \alpha + \gamma, \quad \beta = \alpha + 1, \quad 4\gamma = \alpha + \delta, \quad \delta = u\alpha + n\gamma,$$

which can be solved to yield

$$\alpha = \frac{4-n}{u+1}, \quad \beta = 1 + \frac{4-n}{u+1}, \quad \gamma = 1, \quad \delta = 4 - \frac{4-n}{u+1}. \tag{22}$$

(in this, and in all other cases as well, it turns out that $a_1 = a$, $\beta_1 = \beta$, $\gamma_1 = \gamma$, and $\delta_1 = \delta$.)

When we have a low mass star, so that a H-shell surrounding a He-core is processsing material through the CNO cycle, $u=2$ and n =16 Then, for the variable of most interest to us, we obtain

$$L \propto M_c^8 (1-\tilde{\chi})^8. \tag{23}$$

When we examine the star at fixed core density we have in this instance, using equation (17),

$$L \propto (1-\bar{\chi})^{-12} (1-\tilde{\chi})^8. \tag{24}$$

Case 2 : Gas pressure dominated, convective transport

While equations (21a, b) still hold, in place of (21c) we must use

$$dT \propto T\,(1-\Gamma_2^{-1})\frac{dP}{P}. \tag{25}$$

Using equations (20), (21a, b) and (25) we solve for the exponents in (18) and discover that

$$\alpha=\frac{1}{\Gamma_2-1},\quad \beta=\frac{\Gamma_2}{\Gamma_2-1},\quad \gamma=1,\quad \delta=\frac{u}{\Gamma_2-1}+n, \tag{26}$$

so that the adiabatic index of the convective shell is very important in determining most of these scaling laws. Since, however, $4/3 < \Gamma_2 \lesssim 5/3$ for stable shells, and η is substantially greater than $3u/2$ (the variation in δ allowed by that range in Γ_2), δ is not as relatively dependent on $\Gamma 2$ and $\delta \simeq n + 3u/2$ *This* is always much greater than in Case 1 and larger variations with rotation may therefore be expected if the burning shell is convective.

Case 3: *Radiation pressure dominated*

If the shell is able to become radiation-pressure dominated we utilize equations (21b, c) but replace (21a) with

$$P \propto T^4, \tag{27}$$

so that the exponents in equations (18) are

$$\alpha=\frac{4-n}{4u+n},\quad \beta=1+\frac{4-n}{4u+n},\quad \gamma=\frac{u+1}{4u+n},\quad \delta=1. \tag{28}$$

This implies much more gradual changes in all properties, and since equation (17) still holds in our approximations, we have, at a given ρ_c,

$$L \propto (1-\tilde{\chi})^{-3/2}\,(1-\tilde{\chi}). \tag{29}$$

Case 4: *Degenerate shells*

If the shell ever approaches degeneracy, neither of the basic transport mechanisms we have been using so far is a very good approximation and our approach becomes hopeless. This means that in some cases, once we proceed beyond C-burning (Arnett 1972b, 1973a) where the shells can become somewhat degenerate, none of our valid cases may hold. Bat even though O-burning cores are quite degenerate for $M_\alpha \leqslant 8\ M_\odot$ (M_a is the original mass of the He star, which corresponds to the maximum He core mass built up just prior to He ignition (Arnett 1973b), we calculate that the He and C-burning shells are not very degenerate then, so that this restriction may not be

a serious drawback. Also note that Ne-burning cores in stars with $M_\alpha \leqslant 16\ M_\odot$ are degenerate (Arnett 1974a), so, unless we are dealing with *very* massive stars, our key assumption that the core approximates a white dwarf while the overlaying burning shell is not degenerate is usually reasonable.

Case 5: *Predominantly gas pressure, but non-negligible radiation pressure*

Following Refsdal and Weigert (1970) we introduce

$$\psi = 1 - P_R/P \tag{30}$$

with P_R the radiation pressure , and then, in lieu of equation (21a) we take

$$P \propto \rho T / \psi, \tag{31}$$

where we assume that ψ is not too different from unity. Then

$$L \propto [M_c (1 - \tilde{\chi})\ \psi]^\delta, \tag{32}$$

where δ is given in equation (22); similar relations hold for other shell variables. For a non-rotating star we have

$$\psi_0 = 1 - K' T_0^3/\rho_0 \equiv 1 - K, \tag{33}$$

where $K' = am_p\ \mu/3k$, as long as $P_R \ll P$ Using equation (33), the modifications to T and ρ analogous to that for L in (32), and the scaling laws given in equations (18) and (22), we eventually obtain, to lowest order,

$$\psi \simeq 1 - K\ [M_c\ (1 - \tilde{\chi})]^{3-\alpha}. \tag{34}$$

Then employing equation (17) in (32) and using (34) produces the relation (at constant ρ_c),

$$L \propto (1 - \bar{\chi})^{-3\delta/2}\ (1 - \tilde{\chi})^\delta\ \{1 - K\ [(1 - \bar{\chi})^{-3/2}\ (1 - \tilde{\chi})]^{3-\alpha}\}^\delta. \tag{35}$$

To this order, if $\bar{\chi} = \tilde{\chi}$ (see Section 2.4 below), this reduces to $L \propto (1 + \frac{1}{2}\ \delta\ \tilde{\chi} - \delta\ K)$. As δ is always positive, we see that the effect of radiation pressure is to decrease the photon luminosity. This provides a negative feedback mechanism, since for a given ρ an increase in T raises L, but concomitantly drops Ψ and moderates the flux.

2.4 *Type and Strength of Rotation*

Our results to this point have been characterized by the two parameters $\bar{\chi}$ and $\tilde{\chi}$, representative of the average degree of rotational support in the core and the shell, respectively. Let us now consider what the reasonable ranges for these quantities are. First we note, as mentioned previously, that an upper limit is set by the requirement that our cores be stable against non-axisymmetric perturbations on a secular

(dissipative) timescale. Translating the $T/|W|$ creations of Bodenheimer and Ostriker (1973) leads us to an approximate upper limit of $\chi_{max} = 0{\cdot}187$ for $\bar{\chi}$ This bound is applied to $\bar{\chi}$, not $\tilde{\chi}$, since it is the average degree of rotation in dense core that is of interest in setting instability timescales (Wiita and Press 1976). Since the burning shells are usually much less dense as well as much less massive (Arnett 1973b), they do not dominate the total ratio of rotational to gravitational energy.

Now we follow Maeder (1974) in analyzing the ratio $\bar{\chi}/\tilde{\chi}$, which is representative of the degree of differential rotation in the inner portions of the star. Since the shell is thin and its density low, the weighting factor used in equation (19) falls off quickly, we are safe in evaluating $\tilde{\chi}$ at the surface of the core, using equation(2).if $\bar{r}$ and $M_{\bar{r}}$ correspond to an ' average ' point where $\chi(\bar{r}) = \bar{\chi}$ inside the core, we can write

$$\eta \equiv \frac{\bar{\chi}}{\tilde{\chi}} = \frac{\Omega^2(\bar{r})\,\bar{r}^3\,M_c}{\Omega^2(R_c)\,R_c^3\,M_{\bar{r}}}. \tag{36}$$

As a simple approximation let us set $M_r = \frac{1}{2} M_c$, $\bar{r} = \frac{1}{2} R_c$, and then the ratio η is fixed by the rotation law. Solid body rotation, Ω = const., yields $\eta \simeq 0{\cdot}25$. On the other hand, extreme differential rotation, with $\Omega \propto (r^2 + a^2)^{-2}$, allows for $\eta \simeq 4$ if $a \ll R_c$ A compromise choice would be $\eta = 1$, equivalent to moderate differential rotation and the law $\Omega \propto (r+a)^{-1}$ This last relation is close to the one found in the rotating white dwarf models of Ostriker and Bodenheimer (1968) and has the additional advantage of simplifying the algebra. Thus, unless stated otherwise, we shall illustrate our results by taking $\eta = 1$ in the rest of the paper.

3. Rotational effects on luminosities

3.1 *Photon Luminosities*

The results of the previous section are brought together in Table 1, where the effects of rotation on various core/shell structures are summarized. The temperatures and densities picked are characteristic (for the later stages) of the M_α=4 $M_\odot$ non-rotating models of Arnett (1973a, 1974a), corresponding to main-sequence masses of about 15 $M_\odot$ (Arnett 1972a). The burning shells may be either radiative (Case 1), or convective (Case 2), depending on the exact phase of evolution and the mass of the core. For example, the non-rotating M_a = 4$M_\odot$ star investigated by Arnett has a He-burning shell which starts off as convective, and later switches over to radiative; but by the time a C-burning shell is established the He shell becomes marginally convective again (Arnett 1972b). That C-burning shell also appears to start off as convective but eventually becomes stable. Later shell-burning stages for this type of star are predominantly convective (Arnett 1974a, b). The general trend is for the He and C shells to be convective for a greater fraction of the time as the mass of the star increases, thus increasing the effect of rotation; however, during Ne and O-burning stages the heavier stars allow for radiative shells (Arnett 1972b, 1974a, b). For a few of the later stages some of the shells can become radiation pressure dominated (Case 3) for very massive stars (M_α = 32 $M_\odot$). In attempting somewhat more detailed calculations, particularly for stars with $M_\alpha \geqslant 16\ M_\odot$, the effects of radiation pressure (Case 5) should be included.

Table 1. Rotation and photon luminosities.

Core/Shell	$\log \rho_c$	$\log T_{\rm shell}$	u	n	Case	α	β	γ	δ	L_R/L_0 at $\chi_{\max}$ $\eta = 0{\cdot}25$	$\eta = 1{\cdot}00$	$\eta = 4{\cdot}00$
He/H (CNO)	6·0	7·40	2	16·7	(1)*	−4·23	−3·23	1·00	8·23	1·53 (−4)	2·34	8·69
					(2)† $\Gamma_2 = 5/3$	1·50	2·50	1·00	19·70	7·32 (−10)	7·68	1·77 (+2)
					(3)‡	−0·51	0·49	0·12	1·00	3·94 (−1)	1·11	1·30
C/He (3α)	7·5	8·23	3	22·0	(1)	−4·50	−3·50	1·00	8·50	1·14 (−4)	2·41	9·32
					(2) $\Gamma_2 = 5/3$	1·50	2·50	1·00	26·50	5·14 (−13)	15·54	1·05 (+3)
					(3)	−0·53	0·47	0·12	1·00	3·94 (−1)	1·11	1·30
O, Ne, Mg/C	8·0	8·95	2	12·0	(1)	−2·67	−1·67	1·00	6·67	8·10 (−4)	1·99	5·76
					(2) $\Gamma_2 = 1{\cdot}57$	1·75	2·75	1·00	15·51	6·42 (−8)	4·98	58·78
					(3)	−0·40	0·60	0·15	1·00	3·94 (−1)	1·11	1·30
S, Si/O	9·0	9·30	2	33.0	(1)	−9·67	−8·67	1·00	13·67	4·58 (−7)	4·12	36·25
					(2) $\Gamma_2 = 1{\cdot}55$	1·82	2·82	1·00	36·64	1·02 (−17)	44·38	1·51 (+4)
					(3)	−0·71	0·29	0·07	1·00	3·94 (−1)	1·11	1·30

Notes:

*Case 1 is gas pressure dominated with radiative transport.

†Case 2 is gas pressure dominated with convective transport; the value of Γ_2 is noted.

‡Case 3 is radiation pressure dominated and is purely illustrative because, for the models of this table, the gas pressure is always larger.

Temperatures and densities are taken from Clayton (1968) and Arnett (1972b, 1973b, 1974a, b) for a $M_\alpha = 4\ M_\odot$ core.

For illustrative purposes, let us stay with a $M_\alpha = 4\ M_\odot$ model, and note that when it is undergoing He-shell burning and is radiative (Case 1), $\delta \simeq 8.5$, so using equations (17) and (18) along with the assumption that $\eta = 1$ yields

$$L \propto (1 - \bar{\chi})^{-4.25}. \tag{37}$$

Other Case 1 conditions produce exponents between –3·33 and –6·83. Hence, for moderate differential rotation, the photon luminosity during shell burning stages increases, in accord with the results of Kippenhahn, Meyer-Hofmeister and Thomas (1970) for the earliest post-main sequence phases. But when we recall the stability and linearity limits for our assumptions, such an increase is not terribly dramatic; using $\chi_{\max}$ in equation (37) leads to a rotating to non-rotating luminosity ratio

$$L_R \lesssim 2{\cdot}4\, L_0. \tag{38}$$

This would imply an effective speeding up of the evolution rate by roughly a factor of two during these later stages. Of course an exact value cannot be obtained from this crude analytic approach, as the detailed rotational and chemical history of the star are of great importance. Such variations in the luminosity and in evolutionary speeds, therefore densities on the H-R diagram, are, in principle, detectable. But because this technique cannot make any predictions concerning the surface temperatures we cannot really estimate the shifts on the H-R diagram that would be produced. Two other points militate against observation of these types of perturbations: first, the changes brought about will be hidden in the scatter of the diagram, particularly for these rapidly evolving stars; second, the effects of rotation may cause a star of a given mass to mimic a non-rotating star of a different mass (*e.g.* for main sequence stars see Sackmann 1970).

In all the three major cases of the last section, comparisons of stars at equivalent core temperatures (instead of densities) lead to no changes in the photon luminosities. This is because equation (18) invariably shows that $M_c \propto (1–\bar{\chi})^{-1}$ at fixed T, and that proportionality yields no change in L, independent of y, δ and η.Comparisons at fixed core mass, which although of less physical significance than density may be computationally convenient, always lead to decreases in L, since δ is always found to be positive.

A convective shell (Case 2) allows more latitude in energy transport, and we intuitively expect that rotation will allow for more dramatic effects with regard to the flux permitted to pass. However, changes in density, pressure and temperature are likely to be smaller, due to the mixing over larger regions of the star. These ideas are supported by the results for the exponents listed in Table 1, as the absolute values of α, β and γ are always less than for radiative transport, while that for δ is much higher. Again assuming moderate differential rotation ($\eta = 1$) and setting $\bar{\chi} = \chi_{\max}$ the increase in L at given densities is at least a factor of five for our $M_\alpha = 4M_\odot$ conditions. Changes of this magnitude, and the concomitant speeding up of the evolution, might be detectable and could conceivably provide some badly needed insight into the question of the coupling of convection and rotation.

In the event that the star were to evolve through a radiation pressure dominated phase in the shell (Case 3), the effects of rotation would be quite small and almost certainly undetectable. The essential physical reason for this behaviour is that rota-

tion couples much more tightly to the fluid than to the radiation, and when radiation pressure is large the coupling is weak and all effects are reduced.

As we allow the rotation law to deviate from moderate differential motion we can expect to find more substantial changes. An important result is that solid body rotation throughout the core and shell always leads to a drop in the luminosity (as has long been known on the main sequence, *e.g.* Sackmann 1970). Note that the numbers quoted for η = 0·25 in Table 1 are almost certainly too small, since setting $\bar{\chi} = \chi_{max}$ allowed us to take $\tilde{\chi}$ = 0·748, which, although dynamically possible in the shell, clearly vitiates our basic assumption of sphericity. But even if $\tilde{\chi}$ is forced to stay under 0·2, non-negligible drops in luminosity, and therefore significantly lengthened evolution times, are to be expected if the viscosity and other angular momentum redistribution mechanisms are sufficiently rapid to ensure solid body rotation (Durisen 1975). Under these circumstances, for example, the He-core/H-shell structure can allow L_R/L_0 = 0·3. Such a drop in photon flux may significantly change the internal structure of the star by favouring the growth of convection zones in or above the burning shell. Alternatively, large increases in the luminosity are possible, even for Case 1, if extreme differential rotation can be achieved. While this may be possible in stages where free-fall is approached, as in proto-stellar or supernova collapse phases, in the non-dynamical phases we are concentrating on, such a rotation law does not appear very likely (Endal and Sofia 1978). In this case our comparisons at constant central density lead to results that differ from standard main sequence models, for they compare at constant mass, and as mentioned above, this always leads to a drop in luminosity.

3.2 *Neutrino Luminosities*

Starting from the time when core carbon-burning becomes the dominant source of nuclear energy, neutrino emission becomes the dominant mode for removing energy from a star. Thus the calculations of the previous subsection for the last burning phases are seen to be even less accurate than our many approximations would imply, for equation (20) is no longer nearly exact. It should also be recognized that these neutrino losses imply that the assumption of essentially homologous contraction breaks down, which some calculations (*e.g.* Endal and Sofia 1977) neglect to consider.

Now the relevant question is how rotation affects the total neutrino emission. At this point the distinction between the core and the shell is not so important since the neutrino flux is basically due to the ‘ thermal ’ processes (pair, plasma and photo production) in these stages of stellar evolution (Beaudet, Petrosian and Salpeter 1967; Tubbs *et al.* 1981) and comes from the entire central region. Our analytical treatment is not applicable to the very late stages, when densities get above 10^{10}g cm^{-3} or temperatures rise above 10^{10} K; at that point URCA and other non-thermal processes dominate and homology breaks down completely.

At any given temperature and density we can abstract the temperature and density dependences from the total neutrino (plus anti-neutrino) emission rate, and write $Q \propto \rho^{\nu} T^{k}$, where Q is the emissivity in erg cm^{-3} s^{-1}. Equivalently, the rate S, in erg g^{-1} s^{-1} is

$$S \propto \rho^{\nu-1} T^{k}. \tag{39}$$

In order to estimate the effects of rotation we assume first that the bulk of the neutrino-antineutrino pairs come from the core region, as it is the hottest and the densest region, and we reasonably neglect the contributions of the mantle and envelope. Second we use an average temperature and density characteristic of the core (*cf.* Arnett 1973a) to estimate the flux; this is adequate for our proportionality arguments. Third, we scale this temperature as the shell temperature in equation (18); as long as the core is degenerate this scaling is reasonable, although, of course, the actual average core temperature is higher than that in the surrounding zone. It is important to notice that spherical models show only small temperature gradients in these regimes (Arnett 1974b), so even this—the weakest of our assumptions—is a viable one.

We write the ratio of rotating to non-rotating neutrino luminosities as a product

$$\frac{L_R^\nu}{L_0^\nu} = \left(\frac{M_R}{M_0}\right)\left(\frac{S_R}{S_0}\right) = \left(\frac{M_R}{M_0}\right)\left(\frac{\rho_R}{\rho_0}\right)^{v-1}\left(\frac{T_R}{T_0}\right)^k. \tag{40}$$

If we again compare cores of the same average density we still have equation (17), so $M_R/M_0 = (1 - \chi)^{-3/2}$ Case 3 is no longer amenable to our treatment, but for both Cases 1 and 2 we still may take $T \propto M_c\ (1 - \tilde{\chi})$, as this result is independent of equation (20) which no longer holds. When comparing rotating and non-rotating cores of equal density we then obtain

$$\frac{L_R^\nu}{L} \simeq (1 - \bar{\chi})^{-3(k+1)/2}(1 - \tilde{\chi})^k. \tag{41}$$

In Table 2 this ratio is evaluated for several stages of evolution and for several values of η. The basic conclusions turn out to be similar to the case of photon emission, in that differential rotation can increase the neutrino flux, while solid body rotation suppresses it. Because of the similar k exponents from C-burning through O-burning stages, we find that moderate differential rotation tends to raise the neutrino luminosity in that entire region by a factor of about four or five. Again this will accelerate the evolution through these already short-lived phases. Note that the results for solid body rotation are again almost certainly too low (for the reason discussed above) but it is clear that significant drops in L_ν are possible in this case.

Table 2. Rotation and neutrino luminosities.

Core	log ρ	log T	v	k	L_R/L_0 at χ_{max} $\eta = 0{\cdot}25$	$\eta = 1{\cdot}00$	$\eta = 4{\cdot}00$
He	3·0	8·2	3·0	2·4	0·10	1·76	2·59
C	5·7	8·9	0·0	11·5	6·0(−6)	4·51	28·34
Ne	7·2	9·1	−0·2	11·8	4·7(−6)	4·61	30·03
O	7·3	9·2	−0·7	11·7	5·0(−6)	4·59	29·63

Notes:

Average core values for ρ and T are from Arnett (1972b, 1973b, 1974a, b) for $M_\alpha = 4\ M_\odot$ cores. The neutrino emissivities are from Tubbs *et al.* (1981), assuming that the heavy lepton (τ particle) contributes.

3.3 *Gravitational Radiation*

We now turn to a brief discussion of one aspect of a topic that has excited much recent speculation and calculation: the emission of gravitational radiation by collapsing, rotating cores. One approach has been to concentrate on the star and to attempt to use detailed evolutionary models carried till the late stages in order to model a *somewhat* realistic core collapse (Meier *et al.* 1976; Endal and Sofia 1977, 1978). The other route has been to concentrate on the gravitational waves and to use simple equations of state and models for hypothetical collapsing cores that can be more easily followed numerically (Shapiro 1979; Saenz and Shapiro 1979, and references therein). These latter calculations have yielded an upper limit to energy lost via gravitational radiation of $\Delta E \lesssim 10^{-2}\ Mc^2$ in a time $\lesssim 10^{-2}$ if the collapse is cold, but the more likely initial state of a hot, high entropy core (Schramm and Arnett 1975) implies a slower collapse and yet less emission. However Endal and Sofia (1977) claim a minimum energy loss of the order of 2 per cent through gravitational waves.

No new calculations are presented in this section; we merely wish to point out that the above discrepancy can be understood as arising from several unlikely assumptions made by Endal and Sofia. Their work (Endal and Sofia 1976, 1978) on evolving rotating stars through some post-main sequence phases uses an equipotential technique, which, when coupled with fast computers, allows for significant improvements over earlier work (*e.g.* Kippenhahn, Meyer-Hofmeister and Thomas 1970; Sackmann and Weidemann 1972). Their diffusion technique is a major advance in treating secular angular momentum redistribution mechanisms, but their choice of the size of the diffusion constant is a rather arbitrary one, and slight variations will probably have important—and so far unexplored—consequences (*cf.* the mixing length treatment of convection). They, like most previous workers, probably exaggerate the effectiveness of chemical composition barriers (Huppert and Spiegel 1977).

In Endal and Sofia's (1977) estimate of gravitational radiation emission the key assumption is that their last evolved 10 $M_\odot$ model with central density of $1{\cdot}0 \times 10^6$ g cm^{-3} and central temperature of $5{\cdot}8\times10^8$ K, can be homologously extrapolated down to the much higher central density of 1.9×10^9 g cm^{-3}, while the angular momentum distribution of their last computed model remains the same. But it is exactly during these post-carbon burning phases that neutrino losses break down the homology arguments (Arnett 1972b, 1974a, b), and while the nuclear evolutionary timescales are much shorter by this time, some of the redistribution timescales also drop and the second half of the above assumption is also dubious. Using conservation of specific angular momentum they claim to show that non-axisymmetric, fissioning cores develop before the collapse phase (*e.g.* $\rho = 10^{10}$ g cm^{-3}, taken as the initial state in Saenz and Shapiro 1979); the subsequent collapse of such a triaxial or multiple core could lead to efficient ($\Delta E/Mc^2 > 10^{-2}$) emission of gravitational radiation (Miller 1974; Clark and Eardley 1977).

While this scenario may be possible, we think it highly unlikely for the following reasons. First, observed white dwarfs (as well as neutron stars) never exhibit the distorted shapes or extreme rotational velocities expected if the cores do evolve this way (Hardorp 1974). Although the low values of observed angular momentum for neutron stars may reflect a great deal of dissipation during their violent births, no

such mechanism appears to be available for white dwarfs, and the Endal and Sofia scenario, unlike others, seems to imply rapidly rotating dwarfs. Second, we do not trust either the assumption of specific angular momentum conservation or that of homologous contraction in this critical phase, as explained above. And it should be noted that the question as to whether critical angular velocities (and thus substantial angular momentum dissipation) or high T/ |W| values (and thus axisymmetric evolution) are reached first, is extremely sensitive to these assumptions. Third, this approach (as well as ours) totally neglects magnetic fields, which may put a substantial break on the contraction and spin up. For even if the values of Leblanc and Wilson (1970) and Meier *et al.* (1976) for the field energy are high, and their assumption of pinned field lines overemphasizes the growth of the fields, the fields probably still have significance at this stage. If strong differential rotation does develop, some amplification of fields, removing energy from the rotational mode, is to be expected, for the work of Weiss (1966) is not applicable to this compressible situation. Finally, even if we were to accept the dubious arguments of Endal and Sofia, we must note that the competition between rotational effects is also very sensitive to the initial conditions, *i.e.* the rotation law found for their last computed model. And because of the assumptions that went into their detailed calculations, a large uncertainty in those initial conditions must exist (see Tassoul 1978, p. 352).

4. Conclusions

Rotation can affect the later stages of stellar evolution in several substantial ways. Using an approximate analytical treatment we have shown that moderate differential rotation tends to increase both photon and neutrino fluxes during the post-main sequence phases. If the burning shells are convective these increases can be quite large. But, if the core and the shell somehow manage to rotate rigidly, substantial decreases in luminosity are likely. This great uncertainty emphasizes the gaps in our current understanding of the problem.

We have also argued that a star evolving through the multiple shell burning stages is unlikely to fission or even become substantially axisymmetric. However, when the star reaches the final pre-supernova phase and the core starts to collapse, rotation may produce dramatic effects. One of these is the coupling of rotation with the emission of neutrinos; Kazanas and Schramm (1979) have recently shown that some fraction of the angular momentum can be carried off in this way. But, as convincingly argued by Shapiro (1979) these effects probably do not include the loss of more than 2 per cent of the rest mass energy in the form of gravitational radiation.

Some progress is being made in extending detailed rotating models beyond the main sequence and helium core burning stages (Endal and Sofia 1976, 1978). But a mere listing of the effects that must be included in such calculations underscores their difficulty. Among them are: convection, Solberg-Hoiland instabilities, dynamical and secular shear instabilities, Eddington currents, μ-currents and barriers, Goldreich-Schubert-Fricke instabilities, photon and neutrino viscosities, and magnetic fields. The coupling of the last with rotation is probably the most important question inadequately treated as yet for this stage of evolution. But basic physical questions regarding the interaction of convection and rotation, the shear instabilities (Zahn 1974),

and μ-currents also require more analysis. While most of the other processes appear to be basically understood, their application to evolution has almost always been in terms of drastically simplified approximations.

Future numerical work must strive to clear up many of these problems by either using more sophisticated treatments, or else by demonstrating that the approximations employed are really valid. Until that kind of analysis is performed, we feel that the crude treatment given here is useful, as it serves to illustrate important effects and places bounds on the results expected from more careful numerical calculations.

Acknowledgements

Thanks are due to Drs. W. D. Arnett, D. Kazanas and D. N. Schramm for many stimulating discussions on these topics. This research was supported in part by NSF grants at the University of Chicago, by a NSF-NATO fellowship at the Institute of Astronomy, Cambridge, and by a Faculty Research Fellowship at the University of Pennsylvania.

References

Arnett, W. D. 1972a, *Astrophys. J.*, **176**, 681.
Arnett, W. D. 1972b, *Astrophys. J.*, **176**, 699.
Arnett, W. D. 1973a, *Astrophys. J.*, **179**, 249.
Arnett, W. D. 1973b, in *Explosive Nucleosynthesis*, Eds. D. N. Schramm and W. D. Arnett, University of Texas Press, Austin, p. 236.
Arnett, W. D. 1974a, *Astrophys. J.*, **193**,169.
Arnett, W. D. 1974b, *Astrophys. J.*, **194**, 373.
Arnett, W. D., Schramm, D. N. 1973, *Astrophys. J.*, **184**, L47.
Beaudet, G., Petrosian, V., Salpeter, E. E. 1967, *Astrophys. J.*, **150**, 979.
Bodenheimer, P., Ostriker, J. P. 1973, *Astrophys. J.*, **180**,159.
Boss, A. P. 1980, *Astrophys. J.*, **237**, 866.
Clark, J. P. A., Eardley, D. M. 1977, *Astrophys. J.*, **215**, 311.
Clayton, D. D. 1968, *Principles of Stellar Evolution and Nucleosynthesis*, McGraw-Hill, New York,
Durisen, R. H. 1975, *Astrophys. J.*, **195**,483.
Endal, A. S., Sofia, S. 1976, *Astrophys. J.*, **210**, 184.
Endal, A. S., Sofia, S. 1977, *Phys. Rev. Lett.*, **39**, 1429.
Endal, A. S., Sofia, S. 1978, *Astrophys. J.*, **220,** 279.
Fricke, K. J., Kippenhahn, R. 1972, *A. Rev. Astr. Astrophys.*, **10**,45.
Hainebach, K. L., Norman, E. B., Schramm, D. N. 1976, *Astrophys. J.*, **203**, 245.
Hardorp, J. 1974, *Astr. Astrophys.*, **32**,133.
Huppert, H. E., Spiegel, E. A. 1977, *Astrophys. J.*, **213**, 157.
Kazanas, D., Schramm, D. N. 1979, in *Sources of Gravitational Radiation*, Ed. L. L. Smarr, Cambridge University Press, p. 345.
Kippenhahn, R. 1974, in *IAU Symp. 66: Late Stages of Stellar Evolution*, Ed. R. Tayler, D. Reidel, Dordrecht, p. 20.
Kippenhahn, R., Meyer-Hofmeister, E., Thomas, H. C. 1970, *Astr. Astrophys.*, **5**, 155.
LeBlanc, J. M., Wilson, J. R. 1970 *Astrophys. J.*, **161**, 541.
Maeder, A. 1974, *Astr. Astrophys.* **34**,409.
Meier, D. L., Epstein, R. L., Arnett, W. D., Schramm, D. N. 1976, *Astrophys. J.*, **204**, 869.
Miller, B. D. 1974, *Astrophys. J.*, **187**, 609.
Ostriker, J. P., Bodenheimer, P. 1968, *Astrophys. J.*, **151**,1089.
Refsdal, S., Weigert, A. 1970, *Astr. Astrophys.* **6**, 426.

Sackmann, I.–J. 1970, *Astr. Astrophys.*, **8**, 76.
Sackmann, I.–J., Weidemann, V. 1972, *Astrophys. J.*, **178**, 427.
Saenz, R. A., Shapiro, S. L. 1979, *Astrophys. J.*, **229**, 1107.
Schramm, D. N., Arnett, W. D. 1975, *Astrophys. J.*, **198**, 629.
Schwarzschild, M. 1958, in *Structure and Evolution of the Stars*, Princeton University Press, p. 178.
Shapiro, S. L. 1979, *Astrophys. J.*, **214**, 566.
Tassoul, J.–L. 1978, *Theory of Rotating Stars*, Princeton University Press.
Tubbs, D. L., Margolis, S. H., Schramm, D. N., Wiita, P. J. 1981, In preparation.
Weiss, N. O. 1966, *Proc. R. Soc. London Ser. A.*, **293**, 310.
Wiita, P. J., Press, W. H. 1976, *Astrophys. J.*, **208**, 525.
Wiita, P. J., Schramm, D. N., Symbalisty, E. M. D. 1979, *Proc. Tenth Lunar Planet. Sci. Conf : Geochim. Cosmochim. Acta, Suppl.*, **11**, 1849.
Zahn, J. P. 1974, in *IAU Symp. 59: Stellar Instability and Evolution*, Eds P. Ledoux, A. Noels and A. W. Rodgers, D. Reidel, Dordrecht, p. 185.

J. Astrophys. Astr. (1981) **2**, 405–419

Equilibrium Configuration of the Magnetosphere of a Star Loaded with Accreted Magnetized Mass

Yutaka Uchida and B. C. LOW* *Tokyo Astronomical Observatory, University of Tokyo, Mitaka, Tokyo, 181 Japan*

Received 1981 June 29; accepted 1981 October 14

Abstract. Equilibrium configuration of the magnetosphere of a star loaded by the gravitationally accreted plasma having its own magnetic field is investigated. Axisymmetry around the star's magnetic axis is assumed for simplicity. It is seen that two distinct configurations appear for the cases of parallel and antiparallel magnetic field of the accreted plasma with respect to the star's magnetic moment. If the external field is antiparallel to the star's magnetic moment, the stellar magnetosphere is confined within a spherical region surrounded by the external field with a separatric surface between them. This is an extension of the case of the spherical accretion of non-magnetic plasma dealt with thus far in connection with the mass accretion by the degenerate stars in X-ray binaries. It is noticed that the mass slides down along the field lines to the point closest to the star and is stratified hydrostatically in equilibrium to form a disk in the equatorial plane. The mass loading compresses the sphere as a whole in this case. If, on the other hand, the external field is parallel to the star's magnetic moment, there appears a ring of magnetic neutral point in the equatorial plane. Polar field is open and extends to infinity while the low-latitude field is closed and faces the external field of opposite polarity across the neutral point. The increase of the loaded mass in this case causes a shrink of the closed field region, and the open polar flux is increased. Therefore, the transition between equilibria with small and large amount of the loaded mass requires the reconnection of magnetic lines of force, and the reconnection of the flux through the magnetic neutral ring is proposed as the mechanism of the steady or the intermittent mass leakage like the ones postulated for some X-ray bursters.

Key words: stellar magnetospheres—accretion of magnetized mass—X-ray binaries

*Visiting Scientist supported by the Japan Society for the Promotion of Sciences. Present address: High Altitude Observatory, Boulder, Colorado 80307, USA.

1. Introduction

The magnetosphere of a celestial object treated as a physical system is a useful concept encountered in diverse astrophysical circumstances. Examples of it include the magnetospheres of the earth and planets, the magnetospheres of the stars ranging from that of the sun to that of degenerate objects such as white dwarfs and neutron stars, and the ‘ magnetospheres ’ of the galaxies, *i.e.* galactic magnetic halos. The magnetosphere embodies the physical interaction between the central object and its environment through the magnetic field of the celestial body. Depending on the nature of the central object and its environment, quite different physical situations exist. For example the underlying effect in the case of earth’s magnetosphere is the inter action between the slowly rotating earth and the directed flow of plasma in the solar wind. Stellar magnetosphere may involve the trapping of the heated plasma (corona) and the control of the outflow of the plasma by magnetic field (stellar wind). In contrast, the magnetosphere of a neutron star in X-ray binaries embodies the interaction of the gravitationally accreted plasma with rapidly rotating star having a strong magnetic field.

Although there have been discussions of the phenomena occurring in these magnetospheres and a considerable progress has been achieved, only few attempts have been made to obtain the self-consistent configurations of the global magnetic field structure in them. It is needless to say, however, that the global model field is important because it provides the stage for those various physical processes and may affect even the physical interpretation of the observed phenomena.

In the present paper we confine ourselves to the problem of the axisymmetric non-rotating magnetosphere in equilibrium with the magnetized mass accreted by the central gravitating star, as a first step to more complex problems. This situation may correspond to a magnetic star embedded in a dense cloud of interstellar matter which has its own large-scale weaker magnetic field, as an example. In Section 2, we derive the basic equation describing the axisymmetric magnetosphere with loaded mass. A class of exact solutions are obtained and analysed in Section 3. In Section 4, we give discussion and mention the implication and the application of the results obtained.

2. Axisymmetric magnetostatic equilibrium

Consider an axisymmetric plasma surrounding a spherically symmetric star which has the gravitational potential,

$$\Phi = -\frac{GM}{r} \tag{1}$$

where G is the gravitational constant, M is the mass of the star and r is the distance from the centre. The magnetostatic equilibrium of the plasma is governed by the equation,

$$\frac{1}{c}(\mathbf{j} \times \mathbf{B}) - \nabla p = \rho \nabla \Phi \tag{2}$$

where **B** is the magnetic field, p and ρ are the pressure and the density of the plasma, respectively. **B** fulfils $\nabla \cdot \mathbf{B} = 0$, and $p = \mathcal{R}\,\rho\,T$, where T is the temperature and $\mathcal{R}$ is the gas constant. The task at hand is to derive the solution of equation (2) with these auxiliary relations*.

Let us use the spherical coordinate (r, θ, ϕ) with the pole coinciding with the axis of symmetry. Then, the condition $\nabla \cdot \mathbf{B} = 0$ and the assumption of axisymmetry imply that B is expressible as

$$\mathbf{B} = \left\{ \frac{1}{r \sin\theta} \frac{\partial (\sin\theta\, A_\phi)}{\partial \theta},\ -\frac{1}{r} \frac{\partial (r A_\phi)}{\partial r},\ B_\phi \right\}, \tag{3}$$

where A_ϕ is the ϕ–component of the magnetic vector potential. Note that the magnetic field **B** is defined in terms of two scalar functions, namely, A_ϕ and B_ϕ the current density **j** is given by

$$\frac{4\pi}{c}\mathbf{j} = \nabla \times \mathbf{B} = \left[\frac{1}{r \sin\theta} \frac{\partial (\sin\theta\, B_\phi)}{\partial \theta},\ -\frac{1}{r} \frac{\partial (r B_\phi)}{\partial r},\right.$$
$$\left. -\frac{1}{r}\left\{ \frac{\partial^2 (r A_\phi)}{\partial r^2} + \frac{\partial}{\partial \theta}\left(\frac{1}{r \sin\theta} \frac{\partial (\sin\theta\, A_\phi)}{\partial \theta} \right) \right\} \right]. \tag{4}$$

Substituting equations (3) and (4) into equation (2) and considering the force balance in the azimuthal direction, we have

$$\frac{\partial (A_\phi\, r \sin\theta,\ B_\phi\, r \sin\theta)}{\partial (r, \theta)} = 0, \tag{5}$$

and this demands that

$$\tilde{B} = \text{func}\,(\tilde{A}) \tag{6}$$

where $\tilde{A} = A_\phi\ r \sin\theta$ and $\tilde{B} = B_\phi\, r \sin\theta$ (Lust and Schlüter 1954; Chandrasekhar 1956).

By using this, the r and θ-components of eqution (2) then take the form,

$$\frac{\partial \tilde{A}}{\partial r}\left\{ \frac{\partial^2 \tilde{A}}{\partial r^2} + \sin\theta \frac{\partial}{r\,\partial\theta}\left(\frac{1}{\sin\theta} \frac{\partial \tilde{A}}{r\,\partial\theta} \right) + \frac{1}{2}\frac{d\tilde{B}^2}{d\tilde{A}} \right\} = -4\pi r^2 \sin^2\theta \left(\frac{\partial p}{\partial r} + \rho \frac{\partial \Phi}{\partial r} \right), \tag{7}$$

$$\frac{\partial \tilde{A}}{r\,\partial\theta}\left\{ \frac{\partial^2 \tilde{A}}{\partial r^2} + \sin\theta \frac{\partial}{r\,\partial\theta}\left(\frac{1}{\sin\theta} \frac{\partial \tilde{A}}{r\,\partial\theta} \right) + \frac{1}{2}\frac{d\tilde{B}^2}{d\tilde{A}} \right\} = -4\pi r^2 \sin^2\theta \frac{\partial p}{r\,\partial\theta}, \tag{8}$$

*Comfort, Tandberg-Hanssen and Wu (1979) and Hundhansen and Zweibel (1981) have recently dealt with this problem in a different approach. Approaches in these are ultimately equivalent to ours, as they should be, but we believe that our formulation is more convenient in having insight into the type of the problem to be dealt with in this paper.

respectively. Multiplying equation (7) by $\partial\tilde{A}/r\partial\theta$ and equation (8) by $\partial\tilde{A}/\partial r$ and subtracting one from the other, we obtain

$$\frac{\partial(p, \tilde{A})}{\partial(r, \theta)} + \rho \frac{\partial \Phi}{\partial r} \frac{\partial \tilde{A}}{\partial \theta} = 0. \tag{9}$$

The magnetic field is now expressed in terms of $\tilde{A}$ and $\tilde{B}$ in the form,

$$\mathbf{B} = \frac{1}{r \sin \theta}\left(\frac{1}{r}\frac{\partial \tilde{A}}{\partial \theta}, -\frac{\partial \tilde{A}}{\partial r}, \tilde{B}\right) \tag{10}$$

and the magnetic lines of force are given by integrating the line-of-force equation,

$$\frac{d\mathbf{x}}{ds} = \frac{\mathbf{B}}{|\mathbf{B}|} \tag{11}$$

where $dx/ds \equiv (dr/ds, rd\theta, r \sin \theta\, d\phi/ds)$ and s is the length measured along the field line. If we look at this equation in a meridional plane, ϕ = const, it is easy to see by using equations (10) and (11) that $d\tilde{A} = 0$ along the projection on this plane of each field line. In other words, the curves $\tilde{A}(r, \theta)$ = const represent the lines of force projected on the $r\theta$–plane.

Given $\tilde{A}(r, \theta)$, we may transform an arbitrary function of r and θ into a function of r and $\tilde{A}$. We denote by $\partial/\partial \tilde{A}\, r$ the partial derivative with respect to r in this transformed system. This technique of transformation was used by Low (1975) for a magnetostatic problem in the planar geometry.

Transforming p (r, θ) into $p(r, \tilde{A})$, we have from equation (9),

$$\frac{\partial p}{\partial \tilde{A} r} + \rho \frac{\partial \Phi}{\partial r} = 0, \tag{12}$$

which may be integrated to obtain

$$p(r, \tilde{A}) = p(r_0, \tilde{A}) \exp\left\{-\int_{r_0}^{r} \frac{GMdr}{\mathcal{R}T(r, \tilde{A})\, r^2}\right\}. \tag{13}$$

In deriving equation (13) we made use of the ideal gas law $p = \mathcal{R} \rho T$ and transformed T (r, θ) into T $(r, \tilde{A})$. The integration is to be carried out with $\tilde{A}$ held constant, r_0 is a constant and $p(r_0, \tilde{A})$ is a free function of $\tilde{A}$ arising from the integration with respect to r. Substituting equation (12) into equations (7) and (8), we obtain

$$\mathcal{L}\tilde{A} + \frac{1}{2}\frac{d\tilde{B}^2}{d\tilde{A}} + 4\pi r^2 (1 - \mu^2) \frac{\partial p(r, \tilde{A})}{\partial \tilde{A}} = 0, \tag{14}$$

where

$$\mathscr{L} \equiv \frac{\partial^2}{\partial r^2} + \sin\theta \frac{\partial}{r\,\partial\theta}\left(\frac{1}{\sin\theta}\frac{\partial}{r\,\partial\theta}\right) \equiv \frac{\partial^2}{\partial r^2} + \frac{1-\mu^2}{r^2}\frac{\partial^2}{\partial\mu^2}, \tag{15}$$

$\mu \equiv \cos\theta$, and $\partial/\partial\tilde{A}$ is the partial differential operator with respect to $\tilde{A}$ when r and $\tilde{A}$ are taken to be independent variables.

In our approach to the magnetostatic problem, we must specify a priori the functional forms of $\tilde{B}(\tilde{A})$, $p(r_0, \tilde{A})$ and $T(r, \tilde{A})$. Then equation (13) fixes the functional form of $p(r, \tilde{A})$ and equation (14) poses a problem for $\tilde{A}$ as an unknown. In the final step, the quantities **B**, p, ρ and T are expressed in terms of the spatial coordinates through the explicit solution $\tilde{A}(r, \theta)$. In principle, the functional forms of $\tilde{B}(\tilde{A})$, $p(r_0, \tilde{A})$ and $T(r, \tilde{A})$ should be determined in an unambiguous way from some initial dynamical state if we perform an integration of the equations of motion, mass conservation, energy conservation, and magnetic induction, which govern the dynamical evolution of the system. For the present, however, we shall confine ourselves to a simple approach in which we deal with the equation of the mechanical equilibrium by specifying the functional forms of $\tilde{B}(\tilde{A})$, $p(r, \tilde{A})$ and $T(r, \tilde{A})$ in a reasonable manner and investigate what magnetostatic states are generated by them.

3. A class of exact solutions

For a given set of field lines $\tilde{A}$ = const, the functions $\tilde{B}(\tilde{A})$ and $p(r, \tilde{A})$ describe the amount of the ϕ-component of the magnetic field and the pressure along the individual field lines. Let us consider a simple case in which $\tilde{B} \equiv 0$ and

$$p(r, \tilde{A}) \equiv Q(r)\,\tilde{A} + S(r) \tag{16}$$

where $Q(r)$ and $S(r)$ are free functions. This example leads to analytic solutions and is best suited for demonstrating the basic behaviour of magnetostatic solutions. Substituting for $p(r, \tilde{A})$ in equation (14), we obtain the linear equation,

$$\frac{\partial^2\tilde{A}}{\partial r^2} + \frac{1-\mu^2}{r^2}\frac{\partial^2\tilde{A}}{\partial\mu^2} + 4\pi r^2(1-\mu^2)\,Q(r) = 0. \tag{17}$$

The density and temperature are given from equations (12) and (16) as

$$\rho = -\frac{r^2}{GM}\left(\tilde{A}\frac{dQ}{dr} + \frac{dS}{dr}\right) \tag{18}$$

And

$$T = -\frac{GM}{\mathscr{R}r^2}\frac{\tilde{A}Q + S}{\tilde{A}\dfrac{dQ}{dr} + \dfrac{dS}{dr}} \tag{19}$$

where $\tilde{A}$ is to be a solution of equation (17).

To solve equation (17), we obtain a particular solution of equation (17) and add it to the general solution of the homogeneous version of equation (17),

$$\frac{\partial^2 \tilde{A}}{\partial r^2} + \frac{1-\mu^2}{r^2} \frac{\partial^2 \tilde{A}}{\partial \mu^2} = 0. \tag{20}$$

The particular solution A_1 of equation (17) can be obtained by introducing the transform $\tilde{A}_1$ to u,

$$\tilde{A}_1 = (1-\mu^2)\, r^2\, u(r). \tag{21}$$

Equation (17) then reduces to

$$r\frac{d^2u}{dr^2} + 4\frac{du}{dr} + 4\pi r\, Q(r) = 0, \tag{21}$$

which can be shown to have a particular solution of the form

$$u(r) = -4\pi \int_{r_0}^{r} \frac{dr'}{r'^4} \int_{r_0}^{r'} r''^4\, Q(r'')\, dr''. \tag{23}$$

Equation (20) is just the equation for a potential magnetic field. The complete set of solutions to equation (20) corresponds to the set of multipole potential expansion in an axisymmetric system (Marion 1965). For the purpose of this paper, we consider the case where the solution of equation (20) is made of only the dipole and the uniform field. This solution represents the situation of a stellar dipole field superposed on a uniform interstellar magnetic field in vacuum. The solution of equation (20) which we want is,

$$\tilde{A}_0 = (1-\mu^2)\left(\frac{C_1}{r} + C_2\, r^2\right) \tag{24}$$

where C_1 and C_2 are constants. Direct substitution into equation (10) shows that the terms C_1/r and $C_2\, r^2$ represent a dipole and a uniform field, respectively. The solution to equation (17) that we seek is then

$$\begin{aligned} \tilde{A} &= \tilde{A}_0 + \tilde{A}_1 \\ &= (1-\mu^2)\left(\frac{C_1}{r} + C_2\, r^2 - 4\pi\, r^2\, \Psi_1(r)\right) \end{aligned} \tag{25}$$

where we define

$$\Psi_1(r) \equiv \int_{r_0}^{r} \frac{dr'}{r'^4} \int_{r_0}^{r'} r''^4\, Q(r'')\, dr''. \tag{26}$$

By substituting $\tilde{A}$ into equation (10), we have,

$$B_r(r,\theta) = \frac{1}{r^2 \sin\theta}\frac{\partial \tilde{A}}{\partial \theta}$$

$$= 2\left(\frac{C_1}{r^3} + C_2 - 4\pi\,\Psi_1(r)\right)\cos\theta \tag{27}$$

$$B_\theta(r,\theta) = -\frac{1}{r\sin\theta}\frac{\partial \tilde{A}}{\partial r}$$

$$= 2\left(\frac{C_1}{2r^3} - C_2 + 4\pi\,\Psi_1(r) + 2\pi\,\Psi_2(r)\right)\sin\theta \tag{28}$$

where

$$\Psi_2(r) = \frac{1}{r^3}\int_{r_0}^{r} r'^4\, Q(r')\, dr'. \tag{29}$$

The current density is given from equation (4) as

$$j_\phi(r,\theta) = c\left(r\,Q(r) - \frac{2}{r}\Psi_2(r)\right)\sin\theta. \tag{30}$$

Other components of **B** and **j** all vanish.

Boundary conditions to be set are: (a) The distribution of the magnetic flux on the stellar surface is not altered from the original one since the field lines are anchored by the heavy stellar material at its surface,

$$B_r(r_0,\theta) = B_p\cos\theta. \tag{31}$$

where B_p is the field strength at the star's magnetic pole, and (b) the field at infinity is not affected by the mass-loading around the star,

$$\mathbf{B}(\infty,\theta) = (B_\infty\cos\theta, -B_\infty\sin\theta, 0). \tag{32}$$

These boundary conditions demand that

$\Psi_1(r)$ converges to a finite value as $r\to\infty$, (35)

$\Psi_2(r)$ converges to zero as $r\to\infty$ (36)

and

$$\begin{cases} C_1 = r_0^3\left(\dfrac{B_p - B_\infty}{2} - 4\pi\,\Psi_1(\infty)\right), & (35) \\ C_2 = \dfrac{B_\infty}{2} + 4\pi\,\Psi_1(\infty). & (36) \end{cases}$$

We finally have the magnetic field components fulfilling the boundary conditions as

$$B_r(r,\theta) = \left\{ [B_p - B_\infty - 8\pi \Psi_1(\infty)] \left(\frac{r_0}{r}\right)^3 + B_\infty + 8\pi [\Psi_1(\infty) - \Psi_1(r)] \right\} \cos\theta, \quad (37)$$

$$B_\theta(r,\theta) = \left\{ \frac{[B_p - B_\infty - 8\pi \Psi_1(\infty)]}{2} \left(\frac{r_0}{r}\right)^3 - B_\infty - 8\pi [\Psi_1(\infty) - \Psi_1(r)] + 4\pi \Psi_2(r) \right\} \sin\theta. \quad (38)$$

We discuss simple illustrative examples in the rest of this section in order to demonstrate the properties of our solution. We first note that $S(r)$ does not come into equation (17) for the magnetic vector potential, A The effect of the mass loading comes only through $Q(r)$. A simple interpretation of this may be that $S(r)$ represents the background distribution of the mass in the absence of the magnetic field. $S(r)$ and $-dS/dr$ are required to be positive so that the background pressure and density are positive. The field-related portion of the pressure and the density, A $Q(r)$ and $-(r^2/GM)$ A dQ/dr, can be either positive or negative, corresponding to the enhancement over, or depletion below the background. If we assume that the field-related component of the density is positive outside the boundaries between the stellar and the accreted field, dQ/dr should be negative outside these boundaries and vanish inside, if we want to consider the accreted mass piling up outside these boundaries, deforming the magnetic field due to the effect of the gravity on it.

A simple example of $Q(r)$ fulfilling these conditions may be given by connecting a constant to an inverse-a power function smoothly across the boundary region as

$$Q(r) = Q_0 \left[\frac{\left\{ 1 - \tanh\left(\frac{r - r_b}{d}\right) \right\}}{2} + \frac{\left\{ 1 + \tanh\left(\frac{r - r_b}{d}\right) \right\}}{2} \left(\frac{r_0}{r}\right)^\alpha \right] \quad (39)$$

and we may assume $S(r)$ to be an inverse-a power function as

$$S(r) = S_0 \left(\frac{r_0}{r}\right)^\beta \quad (40)$$

as an example, where r_b is the distance to the boundary from the centre of the star, d is the thickness of the transition between internal and external regions across the boundary and Q_0 and ; are constants. The sign of Q_0 is chosen to make the additional component of the density positive in the external region so that it represents the mass pile-up by accretion.

Two cases arise corresponding to the signs of B_∞ relative to B_p which is assumed to be positive and $|B_p| > |B_\infty|$, $|8\pi \psi_1(\infty)|$. For the convenience of computation, we assume a ratio of $|B_p| / |B_\infty|$ of the order of $10^3 \sim 10^4$ in the following calculation. Much larger ratio of $|B_p| / |B_\infty|$ of degenerate star case is equally permissible except that the calculation requires more time and accuracy.

Case A: $B_\infty > 0$

A neutral point in $r\theta$-plane (actually a ring in three dimensions) appears at $r = r_n$ and $\theta = \pi/2$. In particular, for the case without mass loading ($Q_0=0$, $\psi_1 = \psi_2 = 0$), r_n turns out to be

$$r_{n_0} = \left(\frac{B_p - B_\infty}{2B_\infty}\right)^{1/3} r_0. \tag{41}$$

For $Q_0 \neq 0$ (> 0 in this case to make the additional density positive), we solve an equation,

$$\{8\pi [\Psi_1(\infty) - \Psi_1(r)] - 4\pi \Psi_2(r) + B_\infty\}\left(\frac{r}{r_0}\right)^3 - \tfrac{1}{2}[B_p - B_\infty - 8\pi \Psi_1(\infty)] = 0 \tag{42}$$

to obtain r_n. This equation comes from the condition that the coefficient of $\sin\theta$ in B_θ vanishes. An iterative method is adopted in finding r_b and r_n by assuming $r_b = (1 + \epsilon)\, r_n$, where ϵ *is* a small positive constant.

The field lines in the meridional plane for a typical set of parameter values are given by integrating equation (11) with B_r and B_θ given in equations (37) and (38), and are shown in Figs 1(b), (c). This is to be compared with the case of no mass-loading ($Q_0 = 0$) as given in Fig. 1(a). It is seen that r_n decreases as Q_0 increases, as expected from the gravitational effect of the additional mass introduced by nonzero Q_0. The density and the temperature distributions in $r\theta$-plane are calculated from equations (18) and (19) by using the solution for $\tilde{A}$ and expressions (39) and (40) for Q and S. The distributions of $\tilde{A}$, p, and T *in* r, for given θ for the case of Fig. 1(c) are given in Fig. 2 as examples. It is seen that the present solution has a concentration near the equatorial plane of the mass component due to Q, which interacts with the magnetic field.

Case B: $B_\infty < 0$

A different type configuration appears in this case; singular points occur above the poles. Now the coefficient of $\cos\theta$ in B_r has a zero point which in the mass-free case occurs at $r = r_{s0}$ and $\theta = 0$ and π, where

$$r_{s0} = \left(\frac{B_p - B_\infty}{-B_\infty}\right)^{1/3} r_0. \tag{43}$$

In this case, it is seen from equation (25) that $\tilde{A}$ changes sign from positive to negative as r increases, and we set $Q_0 < 0$ in. order to make the additional density in the region $r \gtrsim r_s$, positive. In order to obtain r_s in the mass-loaded case, $Q_0 \neq 0$ (< 0), we solve an. Equation

$$\{8\pi [\Psi_1(\infty) - \Psi_1(r)] + B_\infty\}\left(\frac{r}{r_0}\right)^3 - [B_p - B_\infty - 8\pi \Psi_1(\infty)] = 0, \tag{44}$$

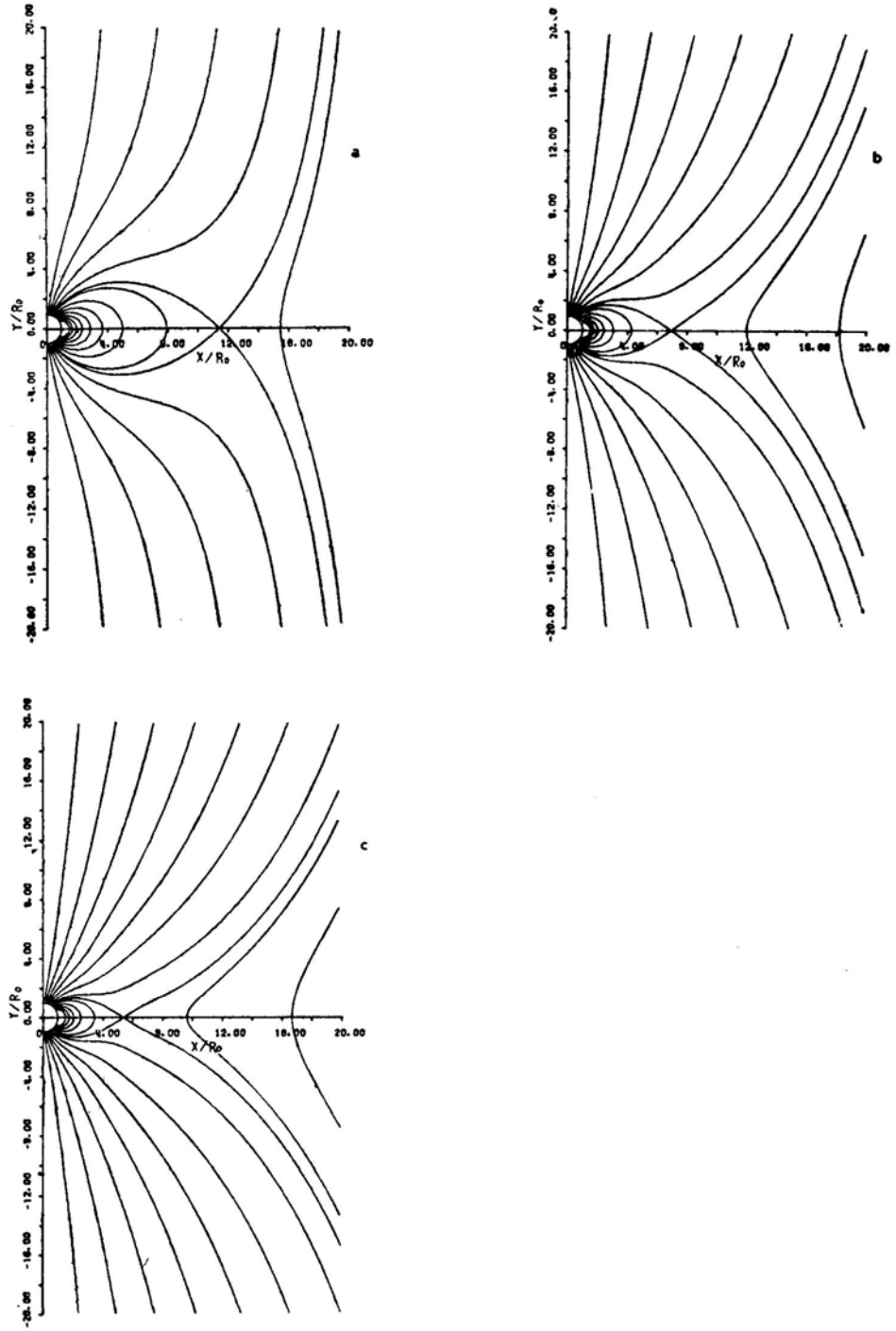

Figure 1. Magnetic field configuration in the meridional plane for Case **A** with $\boldsymbol{B_p}$ = 3 X 10^3 and B_∞, = 1. (a) Q_0 = 0, (b) Q_0 = 1 x 10^{-2}, (c) Q_0 = 4 x 10^{-2}. In this figure and in the following, *a* and *b* in expressions (39) and (40) are both taken to be 4 and $\in \equiv (r_b/r_n - 1)$ is 0 2, to show an example.

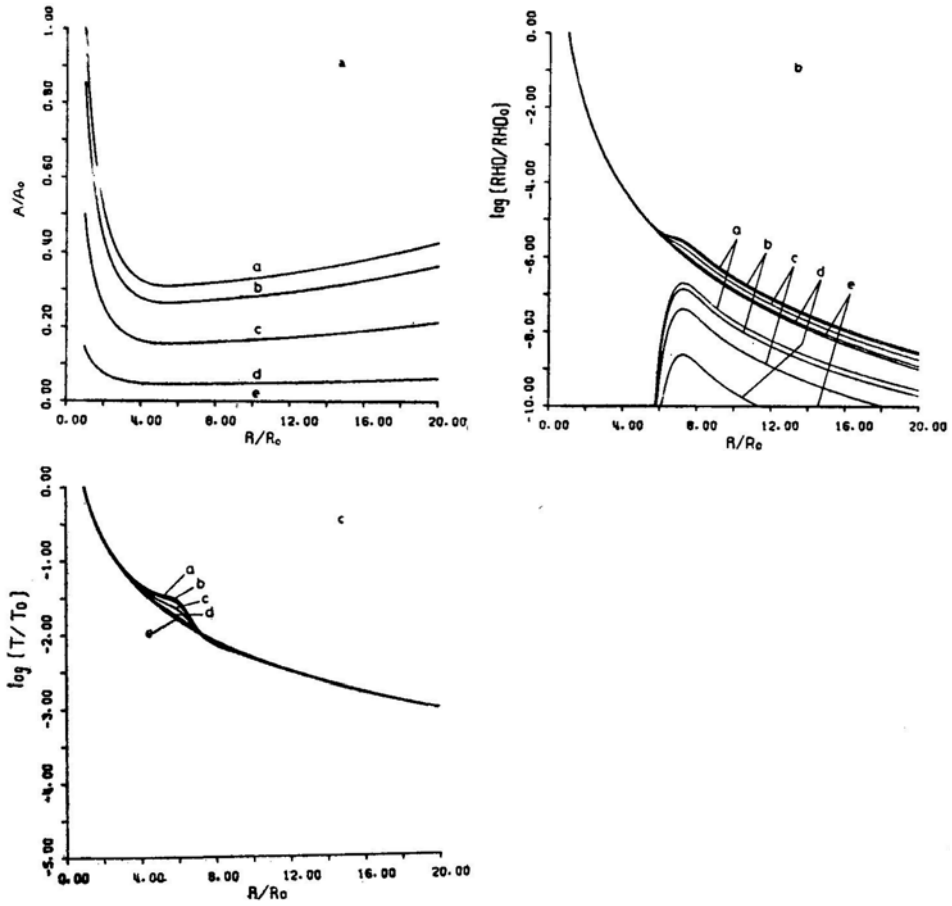

Figure 2 Distributions in r of (a) $\tilde{A}$, (b) the total density, ρ, and the density related to the magnetic field, — (r^2/GM) $A\ dQ/dr$, and (c) the temperature, T, for the case of Fig. I. (c), all normalized to the values at the equatorial surface. Curves (a) through (e) in the figures are for θ= 90°, 67 5°, 45°, 22 5° and 0°, respectively.

which comes from the condition that the coefficient of cos θ in B_r vanishes. r_s is r_s is obtained by the same iterative scheme as in Case A. Fig. 3(a) (Q_0 = 0) and 3(b), (c) ($Q_0 \neq 0$) show that the field configuration in Case B is very different from that in Case A. The distance to the singular point is seen to decrease with increasing Q_0 also in this case due to the shrink of the domain of the stellar field by mass-loading.

Fig. 4 shows the distributions of $\tilde{A}$ ρ and T for the case of Fig. 3(c) as examples. The mass slides down along the field lines to the closest point from the star and distributes itself hydrostatically, and thus its distribution becomes disk-like in the equatorial plane in this case also.

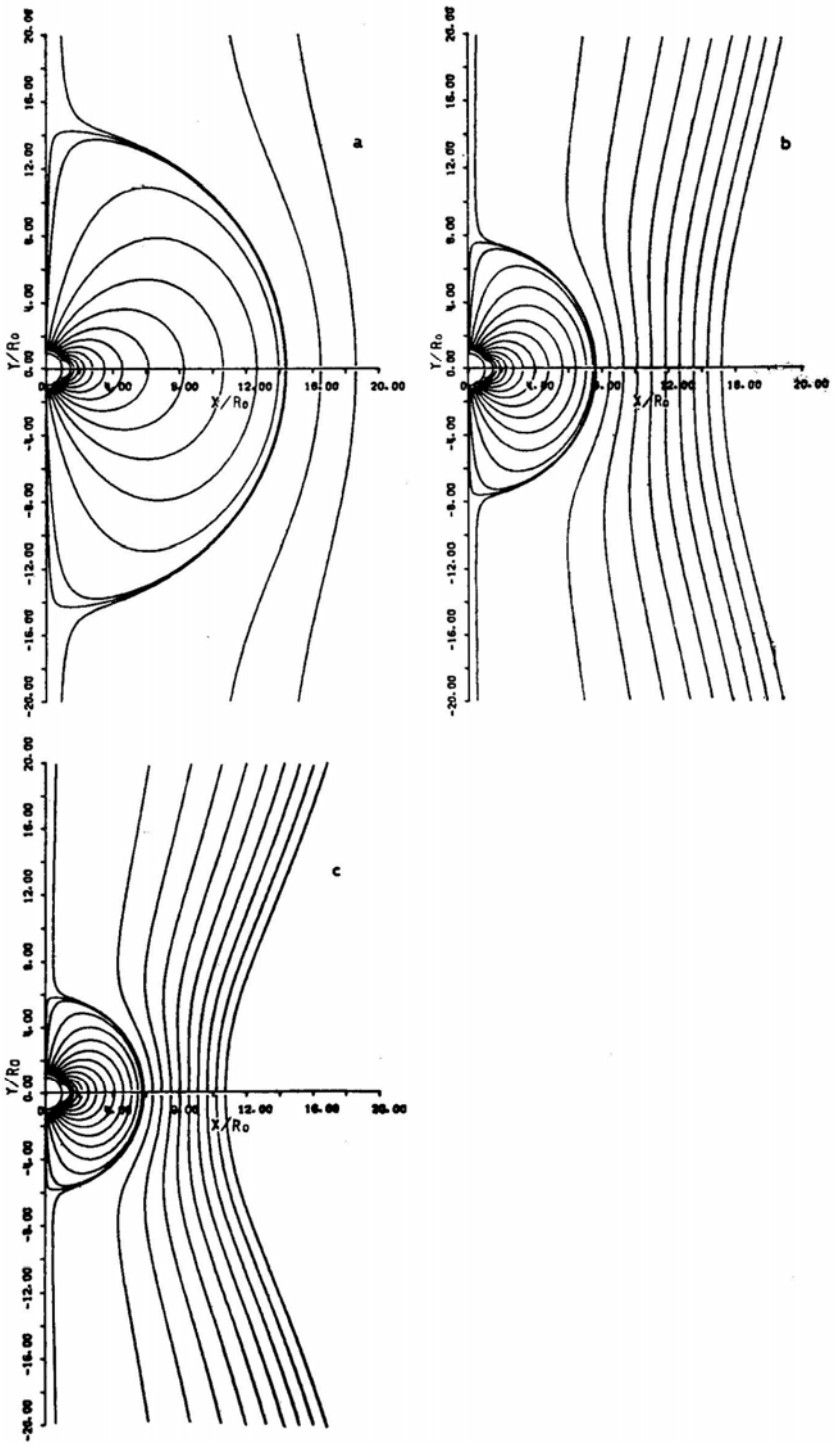

Figure 3. The same as Fig. 1 for Case B, with $B_p = 3 \times 10^3$ and $B_\infty = 1$; (a) $Q_0 = 0$ (b) $Q_0 = 1 \times 10^{-2}$ and (c) $Q_0 = -4 \times 10^{-2}$.

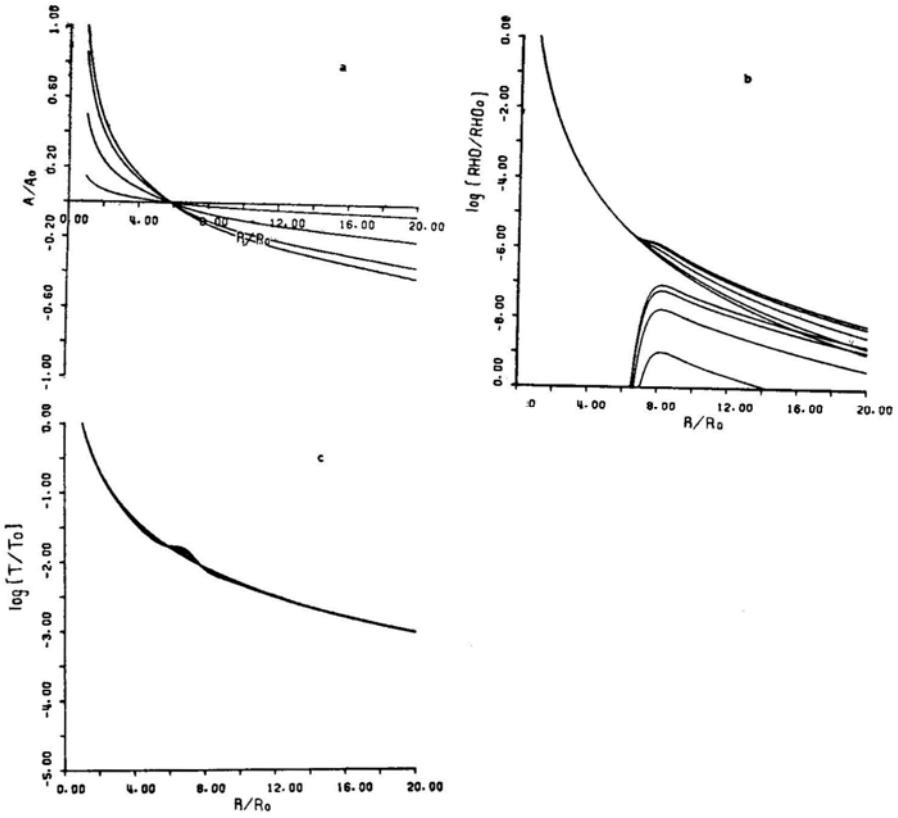

Figure 4. The same as fig. 2 for Case B.

4. Discussion

We have demonstrated simple solutions for the axisymmetric magnetogravitational equilibrium governed by equation (14) in order to obtain the global self-consistent magnetic field configuration of a star loaded by the mass which is, for example, accreted from dense (magnetic) cloud surrounding the star*. It is noteworthy that the inclusion of the axisymmetric magnetic field alone results in the formation of a disk-like density structure. Physically, this is due to the fact that the mass slides down along the field lines to the closest possible points which are—in both Cases A and B —in the equatorial plane. The density is stratified hydrostatically along each tube of force with a scale height corresponding to the temperature given by equation (19), and it has a concentration in the equatorial plane as seen from Figs 2 and 4.

Many models of 'spherical accretion' have been discussed (see review by Lamb 1979) in the context of mass accretion by neutron stars in X-ray binaries, but the global solution of the self-consistent field was not dealt with in full. The configuration

*The situation may also be applicable to a degenerate magnetic star in the companion's magnetic atmosphere if the effect of both rotation of the degenerate star and revolution of the accreted gas around the degenerate star be small. It is, however, likely that these effects are important in this case and we intend to take into account these effects in later papers in certain approximate way.

derived in Case B is related to the shielded-dipole type model argued by Midgley and Davis (1962). They considered no external field, and sought the shielding current layer which cuts off the effect of the internal field to zero beyond certain radius, representing the effect of the gas pressure of the external plasma. Models of the closed magnetosphere extended to include the effect of the accretion disk have been discussed after the introduction of the notion of the accretion disk by Pringle and Rees (1972) and Shakura and Sunyaev (1973). Inoue (1976) and Ghosh and Lamb (1978) have assumed the formation of the indentation of the field configuration at the equator due to the gravity effect on the disk material. It may be noted in this context, however, that the disk-like structure, at least in our solution, squeezes the stellar field as a whole rather than pushing into it like a sharp knife-edge as assumed by them.

In relation to the problem of the mass take-in into the stellar field region, it is often suggested that the mass flows into the polar region. It may be pointed out, however, that the singular openings above the poles are covered up by the field lines in the presence of the external field, and this may affect the mass flow into the polar region assumed in some models. Magnetic field lines should be reconnected in order to allow the mass infall into the closed field region. An alternative mechanism, the Rayleigh-Taylor instability, is proposed to play a role in the process of the mass take-in (Arons and Lea 1976, Elsner and Lamb 1977, Baan 1977). In their models, however, the unmagnetized plasma-blob falling across the star's field will be resisted by the inverse melon-seed effect and may lose the kinetic energy of the free fall.

An interesting situation occurs in our Case A in this context, namely, the field line reconnection can take place at the magnetic neutral ring in the equatorial plane in a very natural way. In this context, note the difference between Figs 1(a) and 1(c) which is due to the difference in the loaded mass. The, open part of the stellar magnetic flux is larger in Fig. 1(c). No dynamical or time-dependent behaviour can be argued from the sequence of the equilibrium models, but it is clear that there should be some reconnection of the field if the state is to change from that of Fig. 1(a) to that of Fig. 1(c) as the result of the increase of the loaded mass. The mass loaded on the external tube of force around the equatorial plane can be transferred to the stellar field by reconnection and can fall to the stellar surface at the edge of the polar cap area along the field lines passing through the neutral point. The reconnected part of the stellar field is now added to the open part of the stellar field. Interchange instability *in* the neutral sheet region was proposed to play an important role in the case of solar flares (Uchida and Sakurai 1977, 1981). The same mechanism may be relevant to the self-quenched mass leakage in a rapid burster type object (Lewin and Joss 1977). We consider this process in some more detail in a following paper. A more detailed discussion in this direction requires the inclusion of the effect of rotation of both the central star and of the accreted mass. The rotation of the disk introduces the pulling of the field lines into ϕ-direction and complicates the problem, but some part of the effects may be represented by $\tilde{B}$ which we ignored in the present paper for simplicity.

Acknowledgements

One of the authors (B. C. Low) acknowledges the support of his ten-month stay

at the Tokyo Astronomical Observatory by Japan Society for the Promotion of Sciences. He also thanks the hospitality of Professor Z. Suemoto, the director, and the staff of Tokyo Astronomical Observatory. The authors also thank Mrs. H. Suzuki for preparing the manuscript. Numerical computation was done on FACOM 230-58 and UNIVAC 1100/80B at the Tokyo Astronomical Observatory.

References

Arons, J., Lea, S. M. 1976, *Astrophys. J.*, **207**, 914.
Baan, W. A. *1977, Astrophys. J.*, **214**, 245.
Chandrasekhar, S. *1956, Astrophys. J.*, **124**, 232.
Comfort, R. H., Tandberg-Hanssen, E., Wu, S. T. 1979, *Astrophys. J.*, **231**, 927.
Elsner, R. F., Lamb, F. K. 1977, *Astrophys. J.*, **215**, 897.
Ghosh, P., Lamb, F. K. 1978, *Astrophys. J.*, **223**, L83.
Hundhausen, A., Zweibel, E. 1981, preprint.
Inoue, H. 1976, *Publ. astr. Soc. Japan*, **28**, 293.
Lamb, F. K. 1979, in *Magnetospheric Boundary Layers*, Eds B. Battrick and J. Mort, E S A, Noordwijk.
Lewin, W. H. G., Joss, P. C. 1977, *Nature*, **270**, 211.
Low, B. C. *1975, Astrophys. I.*, **197**, 251.
Lust, R., Schlüter, A. 1954, *Z. Astrophys.*, **34**, 263.
Marion, J. B. 1965, *Classical Electromagnetic Radiation*, Academic Press, New York.
Midgley, J., Davis, Jr. L. 1962, *J. Geophys. Res.*, **67**, 499.
Pringle, J. E., Rees, M. J. 1972, *Astr. Astrophys.*, **21**, 1.
Shakura, N. I., Sunyaev, R. A. 1973, *Astr. Astrophys.*, **24**, 337.
Uchida, Y., Sakurai, T. 1977, *Solar Phys.*, **51**, 413.
Uchida, Y., Sakurai, T. 1981, *In preparation.*

J. Astrophys. Astr. (1981) **2**, 421–437

Structure and Stability of Rotating Fluid Disks Around Massive Objects. I. Newtonian Formulation

D. K. Chakraborty* and A. R. Prasanna *Physical Research Laboratory, Ahmedabad 380009*

Received 1981 June 29; accepted 1981 September 15

Abstract. In this paper we have presented a very general class of solutions for rotating fluid disks around massive objects (neglecting the self gravitation of the disk) with density as a function of the radial coordinate only and pressure being nonzero. Having considered a number of cases with different density and velocity distributions, we have analysed the stability of such disks under both radial and axisymmetric perturbations. For a perfect gas disk with $\gamma = 5/3$ the disk is stable with frequency $(MG/r^3)^{1/2}$ for purely radial pulsation with expanding and contracting boundary. In the case of axisymmetric perturbation the critical γ_c for neutral stability is found to be much less than 4/3 indicating that such disks are mostly stable under such perturbations.

Key words: Fluid disks—stability

1. Introduction

Study of fluid disks around massive objects has been one of the most important aspects of theoretical astrophysics. Particularly in the case of binary systems where mass transfer is an important feature, one of the major sources of high energy radiation is supposed to be either the hot inner regions of the disk (in the case of continuum emission) or the impact of ruptured unstable disk in the case of burst emissions. A lucid summary with a detailed bibliography of the work on thin disks may be found in the article of Lightman, Shapiro and Rees (1978). Recently, Prasanna and Chakraborty (1981; now onwards referred to as Paper I) have studied the structure and stability of thin disks of charged fluid around compact objects wherein they found that such pressureless thin disks are stable under radial pulsations. It is well known

*On leave of absence from Government College, Jagdalpur 494005

that if the pressure is not negligible then the disk would no longer be thin and one has to consider the structure off the equatorial plane too. Fishbone and Moncrief (1976), and Kozlowski, Jaroszyński and Abramowicz (1978) have respectively considered for isentropic and barytropic fluid disks, solutions of Euler's equations with pressure and rotation. In this paper we consider a similar system (uncharged rotating fluid disks with nonzero pressure) without self gravitation and viscosity and obtain a class of steady state solution and further discuss the stability of such disks under axisymmetric perturbations. We presently restrict the analysis to Newtonian formulation only and shall consider the complete general relativistic discussion in a subsequent article.

We have developed earlier (Paper I) the general set of fluid equations for disks around central massive bodies (including charge density and conductivity); here we shall consider the Newtonian limit of these equations (with $\epsilon = 0$, $\sigma = 0$) and study the structure and stability.

2. Steady state solutions

The equations governing the dynamics of a perfect fluid rotating around a central gravitating source of mass M may be obtained from the general equations (Paper I, equations 2.15–2.17) and are given by

$$\rho\left[\frac{DV^r}{Dt}+\frac{MG}{r^2}-\frac{V^{\theta 2}+V^{\phi 2}}{r}\right]=-\frac{\partial p}{\partial r}, \tag{2.1}$$

$$\rho\left[\frac{DV^\theta}{Dt}+\frac{V^r V^\theta}{r}-\frac{\cot\theta\, V^{\phi 2}}{r}\right]=-\frac{1}{r}\frac{\partial p}{\partial \theta}, \tag{2.2}$$

$$\rho\left[\frac{DV^\phi}{Dt}+\frac{V^r V^\phi}{r}+\frac{\cot\theta\, V^\theta V^\phi}{r}\right]=-\frac{1}{r\sin\theta}\frac{\partial p}{\partial \phi} \tag{2.3}$$

And the continuity equation,

$$\rho\left[\frac{1}{r^2}\frac{\partial}{\partial r}(r^2 V^r)+\frac{1}{r\sin\theta}\frac{\partial}{\partial\theta}(\sin\theta\, V^\theta)+\frac{1}{r\sin\theta}\frac{\partial V^\phi}{\partial\phi}\right]+\frac{D\rho}{Dt}=0, \tag{2.4}$$

wherein p, ρ, V^α denote the pressure, density and velocity as measured in the associated inertial frame and D/Dt is the rate of change operator following the fluid as given by

$$\frac{D}{Dt}=\frac{\partial}{\partial t}+V^r\frac{\partial}{\partial r}+\frac{V^\theta}{r}\frac{\partial}{\partial\theta}+\frac{V^\phi}{r\sin\theta}\frac{\partial}{\partial\phi}. \tag{2.5}$$

For making the system determinate, we further assume the equation of state as expressed by the adiabatic law

$$\frac{D}{Dt}(p\,\rho^{-\gamma})=0, \tag{2.6}$$

γ being the adiabatic index C_p/C_v.

Presently we shall restrict ourselves to the case of pure rotational flow as expressed by $V_0^r = 0$ and $V_0^\theta = 0$ and $V_0^\phi = V_0$. Further as the disk is axisymmetric the equations are given by

$$\rho_0 \left[\frac{MG}{r^2} - \frac{V_0^2}{r}\right] = -\frac{\partial p_0}{\partial r} \tag{2.7}$$

And

$$\rho_0 V_0^2 \cot\theta = \frac{\partial p_0}{\partial \theta}, \tag{2.8}$$

the remaining equations being identically satisfied. In the case when ρ_0 is independent of θ these equations may be solved exactly. Thus considering

$$\rho_0 = \rho_0(r), \tag{2.9}$$

equations (2.7) and (2.8) together give the equation

$$-\frac{1}{r}\frac{\partial}{\partial\theta}(\rho_0 V_0^2) + \cot\theta \frac{\partial}{\partial r}(\rho_0 V_0^2) = 0, \tag{2.10}$$

whose solution is given by

$$\rho_0 V_0^2 = A r^k \sin^k \theta, \tag{2.11}$$

A and k being constants. Substituting these in equations (2.7) and (2.8), we get

$$\frac{\partial p_0}{\partial r} = A r^{k-1} \sin^k\theta - \frac{MG\rho_0}{r^2} \tag{2.12}$$

and

$$\frac{\partial p_0}{\partial \theta} = A r^k \cot\theta \sin^k\theta, \tag{2.13}$$

whose solution may be obtained as

$$p_0 = \frac{A}{k} r^k \sin^k\theta - MG\int \frac{\rho_0 dr}{r^2} + B \tag{2.14}$$

for $k \neq 0$. For the case $k = 0$, the pressure is given by

$$p_0 = A \ln (r \sin \theta) - MG \int \frac{\rho_0 \, dr}{r^2} + B. \tag{2.15}$$

Assuming

$$\rho_0 = \rho_c \, (r/m)^l \tag{2.16}$$

wherein $m = MG/c^2$, ρ_c and l are constants, the expressions for p_0 are given by

$$p_0 = -\frac{MG\,\rho_c}{m^l} \frac{r^{l-1}}{l-1} + \frac{A}{k} r^k \sin^k \theta + B, \qquad l \neq 1, \, k \neq 0, \tag{2.17}$$

$$p_0 = -\frac{MG\,\rho_c}{m^l} \frac{r^{l-1}}{l-1} + A \ln (r \sin \theta) + B, \quad l \neq 1, \, k = 0, \tag{2.18}$$

$$p_0 = -\frac{MG\,\rho_c}{m} \ln r + \frac{A}{k} \sin^k \theta + B, \qquad l = 1, \, k \neq 0 \tag{2.19}$$

and

$$p_0 = A \ln (\sin \theta) + \left(A - \frac{MG\,\rho_c}{m} \right) \ln r + B, \quad l = 1, \, k = 0. \tag{2.20}$$

The special case when $k = -2$ and $l = 0$, corresponds to that of Fishbone and Moncrief. The whole class of solutions obtained above are all physically plausible provided the pressure satisfies the condition $p_0 > O$ throughout the interior of the disk and $p_0 = 0$ over the boundary. The constants A and B may be obtained by using the relation $p_0 = 0$ at r_a and r_b, the inner and outer edges at the plane $\theta = \pi/2$ and from $p_0 > 0$ we can obtain the condition relating k and l. Evaluating the constants thus, we have the pressure given by the expressions

$$\frac{p_0}{c^2} = \frac{\rho_c}{(l-1)} \left\{ \frac{(b^{l-1} - a^{l-1}) \, R^k \sin^k \theta - R^{l-1} (b^k - a^k) + b^k \, a^{l-1} - a^k \, b^{l-1}}{(b^k - a^k)} \right\}, \qquad l \neq 1, \, k \neq 0, \tag{2.21}$$

$$\frac{p_0}{c^2} = \frac{\rho_c}{(l-1)} \left\{ \frac{(b^{l-1} - a^{l-1}) \ln (R \sin \theta) - R^{l-1} (\ln b - \ln a) + a^{l-1} \ln b - b^{l-1} \ln a}{(\ln b - \ln a)} \right\}, \qquad l \neq 1, \, k = 0 \tag{2.22}$$

And

$$\frac{p^0}{c^2} = \rho_c \left\{ \frac{R^k \sin^k \theta \, (\ln b - \ln a) - (b^k - a^k) \ln R + b^k \ln a - a^k \ln b}{(b^k - a^k)} \right\}, \qquad l = 1, \, k \neq 0 \tag{2.23}$$

and $p_0 = 0$ for $l = 1$, $k = 0$. In the above, R, a and b are dimensionless quantities denoting r/m, r_a/m and r_b/m respectively. In order to get the boundary of the disk off the equatorial plane $\theta = \pi/2$, we solve these equations $p_0 = 0$ for $\sin\theta$ and thus for every r we get θ and $(\pi - 0)$ corresponding to the edge of the disk in the meridional plane. Finally using the condition that $p_0 > 0$ throughout the interior of the disk we get the criterion connecting k and l as $k < l - 1$. If $k = l - 1$ then it follows immediately that $P_0 = 0$, $\theta = \pi/2$ and

$$V_0^2 = \frac{MG}{r} \tag{2.24}$$

showing that the disk is a pressureless thin disk confined to the equatorial plane and having Keplerian motion, a well-known result. Thus the nonzero pressure would definitely require a structure off the equatorial plane. As l and k are then related through $k < l - 1$, taking $l - 1 \; k + n$, n being a positive real number, we can write the velocity function to be

$$V_0^2 = A\left(\frac{MG}{r^{1+n}}\right)\sin^k\theta, \tag{2.25}$$

where the constant A for the three different cases is given by

$$A = \frac{k}{l-1}\left(\frac{b^{l-1} - a^{l-1}}{b^k - a^k}\right), \qquad k \neq 0, \; l \neq 1,$$

$$A = \frac{1}{l-1}\left(\frac{b^{l-1} - a^{l-1}}{\ln b - \ln a}\right), \qquad k = 0, \; l \neq 1$$

and

$$A = k\left(\frac{\ln b - \ln a}{b^k - a^k}\right), \qquad k \neq 0, \; l = 1. \tag{2.26}$$

3. Stability analysis

As was done earlier (Paper I) in order to discuss the stability of the configuration, we perturb the system and. consider the equations governing the axisymmetric perturbations and perform the normal mode analysis restricting the perturbations to linear terms only. The general procedure we use is as given by Chandrasekhar and Friedman (1972a, b). The complete set of equations governing the perturbations may be obtained from our earlier work (Paper I, equations 3.1–3.4), in the Newtonian limit as

$$\rho_0\left[\frac{\partial}{\partial t}\delta V^r - \frac{2}{r}V_0\,\delta V^\phi\right] + \delta\rho\left[\frac{MG}{r^2} - \frac{V_0^2}{r}\right] = -\frac{\partial}{\partial r}\delta p, \tag{3.1}$$

$$\rho_0\left[\frac{\partial}{\partial t}\delta V^\theta - \frac{2}{r}\cot\theta\, V_0\,\delta V^\phi\right] + \delta\rho\frac{V_0^2}{r}\cot\theta = -\frac{1}{r}\frac{\partial}{\partial\theta}\delta p, \tag{3.2}$$

$$\frac{\partial}{\partial t}\delta V^\phi + \frac{1}{r}\left(\frac{\partial V_0}{\partial\theta} + V_0\cot\theta\right)\delta V^\theta + \left(\frac{\partial V_0}{\partial r} + \frac{V_0}{r}\right)\delta V^r = 0 \tag{3.3}$$

and

$$\rho_0\left[\frac{1}{r^2}\frac{\partial}{\partial r}(r^2\,\delta V^r) + \frac{1}{r\sin\theta}\frac{\partial}{\partial\theta}(\sin\theta\,\delta V^\theta)\right] + \frac{\partial}{\partial t}\delta\rho + \delta V^r\frac{\partial\rho_0}{\partial r} + \frac{\delta V^\theta}{r}\frac{\partial\rho_0}{\partial\theta} = 0, \tag{3.4}$$

whereas the condition of adiabaticity gives

$$\frac{\partial}{\partial t}(\rho_0^{-\gamma} - \gamma\, p_0\,\rho_0^{-\gamma-1}\,\delta\rho) + \delta V^r\frac{\partial}{\partial r}(p_0\,\rho_0^{-\gamma}) + \frac{\delta V^\theta}{r}\frac{\partial}{\partial\theta}(p_0\,\rho_0^{-\gamma}) = 0. \tag{3.5}$$

Assuming the time dependence of each of the perturbed variable to be of the form

$$e^{i\sigma t}, \tag{3.6}$$

we introduce the Lagrangian displacement ξ^i ($i = r,\theta$) through the relation

$$\frac{\partial\xi^i}{\partial t} = \delta V^i. \tag{3.7}$$

Denoting the perturbed variables to represent only their spatial part we obtain after some rearrangement of terms the following set of equations governing the perturbations

$$\delta V^\phi = -\frac{1}{r}\left(\frac{\partial V_0}{\partial\theta} + \cot\theta\, V_0\right)\xi^\theta - \left(\frac{\partial V_0}{\partial r} + \frac{V_0}{r}\right)\xi^r, \tag{3.8}$$

$$\delta\rho = -\rho_0\left[\frac{1}{r^2}\frac{\partial}{\partial r}(r^2\,\xi^r) + \frac{1}{r\sin\theta}\frac{\partial}{\partial\theta}(\sin\theta\,\xi^\theta)\right] - \xi^r\frac{\partial\rho_0}{\partial r} - \frac{\xi^\theta}{r}\frac{\partial\rho_0}{\partial\theta}, \tag{3.9}$$

$$\delta p = -\gamma\, p_0\left[\frac{1}{r^2}\frac{\partial}{\partial r}(r^2\,\xi^r) + \frac{1}{r\sin\theta}\frac{\partial}{\partial\theta}(\sin\theta\,\xi^\theta)\right] - \xi^r\frac{\partial p_0}{\partial r} - \frac{\xi^\theta}{r}\frac{\partial p_0}{\partial\theta}, \tag{3.10}$$

$$-\rho_0\,\sigma^2\,\xi^r = \frac{2\rho_0\,V_0}{r}\delta V^\phi - \left(\frac{MG}{r^2} - \frac{V_0^2}{r}\right)\delta\rho - \frac{\partial}{\partial r}\delta p \tag{3.11}$$

And

$$-\rho_0\,\sigma^2\,\xi^\theta = \frac{2\,\rho_0\,V_0}{r}\cot\theta\,\delta V^\phi + \frac{V_0^2}{r}\cot\theta\,\delta\rho - \frac{1}{r}\frac{\partial}{\partial\theta}\delta p. \tag{3.12}$$

Equations (3.8) to (3.10) are the initial value equations while (3.11) and (3.12) are the dynamical equations which should be solved as an eigenvalue equation to obtain σ^2. Equation (3.12), being the condition of adiabaticity, is identical with

$$\frac{\Delta p}{p} = \gamma \frac{\Delta \rho}{\rho},$$

wherein Δp and $\Delta \rho$ are the Lagrangian perturbations in p and ρ. At the edge of the disk, we need the boundary condition $\Delta p = 0$, which is satisfied by restricting ξ^i and their derivatives to remain finite everywhere

Following the procedure of Chandrasekhar and Friedman (1972 a, b), we multiply the dynamical equations (3.11) and (3.12) by $\bar{\xi}^r$ and $\bar{\xi}^\theta$ respectively, add them and integrate with respect to r and θ over the entire region of the disk,, Here $\bar{\xi}^r$ and $\bar{\xi}^\theta$ are the ' trial functions ' which satisfy the same boundary conditions as the true eigen functions ξ^r and ξ^θ, but otherwise completely arbitrary. By performing several integrations by parts and using the steady state relations, we can then bring the resultant equation to symmetrical form in barred and unbarred displacements as

$$\begin{aligned}
&\sigma^2 \int\int \rho_0 r^2 \sin\theta\, (\bar{\xi}^r \xi^r + \bar{\xi}^\theta \xi^\theta)\, dr\, d\theta \\
&= \int\int 2\rho_0 r V_0 \sin\theta \left\{ \left(\frac{\partial V_0}{\partial r} + \frac{V_0}{r} \right) \bar{\xi}^r \xi^r + \frac{\cot\theta}{r} \left(\frac{\partial V_0}{\partial \theta} + \cot\theta\, V_0 \right) \bar{\xi}^\theta \xi^\theta \right. \\
&\quad \left. + \frac{V_0}{r} \cot\theta\, (\bar{\xi}^\theta \xi^r + \bar{\xi}^r \xi^\theta) \right\} dr\, d\theta - MG \int\int \frac{\partial \rho_0}{\partial r} \sin\theta\, \bar{\xi}^r \xi^r\, dr\, d\theta \\
&\quad + \int\int V_0^2 r \sin\theta \left\{ \bar{\xi}^r \xi^r \frac{\partial \rho_0}{\partial r} + \frac{\bar{\xi}^\theta \xi^\theta}{r} \cot\theta \frac{\partial \rho_0}{\partial \theta} \right\} dr\, d\theta \\
&\quad - \int\int \left\{ r^4 \sin\theta\, \bar{\xi}^r \xi^r \frac{\partial}{\partial r} \left(\frac{1}{r^2} \frac{\partial p_0}{\partial r} \right) + \sin^2\theta\, \bar{\xi}^\theta \xi^\theta \frac{\partial}{\partial \theta} \left(\frac{1}{\sin\theta} \frac{\partial p_0}{\partial \theta} \right) \right\} dr\, d\theta \\
&\quad - \int\int \left\{ p_0 \frac{\partial}{\partial r} (r \bar{\xi}^r) \frac{\partial}{\partial \theta} (\sin\theta\, \xi^\theta) + p_0 \frac{\partial}{\partial \theta} (\sin\theta\, \bar{\xi}^\theta) \frac{\partial}{\partial r} (r \xi^r) \right. \\
&\quad - p_0 \frac{\partial}{\partial \theta} (r \bar{\xi}^r) \frac{\partial}{\partial r} (\sin\theta\, \xi^\theta) - p_0 \frac{\partial}{\partial r} (\sin\theta\, \bar{\xi}^\theta) \frac{\partial}{\partial \theta} (r \xi^r) \\
&\quad \left. - (\bar{\xi}^\theta \xi^r + \bar{\xi}^r \xi^\theta) \sin\theta \frac{\partial p_0}{\partial \theta} \right\} dr\, d\theta \\
&\quad + \gamma \int\int \left\{ \frac{p_0 \sin\theta}{r^2} \frac{\partial}{\partial r} (r^2 \bar{\xi}^r) \frac{\partial}{\partial r} (r^2 \xi^r) + \frac{p_0}{r} \left[\frac{\partial}{\partial r} (r^2 \bar{\xi}^r) \frac{\partial}{\partial \theta} (\sin\theta\, \xi^\theta) \right. \right. \\
&\quad \left. \left. + \frac{\partial}{\partial \theta} (\sin\theta\, \bar{\xi}^\theta) \frac{\partial}{\partial r} (r^2 \xi^r) \right] + \frac{p_0}{\sin\theta} \frac{\partial}{\partial \theta} (\sin\theta\, \bar{\xi}^\theta) \frac{\partial}{\partial \theta} (\sin\theta\, \xi^\theta) \right\} dr\, d\theta. \qquad (3.13)
\end{aligned}$$

As shown by Chandrasekhar and Friedman, the symmetrical form of σ^2 equation implies a variational principle; for identifying $\bar{\xi}^r$ with ξ^i one can write the following equation for σ^2.

$$\sigma^2 \int\int \rho_0 r^2 \sin\theta \,(\xi^{r^2} + \xi^{\theta^2})\, dr\, d\theta$$

$$= \int\int 2\rho_0 V_0 r \sin\theta \left\{ \left(\frac{\partial V_0}{\partial r} + \frac{V_0}{r}\right)\xi^{r^2} + \frac{\cot\theta}{r}\left(\frac{\partial V_0}{\partial\theta} + \cot\theta\, V_0\right)\xi^{\theta^2} \right.$$

$$\left. + \frac{2V_0}{r}\cot\theta\,\xi^r\,\xi^\theta \right\} dr\, d\theta - MG\int\int \frac{\partial\rho_0}{\partial r}\sin\theta\,\xi^{r^2}\, dr\, d\theta$$

$$- \int\int \left\{ r^4 \sin\theta\,\xi^{r^2}\frac{\partial}{\partial r}\left(\frac{1}{r^2}\frac{\partial p_0}{\partial r}\right) + \sin^2\theta\,\xi^{\theta^2}\frac{\partial}{\partial\theta}\left(\frac{1}{\sin\theta}\frac{\partial p_0}{\partial\theta}\right)\right\} dr\, d\theta$$

$$+ \int\int V_0^2 r\sin\theta \left\{ \xi^{r^2}\frac{\partial\rho_0}{\partial r} + \frac{\xi^{\theta^2}}{r}\cot\theta\frac{\partial\rho_0}{\partial\theta}\right\} dr\, d\theta$$

$$- \int\int \left\{ 2p_0\left[\frac{\partial}{\partial r}(r\,\xi^r)\frac{\partial}{\partial\theta}(\sin\theta\,\xi^\theta) - \frac{\partial}{\partial\theta}(r\,\xi^r)\frac{\partial}{\partial r}(\sin\theta\,\xi^\theta)\right]\right.$$

$$\left. - 2\frac{\partial p_0}{\partial\theta}\sin\theta\,\xi^r\,\xi^\theta \right\} dr\, d\theta + \gamma\int\int \left[\frac{p_0}{r^2}\sin\theta\left\{\frac{\partial}{\partial r}(r^2\,\xi^r)\right\}^2\right.$$

$$\left. + \frac{2p_0}{r}\frac{\partial}{\partial r}(r^2\,\xi^r)\frac{\partial}{\partial\theta}(\sin\theta\,\xi^\theta) + \frac{p_0}{\sin\theta}\left\{\frac{\partial}{\partial\theta}(\sin\theta\,\xi^\theta)\right\}^2\right] dr\, d\theta. \tag{3.14}$$

Now if one evaluates equation (3.14) by two trial displacements ξ^i and $\xi^i + \delta\xi^i$ such that the resultant variation in σ^2 is $\delta\sigma^2$, and trace back the calculations that lead to equation (3.13) starting from equations (3.8) – (3.12), one gets,

$$\delta\sigma^2 \int\int \rho_0 r^2 \sin\theta\,(\xi^{r^2} + \xi^{\theta^2})\, dr\, d\theta$$

$$= \int\int -2\,\delta\xi^r r^2 \sin\theta\left[\rho_0\sigma^2\xi^r + \frac{2\rho_0 V_0}{r}\delta V^\phi - \left(\frac{MG}{r^2} - \frac{V_0^2}{r}\right)\delta\rho - \frac{\partial}{\partial r}\delta p\right] dr\, d\theta$$

$$+ \int\int -2\,\delta\xi^\theta r^2\sin\theta\left[\rho_0\sigma^2\xi^\theta + \frac{2\rho_0 V_0}{r}\cot\theta\,\delta V^\phi\right.$$

$$\left. + \frac{V_0^2}{r}\cot\theta\,\delta\rho - \frac{1}{r}\frac{\partial}{\partial\theta}\delta p\right] dr\, d\theta. \tag{3.15}$$

It is clear from equation (3.15) that demanding $\delta\sigma^2 = 0$ amounts to solving the original eigenvalue equations (3.11) and (3.12) along with the initial value equations

(3.8) – (3.10). Rewriting equation (3.14) in terms of dimensionless quantities R, and V_0, we get

$$\frac{m^2\,\sigma^2}{c^2}\int\int \rho_0\, R^2 \sin\theta\,(\xi^{r^2}+\xi^{\theta^2})\,dRd\theta$$

$$=\int\int\left[2\rho_0\,\mathbf{V}_0\,R\sin\theta\left(\frac{\partial \mathbf{V}_0}{\partial R}+\frac{\mathbf{V}_0}{R}\right)\xi^{r^2}-\frac{\partial\rho_0}{\partial R}\sin\theta\,\xi^{r^2}\right.$$

$$\left.-R^4\sin\theta\,\frac{\xi^{r^2}}{c^2}\frac{\partial}{\partial R}\left(\frac{1}{R^2}\frac{\partial p_0}{\partial R}\right)+\mathbf{V}_0^2\,R\sin\theta\,\xi^{r^2}\frac{\partial\rho_0}{\partial R}\right]dR\,d\theta$$

$$+\int\int\left[2\rho_0\,\mathbf{V}_0\cos\theta\left(\frac{\partial \mathbf{V}_0}{\partial\theta}+\cos\theta\,\mathbf{V}_0\right)\xi^{\theta^2}-\sin^2\theta\,\frac{\xi^{\theta^2}}{c^2}\frac{\partial}{\partial\theta}\left(\frac{1}{\sin\theta}\frac{\partial p_0}{\partial\theta}\right)\right.$$

$$\left.+\xi^{\theta^2}\mathbf{V}_0^2\cos\theta\frac{\partial\rho_0}{\partial\theta}\right]dR\,d\theta+\int\int\left[4\rho_0\,\mathbf{V}_0^2\cos\theta\,\xi^r\,\xi^\theta\right.$$

$$-\frac{2p_0}{c^2}\frac{\partial}{\partial R}(R\,\xi^r)\frac{\partial}{\partial\theta}(\sin\theta\,\xi^\theta)+\frac{2p_0}{c^2}\frac{\partial}{\partial\theta}(R\,\xi^r)\frac{\partial}{\partial R}(\sin\theta\,\xi^\theta)$$

$$\left.+\frac{2}{c^2}\frac{\partial p_0}{\partial\theta}\sin\theta\,\xi^r\,\xi^\theta\right]dR\,d\theta+\gamma\int\int\left[\frac{p_0}{R^2\,c^2}\sin\theta\left\{\frac{\partial}{\partial R}(R^2\,\xi^r)\right\}^2+\frac{p_0}{c^2\sin\theta}\right.$$

$$\left.\left\{\frac{\partial}{\partial\theta}(\sin\theta\,\xi^\theta)\right\}^2+\frac{2p_0}{Rc^2}\frac{\partial}{\partial R}(R^2\,\xi^r)\frac{\partial}{\partial\theta}(\sin\theta\,\xi^\theta)\right]dR\,d\theta,\qquad \mathbf{V}_0=\frac{V_0}{c}. \tag{3.16}$$

In order to evaluate σ^2, we choose two kinds of trial functions (i) with fixed boundary, *i.e.* the Lagrangian displacements ξ^i vanish at the boundary and (ii) expanding or contracting boundary.

For Case (i), corresponding to the three different types of solutions (2.21) – (2.23), we choose a function 'q'

$$q=\sin^k\theta-\frac{k}{AR^k}\left(\frac{R^{l-1}}{l-1}-B\right),\qquad l\neq 1,\ k\neq 0, \tag{3.17}$$

$$q=\sin\theta-\exp\left\{-\frac{R^{l-1}}{A\,(l-1)}-\frac{B}{A}-\ln R\right\},\qquad l\neq 1,\ k=0, \tag{3.18}$$

and

$$q=\sin^k\theta-\frac{k}{AR^k}(\ln R-B),\qquad l=1,\ k\neq 0, \tag{3.19}$$

which vanishes at the boundary and set $\xi^i = q$. With this choice of ξ^r and ξ^θ in equation (3.16) we evaluate the critical value of adiabatic index γ_{c_1} for $\sigma^2 = 0$, which would give the neutral stability. In order to increase the accuracy, we take

$$\xi^r = q + \alpha q^2, \quad \xi^\theta = q + \beta q^2, \tag{3.20}$$

wherein α and β are adjustable parameters determined by extremising the expression for σ^2. With such a choice of ξ^r and ξ^θ, one could obtain better values for γ_{c_1} for the onset of instability

In Case (ii) (a nonstationary boundary), we first consider the case of radial perturbation with $\xi^\theta = 0$. The equations governing such radial perturbation are obtained from the original set of equations (3.8) – (3.12) as follows

$$\delta V^\phi = -\left(\frac{\partial V_0}{\partial r} + \frac{V_0}{r}\right) \xi^r, \tag{3.21}$$

$$\delta\rho = -\frac{\rho_0}{r^2}\frac{\partial}{\partial r}(r^2\,\xi^r) - \xi^r \frac{\partial \rho_0}{\partial r}, \tag{3.22}$$

$$\delta p = -\frac{\gamma p_0}{r^2}\frac{\partial}{\partial r}(r^2\,\xi^r) - \xi^r \frac{\partial p_0}{\partial r}\ , \tag{3.33}$$

$$-\rho_0\,\sigma^2\,\xi^r = \frac{2\rho_0\,V_0}{r}\,\delta V^\phi - \left(\frac{MG}{r^2} - \frac{V_0^2}{r}\right)\delta\rho - \frac{\partial}{\partial r}\,\delta p \tag{3.24}$$

and

$$\frac{2\,\rho_0\,V_0}{r}\,\cot\theta\,\delta\,V^\phi + \frac{V_0^2}{r}\cot\theta\,\delta\rho - \frac{1}{r}\frac{\partial}{\partial\theta}\,\delta p = 0. \tag{3.25}$$

Using initial value equations (3.21) – (3.23) in (3.25) and assuming ξ^r to be a function of r only we obtain the differential equation

$$(1-\gamma)\frac{d}{dr}(r^2\,\xi^r) + 2r\,\xi^r = 0 \tag{3.26}$$

for ξ^r, whose solution is given by

$$\xi^r = \eta\, r^{\frac{4-2\gamma}{\gamma-1}} \tag{3.27}$$

where η is constant of integration. Using this solution for ξ^r in (3.24) we get

$$\rho_0\,\sigma^2\,\xi^r = \eta\frac{\rho_c\,MG}{m^l}\left\{\frac{2\gamma\,(3\gamma-5)}{(\gamma-1)^2}\,B + A\sin^k\theta\,\frac{(3\gamma-5)\,(k\gamma-k+2\gamma)}{k\,(\gamma-1)^2}\,r^k\right.$$

$$+\left[\frac{4-2\gamma}{\gamma-1}-\frac{2\gamma}{(\gamma-1)(l-1)}\left(\frac{3\gamma-5}{\gamma-1}\right)\right]r^{l-1}\Bigg\}\, r^{\frac{6-4\gamma}{\gamma-1}},$$

$$l \neq 1,\ k \neq 0, \tag{3.28}$$

$$\rho_0\,\sigma^2\,\xi^r = \eta\frac{\rho_c\,MG}{m^l}\left\{\frac{2\gamma\,(3\gamma-5)}{(\gamma-1)^2}B + 2A\ln(r\sin\theta)\frac{(3\gamma-5)}{(\gamma-1)^2} + A\frac{(3\gamma-5)}{\gamma-1}\right.$$

$$\left.+\left[\frac{4-2\gamma}{\gamma-1}-\frac{2\gamma}{(\gamma-1)(l-1)}\left(\frac{3\gamma-5}{\gamma-1}\right)\right]r^{l-1}\right\} r^{\frac{6-4\gamma}{\gamma-1}},$$

$$l \neq 1,\ k = 0, \tag{3.29}$$

$$\rho_0\,\sigma^2\,\xi^r = \eta\frac{\rho_c\,MG}{m}\left\{\frac{2\gamma\,(3\gamma-5)}{(\gamma-1)^2}B + A\sin^k\theta\,\frac{(3\gamma-5)\,(k\gamma-k+2\gamma)}{k\,(\gamma-1)^2}r^k\right.$$

$$\left.+\left(\frac{4-2\gamma}{\gamma-1}\right)-(\ln r)\frac{2\gamma}{\gamma-1}\left(\frac{3\gamma-5)}{\gamma-1}\right)\right\} r^{\frac{6-4\gamma}{\gamma-1}},\quad l=1,\ k\neq 0. \tag{3.30}$$

For the special case of ordinary gas with γ = 5/3 the above equations for σ^2 reduce to a very simple form

$$\sigma^2 = \frac{MG}{r^3} \tag{3.31}$$

showing that the disks are stable with 'local' frequency being proportional to $r^{-3/2}$ irrespective of the other parameters like *l, k, a* and *b*. Incidentally this value of γ = 5/3 makes the function ξ^r to be ηr which is exactly the form as used by Bisnovatyi-Kogan and Blinnikov (1972) for analysing the stability of thin gas-disks against expansion and contraction. It is interesting to note that the same frequency is obtained as above for the radial oscillation of a pressureless disk confined to $\theta = \pi/2$ plane, which is in Keplerian motion with. $V_0 = (MG1r)^{1/2}$, as may be seen from equations (3.21) – (3.24) with δp =0.

To consider the stability with a non-stationary boundary (Case and with axi-symmetric perturbations, we choose

$$\xi^r = R + \alpha\, q,\quad \xi^\theta = R + \beta\, q, \tag{3.32}$$

evaluate σ^2 from equation (3.16) and calculate γ_{c_2} by setting σ^2 = 0 after extremising it by adjusting α and β as in Case (i).

4. Discussion and conclusions

As the general solution obtained above refers to a class of solutions with parameters *l* and *k* referring to different density and velocity distributions, we have considered a

number of cases for various values of l and k for different cases of disk radii. The thickness of the disk varies from one case to another depending upon the density and velocity distributions. The general structure of the disks is presented through figures and tables. Figs 1 and 2 show the upper half of the meridional section (r, θ) plane for two typical cases with (i) $a = 4$, $b = 20$, $l = 1$, $k = -1$ and (ii) $a = 4$, $b = 100$, $l = 0$, $k = -2$. For these two cases the corresponding profiles of pressure, density and velocity are plotted in Figs 3 and 4.

Study of the disk structure for a number of cases revealed that the maximum thickness h_m (= $R \cos \theta_m$, θ_m being the minimum value of θ for a given disk) of the disk as well as the shape change with the velocity (n) and density (l) profiles of the disk.

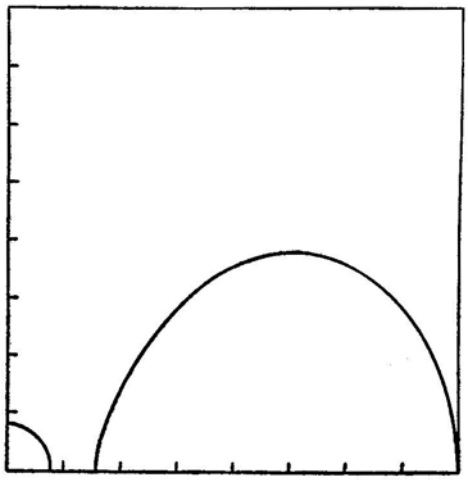

Figure 1. Upper half of the meridional section of the disk for $a = 4$, $b = 20$, $l = 1$, $k = -1$. The circular part at the left is the section of the central massive object with $R = 2$.

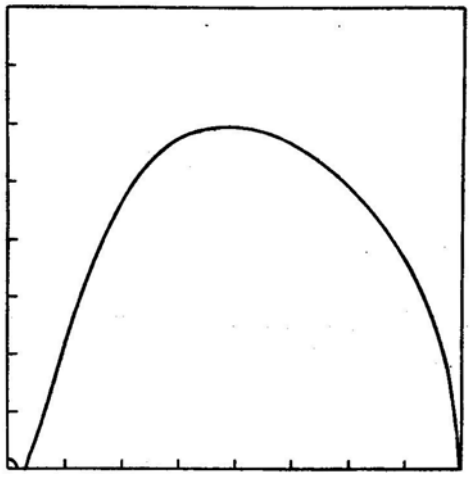

Figure 2. Upper half of the meridional section of the disk for $a = 4$, $b = 100$, $l = 0$, $k = — 2$. The circular part at the left is the section of the central massive object with $R = 2$.

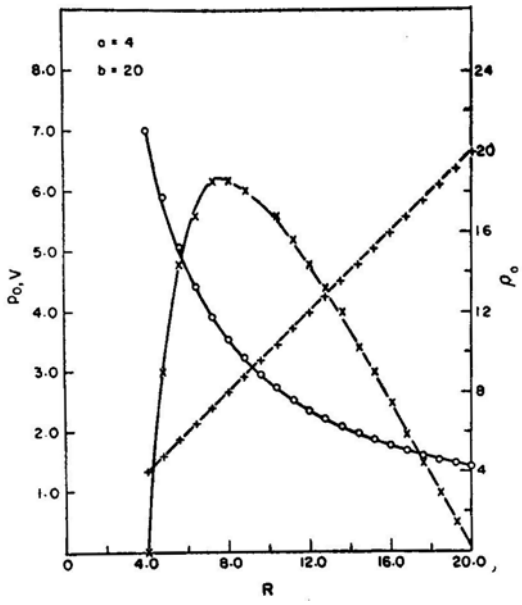

Figure 3. Profiles of pressure, density and velocity at $\theta = \pi/2$ plane for the disk described in Fig. 1; (+ : density, 0 velocity $V_0 \times 10$, × : pressure $P_0 \times 20$).

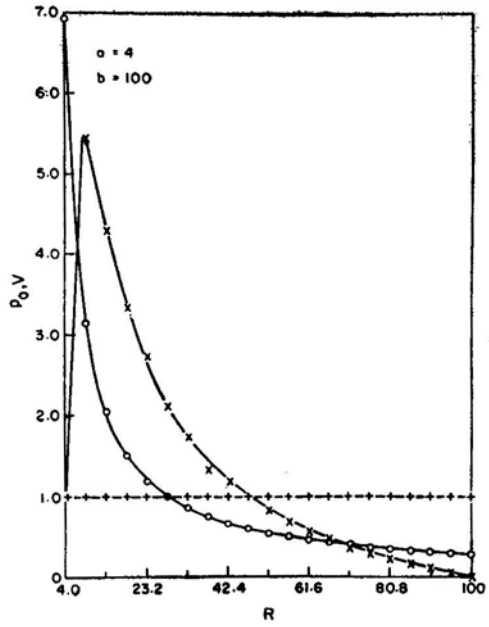

Figure 4. Profiles of pressure, density and velocity at $\theta = \pi/2$ plane for the disk described in Fig. 2; (+ : density, o: velocity $V_0 \times 10$, × : pressure P_0).

For a disk with $a = 4$, $b = 20$, Figs 5 to 8 reveal the nature of such changes. As may be seen from the Figs 5 and 6 the maximum thickness increases as n increases, which is in conformity with the known result that disks with larger angular momentum are thinner than the ones with lesser angular momentum. Also, as regards the shape

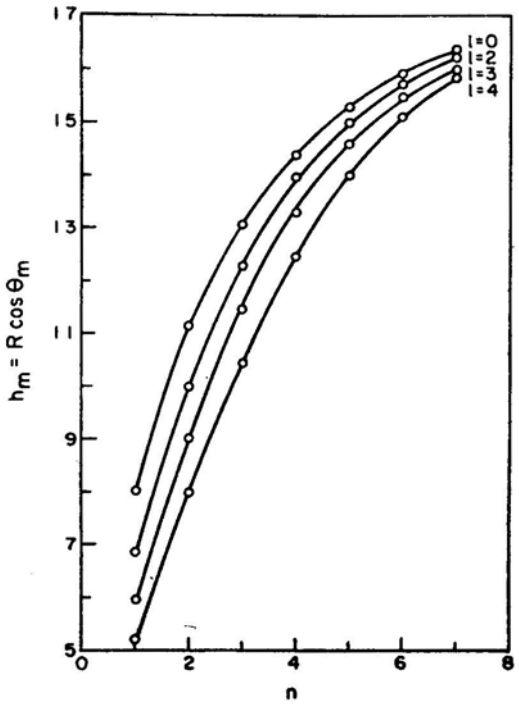

Figure 5. Maximum height $h_m = R \cos \theta_m$ as a function of n for different values of l for the disk with $a = 4$, $b = 20$.

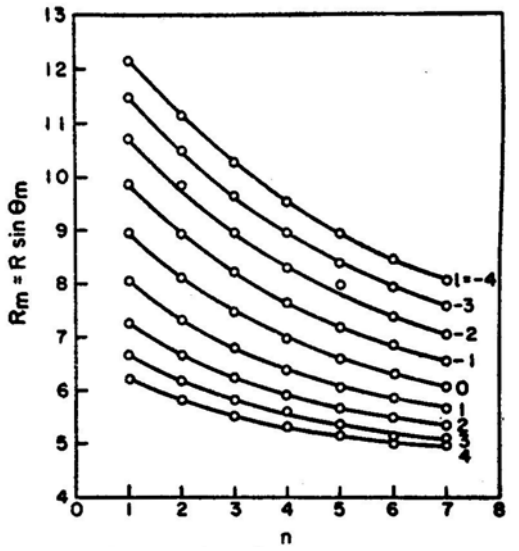

Figure 6. The distance $R_m = R \sin \theta_m$ of the point where the thickness is maximum, as a function of n for different values of l for a disk with $a = 4$, $b = 20$.

of the disks, the maximum thickness occurs nearer to the inner edge as n increases. Fig. 7 shows the variation of the maximum thickness with the density distribution for different values of n. The maximum thickness rises slowly as l increases, attaining a maximum around $l = -2$ to $l = 0$ for $n = 1$ to 7, and then falls off rapidly as l increases, which is consistent with normal distributions.

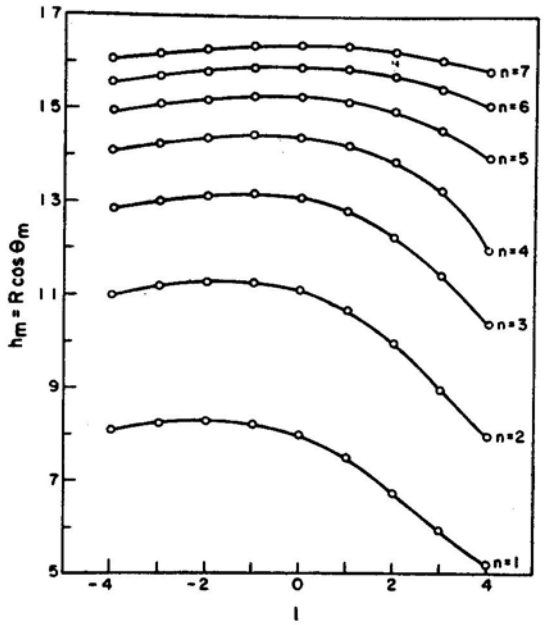

Figure 7. Maximum height $h_m = R \cos \theta_m$ as a function of l for different values of n for a disk with $a = 4$, $b = 20$.

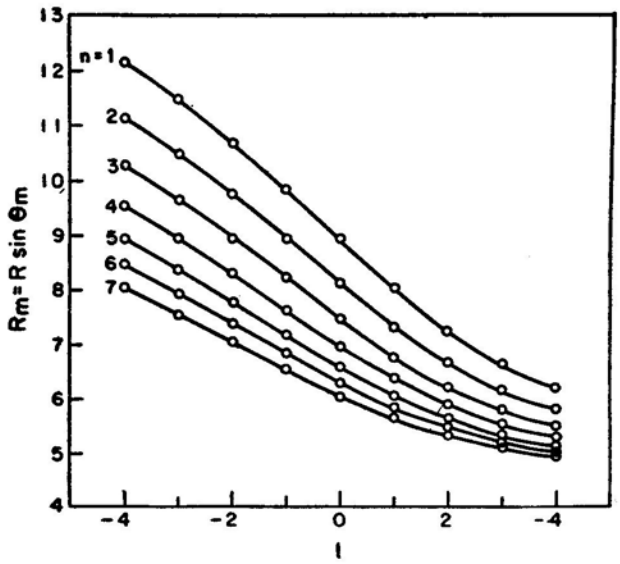

Figure 8. The distance $R_m = R \sin \theta_m$ as a function of l for different values of n for a disk with $a = 4$, $b = 20$.

Regarding the onset of instability as remarked in Section 3, we evaluate the critical adiabatic index γ_c by setting $\sigma^2 = 0$ for different values of a, b, n and l. Table 1 shows the values of γ_c for different l, n, a and b. The table also shows the value of the ratio of the kinetic energy to the potential energy ($I\Omega^2/|W|$) for each disk. Normally, in the case of a self-gravitating fluid sphere, if there is rotation, then the criterion for

Table 1. The ratio of kinetic energy to potential energy $I\Omega^2/|W|$ and y, as a function of n for disks with different values of a, b and l.γ_{c1} refers to the case when $\xi^r = q + \alpha q^2$, and $\xi^\theta = q+\beta q^2$ while γ_{c_2} refers to the case when $\xi^r = R+ \alpha q$, $\xi_\theta = R+ \beta q$.

n	$I\Omega^2/\|W\|$	γ_{c_1}	γ_{c_2}	n	$I\Omega^2/\|W\|$	γ_{c_1}	γ_{c_2}
$a = 4{\cdot}0$,	$b = 100{\cdot}0$,	$l = -3$		$a = 4{\cdot}0$,	$b = 100{\cdot}0$,	$l = 0$	
1	0·037	1·07	1·06	1	0·63	0·89	1·04
2	0·012	1·04	1·17	2	0·24	0·99	1·16
3	0·005	1·02	1·10	3	0·10	0·97	1·15
4	0·003	0·96	0·99	4	0·052	0·92	1·11
5	0·002	0·89	0·90	5	0·031	0·87	1·07
6	0·001	0·83	0·82	6	0·021	0·81	1·04
$a = 4{\cdot}0$,	$b = 100{\cdot}0$,	$l = -2$		$a = 4{\cdot}0$,	$b = 100{\cdot}0$,	$l = 1$	
1	0·15	1·05	1·10	1	1·18	0·62	0·93
2	0·050	1·06	1·17	2	0·49	0·88	1·14
3	0·021	1·02	1·11	3	0·21	0·92	1·15
4	0·011	0·95	1·04	4	0·11	0·89	1·13
5	0·006	0·89	0·97	5	0·066	0·85	1·09
6	0·004	0·83	0·92	6	0·045	0·80	1·06
$a = 4{\cdot}0$,	$b = 100{\cdot}0$,	$l = -1$		$a = 20{\cdot}0$,	$b = 116{\cdot}0$,	$l = 0$	
1	0·35	1·00	1·09	1	1·01	0·47	0·54
2	0·13	1·04	1·17	2	0·70	0·76	0·94
3	0·054	1·00	1·11	3	0·49	0·85	1·04
4	0·028	0·94	1·08	4	0·34	0·86	1·05
5	0·017	0·88	1·04	5	0·25	0·84	1·04
6	0·011	0·82	0·99	6	0·19	0·81	1·02

stability differs from $\gamma = 4/3$ to $\gamma - 4/3 = -2\, I\Omega^2/9\,|W|$ (Lebovitz 1970) showing an increase in the range of stability. However, we find that there is no such simple relation connecting γ_c and the energy ratio for the case of rotating disks. But the critical γ is always less than 4/3 indicating that all the cases considered here correspond to stable configurations under axisymmetric perturbations.

We have thus found that the ordinary perfect fluid ($\gamma = 5/3$) disks rotating around massive objects are stable under radial pulsations with frequency $(MG/r^3)^{1/2}$. In this case the boundary could be expanding or contracting as given by the amplitude function $\xi^r = nr$. On the other hand if the perturbations are axisymmetric the critical value of γ is much less than 4/3, thus indicating stability of such disks. From this detailed study, it appears that the dynamical configuration of a rotating disk around a massive object is similar to that of a self-gravitating fluid sphere. However, in the above analysis, as the consideration of axisymmetric perturbations are restricted only to a specific choice of θ-dependence, the criterion of stability is not very general. In fact, it is at least qualitatively known that the general axisymmetric perturbations do lead to instabilities that would result in either ring structures or spiral structures caused by anisotropies in either temperature or density. In fact it is very much necessary to study the above analysis for more general 0-dependent perturbations, which would perhaps be associated with more general initial configurations. It is also essential to compare the results obtained above with the case of disks when self-gravitation is not neglected.

Acknowledgements

One of us (D. K. C.) would like to thank the University Grants Commission for the award of a Teacher Fellowship.

References

Bisnovatyi-Kogan, G. S., Blinnikov, S. I. 1972, *Astrophys. Sp. Sci.*, **19**, 119.
Chandrasekhar, S., Friedman, J. L. 1972a, *Astrophys. J.*,**175**, 379.
Chandrasekhar, S., Friedman, J. L. 1972b, *Astrophys. .J.*, **176**, 745.
Fishbone, L. G., Moncrief, V. 1976, *Astrophys. J.*, **207**, 962.
Kozowski, M., Jaroszyński, M., Abramowicz, M. A. 1978, *Astr. Astrophys.*, **63**, 209.
Lebovitz, N. R. 1970, *Astrophys. J.*, **160**, 701.
Lightman, A. P., Shapiro, S. L., Rees, M. J. 1978 in *Physics and Astrophysics of Neutron Stars and Black Holes*, Eds R. Giacconi and R. Ruffini, North Holland, Amsterdam, p. 786.
Prasanna, A. R., Chakraborty, D. K. 1981, *J. Astrophys. Astr.*, **2**, 1 (Paper I).

Corrigendum

‘ Mass Segregation in Globular Clusters’ by K. K. Scaria and M. K. V. Bappu was published in *Journal of Astrophysics and Astronomy*, Volume 2, Number 3, September 1981.

Figs 14 and 15 should be replaced by the ones reproduced here.

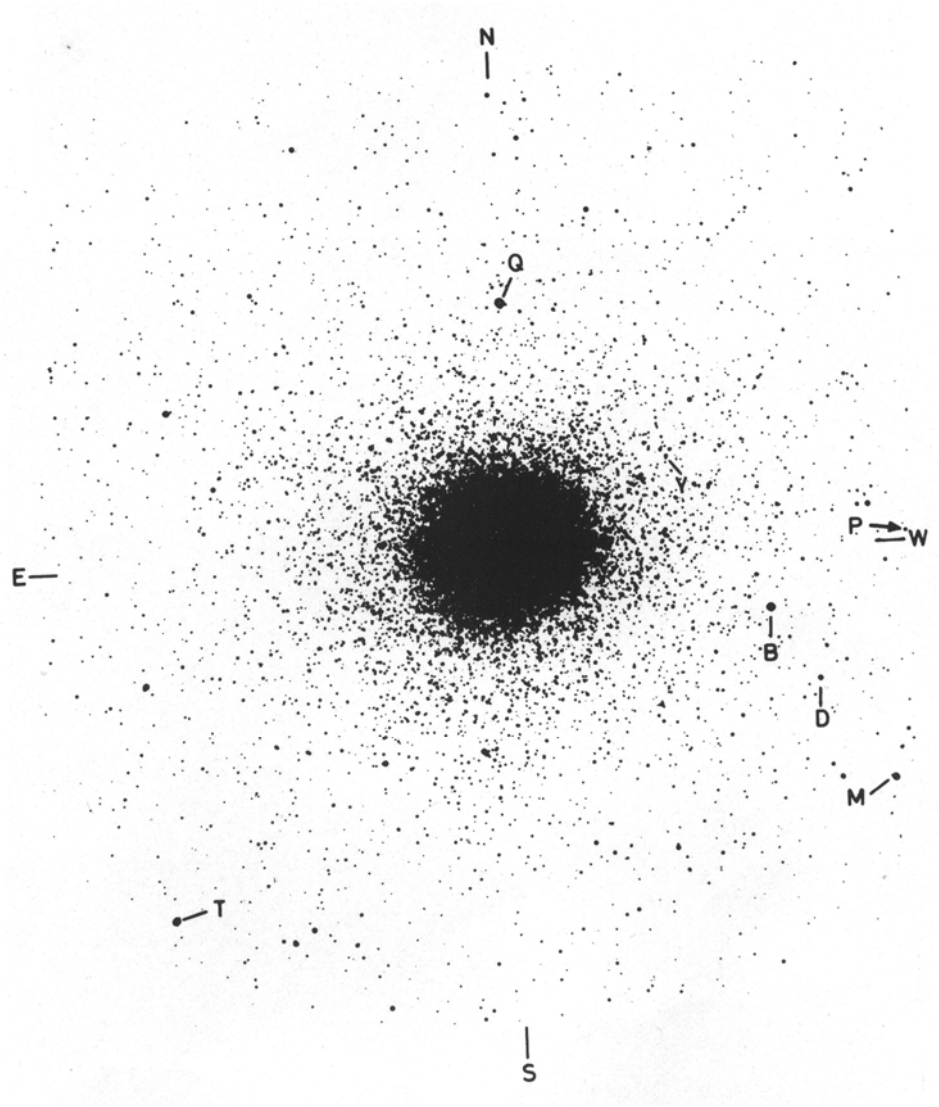

Figure 14. ω Cen in *B* Band taken with the 102 cm reflector at Kavalur. Stars marked *T* and *M* are the reference stars for the equidensitometry of the cluster. Star *P* is the reference star for the scan in the east-west direction and star *Q* is reference star for the north-south scan. Stars *B* and *D* are the two photoelectric standards. Star Y has been identified in Fig. 15(b) which shows the distribution of blue stars.

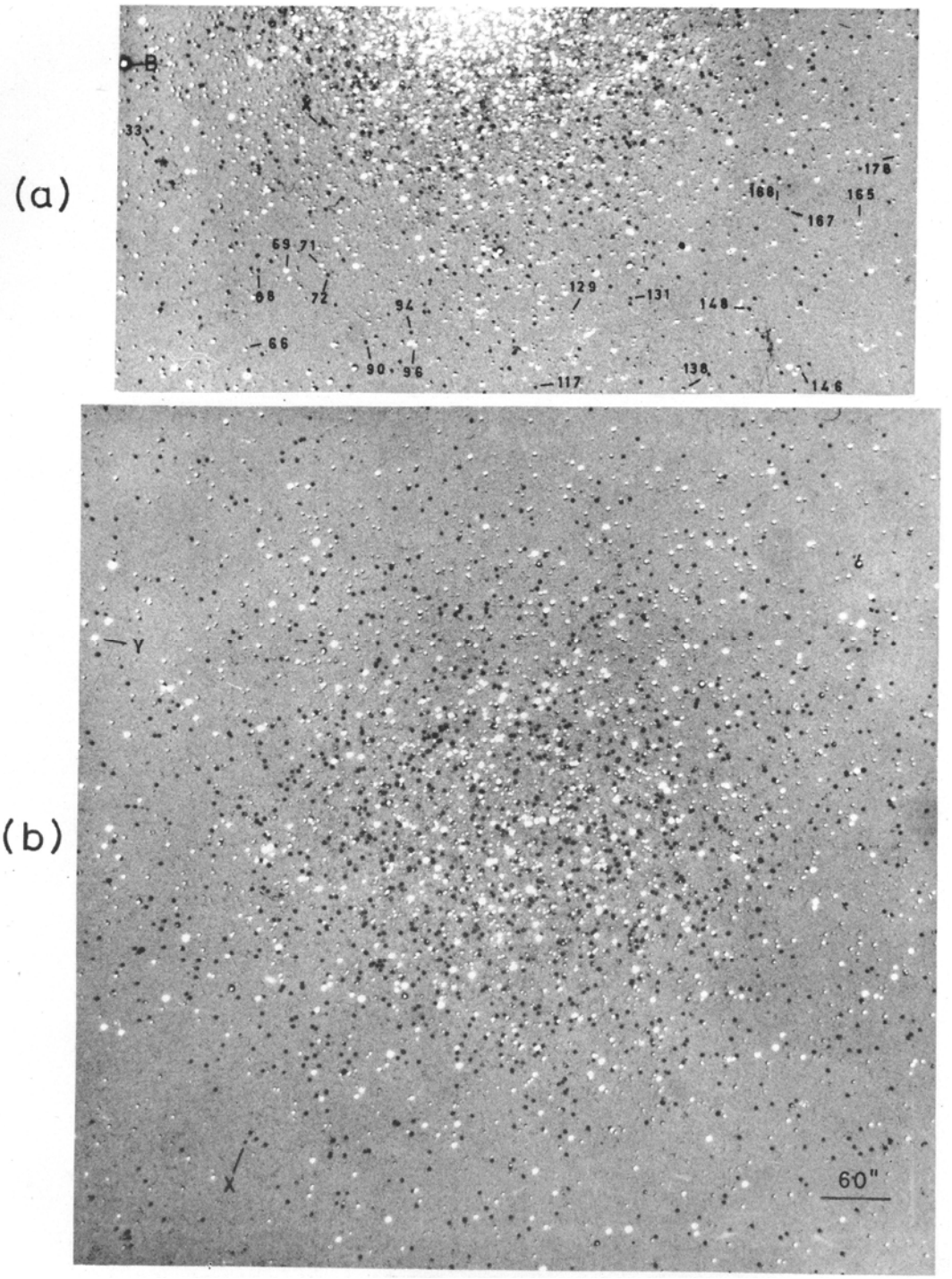

Figure 15. Distribution of horizontal branch stars in w Cen. (a) Outer region: 20 stars with *UBV* photometry by Geyer (1967) are identified. Stars having colour $B–V<0.4$ mag are seen as dark points while red stars are seen as white points. (b) Inner region: Star *X is* marked to allow an easy comparison of the two figures.